JOURNAL OF THE ELECTROCHEMICAL SOCIETY

VOL. 132, NO. 10 OCTOBER 1985

JESOAN 132 (10) 2301-2520, 421C-440C

FUTURE MEETINGS

LAS VEGAS, NEVADA—OCTOBER 13-18, 1985—HEADQUARTERS AT CAESAR'S PALACE

Final program published in the August 1985 issue of **This Journal.**

BOSTON, MASSACHUSETTS—MAY 4-9, 1986—HEADQUARTERS AT SHERATON BOSTON HOTEL

See the detailed Call for Papers published in the July-November 1985 issues of **This Journal.** Final program to be published in the March 1986 issue of **This Journal**.

SAN DIEGO, CALIFORNIA—OCTOBER 19-24, 1986—HEADQUARTERS AT THE TOWN AND COUNTRY HOTEL

The detailed Call for Papers will be published in the December 1985-April 1986 issues of **This Journal**. Final program to be published in the August 1986 issue of **This Journal.**

Planned symposia for the San Diego Meeting include the following Divisions, Groups, Subcommittee, and subjects. **Battery**—Lithium Battery; Stored Hydrogen Batteries; Sodium-Sulfur Battery; General Session. **Battery/Physical Electrochemistry**—Electrochemical and Thermal Modeling; Fuel Cell Electrochemistry and Electrolysis. **Corrosion**—Surfaces, Sorption, and Inhibition (Norman Hackerman 75th Birthday Symposium); Corrosion Protection by Organic Coatings; General Session. **Corrosion/High Temperature Materials**—Corrosion of Aerospace Materials. **Dielectrics and Insulation/Electronics**—Isolation Technology; Sixth Symposium on Plasma Processing; Multilevel Interconnect and Contact Technology. **Dielectrics and Insulation/Electronics/High Temperature Materials**—Silicon Nitride and Silicon Dioxide Thin Films. **Electrodeposition**—Electrodeposition Technology—Theory and Practice in Different Industries; General Session. **Electrodeposition/Physical Electrochemistry**—Electrosolidification and Crystallization. **Electronics**— Entrepreneurship in the Semiconductor Industry. **Electronics/Dielectrics and Insulation**—State-of-the-Art Program on Compound Semiconductors V; Silicon Process Physics and Modeling; Ion Implantation of Compound Semiconductors; Joint General Session; Joint Recent News Papers Session. **Electronics/Luminescence and Display Materials**—Microstructured Silicon Sensors. **Energy Technology**—Electrolyte Management in Electrochemical Energy Systems; Thermodynamic Analysis of Energy Systems; Protonic and Hydroxyl Electrolytes for Use in Electrochemical Devices; Mechanical Properties of Photovoltaic Device Structures; General Session. **Energy Technology/Physical Electrochemistry**—Semiconductor-Electrolyte Interfaces. **High Temperature Materials/Corrosion/Dielectrics and Insulation/Electrodeposition**—Protective Coatings at Elevated Temperatures. **High Temperature Materials/Physical Electrochemistry/Electronics**—Electrical Properties and Applications of Amorphous Materials. **Industrial Electrolytic**—Industrial Processes for the Production of Organic and Specialty Chemicals. **Industrial Electrolytic/High Temperature Materials**—Industrial Electrolysis of Fused Salts. **Luminescence and Display Materials**—Physics and Chemistry of Lamp Phosphors; Lamp Manufacture and Performance; Light Modulation in Optical Processing; X-Ray Imaging; Picosecond and Faster Phenomena in Luminescence; General Session; Recent News Papers Session. **Luminescence and Display Materials/Dielectrics and Insulation**—Materials and Fabrication Techniques for Display Devices. **Luminescence and Display Materials/Electronics**—Sensors for Robot Applications. **Luminescence and Display Materials/Electronics/New Technology Subcommittee**—Robotics for Use in Manufacture of Electronic Devices. **Physical Electrochemistry**—General Session. **Physical Electrochemistry/High Temperature Materials/Battery**—Solid Electrolytes.

PHILADELPHIA, PENNSYLVANIA—MAY 10-15, 1987—HEADQUARTERS AT ADAM'S MARK HOTEL

The detailed Call for Papers will be published in the July-November 1986 issues of **This Journal**. Final Program to be published in the March 1987 issue of **This Journal.**

Planned symposia for the Philadelphia Meeting include the following Divisions, Groups, Subcommittee, and subjects. **Corrosion**—General Sessions. **Corrosion/Energy Technology**—Electrochemistry of Coal Slurries. **Dielectrics and Insulation**—Coatings and Media for Magnetic Recording; Nonblodgett Monomolecular Films. **Dielectrics and Insulation/Electronics**—Fourth International Symposium on VLSI Science and Technology; Semiconductor Manufacturing Science and Clean Room Technology; Contactless Testing of Semiconductor Devices; State-of-the-Art Program on Compound Semiconductors VI; Interconnects and Contacts for Compound Semiconductors; Joint General Session; Joint Recent News Papers Session. **Energy Technology**—General Session. **Energy Technology/Industrial Electrolytic**—Application of Fuel Cell Electrodes in Electrolytic Industries. **Energy Technology/Physical Electrochemistry/Electrodeposition**—Electrochemistry and Tribology. **Energy Technology/Physical Electrochemistry/Organic and Biological Electrochemistry**—Applications of Macromolecules in Energy Conversion. **High Temperature Materials**—Rapidly Solidified Materials. **High Temperature Materials/Battery/Corrosion**—Materials and Processing for Solid Oxide Fuel Cells. **High Temperature Materials/Corrosion/Dielectrics and Insulation/Physical Electrochemistry**—*In situ* Nonelectrochemical Techniques. **High Temperature Materials/Dielectrics and Insulation**—Chemical Interactions in Ceramic Composites; Laser-Induced Chemical Reactions. **Industrial Electrolytic**—General Session. **Industrial Electrolytic/Physical Electrochemistry**—Electrochemistry in Mineral and Metal Processing II. **Physical Electrochemistry**—The Electrical Double Layer; Quantum Effects in Electrochemistry; General Session. **Physical Electrochemistry/Battery**—Nonaqueous Electrochemistry. **Physical Electrochemistry/Battery/Energy Technology**—Electrode Materials and Processes for Energy Conversion and Storage. **Physical Electrochemistry/New Technology Subcommittee**—Magnetic Effects in Electrochemistry.

THE ELECTROCHEMICAL SOCIETY BOOKS IN PRINT

Society Proceedings Series
1980-1985

The following softbound proceedings volumes are sponsored and published by The Electrochemical Society, Inc., 10 South Main Street, Pennington, NJ 08534-2896. Orders filled at the list price given, subject to availability. Enclose payment with order.

Electronic and Optical Properties of Polycrystalline or Impure Semiconductors and Novel Silicon Growth Methods. K. V. Ravi and B. O'Mara, Editors. A 1980 symposium. 280 pages, **$15.00.**

Electron and Ion Beam Science and Technology, Ninth International Conference. R. Bakish, Editor. A 1980 symposium. 672 pages, **$28.00.**

Lithium Nonaqueous Battery Electrochemistry. E. B. Yeager, B. Schumm, Jr., G. Blomgren, D. R. Blankenship, V. Leger, and J. Akridge, Editors. A 1980 workshop. 328 pages, **$18.00.**

Ion Exchange: Transport and Interfacial Properties. R. S. Yeo and R. P. Buck, Editors. A 1980 symposium. 396 pages, **$15.00.**

Materials and New Processing Technologies for Photovoltaics. J. A. Amick, E. Sirtl, P. Rai-Choudhury, and J. P. Dismukes, Editors. A 1980 symposium. 368 pages, **$14.00.**

Lithium Batteries, H. V. Venkatasetty, Editor. A 1980 symposium, 516 pages, **$26.00.**

Semiconductor Silicon 1981. H. R. Huff, R. J. Kriegler, and Y. Takeishi, Editors. A 1981 symposium. 1064 pages, **$25.00.**

Electrocrystallization. R. Weil and R. G. Barradas, Editors. A 1981 symposium. 352 pages, **$13.00.**

Corrosion and Corrosion Protection. R. P. Frankenthal and F. Mansfeld, Editors. A 1981 symposium. 304 pages, **$10.00**

Third International Symposium on Molten Salts. G. Mamantov, M. Blander, and G. P. Smith, Editors. A 1981 symposium, 600 pages, **$23.00.**

Second International Symposium on Molten Salts. J. Braunstein and J. R. Selman, Editors. A 1978 symposium. 420 pages, **$16.00**

High Temperature Materials Chemistry. D. D. Cubicciotti and D. I. Hildenbrand, Editors. A 1981 symposium. 498 pages, **$21.00.**

Electrocatalysis. W. E. O'Grady, P. N. Ross, Jr., and F. G. Will, Editors. A 1981 symposium. 428 pages, **$18.00.**

Photoelectrochemistry: Fundamental Processes and Measurement Techniques. W. L. Wallace, A. J. Nozik, S. K. Deb, and R. H. Wilson, Editors. A 1981 symposium. 736 pages, **$35.00**

The Nickel Electrode. R. G. Gunther and S. Gross, Editors. A 1981 symposium. 324 pages, **$15.00.**

Semiconductor Technology. D. A. Doane, D. B. Fraser, and D. W. Hess, Editors. A 1982 symposium. 264 pages, **$18.00.**

Plasma Processing. J. Dieleman, R. G. Frieser, and G. S. Mathad, Editors. A 1981 symposium. 528 pages, **$25.00.**

VLSI Science and Technology. C. J. Dell'Oca and W. M. Bullis, Editors. A 1982 symposium. 392 pages, **$20.00.**

Materials and New Processing Technologies for Photovoltaics. J. P. Dismukes, E. Sirtl, P. Choudhury, and L. P. Hunt, Editors. A 1982 symposium. 544 pages, **$25.00.**

Inorganic Resist Systems. D. A. Doane and A. Heller, Editors. A 1982 symposium. 320 pages, **$15.00.**

Transport Processes in Electrochemical Systems. R. S. Yeo, T. Katan, and D-T. Chin, Editors. A 1982 symposium. 288 pages, **$18.00.**

Corrosion in Batteries and Fuel Cells and Corrosion in Solar Energy Systems. C. J. Johnson and S. L. Pohlman, Editors. A 1981 symposium. 554 pages, **$22.00.**

Electron and Ion Beam Science and Technology, Tenth International Conference, R. Bakish, Editor. A 1982 symposium. 474 pages, **$30.00.**

Membranes and Ionic and Electronic Conducting Polymers. E. B. Yeager, B. Schumm, Jr., K. Mauritz, K. Abbey, D. Blankenship, and J. Akridge, Editors. A 1982 symposium. 380 pages, **$22.00.**

Aggregation Phenomena of Point Defects in Silicon. E. Sirtl and J. Goorissen, Editors. A 1982 symposium. 216 pages, **$15.00.**

Corrosion in Fossil Fuel Systems. I. G. Wright, Editor. A 1982 symposium. 522 pages, **$20.00.**

Electrochemical Process and Plant Design. R. C. Alkire, T. R. Beck, and R. D. Varjian, Editors. A 1982 symposium. 288 pages, **$20.00.**

High Temperature Materials Chemistry II. Z. A. Munir and D. Cubicciotti, Editors. A 1983 symposium. 480 pages, **$30.00.**

Silicon Nitride Thin Insulating Films. V. J. Kapoor and H. J. Stein, Editors. A 1983 symposium. 522 pages, **$25.00.**

Defects in Silicon. W. M. Bullis and L. C. Kimerling, Editors. A 1983 symposium. 660 pages, **$30.00.**

Plasma Processing. G. S. Mathad, G. C. Schwartz, and G. Smolinsky, Editors. A 1983 symposium. 660 pages, **$35.00.**

Materials and New Processing Technologies for Photovoltaics. J. A. Amick, V. K. Kapur, and J. Dietl, Editors. A 1983 symposium. 512 pages, **$25.00.**

Electroplating Engineering and Waste Recycle—New Developments and Trends. D. D. Snyder, U. Landau, and R. Sard, Editors. A 1982 symposium. 428 pages, **$22.00.**

III-V Opto-Electronics Epitaxy and Device Related Processes. V. G. Keramidas and S. Mahajan, Editors. A 1983 symposium. 289 pages, **$25.00.**

Lithium Batteries. A. N. Dey, Editor. A 1983 symposium. 460 pages, **$35.00.**

Fourth International Symposium on Molten Salts. M. Blander, D. S. Newman, M-L. Saboungi, G. Mamantov, and K. Johnson, Editors. A 1983 symposium. 776 pages, **$35.00.**

Fundamental Aspects of Corrosion Protection by Surface Modification. E. McCafferty, C. R. Clayton, and J. Oudar, Editors. A 1983 symposium. 364 pages, **$25.00.**

Advances in Battery Materials and Processes. J. McBreen, R. S. Yeo, D-T. Chin, and A. C. C. Tseung, Editors. A 1983 symposium. 320 pages, **$26.00.**

The Electrochemistry of Carbon. S. Sarangapani, J. R. Akridge, and B. Schumm, Editors. A 1983 symposium. 648 pages, **$32.00.**

Ninth International Conference on Chemical Vapor Deposition. McD. Robinson, C. H. J. van den Brekel, C. W. Cullen, J. M. Blocher, Jr., and P. Rai-Choudhury, Editors. A 1984 symposium. 824 pages, **$36.00.**

VLSI Science and Technology/1984. K. E. Bean and G. A. Rozgonyi, Editors. A 1984 symposium. 520 pages, **$30.00.**

Porous Electrodes: Theory and Practice. H. C. Maru, T. Katan, and M. G. Klein, Editors. A 1982 symposium. 492 pages, **$18.00.**

Equilibrium Diagrams; Localized Corrosion. R. P. Frankenthal and J. Kruger, Editors. A 1984 symposium. 611 pages, **$36.00.**

Electrochemistry in Mineral and Metal Processing. P. E. Richardson, S. Srinivasan, and R. Woods, Editors. A 1984 Symposium. 677 pages, **$30.00.**

Advances in the Chlor-Alkali and Chlorate Industry. M. M. Silver and E. M. Spore, Editors. A 1984 Symposium. 374 pages, **$18.00.**

The Chemistry and Physics of Electrocatalysis. J. D. E. McIntyre, M. J. Weaver, and E. B. Yeager, Editors. A 1983 symposium. 684 pages, **$27.00.**

Molten Carbonate Fuel Cell Technology. J. R. Selman and T. D. Claar, Editors. A 1982 Symposium. 533 pages, **$15.00.**

Advances in Lead-Acid Batteries. K. R. Bullock and D. Pavlov, Editors. A 1984 Symposium. 548 pages, **$28.00.**

Plasma Processing. G. S. Mathad, G. C. Schwartz, and G. Smolinsky, Editors. A 1984 symposium. 636 pages, **$40.00.**

High Temperature Lamp Chemistry. E. G. Zubler, Editor. A 1985 symposium. 340 pages, **$25.00.**

Computer Aided Acquisition and Analysis of Corrosion Data. M. W. Kendig, U. Bertocci, and J. E. Strutt, Editors. A 1984 symposium. 276 pages, **$17.00.**

Manganese Dioxide Electrode Theory and Practice for Electrochemical Applications. B. Schumm, Jr., R. L. Middaugh, M. P. Grotheer, and J. C. Hunter, Editors. A 1984 symposium. 696 pages, **$40.00.**

VLSI Science and Technology/1985. W. M. Bullis and S. Broydo, Editors. A 1985 symposium. 572 pages, **$35.00.**

Electromigration of Metals/Multilevel Metallization and Packaging. J. R. Lloyd, R. A. Levy, J. Pierce, and R. G. Frieser, Editors. A 1984 symposium. 201 pages, **$16.00.**

9/85

JOURNAL OF THE
ELECTROCHEMICAL SOCIETY
(USPS 284-140)
ISSN 0013-4651

The JOURNAL OF THE ELECTROCHEMICAL SOCIETY (USPS 284-140) is published monthly by The Electrochemical Society, Inc. at 215 Canal St., Manchester, NH 03108. The address for the Executive Offices, Editorial and Advertising Office, and Circulation Department of The Electrochemical Society, Inc., is 10 South Main St., Pennington, NJ 08534-2896. Subscription to members as part of membership service; subscription to nonmembers $135.00 plus $15.00 for postage outside U.S. and Canada. Single copies $7.00 to members, $12.00 to nonmembers. Second Class Postage paid at Pennington, New Jersey and at additional mailing offices.

POSTMASTER: Send address changes to THE ELECTROCHEMICAL SOCIETY, INC., 10 South Main St., Pennington, NJ 08534-2896.

October 1985

ELECTROCHEMICAL SCIENCE AND TECHNOLOGY

TECHNICAL PAPERS

ELECTROCHEMICAL SOCIETY

Vol. 132 • No. 10

Manuscripts submitted to the JOURNAL should be sent in triplicate to the Editorial Office at 10 South Main Street, Pennington, NJ 08534-2896. They should conform to the revised "Instructions to Authors" available from Society Headquarters. Manuscripts so submitted, as well as papers presented before a Society technical meeting, become the property of the Society and may not be published elsewhere in whole or in part without written permission of the Society. Address such requests to the Editor.

The Electrochemical Society does not maintain a supply of reprints of papers appearing in its JOURNAL. A photoprint copy of any particular paper may be obtained from University Microfilms, Inc., 300 N. Zeeb St., Ann Arbor, MI 48106.

Inquiries regarding positive microfilm copies of issues should be addressed to University Microfilms, Inc., 300 N. Zeeb St., Ann Arbor, MI 48106.

Walter J. Johnson, Inc., 355 Chestnut St., Norwood, NJ 07648, have reprint rights to out-of-print volumes of the JOURNAL, and also have available for sale back volumes and single issues with the exception of the last two calendar years.

The JOURNAL OF THE ELECTROCHEMICAL SOCIETY combines the JOURNAL and TRANSACTIONS OF THE ELECTROCHEMICAL SOCIETY. Statements and opinions given in articles and papers in the JOURNAL OF THE ELECTROCHEMICAL SOCIETY are those of the contributors, and The Electrochemical Society, Inc. assumes no responsibility for them.

Claims for a missing issue should be reported within 60 days of normal delivery date to the Circulation Dept., The Electrochemical Society, Inc., 10 South Main Street, Pennington, NJ 08534-2896.

Notice of a change in address should be sent to the Circulation Dept., The Electrochemical Society, Inc., 10 South Main Street, Pennington, NJ 08534-2896. Include the mailing label or the number from the mailing label from your previous issue of the JOURNAL to ensure proper identification.

SOLID-STATE SCIENCE (Cont.)

TECHNICAL NOTES

ACCELERATED BRIEF COMMUNICATIONS

REVIEWS AND NEWS

JOURNAL OF THE ELECTROCHEMICAL SOCIETY

ELECTROCHEMICAL SCIENCE AND TECHNOLOGY

OCTOBER 1985

Physical and Chemical Characteristics of Hermetically Sealed High Rate Li/$SOCl_2$ C-Cells

K. M. Abraham* and L. Pitts

EIC Laboratories, Incorporated, Norwood, Massachusetts 02062

William P. Kilroy*

Naval Surface Weapons Center, White Oak Laboratory, Silver Spring, Maryland 20903-5000

ABSTRACT

Pressure-temperature-voltage relationships in hermetically sealed high rate Li/$SOCl_2$ cells have been studied using specially instrumented C-size cells. The cells generated considerably lower pressures than those expected on the basis of established discharge reactions. This is believed to be due to the SO_2 generated being complexed by $LiAlCl_4$ and/or absorbed by the carbon cathode. Li-limited cells produced lower internal temperatures and pressures towards the end of discharge and during voltage reversal than cathode-limited cells. In high rate discharge involving >10 mA/cm², Co-TAA-catalyzed cathode cells exhibited higher capacities and lower IR heating than uncatalyzed cells. Li-limited Co-TAA catalyzed cathode cells appear to be a desirable design for high rate applications.

The Li/$SOCl_2$ battery is a very attractive high energy density system for many high power applications since it can provide load voltages near 3.0V under high current drains. However, high rate applications are generally limited by safety hazards that occur under certain conditions of operation such as forced overdischarge or by poor cathode performance. Several recent papers have examined some of the factors that can affect cell performance and safety in $SOCl_2$ cells. Cell design is one such factor. Early studies with spirally wound cells revealed that some anode-limited cells exhibited hazardous behavior during forced overdischarge at low rates (1, 2). These cells were considered anode limited rather than Li limited since substantial amounts of Li remained on the anode despite anode potentials greater than 4.0V. This was attributed to poor electrical contact between the Li and the anode grid. Recent studies confirm that during high rate cell reversal, cathode-limited cells were more hazardous than those of Li-limited design (3).

A great deal of work has also been devoted to improving cell performance via the use of catalysts. Studies show that both organic macrocyclic (4) and inorganic (5) additives substantially improve cathode performance, especially at low temperatures. Recently, the use of cobalt tetraazaannulene complexes as catalysts has been proposed to enhance the safety of the $SOCl_2$ system by altering the discharge mechanism so that no pressure building SO_2 product is generated (6).

The presence of water as a safety factor in $SOCl_2$ cells has received little attention. Studies have primarily addressed the effect of water on voltage delay or hydrolysis reactions that produce HCl or H_2 gas (7-9). Water has been shown to increase cell capacity of reverse polarity $SOCl_2$ cells following storage at room temperature (10).

Despite the fact that no energetic products capable of causing detonations have been found, occasionally $SOCl_2$ cells have exhibited explosive behavior. Indeed the mechanism of generating safety hazards is still not well understood.

*Electrochemical Society Active Member.

To date, very little has been reported on the physiochemical characteristics of Li/$SOCl_2$ cells discharged under high rate regimes. In particular, a detailed knowledge of the cell's internal pressure-temperature-electrode potential behavior and its dependence on discharge rates, depth of discharge, and environmental temperatures are extremely important for the ultimate description of safe cells.

By using specially instrumented cells, we have reexamined the effects of cell design, catalysis, and water on the performance-chemistry-safety relationship of Li/$SOCl_2$ cells.

Experimental

Cell construction.—Specially instrumented, spirally wound C-size Li/$SOCl_2$ cells, manufactured by Hellesens Battery Engineering, Incorporated (Hyde Park, Massachusetts), were used in this study. Each cell contained a vent mechanism designed to vent at ~250 psig. A stainless steel threaded bushing fitted with a removable plug was incorporated into the cell top. This allowed electrolyte sampling and the installation of a pressure transducer (Precise Sensor, Incorporated, Monrovia, California) capable of measuring the internal pressure of the cell in the 0-500 psig range. The temperatures at two different points on a horizontal plane perpendicular to the cell wall were measured using internal and external iron-constantan thermocouples. The internal thermocouple was 0.010 in. diam with a 304 stainless steel sheath placed in a 0.020 in. id-0.040 in. od closed tube positioned at the core of the spiral electrode package halfway down the electrode length. This permitted the thermocouple to be isolated from the electrolyte yet provided rapid response to temperature changes. The cell skin temperature was measured by an external thermocouple held in place at the middle of the cell height by the heat-shrinkable cell jacket. Each cell contained a Li reference electrode to enable measurements of individual electrode potentials during discharge. All other components had conventional characteristics of commercial cells.

Cell specifications.—Cells were designed as cathode and Li limited. The specifications of the cathode-limited cells were as follows: dimensions of the Li anode were 0.058 × 29.2 × 3.8 cm: Li weight of 2.4 ± 0.2g. The dimensions of the cathode were 0.064 × 25.4 × 3.8 cm; the carbon weight was 3.3 ± 0.5g. The electrolyte was 1.8*M* $LiAlCl_4$ in $SOCl_2$; its weight was 19.5-20g. The void volume was 1.5-1.8 ml based on electrolyte deletion. The average weight of the cathode-limited cell was 63g. The cell volume was 29.5 cm^3.

The specifications of the Li-limited cells were as follows. The dimensions of the Li anode were 0.023 × 37.5 × 3.8 cm; the Li weight was 1.10 ± 0.15g. The dimensions of the cathode were 0.064 × 33 × 3.8 cm; the carbon weight was 4.3 ± 0.5g. The electrolyte was 1.8*M* $LiAlCl_4$ in $SOCl_2$, and its weight was 24.5-25g. The void volume was 1.5-1.8 ml based on electrolyte deletion. The average weight of the Li-limited cell was 68g, and the cell volume 29.5 cm^3.

Dry electrolyte, containing less than 10 ppm of water, was used for all cells. The "dry" cells contained ~50 ppm water. "Wet" cells containing ~500 ppm of water were prepared by adding water to the dry electrolyte in a controlled manner.

Catalyst.—Cathodes were prepared from Shawinigan acetylene black. In addition to the regular cathodes, those containing 5 weight percent of dibenzotetraazaannulene complex of cobalt (Co-TAA) as a catalyst additive were used. The catalyzed cathodes were prepared by mixing the carbon with the catalyst and then heat-treating the mixture at 500°C under inert gas. After cooling, this mixture was made into a paste with water, isopropanol, and Teflon binder, and then dried below 100°C. The mixture was cured by heating to ~275°C under inert gas. At no time was the catalyst heated above 100°C in air. The possibility exists that the catalyst undergoes structural perturbations during the heat-treatment at 500°C; however, we did not investigate this.

Testing and analysis.—Prior to electrochemical experiments, the cell was housed inside a specially designed test chamber (11) provided with feedthroughs for electrical connections and ports for collecting gases and liquid. A stainless steel capillary tubing with 0.5 cm^3 of void volume connected the pressure transducer located on the outside of the chamber to the cell inside. The chamber was housed in a constant temperature environmental chamber prior to electrochemical tests. Standard electrochemical equipment was used. Data collection and retrieval were done with Bascom-Turner Instruments Series 8000 recorders equipped with microprocessor accessories.

Cell postmortem and sample collection for analyses were done in a Vacuum Atmospheres dry box maintained with an Ar atmosphere. Infrared (IR) spectra were recorded on a Beckman Acculab-5 double-beam spectrometer. X-ray data were obtained by the Debye-Scherrer technique. Gas chromatographic (GC) analysis of volatile materials from the cells were performed on a Varian 920 Gas Chromatograph equipped with a thermal conductivity detector and a 6 ft chromosorb Analabs column.

The water content of the cells was measured by removing electrolyte samples from cells stored one week. The hydrolysis products present were analyzed using infrared spectroscopy and quantitatively measured against IR calibration curves prepared from samples of the dry electrolyte containing known amounts of water.

Results and Discussion

The discharge and overdischarge data and the related pressure-temperature behavior for cathode-limited cells containing uncatalyzed cathodes are given in Fig. 1 and 2. The temperature and pressure changes which accompany the discharge and overdischarge at 0.2A (~1 mA/cm^2) are rather minor. The temperature and pressure increase slightly at the end of discharge when the cell potential approaches 0 V. The internal pressure after the voltage reversal remains at a slightly higher value than that during

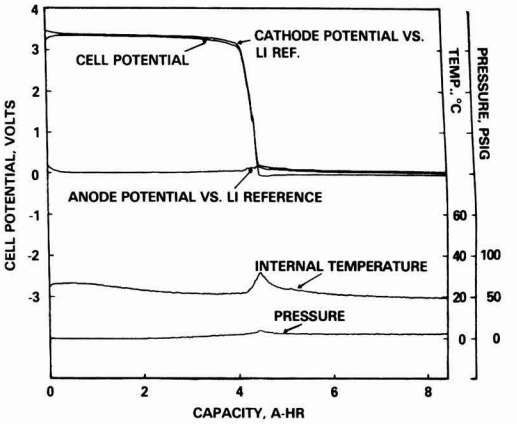

Fig. 1. Temperature, pressure, and voltage data for an uncatalyzed cathode-limited Li/$SOCl_2$ cell discharged at 0.20A at room temperature.

normal discharge. The data in Fig. 2 for the discharge and overdischarge at 2A (~10 mA/cm^2) show that the internal temperature increased to ~50°C during the course of the first 15% of discharge and remained at this value until the end of the normal discharge. The internal pressure increased slightly during the course of the normal discharge, but attained a maximum of only ~25 pounds per square inch (psi) at the 100% depth-of-discharge stage to a 2.0V limit.

By using the following information and the cell geometry and specifications given in the Experimental section, we have calculated the internal pressure of the cells on the basis of the generally accepted cell discharge reaction given below

$$4Li + 2SOCl_2 \rightarrow SO_2 + S + 4LiCl \quad [1]$$

The vapor pressure of SO_2 at 50°C is about 130 psi (12). The solubilities of SO_2 in $SOCl_2$ and $SOCl_2$/$LiAlCl_4$ are given in Ref. (13). The calculated volume reduction which accompanies the Li/$SOCl_2$ cell discharge is 0.56 ml/Ah (14).

The pressure of the cell discharged at 2A was calculated to be at least 130 psi from the 75% depth-of-discharge stage onwards. The observed pressures were much lower. In addition, the internal temperature increases to ~115°C during the early stages of voltage reversal. At this temperature, an amount of SO_2 produced according to Eq. [1] would have generated a pressure of at least 500 psi. The measured maximum pressure is only ~140 psi, slightly lower than the cell venting pressure of ~250 psi. As the data in Table I show, the internal pressures are significantly lower than that expected on the basis of the

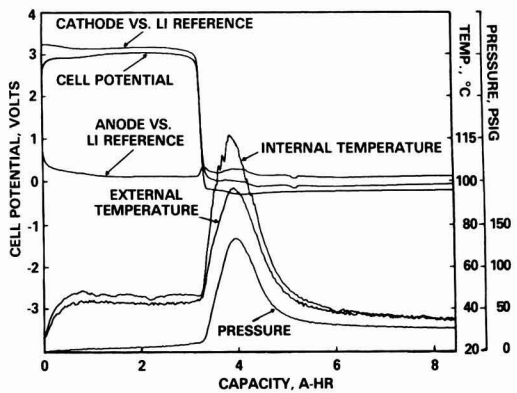

Fig. 2. Temperature, pressure, and voltage data for an uncatalyzed cathode-limited Li/$SOCl_2$ discharged at 2.0A at room temperature.

Table I. Averaged pressure-temperature behavior and safety characteristics of uncatalyzed Li/SOCl$_2$ C-cells

Cell type[a]	Discharge current (A)	Environmental temperature (°C)	Capacity (Ah)[c] to 2.0V	Capacity (Ah)[c] to 0.0 V	Extent of overdischarge (Ah)	Maximum internal temp. (°C)[c]	Maximum internal pressure (psig)[c]
A-W	2.0	20	2.54	2.63	>5	79	73
A-W	2.0	−12	2.20	2.37	>5	54	[b]
A-D	0.2	20	2.90	3.0	>5	30	[b]
A-D	2.0	20	2.66	2.95	>5	73	70
A-D	2.0	−12	2.63	2.90	>5	53	[b]
A-D[d]	3.0	20	2.61	2.90	>5	95	72
C-D	0.2	20	4.75	4.85	>7	30	7
C-D	0.2	−12	2.70	2.88	>5	[b]	[b]
C-D	2.0	20	3.45	3.59	>7	102	138
C-D	2.0	−12	1.60	2.16	>7	58	[b]
C-D	3.0	20	2.25	2.4	>7	130	153
C-W	2.0	20	3.26	3.42	>7	117	158
C-W	2.0	−12	1.74	2.10	>7	71	[b]

[a] A-W: Li-limited wet cells containing 500 ppm added H_2O. A-D: Li-limited dry cells. C-D: cathode-limited dry cells. C-W: cathode-limited wet cells containing 500 ppm added H_2O.
[b] Pressure transducer response at −12°C was poor, so pressure data were unreliable.
[c] Average of five cells for each test current. No cells vented.
[d] At a 3.0A rate, cell became cathode limited and vented after ~3 Ah overdischarge.

SO_2 stoichiometry of Eq. [1]. Complexation of the SO_2 by $LiAlCl_4$ (15), the absorption of SO_2 by carbon (10), and/or the presence of a significant amount of the low volatile $(SO)_x$ rather than its decomposition products S and SO_2 may be occurring (16). The minimum amount of $LiAlCl_4$ in our cells is ~0.02 mol, which is sufficient to complex all the SO_2 produced at the 2.0A rate according to Eq. [1] to form an adduct of the composition $[Li^+(SO_2)_2AlCl_4^-]$. Raman spectroscopic studies have revealed the existence of such complexes in $LiAlCl_4$ solutions in SO_2 (15). However, there is strong evidence for significant absorption of SO_2 by Shawinigan carbon (10). The desorption of this SO_2 gas is reflected in the rapid pressure rise accompanying the temperature increase seen in the early stages of overdischarge. If it were not for a built-in SO_2 scavenging mechanism, the Li/SOCl$_2$ cell would produce excessive internal pressures capable of potentially violent venting, especially during early stages of cell reversal. If the scavenging mechanism involves the formation of SO_2 adducts with $LiAlCl_4$, then the salt concentration is critical: cells with higher salt concentrations should be safer. However, a lower salt concentration is a widely recognized remedy for alleviating voltage delays in the Li/SOCl$_2$ cell (16).

Some typical data for uncatalyzed cells are given in Table I. The temperature and pressure maxima reached in the Li-limited cells were considerably lower than the cathode-limited cells as illustrated by a comparison of the data in Fig. 2 and 3. A substantial fraction of the internal heating at the end of cell life in cathode-limited cells at both 20° and −12°C was associated with cathode polarization. Very little cathode polarization occurred in Li-limited cells.

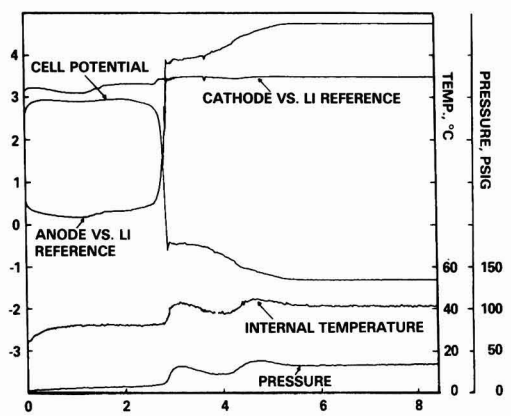

Fig. 3. Temperature, pressure, and voltage data for an uncatalyzed Li-limited Li/SOCl$_2$ cell discharged at 2.0A at room temperature.

The effects of environmental temperature and the addition of 500 ppm H_2O on uncatalyzed cell performance are also tabulated in Table I. The data are averaged over five discharges for each type of cell. Some of the observations follow.

1. Addition of water showed no adverse affect on voltage delay at either 20° or −12°C. Cells with and without the added water showed substantial voltage delays when discharged at >10 mA/cm^2 at −12°C. In both types of cells, the voltage delay exceeded 60s of time to recover to 2.0V. Previous studies have examined the effects of smaller additions of water on voltage delay after storage at 23° and 55°C. Subsequent to room temperature storage for 1 month, cells containing an additional 100 ppm water displayed a decreased delay and attained their running potentials faster (10). Interestingly, partially discharged and stored cells behaved as well as fresh cells. Thus cells discharged for 1 Ah at 2.0A and stored 4 months at ambient room temperature experienced no voltage delay on redischarge at 2.0A (14 mA/cm^2 Li) at room temperature. The same type of cells redischarged at 3.0A (27 mA/cm^2 Li) did exhibit a voltage delay.

2. The internal temperature and pressure maxima at 2A at −12°C were substantially lower than that found at 20°C. The internal temperature of cathode-limited cells was always higher in the presence of added water. Data for a cathode-limited cell overdischarged at −12°C are illustrated in Fig. 4.

3. As seen in Table I, the capacity of the Li-limited cells was decreased ~11% at 20°C and ~18% at −12°C by addition of the water.

4. Two cells each from the four types of uncatalyzed cells were stored 4 months after having been discharged for 1 Ah at 2.0A current. The pressure generated after 4 months storage was 42% greater in the "wet" cells.

In general, the uncatalyzed cathode- and Li-limited cells exhibited safe behavior during extended periods of forced overdischarge at both the 0.2 and 2.0A rates. No cells vented.

Effect of Co-TAA catalyst.—The benefits of Co-TAA catalysis in 1/2 AA Li/SOCl$_2$ cells have been recently cited. These include superior cell performance, significant reduction in voltage delay, and a new SO_2-free reduction mechanism (6, 17). Our studies revealed that the addition of Co-TAA affected the behavior of Li/SOCl$_2$ cells in the following manner.

1. Increased voltages.—The catalyst gives rise to higher load voltages at the 2.0A and higher discharge rates. Typical discharge and overdischarge data at 2.0A at 20°C for

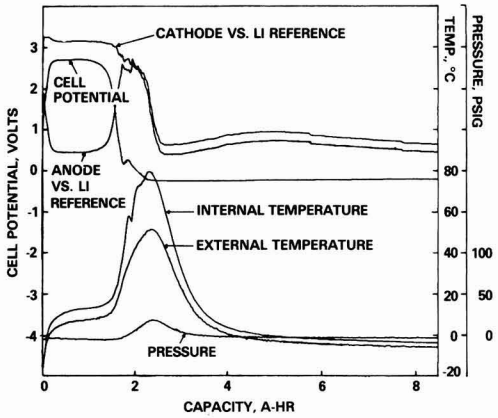

Fig. 4. Temperature, pressure, and voltage data for an uncatalyzed cathode-limited Li/$SOCl_2$ cell containing 500 ppm H_2O discharged at 2.0A at −12°C. Because of the poor response of the transducer, the pressure reading may not be accurate.

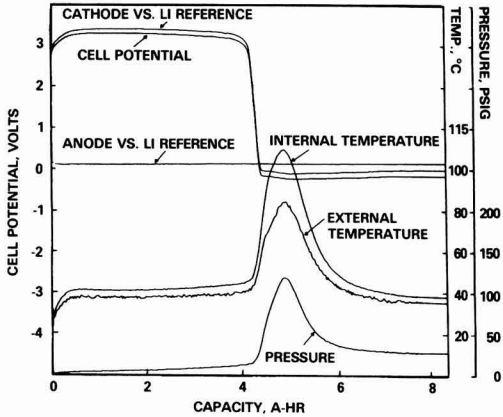

Fig. 5. Temperature, pressure, and voltage data for a catalyzed cathode-limited Li/$SOCl_2$ cell discharged at 2.0A at room temperature.

cathode and Li-limited cells are depicted in Fig. 5 and 6, respectively. The cathode potential profiles *vs.* the lithium reference electrode indicate that the higher voltage results largely from improvements in cathode load voltages—polarization of the catalyzed cathodes at the higher currents is considerably lower than in the uncatalyzed cells. In general, for both wet and dry cells discharged at −12° and 20°C, the average middischarge voltage was ~10 and 20% higher in cathode- and Li-limited cells, respectively, when the catalyst was present.

2. Increased performance.—The effect of catalyst on increasing the average cell capacity is shown in Table III. The data indicate that wet cathode-limited cells discharged at high rates and low temperatures benefit most from the catalyst.

The cells discharged at low temperatures exhibited the most pronounced effect of the catalyst. Even at low rates, where no beneficial effect was expected, cathode-limited cells discharged at −12°C at 0.2A (0.8 mA/cm²) showed a 55% improvement in cell capacity. As Table III indicates, at the 2.0A rate at −12°C these cells had approximately a 74% average increase in cell capacity. At double the rate, 4.0A, the same cells containing catalyst had a 28% larger average capacity at −12°C than uncatalyzed cells discharged at only a 2.0A rate. Indeed, the catalyst was most effective at higher discharge rates. Dry cathode-limited cells discharged at 20°C at 0.2, 2.0, and 3.0A rates showed a 8.6, 20.3, and 61.2% increase, respectively, in cell capacity with added catalyst.

Interestingly, as Table III indicates, the catalyst was most effective in enhancing the capacity of cells containing 500 ppm H_2O. In Li-limited cells, the catalyst appears to have negated the detrimental effect of water, perhaps by inhibiting corrosion of the anode. The water or hydrolysis products may play a role in the catalysis mechanism to increase the capacity of cathode-limited cells.

3. Lower internal temperatures and pressures.—Catalyzed cells exhibited lower average internal temperatures (~40°C) during discharge compared with uncatalyzed cells (~50°C). This difference was also reflected in the temperature maximum accompanying cell reversal. The

Table II. Pressure-temperature behavior and safety characteristics of catalyzed Li/$SOCl_2$ C-cells

Cell type[a]	Discharge current (A)	Environmental temp. (°C)	Capacity (Ah)[c] to 2.0V	Capacity (Ah)[c] to 0.0 V	Extent of overdischarge (Ah)	Maximum internal temp. (°C)[c]	Maximum internal pressure (psig)[c]
C-A-D	0.2	20	3.20	3.24	>5	31	20
C-A-D	2	20	2.92	2.98	>5	65	57
C-A-D	2	−12	2.94	2.90	>5	43	[b]
C-A-W	2	20	3.05	3.15	>5	65	55
C-A-W	2	−12	2.91	3.17	>5	45	[b]
C-A-D[d]	3	20	2.86	2.92	>5	74	[b]
C-A-D[d]	4	20	2.93	3.06	>5	131	140
C-A-W[e]	4	20	2.98	3.02	>5	145	[b]
C-A-W[e]	5	20	2.99	3.02	2	>200	190
C-C-D	0.2	20	5.15	5.20	>7	37	20
C-C-D	0.2	−12	4.60	4.72	>7	4	[b]
C-C-D	2	20	4.16	4.32	>7	102	74
C-C-D[e]	3	20	3.80	3.95	>7	150	236
C-C-D[d]	4	20	3.14	3.53	>7	150	350
C-C-D	2	−12	3.23	3.51	>7	69	[b]
C-C-D	3	−12	3.12	3.40	>7	130	[b]
C-C-W	2	−12	3.52	3.87	>7	68	[b]
C-C-W	2	20	4.39	4.52	>7	84	76
C-C-W[e]	3	20	3.82	3.97	>7	146	218
C-C-W[f]	4	20	3.38	3.53	2	>200	>300

[a] C-A-D: catalyzed Li-limited dry cells. C-A-W: catalyzed Li-limited wet cells. C-C-D: catalyzed cathode-limited dry cells. C-C-W: catalyzed cathode-limited wet cells.
[b] Pressure transducer response at −12°C was too poor to obtain reliable data.
[c] Average of three or four cells for each current.
[d] Only one or two cells used in this category.
[e] One cell vented.
[f] Two out of two cells vented.

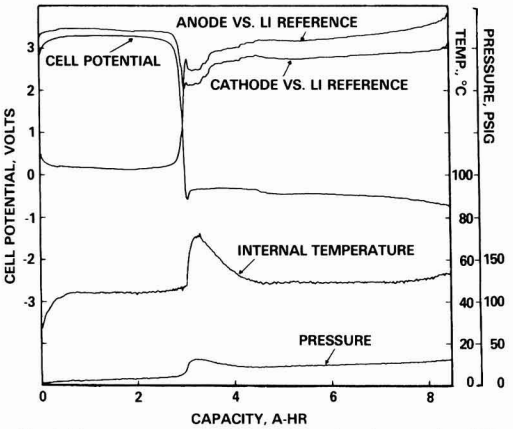

Fig. 6. Temperature, pressure, and voltage data for a catalyzed Li-limited Li/$SOCl_2$ cell discharged at 2.0A at room temperature.

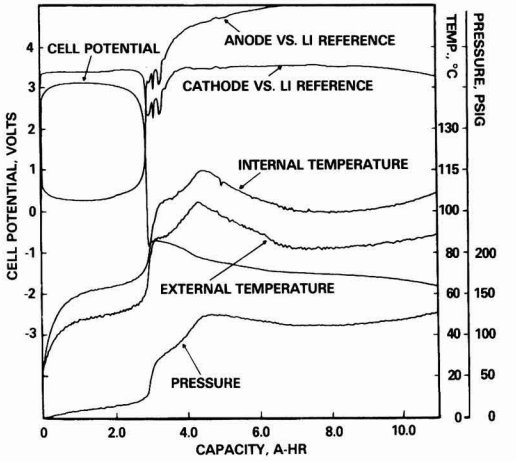

Fig. 7. Temperature, pressure, and voltage data for a catalyzed Li-limited Li/$SOCl_2$ cell discharged at 4.0A at room temperature.

data in Tables I and II reveal that addition of catalyst to cathode-limited wet cells reduced the average internal temperature ~28% during overdischarge at room temperature.

Cells which experienced lower internal temperatures also displayed lower pressure maxima. Upon addition of the Co-TAA catalyst, the average pressure maxima in type A-D, A-W, C-D, and C-W cells were reduced 19, 25, 46, and 52%, respectively.

Our results so far indicate that the catalyst is ineffective in reducing the resistive heating which accompanies the steep drop in cell voltages at the end of discharge and during early stages of cell reversal. On the other hand, the catalyst appears to be effective in lowering cell polarizations during high rate discharge. As a result, the catalyzed cells maintain an overall lower internal temperature profile relative to uncatalyzed cells.

Indeed, the pressure-temperature profiles which accompany cell reversal at high rates were significantly better in the Li-limited cells. Since Co-TAA catalyzed cells exhibited lower cathode polarizations and higher capacities, Li-limited catalyzed cells are a highly desirable design for high rate applications with practically attractive capacities. It should be noted that our Li-limited test cells were not optimized. Larger anodes would have provided additional capacity.

Discharge data for one of the lithium-limited catalyzed cells tested at a constant current of 4.0A are given in Fig. 7. None of the dry Li-limited cells vented at the 4.0A rate. Similar cells have been discharged and forced overdischarged at currents up to 5.0A to monitor their pressure-temperature profiles and safety characteristics.

Co-TAA catalyzed cathode-limited cells have also shown higher useful capacities and lower polarizations at the 3.0 and 4.0A discharge rates. However, in this design, the internal temperature during reversal at 4.0A rises to very high values, approaching the melting point of Li. One of the catalyzed cathode-limited cells tested at 3.0A and two cells tested at 4.0A vented following reversal. The venting occurred during the high temperature excursion. Typically, the cells first vented relieving the internal pressure. Soon after, a second highly exothermic reaction seemed to take place increasing the internal temperatures to excessively high values (Fig. 8). A number of products have been identified in the gases collected from vented cells (*vide infra*).

Table III. Effect of catalyst on increasing the average cell capacity

Temp. (°C)	Discharge rate (A)	Cell balance[a]	Increase in average cell capacity (%) Dry	Wet
20	2.0	A	1	20
20	2.0	C	20	32
20	3.0	C	61	—
−12	2.0	A	0	34
−12	2.0	C	63	84

[a] A = Li limited. C = cathode limited.

Constant current vs. constant load discharge.—The pressure-temperature behavior observed at the end of cell discharge would be different in constant current and constant load discharges. Since the current decreases substantially as the voltage falls towards 0.0 V in a constant load discharge, cell heating would be much less compared to a constant current discharge. This is illustrated in Fig. 9 for a catalyzed cell discharged through a 1.0Ω load. The constant current data are most relevant to cells in series connected batteries.

Cell chemistry.—Gas analysis.—Vapor phase IR spectra and GC analysis were performed on collected gases. The results indicate: (*i*) SO_2 is a discharge product of catalyzed cells; (*ii*) HCl gas was most often found in wet cells with high internal temperatures; and (*iii*) cells exhibiting the largest temperature rise generated the largest amount of the carbonaceous gases, COS, CO_2, and CS_2; specifically, they were cells discharged at high rates, cathode-limited

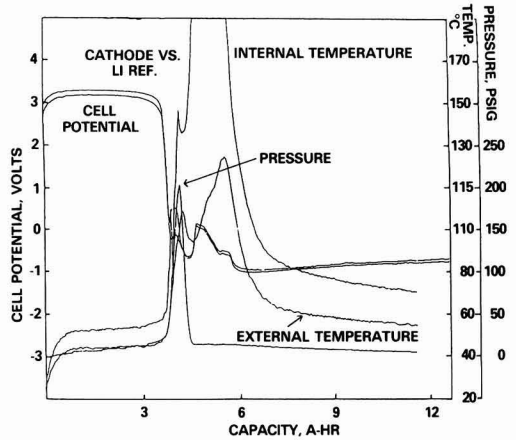

Fig. 8. Temperature, pressure, and voltage data for a catalyzed cathode-limited cell discharged at 3.0A at room temperature.

Table IV. X-ray diffraction data for cathodes from uncatalyzed cells at 2.0A at 20°C

Cell discharged 50%		Cathode-limited cell[a]		Li-limited cell[a]		LiCl[b]		S (rhombohedral)[b]		$LiAlCl_4$[b]		Li_2O[b]	
d (Å)	I/I_o	d (Å)	I/I_o	d (Å)	I/I_o	d (Å)	I/I_o	d (Å)	I/I_o	d (Å)	I/I_o	d (Å)	I/I_o
5.71	40	9.98	Diffuse[c]							5.82	50		
5.09	40	8.44	Diffuse[c]							4.88	40		
3.78	60	5.90	Diffuse[c]					5.40	60	4.76	50		
3.61	60	5.06								4.60	50		
3.21	100	3.82	30	3.87	80			3.89	100	3.25	75		
		3.39	10	3.45	30			3.42	80	3.00	60		
3.05	10	2.99	10	3.21	10					2.89	100		
2.92	20	2.95	100	2.96	40	2.97	100			2.86	75	2.66	100
2.72	10	2.70	40	2.72	100			2.71	100	2.83	75		
2.52	40	2.56	100	2.56	60	2.57	86			2.73	20		
2.27	70			2.49	20								
				2.28	10								
2.16	30			2.21	50								
2.03	60												
1.95	20			2.11	5			2.21	40	2.22	25		
1.92	50			2.03	10			2.08	20	2.19	35		
1.80	20	1.90	20	1.92	80			2.02	80				
		1.81	90	1.86	10			1.95	40				
1.74	50	1.55	80	1.81	30	1.82	58	1.92	80			1.63	40
1.65	10	1.48	70	1.71	20			1.82	80				
1.63	10	1.28	50	1.68	10			1.72	40				
1.50	20	1.21	30	1.57	90			1.65	80				
1.47	30	1.17	60	1.54	10	1.55	29	1.56	80				
		1.15	70	1.48	10	1.48	16	1.49	80			1.39	16
1.40	10			1.42	5								
1.37	10			1.36	60			1.35	60				
1.35	10			1.33	10			1.32	20				
1.31	20			1.28	20	1.28	4						
1.22	40			1.21	70			1.23	10				
				1.18	10	1.18	10	1.19	20				
				1.15	10	1.15	12	1.17	20				

[a] Forced overdischarged > 150% of the discharge capacity.
[b] Literature data from the ASTM files. In contrast to rhombohedral sulfur, the monoclinic form has primarily three strong lines at 6.6 (25), 3.74 (20), and 3.29Å (100%).
[c] The diffuse lines at high d values are carbon background lines.

cells, and cells that vented. Comparison of Fig. 7 and 8 reveals cathode-limited cells have higher internal temperatures.

Gases collected from cathode-limited cells forced overdischarged at > 3A showed small amounts of COS and CO_2, in addition to $SOCl_2$ and SO_2. Appreciable quantities of these carbon containing gases and some CS_2 were found in all cells that vented during forced overdischarge. The cells that vented at high discharge rates generally were those containing the 500 ppm of water. These cells displayed the greatest amounts of HCl.

The formation of these gases typically accompanied or followed the large temperature increase which occurred in the early stages of voltage reversal. It appears the carbonaceous gases are produced in thermally initiated reactions of carbon with S and SO_2. Evidently, rather high temperatures are required for the formation of these materials. Hence, the carbon cathode seems to play a major role in the safety hazards.

Analysis of solids.—Tables IV and V summarize x-ray data on cathodes taken from various discharged and overdischarged uncatalyzed and catalyzed cells. Recent x-ray studies on overdischarged (19) and 100% discharged (20) cells have been interpreted to involve the formation of Li_2O_2 under those circumstances. It should be noted that the x-ray data for Li_2O_2 can be accounted for by the combined x-ray powder patterns of LiCl and rhombohedral sulfur. It has been proposed that the Co-TAA catalyst alters the mechanism of $SOCl_2$ reduction to form Li_2O (6).

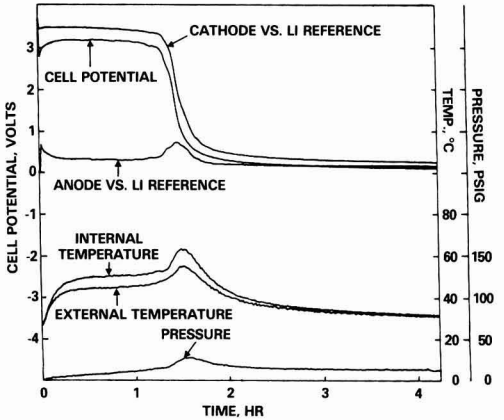

Fig. 9. Temperature, pressure, and voltage data for a catalyzed cathode-limited cell discharged through a 1Ω load at room temperature.

Table V. X-ray diffraction data of cathodes from catalyzed cathode-limited cells

Discharged at 3A to 0.0V at room temperature		Forced overdischarged at 2A at room temperature	
d (Å)	I/I_o	d (Å)	I/I_o
9.38	Diffuse	9.94	Diffuse
8.09	Diffuse	8.53	Diffuse
5.61	Diffuse	5.67	Diffuse
4.88	Diffuse	5.13	Diffuse
3.87	20	3.82	30
3.40	10	2.96	100
3.17	10	2.70	90
3.04	5	2.56	100
2.93	100	2.20	10
2.81	5	1.91	10
2.53	100	1.81	80
2.09	5	1.56	20
1.80	90	1.54	50
1.54	80	1.48	50
1.47	60	1.36	40
1.28	50	1.28	10
1.17	60	1.21	10
1.15	70	1.17	50
		1.09	50

The x-ray data in Table V give little evidence for this and are generally in good agreement with the x-ray patterns for LiCl and S.

In general, the catalyzed and uncatalyzed cells exhibit the same discharge products. While the relative intensities of the LiCl peaks show good agreement to the literature data, the sulfur peaks do not. This may be due to poor crystallinity of the sulfur and/or the existence of more than one allotropic form of S. Furthermore, S exhibits substantial solubility in $SOCl_2$ and, as a result, only small amounts would probably be present in the solid state in partially discharged cells.

Additional x-ray lines are present in the cathodes of partially discharged cells. These may arise from crystallized solvates of $LiAlCl_4$ containing SO_2, $SOCl_2$, or SO_2Cl_2. Evidence for solvates in overdischarged Li-limited cells comes from both the x-ray data and IR spectra.

When the electrolyte solution from overdischarged cells was collected and dried by pumping off the volatiles under vacuum, a glassy solid formed. These extracted salts were examined by IR analysis. Catalyzed and uncatalyzed cells gave identical spectra. However, as observed with the x-ray data, the Li-limited cells displayed a more complex spectral pattern than cathode-limited cells. The IR spectrum of the salt extracted from an overdischarged Li-limited cell is given in Fig. 10. The major absorptions at 1330 and 1070 cm^{-1} are attributed to the complex $Li^+[(SO_2)_x\ (SO_2Cl_2)_y]AlCl_4^-$. Such a complex has recently been proposed (18). The peak at 1195 cm^{-1} may be the S—O absorption associated with $Li^+(SOCl_2)_xAlCl_4^-$ and agrees with the strong band reported for $LiAlCl_4 \cdot 2SOCl_2$ (21). The fact that SO_2Cl_2 is commonly reported in overdischarged Li-limited cells supports the proposed first complex. Additionally, the 1070 and 1195 cm^{-1} bands were not present in the IR spectra of the salts extracted from the overdischarged cathode-limited cells. The peaks at 825 and 695 cm^{-1} are probably due to an oxychloroaluminate salt (18, 22). Studies indicate that the relative amounts of the various materials formed during anode-limited reversal depend on a number of factors including the amount of electrolyte (*i.e.*, flooded or starved cells), the extent of overdischarge, and current density (2, 18, 23).

We also identified $Li_2S_2O_4$ in the cathodes of some overdischarged cathode-limited cells via qualitative tests with naphthol yellow-S (24). IR spectra of the cathode did not show the characteristic absorptions of $Li_2S_2O_4$ (11, 25), indicating it was a minor product. A band at 1015 cm^{-1} appeared only in catalyzed overdischarged cathode-limited cells and may be associated with the catalyst.

Infrared spectra of the liquid collected from extensively overdischarged cells, with or without catalyst, did not differ from the spectra obtained prior to the overdischarge. SO_2 was the only product in the liquid. Previous studies on electrolyte flooded cathode-limited cells showed evidence for $LiAlSCl_2$ formation (2).

The ability of Li-limited cells to sustain extensive periods of overdischarge, as evidenced by their overdischarge voltage profiles, seem to indicate regenerative processes similar to those previously characterized (2).

Cathode-limited cells that were forced overdischarged for extended periods exceeding the amount of Li originally present in the cell suggests cell short-circuiting accompanying plating of lithium onto the cathode. The short-circuited cell apparently shunts current as if it were a resistor. The fact that a substantial amount of Li remains on the anodes of extensively overdischarged cells supports this hypothesis.

Several cathode-limited cells experienced premature anode polarization during discharge. A typical pattern of behavior can be seen in Fig. 4. Polarization of the anode begins after achieving ~1 Ah capacity, initiates a corresponding temperature rise, and appears to trigger the onset of cathodic polarization. This phenomenon was unpredictable, and most frequently occurred in uncatalyzed cells discharged at low temperatures (−12°C) and usually at 2.0A rates or higher. Occasionally, the anode polarized at low rates as shown in Fig. 11. This event was frequently characterized by a subsequent (ganging) or possibly simultaneous (mimicking) failure of the cathode and by the unexplained recovery of the anode to 0 V. It appears that a continuously growing LiCl anode film during discharge or crystallized $LiAlCl_4$ on the surface of the anode as a result of ionic concentration gradients in the cell increases the resistance to Li^+ transport across the anode/solution interphase. Higher current densities and low temperature increase the associated resistance polarization of the anode. Eventually, the voltage of the Li anode recovers, indicating that a disruption or dissolution of the film has occurred. However, the mechanism of this interesting process is not well understood. Lithium has been recently shown to undergo anodic passivation in research cells (26). It has also been shown that a greater passivation occurs when LiCl films are grown quickly (27). A temporary film has been recently shown to exist during anodization of lithium in the SO_2 system (28). Additional studies are warranted to characterize this interesting phenomenon.

Conclusions

The pressure generated in Li/$SOCl_2$ cells has been found to be significantly less than that predicted on the

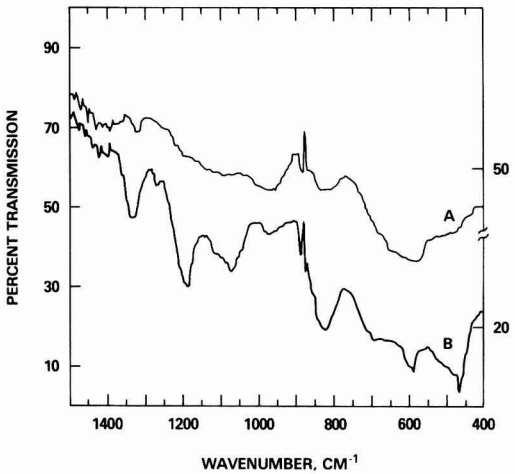

Fig. 10. Infrared spectrum of the glassy solid obtained by evaporating the liquid products from forced overdischarged "dry" cells. Curve A: cathode limited. Curve B: Li limited.

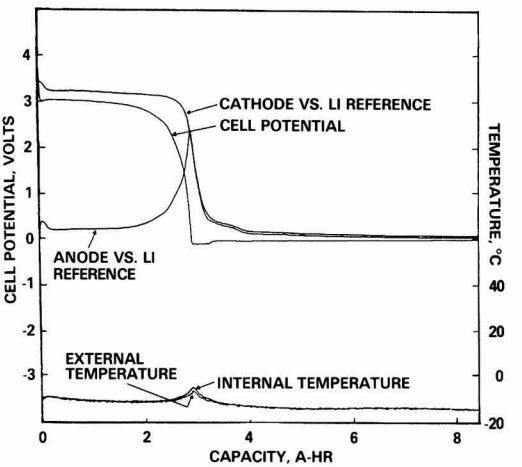

Fig. 11. Temperature and voltage data for an uncatalyzed cell discharged at 0.2A at −12°C.

basis of the accepted discharge reaction. This is believed to be due to the complexation of the generated SO_2 by $LiAlCl_4$ and/or the absorption of SO_2 by the carbon cathode. The highest internal heating was observed towards the end of constant current discharge and during early stages of cell reversal. Cathode polarization was identified as the major contributing factor to this type of internal heating. Runaway reactions and venting were observed in some cathode-limited cells in which the heating caused the internal temperature to exceed the melting point of Li. The generation of CO_2, COS, and CS_2 appeared to be a function of internal temperature—the higher the temperature, the greater the amount of the carbonaceous gases that were produced. Li-limited cells show very little or no cathode polarization towards the end of cell discharge, and they produce considerably less heat than cathode-limited cells. Premature anode polarization has also been observed. This is proposed to be due to a growing anode film or ionic concentration gradients which increases the resistance of Li^+ transport across the anode-solution interface. The addition of water appeared to have no significant effect in voltage delay but generally lowered the capacity of uncatalyzed Li-limited cells, generated greater pressures in stored cells, increased the temperature of cathode-limited cells, and enhanced venting at high rates. Cells incorporating Co-TAA catalyzed cathodes exhibited higher capacities and less internal heating than uncatalyzed cells, especially at low temperatures. Li-limited cells with Co-TAA-catalyzed cathodes appear to be highly desirable for high rate applications.

Acknowledgment

We wish to express our appreciation to N. Marincic and his associates at Hellesens Battery Engineering for the preparation of the Co-TAA catalyst. We are grateful for the continued financial support provided by the Independent Research Program at NSWC and for the High Energy Batteries for Weapons Block Program.

Manuscript received April 22, 1985.

The Naval Surface Weapons Center assisted in meeting the publication costs of this article.

REFERENCES

1. K. M. Abraham, P. G. Gudrais, G. L. Holleck, and S. B. Brummer, in "Proceedings of the 28th Power Sources Symposium," June 12-15, 1978, Atlantic City, NJ, The Electrochemical Society, Inc., p. 251 (1979).
2. K. M. Abraham and R. M. Mank, *This Journal*, **127**, 2091 (1980).
3. N. Doddapaneni, Abstract 47, p. 77, The Electrochemical Society Extended Abstracts, Vol. 83-2, Washington, DC, Oct. 9-14, 1983.
4. N. Doddapaneni, ERADCOM Technical Report, DELET-TR-83-0379-F, Fort Monmouth, NJ (April 1984).
5. G. J. DiMasi, M. Brundage, and L. Jarvis, in "Lithium Batteries," A. N. Dey, Editor, p. 111, The Electrochemical Society, Softbound Proceedings Series, Pennington, NJ (1984).
6. F. Walsh and M. Yaniv, ERADCOM Technical Report, DELET-TR-83-0386-F, Fort Monmouth, NJ (May 1984).
7. K. French, P. Cukor, C. Persiani, and J. Auburn, *This Journal*, **121**, 1045 (1974).
8. R. Staniewitz and R. A. Gary, *ibid.*, **126**, 981 (1979).
9. R. C. McDonald, *ibid.*, **129**, 2453 (1982).
10. W. Clark, F. Dampier, L. Lombardi, and T. Cole, Air Force Report no. AFWAL-TR-83-2083 (Dec. 1983).
11. M. W. Rupich, L. Pitts, and K. M. Abraham, *This Journal*, **129**, 1857 (1982).
12. D. R. Stull, *Ind. Eng. Chem.*, **39**, 517 (1947).
13. K. L. Klinedinst and M. L. McLaughlin, *J. Chem. Eng. Data*, **24**, 203 (1979).
14. N. Marincic, *J. Appl. Electrochem.*, **6**, 51 (1976).
15. Y. Bedfer, J. Corset, M. C. Dhamelincourt, and F. Wallart, *J. Power Sources*, *9*, 267 (1983).
16. A. N. Dey, *ibid.*, **5**, 57 (1980).
17. F. Walsh, R. S. Morris, and M. Yaniv, Abstract 33, p. 54, The Electrochemical Society Extended Abstracts, Vol. 83-2, Washington, DC, Oct. 9-14, 1983.
18. A. I. Attia, C. Sarrazin, K. A. Gabriel, and R. P. Burns, *This Journal*, **131**, 2523 (1984).
19. F. W. Dampier and R. C. McDonald, in "Lithium Batteries," A. N. Dey, Editor, p. 154, The Electrochemical Society Softbound Proceedings Series, Pennington, NJ (1984).
20. B. J. Carter, M. Evans, S. Rao, and R. M. Williams, Abstract 149, p. 228, The Electrochemical Society Extended Abstracts, Vol. 84-2, New Orleans, LA, Oct. 7-12, 1984.
21. R. C. McDonald, F. W. Dampier, P. Wang, and T. Bennett, GTE Final Report NSWC N60921-81-C-0229 (Jan. 1983).
22. J. C. Bailey and G. E. Blomgren, in "Electrocatalysis," W. E. O'Grady, P. N. Ross, Jr., and F. G. Will, Editors, The Electrochemical Society Softbound Proceedings Series, Pennington, NJ (1982).
23. B. J. Carter, R. M. Williams, M. Evans, Q. Kim, S. Kim, F. D. Tsay, and H. Frank, Abstract 38, p. 61, The Electrochemical Society Softbound Proceedings Series, Vol. 83-2, Washington, DC, Oct. 9-14, 1984.
24. L. V. Haff, in "The Analytical Chemistry of Sulfur and Its Compounds," Part 1, J. H. Karchmer, Editor, p. 245, Interscience Publishers, New York (1970).
25. D. M. Oglesby, R. L. Ake, and W. P. Kilroy, in "Proceedings of the 30th Power Sources Symposium," June 7-10, 1982, Atlantic City, NJ, The Electrochemical Society, Inc., p. 127 (1982).
26. S. D. James, *J. Power Sources*, **10**, 105 (1983).
27. A. N. Dey and C. R. Schlaikjer, in "Proceedings of the 26th Power Sources Symposium," Atlantic City, NJ, April 29-30, May 1-2, 1974, p. 47 (1974).
28. P. Zlatilova, Y. Geronov, and R. Moshtev, *J. Power Sources*, **13**, 327 (1984).

Electronmicroscopic Examination of Corroded Aluminum-Copper Alloy Foils

D. Y. Jung,* I. Dumler, and M. Metzger*

Department of Metallurgy and Mining Engineering and Materials Reserach Laboratory, University of Illinois at Urbana-Champaign, Urbana, Illinois 61801

ABSTRACT

The formation of particles of copper through selective dissolution of dilute Al-Cu solid solutions in sulfuric acid was studied by transmission electron microscopy of foils prethinned before corrosion. A technique was employed for prethinning without surface enrichment. At −500 mV *vs.* SCE, a significant fraction of the copper made available by selective dissolution appeared as particles, but not at −100 mV *vs.* SCE. The results are discussed with reference to concurrent AES observations on the Cu-enriched solid solution beneath the anodic film over the main body of the electrode.

Selective dissolution during corrosion of Al-Cu alloys may lead to the formation of metallic copper on the surface and a large enhancement of the cathode reaction rate (1). In HCl solutions, this is displayed through rapid and accelerating pitting corrosion (2, 3). One of the surface reactions in the selective dissolution was recently identified by Strehblow and co-workers (4, 5), who showed by

* Electrochemical Society Active Member.

Rutherford backscattering and ion scattering spectrometry that anodic sweeps of Al-Cu alloys in buffer solutions of pH 5.0-9.2 produced an undoped alumina film with enrichment in Cu of the substrate beneath the film. The observations reported in this paper, which are part of a study that included electrochemical and AES measurements, were concerned with the formation of particles of copper metal on the surface. The identification, distribution, and crystallography of these particles can be examined by TEM with high spatial resolution. The corrosion was performed in sulfuric acid in order to maintain passive conditions and with the intent to employ the body of information on anodic films as an aid in interpreting film behavior. Specimens were thinned to near electron transparency and then exposed to corrosion to a small depth. A problem of specimen preparation arises with these alloys in that electropolishing, which is required to thin specimens properly for microscopy, itself produces surface enrichment in Cu. A procedure was devised to deal with this.

Experimental

The high purity binary alloys, in the form of 1 or 0.1 mm sheet, contained 0.06, 0.20, 0.60, or 2.0% Cu. They were given a final anneal at 580°C to yield solid solutions of grain size >2 mm and water quenched. Testing was done in 2.4*M* H_2SO_4 at 25.0° ± 0.2°C, without deaeration or stirring, at −500 or −100 mV *vs.* SCE. Before switching on the control potential, the rest potential was monitored for a few minutes as a check on specimen surface cleanliness. In all cases, the initial rest potential was ≲ −950 mV *vs.* SCE and near that of 99.999% Al, there being negligible corrosion in this interval. Specimens for electrochemical testing were polished mechanically to avoid initial surface copper enrichment. Mechanical polishing cannot be employed to thin specimens for TEM. Several electropolishing baths were tested and all produced severe surface enrichment in Cu. It was found that the enriched region could be removed by sputtering. This was possible because of the apparent absence of preferential sputtering under the conditions employed, as seen in the AES work. A procedure for thinning from one side, as diagramed in Fig. 1, was developed. After dishing a 0.12 mm sheet just to perforation by electropolishing in a HNO_3-H_2O bath, the specimen was inserted into the Physical Electronics 545 Auger unit and sputtered with 1 keV Xe^+ over a region larger than the dish. The Cu peak at 918 eV was monitored, and the sputtering continued until the Cu signal was indistinguishable from the bulk value as determined on a mechanically polished specimen. After sputtering, both sides of the sheet were exposed in sulfuric acid for a period which would make the equivalent of a few monolayers of Cu available by selective corrosion of the solid solution. In the 0.60% Cu alloy, on which most of the work was done, this required only a fraction of a micrometer depth of corrosion. This, being small and relatively uniform, enlarged the original hole but usually left sufficient thin region for examination.

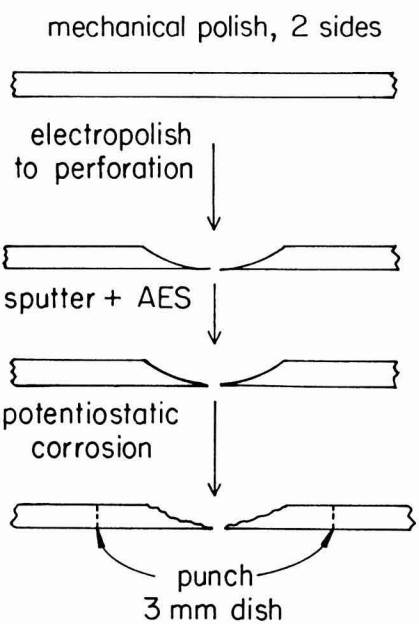

Fig. 1. Preparation of aluminum-copper corrosion specimens for transmission electron microscopy.

Observations were made either on a Phillips 400 microscope at 120 kV or a JSEM 200B microscope at 200 kV, both equipped with EDS capability for chemical analysis.

It was confirmed by electron diffraction of the matrix material that a single-phase solid solution was retained by quenching in all the alloys. Even the 2.0% Cu alloy aged one week at room temperature showed a diffraction pattern in the [100] orientation with no streaking indicative of the formation of Guinier-Preston zones. With this alloy, difficulties were anticipated in completely removing severe surface enrichment without metallurgical changes in the foil corrosion specimens, and it was not examined.

Results and Discussion

−500 mV vs. SCE.—At this potential, no loss of Cu from the solid solution by direct dissolution would be expected. Cu particles or rounded patches were visible in the thinner regions of the corroded foil as dark areas 4-35 nm across (Fig. 2a and 2b). These remained visible during tilting, *i.e.*, they were visible by mass thickness contrast even in the absence of diffraction contrast and thus had thicknesses substantial fractions of their diameters. The particle density was relatively uniform from one field to another and from one foil to another though showing local variations within one field (Fig. 2). There was a tendency for alignment or clustering of particles in the walls of a topographic cell structure.

Figure 3a is a micrograph of the alloy of Fig. 2b after twice as much corrosion. It is seen that the particle density increased but the range of particle diameters remained about the same.

EDS observations in the thinner regions of the foil, employing the ratio of the Cu Kα peak height to that of the Al, readily confirmed the presence of Cu in excess of the bulk value. Observations with selected areas of 0.1 μm diam (Fig. 3) confirmed that local regions of higher particle density gave higher Cu/Al ratios (Fig. 3b and 3c).

The micrographs of copper particles were similar in general appearance to micrographs shown by Tomashov *et al.* (6) of palladium particles in extraction replicas from a steel containing 25% Cr and 0.5% Pd. These were, however, produced under different conditions, *i.e.*, by a few minutes of active dissolution in sulfuric acid.

Selected-area diffraction in regions containing a number of particles (Fig. 4) showed full rings of very fine

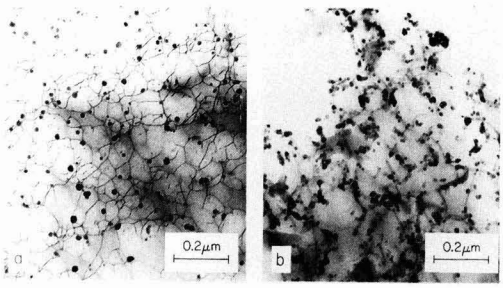

Fig. 2. Transmission micrographs showing copper particles in Al-Cu foils after corrosion at −500 mV vs. SCE. a: 0.06% Cu, 12h. b: 0.60% Cu, 2h.

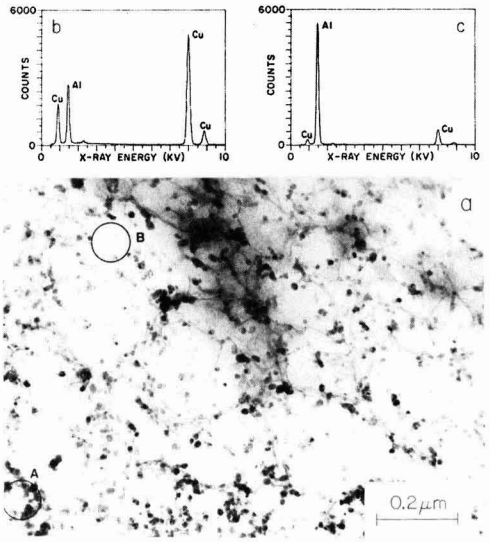

Fig. 3. Analytical examination of 0.60% Cu foil after 4h at −500 mV vs. SCE. a: Transmission electron micrograph. b: EDS spectrum of region A. c: EDS spectrum of Region B.

grained Cu_2O and spotty rings of Cu together with the single-crystal spot pattern (incomplete cross grating) from the selected grain of the aluminum substrate. A layer of Cu_2O would have formed on the surface of the Cu when the specimen was removed from the acid bath and rinsed with water. Al_2Cu was not observed. Darkfield micrographs employing portions of Cu rings imaged the particles. All diffraction patterns represented regions well within a single grain of the substrate so that the observation of closely spaced spots on the Cu rings indicated that a large number of Cu particle orientations arose from a single orientation of the Al-Cu solid solution substrate.

−100 mV vs. SCE.—A second test potential of −100 mV *vs.* SCE was chosen as one at which there is a small corrosion current for pure Cu, *i.e.*, ≈ 80 μA/cm² as indicated by data of Ghandehari *et al.* (7). Thus, any metallic Cu exposed to the acid would suffer some corrosion and would be removed unless it grew faster than it dissolved. The severest case examined was that of the 0.60% Cu alloy exposed 4h at −100 mV *vs.* SCE with a depth of corrosion 0.66 μm and with the amount of Cu which would have been made available by selective corrosion of the Al equivalent to a 1.2 nm thick layer, far greater than in Fig. 2b or 3a. No Cu particles were detected in electron micrographs (Fig. 5a), and an intensive search of thin regions of the foils failed to reveal any Cu or Cu_2O rings in the diffraction pattern.

The topographic cell structure seen in Fig. 5a for 0.60% Cu is characteristic of the potential rather than the copper content since it appeared also with 99.999% Al (Fig. 5b). Impedance data showed that the presence of this structure did not indicate severe surface roughening, as may accompany selective dissolution in some cases (8).

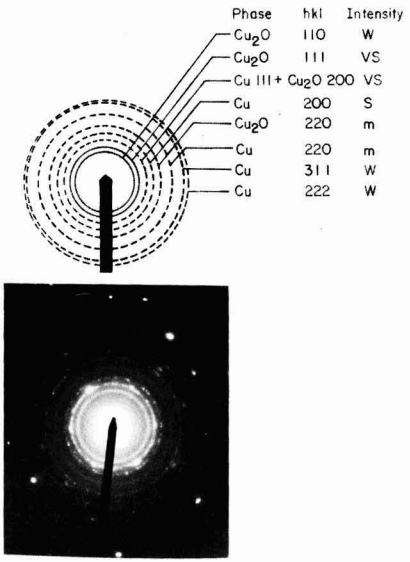

Fig. 4. Diffraction pattern in an area containing many particles and indexing of the rings as Cu and Cu_2O. 0.60% Cu, −500 mV vs. SCE, 4h.

Further Discussion

Quantity of copper in particles.—In many of the micrographs, particles were visible down to projected diameters of about 4 nm. Examination of the micrographs indicated that any smaller particles present probably would have been indistinguishable from the faint phase contrast background, owing to the presence of the amorphous alumina surface film. The distribution of particle diameters had a maximum at 11-14 nm and fell more or less sharply for smaller diameters. It was concluded that in any case only a small fraction of the volume of copper would have been in undetected particles below 4 nm diam.

An estimate of the amount of copper appearing as particles was made from the measured distribution in bright field images. The particles being mainly noncircular in section, a diameter was assigned to each particle to give an equal area. For purposes of estimation, the particles were assumed to be hemispheres and the volume of particles in each size class was calculated and summed. The results for three specimens are compared in Table I with the total copper which would have been made available by selective dissolution. The latter was obtained by integrating the partial anode current during the exposure at −500 mV *vs.* SCE. The estimates show that under the conditions of these experiments a significant fraction up to perhaps one-half of the available copper appeared as particles. It may be noted that an analogous calculation was made for the total surface area of the copper particles in the micrographs. The results were in rough agreement with copper area figures deduced from capacitance measurements and from cathodic polarization data, thus supporting the validity of the TEM data.

An additional portion of the copper made available by selective corrosion should be in the Cu-enriched solid solution beneath the film over the main body of the electrode, according to the results of Strehblow *et al.* (4). To discuss this point, some pertinent results are cited below from the companion AES study, which will be reported separately.

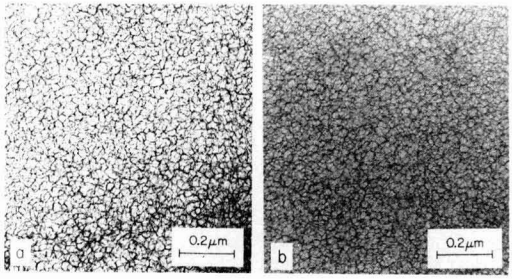

Fig. 5. Transmission electron micrographs of foils after corrosion at −100 mV vs. SCE. a: 0.60% Cu, 4h. b: 99.999% Al, 12h.

Table I. Quantity of copper metal produced by selective corrosion at −500 mV vs. SCE

Cu content (w/o)	Time (h)	Calculated weight loss (g/cm²)	Available Cu (g/cm²)	Estimated Cu as particles, TEM data[a] (g/cm²)	Fraction Cu in particles
0.06	12	3.9×10^{-4}	2.4×10^{-7}	9×10^{-8}	0.4
0.60	2	4.9×10^{-5}	3.0×10^{-7}	1.6×10^{-7}	0.5
0.60	4	9.0×10^{-5}	5.4×10^{-7}	2.3×10^{-7}	0.4

[a] Particles assumed hemispherical.

AES observations.—Figure 6 presents for illustration some AES depth profiles for the 0.60% Cu alloy. The enrichment in Cu of surfaces of Al-Cu alloys prepared by electropolishing, which has been noted previously for an alloy of higher copper content (9), is shown in Fig. 6a. This enrichment appears greater than that of the mechanically polished specimen exposed to sulfuric acid at −500 mV *vs.* SCE (Fig. 6b), but the efficiency of enrichment was actually much greater in the latter case, which was produced by corrosion to a depth two orders of magnitude smaller. The depth profiles in Fig. 6 show a maximum in the copper signal at the oxide-metal interface, indicative of an enriched zone beneath the film. These data do not reveal the lateral distribution of copper or the phases present. In interpreting these depth profiles, it must be borne in mind that the enriched zone will appear thicker than it actually is. The mixing effect of ion bombardment (*i*) causes the enriched zone to be sensed before the nominal sputtered depth has actually reached the outer limit of the zone, and (*ii*) drives some of the excess copper inward so that an excess copper signal persists beyond the original maximum depth of the enriched zone.

Surface at −500 mV vs. SCE.—The Cu particles formed at this potential were up to 25 nm across and thus were too large to be covered by the alumina film (estimated as ≥ 4 nm thick). Even if they had originally formed beneath it, the overlying film would disappear by slow chemical dissolution in the acid since the copper blocks its renewal. The exposed copper metal would be stable at this immune potential. The alloy surface at a particular exposure time is then modeled, as shown schematically in Fig. 7a, as isolated patches of copper covering a few percent of the surface with the remainder, in line with Strehblow's model, consisting of an undoped alumina film overlying a few layers of enriched solid solution. An AES depth profile of such a surface with a 0.03 mm² electron-beam sampling many particles would show a copper concentration of a few percent at the external surface concurrent with the oxide film signals and there would be a maximum at the film-substrate interface, consistent with Fig. 6b. The copper depth profile does not yield a separation of the contributions from particles and enriched zone. Estimates of the total excess copper in these profiles are subject to some uncertainty, but do suggest that a substantial or large fraction of the copper made available by corrosion remains on the electrode at this potential.

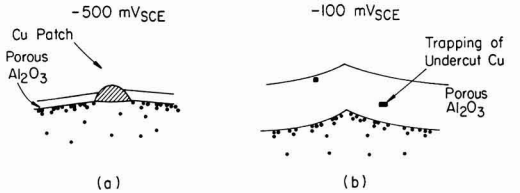

Fig. 7. Schematics of proposed surface conditions after exposure at −500 mV vs. SCE (a) and −100 mV vs. SCE (b).

Although the copper metal particles are immune at this potential, there would be a tendency for them to be undercut and released in the course of continued corrosion. The smallest particles would be most susceptible to undercutting, the ones which achieve larger diameters surviving longer. This could explain why the particle size frequency decreases at the smaller diameters.

Surface at −100 mV vs. SCE.—The processes occurring at this potential are considered to be the same as at −500 mV *vs.* SCE, except for the presence of a significant dissolution current for copper. The cell current was higher and the film thicker.

Consideration is given first to the special case of the 0.60% Cu alloy. The AES depth profile in Fig. 6c shows a Cu-enriched zone beneath the film, but also shows a small copper signal concurrent with the oxygen signal through the film region. The latter would be contrary to Strehblow's model if such signified doping of the film structure with copper ions. The copper signal from within the film cannot be attributed simply to copper metal particles of the size and nature discussed in the previous section because no Cu or Cu_2O was detected in the TEM observations and the cathode polarization data were also not consistent with this. The behaviors of 99.999% Al and 99.999% Cu in this acid are such that an area fraction of exposed copper of only 10^{-5} would produce cathode currents an order of magnitude greater than those of the pure aluminum. It is conceivable that the film formed on this alloy contains fragments of copper, or of copper-aluminum alloy from the enriched zone, which have been undercut from the substrate and trapped in the film, which at this potential is ≥ 20 nm thick. Such fragments are presumably suffering slow corrosion in the porous film. The model is represented schematically in Fig. 7b. Some small particles or clusters yielding the small (≤ 0.6%) Cu signal in Fig. 6c could be undetected by electron microscopy, and, being isolated from the substrate by an alumina film of low electronic conductivity, they would not be effective cathodes.

In the 0.20 and 0.06% Cu alloys exposed at −100 mV *vs.* SCE, the AES depth profiles showed no detectable copper signal from within the film (0.20% Cu still showed copper enrichment beneath the film). This is interpreted as a consequence of a lower rate of particle formation and growth in these alloys so that any copper or copper containing patches exposed at the surface would have dissolved before they could be undercut. Overall, it is concluded that the presence of a Cu signal from within the film may arise from processes other than doping of the

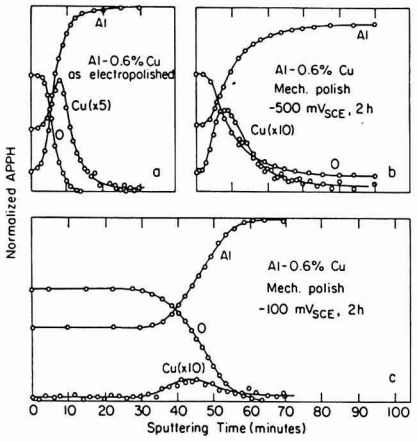

Fig. 6. Auger depth profiles of 0.60% Cu alloy after various treatments. Sputtering was performed with 0.5 keV Xe^+. a: Electropolished in 20% perchloric acid in ethanol. b: Mechanically polished and exposed in 2.4M H_2SO_4, −500 mV vs. SCE, 2h. c: Mechanically polished and exposed in 2.4M H_2SO_4, −100 mV vs. SCE, 2h.

film structure with copper ions and that the present AES observations are not necessarily inconsistent with Strehblow's model.

Orientation relationships.—The dissolution in this system is highly selective at −500 mV *vs.* SCE and it would be expected that the nucleus of a particle of copper metal would have to form by a solid-state process from copper atoms in the alloy and would thus tend to be coherent with the substrate and of the same crystal orientation. This is expected whether the nucleation occurs through aggregation of copper atoms in the enriched zone under the film or if it occurs in conjunction with film breakdown and transient pitting processes. The orientation would persist during growth although misfit dislocations would form. Forty and Durkin (10) made a TEM study of selective dissolution in (111) orientation thin foils of Ag-Au solid solutions and found the substrate orientation retained in the gold-enriched regions; it may be noted that this is a system with minimal coherency strains because the lattice parameter varies by less than 0.2%. However, in the well-formed copper particles noted in the present work, many orientations were present within a single grain of the alloy. Also, in many cases (*e.g.*, Fig. 2b), the particle images showed internal structure indicating that they were not generally monocrystalline. Multiple orientations could have come from nuclei forming in twin relation to the substrate and from growth twinning. The copper requires a strain of 12% to remain coherent with the substrate. It is conceivable that the copper particles do not necessarily nucleate as thin coherent plates but may nucleate in the enriched solid solution beneath the film as incoherent entities too thick to be coherent. The distribution of orientations of the copper particles and its origin needs further study. It is thought unlikely that nucleation at this potential involves transport through the electrolyte. Mechanisms of particle growth will be discussed elsewhere.

Acknowledgments

This work was supported by the National Science Foundation through the Materials Research Laboratory under Contract DMR 80-20250. The authors are indebted to J. A. Eades for advice on contrast questions and particle detectability.

Manuscript submitted April 6, 1984; revised manuscript received July 10, 1985. Part of this article was presented as Paper 80 at the Detroit, Michigan, Meeting of the Society, Oct. 17-21, 1982.

The University of Illinois assisted in meeting the publication costs of this article.

REFERENCES

1. D. Kuhlmann-Wilsdorf and G. Masing, *Z. Metallkd.*, **41,** 497 (1950).
2. G. Tammann and W. Boehme, *Z. Anorg. Allgem. Chem.*, **226,** 82 (1935).
3. M. Metzger and O. P. Arora, *Trans. Met. Soc. AIME*, **227,** 1305 (1963).
4. H. H. Strehblow, C. M. Melliar-Smith, and W. M. Augustyniak, *This Journal*, **125,** 915 (1978).
5. H. H. Strehblow and D. L. Malm, *Corros. Sci.*, **19,** 469 (1979).
6. N. D. Tomashov, G. P. Chernova, V. N. Modestova, T. V. Chukalovskaya, L. N. Volkov, and R. P. Vasilyeva, in "Proceedings of the 4th International Congress on Metallic Corrosion," p. 642, NACE, Houston, TX (1972).
7. M. S. Ghandehari, T. N. Andersen, and H. Eyring, *Corros. Sci.*, **16,** 123 (1976).
8. H. W. Pickering, *This Journal*, **115,** 690 (1968).
9. J. M. Pountney and M. H. Loretto, in "Electron Microscopy 1980," Vol. 3, P. Brederoo and V. E. Cosslett, Editors, p. 180, 7th European Congress on Electron Microscopy, Leiden, The Netherlands (1980).
10. A. J. Forty and P. Durkin, *Philos. Mag. A*, **42,** 295 (1980).

Anodic Oxide Films on $CrSi_2$

A. J. Barcz,[1] M. Bartur,* T. Banwell, and M-A. Nicolet*

California Institute of Technology, Pasadena, California 91125

ABSTRACT

Oxide layers on chromium disilicide of thicknesses up to several thousand angstroms are formed by constant current anodization in ethylene glycol containing different amounts of water. For low H_2O concentrations (1-10%), the films have essentially uniform composition of about 92% SiO_2 and 8% Cr_2O_3; the chromium being dissolved in the electrolyte during the anodic oxidation at a rate of one Cr atom per seven oxygen atoms incorporated. Greater H_2O content leads to increased current efficiency and higher angstrom per volt values for the anodization. In a 50% H_2O electrolyte, Cr-free SiO_2 films can be grown up to a limited thickness. These results are compared with the anodic oxidation of Si and the thermal oxidation of $CrSi_2$.

It is expected that silicides will be applied to interconnection lines in VLSI technology due to silicides, low resistivity relative to the commonly used polysilicon (1) as well as their ability to form insulating layers upon thermal oxidation (2). An exciting feature of the oxidation of most silicides is that the growing oxide appears to be pure SiO_2 while the integrity of the silicide is being preserved. From a purely thermodynamic point of view, assuming equilibrium and unlimited supply of the reactants, one might expect that both silicon and the metal will oxidize since the heat of formation of the silicides is small compared to those of the respective metal oxides [see, for example, the data tabulated per metal atom in Ref. (1)]. The calculations fall closer to the experimentally observed results when the corresponding heats of reaction are taken per one oxygen atom (3). Nevertheless, it seems that kinetic factors such as oxygen transport through the oxide and the rapid migration of Si and metal atoms through the silicide at the temperature of oxidation play a key role in the mechanism which leads to the formation of the metal-free oxide. Several possibilities concerning the mass transport across the silicide layer are discussed in Ref. (2).

In this paper, we report on a study of the formation of anodic oxides on $CrSi_2$ grown in an ethylene glycol containing small quantities of KNO_3 and H_2O, an electrolyte known to produce high quality, compact SiO_2 films when applied to silicon (4). This study gives an interesting opportunity to verify concepts adopted to explain the thermal oxidation processes and, specifically, to identify what is common and what is different in the thermal *vs.* electrochemical mechanism of the oxidation of silicides. First, in anodic oxidation carried out at room temperature any atomic transport across the remaining silicide can be ignored. Second, ionic movement in the high electric

* Electrochemical Society Active Member.

[1] Present address: Institute of Electrical Technology, 02-668 Warsaw, Poland.

field within the oxide includes usually both cationic and anionic components (5), in contrast to the thermal oxidation of Si, in which the mobile species in the oxide is an oxygen containing molecule.

Finally, we point out that the potential advantages of using anodic *vs.* thermal oxides of a silicide could be (*i*) a higher dielectric constant results if the metal oxide is present in the SiO_2 film, and (*ii*) that the silicon-silicide interface is not being affected by the high temperature treatment.

Experimental Procedure

Chromium films about 750Å thick were deposited in an oil-free vacuum of $\sim 10^{-7}$ torr by electron-beam evaporation onto Si <111> substrates. The wafers were then heat-treated in a vacuum furnace (600°C, 20 min, 10^{-7} torr range) to form ~2300Å of the stoichiometric chromium disilicide. The samples to be oxidized were degreased with trichloroethylene, rinsed in deionized water, and blown dry prior to being placed as anodes in an electrolytic cell. The samples were masked so that a limited area (0.3 cm^2) was in contact with the electrolyte. A platinum cathode was positioned about 2 cm from the anode, and the electrolyte was stirred. The solution used in the present experiment was anhydrous ethylene glycol containing 0.5 weight percent (w/o) KNO_3 with different quantities of water: 1, 2, 10, 20, and 50 w/o. Oxidations were performed at a constant anode current density of 3 mA/cm^2 up to a predetermined voltage (V_{max}) followed by a current decay at the maintained voltage V_{max} down to one-quarter of its initial value. After the oxidations, the samples were rinsed in acetone and high resistivity water. Also, some oxidations were made using either 2 atom percent KNO_3 in the electrolyte or 0.5 mA/cm^2 current density. No detectable influence of these parameters changes on the composition of the films was found. Complementary thermal oxidations of $CrSi_2$ were performed in an open-tube furnace at 900°C by steam oxidation. The samples were introduced into the furnace with high N_2 flow to minimize oxidation during the temperature rise of the sample. After the sample had reached the desired temperature, O_2 bubbled through 96°C water was introduced.

It is important to note that the as-evaporated Cr contains about 7 a/o oxygen (6). Also, after thermal oxidation a thin layer of Cr oxide was always observed on the sample surface.

Elemental analysis of the oxidized layers was performed using 2 MeV $^4He^+$ backscattering spectrometry (BS). Samples were positioned normal to the primary beam, and backscattered ions were detected at an angle of 170°. The backscatter analysis provides full information about the composition of the films, since, owing to a large mass difference, signals corresponding to the three components Si, Cr, and O can be independently observed. From these, we derive such quantities as stoichiometric ratios and overall oxygen content. Also, owing to the existing reference plane at the Si-$CrSi_2$ interface, it its possible to detect the loss of Si or Cr atoms by comparing the respective count integrals before and after the anodic processing. The masked edge enables reliable comparison of oxidized and unoxidized $CrSi_2$ at adjacent spots on the sample.

Results

Most oxidations were performed with either 1 or 10 w/o H_2O electrolytes. In these conditions, laterally uniform anodic films were reproducibly grown up to cell voltages of about 125V. Occasionally, it was possible to obtain V_{max} as high as 200V (1% H_2O) before the initial reaction ceased. Typical voltage-time curves for $CrSi_2$ and pure Si substrates oxidized in the above electrolytes are shown in Fig. 1. There is a pronounced difference in the slope of the two curves corresponding to $CrSi_2$, while the curves for Si seem to overlap except for the initial potential rise. Figure 2 depicts the BS spectra of the $CrSi_2$ oxide resulting from the oxidation in the 10% H_2O glycol to V_{max} = 50V; the solid line represents the spectrum of the initial silicide. First, we noticed that the surface film contains

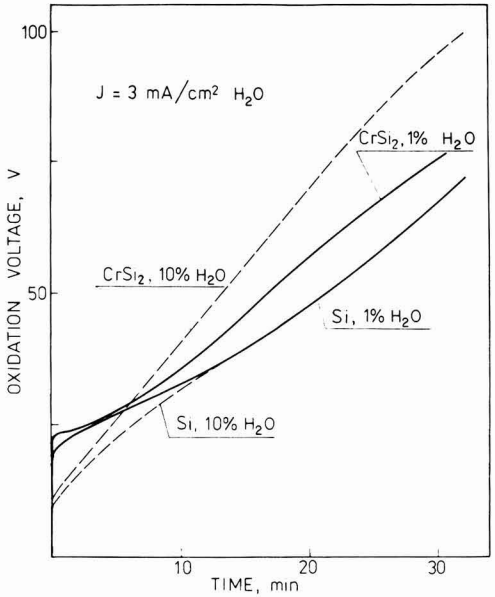

Fig. 1. Voltage-time curves for $CrSi_2$ and Si anodization in glycol with water percentage of either 1 or 10% at constant current density of 3 mA/cm^2.

oxygen, silicon, as well as chromium atoms. The integral over the O peak yields 1.2×10^{18} at./cm^2 of incorporated oxygen. Furthermore, the stoichiometry ratios calculated on the basis of the signal heights give O/Si = 2.27 and Cr/Si = 0.17. It is thus clear that the oxide grows deficient in chromium with regard to the elemental proportions in the silicide (Cr/Si = 0.5). The difference in the Cr integrals confirms the net loss of chromium atoms equal to 1.8×10^{17} at./cm^2, *i.e*, one Cr atom lost per seven O atoms incorporated. No loss of silicon atoms is detected. We also note that the composition profile is uniform and that the oxide-silicide interface is, and Si-silicide interface remains, sharp. A similar picture presented in Fig. 3 concerns the anodization to V_{max} = 75V in a solution containing smaller amounts of water (1 w/o). Here, the resultant oxygen content is 4.9×10^{17} at./cm^2 with a stoichiometry profile comparable to the previous case. A slight Cr enrichment at the surface becomes more evident for the anodic runs in which the electrolyte was not stirred (broken line in the figure). Without

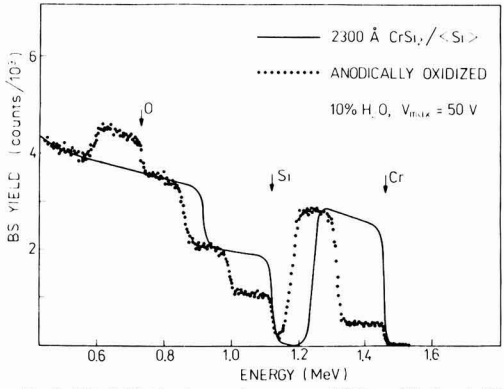

Fig. 2. 2 MeV $^4He^+$ backscattering spectra of $CrSi_2$ on Si before (solid line) and after anodic oxidation in 10% H_2O electrolyte to a voltage of 50V (full dots).

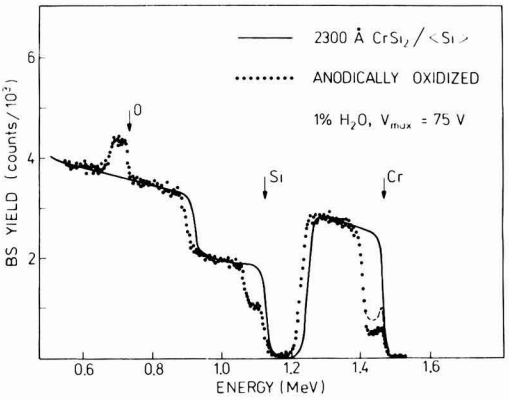

Fig. 3. Backscattering spectrum corresponding to $CrSi_2$ oxide obtained by oxidation in glycol containing 1% water to V_{max} = 75V (dots), when no stirring was applied to the electrolyte (broken line), and with $CrSi_2$/Si substrate (solid line).

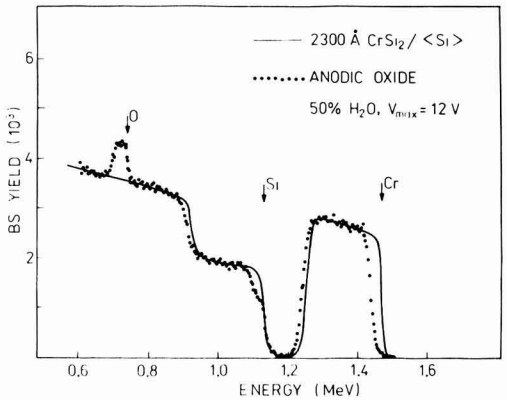

Fig. 5. Backscattering spectra of $CrSi_2$ (solid line) and $CrSi_2$ oxide (dots) produced in 50% H_2O glycol; V_{max} = 12V.

stirring, the current decay stage proceeded down to one-tenth (instead of one-quarter) of its nominal 3 mA/cm², and the Cr appeared at even higher concentrations reaching the ratio of Cr/Si = 0.5.

Considering the above two figures, it is evident that the water content has a large effect on the outcome of the anodization: the sample oxidized in 10% H_2O to a lower voltage contains 2.4 times more oxygen than the one oxidized to the higher voltage in the 1% H_2O electrolyte. This trend is clearly appreciable in Fig. 4, where the oxygen content in atoms per square centimeter is plotted against the maximum effective potential drop ΔV in the oxide ($\Delta V = V_{max}$ minus initial potential rise). For comparison, data for pure Si are also shown. In all cases, the dependence appears to be linear; for $CrSi_2$, the slope for oxidations carried out at 10% H_2O is significantly higher than that for the 1% H_2O electrolyte. Both slopes for $CrSi_2$ are greater than that of Si, which oxidizes at a rate which is nearly independent of the H_2O content. These slopes can be expressed in terms of convenient "electrochemical" units of angstroms per volt by assuming atomic concentration of the oxygen atoms equal to that of pure SiO_2 which is justified by a relatively small contribution of the Cr oxide. The corresponding values are 5.2 Å/V for Si, 18.5 Å/V for $CrSi_2$ (1% H_2O), and 65 Å/V for $CrSi_2$ (10% H_2O).

Anodization in solutions of increasingly aqueous character leads to further increase in the angstroms per volt value and to a more efficient Cr dissolution. At the same time, the maximum voltage that the film can sustain is reduced to 10-20V. An example of this type of behavior is shown in Fig. 5, where the anodic growth proceeded only to V_{max} = 12V (from the starting potential of 7.5V, V = 4.5V). The oxide layer is practically free of Cr and constitutes a pure SiO_2 of a thickness of about 850Å. This result is thus similar to thermally grown oxides except that the silicide is not preserved as a whole, and Cr is lost into the solution.

Additional information about the growth mechanism can be acquired by analyzing an oxide layer produced by anodic followed by thermal oxidation. In Fig. 6, backscatter spectra are shown for the individual oxidations of $CrSi_2$: anodic oxidation (10% H_2O, V_{max} = 30V producing incorporation of 5×10^{17} O at./cm²), thermal oxidation (900°C, wet, 30 min) resulting in an oxide with 8.5×10^{17} O at./cm², together with the spectrum resulting from thermal oxidation of the already preformed anodic

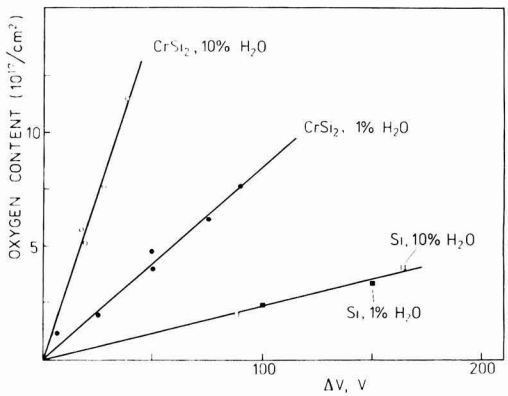

Fig. 4. Amount of oxygen incorporated during oxidation vs. effective potential drop in the film for $CrSi_2$ and Si, processed at constant current density of 3 mA/cm² in 1 and 10% H_2O glycol.

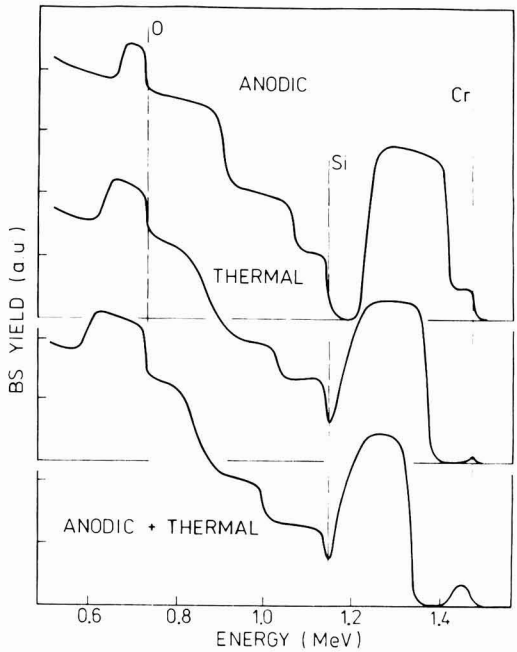

Fig. 6. Schematic BS spectra of chromium disilicide oxides. Anodic: 10% H_2O; V_{max} = 30V. Thermal: 90°C, wet, 30 min. Anodic followed by thermal.

oxide (11.5×10^{17} O at./cm^2 incorporated). A most interesting feature in these spectra is the observation of the Cr exclusion within the films. As far as the concentration level of Cr in the anodic oxide is concerned, only a trace amount is detected at the surface in the thermal case. In the double-oxidized sample, the Cr profile in the oxide seems to be divided into two regions: a surface region (1.4-1.45 MeV) with similar Cr concentration as in the anodic oxide, and a chromium-free layer underneath (1.35-1.4 MeV). The deleterious effect of the heat-treatment on the Si-$CrSi_2$ interface is also visible in the bottom spectra as broadening of the step at 0.85 MeV.

For a sample that was initially oxidized thermally, followed by anodic oxidation and finally thermal oxidation again, Cr was not detected in the oxide layer.

Discussion and Conclusion

The experiment described in this paper gives evidence that thick uniform oxides can be grown on chromium disilicide by anodic oxidation in ethylene glycol + potassium nitrate + water electrolyte. This may be regarded as the main result of this work. In view of a still inadequate understanding of the anodic processes, it is not possible to rigorously predict whether a given material in a given oxidizing medium will yield substantial oxide films (7, 8). Apart from valve metals such as Al, Hf, or Ta that oxidize with 100% current efficiency to voltages of at least 200V and sustain high electric fields ($>10^6$ V/cm), there exist many other materials that only partially fulfill these criteria. Such behavior is exhibited by silicon, which in organic electrolytes can be oxidized to several hundreds volts, though exhibiting a poor current efficiency suggesting the evolution of an appreciable amount of oxygen (9). On the other hand, chromium, which passivates to form Cr_2O_3 (10), has not been reported to produce thick oxides. In the electrolytes employed here, anodization of a pure Cr film does not induce any potential buildup, and creates a black spot on the Cr film surface containing no oxygen detectable by He backscatter spectrometry. Consequently, the $CrSi_2$ compound seems to be a rather complicated system as far as its anodic behavior is concerned. It is known that compounds or single phase alloys composed of valve or near-valve metals oxidize easily (11). The general situation becomes more complicated. Extensive studies on the anodization of GaAs (12), for example, show that several factors (*e.g.*, current density, oxide thickness) determine the composition and quality of the compound oxide formed. As for silicides, data on anodic oxidation are not available; the corrosion study of Cu, Co, and Ni silicides published in Ref. (13) was oriented primarily toward electrorefining and electrowinning from ores.

Summarizing the oxidation of $CrSi_2$ in glycol with a water content ranging from 1 to 10%, it can be concluded that the oxide has a fixed composition with a relative concentration of the constituents given by O/Si = 2.27 and Cr/Si = 0.17. Assuming that the film is composed of SiO_2 and Cr_2O_3 molecules, these numbers are consistent with a composition of 92% SiO_2 and 8% Cr_2O_3. This indicates that during the film formation, a substantial segregation takes place; preservation of the Cr/Si proportion in the silicide would require an oxide composition of 83% SiO_2, and 17% Cr_2O_3. Undoubtedly, the excess Cr is dissolved in the electrolyte. From the corrosion behavior of chromium, it is known that at higher potentials Cr atoms enter the electrolyte as CrO_4^{2-} anions (14). Also, chromium tends to lose its passivity rather easily in the presence of certain contaminants, especially chloride ions (9). The accumulation of Cr at the oxide surface observed when the 1% H_2O electrolyte was not stirred during the anodization suggests that the dissolution could be further reduced by saturating the solution with Cr ions. Alternatively, more Cr atoms are leached out of the film for electrolytes with greater water content. Hence, the Cr-to-Si ratio in the oxide can be controlled by choosing adequate experimental conditions.

The current efficiency for oxide formation on $CrSi_2$ increases from 3 to 16% when the H_2O content of the electrolyte is raised from 1 to 10%. This is probably associated with enhanced field-assisted ionic transport across the (porous) oxide. It is unlikely that there is suppression of the current contribution from parasitic reactions and/or electronic conduction, since the oxide breakdown voltage dropped with increasing H_2O content as one might anticipate (15). The ionic current associated with Cr dissolution also degrades the current efficiency.

Anodic vs. Thermal

Comparison between anodic and thermal oxidation gives further insight to the prevailing processes.

1. In both cases, the silicide dissociates readily. In thermal oxidation, the excess Cr diffuses through the silicide to the Si substrate, where it reacts and reforms silicide, hence preserving the silicide (16). But, during anodic oxidation, Cr diffuses through the growing oxide and a fraction of the dissociated Cr oxidizes while the rest is dissolved in the electrolyte.

2. Increasing the water content in the oxygen gas during thermal oxidation increases the oxidation rate. In anodic oxidation, a higher water content also results in a higher oxide formation rate. Possibly, it has to do with the oxygen containing molecule that diffuses through the oxide. In the thermal oxidation case, the effective diffusion coefficient changes, while in anodic oxidation it may be only the boundary condition at the oxide/electrolyte interface.

3. With the assumption that the heat capacity of the reactants and products are similar, the heat of the reaction ΔH at room temperature and at high temperatures (for thermal oxidation) never exceeds 3 kcal/gatom (17). So the thermodynamic predictions (3) are the same by definition for anodic and thermal oxidation. The observed different results are due to different kinetic limitations.

4. From the sequential thermal/anodic oxidation results, we conclude that (*i*) chromium cannot diffuse through thermal SiO_2 (see Fig. 6 and also the results of thermal/anodic/thermal), and (*ii*) an oxygen containing molecule diffuses through the anodic oxide driving wet oxidation faster than through thermal oxide. This conclusion is reached with the assumption that the thermal oxidation is parabolic rate limited. The predicted oxygen content of anodic and thermal oxides, assuming the same diffusion coefficient in anodic and thermal oxides, is 10^{17} $(5^2 + 8.5^2)^{1/2} = 9.9 \times 10^{17}$ O at./cm^2; while we get 11.5×10^{17} O at./cm^2, which is indicative of a faster diffusion rate in the anodic oxide.

Since no electrical characterization of the layers was conducted and no data on insulating properties of anodic Cr_2O_3 have been published, it is difficult to predict dielectric constant ϵ or breakdown voltage of the films. There are indications, however (9), that the anodic oxide of Cr, having a low formation field, should have a high ϵ value (> 40), as it is known that low ϵ values (*e.g.*, SiO_2) tend to be associated with high anodization fields and vice versa. Additionally, the breakdown voltage can be roughly estimated from the angstrom per volt values because they are nearly linearly correlated (18). (However, it is uncertain how the individual properties of SiO_2 and Cr_2O_3 will contribute in the mixed oxide.)

Acknowledgment

The authors would like to thank Dr. M. Croset (Thomson-CSF) and J. Siejka (Ecole Normall Superieuve) for fruitful discussions and final comments.

Manuscript submitted Dec. 26, 1984; revised manuscript received June 23, 1985.

The California Institute of Technology assisted in meeting the publication costs of this article.

REFERENCES

1. F. M. d'Heurle, in "VLSI Science and Technology/1982," C. Dell'Oca and W. M. Bullis, Editors, p. 194, The Electrochemical Society Softbound Pro-

ceedings Series, Pennington, NJ (1982).
2. M. Bartur and M-A. Nicolet, *This Journal*, **131**, 1118 (1984).
3. M. Bartur, *Thin Solid Films*, **107**, 55 (1983).
4. M. Croset, E. Petreanu, D. Samuel, G. Amsel, and J. P. Nadai, *This Journal*, **118**, 717 (1971).
5. A. Damjanovic and A. T. Ward, in "Electrochemistry," Vol. 6, J. O'M. Bockris, Editor, pp. 105-106, Butterworths, Boston (1976).
6. C.-D. Lien, L. S. Wieluński, and M-A. Nicolet, *Thin Solid Films*, **104**, 235 (1983).
7. L. Young, "Anodic Oxide Films," Academic Press, New York (1961).
8. S. P. Maminova and L. L. Odynets, *Elektrokhimiya*, **2**, 346 (1966).
9. A. K. Vijh, in "Oxides and Oxide Films," Vol. 2, J. W. Diggle, Editor, p. 1, Marcel Dekker, New York (1972).
10. N. Hackerman, *Z. Electrochem.*, **62**, 632 (1958).
11. G. C. Wood and S. W. Khoo, *J. Appl. Electrochem.*, **1**, 189 (1971).
12. M. Croset, J. Diaz, D. Dieumegard, and L. M. Mercandalli, *This Journal*, **126**, 1543 (1979).
13. A. T. Kuhn, H. Shalaby, and D. W. Wakeman, *Corros. Sci.*, **17**, 833 (1977).
14. T. P. Hoar, *Corros. Sci.*, **7**, 341 (1967).
15. S. Ikonopisov, *Electrochim. Acta*, **22**, 1077 (1977).
16. M. Bartur and M-A. Nicolet, *This Journal*, **131**, 371 (1984).
17. R. Pretorius, J. M. Harris, and M-A. Nicolet, *Solid State Electron.*, **21**, 667 (1978).
18. P. J. Harrop and D. S. Campbell, *Thin Solid Films*, **2**, 273 (1968).

Application of Kramers-Kronig Transforms in the Analysis of Electrochemical Systems

I. Polarization Resistance

Digby D. Macdonald* and Mirna Urquidi-Macdonald

Chemistry Laboratory, SRI International, Menlo Park, California 94025

ABSTRACT

A Kramers-Kronig transform that is useful for validating electrochemical and corrosion impedance data is employed to calculate the polarization resistance from the frequency-dependent imaginary component. Applications of the transform in the analysis of experimental impedance data for TiO_2-coated carbon steel in HCl/KCl solution at ambient temperature and for aluminum and Al-0.1P-0.1In-0.2-Ga-0.01Tl alloy in 4*M* KOH solution at 25°C are discussed.

Electrochemical techniques are now used extensively for investigating the mechanisms of electrochemical and corrosion processes, and for the measurement of corrosion rates (1-4). With respect to the latter, the advantages offered by electrochemical methods are that they can be applied *in situ* in hostile environments and that they require minimal manipulation of samples or post-test analyses. In all electrochemical methods for estimating corrosion rates, the objective is to measure the polarization resistance (R_p), from which the corrosion current and corrosion rate may be calculated using the Stern-Geary relationship (5, 6), provided that the Tafel constants are known.

A widely used technique for measuring R_p is impedance spectroscopy (1-3), in which the impedance of the corroding interface is measured over an effectively infinite bandwidth. The polarization resistance is therefore given by

$$R_p = |Z(j\omega)|_{\omega\to 0} - |Z(j\omega)|_{\omega\to\infty} \quad [1]$$

$$= \mathrm{Re}\,[Z(j\omega)]_{\omega\to 0} - \mathrm{Re}\,[Z(j\omega)]_{\omega\to\infty} \quad [2]$$

where Re denotes the real part of the complex impedance $Z(j\omega)$. In other words, the polarization resistance may be obtained from only the real component of the impedance, provided that it is measured over a sufficiently wide frequency range.

A critical problem in any impedance analysis involves validation of the data. This is particularly true because of the need to employ low amplitude excitations, and when working with inherently "noisy" systems. In this paper, we describe how Kramers-Kronig transforms may be used to estimate R_p from the imaginary component of the impedance. We also argue that comparison of the R_p value computed from the imaginary component via the K-K transforms with that derived directly from Eq. [2] represents a simple and convenient test of the validity of corrosion impedance data.

*Electrochemical Society Active Member.

Kramers-Kronig Transforms

Derivation of the Kramers-Kronig transforms (7-11) is based upon four quite general conditions of the system being fulfilled.

Causality.—the response of the system is due only to the perturbation applied, and does not contain significant components from spurious sources.

Linearity.—the perturbation/response of the system is described by a set of linear differential laws. Practically, this condition requires that the impedance be independent of the magnitude of the perturbation.

Stability.—the system must be stable, in the sense that it returns to its original state after the perturbation is removed.

Impedance values.—the impedance must be finite valued at $\omega\to 0$ and $\omega\to\infty$, and must be a continuous and finite valued function at all intermediate frequencies.

Provided that the above conditions are satisfied, the K-K transforms are purely a mathematical result, and do not reflect any other physical property or condition of the system. The transforms have been used extensively in the analysis of electrical circuits (9), but only rarely in the case of electrochemical systems (10-14).

Two of the more important transforms may be stated as follows (9, 11)

$$Z'(\omega) - Z'(\infty) = \left(\frac{2}{\pi}\right)\int_0^\infty \frac{xZ''(x) - \omega Z''(\omega)}{x^2 - \omega^2}\,dx \quad [3]$$

$$Z'(\omega) - Z'(0) = \left(\frac{2\omega}{\pi}\right)\int_0^\infty \left[\left(\frac{\omega}{x}\right)Z''(x) - Z''(\omega)\right]\cdot\frac{1}{x^2 - \omega^2}\,dx \quad [4]$$

where Z' and Z'' are the real and imaginary components of the impedance, respectively. Therefore, according to Eq. [2], the polarization resistance simply becomes

$$R_p = \left(\frac{2}{\pi}\right)\int_o^{\infty}\left[\frac{Z''(x)}{x}\right]dx \approx \left(\frac{2}{\pi}\right)\int_{x_{min}}^{x_{max}}\left[\frac{Z''(x)}{x}\right]dx \quad [5]$$

The forms of Eq. [3]-[5] deserve brief comment. First, it is evident that if the integral in Eq. [5] is to be convergent and finite, then $Z''(x)/x \to 0$ as $x \to x_{min} \to 0$ and $x \to x_{max} \to \infty$. The approximation is valid when the integrals from $x = 0$ to x_{min} and from x_{max} to ∞ are negligible compared with the integral from x_{min} to x_{max}. Second, it appears that the functions beneath the integrals in Eq. [3] and [4] contain singularities at $x = \omega$. However, as we show later (16), expansion of $(x^2 - \omega^2)^{-1}$ reveals that no singularity actually exists, and hence that the precision of integration is not compromised on passing through $x = \omega$, as is sometimes claimed.

In this study, we evaluate the integral in Eq. [5] in a piece-wise fashion by fitting a fifth-order polynomial to experimental Z'' *vs.* frequency (x) data using a least squares technique

$$Z''(x) = a_o + a_1x + a_2x^2 + a_3x^3 + a_4x^4 + a_5x^5 \quad [6]$$

The segments over which the integral is evaluated are chosen to coincide with changes in the sign of $Z''(x)$ and/or with changes in the gradient of $Z''(x)$ *vs.* frequency. The total integral is then evaluated as

$$R_p \approx \left(\frac{2}{\pi}\right)\sum\left[a_o\ln x + a_1x + \frac{a_2x^2}{2} + \frac{a_3x^3}{3} + \frac{a_4x^4}{4} + \frac{a_5x^5}{5}\right]_{x_i}^{x_{i+1}} \quad [7]$$

where i is the segment number. The limitation on the size of the segment is that the number of data points must exceed the highest order of the polynomial; we have found that a fifth-order polynomial is well suited for the cases discussed later in this paper.

The use of Eq. [5] in the analysis of impedance data for corroding systems has also been proposed by Kendig and Mansfeld (12) and was subsequently used by Mansfeld *et al.* (13). However, these workers propose that this equation is a basis for estimating polarization resistance data from the imaginary component of the interfacial impedance at high frequencies, thus avoiding the need to obtain impedance data at time consuming low frequencies. As noted by Kendig and Mansfeld (12), this approach is valid only if the plot of Z'' *vs.* log ω (*e.g.*, see Fig. 2) is symmetrical. This is true only for those systems that exhibit single semicircles in the complex plane that are either depressed or centered on the real axis; it is generally not valid for systems that exhibit multiple resistive/capacitive or resistive/inductive relaxations or for those systems that are best described in terms of a diffusional impedance or a transmission line. Accordingly, the method described by these workers is not expected to be generally applicable to experimental impedance data, except in those cases for which the condition noted above holds.

In this work, we adopt a more general approach in the application of Eq. [5], in that the integration is carried out over the entire frequency range and not just over the high frequency arm of the Z'' *vs.* log ω region, as proposed by Kendig and Mansfeld (12). Accordingly, our analysis is not restricted by the shape of the Z'' *vs.* log ω correlation, but should be applicable to all impedance data, provided that the four general conditions for a valid impedance are fulfilled and that the integral in Eq. [5] can be evaluated. This then forms the basis for using Eq. [5] as a diagnostic criterion for determining the validity of impedance data.

Analysis of Experimental Data

In order to illustrate the application of the K-K transformation method for validating polarization resistance measurements in particular and for verifying impedance data in general, we consider three systems: TiO_2-coated steel in a HCl/KCl solution of pH = 2 at 25°C, Al-0.1P-0.1In-0.2Ga-0.01Tl alloy in 4*M* KOH at 25°C, and pure aluminum (99.99%) also in 4*M* KOH at 25°C. The first system was chosen because it is characterized by an extensive (Z', Z'') *vs.* frequency data set that appears to satisfy the four conditions listed previously for a valid impedance. The second and third systems are included because aluminum corrodes rapidly in KOH solution, so that the condition of stability may not be satisfied. Furthermore, the third system exhibits characteristics that suggest the presence of experimental artifacts in the experimental impedance data. Accordingly, this system affords an opportunity to examine the sensitivity of the transform currently being considered to apparently "bad" data.

The complex plane plot for TiO_2-coated carbon steel in HCl/KCl solution, pH = 2, at 25°C is shown in Fig. 1. The high frequency region exhibits a slope of $\sim \pi/4$, indicating that the interfacial properties are dominated by a mass-transfer process. At lower frequencies, the locus of data points curls over and ultimately intercepts the real axis at a frequency of less than 0.01 Hz. The measured polarization resistance is readily computed from the high frequency and low frequency intercepts as $R_p = 158.48 - 1.35 = 157.13\Omega$. The experimental Z'' *vs.* $\log_{10} x$ (x = frequency in hertz) data are plotted in Fig. 2, and demonstrate that this system exhibits a single dispersed relaxation centered about $x = 0.58$ Hz. Also plotted on this figure are data calculated from the least squares piecewise fit of Eq. [6] to the experimental data. In this case, five segments were used, corresponding to one for $x < 0.58$ Hz and four for $x > 0.58$ Hz. The value of R_p calculated from the integral (Eq. [7]) was found to be 158.20Ω which differs from the experimental value noted above by less than 0.7%. This error is of the same order (1-1.5%) as that found by transforming data calculated from equivalent electrical circuits; systems that we know *a priori* satisfy the conditions for a valid impedance. Thus, the observed error may be attributed principally to the algorithm itself.

In the second case Al-0.1P-0.1-In-0.2-Ga-0.01Tl alloy in 4*M* KOH at 25°C, (Fig. 3 and 4), both the complex plane and the Z'' *vs.* $\log_{10} x$ plots demonstrate the existence of resistive/capacitive and resistive/inductive relaxations at high and low frequencies, respectively. The data plotted in Fig. 4 were analyzed in three segments: A-B, B-C, and C-D. Agreement between the experimental data and that recalculated from Eq. [6] is clearly less exact in this case than in the previous one. Also, it was necessary to use much wider segments in the evaluation of the integral in Eq. [5]. The calculated R_p value was found to be 82.4Ω compared with $90 \pm 5\Omega$ obtained by extrapolating the

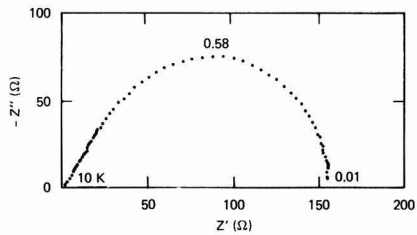

Fig. 1. Complex plane impedance plot for TiO_2-coated carbon steel in HCl/KCl solution. pH = 2. T = 25°C. The numbers refer to frequencies in hertz.

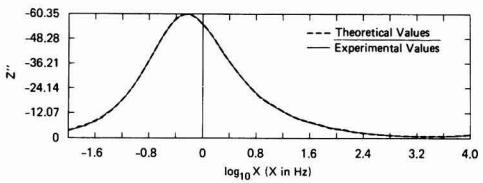

Fig. 2. Plot of Z'' *vs.* $\log_{10} x$ (x in hertz) for TiO_2-coated carbon steel in HCl/KCl solution. pH = 2. T = 25°C. Dashed line: polynomial fit (Eq. [6]). Solid-line: experimental data.

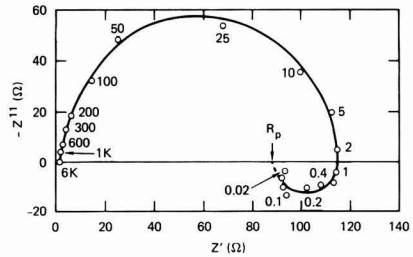

Fig. 3. Impedance diagram for Al-0.1P-0.1In-0.2Ga-0.01Tl alloy in 4M KOH at 25°C and at the open-circuit potential (−1.760V vs. Hg/HgO). Numbers next to the experimental points are frequencies in hertz.

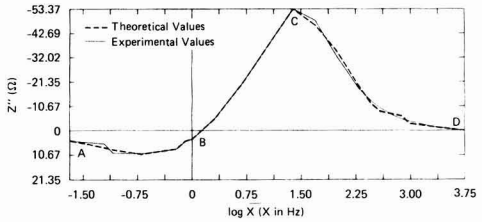

Fig. 4. Plot of Z″ vs. log x (x in hertz) for Al-0.1P-0.1In-0.2Ga-0.01Tl alloy in 4M KOH at 25°C under open-circuit conditions (E = −1.76V vs. Hg/HgO). Dashed line: polynomial fit (Eq. [6]). Solid line: experimental data.

measured impedance to intercept the real axis in the limit of zero frequency. We believe that the difference is significant, and that it reflects not only an overall lower quality of data, as expected for a rapidly corroding system, but also a less extensive data set, particularly in the critically low frequency region. Nevertheless, the transform is quite satisfactory, considering the dubious fulfillment of the stability condition.

The final case considered in this paper (Fig. 5 and 6) was chosen because the system apparently exhibits a negative resistance at high frequencies and multiple intersecting loops at low frequencies. This latter characteristic is frequently observed experimentally, and is predicted

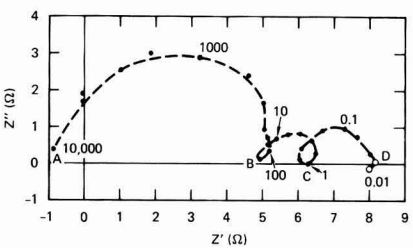

Fig. 5. Complex plane impedance plot for pure Al (99.99%) in 4M KOH at 25°C. E = −1.56V vs. Hg/HgO. Numbers next to the experimental points are frequencies in hertz.

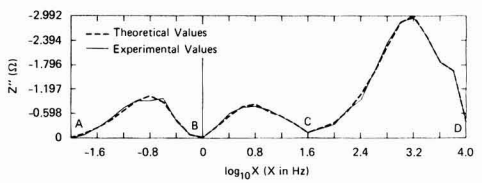

Fig. 6. Plot of Z″ vs. $\log_{10} x$ (x in hertz) for Al in 4M KOH at 25°C. E = −1.56V vs. Hg/HgO. Dashed line: polynomial fit (Eq. [6]). Solid line: experimental data.

theoretically for certain dissolution reactions (12), so that verification that data of this type correctly transform is a matter of considerable interest. The negative resistance at high frequencies is almost certainly an experimental artifact, presumably arising from poor cell design. In carrying out the transformation, a three-segment (A-B, B-C, C-D, Fig. 6) integration was used to yield an R_p value of 7.55Ω. This value is significantly lower (by 18%) than the value of 9.2Ω obtained by extrapolating the high and low frequency arms to the real axis. Part of the difference may be due to the fact that the data were not obtained at a sufficiently low frequency to detect an inductive loop; note that the data point at 0.01 Hz does in fact lie below the real axis. However, a more likely explanation is that the real component of the impedance is distorted by some cause that results in the appearance of an apparent negative resistance at high frequency. Indeed, if it is assumed that the high frequency data intersects the real axis at the origin, then an experimental value for R_p of 8.2 ± 0.5Ω is obtained. This value is in much better agreement with that calculated above using the K-K transform.

Discussion

The analyses described above demonstrate that the Kramers-Kronig transform, as embodied in Eq. [5], is an accurate and convenient tool for assessing the validity of electrochemical impedance data.

From the present analysis, it is evident that the quality of electrochemical impedance studies depends heavily upon the size and accuracy of the experimental data set, as exemplified by the first example analyzed in this study. It is also apparent that psuedoinductive impedances (second case), and possibly those exhibiting intersecting loops (third case), also transform correctly, and hence may be regarded as valid characteristics of an observed impedance function. Finally, the transform apparently is sensitive to experimental artifacts that may, for example, lead to the distortion of one component; in the third case analyzed here, the distortion results in negative resistance at high frequencies. It is important to note, however, that the entire weight of the validation test afforded by Eq. [5] is placed on a knowledge of the real and imaginary components of the impedance over an effectively infinite frequency bandwidth. Since reliable impedance data for the low frequency region are not always available, considerable care must be exercised in applying Eq. [5] as a quantitative validity test. It is possible that more accurate and convenient validation analyses might be developed by considering the full set of K-K transforms, including Eq. [3] and [4], in order to deemphasize the importance of the low frequency region. This possibility is currently being explored, and will be discussed in the second part of this series (16).

Acknowledgments

Financial support of this work from the Department of Energy and Eltech Systems, Incorporated, through Contract LNL-1806205, is greatly appreciated. The authors also thank Dr. M. C. H. McKubre for supplying data on TiO_2-coated carbon steel and Ms. Silvia Real for some of the experimental data for aluminum.

Manuscript submitted Feb. 8, 1985; revised manuscript received June 10, 1985.

SRI International assisted in meeting the publication costs of the article.

REFERENCES

1. D. D. Macdonald and M. C. H. McKubre, in "Modern Aspects of Electrochemistry," Vol. 14, J. O'M. Bockris, B. E. Conway, and R. E. White, Editors, p. 61, Plenum Press, New York (1982).
2. D. D. Macdonald and M. C. H. McKubre, in "Electrochemical Corrosion Testing," STP727, ASTM, Philadelphia (1981).
3. D. D. Macdonald, "Transient Techniques in Electrochemistry," Plenum Press, New York (1977).
4. A. J. Bard and L. R. Faulkner, "Electrochemical Methods," John Wiley and Sons, New York (1980).

5. M. Stern and A. L. Geary, *This Journal*, **104,** 56 (1957).
6. F. Mansfeld, *Adv. Corr. Sci. Technol.*, **6,** 163 (1976).
7. H. A. Kramers, *Physiol. Zool.*, **30,** 522 (1929).
8. R. de L. Kronig, *J. Opt. Soc. Am.*, **12,** 547 (1926).
9. H. W. Bode, "Network Analysis and Feedback Amplifier Design," Chap. 14, Nostrand, New York (1945).
10. V. A. Tyagai and G. Ya. Kolbasov, *Elektrokhimiya*, **8,** 59 (1972).
11. R. L. Van Meirhaeghe, E. C. Dutoit, F. Cardon, and W. P. Gomes, *Electrochim. Acta*, **21,** 39 (1976).
12. M. Kendig and F. Mansfeld, *Corrosion*, **39,** 466 (1983).
13. F. Mansfeld, M. W. Kendig, and W. J. Lorenz, *This Journal*, **132,** 290 (1985).
14. C. D. S. Tuck, Abstract 191, p. 276, The Electrochemical Society Extended Abstracts, Vol. 84-2, New Orleans, LA, Oct. 7-12, 1984.
15. M. Keddam, O. R. Mattos, and H. Takemouti, *This Journal*, **128,** 257 (1981); *ibid.*, **128,** 266 (1981).
16. M. Urquidi and D. D. Macdonald, To be submitted to *This Journal*.

Anodic Oxide Growth on Aluminum in the Presence of a Thin Thermal Oxide Layer

Walter J. Bernard* and Steven M. Florio

Sprague Electric Company, North Adams, Massachusetts 01247

ABSTRACT

The presence of a thin film of thermal oxide on the surface of aluminum promotes the growth of additional crystalline (γ'-Al_2O_3) oxide during subsequent anodization in an aqueous phosphate solution. It was shown through the use of phosphorus-32 tracer and chemical thinning procedures that the anodic crystalline oxide is formed beneath a discrete, continuous layer of amorphous oxide, and that the original thermal oxide is incorporated in the anodic crystalline film. The concentration of phosphorus in the amorphous layer is greater than that which occurs in the absence of crystalline oxide. Evidence is given that the occluded phosphorus species has some ionic mobility in both oxides.

The anodic oxidation of aluminum in aqueous borate or phosphate solutions generally results in the growth of oxide films that appear amorphous by x-ray or electron diffraction. Under some conditions, however, these dielectric films may display some degree of crystallinity. For example, if the metal is treated with hot water before anodic oxidation to a high voltage in aqueous borate, a portion of the dielectric contains crystals of γ'-Al_2O_3 (1, 2). This has been studied in some detail. Low voltage films grown in citric acid after a boiling water treatment have also been shown to have a partial crystalline character (3).

Crystalline oxide growth may also be promoted by the use of a brief thermal oxidation prior to the anodic oxidation (4, 5). The thermal oxide, identified as γ-Al_2O_3 (6), has been shown (7, 8) to consist of small crystallites that nucleate below the pre-existing amorphous oxide, spreading laterally to cover the entire metal surface.

The presence of the thermal oxide modifies the mechanism of anodic oxidation so that the growth of additional crystalline oxide is promoted, and it may also affect the composition of the layers of oxide that comprise the overall complex film structure. That such compositional modification can be brought about by the presence of an existing film was shown (9) in the case of anodic oxidation of aluminum in an aqueous phosphate solution. When the surface is free of oxide the dielectric contains substantial amounts of phosphorus (10, 11), but when the foil is first covered with a hydrous oxide layer the subsequently formed anodic oxide is essentially free of phosphorus. One purpose of this study was to see if the thermal oxide behaves analogously.

The location of the thermal oxide during anodization may be conveniently observed by the use of a pretreatment of the foil in hot phosphoric acid containing ^{32}P. As a result of this treatment, the aluminum surface becomes covered with a monolayer of the acid (or other phosphate species). This phosphorus is retained during thermal oxidation, becoming incorporated into the thin thermal film and thereby acts as a marker during the following anodization. The location of the tagged thermal oxide may be determined by measuring the amount of residual ^{32}P during chemical sectioning of the composite films.

Further information on the mechanism of the reaction was obtained by carrying out the foil pretreatment in nonradioactive phosphoric acid; in this case, the thermal step was followed by anodization in a radioactive solution of ammonium dihydrogen phosphate.

*Electrochemical Society Active Member.

Experimental

The aluminum specimens were cut from 76 μm thick Alcoa foil of 99.99% purity. Prior to phosphoric acid treatment, the specimens were electropolished in a perchloric acid/acetic anhydride mixture for 150s at 10 mA/cm^2, and then rinsed with distilled water and dried with acetone. This electropolishing procedure produces a smooth metal surface covered with a very thin (<20Å) oxide film (12).

Carrier-free ^{32}P isotope was obtained from New England Nuclear as H_3PO_4 in water. A 2.0 mCi portion of this acid was incorporated into a 0.01*M* solution of H_3PO_4; a similar 0.01*M* H_3PO_4 solution without tracer was also prepared. A second 2.0 mCi portion of the radiolabeled acid was incorporated into a 0.01*M* solution of ammonium dihydrogen phosphate (ADP); a similar 0.01*M* ADP solution without tracer was also prepared.

Standards for determining activity were prepared by the uniform distribution of an aliquot (either 50 or 100 μliter) of the active solutions, in small droplets, over an area of aluminum equivalent to that used for counting experimental specimens. The phosphoric acid for these standards was neutralized with 0.01*N* NaOH before use. The foils were then dried at 60°C before counting.

For all radioactive specimens, a circular area of 7.9 cm^2 was measured with a Geiger-Müller counter. A tantalum mask, 0.76 mm thick, served to define the counting area. The aluminum foil itself was transparent to β-radiation emitted by ^{32}P, and hence both sides of the experimental samples were counted simultaneously.

Acid pretreatment was carried out in vigorously boiling solutions of 0.01*M* H_3PO_4 for 90s. These foils were then thoroughly washed with distilled water, dried with acetone, weighed, and counted when applicable. The weight changes for this step and all subsequent operations were determined with a digital microbalance. Specimens were oxidized in air at 600°C for 5 min, and then reweighed and counted.

After thermal oxidation, the active specimens were anodized in nonactive 0.01*M* ADP solution; foils that had been pretreated with nonradioactive H_3PO_4, on the other hand, were anodized in ADP solutions containing the ^{32}P tracer.

Anodizations were performed in glass-jacketed cells, using Teflon supports for platinized-platinum counter-electrodes. Stirring of the electrolyte was accomplished with a magnetically driven stirring bar. A constant-temperature liquid pumped through the cell jacket maintained the anodizing solution at 85° ± 0.2°C. The current density was 1.0 mA/cm², and during the constant-voltage period it was allowed to decay to 0.05 mA/cm².

Measurements of series capacitance, at 120 Hz, were made in a similar cell using aqueous ammonium borate at 25°C.

The distribution of radiotracer in the films was determined by dissolving the films stepwise in a stirred solution of 2% CrO_3/5% H_3PO_4 at 65°C. This solution has been shown to attack amorphous Al_2O_3 uniformly at a moderately fast rate, with extremely little attack on the metal (13). However, the rate of attack on crystalline Al_2O_3 has been shown to be much slower (14, 15). As such, this procedure is effective for discriminating between the two types of oxide.

In addition to the determination of weight loss and residual radioactivity following the chemical sectioning steps, capacitance and remaining barrier voltage were obtained to give a measure of the film thickness. The barrier voltage was determined by applying a small constant current (*i.e.*, 10% of the formation current density) in the original anodizing electrolyte, and observing the knee of the V-t curve. The point which is taken as V_R is the beginning of the constant slope corresponding to the calculated rate of new film growth. This is found by extrapolation of the straight line to the point of curvature, and is indicated by vertical lines on the tracings in Fig. 3. For short chemical treatment times, the break in the curve is satisfactorily sharp, and observations were reproducible to a volt or two. For longer periods, where film undercutting may occur, there is correspondingly less certainty in the value.

Results and Discussions

The amount of thermal oxide grown on aluminum depends on both the temperature and the reaction time. Crystalline oxide can be formed at temperatures as low as 450°C (6), but more complete coverage of the foil is achieved under more vigorous conditions; this, in turn, increases the amount of crystalline anodic oxide. Five minutes at 600°C gave satisfactory results for the work reported here.

Under the experimental conditions used, it is believed that after thermal treatment the oxide present on the metal surface is almost entirely crystalline. The exposure to dilute phosphoric acid serves to dissolve the natural amorphous oxide as well as to create an adsorbed layer of phosphate. The oxide-free aluminum is thus largely protected from regrowth of oxide until exposure to temperatures which permit the growth of crystalline oxide. This sequence of events is supported by weight measurements showing that the loss in weight during exposure to phosphoric acid corresponds to the removal of the original amorphous film; no substantial weight gain occurs until high temperature oxidation takes place. Only a small fraction of the resulting film is soluble in phosphoric acid. Details will be given in a future publication.

In the first series of experiments foil samples were treated with active H_3PO_4, thermally oxidized, and then anodized in nonactive ADP. When these foils were subjected to the chemical sectioning procedure, the ^{32}P activity and oxide weight varied with time, as shown in Fig. 1.

The duplex nature of the anodic films can be deduced from these results. It is apparent from the weight loss curve that a soluble oxide is positioned above an insoluble layer, as shown by the abrupt reduction in weight loss after 2 min. The insoluble layer was identified by electron diffraction as γ'-Al_2O_3, confirming earlier reports (14, 16). In addition, the fact that only about 10% of the original activity is lost during chemical stripping shows that the bulk of the original adsorbed species has become a constituent of the insoluble crystalline oxide. This can only have come about by nearly complete incorporation

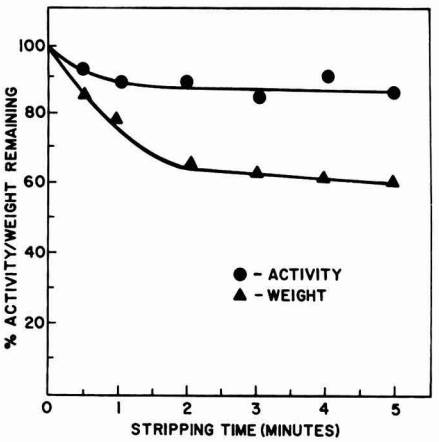

Fig. 1. Loss of activity and weight during chemical sectioning of 100V ADP films. Pretreated with active H_3PO_4 and then thermally oxidized.

of phosphorus in the thermal oxide that was grown at 600°C; upon anodization this thermal oxide, which enhances the anodic growth of γ'-Al_2O_3, occupies the same location in the complex film as the thicker crystalline film.

It is not clear why the thermal oxide failed to tie up the entire layer of adsorbed phosphoric acid, allowing about 10% of the phosphorus to be removed during the early stage of the chemical sectioning. It might have been reasonable to expect the γ'-Al_2O_3 film to have sufficient mass to accommodate all the phosphorus available; using a density of 3.6 g/cm³ (5) and an oxide weight of 5.7 μg/cm², the film thickness is estimated to be about 160Å.

The very small amount of phosphorus introduced as a marker has apparently no significant effect on the mechanism. From activity data, it was calculated that only about 0.035 μg/cm² was present before thermal treatment, and that about 0.030 μg/cm² remained in the final duplex oxide before chemical sectioning. These figures were essentially independent of the anodization voltage, as shown in Table I.

The curves of weight loss and residual activity do not show the limiting horizontal lines which would be anticipated for ideal behavior. This is most likely a result of the incompletely continuous nature of the crystalline oxide, which permits some degree of penetration and undercutting of the crystalline particles, followed by mechanical dislodging of these grains.

The curves in Fig. 2 provide further evidence for the layered structure of the dielectric film. Separate foil specimens were chemically stripped and reanodized to determine the amount of barrier remaining (V_R), as well as the capacitance of the remaining film. The shape of the V_R curve is similar to that of the weight loss curve of Fig. 1, and for a 100V film it indicates that about 35% of the original barrier consists of the easily soluble amorphous oxide. The remainder of the film appears to be largely crystalline, although the presence of an additional thin amorphous layer at the metal/oxide interface is likely (3), and is supported by the manner in which the crystalline

Table I. Weight of phosphorus on aluminum surface (ng/cm²)

	Anodization voltage		
	50V	100V	150V
Before 600°C treatment	38	35	33
After 600°C treatment	34	36	35
Final weight in oxide	30	29	27

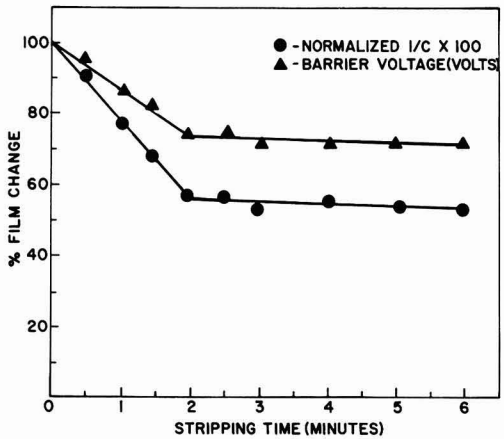

Fig. 2. Change in barrier voltage and reciprocal capacitance during chemical sectioning of 100V ADP films. Pretreatment as in Fig. 1.

film may be undercut after extended chemical stripping. When carried out for sufficiently long periods, it was possible to observe minute particles of insoluble oxide suspended in the stripping solution.

Reanodization curves also demonstrate that the crystalline layer is not a completely inpenetrable barrier, but consists, in part at least, of some defects and channels in which amorphous film is grown. A typical reanodization curve, shown in Fig. 3, demonstrates that a small but significant charge is required to refill gaps in the crystalline layer when chemical sectioning approaches the amorphous/crystalline interface. A 30s stripping (curve I) required only 6.8 mC/cm² to recharge the film to 97V, corresponding to 3.6% of the charge passed during the original formation to that voltage. A longer reaction time of 120s, on the other hand, required the passage of 9.3 mC/cm² to reach the residual barrier level of 71V (curve II); in terms of anodization charge, this amounts to 6.6% of that needed to form a 71V film.

Figure 2 also shows the dependence of reciprocal capacitance on stripping time; a constant value of 1/C is reached after about 120s, the same point at which V_R becomes constant. The data in this plot represent measurements made immediately after reanodization, which gave stable reproducible values. If measured before reanodization, however, capacitances were unstable and fictitiously high, either through the dissolution of intergranular amorphous oxide, or because of some degree of dielectric instability revealed by the chemical treatment. This type of dielectric relaxation is commonly observed in high voltage films that have been formed in the presence of a hydrous oxide layer, but has also been observed with low voltage films of the type described here (2, 17).

The two forms of anodic oxide differ not only in their degree of crystallinity, but also in other properties. The growth constant (reciprocal field strength) of the crystalline layer is obviously greater than that of the amorphous film, and it should be possible to estimate its value from the curves in Fig. 2 and from the appropriate physical constants of the amorphous oxide, *i.e.*, 14.8 Å/V[1] and ϵ = 8.5 (18).

The voltage across the crystalline film is 71V (assuming that there is only a negligible amount of amorphous oxide at the metal interface), while its reciprocal capacitance is only 54% of the total film. If its dielectric constant is 8.6, as reported (5), its growth rate is calculated as 7.2 Å/V. This suggests that the field in the crystalline oxide is much higher than has been reported previously; weight measurements, on the other hand, lead to different results. From the curve in Fig. 1, and using an oxide density of 3.61 g/cm³ (5) for the crystalline layer, the growth rate is calculated to be 9.2 Å/V, in good agreement with Alwitt and Takei (5).

These discrepant results could perhaps be reconciled if a higher value of ϵ for γ'-Al_2O_3 were used. In view of the relatively high values that have been published for polycrystalline aluminas—10.5 and higher (19)—it would not be surprising to find the value for γ'-Al_2O_3 to be somewhat greater than 8.6.

The second set of experiments involved the use of active phosphorus in ADP solution to tag the growing anodic film. The amount of phosphorus takeup (Fig. 4) was constant with formation voltage up to 150V, as was ob-

[1]The cited paper reported 12.3 Å/V at a current density of 0.05 mA/cm² at 25°C. From this value, we have made an estimate of the thickness of the amorphous film at 85°C.

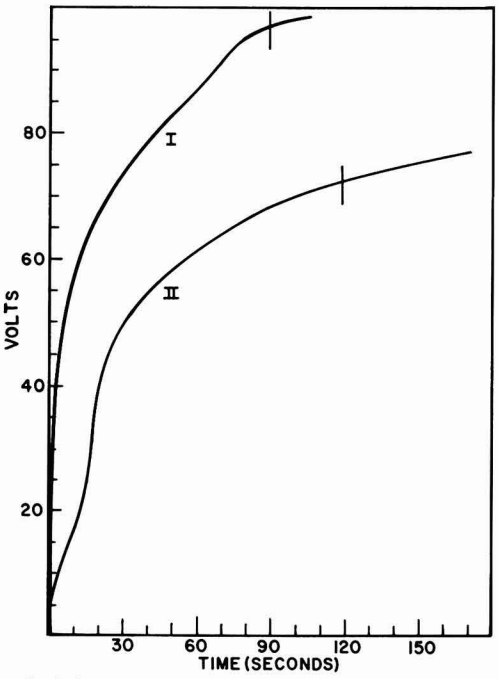

Fig. 3. Recorder tracings of reanodization of 100V ADP films chemically stripped for 30s (curve I) and 120s (curve II). Foils pretreated as in previous figures.

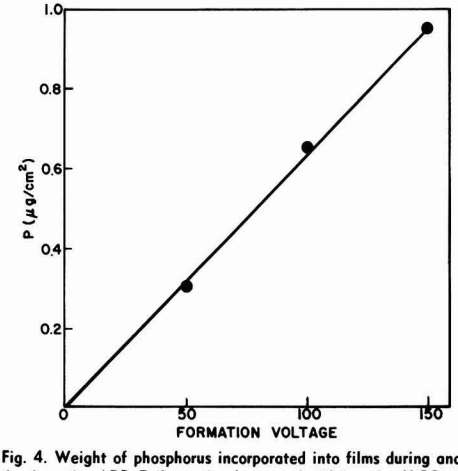

Fig. 4. Weight of phosphorus incorporated into films during anodization in active ADP. Foils previously treated with inactive H_3PO_4, followed by thermal oxidation.

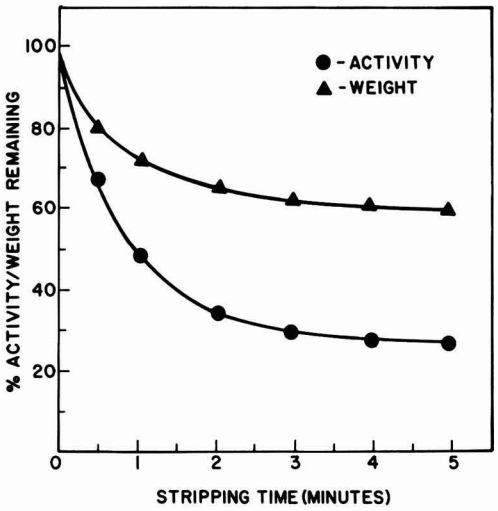

Fig. 5. Loss of activity and weight during chemical sectioning of 100V films anodized in active ADP. Foils pretreated as in Fig. 4.

served earlier in films formed in the absence of a thermal oxide (10), but the distribution was quite different. Figure 5 shows the rate at which activity was lost in the chemical stripping solution; the rate of weight loss is also depicted, in good agreement with the previous independent set of measurements. The bulk of the phosphorus (about 65%) is in the outer amorphous layer, but a significant amount is incorporated in the crystalline film.

The concentration of phosphorus in the amorphous layer is influenced by the presence of the underlying crystalline material. When anodization conditions are chosen so that a fully amorphous oxide is grown, a 100V film has a [P] of 640 ng/cm^2 (20, 21). But since phosphorus is found only in the outer 70% of the film, where it is homogeneously distributed (10), the concentration may be better expressed as 9.1 ng/cm^2 for each volt of film. In the case of the duplex film described in the paper, however, the outer amorphous layer does not appear to be as homogeneous, judging from the absence of a sharp transition in the rate of activity lost during chemical sectioning, and the phosphorus concentration is much greater. From the activity data, it was calculated to be 19 ng/cm^2-V or about twice that found in the conventional film. The crystalline portion of the film, on the other hand, has a [P] of only 4.4 ng/cm^2-V.

These data suggest that the crystalline oxide acts as a conductor not only for aluminum ions during film growth, but also for oxygen and phosphate ions. The presence of phosphorus in that portion of the dielectric cannot come about by direct occlusion from solution as it does for the outer amorphous film, since the crystalline layer is never in contact with the solution once the first contribution to film growth by metal ion migration takes place. The results cannot therefore be reconciled to the picture of P as an inert marker, but rather as a film component with ionic mobility.

The difference in the phosphorus concentration in the amorphous and crystalline oxide forms can thus be attributed to its lower mobility in the γ'-modification. In the case of a wholly amorphous film, it was found (10) that the rate of phosphorus incorporation from the advancing oxide/solution interface is constant at constant current density; the rate of phosphorus diffusion into the phosphorus-free region grown at the metal/oxide interface is such that a uniform distribution results in the outer layer of the duplex film. In the present case, however, because the diffusing ions encounter the environment of γ'-Al_2O_3 in which mobility is sharply reduced, the concentration in the amorphous layer is increased.

It is also significant that the total amount of phosphorus in the overall film structure is greater than the parallel case with an all-amorphous film, the figures being 950 and 640 ng/cm^2, respectively. This can be accounted for if the contribution to film growth by aluminum ion motion is greater in the presence of the crystalline film, since this would lead to greater growth at the electrolyte interface and increased inclusion of phosphate ion.

A more detailed description of the process—in particular, the transport numbers of the ions—is not justified by the available data. If the P species is not an immobile marker, the measurement of its profile in the outer layer alone cannot be used to estimate transport numbers. A concentration profile of P in the crystalline films by means other than chemical sectioning might do much to throw more light on the overall process.

Manuscript submitted April 3, 1985; revised manuscript received May 27, 1985. This was Paper 54 presented at the Toronto, Ontario, Canada, Meeting of the Society, May 12-17, 1985.

Sprague Electric Company assisted in meeting the publication costs of this article.

REFERENCES

1. R. S. Alwitt, *This Journal*, **114,** 843 (1967).
2. R. S. Alwitt and C. K. Dyer, *Electrochim. Acta*, **23,** 355 (1978).
3. C. Crevecoeur and H. J. deWit, Abstract 174, p. 413, The Electrochemical Society Extended Abstracts, Vol. 78-1, Seattle, Washington, May 21-26, 1978.
4. C. Crevecoeur and H. J. DeWit, Paper 132 presented at the 27th Meeting of the International Society of Electrochemistry, Zurich (1976).
5. R. S. Alwitt and H. Takei, in "Passivity of Metals and Semiconductors," M. Froment, Editor, p. 741, Elsevier, Amsterdam (1983).
6. A. F. Beck, M. A. Heine, E. J. Caule, and M. J. Pryor, *Corros. Sci.*, **7,** 1 (1967).
7. P. E. Doherty and R. S. Davis, *J. Appl. Phys.*, **34,** 619 (1963).
8. J. J. Randall, Jr., and W. J. Bernard, *ibid.*, **35,** 1317 (1964).
9. R. S. Alwitt and W. J. Bernard, *This Journal*, **121,** 1019 (1974).
10. J. J. Randall, Jr., and W. J. Bernard, *Electrochim. Acta*, **20,** 653 (1975).
11. M. F. Abd Rabbo, J. A. Richardson, and G. C. Wood, *Corros. Sci.*, **16,** 689 (1976).
12. Z. Fujimura, *J. Electrochem. Soc. Jpn.*, **31,** 7 (1963).
13. J. E. Lewis and R. C. Plumb, *This Journal*, **105,** 496 (1958).
14. D. J. Stirland and R. W. Bicknell, *ibid.*, **106,** 482 (1959).
15. K. Shimizu, S. Tajima, G. E. Thompson, and G. C. Wood, *Electrochim. Acta*, **25,** 1481 (1980).
16. N. F. Jackson and P. D. S. Waddell, *J. Appl. Electrochem.*, **2,** 345 (1972).
17. W. J. Bernard and P. G. Russell, *This Journal*, **127,** 1256 (1980).
18. W. J. Bernard and J. W. Cook, *ibid.*, **106,** 643 (1959).
19. "Alumina as a Ceramic Material," W. H. Gitzen, Editor, p. 78, The American Ceramic Society, Columbus, OH (1970).
20. R. C. Plumb, *This Journal*, **105,** 498 (1958).
21. H. Takahashi, K. Fujimoto, H. Konno, and M. Nagayama, *ibid.*, **131,** 1856 (1984).

Anodic Oxidation of Reductants in Electroless Plating

Izumi Ohno,[1] Osamu Wakabayashi,[2] and Shiro Haruyama

Tokyo Institute of Technology, Faculty of Engineering, O-okayama, Meguro-ku, Tokyo 152, Japan

ABSTRACT

The anodic oxidation of reductants (hypophosphite, formaldehyde, borohydride, dimethylamine borane, and hydrazine) was studied on different metal electrodes (Au, Pt, Pd, Ag, Cu, Ni, and Co) at various temperatures, with special interest in the catalytic aspect of electroless plating. The rate of the anodic oxidation strongly depended on the pH value, the concentration of reductants, and the nature of the metal electrode. The catalytic activities of the metals for the anodic oxidation of different reductants were evaluated by the potentials at a reference current density. The order of the catalytic activity with metal varied depending on the nature of the reductants. The catalytic activity series thus obtained can be utilized for choosing the reductant suitable for the metal to be deposited. Arrhenius plots of the anodic currents on different metals at a reference potential yielded their respective straight lines. Some correlations were observed between the catalytic activity and the activation energy. The catalytic activity series was discussed in connection with that for hydrogen electrode reaction.

It is widely accepted that electroless plating proceeds along the electrochemical mechanism as the simultaneous reaction of cathodic metal deposition and anodic oxidation of reductant (1-5). The electrochemical conditions for electroless plating taking place are, first, the oxidation potential of the reductant's being less noble to the reversible potential of the metal to be deposited, and, second, the metal's having enough catalytic activity for the anodic oxidation taking place with reasonable rate. The first condition can be readily provided by simple thermodynamic consideration. Therefore, the rate of anodic oxidation of the reductant is, in some sense, a dominant factor in electroless plating.

The reductants used in electroless plating have a special feature. A limited variety of reductants is used in an electroless process, *e.g.*, hypophosphite, formaldehyde, borohydride, dialkylamine borane, and hydrazine. Electroless plating usually accompanies hydrogen evolution, the rate of which is not directly related to that of metal deposition. Different reaction mechanisms have been proposed to account for the hydrogen evolution during electroless plating: (*i*) the proton discharge mechanism (6, 7), (*ii*) the hydroxide mechanism (8, 9), and (*iii*) the hydride ion mechanism (10, 11) and atomic hydrogen mechanism (12, 13). It was found by Gorbunova *et al.* (14) and Holbrook *et al.* (15) that the hydrogen evolved during electroless plating was originated mainly from the reductant molecule. Electroless plating proceeds mostly on certain metals that are known to be hydrogenation-dehydrogenation catalysts. It was reported by Gorbunova *et al.* (16) and Pearlstein *et al.* (17) that the poison for hydrogenation catalysts such as thiourea and mercaptobenzothiazole functions as stabilizer in an electroless process.

Various reaction mechanisms were presented for respective electroless processes (18-25). It was suggested by several workers that the key step in the reaction is the dissociative chemisorption to form adsorbed atomic hydrogen and an adsorbed anion radical. Van der Meerakker (26) claimed that all the electroless plating processes can be explained by a universal mechanism with the dehydrogenation of the reductant as the first step, thus

$$RH \longrightarrow R + H \quad [1]$$

$$R + OH^- \longrightarrow ROH + e^- \quad [2]$$

$$H + H \longrightarrow H_2 \quad [3]$$

$$H + OH^- \longrightarrow H_2O + e^- \quad [4]$$

$$M^{n+} + ne^- \longrightarrow M \quad [5]$$

where RH represents the reductants. Reactions [3] and [4] represent the recombination and ionization of adsorbed atomic hydrogen, respectively, which can occur in parallel. Van den Meerakker also advocated that the catalytic aspect in electroless plating is originated from the catalytic property of the metal for reaction [3]. There are, however, only a few works on the anodic oxidation of the reductant in connection with the catalytic activity of the metal.

The aim of this paper is to establish the anodic oxidation behavior of the reductants on different metal electrodes with special interest in the catalytic activities of the metals in electroless plating.

Experimental Details

Polarization experiments were carried out on gold, platinum, palladium, silver, copper, nickel, and cobalt electrodes in the appropriate complex solutions containing sodium hypophosphite, formaldehyde, sodium borohydride, dimethylamine borane, and hydrazine, respectively. The standard compositions of the baths and the experimental conditions are summarized in Table I. Platinum, gold, and silver plates of surface area 0.4 cm² were used as the working electrodes. A platinum plate of the same surface area plated with the metal under investigation was also used as the working electrode. The counter-

Table I. Electrolytic solutions and experimental conditions for anodic oxidation of reductants

Reductant	Electrolyte	
NaH_2PO_2	NaH_2PO_2	0 ~ 0.4*M*
	Na-citrate	0.2*M*
	H_3BO_3	0.5*M*
	*p*H	7.0 ~ 9.5
	Temperature	290.2 ~ 350.2 K
	Air atmosphere	
HCHO	HCHO	0 ~ 1*M*
	EDTA · 2Na	0.175*M*
	*p*H	11.0 ~ 13.2
	Temperature	278.2 ~ 330.2 K
	Nitrogen atmosphere	
$NaBH_4$	$NaBH_4$	0.01 ~ 0.1*M*
	EDTA · 2Na	0.175*M*
	*p*H	11.5 ~ 13.8
	Temperature	277.2 ~ 320.2 K
	Nitrogen atmosphere	
DMAB*	DMAB	0 ~ 8 g/liter
	Na-citrate	0.2*M*
	H_3BO_3	0.5*M*
	CH_3OH	2 ml/liter
	*p*H	6.0 ~ 8.0
	Temperature	287.2 ~ 329.2 K
	Nitrogen atmosphere	
NH_2NH_2	$NH_2NH_2 \cdot H_2O$	0 ~ 2*M*
	EDTA · 2Na	0.175*M*
	*p*H	11.0 ~ 13.0
	Temperature	298.2 ~ 339.2 K
	Nitrogen atmosphere	

* Dimethylamine borane.

[1]Permanent address: Tokyo Institute of Technology, Graduate School at Nagatsuta, Midori-ku, Yokohama 227, Japan.

[2]Present address: Komatsu Limited, Technical Research Center, 2597, Shinomiya, Hiratsuka 254, Japan.

electrode was a platinum plate of surface area 18 cm^2. The electrolytic cell was a Pyrex cylinder 5 cm in diameter and 8.5 cm in height. The potential of the working electrode was measured against a saturated calomel electrode (SCE) via a Luggin capillary and a salt bridge. Polarization measurements were made in potentiodynamic mode with a sweep rate of 0.002 V/s using an electronic potentiostat and a function generator. The experiments were carried out without agitation at 298.2 K unless otherwise noted. Some of the experiments were performed by using a rotating disk electrode. The rotating electrode was a platinum disk 0.3 cm in diameter plated with the metal under investigation. It was found, however, that the rotation of the electrode had no significant effect on the polarization behavior.

Results and Discussions

The anodic and cathodic reactions in electroless plating are more or less interdependent when they occur simultaneously (27, 28). The rate of the anodic oxidation of the reductant is in many cases accelerated in the presence of the cathodic deposition of the metal. As a first approximation, however, it can be assumed that the anodic polarization curve obtained in the absence of the metallic ion represents the true partial anodic reaction that would occur in the complete baths. In order to understand the catalytic aspect in electroless plating, the anodic polarization experiments were carried out on gold, platinum, palladium, silver, copper, nickel, and cobalt electrodes in the baths containing the reductants as listed in Table I. Similar polarization experiments were carried out in the baths in the absence of the reductant to distinguish the anodic current attributable to the dissolution of the metal.

Effect of pH and the concentration of reductant.—The rate of the anodic oxidation of the reductants increases with increasing either pH value or the concentration of the reductant. As the examples, the effects of the concentration on the anodic polarization curve of nickel in the solution containing hypophosphite are shown in Fig. 1. The polarization curves exhibit a maximum in current

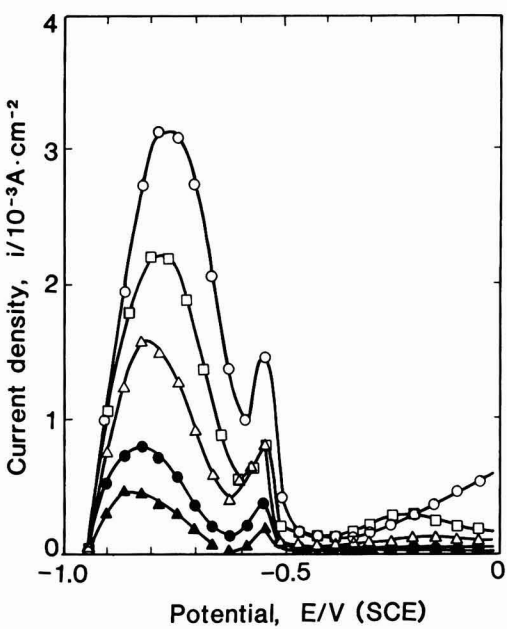

Fig. 1. Current-potential curves of anodic oxidation of hypophosphite on nickel at different concentrations. Bath composition: 0.2M Na-citrate + 0.5M H_3BO_3 + NaH_2PO_2 (varied), pH 9.0, 343 K. Concentration of NaH_2PO_2(mol/dm^3): open circles, 0.40; open squares, 0.20; open triangles, 0.10; solid circles, 0.06; solid triangles, 0.03.

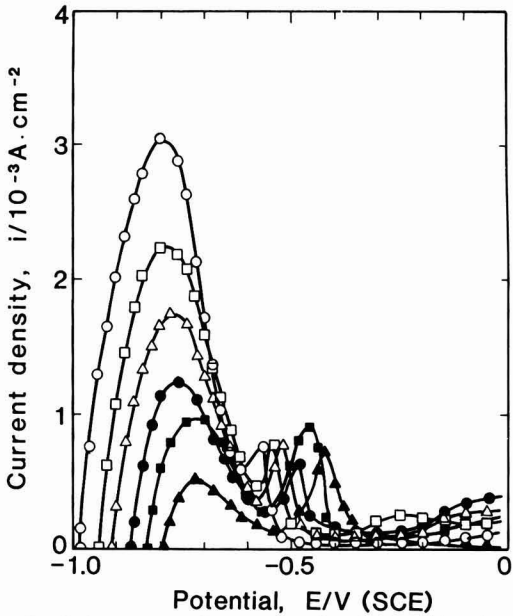

Fig. 2. Current-potential curves of anodic oxidation of hypophosphite on nickel at different pH values. Bath composition: 0.2M NaH_2PO_2 + 0.2M Na-citrate + 0.5M H_3BO_3, 343 K. pH: open circles, 9.5; open squares, 9.0, open triangles, 8.5; solid circles, 8.0; solid squares, 7.5; solid triangles, 7.0.

which increases with increasing the concentration. Although the depression of current after the maximum has been often attributed to the formation of an oxide film on surface, it occurs sometimes on noble metals and the depression potentials are mostly less noble compared to the reversible potentials for the oxide formation of the metals.

Figure 2 shows the effect of pH value on the anodic oxidation of hypophosphite on nickel. The current increases with increasing the pH value, shifting the current maximum to less noble potentials. The effects of the concentration of hypophosphite and the pH value on the anodic current at a fixed potential are summarized on logarithmic diagrams in Fig. 3 and 4, respectively. The slopes of the current-concentration diagram in Fig. 3 scattered between 0.44 and 0.80, depending on the nature of metal. The reaction orders with respect to hydroxyl ion were obtained from Fig. 3 to be approximately 0.25, except that for platinum (29).

Polarization experiments similar to those described above were carried out in the other baths shown in Table I. The dependencies of the current on pH value and the concentration of reductant in the other baths were very complicated, and the logarithmic plots of the relation similar to Fig. 3 and 4 did not exhibit a straight line (30, 31). Summarizing all the results, the reaction orders with respect to the reductants seem to scatter between 0.4 and 0.8, regardless of the natures of metal and reductant. The reaction orders regarding hydroxyl ion ranged from 0.2 to 0.4. Since the anodic oxidation of the reductants in the complex solutions is affected by pH in various ways, however, the apparent reaction orders may not be so helpful for the diagnosis of the reaction mechanism.

Effect of the nature of metals.—The polarization curves for the anodic oxidation of hypophosphite on different metals in sodium citrate solution are shown in Fig. 5. Anodic current attributable to the oxidation of hypophosphite was not observed on copper and silver electrodes, which simply dissolved anodically as indicated by the dotted line in Fig. 5. The polarization curve on palladium electrode exhibits a monotonous increase in current with

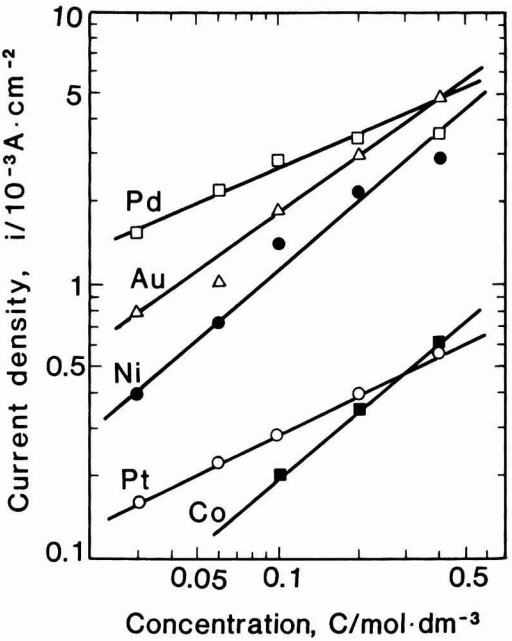

Fig. 3. Dependency of the anodic oxidation current at constant potential on the concentration of hypophosphite. Bath composition: 0.2M Na-citrate + 0.5M H_3BO_3 + NaH_2PO_2 (varied), pH 9.0, 343 K. Potentials (vs. SCE): −0.80V (for Pd, Au, Ni, Co), +0.20V (for Pt).

shifting the potential to noble direction. The polarization curve on gold shows three maxima of current, and the current falls off finally at around 0 V. The current on nickel electrode reaches a maximum at −0.7V and falls off at −0.4V. Cobalt electrode dissolved anodically at the potentials noble to the current maximum. It is readily seen in Fig. 5 that platinum is less active for the anodic oxidation of hypophosphite.

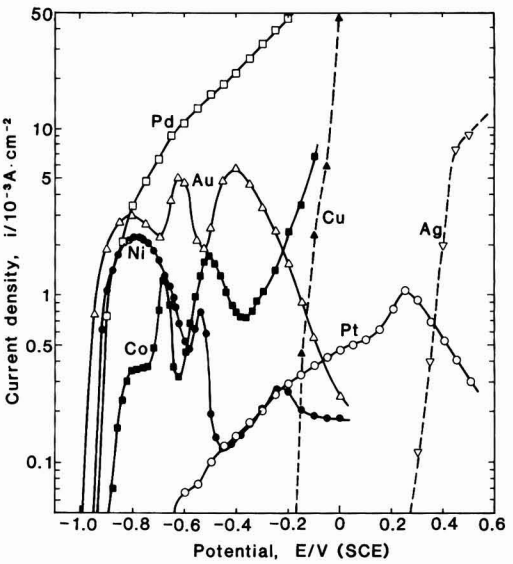

Fig. 5. Polarization curves for the anodic oxidation of hypophosphite on different metals. Bath composition: 0.2M NaH_2PO_2 + 0.2M Na-citrate + 0.5M H_3BO_3, pH 9.0, 343 K. Dotted line: current attributable to the anodic dissolution of Ag and Cu electrodes.

The polarization curves for the anodic oxidation of formaldehyde on different metals in a EDTA solution are shown in Fig. 6. Cobalt and nickel electrodes exhibit the anodic current attributable to oxidation of formaldehyde only at the potentials noble to 0.3V. The anodic current on copper starts to rise at −0.95V and falls off at −0.3V, exhibiting a maximum in current. The polarization curves on gold, silver, platinum, and palladium electrodes obey the Tafel relation at less noble potentials, exhibiting a limiting current at noble potentials. The limiting current was scarcely affected by the rotation of the electrode.

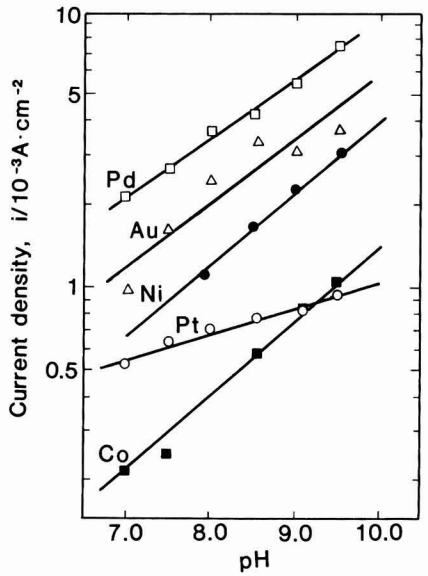

Fig. 4. Dependency of the anodic oxidation current of hypophosphite on pH value. Bath composition: 0.2M NaH_2PO_2 + 0.2M Na-citrate + 0.5M H_3BO_3, 343 K. Potential (vs. SCE): −0.80V (for Au, Ni), −0.70V (for Pd, Co), +0.20V (for Pt).

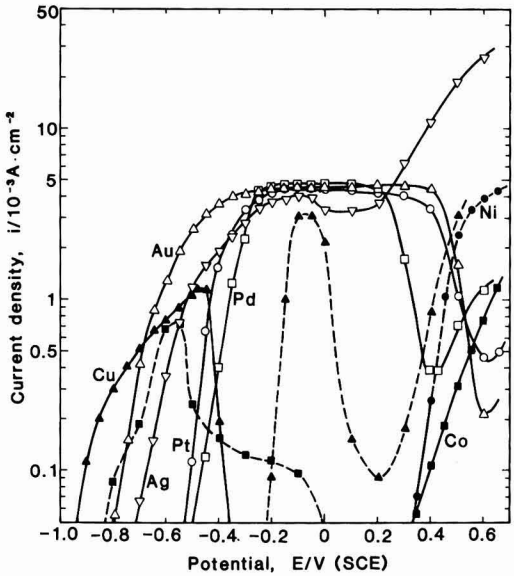

Fig. 6. Polarization curves for the anodic oxidation of formaldehyde on different metals. Bath composition: 0.1M HCHO + 0.175M EDTA.2Na, pH 12.5, 298 K. Dotted line: current attributable to the anodic dissolution of Cu and Co electrodes.

It is seen in Fig. 6 that the apparent oxidation potential of formaldehyde on copper is less noble than that on the other metals.

The polarization curves for the anodic oxidation of borohydride on different metals are shown in Fig. 7. Most of the polarization curves obey the Tafel relation exhibiting an asymptotic behavior at noble potentials, whereas those on cobalt and nickel electrodes show a current maximum.

Figure 8 shows the polarization curves for the anodic oxidation of dimethylamine borane on different metals. Copper electrode simply dissolved without exhibiting the current attributable to anodic oxidation of dimethylamine borane. The current maximum behavior was observed on nickel, cobalt, and platinum electrodes.

The polarization curves for the anodic oxidation of hydrazine on different metals are shown in Fig. 9. The polarization curves on cobalt and nickel show a maximum current behavior, whereas those on platinum, palladium, copper, gold, and silver exhibit well-defined Tafel lines.

Referring to the results shown in Fig. 5-9, it is seen that the shapes of the polarization curves can be classified into three categories: the Tafel type, the Tafel type with limiting current, and the volcano type. The limiting current has been attributed to a limited diffusion of reactant in solution, whereas it is less sensitive to agitation of solution. Occurrence of the volcano type of polarization curve has been often attributed to the formation of anodic oxide film on surface, although the potential of falling off of current is usually less noble than the reversible potential of oxide formation. It is highly probable that these polarization behaviors reflect the mechanism of anodic oxidation of reductants as such. It is also noted that electroless plating usually takes place at the potentials corresponding to the less noble branch of the polarization curves.

Effect of temperature.—The anodic polarization experiments similar to those described above are carried out on various metals and reductants at different temperatures. The Arrhenius plots of the currents on different metals at appropriate potentials for the anodic oxidation of hypophosphite, formaldehyde, borohydride, dimethylamine borane, and hydrazine are shown in Fig. 10, 11, 12, 13, and 14, respectively. The reference potential was so selected in the Tafel region at less noble potentials in Fig. 5-9 that the temperature dependency of the current on different metals could be evaluated on the basis of a common potential. Because of difference in the shape of polarization curves and in its temperature dependency, however, all the data on different metals could not be covered by

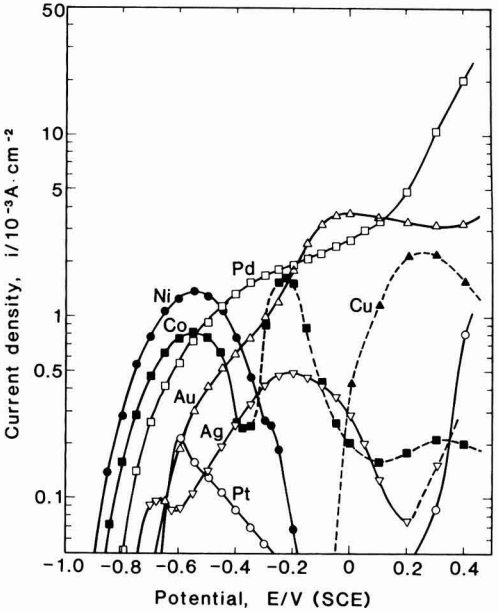

Fig. 8. Polarization curves for the anodic oxidation of dimethylamine borane (DMAB) on different metals. Bath composition: 2.0 g/dm³ DMAB + 0.2M Na-citrate + 0.5M H_3BO_3, pH 7.0, 298 K. Dotted line: current attributable to the anodic dissolution of Cu and Co electrodes.

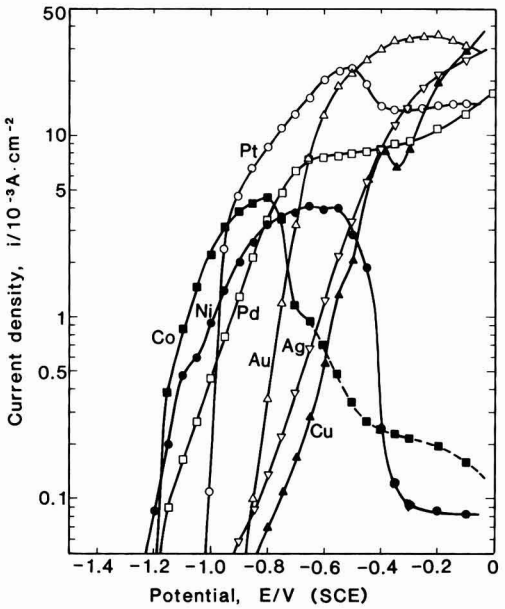

Fig. 7. Polarization curves for the anodic oxidation of borohydride on different metals. Bath composition: 0.03M $NaBH_4$ + 0.175M EDTA.2Na, pH 12.5, 298 K. Dotted line: current attributable to the anodic dissolution of Co electrode.

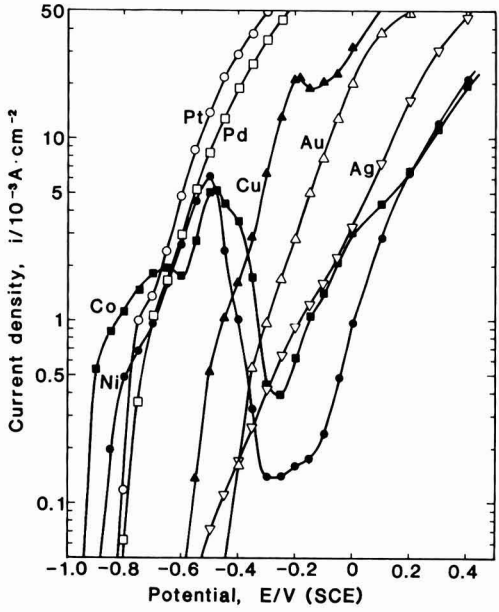

Fig. 9. Polarization curves for the anodic oxidation of hydrazine on different metals. Bath composition: 1.0M N_2H_4 + 0.175M EDTA.2Na, pH 12.0, 298 K.

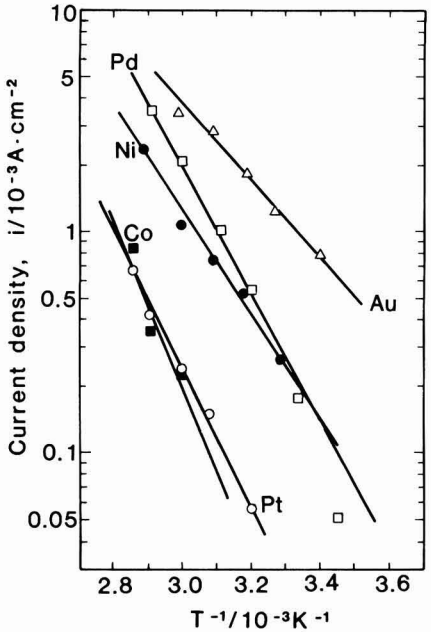

Fig. 10. Arrhenius plots of the anodic oxidation current of hypophosphite at a reference potential. Bath composition: 0.2M NaH_2PO_2 + 0.2M Na-citrate + 0.5M H_3BO_3, pH 9.0. Reference potential (vs. SCE): −0.80V (for Au,Pd, Ni, Co), +0.20V (for Pt).

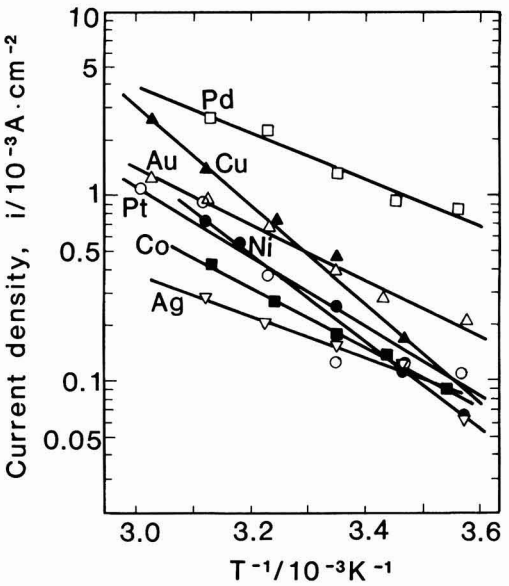

Fig. 11. Arrhenius plots of the anodic oxidation current of formaldehyde at a reference potential. Bath composition: 0.1M HCHO + 0.175M EDTA.2Na, pH 12.5. Reference potential (vs. SCE): −0.70V (for Au, Cu), −0.65V (for Ag), −0.50V (for Pt), −0.35V (for Pd), 0.40V (for Ni), 0.45V (for Co).

single reference potential. The apparent activation energies and the frequency factors obtained from Fig. 10-14 are summarized in Table II, together with the reference potentials. The activation energies (kJ/mol) hitherto published on the rate of electroless plating in the net electroless baths are 74.1 for NiP-hypophosphite (18), 49.0 for Cu-formaldehyde (32), 44.4-64.0 for NiB-dimethylamine borane (33), 80 for Au-borohydride (22), and 66.5 for Co-hydrazine (34). The activation energies for the anodic oxidation of reductants shown in Table II seem to be appreciably low in comparison with those for the rate of electroless plating in the net electroless baths, probably because the latter values involve the temperature depend-

Table II. Potentials at 1.0×10^{-4} A/cm² (E^*), apparent activation energies (E_a), and frequency factors (log i^*) for the anodic oxidation of reductants on different metals. For conditions, see the captions of Fig. 10-14

Reductants	Metal	E^* (V vs. SCE)	E_a (kJ/mol)	log i^* (10^{-3} A/cm²)	Reference potential (V vs. SCE)
NaH_2PO_2	Au	−0.982	33	5.7	−0.80
	Ni	−0.935	46	9.2	−0.80
	Pd	−0.910	54	8.9	−0.80
	Co	−0.854	88	11	−0.80
	Pt	−0.300	59	8.8	0.20
HCHO	Cu	−0.906	50	8.5	−0.70
	Au	−0.770	29	4.7	−0.70
	Ag	−0.675	29	4.3	−0.65
	Pt	−0.508	38	6.1	−0.50
	Pd	−0.464	24	4.4	−0.35
	Ni	0.366	46	7.3	0.40
	Co	0.450	31	4.8	0.45
$NaBH_4$	Ni	−1.190	40	7.2	−0.95
	Co	−1.180	40	8.2	−0.95
	Pd	−1.136	54	10	−0.95
	Pt	−0.983	46	8.4	−0.95
	Au	−0.850	39	7.4	−0.70
	Ag	−0.832	46	7.4	−0.70
	Cu	−0.761	46	7.3	−0.70
DMAB	Ni	−0.866	35	6.2	−0.55
	Co	−0.832	37	6.3	−0.55
	Pd	−0.766	41	7.1	−0.55
	Au	−0.650	42	6.8	−0.55
	Pt	−0.633	14	1.6	−0.55
	Ag	−0.565	50	8.0	−0.55
NH_2NH_2	Co	−0.940	31	5.7	−0.75
	Ni	−0.871	33	5.5	−0.75
	Pt	−0.800	17	3.0	−0.75
	Pd	−0.797	38	6.1	−0.75
	Cu	−0.556	33	5.3	−0.50
	Ag	−0.460	42	6.3	−0.50
	Au	−0.413	59	8.1	−0.50

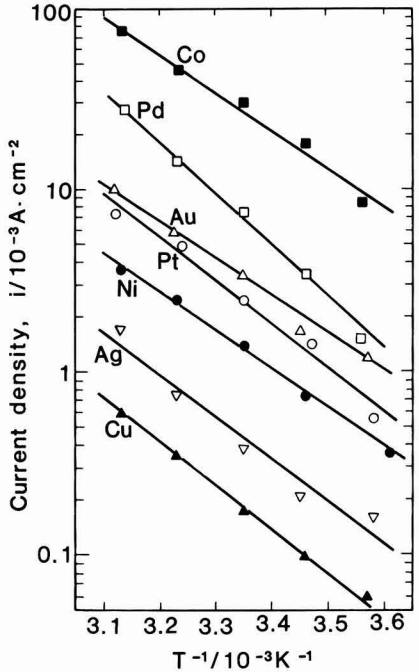

Fig. 12. Arrhenius plots of the anodic oxidation current of borohydride at a reference potential. Bath composition: 0.03M $NaBH_4$ + 0.175M EDTA.2Na, pH 12.5. Reference potential (vs. SCE): −0.95V (for Pt, Pd, Ni, Co), −0.70V (for Au, Ag, Cu).

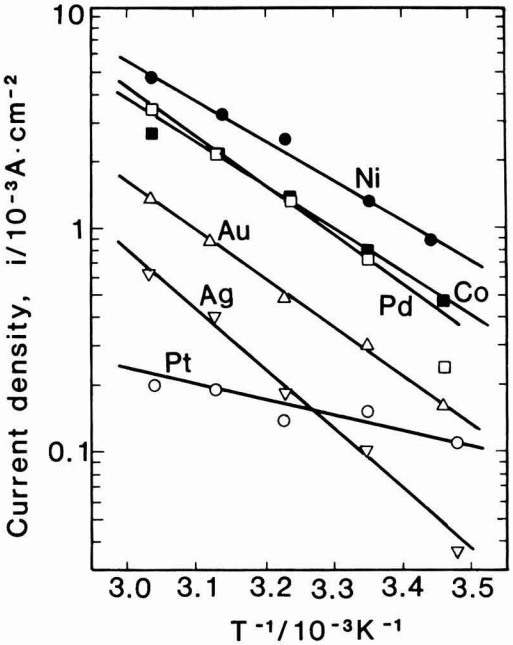

Fig. 13. Arrhenius plots of the anodic current of dimethylamine borane (DMAB) at −0.55V (vs. SCE). Bath composition: 2.0 g/dm³ DMAB + 0.2M Na-citrate + 0.5M H_3BO_3, pH 7.0.

encies of the rate of cathodic metal deposition and of the dissolution equilibrium of complex ion.

Hydrogen evolution during anodic oxidation of reductant.—Before the polarization experiments start, evolution of hydrogen gas was observed on some electrodes at open-circuit condition, especially in the solutions containing either hypophosphite or borohydride or dimethylamine borane. With shifting the potential to noble potentials, however, hydrogen evolution on cobalt, nickel, palladium, and platinum electrodes decreased and finally ceased. Therefore, it is probable that the hydrogen evolution in open circuit is attributable to the cathodic proton discharge under mixed potential control, thus

$$2H^+ + 2e^- \longrightarrow H_2 \qquad [6]$$

$$RH + 2\,OH^- \longrightarrow ROH + H_2O + 2e^- \qquad [7]$$

On the other hand, the rate of hydrogen evolution on copper, silver, and gold electrodes increased with shifting the potential to noble direction, regardless of the nature of the reductant. This means that the reductants are anodically oxidized on copper, silver, and gold electrodes accompanied by evolution of hydrogen gas that is originated from the reductant molecule. Accordingly, it is likely that the anodic oxidation of the reductants proceeds mainly along the hydrogen evolution mechanism on copper, silver, and gold, and the hydrogen ionization mechanism predominates on cobalt, nickel, palladium, and platinum.

Catalytic activity of the metal.—As is shown in Fig. 5-9, the shape of the polarization curves of anodic oxidation of the reductants varies in a complicated way depending on the natures of metals and reductants, probably because of complexity in reaction mechanism. Therefore, it seems difficult to evaluate the catalytic activity of the metal for respective reductants on the basis of a unified theoretical standard. As a first approximation, however, it can be assumed that the catalytic activities of the metals are characterized by the potential at a reference current density on the polarization curves shown in Fig. 5-9. The characteristic potentials at 1.0×10^{-4} A/cm² are summarized in Fig. 15. The oxidation-reduction potentials of the reductants and the reversible hydrogen potentials in respective solutions are also indicated in Fig. 15.

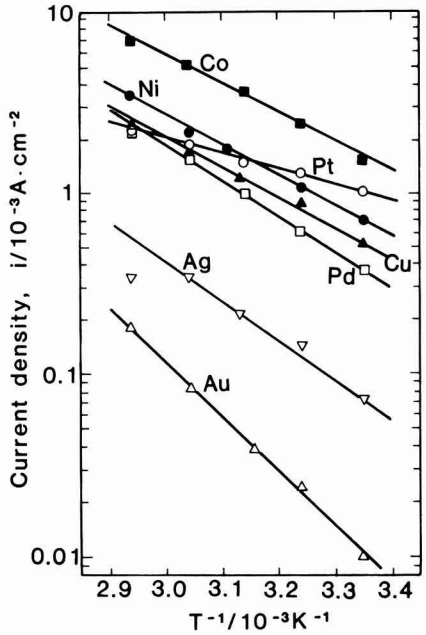

Fig. 14. Arrhenius plots of the anodic oxidation current of hydrazine at a reference potential. Bath composition: 1.0M N_2H_4 + 0.175M EDTA.2Na, pH 12.0. Reference potentials (vs. SCE): −0.75V (for Pt, Pd, Ni, Co), −0.50V (for Au, Ag, Cu).

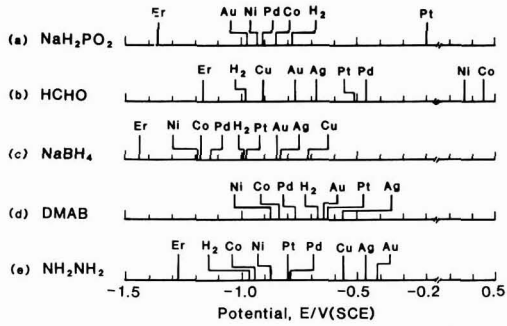

Fig. 15. Catalytic activities of metals (the potentials at 10^{-4} A · cm^{-2}), for anodic oxidation of different reductants. E_r: oxidation-reduction potentials of reductants. H_2: reversible hydrogen potentials. Conditions: (a) 0.2M NaH_2PO_2 + 0.2M Na-citrate + 0.5M H_3BO_3, pH 9.0, 343 K; (b) 0.1M HCHO + 0.175M EDTA.2Na, pH 12.5, 298 K; (c) 0.03M $NaBH_4$ + 0.175M EDTA.2Na, pH 12.5, 298 K; (d) 2.0 g/dm^3 DMAB + 0.2M Na-citrate + 0.5M H_3BO_3, pH 7.0, 298 K; (e) 1.0M N_2H_4 + 0.175M EDTA.2Na, pH 12.0, 298 K.

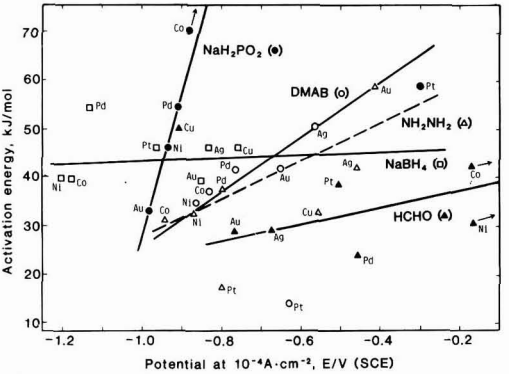

Fig. 16. Relation between activation energies and the potentials at 10^{-4} A · cm^{-2}.

It can be seen in Fig. 15 that the catalytic activity of the metals for the anodic oxidation of different reductants decreases in the following order, respectively: Au, Ni, Pd, Co, and Pt for hypophosphite, Cu, Au, Ag, Pt, Pd, Ni, and Co for formaldehyde, Ni, Co, Pd, Pt, Au, Ag, and Cu for borohydride, Ni, Co, Pd, Au, Pt, and Ag for dimethylamine borane, Co,Ni, Pt, Pd, Cu, Ag, and Au for hydrazine. Although there is no simple rule governing these orders, it is noted that the order of the catalytic activity for borohydride is almost the same as that for dimethylamine borane. This fact seems to imply that the anodic oxidation of these two boron containing reductants involve the same adsorbed intermediate in the rate determining step as was suggested by Okinaka (3). It must be also pointed out that copper, silver, and gold are very active for the anodic oxidation of formaldehyde, whereas they are less active for the other reductants.

The requisite kinetic condition for the electroless plating taking place with a reasonable rate is the characteristic potentials being less noble to the reversible potential of the metal to be deposited. According to this approach, Fig. 15 can be utilized for choosing the reductant suitable for electroless process of respective metals. Since the reversible potentials of metals in the complex solutions that are utilized in electroless processes are mostly in the range from −0.65 to −0.45V (SCE) (35, 36), it is said that the reductants available for depositing the metals are hypophosphite for Au, Ni, Pd, and Co, formaldehyde for Cu, Au, Ag, (Pt), and (Pd), borohydride for Ni, Co, Pd, Pt, Au, Ag, and (Cu), dimethylamine borane for Ni, Co, Pd, and (Pt), and hydrazine for Co, Ni, Pt, Pd, and (Cu). It can be seen that borohydride can be utilized for the electroless process of most metals and formaldehyde is substantially the only reductant which can be used in high speed electroless copper process. Such speculations based on Fig. 15 are in accord with the conventional usage of the reductant in electroless process.

The characteristic potentials at 1.0×10^{-4} A/cm^2 are listed in Table II, together with the activation energies. The activation energies are plotted against the characteristic potentials in Fig. 16. For the anodic oxidation of hypophosphite and dimethylamine borane, the characteristic potential shifts, except for platinum, to noble potentials with increasing the activation energy. Somewhat similar correlation is observed on hydrazine. Although the physical meaning of the activation energy is not clarified yet, the observed parallelism between the catalytic activity and the activation energy is quite acceptable from the usual understanding of chemical reaction. On the other hand, the correlation as described above is not observed for borohydride and formaldehyde. The activation energies for borohydride and formaldehyde scatters around 42 and 30 kJ/mol, respectively, regardless of the nature of metal.

Since the electroless plating accompanies hydrogen evolution originated from the reductant molecule, the catalytic nature in electroless plating has been often discussed in connection with that in hydrogen electrode reaction (12, 13, 16). According to Van den Meerakker (26), the anodic oxidation of the reductant proceeds along four elementary steps: dissociative adsorption, anodic oxidation of adsorbed radical, and recombination and/or ionization of adsorbed hydrogen. Namely, the adsorbed atomic hydrogen formed by dissociative adsorption of reductant is removed by either recombination or ionization, as similar with that in hydrogen electrode reaction. It is known (37) that the exchange current density of hydrogen electrode reaction decreases in the following order with metal: Pt, Pd, Ni, Co, Cu, Ag, and Au. It is probable that the anodic oxidation of the reductants proceeds mainly along the hydrogen evolution mechanism on copper, silver, and gold electrodes which are less active for hydrogen electrode reaction. Thus, it seems likely that the preferential reaction path for removing the adsorbed atomic hydrogen is related to the activity of metal for hydrogen electrode reaction. However, there is no simple correlation between the order of catalytic activity with metal for hydrogen electrode reaction and that for the anodic oxidation of the reductants. Therefore, it is not likely that the rate of anodic oxidation of the reductants is controlled by the removal of the adsorbed hydrogen. Much attention should be focused on the electrochemical step for removing the adsorbed anion radical.

Summary

The catalytic activity of metals for the anodic oxidation of different reductants in electroless plating was evaluated by the potentials at a reference current density. The catalytic activity series thus obtained serve to choose the reductant suitable to the metal to be deposited. Some correlations were observed between the catalytic activity and the apparent activation energy.

It is suggested that the anodic oxidation of the reductants proceeds mainly along hydrogen evolution mechanism on copper, silver, and platinum, whereas the hydrogen ionization mechanism predominates on cobalt, nickel, palladium, and platinum. It is found, however, that the catalytic activity series of metal for anodic oxidation of reductants does not coincide with that for hydrogen electrode reaction.

Manuscript submitted Dec. 10, 1984; revised manuscript received May 9, 1985. This was Paper 444 presented at the New Orleans, Louisiana, Meeting of the Society, May 12-17, 1985.

Tokyo Institute of Technology assisted in meeting the publication costs of this article.

REFERENCES
1. M. Saito, *J. Met. Finish. Soc. Jpn.*, **16,** 300 (1965); **17,** 14 (1966).
2. M. Paunovic, *Plating*, **55,** 1161 (1968).
3. Y. Okinaka, *This Journal*, **120,** 739 (1973).
4. M. Matsuoka and T. Hayashi, *Denki Kagaku*, **41,** 211 (1973).
5. I. Ohno, *Surf. Technol.*, **4,** 515 (1976),
6. W. Machu and S. El-Gendi, *Metalloberflaeche*, **13,** 97 (1959).
7. C. H. de Minjer, *Electrodeposition Surf. Treat.*, **3,** 261 (1975).
8. P. L. Gavallotti and G. Salvago, *Electrochim. Met.*, **3,** 239 (1968).
9. G. Salvago and P. L. Gavallotti, *Plating*, **59,** 665 (1972).
10. P. Hersh, *Trans. Inst. Met. Finish.*, **33,** 417 (1955-1956).
11. R. M. Lukes, *Plating*, **51,** 969 (1964).
12. A. Brenner and G. E. Riddell, *J. Res. Nat. Bur. Stand.* **37,** 1 (1946).
13. F. M. Donahue. *Oberflaeche*, **13.** 301 (1972).
14. K. M. Gorbunova, M. V. Ivanov, and V. P. Moiseev, *This Journal*, **120,** 613 (1973).
15. K. A. Holbrook and P. J. Twist, *J. Chem. Soc. A.*, 890 (1971).
16. K. M. Gorbunova, M. V. Ivanov, and A. A. Nikiforova, *Prot. Met.*, **6,** 470 (1970).
17. F. Pearlstein and R. F. Weightman, *Plating*, **61,** 154 (1974).
18. G. Gutzeit, *ibid.*, **46,** 1158 (1959).
19. J. P. Elder and A. Hickling, *Trans. Faraday Soc.*, **58,** 1852 (1962).
20. D. J. Levy, *Electrochem. Technol.*, **1,** 38 (1963).
21. J. W. Dini and P. R. Coronado, *Plating*, **54,** 385 (1967).
22. Y. Okinaka, *ibid.*, **57,** 914 (1970).
23. J. P. Randin and R. F. Weightman, *ibid.*, **54,** 523 (1967).
24. A. Molenaar, M. F. E. Holdrinet, and L. K. H. van Beek, *ibid.*, **61,** 238 (1974).
25. J. Dumesic, J. A. Koutsky, and T. W. Chapman, *This Journal*, **121,** 1405 (1974).
26. J. E. A. M. Van den Meerakker, *J. Appl. Electrochem.*, **11,** 395 (1981).
27. I. Ohno and S. Haruyama, *Surf. Technol.*, **13,** 1 (1981).
28. I. Ohno, M. Suzuki, and S. Haruyama, "Proceedings of the First AES Electroless Plating Symposium," American Electroplaters' Society, Winter Park, FL (1982).
29. I. Ohno, O. Wakabayashi, and S. Haruyama, *J. Met. Finish. Soc., Jpn.*, **34,** 594 (1983).
30. I. Ohno, O. Wakabayashi, and S. Haruyama, *Denki Kagaku*, **53,** 190 (1985).
31. I. Ohno, O. Wakabayashi, and S. Haruyama, *ibid.*, **53,** 196 (1985).
32. F. L. Shippey and F. M. Donahue, *Plating*, **60,** 43 (1973).
33. A. F. Schmeckenbecher, *ibid.*, **58,** 905 (1971).
34. D. J. Levy, *ibid.*, **50,** 29 (1963).
35. C. Milazzo and S. Caroli, "Tables of Standard Electrode Potentials," Project of the IUPAC Electrochemistry Commission, John Wiley and Sons, New York (1978).
36. I. Ohno and S. Haruyama, *Bull. Jpn. Inst. Met.*, **20,** 979 (1981).
37. H. Kita, *This Journal*, **113,** 1095 (1966).

Copper Electrodeposition onto Moving High Resistance Electroless Films

J. F. D'Amico* and M. A. DeAngelo

AT&T Technologies, Incorporated, Princeton, New Jersey 08540

F. R. McLarnon*

Applied Science Division, Lawrence Berkeley Laboratory, Berkeley, California 94720

ABSTRACT

The electrodeposition of Cu from aqueous $CuSO_4$-H_2SO_4 electrolyte onto a high resistance moving substrate has been studied. Substrate speeds of 0.5-2.0 cm/s, average current densities of 12-50 mA/cm^2, input Cu thicknesses of 0.1-0.5 μm, and cell depths of 30-74 cm were employed. Measured Cu metal thickness distributions showed good agreement with those predicted by a steady-state "terminal effect" model.

The production of printed circuits by additive methods (1) is initiated by the electroless deposition of a thin (0.1 μm) conductive coating of Cu onto an insulating substrate. This coating may be patterned (1) or may be a uniform deposit over the dielectric. The thickness of this coating can then be increased to practical values (*ca.* 35 μm) by electrodeposition of Cu. The patterned electroless coating may be built up by electrodeposition (if the pattern is continuous) or by high speed electroless plating. The unpatterned electroless deposit will most often be used as a cathodic connection for pattern electrodeposition through a plating mask. The latter process is usually referred to as "semiadditive" plating.

Additive production methods permit an inventory of Cu metal which is smaller than that required by standard printed-circuit production methods, where the starting material is (typically) an insulating substrate clad with 35 μm thick Cu foil. The additive printed-circuit production method minimizes reliance on etching processes, which thereby enhances the process capability for definition of fine-line patterns.

Continuous or semicontinuous production of flexible printed circuits may be carried out by passing a sheet of substrate material through a series of processing tanks, using rollers to guide the substrate along its desired path.

*Electrochemical Society Active Member.

A schematic diagram of the electrodeposition portion of such a continuous processing machine is illustrated in Fig. 1. Electrodeposition apparatus similar to that shown might be expected to increase the thickness of the Cu deposit from 0.1 to 5 μm. The apparatus, with dimensions as shown in Fig. 1, accommodates substrate speeds of 1-5 cm/s in order to be compatible with the remainder of the additive process. Economic constraints dictate that the apparatus should be compact and have the capability of operating at high current densities.

Previous studies by D'Amico *et al.* (2) showed that practical current densities in the electrodeposition apparatus (Fig. 1) were well below mass-transfer-limited values. Measurements of Cu thickness distributions indicated that this limitation was a consequence of highly nonuniform current distributions; the local current density was a strong function of axial position of the substrate in the apparatus. This highly nonuniform current density distribution was attributed to the so-called "terminal effect" (3), caused by the relatively high resistance (small Cu thickness) of the substrate on which the Cu metal is electrodeposited. Another source of nonuniform current distribution is the uneven division of current between different loops of Cu-clad substrate connected to one or more metallic rollers that are held at the same cathodic potential. Proportionately more current is distributed to sub-

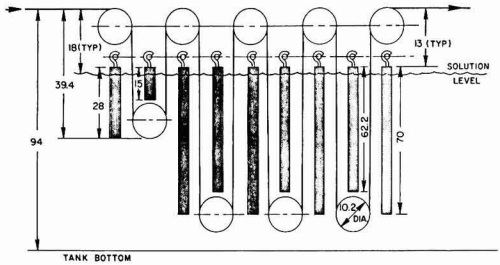

Fig. 1. Schematic diagram of a continuous, multipass electrodeposition apparatus. The five top rollers (stainless steel) are parallel-connected cathodes. The (hanging) copper bars are parallel-connected anodes. A side view of the complete apparatus is shown. A plan view of a single section is similar to that presented in Fig. 2. All dimensions are in centimeters.

strate loops with thicker Cu deposits; *i.e.*, higher currents are observed closer to the location where the substrate exits the electrodeposition apparatus. D'Amico *et al.* evaluated several designs that provided more even current density distributions, including "field shields," additional cathode connections located within the electrolyte phase, and shorter loops near the location where the substrate enters the electrodeposition apparatus.

The purpose of the present work is to apply basic models of current density distribution to evaluate measured Cu deposit thickness variations in a pilot-scale continuous electrodeposition apparatus. It is expected that these models can be used as a predictive basis for the design of full-scale electrodeposition equipment employed in the production of printed circuits by additive methods.

Other investigators have studied the problem of nonuniform current density distribution during electrodeposition onto a substrate of high ohmic resistance. Both steady-state (3) and transient (4) analyses of the current density distribution on resistive, stationary plane-parallel electrodes have been performed, and the transient current density distribution on a resistive, stationary wire electrode has been studied (5). The problem of nonuniform current density distribution during electrodeposition onto a moving wire electrode of high ohmic resistance has been analyzed (6, 7). Both steady-state (8) and transient (9) analyses of forced-convection mass transfer to a moving sheet electrode of negligible resistance have been performed. None of these investigations has studied the problem of nonuniform current density distribution along resistive, moving plane-parallel electrodes.

Experimental

Electrodeposition apparatus.—Copper electrodeposition was carried out in the "single-pass" cell shown in Fig. 2. This cell is intended to model a single loop of a "multipass" apparatus, such as that shown in Fig. 1. The anodes were 0.64 cm thick, 15.2 cm wide oxygen-free, high conductivity Cu sheets of various lengths. The 6.5 cm wide, 0.05 mm thick polyimide (du Pont Kapton®) flexible substrate material, initially coated with a 0.1-2.5 μm layer of Cu (unpatterned), passed over 3.5 cm diam stainless steel rollers, which served not only to guide the substrate through the cell, but also to make electrical contact to the substrate. Electrical connection to the substrate on the side not in contact with these rollers was made through numerous Cu-plated through-holes in the

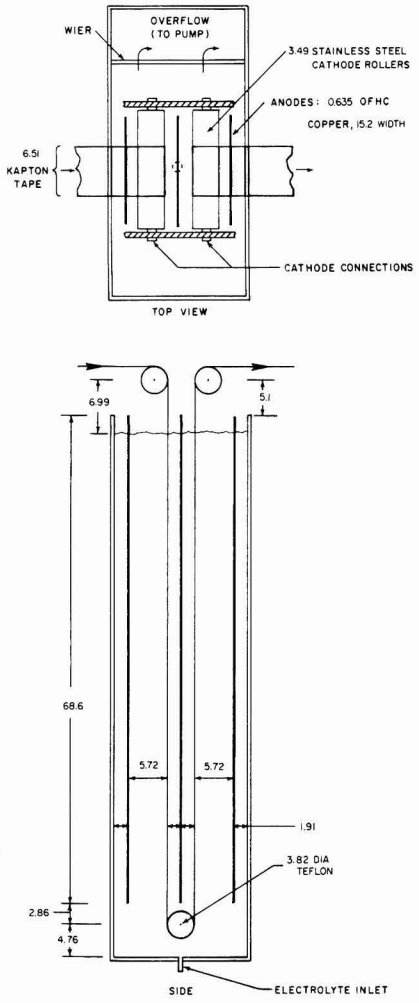

Fig. 2. Schematic diagram of electrodeposition cell. A side view of the cell is shown in the lower portion of the figure, and a plan view of the cell is shown in the upper portion of the figure. All dimensions are in centimeters.

substrate, as described previously in Ref. (2). Anode/cathode spacings were 1.9 and 5.7 cm, as shown in Fig. 2. A mean electrode separation of 3.8 cm was employed in the subsequent analysis. Average electrolyte flow velocities were 2.8-3.8 cm/s.

Electrolyte.—The electrolytes used were acid copper sulfates, having compositions and conductivities as listed in Table I. Electrolytes I and II were proprietary compositions, Cubath I® and Cubath II® supplied by Sel-Rex Company (Nutley, New Jersey). Electrolyte III was a 50-50 (volume percent) mixture of I and II. In addition to the sulfate ingredients listed, these baths contained trace amounts of electroplating additives, including 30 ppm Cl^-. These additives are expected to have little effect on the electrolyte conductivity.

The conductivities reported in Table I were measured with a direct reading conductance bridge (Industrial Instruments, Incorporated) at 1 kHz. The conductance cell was platinum-glass, with a cell constant of 1.0 cm^{-1}. Measurements were made at 22°-24°C in reagent-grade $CuSO_4$-H_2SO_4 mixtures. The conductivity of electrolyte III was not measured, so an interpolated value $\kappa = 0.319$ was used in subsequent calculations.

Table I. Electrolyte properties

Electrolyte	Concentrations (mol/liter) $CuSO_4$	Concentrations (mol/liter) H_2SO_4	Conductivity (Ω^{-1}-cm^{-1})
I	0.27	1.76	0.475
II	0.90	0.57	0.162
III	0.59	1.17	—

The electrolyte temperature was maintained at 22°-25°C, and it was continuously pumped through polypropylene and carbon filters in a recirculation loop. The electrolyte composition was monitored by periodic measurement of Cu^{++}, pH, and Cl^-. Electrolyte losses due to water evaporation and mechanical loss (*i.e.*, the small amount of electrolyte that adhered to the substrate) were compensated for by periodic additions of H_2O, $CuSO_4$, H_2SO_4, and/or HCl, as necessary.

Electrodeposition experiments.—Electroless Cu-clad substrate was passed through the electrodeposition cell shown in Fig. 2. After setting the substrate speed and cell current, the cell was operated for an interval corresponding to three to four times the substrate residence time within the electrolyte, in order to assure that steady-state conditions were reached. The cell circuit was then opened and the substrate movement was simultaneously halted. The two locations where the substrate rested at the top of the stainless-steel rollers were marked on the substrate, and the substrate was then fed out of the cell at 3 cm/s. This procedure resulted in an open-circuit residence time within the electrolyte of not more than 1 min. Other experiments showed that during a 1 min interval, not more than 0.01 μm of Cu would be etched by the $CuSO_4/H_2SO_4$ electrolyte. This amount of etching could create errors as high as 10% (near the entrance to the cell) in subsequent determinations of Cu thickness.

Copper thicknesses were determined by weighing the deposited metal. The substrate was cut in to 3.2 cm long specimens, which were then weighed on a Mettler H-15 balance (accuracy of approximately 0.1 mg). The specimens were then dipped in dilute HNO_3 solution to remove the Cu metal, and the substrate was dried and reweighed to arrive at the net weight of Cu metal. The weight of the 3.2 cm long Cu-free substrate was 135 mg. The standard bulk Cu density of 8.93 g/cm^3 and the measured specimen area of 40 cm^2 (both sides) was used to calculate the average Cu metal thickness on the specimen.

Analysis

A complete analysis of the electrodeposition cell used in this study would necessarily consider the interrelated electric-field, kinetic, hydrodynamic, and mass-transfer effects, as well as the spatially and temporally variable ohmic resistance of the cathode substrate. However, consideration of the conditions that exist in a continuous electrodeposition cell suggests that the following approximations may be made (refer to the cell geometry shown in Fig. 3). (*i*) The anode/cathode separation is typically much smaller than the depth and width of electrodes, so the primary current density distribution (in the limiting case where the cathode substrate resistance is zero) is fairly uniform. (*ii*) The electrolyte is continuously agitated by pumping, so that concentration and temperature gradients within the cell are relatively small. Mass-transfer limiting conditions are not approached anywhere in the cell. (*iii*) The net thickness change ($\leq$ 35 μm) of electrodeposited metal in a multiloop electrodeposition apparatus (Fig. 1) is much smaller than the anode/cathode separation. Therefore, provided that electrodeposition conditions lead to a uniformly smooth metal deposit, the anode/cathode separation is constant. (*iv*) The net Cu electrodeposit thickness change (0.5-5 μm) over the cathode substrate length L (which corresponds to one-half of a loop in a multiloop electrodeposition apparatus) is small relative to the local electrodeposit thickness (0.1-35 μm). This approximation is most likely to be valid near the exit of the electrodeposition apparatus where the metal deposit is relatively thick, and it is least likely to be valid near the entrance to the device where the metal deposit is relatively thin. However, it has been shown (2) that it is appropriate to use lower currents and shorter loops (smaller values of L) where the metal deposit is relatively thin, which leads to a smaller net Cu electrodeposit thickness change per loop near the entrance to the device. This approximation permits the effective resistance of the cathode substrate to be defined by a single value that is characteristic of the average (*i.e.*, averaged over the Z-direction) thickness of the Cu deposit at some location $0 \leq x \leq L$. (*v*) Because the Cu metal is either shielded (upward facing side of the cathode substrate) or remote (downward facing side of the cathode substrate) from the anodes, little metal deposition (or dissolution) occurs as the cathode substrate passes around the lower guide roller ($x > L$). (*vi*) Negligible rates of metal deposition (or dissolution) occur after the cathode substrate leaves the electrolyte phase and enters air. (*vii*) The electrode kinetics for Cu electrodeposition on the cathode substrate and Cu electrodissolution from the anode may be described by linear expressions. This should be a good approximation if the cell design leads to a fairly uniform current density distribution, because even if the levels of current density correspond to operation in the Tafel region, the Tafel expression can be linearized if there are only small excursions from average current density values. (*viii*) The electrodeposition process is 100% efficient, *i.e.*, there are no side reactions such as H_2 evolution. (*ix*) Steady-state conditions prevail.

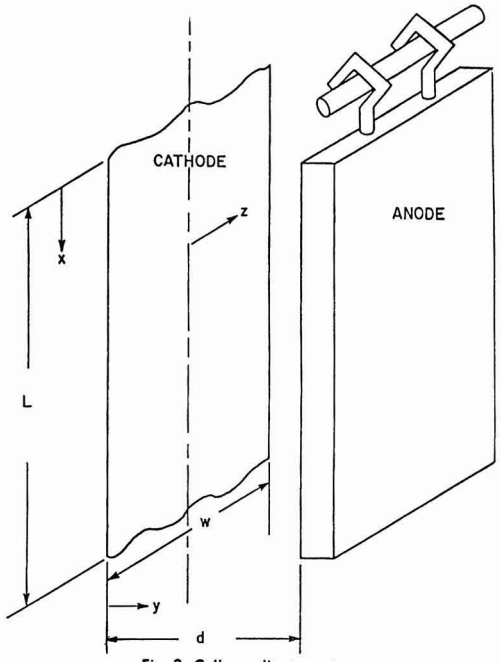

Fig. 3. Cell coordinate system

By making the nine approximations listed above, it is possible to treat each half-cell as a classical steady-state "terminal effect" problem, solved by Tobias and Wijsman (3). They found the current density distribution to be a strong function of a single parameter ϕ (defined in Eq. [2]), that represents the ratio of the electrode resistance to the electrolyte resistance, and identified conditions under which a simplified model could be applied. Their results show that the simplified model can be used when $d/L < 0.1$, $(\lambda_a + \lambda_d)$ is not $>> 1$, and $(\mu_a + \mu_d)$ is not $>> 1$. For the conditions employed in the present work, $0.05 < d/L < 0.12$, $0.04 < (\lambda_a + \lambda_d) < 4.0$, and $0.02 < (\mu_a + \mu_d) < 0.06$. Even when $d/L = 0.12$, the computed results shown in Fig. 10 of Ref. (3) suggest that the simplified model will predict values of local current densities that fall within about 2% of those calculated for the exact solution, $0.05 < x/L < 1$. The simplified model is easier to apply than the exact model, and it thereby permits rapid estimation of the current density distributions that will result from various designs of the electrodeposition apparatus. The simplified Tobias-Wijsman model can now be ap-

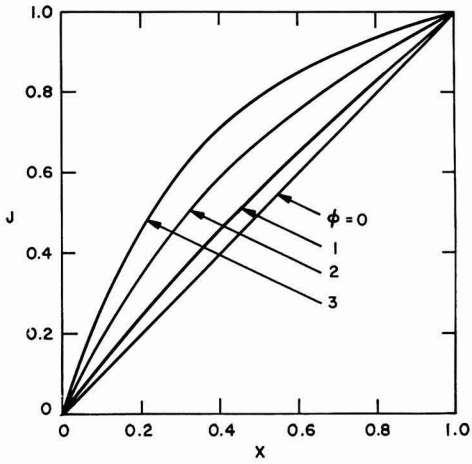

Fig. 4. Dimensionless current per unit cathode substrate width for various values of the parameter ϕ.

plied directly. The dimensionless current J per unit width (in the Z-direction) of Cu is given by

$$J(X) = 1 - \frac{\sinh [\phi(1 - X)]}{\sinh \phi} \quad [1]$$

where

$$\phi^2 = \frac{\rho_e \kappa L^2}{T(d + 2\kappa b)} \quad [2]$$

is a parameter related to the ratio of the X-direction potential gradient in the resistive cathode substrate to the potential gradient in the electrolyte phase. The corresponding local current density distribution is given by

$$\frac{i(X)}{i_{avg}} = \phi \frac{\cosh [\phi(1 - X)]}{\sinh \phi} \quad [3]$$

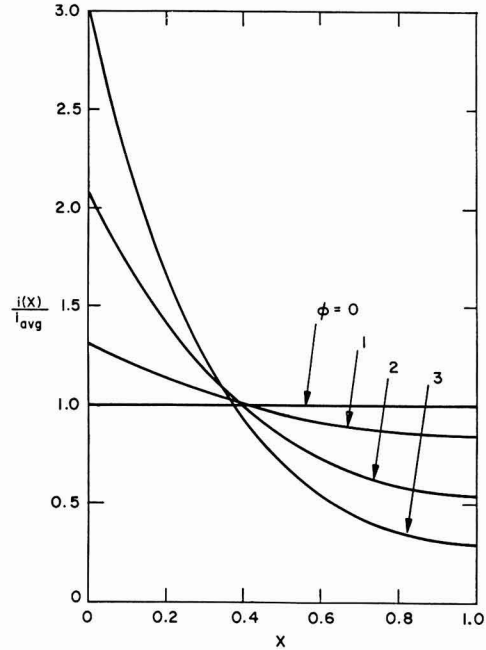

Fig. 5. Dimensionless current density distributions for various values of the parameter ϕ.

Equations [1] and [3] are plotted in Fig. 4 and 5, respectively, for various values of the parameter ϕ. Small values of ϕ correspond to uniform local current densities and a linear variation of J *vs.* X. Large values of ϕ correspond to nonuniform local current densities and a nonlinear variation of J *vs.* X.

The local Cu metal thickness can be related to the local current density through Faraday's law

$$T(x) = T(0) + \frac{M}{n\mathbf{F}\rho v} \int_0^x i(x)\, dx \quad [4]$$

or it may be equivalently related to the current per unit width (in the Z-direction) of Cu

$$T(x) = T(0) + \frac{M}{n\mathbf{F}\rho v} j(x) \quad [5]$$

Equations [1] and [5] can be combined to predict the axial distribution of Cu metal thickness in the electrodeposition cell.

Results and Discussion

Electrolyte composition, loop depth, substrate speed, cell current, average cathodic current density, and entering Cu deposit thickness are listed for ten separate experiments in Table II. The measured steady-state axial Cu thickness distributions are shown as the filled circles in Fig. 6-10.

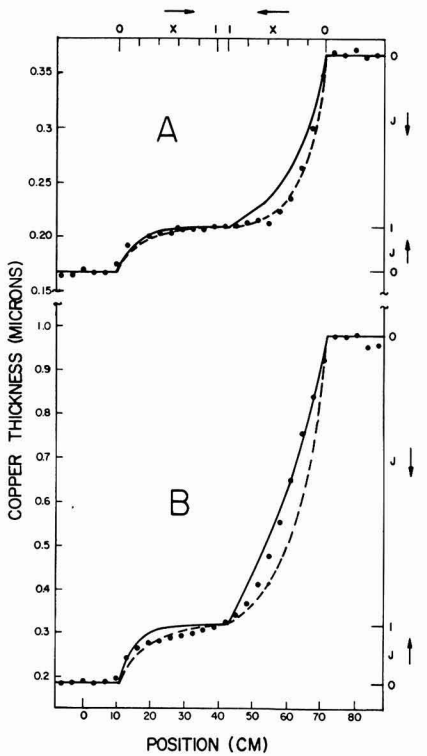

Fig. 6. Axial Cu thickness distributions. Lower abscissa: distance along cathode substrate (cm). Upper abscissa: dimensionless axial distance x/L. Left ordinate: Cu thickness (μm). Right ordinate: dimensionless Cu thickness $J(X)$. Dashed line: dimensionless thickness distribution $J(X)$, computed using the Cu thickness at the lower guide roller location $x = L$ to calculate the effective substrate resistivity ρ_e. Solid line: dimensionless thickness distribution $J(X)$, computed using the Cu thickness where the substrate enters the electrolyte (for the portion of the solid curve to the left of the inflection point), or where the substrate leaves the electrolyte (for the portion of the solid curve to the right of the inflection point). Solid circles: measured axial Cu thickness distributions. The experimental parameters employed for the data shown in the upper half (A) and lower half (B) of the figure are listed in Table II.

Table II. Experimental conditions

Figure	Electrolyte[a]	L (cm)	v (cm/s)	I (A)	i_{ave} (mA/cm²)	$T(0)$ (μm)
6A	I	30.5	1.45	9.3	11.7	0.17
6B	I	30.5	0.55	14.7	18.5	0.19
7A	I	30.5	1.93	23.2	29.2	0.51
7B	I	30.5	1.09	23.0	29.2	0.50
8A	I	30.5	0.53	23.2	29.2	0.41
8B	I	30.5	0.54	32.9	41.5	0.44
9A	II	30.5	0.78	11.5	14.5	0.08
9B	II	30.5	0.78	40.1	50.5	0.08
10A	III	74.1	1.94	45.3	23.5	0.54
10B	III	74.1	1.06	45.5	23.6	0.51

[a] See Table I.

The Cu deposit resistivities were measured using the standard four-point probe method. Strips 1.27 cm wide and 15.2 cm long were cut from sections of the plated substrate, and their resistances were measured on a special fixture designed to accommodate these specimens. The copper thickness of the same specimens was then determined using the weighing method previously described. This method requires that the deposit density be known, and the literature value for electrolytic copper was used for both electroless and electroplated Cu. The density of electroless Cu is reported (10) to be only a few percent lower than that of electrolytic Cu.

Electroplated Cu deposit resistivity ρ_c was 2.0×10^{-6} Ω-cm, which is close to the literature value of 1.8×10^{-6} Ω-cm. Electroless Cu deposit resistivity was three times higher, 6.0×10^{-6} Ω-cm. The linear polarization parameter $b = 1.3$ Ω-cm² was estimated by linearizing Cu electrode kinetic data, reported by Turner and Johnson (11), about the average cathode current density. The use of a single polarization parameter will not account for asymmetry of the anodic and cathodic polarization curves, nor will it apply when there are large variations in local current density [see approximation (*vii*) above]. However, the effect of electrode kinetics on the current density distribution is expected to be relatively small. This effect can be estimated from the magnitude of the last term in the denominator of Eq. [2]; even if this term is neglected, there results only a 5-15% error in the value of ϕ, which corresponds to a similar error in the associated current density distribution Eq. [3]. The assumption that both the anode and cathode exhibit the same linear electrode kinetic behavior, which is consistent with the assumptions made in the derivation of Eq. [2], is therefore expected to lead to small errors in calculated current density distributions and metal thickness distributions. Values of the computed dimensionless parameter ϕ ranged from 0.7 to 6.0.

Computed dimensionless thickness distributions $J(X)$ are plotted as the dashed and solid curves in Fig. 6-10. The dashed curves correspond to the value of ϕ calculated using the measured Cu deposit thickness at the bottom guide roller. The solid curves to the left of the inflection points correspond to the value of ϕ calculated using the measured Cu deposit thickness on the substrate as it enters the electrolyte [*i.e.*, $T(0)$ listed in Table II]. The solid curves to the right of the inflection points correspond to the value of ϕ calculated using the measured Cu deposit thickness on the substrate as it leaves the electrolyte. The solid and dashed curves therefore represent extremes of effective cathode substrate resistivity along a single half-loop. The spread between the solid and dashed curves indicates the uncertainty associated with employing a single value of Cu deposit thickness to characterize the effective resistance of the cathode substrate.

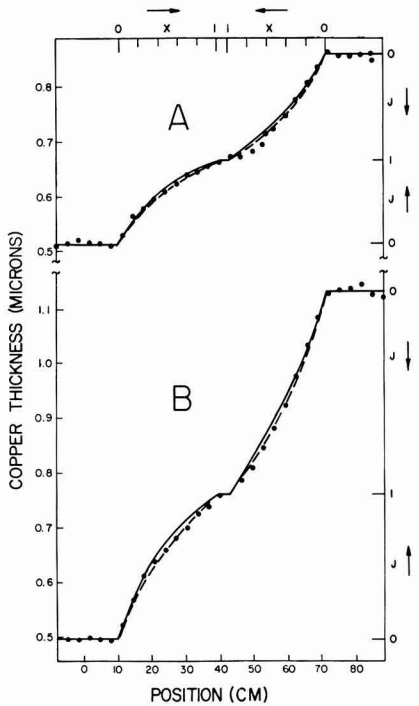

Fig. 7. Axial Cu thickness distributions. Designations are identical to those listed in the caption for Fig. 6.

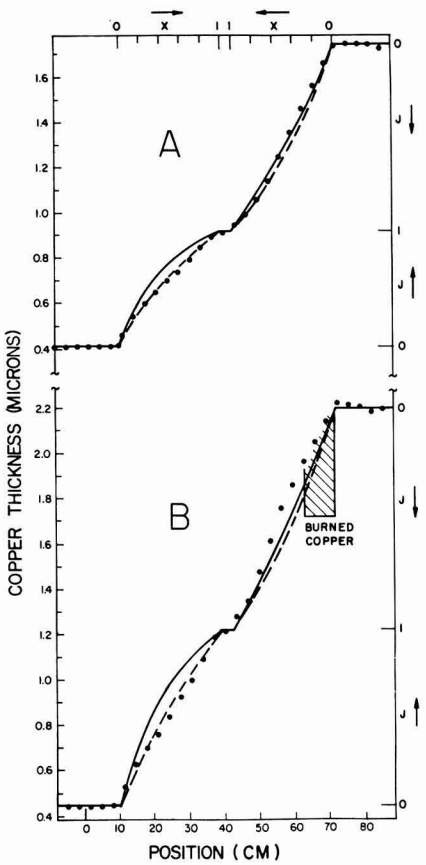

Fig. 8. Axial Cu thickness distributions. Designations are identical to those listed in the caption for Fig. 6.

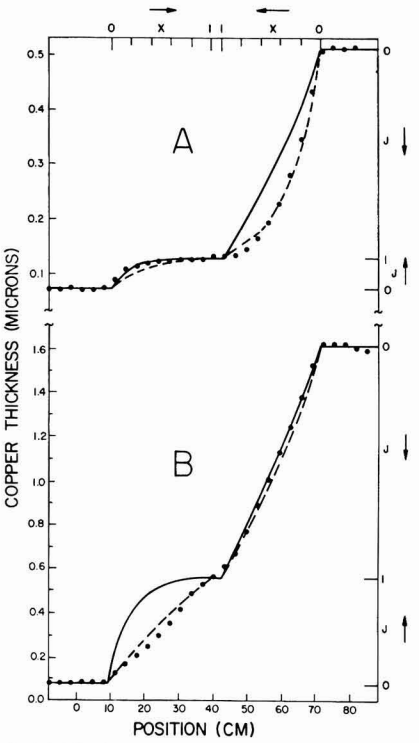

Fig. 9. Axial Cu thickness distributions. Designations are identical to those listed in the caption for Fig. 6.

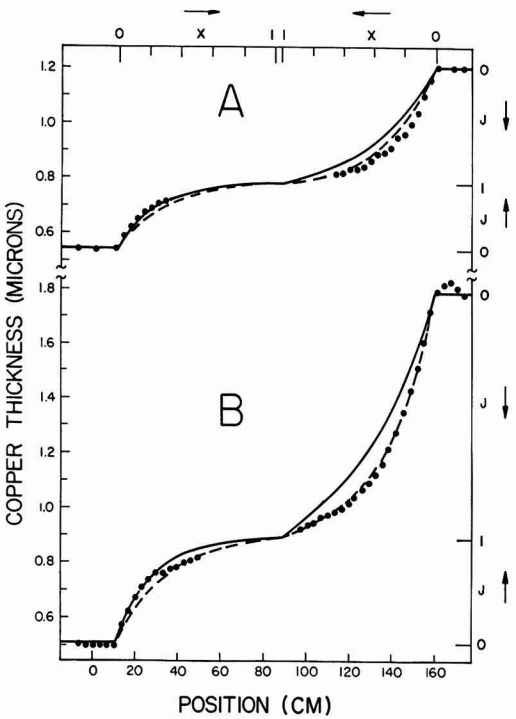

Fig. 10. Axial Cu thickness distributions. Designations are identical to those listed in the caption for Fig. 6.

For example, the large spread between the solid and dashed curves to the left of the inflection point on Fig. 9B suggests that the use of a single value of Cu deposit thickness to compute a characteristic value of ϕ may lead to considerable error. In this case, the experimental parameters give rise to an increase in Cu deposit thickness from 0.08 to 0.55 μm, which violates the conditions leading to approximation (*iv*). The failure of the present analysis to accurately predict the measured axial Cu thickness distribution to the left of the inflection point in Fig. 9B is, therefore, not unexpected.

Another case where the predicted axial thickness distributions do not agree well with the measured distributions is in Fig. 8B, where the measured thickness distribution is more uniform than that predicted. Note that a relatively high average current density of 41.5 mA/cm^2 was employed with the low Cu^{++}-concentration electrolyte, and a discolored ("burned") Cu electrodeposit was observed near the location where the substrate exits the cell. These observations suggest that mass-transfer limiting conditions were approached, which violates approximation (*ii*). Again, therefore, it is not surprising that in Fig. 8B the measured axial thickness distributions do not agree well with those predicted.

Figures 6-10 show that the "terminal-effect" model provides a good basis for predicting axial metal thickness distributions (and the associated current density distributions Eq. [4]) under a range of electrolyte compositions, cell depths, substrate velocities, average current densities, and initial Cu thicknesses. The uniformity of current density distribution (linearity of Cu thickness distribution) is enhanced by: (*i*) more shallow loops (*cf.* Fig. 7A and 10A), (*ii*) thicker initial Cu deposits (*cf.* Fig. 6B and 7B), (*iii*) slower substrate speeds (which leads to thicker Cu electrodeposits) (*cf.* Fig. 7A and 7B), (*iv*) higher average current densities (which leads to thicker Cu deposits) (*cf.* Fig. 9A and 9B), and (*v*) lower electrolyte conductivity (see Eq. [2]).

Conclusions

The steady-state "terminal effect" model has been shown to provide a good basis for the prediction of axial metal thickness distributions along a resistive cathode substrate in a continuous electrodeposition cell. Good agreement between predicted and measured thickness distributions is found for a wide range of experimental parameters; for example, the dimensionless parameter ϕ ranged from 0.7 to 6.0. These results indicate that the current density distribution is typically determined by the value of ϕ, which includes several factors: ohmic potential drop in the resistive cathode, ohmic potential drop in the electrolyte, kinetic overpotential at the electrodes, and cell geometry. Other factors, such as the concentration overpotential, are of secondary importance. Conditions leading to cases where the model may not apply have been identified; these conditions can correspond to cell designs and operating parameters (*e.g.*, those leading to local mass-transfer limiting currents) that can produce electrodeposited metal exhibiting undesirable properties.

Acknowledgment

Manuscript submitted March 15, 1985; revised manuscript received June 26, 1985. This was Paper 270 presented at the Washington, DC, Meeting of the Society, May 2-7, 1976.

AT&T Technologies, Incorporated, assisted in meeting the publication costs of this article.

LIST OF SYMBOLS

b	kinetic polarization parameter (Ω-cm^2)
d	anode/cathode separation (cm)
$\mathbf{F}$	Faraday constant (C/eq)
i	local current density (A/cm^2)
i_{avg}	average current density (A/cm^2)
I	cell current (A)
j	current per unit substrate width (A/cm)
J	$j(x)/j(L)$

L electrode length (cm)
M molecular weight of electrodeposited metal (g/mol)
n cation valence (eq/mol)
T metal deposit thickness (cm)
v substrate speed (cm/s)
w electrode width (cm)
x axial coordinate (cm)
X x/L
z horizontal coordinate (cm)
κ electrolyte conductivity (Ω^{-1}-cm^{-1})
λ_o, λ_d dimensionless parameter $\rho_c\kappa L/T$ for the electrodes at $y = 0$ and $y = d$, respectively
μ_o, μ_d dimensionless parameter $\kappa b/L$ for the electrodes at $y = 0$ and $y = d$, respectively
ρ density of electrodeposited metal (g/cm^3)
ρ_c resistivity of electrodeposited metal (Ω-cm)
ϕ dimensionless parameter (Eq. [2])

REFERENCES

1. J. F. D'Amico, M. A. DeAngelo, J. F. Henrickson, J. T. Kenney, and D. J. Sharp, *This Journal*, **118,** 1695 (1971).
2. J. F. D'Amico, M. A. DeAngelo, and L. D. Noble, *ibid.*, **123,** 478 (1976).
3. C. Tobias and R. Wijsman, *ibid.*, **100,** 459 (1953).
4. R. Alkire, *ibid.*, **118,** 1935 (1971).
5. R. Alkire and A. Tvarusko, *ibid.*, **119,** 340 (1972).
6. R. Alkire and R. Varjian, *ibid.*, **124,** 388 (1977).
7. R. Alkire and R. Varjian, *ibid.*, **121,** 622 (1974).
8. D. T. Chin, *ibid.*, **122,** 643 (1975).
9. R. S. R. Gorla, *ibid.*, **125,** 865 (1978).
10. J. Hajdu and J. Wynschenk, Abstract 211, p. 530, The Electrochemical Society Extended Abstracts, Miami, FL, Oct. 8-13, 1972.
11. D. R. Turner and G. R. Johnson, *This Journal*, **109,** 798 (1962).

Electrochemical Production of Potassium Carbonate

F. Hine,* M. Yasuda,* Y. Ogata, and T. Kojima

Nagoya Institute of Technology, Nagoya 466, Japan

Yang Weiyi*,[1]

Jinxi Research Institute of Chemical Industry, China

ABSTRACT

Direct production of potassium carbonate by electrolysis of potassium chloride solution with the membrane cell was studied. The current efficiency was high since the hydroxyl ion concentration in the cathode compartment was low, resulting in minimum back-migration of OH^- through the membrane. The reduction of the cell voltage is discussed in some detail. The anode and cathode materials having low overvoltages were studied, and Nafion 423 was used as the separator. The operation of a separate reactor for carbonating the catholyte liquor is also described briefly.

Although the production capacity and the market of caustic and carbonate potash are small in comparison with the soda products, they are still important chemicals. Potassium carbonate is produced only by absorption of carbon dioxide with caustic potash, and there is no direct route from chloride such as the Solvay process for making soda ash because of the large solubility of potassium carbonate: 127g/100g H_2O compared to 46g/100g H_2O of Na_2CO_3 at 60°C (1).

Caustic potash is produced by electrolysis of potassium chloride solution. However, the current efficiency of the membrane cell is said to be low somewhat caused by small transport number of K^+ in the membrane compared to the case of NaCl electrolysis (2).

There are several publications on the electrolytic production of sodium carbonate where the caustic catholyte is carbonated to keep the OH^- concentration low, resulting in high current efficiency (3, 4). In fact, it is troublesome since sodium carbonate and bicarbonate deposit in the cathode compartment.

In the case of potassium salts, on the other hand, this process would be desirable because of no unwanted deposition (5). This paper deals with a small cell experiment and a pilot test for the direct electrolytic production of potassium carbonate from potassium chloride solution with a membrane cell followed by absorption of carbon dioxide with the catholyte effluent.

Flowsheet and Reaction Sequence

A proposed flowsheet is illustrated in Fig. 1. Concentrated and purified KCl solution is pumped to the anode compartment of the membrane cell, and its effluent is sent back to the reservoir through the gas-solution separator where chlorine gas is recovered. Polishing of the feed brine with the chelating resin column is of great importance in eliminating a trace of hardness ions so as to keep the cell performance high and in extending the membrane service life (6, 7). The depleted brine is sent to the brine treatment yard. It is not shown in this figure.

* Electrochemical Society Active Member.
[1] Exchange scholar at Nagoya Institute of Technology (1981-1982).

The catholyte liquor flows down from the top of the CO_2 absorption tower packed with the Raschig rings to carbonate caustic solution into carbonate, then bicarbonate after separation of hydrogen. A part of the catholyte liquor is bypassed to the second stage of the absorption tower, where carbonate is converted into bicarbonate.

Water is supplied to the catholyte reservoir to adjust the water balance and the solution concentration.

The reaction sequence is simple. In the electrolytic cell, chlorine and hydrogen are liberated at the anode and the cathode, respectively

$$2Cl^- = Cl_2 + 2e \quad [1]$$

and

$$2H_2O + 2e = H_2 + 2\,OH^- \quad [2]$$

Since the catholyte contains bicarbonate ions, reaction [3] takes place in the bulk of solution

$$OH^- + HCO_3^- = CO_3^{2-} + H_2O \quad [3]$$

The catholyte effluent is further carbonated in the absorption tower to keep the OH^- concentration low, but the bicarbonate content in the product should also be controlled.

An excess solution absorbs more CO_2 to convert into bicarbonate in the second stage of the tower

$$CO_3^{2-} + CO_2 + H_2O = 2HCO_3^- \quad [4]$$

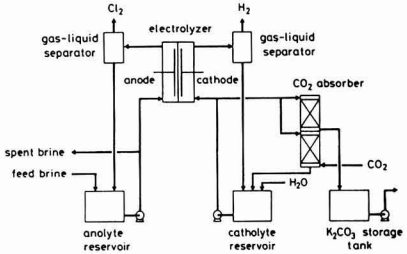

Fig. 1. Flowsheet for the electrolytic production of potassium carbonate

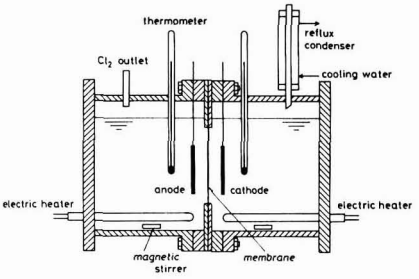

Fig. 2. A small Lucite cell

Experimental Procedure

A small Lucite cell, shown in Fig. 2, was fabricated to determine the electrode polarization, the IR drop through the membrane, and the cathode current efficiency in the batch-wise system. That is, four Luggin-Haber probes were positioned on the front of the anode and cathode, and both sides of the membrane. The Luggin probes located at the cathode compartment were connected with respective reference electrodes composed of Hg/HgO/1*M* KOH, while the probes in the anode side were referred to the saturated calomel electrodes (SCE).

The solution gaps in both the anode and cathode compartments were large enough for the convenience of experiment.

The DSA-type (RuO_2+ TiO_2) anode was prepared by a conventional manner, and another material—named MODE—was also used. The MODE is a platinized Ti mesh loaded with IrO_2 as the electrode catalyst (8). A nickel sheet was used as the cathode.

The solutions, 0.2 liter each in volume at the anode and cathode sides, were agitated by the magnetically driven stirrer, and the temperature was controlled at 60°C by electric heater.

The flowsheet of the pilot experiment was almost the same as shown in Fig. 1, with some exceptions. A major difference was the separate operation of the electrolyzer from the gas absorber.

A vertical and rectangular-type electrolytic cell, also made of Lucite resin, is illustrated in Fig. 3. The Nafion membrane of 5 cm wide and 40 cm long was flanged by two frames, and supported by the anode mesh. The

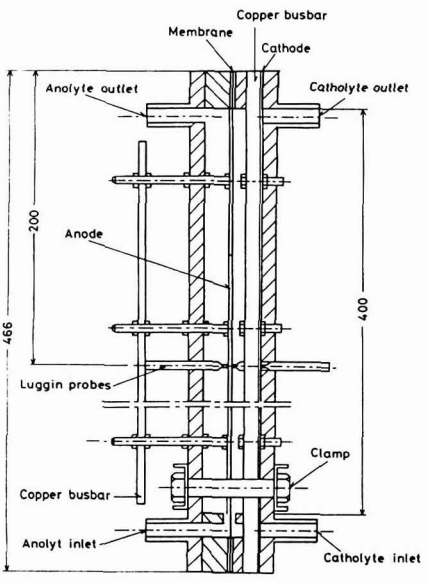

Fig. 3. A vertical cell

membrane-to-cathode gap was adjusted by a frame of a certain thickness. A MODE mesh was employed with this cell. A plain Ni sheet was mostly used as the cathode, and some experiments were conducted with an activated mesh cathode consisting of a steel coated with the Raney nickel. An alloy composed of 50% Ni and 50% Al was plasma-sprayed on a steel mesh substrate, then aluminum was leached out with hot concentrated caustic soda for a day. The apparent electrode area was about the same as of the membrane, so that the current density on both electrode and membrane was *ca.* 40 A/dm² at 80A in total amperage. The current density presented in this paper is referred to the membrane surface.

Nafion membranes 315, 417, and 423 were employed. Most experiments were conducted with 423. These membranes were treated with boiling water for about an hour prior to experiment.

The temperature was controlled by the electric heater immersed in the reservoir. The solution volume was 8 liters each side. The anolyte flow was kept constant at 3 liter/min, and was large enough to keep the solution composition to be unchanged during experiment. On the other hand, the catholyte flow rate was varied in a wide range, 0.04-3.0 liter/min. All the catholyte flows through the gap between the membrane and the flat plate cathode. On the other hand, a part of the catholyte and hydrogen bubbles evolved may pass through the back-space when the mesh cathode is provided.

Potassium chloride of 4.2*M* in concentration was fed to the anode compartment. The catholyte was composed of a mixture of $KHCO_3$ and K_2CO_3. The total molarity was kept constant at 2.0*M*, and the concentration ratio of the constituents was varied in a wide range. Its composition and concentration are not optimum, but it is just for the convenience of experiment. In practice, the higher the catholyte concentration, the higher is the performance of the cell. Potassium hydroxide was also added to the catholyte if necessary. These electrolytes were prepared with reagent-grade chemicals and deionized water. Also, the anolyte was further treated by passing through the chelating resin column when the hardness content reached unacceptable levels.

The catholyte was titrated with HCl solution and the indicator composed of methyl red and bromocresol green before and after electrolysis to evaluate the current efficiency for the cathode products. The solution composition was determined by *p*H titration.

A vertical cell was normally operated continuously for 30 Ah at various current densities, while a small batch cell was operated for 2.1 Ah.

Results and Discussion

As is shown in Eq. [3] and [4], the reaction of KOH with $KHCO_3$ is just a neutralization, so that OH^- and CO_3^{2-} may exist in alkaline solution. On the other hand, the solution containing excess CO_2 or HCO_3^- is composed of $KHCO_3$ plus K_2CO_3, but no KOH. In consequence, a parameter α shown by Eq. [5] is used to represent a nature of the mixed solution or the KOH-K_2CO_3-$KHCO_3$ system instead of the molar concentration *C* of the components

$$\alpha = \frac{C_{CO_3^{2-}} + C_{OH^-}}{C_{HCO_3^-} + C_{CO_3^{2-}}} \qquad [5]$$

At α = 1, neither OH^- nor HCO_3^- exist in the solution; that is, the solution contains only K_2CO_3. If $\alpha < 1$, the solution contains excess $KHCO_3$, but no KOH. On the other hand, OH^- remains in the solution, but there is no $KHCO_3$ when $\alpha > 1$. It is useful to compare the electrolyte of different composition and concentration.

Figure 4 shows an example of the current efficiency and the terminal voltage of a small cell shown in Fig. 2 as functions of α. It is clear that the current efficiency decreases when α increases, especially in the region larger than unity of α caused by a significant migration of OH^- from the cathode compartment to the anode side through the membrane. On the other hand, the cell voltage goes down with the increase of α because the IR drop between

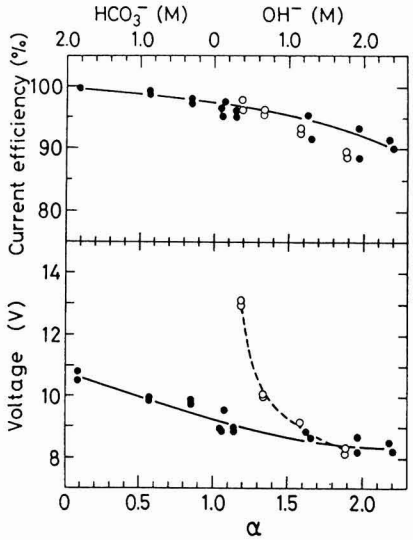

Fig. 4. Current efficiency and voltage of the small cell as functions of the solution composition. Closed points: solution containing carbonate. Open points: solution free of carbonate. Anode: DSA. Cathode: plain Ni. Membrane: Nafion 423. Anode-to-membrane gap: 27 mm. Cathode-to-membrane gap: 27 mm. Current density: 20 A/dm². Temperature: 60°C.

the cathode and the membrane decreases with the increase of the ionic strength and/or the KOH concentration. The cell voltage in this figure is very large and is shown as reference because the solution gaps in both the anode and cathode sides are large.

This figure also shows the current efficiency and the cell voltage obtained with the KOH catholyte free of carbonate. The current efficiency is almost equal to that of the cell operated with mixed solutions. It represents that the back-migration of OH^- through the membrane is not affected significantly by carbonate ions. The cell voltage was, of course, very high in weak solutions whereas it was almost the same as of the cell filled with mixed solutions in the concentration range of OH^- more than 1.5*M*.

The current efficiency and the voltage of the vertical cell equipped with Nafion 423 as functions of the catholyte composition are shown in Fig. 5. The current density was 20 A/dm², and the solution temperature was kept constant at 60°C. The catholyte flow was 3 liter/min or *ca.* 16.7 cm/s in a 6 mm gap between the flat plate cathode and the membrane. As is shown by the top draft in this figure, the current efficiency of the vertical cell was almost equal to that of the small cell described above. The cell voltage in this case is relatively low in comparison with that of the small cell because the membrane touches on the anode mesh and the cathode gap is small, but is still insufficient. The flow rate was a small factor on the current efficiency as shown in Fig. 6. Of course, electrolytic hydrogen bubbles associate with forced circulation to agitate the catholyte and to keep the solution composition uniform across the vertical cell.

At the flow rate lower than 0.1 liter/min or 0.6 cm/s, the OH^- concentration in the cathode compartment increases and causes the current inefficiency.

Figure 7 illustrates that the current efficiency is almost independent of the current density in the range 10-40 A/dm² if α does not exceed unity. Also, the current efficiency did not change in the temperature range 40°-70°C. The cell voltage is almost linear with the current density in the range 10-40 A/dm² (see bottom of the figure), which represents that the major factor of the cell voltage is the ohmic component, either membrane or electrolyte, rather than the overvoltage.

From the viewpoint of product quality, potassium carbonate is contaminated by either caustic potash or bicarbonate depending on α, and hence α must be controlled as exactly as possible.

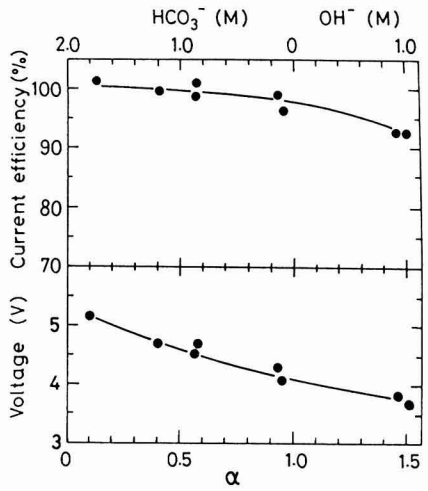

Fig. 5. Current efficiency and voltage of the vertical cell as functions of the solution composition. Anode: MODE. Cathode: plain Ni. Membrane: Nafion 423. Cathode-to-membrane gap: 6 mm. Current density: 20 A/dm². Temperature: 60°C. Catholyte flow rate: 3 liter/min.

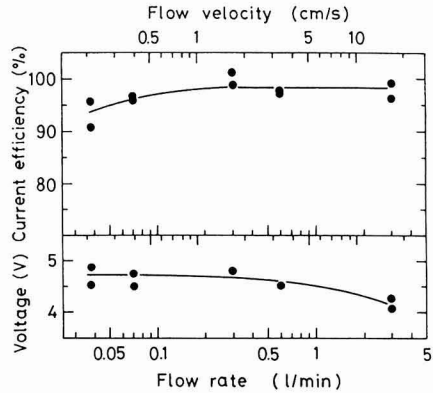

Fig. 6. Current efficiency and voltage of the vertical cell as functions of the catholyte flow. Operating conditions were the same as in Fig. 5, except α = 0.9-1.0.

Table I shows the breakdown of the terminal voltage of the small cell and the vertical cell at a given current density (20 A/dm²) and temperature (60°C). The figures for the small cell were obtained by experiment with the exception of the catholyte IR drop. Its IR drop was calculated with an assumption of 6 mm for the electrolysis gap to compare the voltage drop in two cells under the same conditions. The solution conductivity was measured with a separate cell for this treatment. The anolyte IR drop of the small cell was dropped from the list for the same reason. Both cells were equipped with a mesh-type MODE anode, a plain Ni cathode, and Nafion 423. As shown in Fig. 2, since the solution gaps in both the anode and cathode compartments of the small cell are large enough, the gas voidage is small, and hence it is concluded that the experimental results do not contain any bubble effect of hydrogen and chlorine in this case.

In the vertical cell, on the other hand, Nafion membrane is supported by the anode mesh while the cathode plate is located at 6 mm from the membrane, and the catholyte is circulated in between at a constant rate (3 liter/min). Therefore, detachment of chlorine bubbles from the anode-membrane structure is delayed, and the

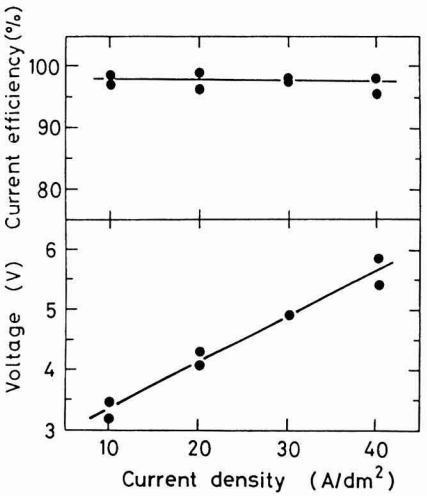

Fig. 7. Current efficiency and voltage of the vertical cell as functions of the current density. Operating conditions were the same as in Fig. 5, except for α = 0.9-1.0.

catholyte in the electrolysis zone is crowded by hydrogen bubbles to some extent. As a result, the overvoltages at the anode and the cathode, and also the membrane IR drop, increase considerably depending on the blinding of these surfaces.

The reversible potentials for the hydrogen and chlorine electrode processes under operating conditions of solution composition and temperature were measured with the small cell and agreed with theory. These results were used to break down the cell voltage shown in Table I.

The overvoltages obtained with the small cell are also shown in Fig. 8. In this case, the IR drop between the working electrode and the Luggin probe was calibrated by the current interruption technique. However, the anode potential of the vertical cell in Table I contains some IR drops between the anode and the Luggin probe.

The membrane IR drop in the small cell was some 0.6V, as shown in Table I, and did not contain any disturbance as the vertical cell was affected. However, it is still very large in comparison to the IR drop of similar Nafion employed in the NaCl cell: *ca.* 0.3V at 80°C with Nafion 427 (9) due to different conductivity in both cases.

As is shown in Table IIA as example with Nafion 315, the resistance of Nafion membranes immersed in potassium electrolyte is larger than that in sodium salt solution due to different permeability of K^+ and Na^+. Also, the specific resistance in carbonate solution is large compared to hydroxide solution. These factors reflect directly the IR drop through the membrane in potassium

Table I. Breakdown of the cell voltage at 20 A/dm². Membrane: Nafion 423. Anode: MODE mesh. Cathode: plain Ni plate. Cathode-to-membrane gap: 6 mm. Flow rate: 3 liter/min. α = 1. Temperature: 60°C

	Small cell (V)	Vertical cell (V)
Anode potential	1.350	1.563
Reversible potential	*1.300*	*1.300*
Overvoltage	*0.050*	0.263
Cathode potential	−1.315	−1.321
Reversible potential	*−0.735*	*−0.735*
Overvoltage	*−0.580*	*−0.586*
Catholyte IR drop	0.348	0.368
Membrane IR drop	0.662	1.130
Membrane potential	−0.010	−0.025
(Sum) Terminal voltage	3.665	4.357

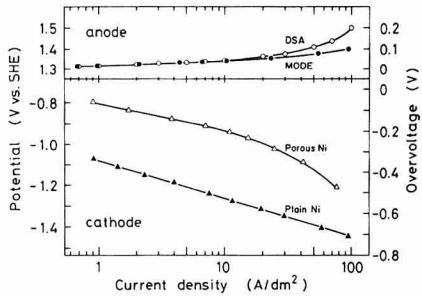

Fig. 8. Polarization curves of various electrodes. Anolyte: 4.2M KCl. Catholyte: 2.0M K_2CO_3. Temperature: 60°C.

carbonate cell under discussion. Table IIB lists the nominal resistance of Nafion membranes in a dilute KCl solution (0.6*N* KCl at 25°C, reported by du Pont) and the test results obtained in the small cell under operating conditions.

On the other hand, very large IR drop through the membrane positioned in the vertical cell was recorded as shown in Table I. Because the membrane was supported by the anode mesh, chlorine bubbles liberated from the anode were disturbed to escape, and hence the membrane surface was covered by gas bubbles to a great extent. This causes large IR drop through the membrane, also the anode overvoltage. It is known that gas bubbles can detach from the membrane if the surface is hydrophilic.

Uneven current distribution in the membrane attached to the mesh electrode is also a factor on high voltage drop; that is, the effective area for passing electrolytic current reduces to some extent, which is a common problem for the membrane cell technology. Consequently, an adequately designed electrode must be employed to eliminate, or minimize at least, these troubles.

The cathode overvoltage is the second largest factor of the terminal voltage after the membrane IR drop when the plain Ni cathode is used. Several cathode materials showing low hydrogen overvoltage are available in the market. The hydrogen overvoltage of a Raney-type porous Ni cathode is very low (see Fig. 8), and its Tafel slope is somewhat small, *ca.* 110 mV/decade, in comparison with 142 mV/decade of a plain Ni cathode.

The solid line labeled 423 in Fig. 9 shows the voltampere curve of the cell equipped with Nafion 423 and a porous Ni-coated mesh cathode attached with Nafion. The voltage saving from the cell with a plain Ni cathode (see dotted line) is *ca.* 0.6V at 20 A/dm². The experimental

Table II. Resistance of Nafion membranes

A. Nafion 315 in various solutions at 60°C

Anolyte	Catholyte	Resistance (Ω-cm²)
4.2*M* KCl	2*M* K_2CO_3	4.0
	1*M* K_2CO_3 + 2*M* KOH	3.2
	4*M* KOH	2.7
5.4*M* NaCl	2*M* Na_2CO_3	2.7
	1*M* Na_2CO_3 + 2*M* NaOH	2.0
	4*M* NaOH	1.6

B. Nafion 423, 417, and 315

Type of Nafion membranes		Resistance (Ω-cm²) Nominal[a]	Measured[b]
423	5-1200/T-12	5.4	3.3
417	7-1100/T-12	4.1	2.3
315	2-1500/4-1100/T-12	5.5	4.0

[a] In 0.6*N* KCl at 25°C, quoted from du Pont's brochure.
[b] Anolyte: 4.2*M* KCl. Catholyte: 2.0*M* K_2CO_3 at 60°C.

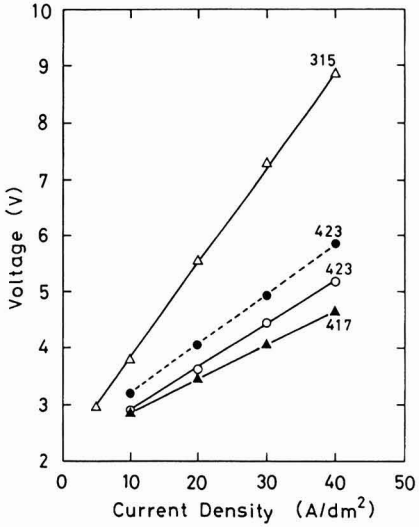

Fig. 9. Voltage vs. current density curves (solid line) of the vertical cell equipped with MODE and a porous Ni cathode attached with Nafion membrane at 60°C. Dotted line shows the results with a plain Ni cathode located at 6 mm for the membrane (see Fig. 8). Catholyte flow: 3 liter/min. α = 0.9-1.0.

results with other membranes are also shown. The cathode current efficiency at 20 A/dm² was, of course higher than 95% in all cases.

The solution temperature is an important factor for cell operation. The higher the temperature, the lower is the cell voltage. The cell voltage could be reduced further by 0.2V when the operating temperature is raised from 60° to 90°C, whereas only few experiments were conducted under such conditions since the plastic cell was affected by chemical attack.

Most experiments described here were conducted with the catholyte of 2*M* total concentration and at the current density of 20 A/dm² for the convenience of experiment. Of course, the higher the concentration, the lower was the cell voltage. The current efficiency was almost independent of the total catholyte concentration. Therefore, the concentration must be kept as high as possible. Also, we estimate that an optimum current density may exist at higher levels than 20 A/dm², so that the investment or the fixed charge is lowered while further experiment and engineering considerations are required for evaluating the economy of this process.

Absorption of carbon dioxide with potassium hydroxide solution (reaction [6]) followed by reaction [4] or [7] is a typical process of gas absorption accompanied with chemical reaction (10-12), and is very fast, especially at high temperatures

$$CO_2 + 2KOH = K_2CO_3 + H_2O \quad [6]$$

and

$$CO_2 + K_2CO_3 + H_2O = 2KHCO_3 \quad [7]$$

The catholyte can be carbonated by introducing CO_2 gas into the cathode compartment, while the cell configuration is complicated somewhat (4). However, use of a separate reactor in parallel with the electrolyzer is preferable for easy operation and reduction of the energy consumption, as is illustrated in Fig. 1.

Excess caustic in the catholyte effluent is neutralized in the upper column of the absorption tower (see Fig. 1), and a part of solution is recovered as an intermediate of the product, which is concentrated or evaporated, depending on the market. Remains flow down to the second stage of the tower where the solution absorbs more CO_2 to obtain bicarbonate (reaction [4A]) to prepare the catholyte liquor.

In conclusion, electrochemical production of potassium carbonate with a membrane cell was studied. The cathode current efficiency was high at almost 100% in a wide range of the operating conditions since the OH^- concentration in the cathode compartment was low. The IR drop through the membrane was the largest factor of the terminal voltage. Although Nafion 423 was employed most often in this experiment, any membrane having lowest resistivity is preferable since the OH^- concentration in the catholyte liquor is sufficiently low, and further reduction of the cell voltage is thus anticipated. The flowsheet shown in Fig. 1 is applicable to practice because of easy operation of the whole process of interest.

Acknowledgments

The Nafion membranes were supplied by the Experimental Station of E. I. du Pont de Nemours and Company, Wilmington, Delaware, by arrangements of Mr. S. Higuchi of du Pont Japan, Tokyo. The Raney-type Ni-coated cathode was prepared by Showa Company, Nara, Japan. The authors wish to thank Y. Ishida, A. Kuroyanagi, and N. Yamauchi for their laboratory efforts.

Manuscript submitted March 19, 1985; revised manuscript received *ca.* June 28, 1985. This was Paper 423 presented at the Toronto, Ontario, Canada, Meeting of the Society, May 12-17, 1985.

Nagoya Institute of Technology assisted in meeting the publication costs of this article.

REFERENCES

1. "Lange's Handbook of Chemistry," 12th ed., J. A. Dean, Editor, Section 10, McGraw-Hill, New York (1979).
2. W. Yang, K. Hara, and F. Hine, *Soda to Enso*, **33,** 123 (1982).
3. H. Kaden, P. Volland, K. Zimmermann, and H. Hofmann, *Chem. Technol.*, **27,** 356 (1975).
4. D. L. DeRespiris and T. J. Gilligan, Abstract 451, p. 1130, The Electrochemical Society Extended Abstracts, Vol. 78-1, Seattle, WA, May 21-26, 1978.
5. W. Yang and F. Hine, *Soda to Enso* **33,** 192 (1982).
6. K. Sekine and C. Motohashi, *ibid.*, **33,** 66 (1982).
7. C. Motohashi, *ibid.*, **34,** 516 (1983).
8. T. Asaki, Y. Kamegaya, and K. Takayasu, in "Advances in the Chlor-Alkali and Chlorate Industry," M. M. Silver and E. M. Spore, Editors, p. 165, The Electrochemical Society Softbound Proceedings Series, Pennington, NJ (1984).
9. T. Berzins, Abstract 437, p. 1137, The Electrochemical Society Extended Abstracts, Vol. 77-2, Atlanta, GA, Oct. 9-14, 1977.
10. "Chemical Engineers' Handbook," 5th ed., R. H. Perry and C. H. Chilton, Editors, Section 14, McGraw-Hill, New York (1973).
11. S. Hatta, *Kogyo Kagaku Zasshi*, **31,** 869 (1928); *ibid.*, **32,** 809 (1929).
12. S. Hatta, *ibid.*, **35,** 1397 (1932); *ibid.*, **36,** 7 (1933).

Analysis of Laboratory Data in Early Stages of Evaluation of Electro-Organic Reactions

Edward K. Yung*,[1] and Richard C. Alkire*

Department of Chemical Engineering, University of Illinois, Urbana, Illinois 61801

ABSTRACT

The production of 1,2-dichloroethane and ethylene chlorohydrin by electrolysis of ethylene containing hydrochloric acid solutions was studied with a bench-scale continuous-flow undivided parallel-plate cell. The product distribution was independent of electrolyte flow rate and current density, but was significantly influenced by the chloride ion concentration. The cell current-voltage curves were found to be independent of electrolyte flow rate. Engineering models which included consideration of the chemical environment in the electrolysis zone were developed from fundamental principles of mass transport, ohmic resistance, and reaction kinetics. The models were verified by comparison with experimental findings, and were subsequently used to explore engineering aspects of scale-up and optimization. These models were incorporated with economic analyses to study the influence of design and operating parameters on the cost of 1,2-dichloroethane. A successive quadratic programming method was used to identify optimal operating conditions as well as the most sensitive parameters of the system.

Development of new electro-organic synthesis processes depends on knowledge of chemical mechanism as well as on engineering design trade-offs. The unification of these perspectives at an early stage of development can promote a more cost-effective exploration of those factors which control the candidate process. The purpose of the present study was to provide methodology by which small-scale experiments can be exploited to evaluate process limitations at an early stage. The emphasis of the work was on a methodology which is simple and portable to other applications, and not on development of a specific candidate process.

The process chosen for study was the production of 1,2-dichloroethane (DCE) and ethylene chlorohydrin (EC) by electrolysis of hydrochloric acid solutions containing ethylene. The synthesis was an indirect electrochemical process in which chlorine was produced at the anode, and products were generated by electrophilic addition of chlorine to ethylene

$$C_2H_4 + Cl_2 + \frac{R}{R+1}H_2O \rightarrow \frac{1}{R+1}C_2H_4Cl_2 + \frac{R}{R+1}C_2H_3OCl + \frac{R}{R+1}HCl$$

where R is the product ratio defined as $R = [EC]/[DCE]$. The reaction mechanism consists of formation of a chloronium ion intermediate followed by attack from nucleophiles (1).

A series of feasibility studies for electrochemical chlorination of ethylene was carried out by Tedoradze *et al.* (2-5). Experiments were carried out in ethylene-sparged beaker cells with planar electrodes. Parameters investigated included purity and concentration of HCl solutions, temperature, current density, electrode materials, and ethylene feed rate. The dependence of yield and product spectrum upon these parameters was reported. These studies made their contribution in demonstrating feasibility and identifying the proper chemical environment for the process.

Early aspects of process evaluation also require quantitative data obtained in well-characterized experimental systems. The scope of the present work included bench-scale experiments, formulation of models of the reaction chemistry and of the electrolytic cell, scale-up, cost evaluation, optimization, and sensitivity analysis.

Fundamental analyses of the parallel-plate cell geometry have been reported (6). For the system under study, however, gas evolution on both electrodes complicated the mass transfer and ohmic resistance aspects. The influence of gas bubbles on the current distribution in electrolytic cells has been reported (7, 8) for situations where the population distribution of bubbles was uniform. A review of gas evolving electrodes has been provided by Vogt (9).

The scale-up of electrochemical processes has recently been reviewed (10) with emphasis on the value of engineering models to exploit limited bench-scale laboratory data. Capital costs for electrochemical cells have become available (11), and examples of economic evaluations have been reported (12).

Methods for optimization of electrochemical processes (13) are beginning to emerge for analysis of individual cells (14, 15) as well as entire electrolytic processes (16). In general, optimization considerations should be based on the entire flowsheet, since in some cases it is worthwhile to accept cell modifications in order to achieve better downstream operations.

Experimental

Apparatus.—The electrochemical cell was of undivided parallel-plate geometry and consisted of two cell housing pieces and a spacer, all of polypropylene. The electrodes were mounted flush with the flow channel surfaces, opposite each other, and were held in place by the spacer which also served to establish the gap distance between electrodes. The anode material was Karbate® no. 22 (Union Carbide), a graphite material impregnated with a standard phenolic resin, impervious to liquids. [Results of auxiliary limiting current experiments (17) for chlorine reduction with a Karbate® rotating disk electrode indicated that deviation of the active surface area from the apparent surface area was less than 5%.] The cathode was platinized graphite (17) on a substrate of Poco AXF-5Q (Union Oil) graphite. The exposed electrode surface had a dimension of 10.2 × 2.54 cm. A hydrodynamic entrance length (43.2 cm) was provided for flow development upstream from the electrodes. For a typical cell gap of 0.635 cm, this hydrodynamic entrance length was adequate up to a Reynolds number of 1700, where the Reynolds number was based on the cell gap (18). The downstream calming region was 10.2 cm long. Current feeders consisted of threaded oxygen-free copper rods (1/8 in. diam) connected to the back side of the electrodes.

The flow system is shown schematically in Fig. 1. A bubble column (4 ft length) was included for ethylene (Air Products, C.P. Grade, 99.8%) absorption. The ethylene stream eventually passed through a Dry Ice cold trap for recovery of residual 1,2-dichloroethane. The liquid stream passed through flow measurement devices (Gilmont, F1500 and F1300), flow stabilizer, the electrochemical cell, and then returned to the reservoir. The function of the flow stabilizer was to collect the gradually released

*Electrochemical Society Active Member.

[1]Present address: International Business Machines Corporation, Thomas J. Watson Research Center, Yorktown Heights, New York 10598.

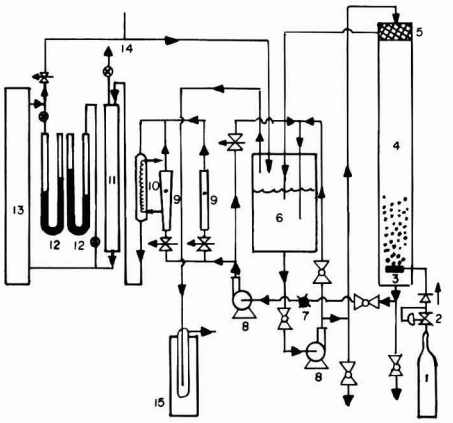

Fig. 1. Flow system. 1: Ethylene cylinder. 2: Regulator. 3: Gas sparger. 4: Bubble column. 5: Rasching ring packing. 6: Reservoir. 7: Sampling port. 8: Pump. 9: Rotameter. 10: Condenser. 11: Flow stabilizer. 12: Manometer. 13: Cell. 14: Thermometer. 15: Dry ice cold trap.

ethylene gas so that a steady, bubble-free electrolyte would enter the cell. For electrolysis experiments, the cell pressure was monitored at 1.2 atm, for which release of ethylene gas was found to be sufficiently slow. Tubing and piping were of 1/2 in. polypropylene.

Flow electrolysis experiments were carried out in constant current mode. A current controlling resistor (Koolohm®, 10W, 1Ω) was connected to the power supply (PAR, 371) for cell current monitoring. Current readout was given by a digital multimeter (Keithley, 179A). For cell current-voltage measurements, a function generator was connected to the potentiostat to provide the voltage scan, and the cell current was recorded by an X-Y recorder (Houston Instrument, 2000). HCl (Mallinckrodt, AR) and deionized water were used in electrolyte preparation.

A rotating disk (Pine Instrument, AFDD 20) was used to determine charge transfer parameters. A Karbate® disk (0.318 cm diam) was used for chlorine evolution, and a platinized graphite disk (0.159 cm diam) for hydrogen evolution. The disk sizes were chosen so that the current distribution would be uniform to within 20% up to a current density of 100 mA/cm² (25).

Procedures.—Prior to each electrolysis experiment, ethylene was bubbled for at least 20 min with electrolyte circulation. The period of electrolysis was typically 2h, following which the bulk solution and cold trap were sampled and analyzed by gas chromatography (Varian 3740 Chromatograph and Vista 401 Data Station). The combinations of operating parameters which were investigated included three electrolyte flow rates (95, 328, 1380 ml/min) and four current levels (200, 400, 800, 1600 mA). Four electrolyte concentrations (1, 2, 4, 8*M* HCl) were used to study the effect of chloride ion concentration on the product spectrum. Temperature range was (25 ± 4)°C.

No organic impurities were found in the electrolyte that would interfere with the chemical analysis. The column was 2 mm glass, 6 ft length, and packed with 1% SP-1000 on 60/80 Carbopack (Supelco, Incorporated). A prepacking of sodium bicarbonate was used to retard attack of HCl on the packing. Helium was the carrier gas; the flow rate was 30 ml/min at an inlet pressure of 50 psig. The flame ionization detector was held at 210°C, while the flash injector was held at 180°C. For analysis, the column was held at 50°C for 2 min and then subjected to temperature programming at a ramp rate of 10°C/min to a final temperature of 150°C. Ethanol was used as the internal standard.

Cell current-voltage curves were recorded for various combinations of cell gap and flow rate. Voltage sweep rate was 10 mV/s, which appeared to be slow enough to minimize double-layer charging effects as well as to allow the cell to operate at pseudo-steady state.

Results and Discussion

The amount of the two major products, 1,2-dichloroethane (DCE) and ethylene chlorohydrin (EC), was a linear function of the electrolysis period. For most experimental runs, the material yield (*Y*)

$$Y = \frac{\text{sum of the amount of EC and DCE}}{\text{total amount of chlorine generated at 100\% current efficiency}}$$

was in the range of (100 ± 5)%. Therefore, the current efficiency for chlorine evolution was 100% at all current densities investigated. Electrolyte flow rate and cell current were found to have little influence on the product spectrum.

Chloride ion concentration was found to have significant influence on the product distribution. As the chloride ion concentration was increased, the product spectrum shifted towards 1,2-dichloroethane. Supplementary experiments for the study of solution phase reaction between ethylene and chlorine were carried out with a chemical flow reactor having no electrodes. To within experimental error, it was found that the product distribution was practically identical to that from the electrolysis experiments. It was concluded that, even in the presence of electrodes, the reaction was still occurring in the solution phase. Figure 2 shows the dependence of the product distribution upon the ratio $[H_2O]/[HCl]$. The equation which fits these data is

$$R = \frac{[EC]}{[DCE]} = -0.102 + 0.132\,\frac{[H_2O]}{[HCl]} \qquad [1]$$

The product distribution results in Fig. 2 agree with the commonly accepted mechanism of chlorination of olefins (1)

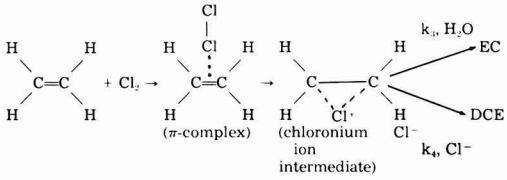

According to this mechanism, the slope of the straight line would be the ratio (k_3/k_4) of the two rate constants leading to the formation of the two major products. Evidence given by Serguchev and Konyushenko (19, 20) indicated that the ratio k_3/k_4 was relatively independent of the reactivity of the unsaturated compounds. The number obtained in our experiments (0.132) compares favorably with that for chlorination of styrene in aqueous system (0.133) as well as that for chlorination of allyltrimethylammonium perchlorate (0.156). The activity of styrene has been estimated to be 1.2×10^5 times that of allyltrimethylammonium perchlorate. However, there was evidence (20) that the ratio depended upon the solvent composition. Therefore, extension of the experimental finding to systems other than aqueous hydrochloric acid would not be recommended.

The product ratio resulting from thermodynamic equilibrium between the two products following the reaction

$$C_2H_4Cl_2 + H_2O \rightleftharpoons C_2H_5OCl + HCl;$$

$$K_{eq} = [C_2H_5OCl][HCl]/[C_2H_4Cl_2][H_2O]$$

would be expected to be pH dependent. However, supplementary experiments with mixed electrolytes of HCl and NaCl showed that the product distribution depended upon total chloride ion concentration but not upon HCl concentration. It was therefore concluded that the product distribution was controlled by the kinetics of the homogeneous reaction.

It was found that the same I-V curve was recorded for both 1*M* HCl and for ethylene-saturated 1*M* HCl as long as

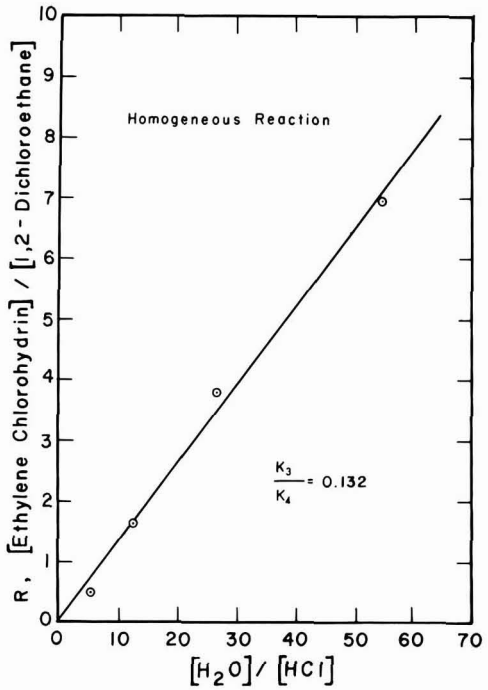

Fig. 2. Determination of the ratio of rate constants (k_3/k_4)

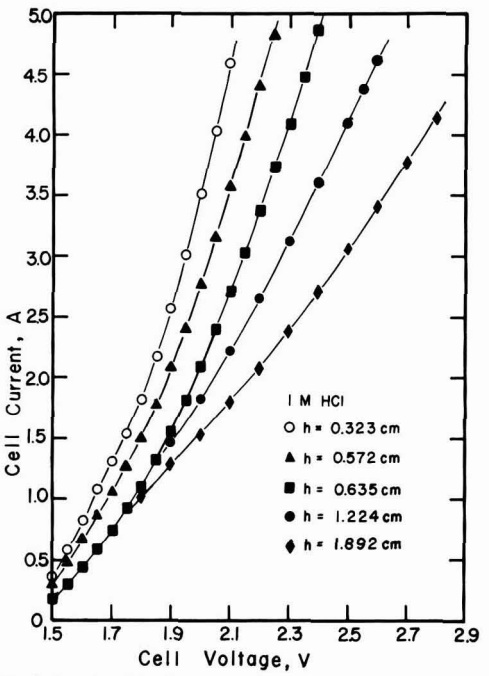

Fig. 3. Experimental cell current-voltage curves for different cell gaps

the cell was kept continuously active. If the power was turned off, the I-V curve from the first subsequent voltage scan would then be different, but subsequent scans eventually reverted to the curve found in ethylene-free electrolyte. These observations suggest that as long as the cell is continuously activated, there will be no possibility for the adsorption of ethylene to occur and the electrode will not respond to the presence of ethylene. These results support the interpretation that rapid reaction between ethylene and chlorine occurs in the solution phase and that the cell plays only the role of a chlorine source.

For a fixed cell gap, the I-V curves were found to be independent of the electrolyte flow rate over a range from 50 to 2000 ml/min. The I-V curves recorded for various cell gaps ranging from 0.323 to 1.892 cm are shown in Fig. 3. It can be seen from the slope of the high current portion of the curves that at the same cell voltage the cell current is smaller for larger cell gap, owing to larger ohmic loss in solution phase. Also, the cell gap influences the overall shape of the curves; the curves become straight lines at lower current levels for larger cell gaps. These measurements were clarified by visual observations described in the following paragraphs.

For visual observation of flow pattern in the electrolysis region, a transparent Plexiglas[16] spacer 1.224 cm thick was used. While the results are qualitative in nature, the phenomena which were observed were essential for resolution of I-V data.

Gas evolution was observed at both electrodes. Three distinct regions were seen. Next to the anode surface, a thin layer containing a chlorine bubble swarm was observed. All bubbles seemed to move at the same velocity. Coalescence of bubbles was not apparent. A similar bubble layer containing hydrogen bubbles was seen adjacent to the cathode. The central portion of the flow channel was free of bubbles. The diameter of hydrogen bubbles was estimated to be 200 μm and that of chlorine bubbles was estimated to be 100 μm. Bubble size distribution seemed to be narrow. Neither cell current nor electrolyte flow rate seemed to influence the bubble sizes. The thickness of the moving bubble layers was not uniform over the entire electrode length; it increased with the distance from the leading edge. The thickness of the moving bubble layers increased slightly with decreasing electrolyte flow rate. The current level was found to have little influence on the thickness. The hydrogen layer was thicker than the chlorine layer. For a flow rate of 1560 ml/min, hydrogen layer thickness at the center of the electrode was estimated to be 0.05 cm, while the corresponding chlorine layer thickness was estimated to be 0.02 cm. The thickness of the moving bubble layers, δ_{avg}, is represented by

$$\delta_{avg,a} = 0.02(Q/26.0)^{-0.5} \quad [2]$$

$$\delta_{avg,c} = 0.05(Q/26.0)^{-0.5} \quad [3]$$

The rise velocity of bubble swarms was not influenced by the change of electrolyte flow rate for a fixed cell current. Over the cell current range under study (1-3A), the rise velocity varied nearly proportionally with the cell current for fixed electrolyte flow rate, while the layer thickness did not change. For a cell current of 1A, the rise velocity of hydrogen bubble swarm was estimated to be 6 cm/s. The corresponding value for chlorine bubbles was 2 cm/s. These values were in reasonably good agreement with values calculated on the assumption of Stoke's law (21) for an isolated bubble without internal circulation. The rise velocity of bubble swarms was therefore represented as

$$u_{g,Cl_2} = 2I_{cell} \quad [4]$$

$$u_{g,H_2} = 6I_{cell} \quad [5]$$

According to observation of others on bubble formation at solid surfaces (9), it is reasonable to expect that a layer of small stationary bubbles exists underneath each moving bubble layer. This immobile layer would not be expected to be affected by liquid flow, owing to its thinness and the attachment of the bubbles to the electrode surfaces.

A schematic of the flow pattern in the electrolysis region, based on visual observation, is summarized in Fig. 4. This flow pattern will play a central role in formulation of the cell model which follows.

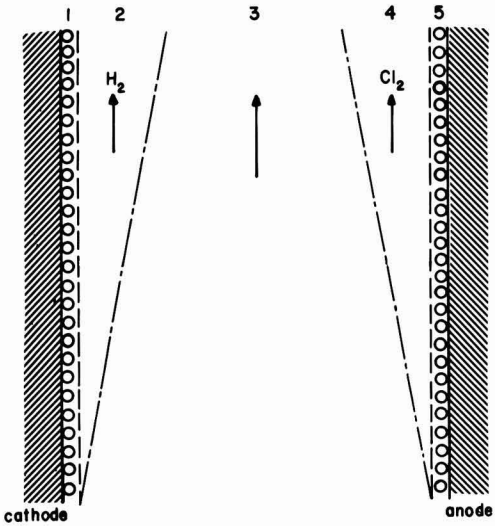

Fig. 4. Schematic of the flow pattern in the experimental cell. Layer 1: Fixed hydrogen layer. Layer 2: Moving hydrogen layer. Layer 3: Bubble-free liquid layer. Layer 4: Moving chlorine bubble layer. Layer 5: Fixed chlorine bubble layer.

Charge transfer measurements with the rotating disk electrode were carried out at four concentrations (1, 2, 4, and 8*M* HCl), and were corrected for the ohmic component by assuming that the reference electrode was infinitely far away. The data for both reactions followed the Tafel equation

$$i_c(x) = i_{c0}\left\{\frac{[H^+]_s(x)}{C^*}\right\}^2 \exp\left\{\frac{-\alpha_c n_c \mathbf{F}}{RT}[-E_{eq,c} - \phi_{s,c}(x)]\right\} \quad [6]$$

$$i_a(x) = i_{a0}\left\{\frac{[Cl^-]_s(x)}{C^*}\right\} \exp\left\{\frac{\alpha_a n_a \mathbf{F}}{RT}[V_{cell} - E_{eq,a} - \phi_{s,a}(x)]\right\} \quad [7]$$

By examination of the data represented by Eq. [7], a value of 1.05V *vs.* SCE was assigned to $E_{eq,a}$, and the exchange current density (i_{a0}) was therefore evaluated at a reference concentration ($[Cl_2]_0$) for each electrolyte such that the combination of $[Cl^-]$ and $[Cl_2]_0$ yielded a value of 1.05V for $E_{eq,a}$. By examination of the data represented by Eq. [6], a value of −0.123V *vs.* SCE was assigned to $E_{eq,c}$; the exchange current density (i_{c0}) was then evaluated at a reference concentration ($[H_2]_0$) which yielded a value of −0.123V for $E_{eq,c}$. These data are listed in Table I.

Theoretical

Reaction chemistry near the anode.—Chlorine produced at the anode reacts homogeneously with ethylene which is dissolved in the solution. The concentration profiles near the electrode were investigated theoretically with use of a transport model, described in the Appendix. Calculations were carried out for combinations of flow rates (3, 10, 20 ml/s) and current densities (8, 16, 32, 64, and 128 mA/cm²). A rate constant of 2×10^5 cm³/mol-s was used since this value had been reported for the uncatalyzed reaction (23); the actual overall rate constant is probably larger since the HCl-catalyzed reaction path would also be available. Details on computation aspects are available in Ref. (17).

Results of these calculations indicated that the homogeneous reaction takes place in a very sharply defined zone at a distance from the anode. At this reaction plane, the chloride ion concentration is essentially identical to that in the bulk solution. Therefore, the product distribution would be expected to be the same as if the chlorine had been bubbled directly into the solution, in agreement with experimental findings. Also, it was computed that the product distribution varied by less than 0.5% for all combinations of flow rates and current densities. These results supported the experimental finding that the product distribution was not affected by either flow rate or current density. Also, the calculations demonstrated that the ethylene concentration between the reaction plane and the anode would be zero, supporting the view that ethylene is not adsorbed on the anode as long as the electrode is maintained in the active state.

The discussion in the first paragraph of the Appendix suggests that the effect of gas bubbles is to increase the rate of transport in comparison with the rate of homogeneous reaction. One simple way to achieve such alteration in relative rates in the present model is to decrease the reaction rate constant (or to increase the diffusion coefficient). When calculations were carried out with rate constants which were 10^6-fold smaller (that is, a value of 2×10^{-1} cm³/mol-s), it was found that the qualitative features of behavior described in the previous paragraph remained valid. It was therefore concluded that the general features described above would not be qualitatively different had a more detailed treatment of bubble evolution been carried out.

Analysis of the electrolytic cell.—An undivided parallel-plate reactor was modeled. The present analysis differs from previous treatments of parallel-plate flow cells owing to the presence of gas bubbles which requires consideration of flow pattern in the formulation of effective electrolyte conductivity. Phenomena under consideration included charge transfer, ohmic resistance, and mass transfer. Parameters for each phenomena were determined experimentally or were obtained from the literature for use in model calculations; these parameters are compiled in Table I. The mathematical articulation of these components into a unified representation of the entire cell constitutes an important task. While each element of the following overall model could be represented in a more sophisticated manner, it is rarely cost effective to do so in early stages of process evaluation. By the method described below, the most sensitive features of an optimized simple model can be identified. In turn, these components can then be upgraded in order to improve in a selective manner the most important features of the cell model.

The charge transfer characteristics of the chlorine and hydrogen evolution reactions on the electrode materials used in this study were obtained experimentally as discussed in the presentation of Eq. [6] and [7] above.

The solution phase ohmic resistance was assumed to be the sum of the resistance of each layer represented in the flow pattern depicted in Fig. 4. The effective conductivity of the bubble curtains was assumed to be 1/5 of the bulk value (27). A thickness of 50 μm was assigned to the chlorine bubble curtain, and a value of 60 μm was assigned to the hydrogen bubble curtain (27).

Bruggeman's equation (28) was used to describe the effective conductivity of the moving bubble layers on each electrode

$$\kappa_{avg,a} = \kappa_0\left[1 - \frac{RT(I_{cell}/2)}{2\mathbf{F}P_{cell}\delta_{avg,a}u_{g,Cl_2}W}\right]^{3/2} \quad [8]$$

$$\kappa_{avg,c} = \kappa_0\left[1 - \frac{RT(I_{cell}/2)}{2\mathbf{F}P_{cell}\delta_{avg,c}u_{g,H_2}W}\right]^{3/2} \quad [9]$$

The total solution phase ohmic resistance was expressed as

$$R_s = 5(0.005)/A\kappa_0 + 5(0.006)/A\kappa_0 + \delta_{avg,a}/A\kappa_{avg,a} + \delta_{avg,c}/A\kappa_{avg,c} + (h - 0.005 - 0.006 - \delta_{avg,a} - \delta_{avg,c})/A\kappa_0 \quad [10]$$

Table I. System parameters used in the modeling of the experimental cell

Parameter	Physical meaning	Value or functional	Ref.
C	HCl concentration	Variable (M), normally 1M	
h	Cell gap	Variable (cm)	
L	Cell length	10.16 cm	
W	Cell width	2.54 cm	
Q	Flow rate	Variable (ml/s)	
V_{cell}	Cell voltage	Variable (V)	
C_0	C_2H_4 concentration	$5.0 \times 10^{-3}M$	
T	Temperature	298.15 K	
P_{cell}	Cell pressure	1 atm	
i_{a0}	Exchange current density for Cl^-/Cl_2 redox pair	4.78×10^{-4} A/cm^2 for 1M HCl	(17)
i_{c0}	Exchange current density for H_2/H^+ redox pair	4.523×10^{-5} A/cm^2 for 1M HCl	(17)
i'_{a0}	Exchange current density for H_2O/O_2 redox pair	1.0×10^{-6} A/cm^2	(17)
$\alpha_a n_a$	Anodic transfer coefficient for chlorine evolution	0.2779 for 1M HCl	(17)
$\alpha_c n_c$	Cathodic transfer coefficient for hydrogen evolution	1.2986 for 1M HCl	(17)
$\alpha'_a n'_a$	Anodic transfer coefficient for oxygen evolution	0.30	(17)
$E_{eq,a}$	Equilibrium potential for Cl^-/Cl_2	1.05V	(17)
$E_{eq,c}$	Equilibrium potential for H_2/H^+	$-0.123V$	(17)
$E'_{eq,a}$	Equilibrium potential for H_2O/O_2	1.01V	(17)
d_{b,Cl_2}	Chlorine bubble departure diameter	50 μm	(27)
d_{b,H_2}	Hydrogen bubble departure diameter	60 μm	(27)
κ_0	Electrolyte conductivity	$\kappa_0 = 0.0126143 + 0.380292C - 0.0591346C^2 + 0.00365068C^3 - 0.0000842448C^4$ (mho/cm)	(35)
D_{HCl}	Diffusion coefficient of HCl	$D_{HCl} = (2.87445 + 0.58244C) \times 10^{-5}$ (cm^2/s)	(35)
ρ	Density	$\rho = 0.999802 + 0.0159094C$ (g/ml)	(35)
η	Viscosity	$\eta = (0.896375 + 0.0393314C + 0.00251171C^2) \times 10^{-2}$ (g/cm-s)	(36)
t_{H^+}	Transference number of H^+	$t_{H^+} = 0.811794 + 0.0302287C - 0.00525897C^2 - 0.000472662C^3 + 0.0000514969C^4$	(35)
D_{Cl_2}	Diffusion coefficient of chlorine	$D_{Cl_2} = 1.44T/(293.15\eta) \times 10^{-7}$ (cm^2/s)	(17)

Note: Range of applicability: 1-8M HCl.

A correlation for mass transfer in the presence of microconvection owing to bubble growth on an electrode surface (24) was used

$$\mathrm{Sh} = 0.93\ \mathrm{Re}^{0.5}\mathrm{Sc}^{0.487} \qquad [11]$$

The equations governing mass transfer were

$$i_a(x) = \mathbf{F}k_{mt,a}[C_b(x) - [Cl^-]_s(x)] \qquad [12]$$

$$i_c(x) = \mathbf{F}k_{mt,c}[C_b(x) - [H^+]_s(x)] \qquad [13]$$

Variation of bulk concentration of HCl was obtained from a differential mass balance

$$C_b(x) = C^* - \frac{W}{2\mathbf{F}Q}\left(\frac{R_0 + 2}{R_0 + 1}\right)\int_0^x i_a(x')\,dx' \qquad [14]$$

The solution phase potential on both electrode surfaces were related by the following equations

$$\phi_{s,a}(x) = \phi_{s,c}(x) + i_c(x)AR_s + \eta_{c,c}(x) + \eta_{c,a}(x) \qquad [15]$$

The concentration overpotentials were formulated on the assumption of dilute solution theory as well as linear concentration profile in the mass-transfer boundary layer (29)

$$\eta_{c,c}(x) = \frac{2RT}{\mathbf{F}}\ln\left[\frac{C^*}{[H^+]_s} - t_{H^+}\left(1 - \frac{[H^+]_s}{C^*}\right)\right] \qquad [16]$$

$$\eta_{c,a}(x) = \frac{2RT}{\mathbf{F}}\ln\left[\frac{C^*}{[Cl^-]_s} - t_{Cl^-}\left(1 - \frac{[Cl^-]_s}{C^*}\right)\right] \qquad [17]$$

The last equation needed is for current balance

$$i_c(x) = i_a(x) \qquad [18]$$

Equations [1]-[18] constitute a system of 18 independent equations for 18 variables at each location of the cell. The variables are i_a, i_c, $k_{mt,a}$, $k_{mt,c}$, $[Cl^-]_s$, $[H^+]_s$, $\phi_{s,a}$, $\phi_{s,c}$, $\eta_{c,a}$, $\eta_{c,c}$, $\delta_{avg,a}$, $\delta_{avg,c}$, u_{g,Cl_2}, u_{g,H_2}, $\kappa_{avg,a}$, $\kappa_{avg,c}$, R_s, and C_b. This set of equations contains parameters the values of which are set according to literature sources or laboratory measurement as well as estimations when literature values were unavailable. Table I lists the values used in the present study.

Method of solution.—It is convenient to arrange the integral in Eq. (14) by approximating it as

$$\int_0^x i_a(x')\,dx' \cong \sum_{j=1}^{m-1} i_a(j)\frac{L}{N} + \left(x - \frac{L}{N}(m-1)\right) i_a(m) \cong \sum_{j=1}^{m-1} i_a(j)\frac{L}{N} \qquad [19]$$

where

$$(m-1)\frac{L}{N} < x \leq m\frac{L}{N}$$

since no iterations were then required for the solution of the equations. Integration was carried out by dividing the cell into N sections along the flow direction, and proceeding section-wise starting from the upstream end of the cell. The set of equations was combined into two nonlinear algebraic equations, and IMSL subroutine ZSPOW was used on the Cyber 175 computer to solve them. Subsequently, the cell current was evaluated by

$$I_{cell} = W\int_0^L i_c(x)\,dx = W\sum_{j=1}^{N} i_c(j)\frac{L}{N} \qquad [20]$$

Results

The calculated cell current-voltage curves for various cell gaps and flow rates are listed in Table II and their comparison with experimental curves is shown in Fig. 5. The discrepancy at low current densities is probably the result of errors in evaluation of kinetic parameters. However, for current densities above 100 mA/cm^2 ($I_{cell} > 2.6$A),

Table II. Calculated I-V curves based on the actual flow pattern

h (in.)	0.127		0.225		0.250		0.482		0.745	
Q (ml/s)	3.6	15.7	3.6	15.7	3.6	15.7	3.6	15.7	3.6	15.7
V (V)	I (mA)									
1.4	58.3	58.3	57.5	57.5	57.3	57.3	55.5	55.5	53.7	53.6
1.5	135.4	135.1	131.3	131.0	130.3	130.0	122.0	121.8	114.2	114.0
1.6	300.8	299.5	282.6	281.5	278.5	277.4	246.7	245.9	220.5	220.0
1.7	621.2	616.3	556.8	553.2	543.1	539.8	448.4	446.4	381.0	379.6
1.8	1162	1148	984.8	975.6	950.0	941.6	730.6	726.2	592.7	590.1
1.9	1951	1919	1567	1548	1497	1480	1083	1075	846.7	842.5
2.0	2970	2910	2281	2249	2161	2133	1491	1479	1133	1127
2.1	4178	4082	3099	3051	2918	2875	1941	1925	1444	1436
2.2	5533	5394	3996	3929	3744	3686	2424	2402	1774	1763
2.3	6999	6812	4953	4866	4625	4550	2931	2903	2119	2105
2.4	8551	8313	5957	5848	5546	5453	3457	3423	2474	2458
2.5	10170	9878	6998	6866	6501	6388	3998	3958	2839	2820
2.6	11841	11493	8067	7913	7481	7349	4552	4506	3211	3189

the error between experimental and calculated curves was less than 30 mV. The model also indicated that the cell current-voltage curves will be insensitive to the flow rate change (see Table II), a phenomenon also observed during the experiments. Reasonable variation in the choice of values of δ_{avg} and u_g (Eq. [2]-[5]) did not affect this conclusion. For a comparison, formulation of the cell model based on a commonly used flow pattern, namely, homogeneous gas-liquid mixture with no slip between phases, was done; the results showed strong dependence of I-V curves on flow rate. The comparison demonstrates that understanding of flow pattern, which in turn can vary with design considerations and operating conditions, is essential for predicting cell behavior of gas evolving systems.

Scale-up and cost analysis.—The application of the cell model to scale-up was made with the following modifications to the foregoing model.

1. The flow pattern was assumed to be a homogeneous gas-liquid mixture over the entire cell domain because of the merging of bubble layers in cells of very large length/gap ratio.

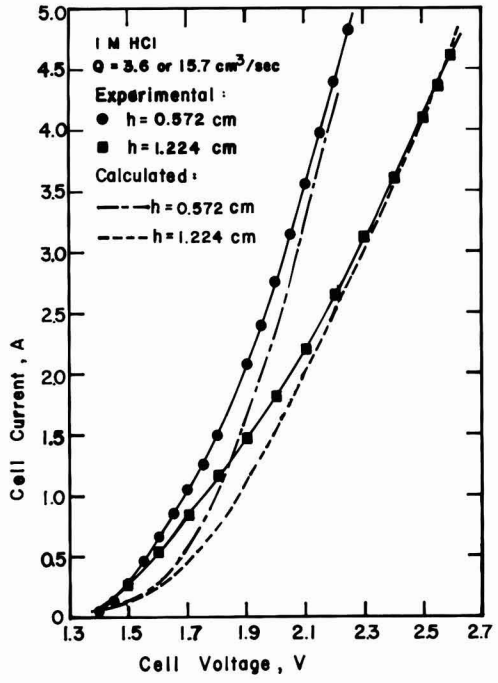

Fig. 5. Comparison of experimental and calculated cell current-voltage curves.

2. Pumping power requirement was included in the scale-up. A correlation proposed by Vogt (30) was used for pressure drop estimation for gas-liquid mixture.

3. The mass-transfer rate was described by a correlation proposed by Vogt (31) which considered the mass transfer to be jointly controlled by gas evolution and hydrodynamic flow.

4. Oxygen evolution following Tafel kinetics was included as an anodic side reaction.

Analyses were carried out for a hypothetical production facility operating at 10^4 metric tons of DCE per year. The overall cost was composed of three components: capital cost, operating cost, and raw material cost. The capital cost was evaluated to the cell battery limit, *i.e.*, cell banks together with their peripheries including rectifiers and bus bars, pumps, piping, instrumentation, etc. Equipment cost of upstream feed preparation and downstream product recovery operations was not included. Operating cost, which included energy cost, labor, and maintenance, was also considered to cell battery limit. Economic information by Keating and Sutlic (11) and supplementary data by Danly (32) for electrochemical cells was used. All cost information was corrected to March 1983 prices. Electricity cost was assumed to be 5 ¢/kWh.

The raw material cost included reactant cost and credit for useful by-products. A price (12 ¢/lb), or half the market price for ethylene glycol, was arbitrarily assigned for ethylene chlorohydrin credit. Credit was also given to hydrogen based on its heat of combustion at an assumed thermal efficiency of 90%. A payback time of seven years was selected. The production cost of DCE was determined so that the total revenue would be equal to the total cost at the end of the payback period.

Calculations were carried out initially for 1*M* HCl to investigate the influence of design and operating parameters on DCE cost. Two parameters, cell gap and flow rate, showed pronounced effects. The variation of DCE cost with cell gap is shown in Fig. 6. A sharp minimum can be seen. For smaller cell gaps, unit cell production rate was higher at a fixed cell voltage, which would lead to smaller capital investment. However, pumping power, as a fraction of operating cost, was strongly influenced by the cell gap ($\Delta P \sim h^{-3}$, approximately) so that pumping cost dominated the operating cost and outweighed gains in capital investment. For larger cell gaps, unit cell production rate was lower at fixed cell voltage due to larger ohmic loss in the solution phase.

The variation of DCE cost with flow rate is shown in Fig. 7. Since over the range under investigation mass-transfer rate was mainly dominated by gas evolution phenomenon, increase of electrolyte flow rate would not substantially increase the production rate. Instead, operating cost would be significantly increased owing to pumping power. For very low flow rate, ohmic loss in the solution phase owing to the high gas content lowered the unit cell production rate which resulted in higher capital investment. However, the effect of high gas content was not very strong and, therefore, the minimum seen in Fig. 7 is not very sharp.

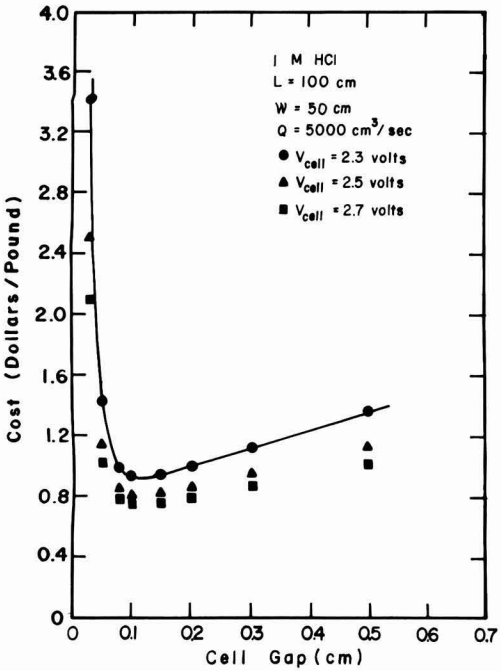

Fig. 6. Influence of cell gap on 1,2-dichloroethane cost

Results shown in Fig. 6 and 7 were carried out for 1*M* HCl because of the more distinct variation with the parameters under study.

The market price of DCE was 17 ¢/lb (July 1983 price) which is substantially lower than these calculated costs. It has been shown in Fig. 2 that the product distribution depends on $[Cl^-]/[H_2O]$. In particular, DCE cost will decrease as HCl concentration increases. For example, when 8*M* HCl is used as the electrolyte, a calculated cost of 22 ¢/lb for DCE is obtained at a current density less than 1 A/cm².

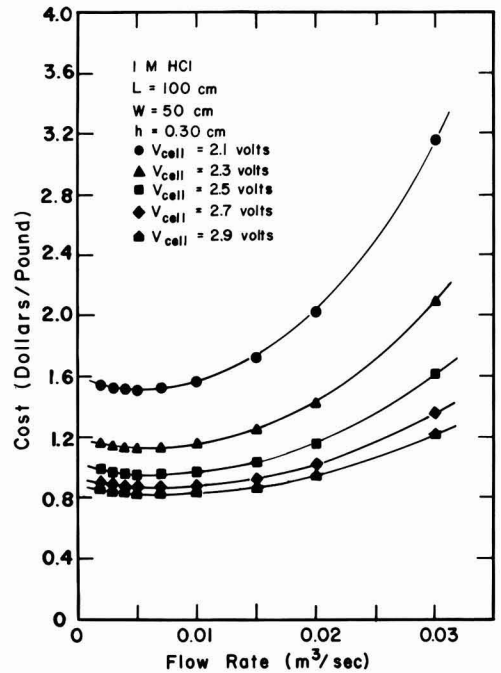

Fig. 7. Influence of electrolyte flow rate on 1,2-dichloroethane cost

Optimization.—An enhanced successive quadratic programming (SQP) method (14) was applied to the cost model described in the previous section in order to locate the optimal design parameters and operating conditions. The SQP method was chosen because it is known to be successful in situations where a large number of function and derivative evaluations are required, a category to which our system belongs. The SQP method has only recently been reported for electrochemical applications (15), and the present study represents the first known application of its use in directing bench-scale studies.

Starting with an initial set of values for the independent variables, a quadratic programming problem was formulated by taking a quadratic approximation of the objective function as well as linearization of the constraint functions. Solution of this problem by the Han-Powell algorithm (33) produced a search direction. Improvement of the objective function value was attempted along this search direction, and a new set of values was thereby obtained. The same procedure repeated itself until no further improvement was made. Five independent variables (cell gap, cell length, electrolyte flow rate, cell voltage, and cell width) were considered in the present analysis. The objective was minimization of DCE cost. Other more sophisticated objectives could be chosen for evaluation, but the general method would be the same. Three constraint functions were implemented: an upper limit was set on the maximum current density for anode protection, an upper limit (0.40) was also set for gas volume fraction at the outlet of the cell to prevent development of hot spots, and the maximum electrode area was set to be 0.8 m².

The software package SQPHP for solving nonlinear programming problems using an enhanced version of the Han-Powell method for successive quadratic programming was developed by Chen (33, 34), and is available commercially.[2] The program requires 41.4K words of core on the CDC Cyber 175 computer.

Results of optimization calculations for 1*M* HCl are summarized in Table III. It was found that the major fraction of computer time was consumed in function and derivative evaluations, not in the optimization procedure. For example, in Run no. 10, 120.526 CP seconds were consumed, of which only 0.154 CP seconds were used for 19 calls of SQPHP. Most runs terminated when there was lack of improvement of objective function value along the final search direction. In these cases, the final solution is believed to be very close to a local minimum. The results of Runs 1-4 suggest the possibility of local minima since different initial guesses ended up with different sets of optimal values for the variables.

Sensitivity analysis was carried out by finite difference evaluation of the cost change for small changes in each independent variable at the optimal condition. The strong influence of cell gap and cell voltage on the economy was demonstrated by the sensitivity analysis results shown in the footnote of Table III.

A simplified method for determining which phenomenon controls the cell resistance is to calculate the cell current that would pass if the entire driving force (cell voltage) were consumed by the particular phenomenon under consideration. That phenomenon which gives the smallest current is the limiting process. When such calculations were done for the optimal conditions corresponding to a maximum current density of 0.5 A/cm² (Run no. 4 of Table III), values of 2.12, 20.73, and 1.84 for dimensionless cell current were obtained in response to charge transfer, mass transfer, and ohmic resistance-controlled system, respectively. Therefore, it was concluded that mass transfer will not control the cell; measures towards

[2]M. Stadtherr, Department of Chemical Engineering, University of Illinois, Urbana, Illinois 61801.

Table III. Results of optimization calculations for 1M HCl

Run no.	Initial guess set no.[a]	Scaling factor set no.[b]	Stop mode[c]	Optimal cost (¢/lb)	Maximum c.d., x_1 i_{max} (A/cm²)	Cell gap, x_1 (cm)	Cell length, x_2 (cm)	Electrolyte flow rate, x_3 (ml/s)	Cell voltage, x_4 (V)	Cell width, x_5 (cm)	Y[d]
1	1	1	B	89.26	0.5	0.790 $E-1$	0.718 $E+2$	0.287 $E+4$	0.221 $E+1$	100	0.324 $E-1$
2	2	1	A	89.98	0.5	0.426 $E-1$	0.540 $E+2$	0.157 $E+4$	0.215 $E+1$	100	0.625 $E-3$
3	3	1	B	89.18	0.5	0.862 $E-1$	0.769 $E+2$	0.334 $E+4$	0.222 $E+1$	100	0.244 $E-1$
4	4	1	B	89.19	0.5	0.883 $E-1$	0.800 $E+2$	0.343 $E+4$	0.222 $E+1$	100	0.299 $E-2$
5	5	1	B	89.72	0.5	0.529 $E-1$	0.563 $E+2$	0.171 $E+4$	0.217 $E+1$	100	0.423 $E-1$
6	4	2	B	89.16	0.5	0.931 $E-1$	0.794 $E+2$	0.348 $E+4$	0.223 $E+1$	100	0.984 $E-2$
7	4	3	B	89.26	0.5	0.912 $E-1$	0.688 $E+2$	0.318 $E+4$	0.223 $E+1$	100	0.269 $E-1$
8	5	1	B	142.4	0.2	0.889 $E-1$	0.800 $E+2$	0.233 $E+4$	0.199 $E+1$	100	0.920 $E-2$
9	4	1	A	98.05	0.4	0.640 $E-1$	0.687 $E+2$	0.224 $E+4$	0.213 $E+1$	100	0.705 $E-3$
10	4	1	A	83.65	0.6	0.905 $E-1$	0.791 $E+2$	0.372 $E+4$	0.229 $E+1$	100	0.472 $E-3$
11	4	1	B	76.83	0.8	0.656 $E-1$	0.534 $E+2$	0.270 $E+4$	0.235 $E+1$	100	0.344 $E-2$
12	4	1	A	72.98	1.0	0.549 $E-1$	0.500 $E+2$	0.245 $E+4$	0.242 $E+1$	100	0.349 $E-3$
13	4	1	A	67.40	5.0	0.558 $E-1$	0.500 $E+2$	0.347 $E+4$	0.290 $E+1$	100	0.475 $E-3$

[a] Initial guess
Set no. 1: $x_1 = 0.1$, $x_2 = 80$, $x_3 = 4000$, $x_4 = 2.2$, $x_5 = 100$.
Set no. 2: $x_1 = 0.03$, $x_2 = 100$, $x_3 = 20{,}000$, $x_4 = 2.0$, $x_5 = 50$.
Set no. 3: $x_1 = 0.3$, $x_2 = 60$, $x_3 = 2500$, $x_4 = 2.5$, $x_5 = 90$.
Set no. 4: $x_1 = 0.1$, $x_2 = 80$, $x_3 = 4000$, $x_4 = 2.1$, $x_5 = 100$.
Set no. 5: $x_1 = 0.2$, $x_2 = 75$, $x_3 = 5000$, $x_4 = 1.95$, $x_5 = 100$.

[b] Scaling factor
Set no. 1: $\delta_1 = 10$, $\delta_2 = 100$, $\delta_3 = 100{,}000$, $\delta_4 = 0.1$, $\delta_5 = 1000$, $\delta_6 = 2.0$.
Set no. 2: $\delta_1 = 100$, $\delta_2 = 100$, $\delta_3 = 10{,}000$, $\delta_4 = 1$, $\delta_5 = 1000$, $\delta_6 = 2.0$.
Set no. 3: $\delta_1 = 1$, $\delta_2 = 100$, $\delta_3 = 100{,}000$, $\delta_4 = 0.01$, $\delta_5 = 100$, $\delta_6 = 5.0$.

[c] Stop mode
A Convergence criteria are satisfied.
B Five calls of SQPHP are required.

Sensitivity analysis for run no. 9
$s_1 = 0.239E + 2$ \$/cm.
$s_2 = -0.444E - 3$ \$/cm.
$s_3 = -0.995E - 4$ \$/(ml/s).
$s_4 = -0.167E + 2$ \$/V.
$s_5 = -0.202E - 2$ \$/cm.

[d] Sum in convergence test.

enhancement of mass-transfer rate, such as implementation of turbulence promoters, would not be expected to improve the cell economic performance. The present system is controlled primarily by ohmic resistance and, to a lesser degree, by a charge transfer resistance. Increasing the solution conductivity with a different electrolyte seems unlikely since the most mobile cation, H^+, is already present in the electrolyte. Development of a more active electrode surface for enhancement of charge transfer rate would represent only a limited contribution to process improvement. Further improvement in yield would be achieved by increasing the total chloride ion concentration beyond that obtainable with pure HCl electrolyte, such as by addition of chloride ion containing salts.

Conclusions

Because electrochemical processes can be complex, early stages of process evaluation must be guided so that efficient use is made of development efforts. Simple methods need to be used for modeling cells, their scale-up properties, and their economic features, and for predicting their optimal configuration. The incorporation of such methods along with bench-scale laboratory data can be carried out with numerical software available commercially on most mainframe systems.

In the present investigation, the most sophisticated numerical computations were those used to clarify the chemical reaction sequence which occurred near the electrode surface, summarized in the Appendix. The development of a model of an entire cell involved a few dozen equations, primarily nonlinear algebraic equations, which in the present study were easily solved by commercial software. Optimization and identification of the most sensitive parameters were also found to be readily accomplished with successive quadratic programming methods. While the present study did not include aspects of the process flow sheet other than the electrolytic cell, methods for flowsheet simulation and optimization represent an area of active research where rapid advances may be anticipated in the near future.

As a model system for the investigation of these methods, the electrochemical process for 1,2-dichloroethane production by electrolysis of ethylene containing hydrochloric acid solutions was studied with a bench-scale continuous-flow undivided parallel-plate cell. Ethylene chlorohydrin was the only by-product. The product spectrum was found to be independent of both electrolyte flow rate and cell current, but was found to be significantly influenced by the chloride ion concentration. Product distribution data supported the reaction mecha-

nism involving a chloronium ion intermediate and subsequent attack by nucleophiles (chloride ion and water molecule).

An approximate model which considered the chemical environment in the electrolysis zone was developed from fundamental principles of mass transport and reaction kinetics. The calculations supported the view that the cell served to generate chlorine, and that reaction of ethylene occurred solely by homogeneous chemical reaction.

The cell current-voltage curves were found to be independent of electrolyte flow rate. The flow patterns arising from gas evolution in the cell were observed experimentally and were used to establish a mathematical model of the cell. The cell model took into account mass transfer, charge transfer, and solution phase ohmic resistance. When a correlation was constructed for solution phase ohmic resistance based on the observed gas bubble flow pattern, the model characterized the experimental cell accurately, particularly the observation that the I-V curve was independent of flow rate.

Economic analyses were carried out for a hypothetical production facility. Influence of key operating and design parameters on the balance of capital cost and operating cost was demonstrated. An enhanced successive quadratic programming code was applied to locate the optimal operating conditions and to identify the most sensitive variables. The methods developed in this study are portable and can be applied to a wide variety of electrolytic processes.

Acknowledgments

Financial support of this work was provided by the American Chemical Society Petroleum Research Fund (13402-AC7). Computer costs were partially supported by the University of Illinois Research Board.

Manuscript submitted March 22, 1985; revised manuscript received May 28, 1985. This was Paper 318 presented at the Cincinnati, Ohio, Meeting of the Society, May 6-11, 1984.

The University of Illinois assisted in meeting the publication costs of this article.

APPENDIX

Reaction Chemistry Near the Anode

A two-dimensional representation of the reaction zone, illustrated in Fig. A-1, was used to calculate concentration profiles near the anode. Reference (17) contains a complete discussion of the summary which follows. The primary assumptions were (*i*) constant physical properties, (*ii*) well-developed laminar flow with a linear velocity field in the thin reaction region, (*iii*) homogeneous reaction which is first order in both chlorine and ethylene concentrations, (*iv*) 100% current efficiency for chlorine evolution, and (*v*) transport by convection along the electrode and by diffusion normal to the electrode. The last assumption represents a limiting case of behavior which does not include the effect of gas bubbles. The presence of such bubbles would serve to increase mass transfer of Cl^- and ethylene toward the anode, and to transport Cl_2 into the bulk at rates faster than given by the model. That is, the consequence of gas bubbles would be to increase rates of transport with respect to rates of chemical reaction, a point to which discussion will return.

The differential mass balances for chlorine and ethylene

$$D_{Cl_2}\frac{\partial^2[Cl_2]}{\partial y^2} - u_x(y)\frac{\partial[Cl_2]}{\partial x} = k[Cl_2][C_2H_4] \quad [A\text{-}1]$$

$$D_{C_2H_4}\frac{\partial^2[C_2H_4]}{\partial y^2} - u_x(y)\frac{\partial[C_2H_4]}{\partial x} = k[Cl_2][C_2H_4] \quad [A\text{-}2]$$

where the linear velocity field is represented by

$$u_x(y) = 6\langle u\rangle\left(\frac{y}{h} - \frac{y^2}{h^2}\right) \simeq 6\langle u\rangle\frac{y}{h} \quad [A\text{-}3]$$

The six boundary conditions are

$$[Cl_2] = 0 \text{ at } y = \delta_R \text{ for all } x \quad [A\text{-}4]$$

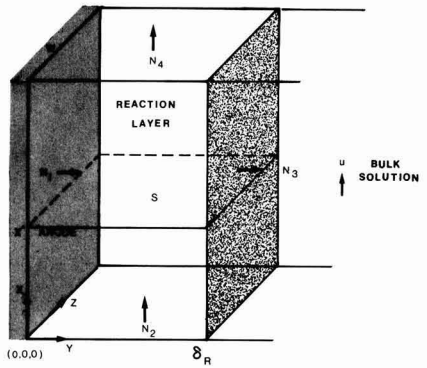

Fig. A-1. Basis of the reaction chemistry model. N_1: chlorine flux at anode. N_2: convective flux of chlorine into the reaction zone. N_3: diffusional flux of chlorine into bulk solution. N_4: convective flux of chlorine out of the reaction zone. S: rate of consumption of chlorine in the reaction zone.

$$[C_2H_4] = C_0 \text{ at } y = \delta_R \text{ for all } x \quad [A\text{-}5]$$

$$-D_{Cl_2}\frac{\delta[Cl_2]}{\partial y} = \frac{i}{2\mathbf{F}} \text{ at } y = 0 \text{ for all } x \quad [A\text{-}6]$$

$$\frac{\partial[C_2H_4]}{\partial y} = 0 \text{ at } y = 0 \text{ for all } x \quad [A\text{-}7]$$

$$[C_2H_4] = C_0 \text{ at } x = 0 \text{ for all } y \quad [A\text{-}8]$$

$$[Cl_2] = 0 \text{ at } x = 0 \text{ for all } y \quad [A\text{-}9]$$

Different concentration profiles will be obtained for different values of reaction layer thickness δ_R. The value of δ_R must be chosen so that it satisfied a chlorine mass balance

$$\frac{iWL}{2\mathbf{F}} = W\int_0^{\delta_R}[Cl_2](y)\Big|_{x=L}u_x(y)\,dy + W\int_0^L\int_0^{\delta_R}r(x, y)\,dydx \quad [A\text{-}10]$$

The differential mass balance for chloride ion is

$$D_{HCl}\frac{\partial^2[Cl^-]}{\partial y^2} - u_x(y)\frac{\partial[Cl^-]}{\partial x} + \frac{R}{R+1}r = 0 \quad [A\text{-}11]$$

where r is the local reaction rate, which can be calculated after the concentration profiles for both chlorine and ethylene have been obtained. Diffusion coefficient of HCl molecule, D_{HCl}, is used in Eq. [A-11] because of the binary nature of the electrolyte (22). The last term accounts for chloride generation following the stoichiometric reaction

$$C_2H_4 + Cl_2 + \frac{R}{R+1}H_2O \rightarrow \frac{1}{R+1}C_2H_4Cl_2 + \frac{R}{R+1}C_2H_5OCl + \frac{R}{R+1}HCl$$

The local product ratio was

$$R(x, y) = \frac{[EC]}{[DCE]}(x, y) = -0.102 + 0.132\,[H_2O]/[Cl^-](x, y) \quad [A\text{-}12]$$

The boundary conditions associated with Eq. [A-11] are

$$D_{HCl}\frac{\partial[Cl^-]}{\partial y} = \frac{i}{\mathbf{F}} \text{ at } y = 0 \quad [A\text{-}13]$$

$$[Cl^-] = [Cl^-]_0 \text{ at } y = \delta_R \quad [A\text{-}14]$$

$$[Cl^-] = [Cl^-]_0 \text{ at } x = 0 \quad [A\text{-}15]$$

where $[Cl^-]_0$ is the chloride ion concentration in the bulk solution.

The overall product ratio can be calculated by

$$R_{\text{overall}} = \left(\frac{[\text{EC}]}{[\text{DCE}]}\right)_{\text{overall}} = \frac{\dfrac{iLfR_0}{2\mathbf{F}(R_0+1)} + \displaystyle\int_0^L\int_0^{\delta_R} \frac{r(x,y)R(x,y)}{R(x,y)+1}\,dydx}{\dfrac{iLf}{2\mathbf{F}(R_0+1)} + \displaystyle\int_0^L\int_0^{\delta_R} \frac{r(x,y)}{R(x,y)+1}\,dydx} \qquad \text{[A-16]}$$

where R_0 is the ratio obtained from reaction in the bulk solution and f is the fraction of chlorine being carried out of the reaction layer by convection

$$f = \int_0^{\delta_R} u_x(y)[\text{Cl}_2](y)|_{x=L}\,dy \Big/ \left(\frac{iL}{2\mathbf{F}}\right) \qquad \text{[A-17]}$$

Concentration profiles were computed by a finite difference method (IMSL subroutine ZSPOW) implemented on a Cyber 175 computer. Additional details are available in Ref. (17).

LIST OF SYMBOLS

A	electrode area (cm²)
C_b	bulk concentration of HCl (mol/cm³)
C_0	ethylene concentration in electrolyte (mol/cm³)
C^*	bulk concentration of HCl at cell inlet (mol/cm³)
d_b	bubble departure diameter (cm)
D_i	diffusion coefficient of species i (cm²/s)
E_{eq}	equilibrium potential (V)
f	fraction of chlorine flux out of the reaction layer
$\mathbf{F}$	Faraday's constant (96,487 C/eq)
h	cell gap (cm)
i	current density (A/cm²)
i_0	exchange current density (A/cm²)
I_{cell}	cell current (A)
k	reaction rate constant for chlorination of ethylene (cm³/mol-s)
k_3	rate constant for ethylene chlorohydrin formation (cm³/mol-s)
k_4	rate constant for 1,2-dichloroethane formation (cm³/mol-s)
k_{mt}	mass transfer coefficient (cm/s)
L	cell length (cm)
n	number of electrons involved in the electrochemical reaction
$N_1 - N_4$	chlorine fluxes in Fig. A-1 (mol/cm²-s)
P_{cell}	cell pressure (atm)
Q	electrolyte flow rate (cm³/s)
R	product ratio ([EC]/[DCE]); gas constant (8.3144 J/g-mol-K), when appearing as RT
R_0	product ratio in bulk electrolyte
R_s	solution phase ohmic resistance (Ω)
Re	$V_g d_b/A\nu$, Reynolds number (dimensionless)
S	amount of chlorine reacted in the reaction layer per unit time (mol/s)
Sc	ν/D_{HCl}, Schmidt number (dimensionless)
Sh	$\kappa_{mt}d_b/D_{HCl}$, Sherwood number (dimensionless)
t_i	transference number of ionic species i
T	temperature (K)
$<u>$	average velocity of electrolyte flow, (cm/s)
u_g	rise velocity of bubble swarm, (cm/s)
V_{cell}	cell voltage (V)
V_g	volume rate of gas bubble formation (cm³/s)
W	cell width (cm)

Greek Symbols

α	symmetry factor in Butler-Volmer equation
δ_{avg}	average thickness of moving bubble layer (cm)
δ_R	reaction layer thickness (cm)
η_c	concentration overpotential (V)
κ_{avg}	effective conductivity of moving bubble layer (mho/cm)
κ_0	conductivity of gas bubble-free electrolyte (mho/cm)
ν	kinematic viscosity (cm²/s)
ϕ_s	solution phase potential (V)

Subscripts

a	anodic
c	cathodic
s	surface

REFERENCES

1. R. C. Fahey and H.-J. Schneider, *J. Am. Chem. Soc.*, **90,** 4429 (1968).
2. G. A. Tedoradze, V. A. Paprotskaya, and A. P. Tomilov, *Elektrokhimiya*, **10,** 1103 (1974).
3. V. A. Paprotskaya, G. A. Tedoradze, and A. P. Tomilov, *ibid.*, **12,** 206 (1976).
4. G. A. Tedoradze, V. A. Paprotskaya, and A. P. Tomilov, *ibid.*, **10,** 1612 (1974).
5. G. A. Tedoradze Yu.M. Sokolov, E. A. Panomarenko, V. A. Papotskaya, and A. P. Tomilov, PCT Int. Appl. 80 01,686, Aug. 21, 1980 (C.A.:93:247451).
6. W. R. Parrish and J. Newman, *This Journal*, **117,** 43 (1970).
7. C. W. Tobias, *ibid.*, **106,** 833 (1959).
8. I. Rousar, *ibid.*, **116,** 676 (1969).
9. H. Vogt, "Comprehensive Treatise of Electrochemistry," Vol. 6, E. Yeager *et al.*, Editors, p. 445, Plenum Press, New York (1983).
10. J. R. Selman, in "Tutorial Lectures in Electrochemical Engineering and Technology," Part II, R. Alkire and D. Chin, Editors, p. 101, AIChE Symposium Series 229, AIChE, New York (1983).
11. K. B. Keating and V. D. Sutlic, in "Electro-Organic Synthesis Technology," M. Krumpett, E. Weismann, and R. Alkire, Editors, p. 119, AIChE Symposium Series 185, AIChE, New York (1979).
12. R. E. W. Jansson, in "Tutorial Lectures in Electrochemical Engineering and Technology," Part II, R. Alkire and D. Chin, Editors, p. 119, AIChE Symposium Series 229, AIChE, New York (1983).
13. T. R. Beck, in "Techniques of Electrochemistry," Vol. 3, E. Yeager and A. J. Salkind, Editors, Wiley-Interscience, New York (1978).
14. R. C. Alkire, G. D. Cera, and M. A. Stadtherr, *This Journal*, **129,** 1225 (1982).
15. R. Alkire, S-A. Soon, and M. A. Stadtherr, *ibid.*, **132,** 1105 (1985).
16. R. C. Alkire, R. D. La Roche, G. D. Cera, and M. A. Stadtherr, Paper 410 presented at the Toronto, Ont., Canada Meeting of the Society, May 12-17, 1985.
17. E. K. Yung, Ph.D. Thesis, University of Illinois, Urbana, IL (1985).
18. H. Schlichting, "Boundary-Layer Theory," 7th ed., p. 185, McGraw-Hill, New York (1979).
19. V. P. Konyushenko, Yu. A. Serguchev, and V. I. Staninets, *Khim. Prom.*, 146 (1979).
20. Yu. Serguchev and V. P. Konyushenko, *Ukr. Khim. Zhurn.*, **42,** 100 (1976).
21. R. B. Bird, W. E. Stewart, and E. N. Lightfoot, "Transport Phenomena," p. 59, John Wiley and Sons, New York (1960).
22. J. Newman, "Electrochemical Systems," p. 223, Prentice-Hall, Englewood Cliffs, NJ (1973).
23. P. W. Dun and T. Wood, *J. Appl. Chem. Lond.*, **17,** 53 (1967).
24. K. Stephan and H. Vogt, *Electrochim. Acta*, **24,** 11 (1979).
25. J. Newman, *This Journal*, **113,** 1235 (1966).
26. J. Newman, *ibid.*, **113,** 501 (1966).
27. H. Vogt, *Electrochim. Acta*, **26,** 1311 (1981).
28. D. A. G. Bruggeman, *Ann. Phys.*, **24,** 659 (1935).
29. J. Newman, "Electrochemical Systems," p. 383, Prentice-Hall, Englewood Cliffs, NJ (1973).
30. H. Vogt, *J. Appl. Electrochem.*, **12,** 261 (1982).
31. H. Vogt, *Electrochim. Acta*, **23,** 203 (1978).
32. Kirk-Othmer, "Encyclopedia of Chemical Technology," Vol. 8, p. 704, John Wiley and Sons, New York (1979).
33. H. S. Chen, Ph.D. Thesis, University of Illinois, Urbana, IL (1982).
34. H. S. Chen and M. A. Stadtherr, *Comp. Chem. Eng.*, **8,** 229 (1984).
35. T. W. Chapman and J. Newman, "A Compilation of Selected Thermodynamic and Transport Properties of Binary Electrolytes in Aqueous Solution," AEC Contract w-7405-eng-48 (1968).
36. "CRC" Handbook of Chemistry and Physics," 63rd ed., R. C. Weast and M. J. Astle, Editors, p. D-240, CRC Press, Boca Raton, FL (1982).

Charge-Discharge Behavior of Polyacetylene Electrodes

Fritz G. Will*

General Electric Company, Corporate Research and Development, Schenectady, New York 12301

ABSTRACT

The charge-discharge and open-circuit behavior of polyacetylene electrodes, p-doped with BF_4, is examined. Discharge curves for controlled current are interpreted quantitatively in terms of a model involving slow dopant diffusion and slow discharge at the polymer/electrolyte interface. The open-circuit potential is measured as a function of mean dopant level. It is shown that, due to the slow dopant diffusion, no steady-state potentials are attained. The coulombic efficiency of pristine polyacetylene electrodes in identical states of doping is determined as a function of discharge current. Discrepancies among results of different authors are related to different dopant states near the polymer surface. A quantitative relationship between efficiency and current is derived which is shown to be valid for small polarizations and short discharge times.

Polyacetylene $(CH)_x$ can be doped and undoped electrochemically (1) with a variety of ions and can, therefore, principally be used as novel electrode material in rechargeable batteries. Certain aspects of repetitively charging (p-doping or anion incorporation) and discharging (undoping) polyacetylene electrodes have been described in the literature. Nigrey *et al.* (1) applied controlled current charges and discharges of short duration to polyacetylene films in solutions of $LiClO_4$ in propylene carbonate. This resulted in ClO_4 dopant level changes of the order of 0.5 mole percent (m/o). Kaneto *et al.* (2) described the open-circuit voltage behavior following consecutive controlled potential charge and discharge pulses and determined the coulombic and energy efficiency of ClO_4-doped polyacetylene at various constant current discharges. They observed an unexplained increase in coulombic efficiency from 74 to 87% for a ten-fold increase in discharge current. Farrington *et al.* (3) found quite different open-circuit voltage behavior after p-doping with ClO_4 or AsF_6, characterized by a pronounced voltage step at 2 m/o doping level and a linear increase in voltage at higher doping levels. Furthermore, coulombic efficiencies reported in Ref. (3) for controlled current discharge from identical dopant levels as in Ref. (2) are only approximately half of the values reported in Ref. (2), that is, only 41-51%.

In the present paper, we study the open-circuit voltage behavior of polyacetylene electrodes p-doped with BF_4, following consecutive controlled current charges and discharges of 0.1-100s duration. Furthermore, we establish the coulombic efficiency of pristine polyacetylene film electrodes for various controlled current charges and discharges of typically 1h duration. We show that the coulombic efficiency is determined by slow dopant diffusion (4, 5) in the polyacetylene structure. The anomalies of efficiency *vs.* discharge current observed by others (2) and the discrepancies among the efficiency values reported by different groups (2, 3) can be reconciled by the nonsteady-state nature of dopant diffusion and concentration in polyacetylene.

Experimental

Polyacetylene films had been prepared by the Rohm and Haas Company and shipped in sealed glass vials, filled with inert gas. Prior to electrochemical experiments, films were predominantly in the *cis* form as evidenced by infrared spectroscopy (6). They had an apparent density of 0.56 g/cm³, corresponding to 48% of the theoretical density and a true surface area of 40-50 m²/g. The internal void space of 52% consists of interconnected micropores of a few hundred to a few thousand angstroms diameter between individual polyacetylene fibers of a few hundred angstroms diameter. This microfibrillar structure of polyacetylene is well established (7, 8).

Details of the film preparation and characterization have been described elsewhere (6). Circular electrodes A of 2 cm² area with 89 μm thickness and B of 1.25 cm² area with 68 μm thickness were cut from the films. The former corresponds to 2.7 m/o dopant per A-s/cm² charge, the latter to 3.5 m/o/A-s/cm². Electrodes were provided with 1000Å sputtered Au films on the back side. Contact was made by attaching Au wires with Au-epoxy cement. Experiments were carried out in PTFE cells using Li counter and reference electrodes. Approximately 1 cm³ electrolyte was employed, consisting of 30% by weight solutions of $LiBF_4$ in sulfolane for electrodes A and 10% solution for electrodes B. These electrolytes have very high viscosity. Handling of and experimentation with the polyacetylene were carried out in a high quality dry box.

Coulombic efficiency studies were performed for each different discharge current on a pristine polyacetylene electrode, charged with identical current density of 0.24 mA/cm².

Controlled currents were generated with a PAR Model 175 Universal Programmer and applied with a PAR Model 175 Galvanostat/Potentiostat equipped with Digital Coulometer Model 179. Voltage-time traces were recorded on a Nicolet Model 206 Storage Oscilloscope or a Hewlett-Packard Model 17501A Recorder, depending on pulse duration.

Results

Nonsteady-state polarization behavior.—Figure 1 shows polarization-time transients for electrode A, subjected to short-duration discharge and charge pulses separated by open-circuit periods. Electrode A had been previously charged to 7 m/o BF_4 dopant level. The polarization data are corrected for the ohmic voltage drop between test and reference electrode and are referred to the open-circuit potential of 3.8V obtained after 7 m/o doping. It is seen from Fig. 1 that discharge and charge with current densities as small as 0.05 and 0.5 mA/cm² yield low polarizations which do not appear to change significantly after the first few hundredths of a second.[1] Open-circuit stand for 0.1s following discharge or charge with 0.05 mA/cm² for 0.1s results in negligible remaining polarization, whereas a current density of 0.5 mA/cm² for 0.1s al-

[1] Closer examination of the curves and charging or discharging for longer periods of time, however, reveals that the polarizations do not attain steady-state values.

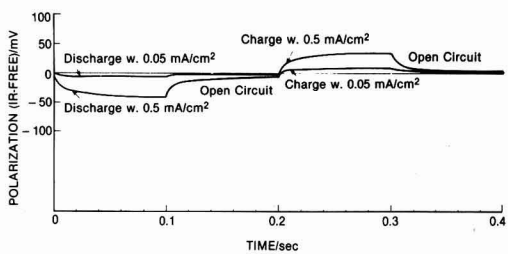

Fig. 1. Short-term charge, discharge, and open-circuit behavior of BF_4-doped polyacetylene electrodes; doping and undoping with 0.1s current pulses.

* Electrochemical Society Active Member.

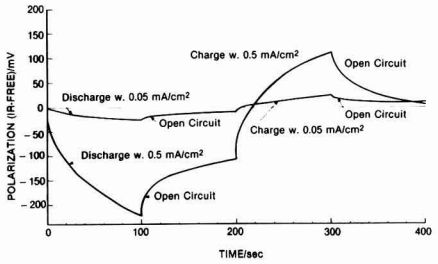

Fig. 2. Short-term polarization behavior of BF_4-doped polyacetylene electrodes; doping and undoping with 100s current pulses.

ready produces a perturbation which does not dissipate completely on open circuit in 0.1s. Charge or discharge with 0.5 mA/cm² for 0.1s corresponds to a dopant injection or removal of 3.1×10^{14} BF_4 molecule/cm².

Figure 2 shows polarization-time transients for pulse lengths and open-circuit periods of 100s each. Thus, dopant injection or removal corresponds to 3.1×10^{16} and 3.1×10^{17}/cm² in a single 0.05 and 0.5 mA/cm² pulse. It is seen that even for the small current density of 0.05 mA/cm² steady-state polarizations are never attained. This is even more pronounced for the 0.5 mA/cm² pulse. During the 100s open-circuit periods following current pulses, the perturbations caused by the charge injection or removal do not relax. Slow diffusion (4, 5) prevents steady state from being attained.

Open-circuit potential-dopant level relationship.—Prior to establishing the open-circuit potential-dopant level relationship, electrode A had been cycled several times, discharged to 1.3V, and left on open circuit for 1h, which led to recovery of the potential to 3.33V. The electrode was then p-doped in a series of 100s charging pulses of 0.25 mA/cm², each followed by an open-circuit period of 100s (part a of curve). In part b of the curve, the open-circuit period was increased from 100 to 500s. The potential-time transients were equivalent to those shown in Fig. 2. The charge input and the open-circuit potential were both recorded and the potential at the end of the open-circuit stand plotted in Fig. 3 against the incremental charge input. The upper abscissa shows the incremental dopant level if the dopant were uniformly distributed throughout the entire polyacetylene film.[2] It is appreciated from the discussion in the preceding paragraph that the potentials plotted in Fig. 3 are nonsteady-state values. The open-circuit potential increases monotonically from 3.35 to 3.72V for a mean dopant level change of 1.5 m/o. The decrease at 3.62V is due to the change of open-circuit stand from 100 to 500s. Discharge in a series of 100s pulses of 0.25 mA/cm² with 500s stand after pulses results in decreasing open-circuit potentials as shown in Fig. 3. The relevant curve exhibits considerable hysteresis such that the open-circuit potentials on discharge are by an average of 0.2V lower than those on charging at identical mean dopant levels. Under the conditions applied, namely, charging with 100s pulses of 0.25 mA/cm² followed by open circuit for 500s and discharging with the same pulse regime, polyacetylene electrodes do not behave reversibly, and no unique relationship between open-circuit potential and mean dopant level is established.

Charge-discharge cycling simulating battery applications.—The charge-discharge curves of Fig. 1 and 2 are of little interest to practical battery operation as the discharge times are too short and the doping level changes too small to yield energy densities competitive with other batteries. Figure 4 shows the results of three consecutive charges and discharges of longer duration. Pristine film was charged initially at controlled potentials of 3.5, 4, and 4.5V for a total of 2h. A charge of 1.5 A-s/cm² was thus injected over a time period of 2h, corresponding to a mean

[2] Referred to as mean dopant level or mean concentration from here on.

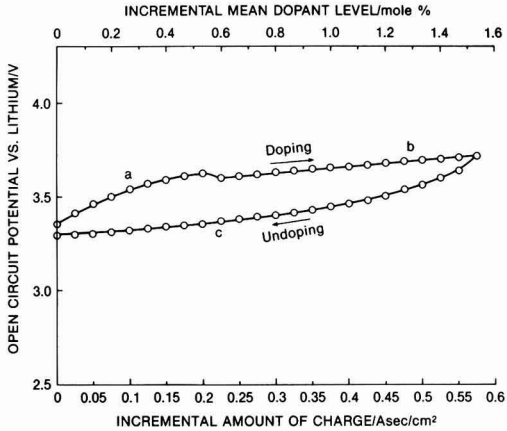

Fig. 3. Open-circuit potential of BF_4-doped polyacetylene vs. incremental state of charge or mean dopant level. a: 100s on open circuit after 0.25 mA/cm² × 100s charging pulses (doping). b: 500s on open circuit after doping. c: 500s on open circuit after 0.25 mA/cm² × 100s discharge pulses (undoping).

dopant level of 4 m/o. Subsequent discharges were performed at 0.25 mA/cm² to a lower voltage limit of 1.3V and alternate charges at 0.25 mA/cm² for 1-2.5h. The charging, discharging, and open-circuit conditions are summarized in Table I, as are the coulombic efficiencies. The latter values vary greatly, from 19 to 55%, in spite of identical current densities during charge and discharge in these three cycles. It appears from Table I that a short open-circuit period between charge and discharge leads to high coulombic efficiencies and vice versa.

Coulombic efficiency of pristine polyacetylene.—The nonreproducibility of consecutive charge-discharge curves of polyacetylene films subjected to different open-circuit periods prior to discharge suggests that the film is in different dopant states. This makes an evalua-

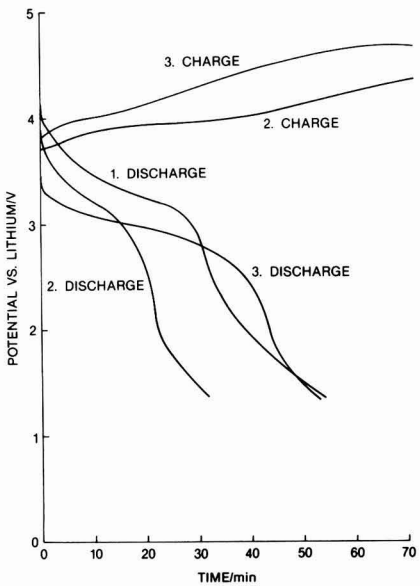

Fig. 4. Consecutive charge-discharge curves of BF_4-doped polyacetylene. First charge potentiostatically at 3.5, 4, and 4.5V; subsequent charges and discharges galvanostatically at 0.25 mA/cm². Additional details in Table I.

Table I. Coulombic efficiencies in consecutive cycling

Charging			Open circuit	Discharging			Open circuit	Efficiency
i (mA/cm²)	t (min)	Q_{in} (A-s/cm²)	t (min)	i (mA/cm²)	t (min)	Q_{out} (A-s/cm²)	t (min)	Q_{out}/Q_{in}
Const. V	120	1.45	10	0.25	54	0.80	30	0.55
0.25	160	2.39	50	0.25	31	0.46	60	0.19
0.25	120	1.75	10	0.25	54	0.82	60	0.47

tion of the effect of current density on discharge performance difficult or impossible.

Therefore, a comparative study of the very first charge and discharge on pristine polyacetylene films was undertaken with discharges performed at different current densities. This enables determination of the coulombic efficiency as a function of current density for polyacetylene identically pretreated and hence presumably in identical initial dopant states. Figure 5 shows charge-discharge curves for three pristine film electrodes B. Charging was carried out with 0.24 mA/cm² for 70 min, equivalent to 1 A-s/cm² or a dopant level of 3.5 m/o. The charging curves for all three films were identical. Discharging was performed after 1h open-circuit stand with current densities of 0.08, 0.24, and 1.2 mA/cm², respectively. A voltage plateau occurs with inflection points at 3.5, 3.45, and 3.03V, respectively. The coulombic efficiencies for discharge to 2.5V decrease from 70% at 0.08 mA/cm² to 64% at 0.24 mA/cm² and to 30% at 1.2 mA/cm².

Reproducibility of the charge-discharge curves was ascertained at 0.24 mA/cm² by employing a fourth pristine film. A charge-discharge curve identical to the relevant curve in Fig. 5 was obtained.

Discussion

Nonsteady-state polarization behavior.—Polarization-time transients of short duration such as those shown in Fig. 1 and 2 are quantitatively interpreted (4) in terms of a semi-infinite linear diffusion model with charge transfer through the polyacetylene/solution interface superimposed on the very slow diffusion (5) of dopant in the polyacetylene. Applicability of semi-infinite linear diffusion to the microporous structure of polyacetylene films is tantamount to the assumption that only the exterior surface of the film is wetted by the electrolyte and that the large interior surface (2000 times larger than the projected area) remains essentially electrolyte free. This assumption is justified by the fact that the observed double-layer capacitance (4, 5) is 14 and 22 μF for electrodes B and A, respectively. Such values yield 11 μF/cm² if only the exterior surface is wetted and 0.005 μF/cm² if the large interior surface is also wetted. Clearly, only the former value is in agreement with generally accepted double-layer capacitance values. Considering the high viscosity of the electrolytes used in this study, the nonpenetration of the micropores is not surprising. This condition may not apply to electrolytes with low viscosities, especially if the electrodes are carefully vacuum impregnated. Vacuum impregnation, however, has not been applied in this study or, apparently, in other studies (1-3).

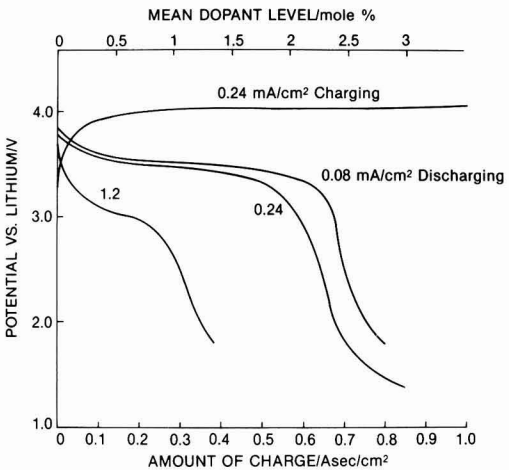

Fig. 5. First charge-discharge curves of pristine BF_4-doped polyacetylene at various discharge currents; 1h on open circuit following charging to 3.5 m/o.

The mathematical model further assumes a solid slab of homogeneous physical properties. This means that the fibrous structure is neglected and that an isotropic diffusion coefficient is assumed. In fact, however, the diffusion coefficient is expected to be different parallel and perpendicular to the fiber axis. More complex future models may take these features into account and future experiments may establish the diffusion coefficients parallel and perpendicular to the fiber axis.

The effect of charging the double-layer capacitance is only significant in the first few milliseconds of the transient and can be neglected thereafter. For times short compared to the time constant for diffusion through the entire film and for small polarizations η, the transient is given (9) by

$$\eta = (RT/\mathbf{F})\,(i/i_o + 2i\,\sqrt{t}/\sqrt{\pi D}\,\mathbf{F}c_o) \qquad [1]$$

where i is the applied current density, i_o the exchange current density, t the time, c_o the initial dopant concentration, D the dopant diffusion coefficient, R the gas constant, T the temperature, and $\mathbf{F}$ the Faraday constant. The current densities are related to the wetted exterior (or projected) surface area where ion charge and discharge is thought to occur.[3]

Validity of Eq. [1] assumes that the dopant concentration is nearly constant (c_o) over a distance from the exterior surface into the interior comparable to the diffusion depth relevant to the subsequent transient. Whether or not this is the case depends on the duration of the pulses and open-circuit periods. Figure 6 shows the polarization transients of Fig. 2 for both charge and discharge at 0.5 mA/cm² in a plot of η against $\sqrt{t}$. The curves exhibit the straight line behavior required by Eq. [1]. The slope of the straight line yields the diffusion coefficient, and the intercept with the axis $\sqrt{t} = 0$ yields the exchange current density. It is, therefore, clear that the nonsteady-state behavior of polyacetylene electrodes results from the very slow diffusion of dopants into and out of the polymer.

The concentration gradients relevant to a pulse sequence are qualitatively shown in Fig. 7. Figure 7a corresponds to charging (doping) of a pristine or well-equilibrated film. The constant value of dc/dx is dictated by the constant applied current density. Figure 7b shows the partial relaxation of the concentration profile during open circuit. At the interface, $dc/dx = 0$ as the current is zero. Figure 7c shows commencement of discharge with concentration gradients from the preceding charging event still present. Figure 7d shows the relaxation on open circuit of the concentration gradients left from the previous discharge. For comparison with Fig. 7c, Fig. 7e shows the concentration profile for discharge of a well equilibrated film, kept on open circuit for a long time.

[3] It is for this reason that we refer to doping and diffusion of BF_4 rather than BF_4^- ions in the polyacetylene structure.

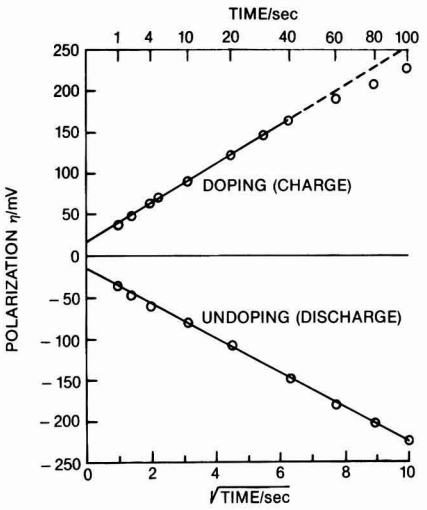

Fig. 6. Polarization-time transients of polyacetylene, BF_4-doped to 7 m/o, during charging and discharging with 0.5 mA/cm² × 100s current pulses; η plotted against $\sqrt{t}$ according to Eq. [1].

Open-circuit potential-dopant level relationship.—The open-circuit potential is dependent on the activity or concentration of dopant at the polyacetylene/solution interface. In view of the small diffusion coefficients of dopants in polyacetylene, very long times of equilibration are required after charging or discharging before steady-state open-circuit potentials are obtained which correspond to uniform dopant concentration throughout the polyacetylene. For a 70 μm thick film, equilibration times are in excess of 300h, and for a 7 μm film, in excess of 8h. The open-circuit potential *vs.* charge data in Fig. 3 are thus nonsteady-state data, and the dopant levels near the surface deviate considerably from the mean levels in Fig. 3. The surface values decrease or increase toward the interior after charge or discharge, respectively, in a way qualitatively shown in Fig. 7. The decrease in open-circuit potential with longer open-circuit time and the hysteresis of the curves on charge and discharge, as shown in Fig. 3, are thus explained in terms of nonsteady-state diffusion.

Kaneto *et al.* (2) determined the open-circuit potential as a function of dopant level at different times after charging with a series of potential steps. Their results after 2s and 24h open-circuit stand are plotted in Fig. 8 together with the present results. Straight lines result in a semilog plot with slopes between 300 and 400 mV/decade. The open-circuit potentials are highest after the consecutive 0.25 mA/cm² × 100s current pulses and 100s open-circuit times employed in this study, since the surface concentration of dopants is highest. The consecutive voltage pulses applied by Kaneto *et al.* allowed more time for the dopant to diffuse into the interior. Hence, the open-circuit potentials are lower after only 2s open-circuit time. The values after 24h open-circuit time are lower yet, but still cannot be regarded as steady-state values. Farrington *et al.* (3) employed 0.05 mA/cm² current pulse charges of various durations. Discharge for more than 16h had preceded charging. Open-circuit potentials were observed at unspecified time after charging. The data are also shown in Fig. 8. The high mean dopant levels employed in this study correspond to exceedingly large dopant levels near the surface. Such high dopant levels, in the region of 10-50 m/o, may result in formation of a second phase which would explain the step change in open-circuit potential at 3 m/o mean dopant level.

The large observed slopes of 300-400 mV/decade in Fig. 8 are not readily explained in terms of simple solution behavior as it applies, for example, to the alkali intercalates of graphite (10). Such large changes in open-circuit potential with doping have, however, been observed (11) in other intercalation compounds, such as Li_xTiS_2 and Na_xTaS_2; they are consistent with a salt-like model, requiring lattice rearrangement energy, and may also be associated with shifts in the Fermi level energy brought about by the donation of p-type charge carriers from the dopant molecules to the conduction band.

It appears that the slow diffusion of dopants in polyacetylene is responsible for the different behaviors observed by different authors. The boundary conditions established at the surface depend on the previous history of the polyacetylene, such as potentiostatic *vs.* galvanostatic conditions, applied current density, duration of open-circuit periods, etc. The open-circuit potential, in turn, depends only on the surface concentration. In all studies to date, open-circuit times have been too short to establish the true steady-state relationship between open-circuit potential and dopant level.

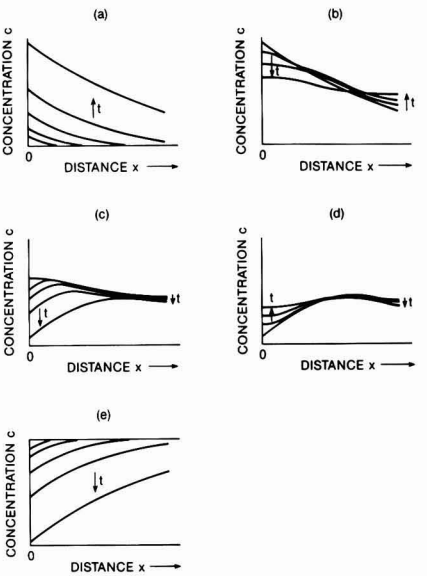

Fig. 7. Dopant concentration profiles in polyacetylene electrodes (qualitatively) at different times during consecutive (a) charging, (b) 1. open circuit, (c) discharging, and (d) 2. open circuit; (e) discharge of previously equilibrated charged film.

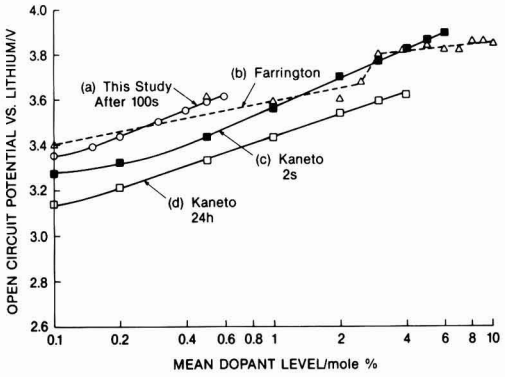

Fig. 8. Open-circuit potential of p-doped polyacetylene *vs.* logarithm of mean dopant level at specified times after charging. (a) 100s after BF_4 doping with 0.25 mA/cm² pulses; (b) unspecified time after ClO_4 doping with 0.05 mA/cm²; (c) 2s after ClO_4 doping with increasing voltage pulses; (d) 24h after ClO_4 doping with voltage pulses.

Charge-discharge cycling.—Short-duration charge and discharge curves such as those shown in Fig. 1 and 2 can be readily interpreted in terms of the simple Eq. [1]. For such short times, the polarization η remains small and the linearization of the exponential terms in the discharge equation leads to cancellation of the terms containing the transfer coefficient α.

However, for longer charge and discharge times, as they are of interest to battery applications, the polarization becomes large enough so that the expression

$$\eta = -[RT/(1-\alpha)\mathbf{F}]\,[\ln(-i/i_0) - \ln(1-\sqrt{t/\tau})] \quad [2]$$

must be used (12). The transition time τ is given by

$$\tau = \pi D\mathbf{F}^2c_0^{\,2}/4i^2 \quad [3]$$

and signifies the time at which the dopant concentration at the polyacetylene surface has become zero; τ must not be confused with the time constant for dopant diffusion through the entire film.

When τ has been reached, η increases rapidly; this is the case for τ = 7200s for the discharge curve at 0.08 mA/cm² on pristine polyacetylene, shown in Fig. 5. From Eq. [3] with $D = 5.7 \times 10^{12}$ cm²/s, we calculate a dopant concentration of 3.1×10^{-2} mol/cm³. This corresponds to 34.8 m/o doping when averaged over the penetration depth $\sqrt{Dt}$ of approximately 3 μm during 1h charging and 1h on open circuit. Figure 9 shows the discharge curve for 0.08 mA/cm² of Fig. 5 in a plot of η *vs.* $-\log(1-\sqrt{t/\tau})$. A straight line results at large η as required by Eq. [2]. The slope yields an α value of 0.77 and the intercept with the ordinate at $\sqrt{t/\tau} = 0$ results in an i_0 value of 3.6×10^{-5} A/cm². Discharge curves published by Kaneto *et al.* (2) for discharge of polyacetylene doped with 7 m/o ClO_4 also yield straight lines for large η when plotted in terms of η *vs.* $-\log(1-\sqrt{t/\tau})$. As an example, the lower curve in Fig. 9 corresponds to discharge at approximately 0.5 mA/cm² with τ = 2400s. The slope yields α = 0.93, and the intercept $i_0 = 2.1 \times 10^{-4}$ A/cm². To arrive at these numbers, we have made the reasonable assumption that the diffusion coefficients of BF_4 and ClO_4 are approximately the same. Hence, the model of slow diffusion and discharge explains the present data and those of Kaneto *et al.* equally well. We find no support for the recent model of field-enhanced diffusion of Kaufman *et al.* (13), which they employ to explain a perceived three orders of magnitude discrepancy between observed discharge currents and currents predicted on the basis of a standard diffusion model. The perceived discrepancy is based upon an estimate of the diffusion coefficient which is six orders of magnitude in error [see Ref. (5)]; in addition, the model of field-enhanced diffusion which has been applied to O_2 diffusion in thin SiO_2 films on Si (14) is not applicable to highly doped polyacetylene, as the Debye length for such high charge-carrier densities is far too small.

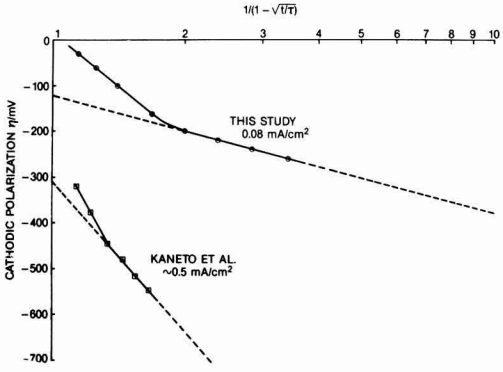

Fig. 9. Cathodic polarization or discharge curves during undoping *vs.* $-\log(1-\sqrt{t/\tau})$ according to Eq. [2]. (a) 1h discharge of pristine 3.5 m/o BF_4-doped polyacetylene with 0.08 mA/cm² (see Fig. 5); τ = 7200s; (b) 0.7h discharge of 7 m/o ClO_4-doped polyacetylene with ~ 0.5 mA/cm², τ = 2400s.

Coulombic efficiency as function of discharge current.—In consecutive cycling of polyacetylene electrodes with 0.25 mA/cm², we have observed variations of the coulombic efficiency from 19 to 55% (Table I) and have found that long open circuit results in low efficiencies and vice versa. This behavior is due to a larger fraction of the dopant diffusing into the bulk of the polyacetylene during longer open-circuit stand. Figure 7 shows the relevant time-dependent concentration profiles.

Farrington *et al.* (3) observed variations in efficiency from 21 to 46% in three consecutive cycles with approximately identical mean dopant levels of 3 m/o and charge/discharge currents of 0.05/0.5 mA/cm². The open-circuit time between charge and discharge was not specified, and we speculate that the variations in their efficiency values too may have been caused by different open-circuit periods.

A study of the effect of current density on coulombic efficiency also requires identical previous history and, hence, identical states of doping. This was assured in the present study by employing pristine polyacetylene and identical charging conditions and open-circuit times prior to discharge. According to the results in Fig. 4, the coulombic efficiency of pristine film, charged and discharged once, decreases significantly with increasing discharge current density. Such behavior may be suspected again to result from the slow diffusion of dopants in polyacetylene. The effect of slow diffusion and simultaneous slow discharge on the coulombic efficiency can be predicted from Eq. [1] or [2], for small or large values of η, respectively. For discharge performed at various current densities i_d to small fixed polarization η_F, the relevant discharge times t_d follow from Eq. [1] as

$$\sqrt{t_d} = (\sqrt{\pi D}\,\mathbf{F}c_0/2)\,(\mathbf{F}\eta_F/RTi_d - 1/i_0) \quad [4]$$

The mean dopant concentration c_0 is related to the input charge $q_{in} = i_c t_c$ by

$$c_0 = q_{in}/\mathbf{F}\delta \quad [5]$$

where i_c, t_c are charge current density and time, respectively, and δ the film thickness. The coulombic efficiency $e_{coul} = q_{out}/q_{in}$ then follows from Eq. [4] as

$$e_{coul} = (\pi D q_{in} i_d/4\delta^2)\,(\mathbf{F}\eta_F/RTi_d - 1/i_0)^2 \quad [6]$$

According to Eq. [4], for discharge to a fixed small polarization η_F, a plot of $\sqrt{t_d}$ *vs.* the reciprocal discharge current ($1/i_d$) should yield a straight line. Figure 10 shows a plot of this type for η_F = 50 mV and 100s discharge pulses applied to electrode A. A straight line is indeed obtained, and the observed discharge times are predicted very well for a doping concentration near the surface of 5 m/o, which is somewhat smaller than the 7% derived from the charge input under the assumption of a flat concentration profile throughout the polyacetylene.

No quantitative agreement between observed and predicted coulombic efficiencies is obtained for large polarizations as they apply to the discharge curves in Fig. 4 and 5. Only the general trend is predicted correctly; namely, that for polyacetylene in identical dopant state just prior to discharge, the efficiency decreases significantly (70, 64, and 30%) with increasing current density (0.08, 0.24, and 1.2 mA/cm²).

On polyacetylene in different dopant states prior to discharge, Kaneto *et al.* (2) observed an unexplained increase in coulombic efficiency (74, 79.3, and 86.7%) with increasing current (0.1, 0.55, and 1.0 mA). Charging in all three cases had been carried out to a mean dopant level of 7 m/o but for times of 12, 7, and 5.5h, respectively. The results of the present study provide a ready explanation for the anomalous observed behavior: during longer charging time, a larger fraction of the total amount of dopant diffuses into the polyacetylene, thus leaving a smaller dopant concentration near the surface for reduction dur-

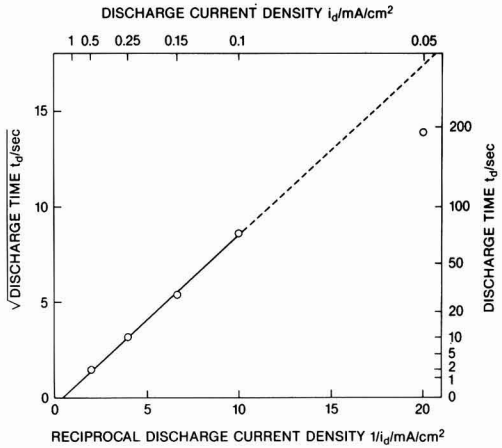

Fig. 10. Discharge time $\sqrt{t_d}$ vs. reciprocal discharge current density to fixed polarization of −50 mV according to Eq. [4]; evaluation of transients from 0.05 to 0.5 mA/cm² shown in Fig. 2.

ing subsequent discharge. This behavior is evident from the time-dependent concentration profiles shown in Fig. 7.

Conclusions

The behavior of BF_4-doped polyacetylene electrodes during charge, discharge, and open circuit is controlled by slow solid-state diffusion of the dopant in the polymer. Steady-state potentials are therefore usually not attained, unless the amount of charge (dopant) injected or removed is of the order of only 0.01 mA-s/cm² or open-circuit times between charges or discharges are exceedingly long, *i.e.*, in excess of 300h for a 70 μm thick film. Since such long times have not been employed in this or other studies, no unique relationship between open-circuit potential and state of charge or dopant level has been established as yet.

Discharge curves of BF_4-doped polyacetylene reported here and of ClO_4-doped polymer obtained by others are interpreted quantitatively by a model involving slow diffusion and discharge. There appears to be no need to invoke a field-enhanced diffusion model.

Coulombic efficiencies observed on pristine polyacetylene electrodes, identically BF_4-doped for 1h with 0.24 mA/cm² to 3.5 m/o followed by 1h on open circuit, are 70, 64, and 30% for discharge with 0.08, 0.24, and 1.2 mA/cm², respectively. The dependency of efficiency on current is predicted quantitatively by a semi-infinite diffusion model if the discharge polarizations and times are small. The anomalous increase in efficiency with increasing discharge current observed by other authors is readily explained by different dopant concentrations near the surface caused by very different charging times.

Acknowledgments

The preparation of the polyacetylene films and the electrolytes by the Rohm and Haas Company, and the help of J. J. Rogers in the experimentation, are gratefully acknowledged.

Manuscript submitted Dec. 26, 1984; revised manuscript received May 24, 1985. This was Paper 616 presented at the New Orleans, Louisiana, Meeting of the Society, Oct. 7-12, 1984.

General Electric Company assisted in meeting the publication costs of this article.

REFERENCES

1. P. J. Nigrey, D. MacInnes, Jr., D. P. Nairns, and A. G. MacDiarmid, *This Journal*, **128,** 1651 (1981).
2. K. Kaneto, M. R. Maxfield, D. P. Nairns, and A. G. MacDiarmid, *J. Chem. Soc., Faraday Trans.*, **78,** 3417 (1982).
3. G. C. Farrington, B. Scrosati, D. Frydryk, and J. DeNuzzio, *This Journal*, **131,** 7 (1984).
4. F. G. Will, *ibid.*, **132,** 2093 (1985).
5. F. G. Will, *ibid.*, **132,** 743 (1985).
6. F. G. Will, R. S. McDonald, R. D. Gleim, and M. R. Winkle, *J. Chem. Phys.*, **78,** 5847 (1983).
7. T. Ito, H. Shirakawa, and S. Ikeda, *J. Polym. Sci.*, **12,** 11 (1974).
8. K. Shimamura, F. E. Karasz, J. A. Hirsch, and J. C. W. Chien, *Macromol. Chem. Rapid Commun.*, **2,** 473 (1981).
9. T. Berzins and P. Delahay, *Z. Elektrochem.*, **59,** 792 (1955).
10. S. Aronson, F. J. Salzano, and D. Ballafiore, *J. Chem. Phys.*, **49,** 434 (1968).
11. M. S. Whittingham, in "Progress in Solid State Chemistry," Vol. 12, G. M. Rosenblatt and W. L. Worrell, Editors, pp. 41-100, Pergamon Press, Elmsford, NY (1980).
12. T. Berzins and P. Delahay, *J. Am. Chem. Soc.*, **77,** 6448 (1955).
13. J. H. Kaufman, E. J. Mele, A. J. Heeger, R. Kaner, and A. G. MacDiarmid, *This Journal*, **130,** 571 (1983).
14. W. A. Tiller, *ibid.*, **127,** 625 (1980).

Kinetic Investigation on the Mechanism of the Photoelectrochemical Oxidation of Water and of Competing Hole Processes at the TiO_2(Rutile) Semiconductor Electrode

F. Vanden Kerchove, A. Praet, and W. P. Gomes*

Rijksuniversiteit Gent, Laboratorium voor Fysische Scheikunde, B-9000 Gent, Belgium

ABSTRACT

The competition between the oxidation of H_2O and that of Br^- ions at the illuminated surface of the semiconducting rutile anode was studied as a function of the Br^- concentration at the surface, the light intensity, the electrode potential, and the surface pretreatment by means of the rotating ring-disk electrode (RRDE) technique. The results allow one to propose a mechanism for the multistep oxidation of H_2O to O_2 as well as for the oxidation of Br^-, the latter reaction being assumed to occur with the surface intermediate H_2O_2 of the former. The data also indicate the occurrence of a surface electron-hole recombination process involving intermediates of the H_2O oxidation, and demonstrate the influence of surface imperfections upon the competition studied.

The anodic oxidation of water to oxygen by photogenerated holes at the semiconducting TiO_2 (rutile) electrode is the reaction which led, more than a decade ago, to the concept of solar-to-chemical energy conversion in photoelectrochemical cells (1). However, the mechanism of this important reaction is not known in detail yet. Indeed, the saturation photocurrent density only depends on the light intensity. Therefore, data on the reactivity of water for holes and on the different steps of this oxidation are not directly accessible by kinetics, and can only be obtained by studying the competition between different reagents for the holes at the electrode surface. One possible method, which was formerly used for TiO_2 (2) and $SrTiO_3$ (3), consists of the measurement of the photocurrent under the addition of so-called current doubling reagents to the photoelectrochemical cell. A more recent technique uses the rotating ring-disk electrode (RRDE): the reaction product of one of the competitive photoreactions at the semiconductor disk electrode is detected specifically at the metal ring electrode. A competitive reagent, which is well suited for this study, is the bromide ion. Its oxidation product, Br_2, is stable in acid solutions and can be easily detected at the ring electrode.

Other investigators have already presented results, obtained by means of this method at monocrystalline TiO_2 electrodes, where Br^- competed with water for holes. Kobayashi *et al.* (4) observed at pH = 2 that Br^- was very reactive as compared to water. At high concentrations of Br^- ($c \geq 10^{-2}$ mol-dm^{-3}), the fraction n of the photocurrent that oxidizes Br^- appeared to be independent of the light intensity. At lower bromide concentrations, n decreased when the light intensity increased, apparently because of the diffusion limitation of the bromide transport to the electrode. Also, Fujishima *et al.* (5) studied the competition between Br^- and H_2O. They also stated that n was independent of the light intensity, without mentioning, however, at which values of pH and c this observation was made. Both groups of investigators found that the reactivity of Br^- decreases with respect to that of water when the pH of the solution is increased. Hence, higher concentrations of bromide can be used for competition studies in less acid solutions, so that the oxidation of Br^- at the anode is no longer limited by the diffusion rate. However, at higher pH, several complications must be taken into account: dismutation of Br_2 to hypobromite and bromide is possible (6); in unbuffered solutions, the pH at the photoanode changes because of the photooxidation of water; and in buffered solutions, the buffer (*e.g.*, acetate) may react with the holes (7).

Therefore, we preferred to confine our measurements to solutions of a pH less than 2, so that the addition of buffers could be avoided and nevertheless changes in pH could be neglected. At these pH values, the range of bromide concentrations, in which changes of n can be observed without the influence of diffusion limitation, is rather small; however, the concentration range can be considerably extended by exploiting the properties of the RRDE. By varying the rotation speed of the RRDE, the flux of bromide to the disk can be monitored. By application of the diffusion laws, c_s (the concentration of bromide at the disk surface) can be calculated (see results). Thus, n can be measured as a function of c_s under different circumstances of light intensity, electrode potential, and surface pretreatment. Such measurement may yield interesting indications on reaction mechanisms, as was recently shown in the case of III-V semiconductor electrodes [see, *e.g.*, Ref. (8) and (9)]. By measuring n at different stages of the photoetching procedure, the influence of the surface pretreatment on the photoelectrochemical behavior of TiO_2 can be studied.

Experimental

All TiO_2 electrodes were cut from one monocrystalline sample, purchased from NL Industries (South Amboy, New Jersey). The sample was doped with 0.05 weight percent (w/o) Nb_2O_5. The electrodes were worked to a cylinder with a height of 5.0 mm and a diameter of 5.0 mm. The front side was the (001) face. Before the TiO_2 sample was mounted as the disk electrode, indium was evaporated on the back and then it was heated in a nitrogen flow during 20 min at 400°C. After cooling, the disk was fitted in a Teflon® tube, which was in turn fitted in a copper tube, on top of which a platinum ring was soldered. Around the ring and the copper tube, a PVC shaft of a suitable shape was mounted. In order to avoid leaks to the back of the electrodes, Cyanolit® 202, a cyanoacrylate ester, was applied between the electrodes and the Teflon and solidified there. Before any measurement, the electrode surface was successively polished with abrasive papers and Al_2O_3 powders of decreasing grain size (0.3 μm final polish) and the previously described photoetching procedure (10) was applied.

Six electrodes were assembled in this way. All but one, exhibiting an inhomogeneous surface, showed very similar behavior. The results reported below were all obtained on two of them, indicated by A and B, respectively. The dimensions of the RRDE r_1, r_2, r_3 (being the radius of the disk, and the inner and the outer radius of the ring, respectively), and the theoretical collection efficiency N are given in Table I. For the calculation of N from the dimensions of the RRDE, the theoretical treatment of Albery and Bruckenstein (11) was followed.

The combined ring-disk electrode was fixed in the cover of the perspex electrochemical cell. In the cell, an auxiliary electrode made of platinized platinum gauze was present; a saturated K_2SO_4-Hg_2SO_4 reference electrode (Radiometer K601) was connected to the cell

* Electrochemical Society Active Member.

Table I. Characteristics of the electrodes used

Specimen	r_1 (mm)	r_2 (mm)	r_3 (mm)	N
A	2.37	3.47	3.88	0.213
B	2.40	3.45	3.92	0.232

through a saturated K_2SO_4 salt bridge. The four electrodes were connected to a bipotentiostat (Bipad Tacussel). The potential of the disk or the ring could be swept by a homemade voltage programmer. All electrode potentials will be expressed in volts *vs.* the saturated sulfate electrode (SSE). The cell was installed in an earthed metal case. The ring-disk electrode could be rotated by means of an electric motor (Tacussel); the rotation speed could be varied between 0 and 2400 rpm. The speed was measured by means of an opto-digital tachometer.

The disk was illuminated by a 450W xenon arc lamp with a stabilized power supply (Oriel). The light was entering the electrochemical cell through a Pyrex window. By placing neutral density filters (Balzers) in the light beam, different light intensities were obtained. No absolute measurement of the light intensity was performed. The saturation photocurrent was always proportional to the light intensity for each state of the electrode surface and was hence considered as a measure of the light intensity for the electrode state considered. All electrodes were mounted in the same position relative to the lamp; thus, the saturation photocurrent under full light intensity can be used as a reference for the measurement of the light intensity at the different states (damaged or etched) of the surface.

All solutions were prepared with reagent-grade chemicals (Merck) in deionized water. During the measurements, pure N_2 (99.98%) was bubbled through the electrolyte solution in order to remove the dissolved and formed oxygen.

The value of N was checked experimentally by dark reduction of $Fe(CN)_6^{3-}$ at the disk and reoxidation of the resulting $Fe(CN)_6^{4-}$ at the ring. The mean experimental value of N differed from the calculated one by less than 0.2% for electrode A and by less than 0.1% for electrode B.

Results on the competition between Br^- and H_2O are expressed by the competition ratio n. The value of n is calculated from the currents at the ring-disk electrode

$$n = I_{Br}/I_D = |I_R|/NI_D \qquad [1]$$

where I_{Br} is the photocurrent associated with the oxidation of bromide, and $|I_R|$ and I_D the absolute increase of the (negative) ring and the (positive) disk current, respectively, resulting from the illumination of the disk. Unless otherwise stated, the disk was kept at +1.00V, *i.e.*, in the saturation region of the photocurrent, and the ring at −0.20V, *i.e.*, in the saturation region of the bromine reduction.

Results

Fully etched electrodes.—Influence of the light intensity and of the bromide concentration on n.—In accordance with the results of Kobayashi *et al.* (4) and Fujishima *et al.* (5), it is a general observation that, for relatively high concentrations of Br^-, n is independent of the light intensity, while for lower concentrations a strong dependence of n on the light intensity is observed. This is illustrated in Fig. 1, when n is given as a logarithmic function of the saturation photocurrent density i for three different concentrations of Br^-. These curves are very similar to those presented by Kobayashi *et al.* (4). As part of these curves are influenced by diffusion limitation of Br^-, we will, in order to isolate the effect of the light intensity, consider in what follows the concentration of Br^- ions at the surface, c_s. Under circumstances of diffusion control, c_s is smaller than the bromide concentration in the bulk, c. In the steady state, the flux of material reacting at the electrode surface must equal the flux being transported through the diffusion layer. Hence

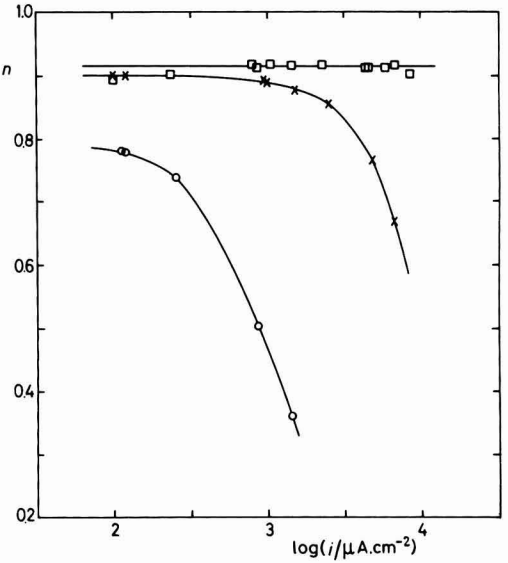

Fig. 1. The competition ratio n as a function of the logarithm of the total photocurrent density i at different concentrations c of bromide. n-TiO_2 (specimen A), surface area 17.6 mm^2, disk potential +1.0V *vs.* SSE, ring potential −0.2V *vs.* SSE, rotation speed 600 rpm, supporting electrolyte 0.33 mol·dm^{-3} $HClO_4$. Bromide concentration c/mol·dm^{-3}: (□) 0.1; (×) 0.01; (○) 0.001.

$$i_{Br} = \frac{I_{Br}}{A} = \frac{FD(c - c_s)}{x_D} \qquad [2]$$

i_{Br} being the part of the photocurrent density corresponding to the oxidation of Br^-, A the surface area of the disk, F the Faraday constant, x_D the thickness of the diffusion layer, and D the diffusion constant of Br^-. The value of x_D (in SI units) is given by (12)

$$x_D = 0.643\ W^{-1/2}\ \nu^{1/6}\ D^{1/3} \qquad [3]$$

with W the rotation speed of the RRDE (in revolutions per second) and ν the kinematic viscosity of the solution ($\nu = 0.9 \times 10^{-6}$ m^2-s^{-1}).

The value of D can be calculated from the slope of the plot of I_{Br} *vs.* $W^{1/2}$ under circumstances of pure diffusion control. Indeed, when $c_s \approx 0$ and c is kept constant, I_{Br} is a function of the rotation speed only (see Eq. [2] and [3]). A value of $D = 1.56 \times 10^{-9}$ m^2-s^{-1} was obtained in 0.33 mol-dm^{-3} $HClO_4$ as the supporting electrolyte, which is in good agreement with that measured by Johnson and Bruckenstein (13) in 1 mol-dm^{-3} H_2SO_4 ($D = 1.58 \times 10^{-9}$ m^2-s^{-1}).

From Eq. [1]-[3], Eq. [4] can be derived, which shows that c_s can be varied by varying the rotation rate and the bulk concentration of Br^-, and can be determined by measuring $|I_R|$ at given c and W, the values of N, A, ν, and D being known

$$c_s = c - \frac{0.643\nu^{1/6}}{NFAD^{2/3}} \cdot \frac{|I_R|}{W^{1/2}} \qquad [4]$$

Values of n were measured at three different light intensities as a function of c_s. The results for the etched electrode A are plotted in Fig. 2(a). At high values of c_s, n tends to a constant value, but at lower values of c_s, n appears to be a function of both c_s and of the light intensity and, hence, of the total photocurrent density i.

Influence of the electrode potential on n.—The photocurrent at the disk remains nearly unaffected by variations of the disk potential, if larger than +0.25V. However, when the potential is decreased gradually to −0.5V, the photo-

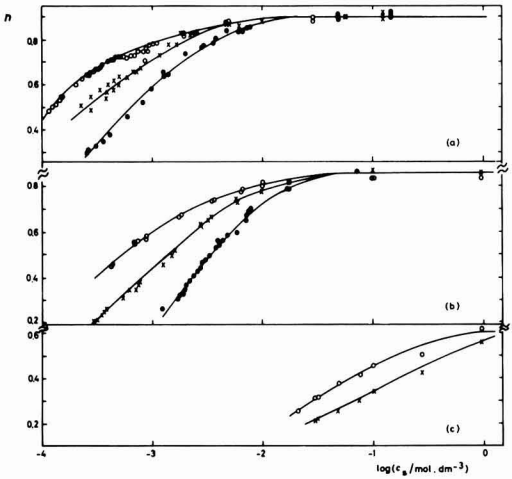

Fig. 2. The competition ratio n as a function of the logarithm of the bromide concentration at the surface c_s at different light intensities corresponding to three values of the disk current density $i/\mu A \cdot cm^{-2}$: (○) 142; (×) 568; (●) 2840. Surface pretreatment: (a) photoelectrochemically etched; (b) damaged by polishing on Al_2O_3 powder of 0.3 μm grain size; (c) as in (b), but 1.0 μm grain size. n-TiO_2 (specimen A), disk potential +1.0 V vs. SSE, ring potential −0.2 V vs. SSE, supporting electrolyte 0.33 mol·dm^{-3} $HClO_4$.

current declines to almost zero because of the recombination of holes with electrons, and simultaneously n is observed to increase. In Fig. 3, the top curve represents results obtained at a fully etched electrode. In order to avoid complications by diffusion limitation, the light intensities were kept low enough. It can be noticed that the photocurrent can be decreased by decreasing either the light intensity or the disk potential, the effect on n being generally more pronounced in the latter case. This phenomenon is illustrated clearly in Fig. 4, by plotting n as a

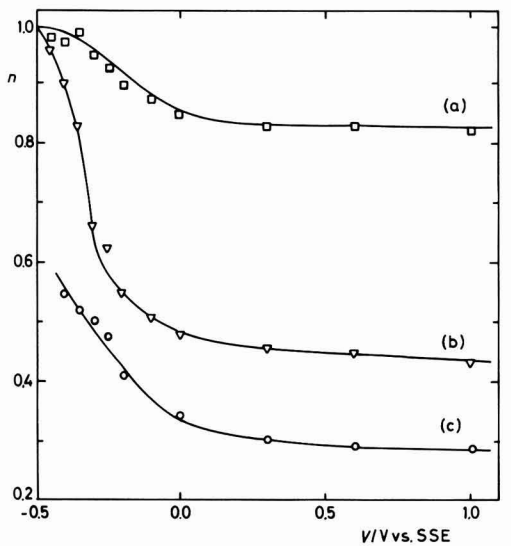

Fig. 3. The competition ratio n as a function of the disk potential V, with a limiting photocurrent density (at $V = +1.0$V vs. SSE) of 616 $\mu A \cdot cm^{-2}$, after different periods of photoetching: (a) 20h (fully etched); (b) 13h; (c) 6.5h. n-TiO_2 (specimen B), ring potential −0.2V vs. SSE, rotation speed 600 rpm, supporting electrolyte 0.33 mol·dm^{-3} $HClO_4$, bromide concentration 0.01 mol·dm^{-3}.

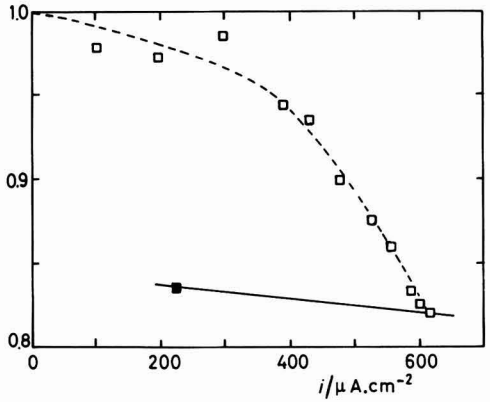

Fig. 4. Plot of n vs. the total photocurrent density i, changed by either varying the electrode potential (□) (same data as in curve (a) of Fig. 3) or the light intensity (■).

function of the photocurrent density. The full line shows the change of n when the photocurrent is varied by a change of the light intensity. As the broken line indicates, the variations of the photocurrent, due to changes of the disk potential, are by far more considerable; in that case, n can rise to its maximum value of 1.

Damaged electrodes.—Influence of the light intensity and of the bromide concentration on n.—After the measurements represented in Fig. 2(a), the electrode was polished with Al_2O_3 powder of 0.3 μm so that damage was induced to the surface and to the underlying region. As a consequence of the ensuing enhanced electron-hole recombination (10), the light intensities had to be increased by a factor of 2.1 in order to obtain nearly the same photocurrents as in Fig. 2a. Then the dependence of n on the light intensity and on c_s was studied again [see Fig. 2b]. Finally, the polishing was repeated with Al_2O_3 powder of 1 μm. As a result of the larger degree of damaging, the light intensities had to be increased again, now by a factor of about 5 relative to those used for Fig. 2(b). Even with full illumination, it was no longer possible to produce a photocurrent of 500 μA in this case. The results obtained after the final polish are plotted in Fig. 2(c).

For damaged surfaces, the concentration range where the influence of the light intensity on n is observed, is extending to higher values of c_s; this effect is very pronounced in Fig. 2c. By comparing parts a, b, and c of Fig. 2, it is obvious that the more the surface has been damaged, the lower the value of n is for each pair of parameters (i and c_s).

Influence of the electrode potential on n.—Similarly, as with fully etched electrodes, it is observed with damaged disks that in the onset region of the photocurrent-voltage curve, n increases significantly as the potential is decreased. In Fig. 3, below curve a representing data for the fully etched electrode B, two other curves (b and c) are given, representing data, obtained before the photoelectrochemical etching of the electrode was completed. The values of n, corresponding with curve c were measured after about 6.5h of photoetching (the limiting photocurrent was at that moment 100 μA with full illumination). The values of curve b were measured after another 6.5h of etching; the limiting photocurrent had risen to 300 μA, while the complete etching lasted 20h and led to a maximum photocurrent of 400 μA.

In all cases, n decreases with increasing V to reach a constant value in the voltage region where, also, the photocurrent is almost constant.

Discussion

Other investigators (4) obtained results, similar to those shown in Fig. 1, but ascribed the decrease of n at increas-

ing light intensity in dilute bromide solutions fully to the diffusion limitation of Br^- transport. The measurements reported here, however, reveal a clear influence of the light intensity and hence of the total photocurrent density on n, at given concentration of Br^- at the surface, for etched as well as for damaged electrodes. Such influence shows that the competing anodic oxidation reactions, *i.e.*, those of H_2O and Br^-, do not occur through parallel pathways involving consecutive one-hole steps, since in that case n should be independent of the light intensity.

In several recent publications by our research group, the kinetics of competing hole processes at semiconductor photoanodes have been analysed (8, 9, 14, 15). Although stabilization of photocorroding n-type III-V semiconductor electrodes is particularly stressed, the kinetic models developed there can be easily adapted to the treatment of the competition between the oxidation of H_2O and that of Br^- at the TiO_2 surface. With III-V compounds as well as with TiO_2, one reagent is always present in large excess (*i.e.*, the electrode material itself in the case of III-V compounds and H_2O in the case of TiO_2) and is oxidized in a multistep reaction, whereas another reducing agent is added to the solution, oxidized in a relatively simple reaction, and detected in a quantitative way. The analysis of competing electrode reactions mentioned leads to the conclusion that those mechanisms, which lead to a light-intensity-dependent competition ratio, are grouped kinetically into two classes, in which n is either a function of the single variable c_s/i or of c_s^2/i. The present experimental results were found to belong to the latter class, as is illustrated by Fig. 5, where the data of Fig. 2a have been replotted as n *vs.* log (c_s^2/i), leading to one single curve. All but one (a chemically improbable one) of the previously derived kinetic relationships in which n is a function of (c_s^2/i) are of the type $n^2/(1-n) \sim c_s^2/i$. This relationship appears not to be obeyed in the present case, however.

Therefore, in order to account for the experimental kinetics of the H_2O *vs.* Br^- competition on the TiO_2 electrode, we propose a reaction mechanism which is to a certain extent analogous to mechanisms devised earlier for cases in which the competition ratio is a function of c_s^2/i and which is furthermore based upon various literature data on the photooxidation of H_2O on TiO_2. By spin trapping and electron spin resonance techniques, Jaeger and Bard (16) revealed the existence of adsorbed hydroxyl and perhydroxyl radicals on illuminated TiO_2 powder, which were dispersed in aqueous solutions. Wilson (17) proposed associating intermediates of the O_2 evolution process with surface states within the bandgap of TiO_2. It is presently accepted that $OH^\cdot$ radicals and adsorbed H_2O_2 molecules are involved as intermediates and as surface states in the photo-oxidation of H_2O on TiO_2; in a number of recent papers, Salvador and Gutierrez dealt with this subject (18-20). These authors proposed the following mechanism for the photo-oxidation of H_2O to H_2O_2: (*i*) capture of a photogenerated hole by a Ti-OH^- surface group, creating a surface $OH^\cdot$ radical; (*ii*) electron transfer from an OH^- ion, physisorbed from solution, to a surface $OH^\cdot$ radical; (*iii*) formation of H_2O_2 from two $OH^\cdot$ radicals. Oxygen is then suggested to be formed either by decomposition of H_2O_2 or by further capture of two holes. Details about these eventual reactions are not given in the references cited. Neither of both these proposed pathways for further reaction of H_2O_2 can account for the n *vs.* c_s^2/i relationship describing the competition between H_2O and Br^- (see below), so that we propose the following mechanism for the photoanodic oxidation of H_2O

$$4(H_2O + h^+ \xrightarrow{k_1} H^+ + OH^\cdot) \quad [5]$$

$$2\,OH^\cdot \xrightarrow{k_2} H_2O_2 \quad [6]$$

$$H_2O_2 + OH^\cdot \xrightarrow{k_3} OOH^\cdot + H_2O \quad [7]$$

$$OOH^\cdot + OH^\cdot \xrightarrow{k_4} O_2 + H_2O \quad [8]$$

Hence, the overall reaction is

$$2H_2O + 4h^+ \rightarrow 4H^+ + O_2 \quad [9]$$

Reaction [7] was already considered by Jaeger and Bard (16) as a possible source of the observed $OOH^\cdot$ at TiO_2 surfaces. Reactions [7] and [8] are assumed to occur during the gas phase decomposition of H_2O_2 (21).

The general kinetic analysis mentioned above (8) suggests consideration of the reaction of Br^- with the surface intermediate H_2O_2, which is known to proceed in the case of a homogeneous liquid phase and to take place according to (22)

$$H_2O_2 + Br^- + H^+ \xrightarrow{k_{Br}} HOBr + H_2O \quad [10]$$

followed by the much faster reaction

$$HOBr + H^+ + Br^- \rightleftharpoons Br_2 + H_2O \quad [11]$$

Note that in this mechanism (reactions [5]-[8], [10], and [11]), the competition between the formation of O_2 and that of Br_2 is actually a competition for H_2O_2 between $OH^\cdot$ radicals and Br^- ions, as expressed in Eq. [7] and [10], and that the light-intensity dependence originates from the fact that the $OH^\cdot$ radicals are formed by holes (Eq. [5]) and hence by light. The intermediates $OH^\cdot$, H_2O_2, and $OOH^\cdot$ are assumed to be adsorbed to the surface. The $OH^\cdot$ radical is considered as being mobile along the surface (a layer of adsorbed H_2O can be conceived in which the $OH^\cdot$ radical captures an electron from a neighboring H_2O molecule). The adsorbed H_2O_2 is assumed to react with a bromide ion from the adjacent solution layer (reaction [10]).

Under steady-state conditions, the concentrations of the intermediates $OH^\cdot$, H_2O_2, and $OOH^\cdot$ are constant, resulting in Eq. [12]-[14]

$$\frac{dx_1}{dt} = k_1 p_s - 2k_2 x_1^2 - k_3 x_1 x_2 - k_4 x_1 x_3 = 0 \quad [12]$$

$$\frac{dx_2}{dt} = k_2 x_1^2 - k_3 x_1 x_2 - k_{Br} x_2 c_s = 0 \quad [13]$$

$$\frac{dx_3}{dt} = k_3 x_1 x_2 - k_4 x_1 x_3 = 0 \quad [14]$$

Here x_1, x_2, and x_3 represent the surface concentrations of $OH^\cdot$, H_2O_2, and $OOH^\cdot$, respectively, and p_s the concentration of holes at the electrode surface.

The total steady-state current density is proportional to the light intensity and is given by the following expression, in view of Eq. [5] and considering the surface H_2O concentration to be constant

$$i = ek_1 p_s \quad [15]$$

where e is the absolute value of the elementary charge. According to Eq. [10] and [11], the part of i corresponding to the oxidation of Br^- is given by

$$ni = i_{Br} = 2ek_{Br} x_2 c_s \quad [16]$$

Elimination of the unknown quantities p_s, x_1, x_2, and x_3 from Eq. [12]-[16] leads to the expression

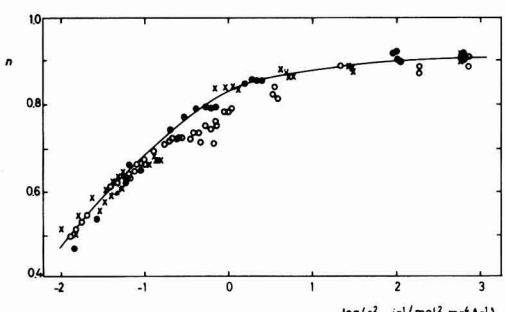

Fig. 5. Plot of n *vs.* log(c_s^2/i). Same data as in Fig. 2(a).

$$\frac{n^2(1+n)}{(1-n)^2} = \frac{ek_2k_{Br^-}^2}{k_3^2} \cdot \frac{c_s^2}{i} \qquad [17]$$

which conforms to the experimental result that n is a function of the single variable c_s^2/i (Fig. 5).

It should be remarked that, in this equation, k_1 and k_4 are absent: only reactions [6], [7], and [10] determine the competition. It has been found that the shape of the function (Eq. [17]) is not changed if reaction [5] is assumed to be reversible. Neither is it changed when reaction [8] is replaced by another plausible reaction (21)

$$2\ OOH \rightarrow H_2O_2 + O_2 \qquad [18]$$

Under the latter assumption, only the ratio of the reaction constants in Eq. [17] must be adapted. On the other hand, if further oxidation of H_2O_2 by a hole instead of reaction [7] were assumed, an expression would result in which n is a function of (c_s/i) instead of (c_s^2/i); if decomposition of H_2O_2 were assumed, an i-independent expression for n would be obtained.

When the experimental results are plotted as $n^2(1+n)/(1-n)^2$ *vs.* c_s^2/i, the linearity is not completely satisfactory. However, it can be improved by inserting, instead of n, a quantity n' defined by

$$n' = n/n_{max} \qquad [19]$$

and in which n_{max} represents the observed maximum value of n (in Fig. 2, n_{max} is equal to 0.90, 0.86, and 0.59 for parts a, b, and c, respectively). In Fig. 6, the data of Fig. 2 have been replotted as $\log[n'^2(1+n')/(1-n')^2]$ *vs.* $\log(c_s^2/i)$. It is seen that the sets of data a, b, and c can be represented in a very satisfactory way by linear plots with slope 1, demonstrating that Eq. [17] holds for n' and hence indicating that the proposed competing reaction mechanism (Eq. [5]-[7], [10], and [11]) is valid.

Kobayashi *et al.* (23) already remarked that, at damaged TiO_2-electrodes, n does not tend to 1 when the concentration of bromide is increased. This was explained by the assumption that polishing results in the creation of special surface sites (*e.g.*, Ti^{3+}-Ti^{3+} pairs), where the formation of O_2 (and surface electron-hole recombination) would occur by preference. Hence, the surface might be conceived as being composed of two parts, *i.e.*, a nondamaged one, where the competition between the formation of Br_2 and that of O_2 proceeds according to reactions [5]-[11], and a damaged one, where only O_2 is formed. This reasoning would be compatible with the correction of n by the factor $(1/n_{max})$. Also, with the fully etched electrode, the limiting value of n remains less than 1. It is therefore supposed that even after prolonged etching, a certain fraction of the surface consists of special Ti^{3+}-Ti^{3+} sites.

The foregoing considerations refer to situations in which surface electron-hole recombination can be excluded because of the large band bending. Recombination mechanisms, in which conduction band electrons are captured in surface states, associated with intermediates of the anodic decomposition of the semiconductor, have been treated kinetically in a recent paper (9). Specifically it was shown that, if the intermediate involved in recombination corresponds to a higher degree of oxidation than that involved in the competing reaction with the solved reducing agent, then decreasing the voltage in the photocurrent onset (*i.e.*, increasing the conduction band electron concentration at the surface) should result in a change in the competing rates in favor of the solved reducing agent. This conclusion has very recently been verified experimentally on the system n-GaAs/Fe^{2+} (24). In an analogous way, the results presented in Fig. 4 may be interpreted by assuming the occurrence, not only of ordinary electron-hole surface recombination, but also of a recombination step in which conduction band electrons are captured by OOH^- radicals according to

$$e^- + OOH^- + H^+ \rightarrow H_2O_2 \qquad [20]$$

It can be easily seen from a simplified reaction scheme (Fig. 7, in which protons and ordinary surface recombination have been omitted) that this recombination step prevents the oxidation of H_2O_2 to O_2 and hence leads to the enhancement of the competition ratio n. Reaction [20] is conceivable to occur in view of the energetic position of the OOH^-/H_2O_2 redox couple [$U^0 = 1.5V$ *vs.* SHE at pH = 0 (16), corresponding to an energy level at -1.5 eV *vs.* SHE, *i.e.*, about midgap].

Another recombination step, in which conduction band electrons are captured by H_2O_2, adsorbed at the TiO_2 surface, has been suggested in the literature (19). The occurrence of this step is in principle not excluded by the present results, but may contribute to a minor extent only when H_2O_2 is much more reactive with respect to bromide ions than to conduction band electrons.

It should be remarked that, also, Kobayashi's concept (23) of special sites for preferential H_2O oxidation and surface recombination may explain the influence of the electrode potential upon V: when V is decreased and hence the conduction band electron concentration at the surface increased, surface recombination competes in these sites only with the H_2O oxidation, resulting in an increase in the observed value of n.

Conclusions

The present study on competing hole processes has allowed us to propose a mechanism for the oxidation of water molecules at the TiO_2 photoanode, in which hydroxyl radicals are assumed to be involved in at least three of the subsequent reaction steps. The results also indicate that the hole processes occurring simultaneously with the H_2O oxidation reaction, *i.e.*, oxidation of Br^- and to a certain extent also surface electron-hole recombination, do not occur in parallel with the water oxidation, but that these three processes are linked through the intermediates of the latter, analogously to what has previously been observed on n-type III-V electrodes. In particular, the oxidation of Br^- ions appears to occur by reaction with the surface intermediate H_2O_2 of the H_2O oxidation. If this type of oxidation mechanism for reducing agents at the TiO_2 photoanode were general, this would evidently have important implications as to the factors which determine the reactivity and selectivity behavior of this electrode: these factors would then be connected with the thermodynamics and kinetics of reactions between solved reducing agents and adsorbed hydrogen

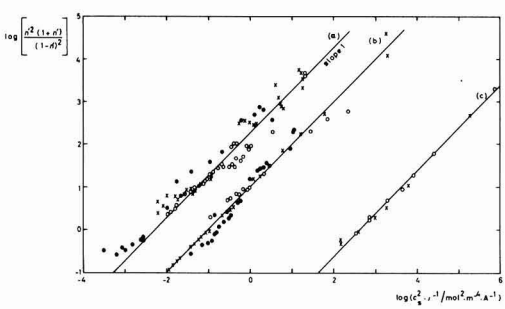

Fig. 6. Plot of $\log[n'^2(1+n')/(1-n')^2]$ *vs.* $\log(c_s^2/i)$. Same data as in Fig. 2 (a, b, and c).

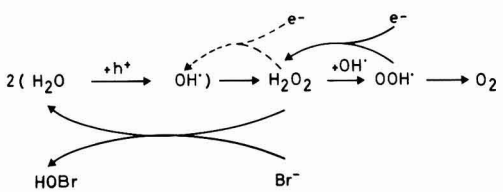

Fig. 7. Reaction scheme for processes occurring at the illuminated TiO_2 electrode.

peroxide. Experimental work with reducing agents different from bromide will be needed in order to clarify this point.

Acknowledgments

One of the authors (F. V. K.) wishes to thank the Nationaal Fonds voor Wetenschappelijk Onderzoek (N.F.W.O.) for a research grant. Acknowledgment is made to Lic. J. Willaert for performing part of the experiments.

Manuscript submitted Nov. 14, 1984.

REFERENCES

1. A. Fujishima and K. Honda, *Nature*, **238**, 37 (1972).
2. E. C. Dutoit, F. Cardon, and W. P. Gomes, *Ber. Bunsenges. Phys. Chem.*, **80**, 1285 (1976).
3. F. Vanden Kerchove, J. Vandermolen, W. P. Gomes, and F. Cardon, *ibid.*, **83**, 230 (1979).
4. T. Kobayashi, H. Yoneyama, and H. Tamura, *J. Electroanal. Chem.*, **122**, 133 (1981).
5. A. Fujishima, T. Inoue, and K. Honda, *J. Am. Chem. Soc.*, **101**, 5582 (1979).
6. F. A. Cotton and G. Wilkinson, "Advanced Inorganic Chemistry," p. 477, Interscience, New York (1972).
7. K. Hirano and A. J. Bard, *This Journal*, **127**, 1056 (1980).
8. F. Cardon, W. P. Gomes, F. Vanden Kerchove, D. Vanmaekelbergh, and F. Van Overmeire, *Faraday Disc.*, **70**, 153 (1980).
9. D. Vanmaekelbergh, W. P. Gomes, and F. Cardon, *J. Chem. Soc., Faraday Trans. 1*, **79**, 1391 (1983).
10. A. Praet, F. Vanden Kerchove, W. P. Gomes, and F. Cardon, *Solar Energy Mater.*, **7**, 481 (1983).
11. W. J. Albery and S. Bruckenstein, *Trans. Faraday Soc.*, **62**, 1920 (1966).
12. W. J. Albery, "Electrode Kinetics," p. 53, Clarendon Press, Oxford (1975).
13. D. C. Johnson and S. Bruckenstein, *This Journal*, **117**, 460 (1970).
14. D. Vanmaekelbergh, W. P. Gomes, and F. Cardon, *ibid.*, **129**, 546 (1982).
15. D. Vanmaekelbergh, W. Rigole, W. P. Gomes, and F. Cardon, *J. Chem. Soc., Faraday Trans. 1*, **79**, 2813 (1983).
16. C. J. Jaeger and A. J. Bard, *J. Phys. Chem.*, **83**, 3146 (1979).
17. R. H. Wilson, *This Journal*, **127**, 228 (1980).
18. C. Gutierrez and P. Salvador, *J. Electroanal. Chem.*, **138**, 457 (1982).
19. P. Salvador and C. Gutierrez, *Surf. Sci.*, **124**, 398 (1983).
20. P. Salvador and C. Gutierrez, *J. Phys. Chem.*, **88**, 3696 (1984).
21. A. Tessier and W. Forst, *Can. J. Chem.*, **52**, 794 (1974).
22. A. A. Frost and R. G. Pearson, "Kinetics and Mechanism," 2nd ed., p. 207, John Wiley, New York (1961).
23. T. Kobayashi, H. Yoneyama, and H. Tamura, *J. Electroanal. Chem.*, **138**, 105 (1982).
24. D. Vanmaekelbergh, W. P. Gomes, and F. Cardon, *Ber. Bunsenges. Phys. Chem.*, To be published.

Ellipsometry of the Growth and Dissolution of Anodic Oxide Films on Aluminum in Alkaline Solution

R. Greef* and C. F. W. Norman**

Department of Chemistry, The University, Southampton, England 509 5NH

ABSTRACT

Ellipsometry has been used to study the growth of anodic films on superpure aluminum in sodium hydroxide of concentration range 0.1-4*M*. The ellipsometer used was a self-nulling type, and all experiments were performed *in situ* at a constant wavelength of 632.8 nm. The results are explained by the growth and dissolution of anodic films that are duplex in nature. During the dissolution process, at certain potentials, a highly reproducible transient effect in the optical signal is seen. This effect has been related to roughening of the underlying aluminum substrate, followed by subsequent smoothing upon completion of the dissolution process. The latter is indicated by the optical signal returning close to its initial value prior to film growth.

Until comparatively recently, interest in oxygen containing films on aluminum has focused largely on their protective and decorative properties. Newer applications for aluminum and aluminum alloys include their use in corrosion control as sacrificial anodes, and as primary battery anodes (1-3). In the latter role, the presence of passivating oxide films is detrimental to the primary function of the substrate, which is to dissolve electrochemically at the lowest possible overpotential.

Aluminum used in these applications is alloyed with such elements as zinc, tin, indium, and gallium, the effect of which is to improve reactivity (4-7). The full reasons for the effect of alloying with these metals is not yet clear, and recent work (8) with zinc-tin and zinc-indium alloys in 0.1*M* NaOH has shown the system to be complex. To help understand the mechanisms involved, it was acknowledged that investigation with super-pure aluminum would be of fundamental importance.

A method of monitoring the surface condition of the metal under working conditions with the metal *in situ* in the electrolyte was required. Ellipsometry provides such a technique (9, 10) and allows precise monitoring of the electrode surface by measuring the change in the state of polarization of a beam of light specularly reflected from the surface. These changes can be interpreted in terms of the thickness and refractive index of overlayers on the metal surface.

Previous ellipsometric studies of pure aluminum are available and are concerned with anodic film growth in acidic or buffered solutions (11-14) or in hot water (15). This paper describes an ellipsometric study of aluminum in sodium hydroxide solutions, in which aluminum oxide is soluble, and which for this reason is a medium of importance in battery applications.

Ellipsometry is shown to be capable of monitoring the growth and dissolution of surface films over a range of potentials and alkali concentrations, and the results can be interpreted in terms of the porosity of the films. The results are explained with a detailed model of changes in density profile through the thickness of the film as a function of time.

When the surface film dissolves, it does so finally to leave a smooth aluminum surface, but an unexpected and large transient optical signal is observed just before the last of the porous film disappears. This is explained by the short-lived presence of a microrough metal surface formed by exposure and corrosion of the substrate as the overlying layer becomes discontinuous. When all the protective layer dissolves, the peaks of the rough metal surface are preferentially attacked and dissolve, and the substrate again becomes smooth, as is shown by a return of the optical signal to a point closely corresponding to its starting point before the initiation of anodic film growth.

*Electrochemical Society Active Member.
**Electrochemical Society Student Member.

Experimental Method

Materials.—Aluminum rods (99.999% Al) were cut into cylindrical electrodes of 6 mm diam. Electrical connection was made with a copper wire attached with thermosetting silver-loaded epoxy resin. The samples were mounted in epoxy resin.

Smoothing.—The electrodes were ground on 400 grit, then mechanically polished for 6 min on 6 μm diamond, and finished on alumina (0.05 μm). The powder was mixed with distilled water.

Cell.—The electrodes were mounted in a polypropylene cell, designed to support the surface horizontally at the optical center of the ellipsometer. The cell contained a platinum counterelectrode and a reversible hydrogen reference electrode. The reference electrode consisted of a platinized platinum electrode sealed into a tube with a closed upper end and an open lower end immersed in the electrolyte. It was prepared by passing a cathodic current of approximately 10 mA-cm^{-2} until a bubble of hydrogen formed enveloping half of the platinum. Electrode potentials are reported throughout *vs.* this reversible hydrogen electrode in the same solution. The electrolyte was air-saturated, AR-grade sodium hydroxide solution.

Electrochemical measurement.—The electrode potential was controlled by a Wenking potentiostat (70TS1) coupled to a Wenking voltage scan generator (VSG72). Cyclic voltammograms were recorded on a analog X-Y recorder.

Optical measurements.—The ellipsometer is a self-nulling fully automated type, employing Faraday modulation and compensation. The optical and mechanical parts of the ellipsometer have been described elsewhere (16).

The ellipsometer was used in the monochromatic mode, the source being a He-Ne laser of wavelength 633 nm. The time constant for the self-nulling process is of the order of 0.1s.

The ellipsometer is linked to a SWTPC M6809 microcomputer which controls the operation and data acquisition. The computer is interfaced with a Hewlett-Packard Type 7470A plotter, which enables direct monitoring of the results while the experiment is running. Data points consisting of readings of time, the ellipsometric parameters Δ and ψ, and the working electrode potential and cell current were recorded on diskette.

Electrochemical results.—Cyclic voltammograms for super-pure aluminum in 0.1 and 1.0*M* NaOH are given Fig. 1a and 1b.

On the forward anodic sweep, at a potential close to −0.5V there is a region where little hydrogen evolution occurs together with no film growth. Here we have a small net anodic current and, ellipsometrically, an almost steady signal.

At higher anodic potentials there is an increase of current and the resulting broad plateau is characteristic of film growth. Currents are slightly lower on the reverse sweep and indicate a continuation of film growth.

Current time transients were recorded by stepping the potential from −0.5V to other more anodic potentials. The resultant transients shown in Fig. 2 show a fall of current with respect to time indicative of the growth of a porous film. Hurlen and Haug (17) have recently obtained transients that are similar in structure, but the potential steps are much smaller than in our experiments.

When the potential is stepped back to −0.5V, the current becomes zero very quickly and after several seconds rises to the small anodic value it had prior to the anodic pulse. This time period is known as the recovery time, and previous accounts of similar phenomena in acidic electrolytes are available (18-21).

The recovery time depends upon the electrolytic concentration and the height of the anodic peak. The recovery time is longer for more dilute concentrations and higher anodic pulses.

Optical terminology.—Ellipsometry measures the quantity ρ, which is the ratio of the reflection coefficients parallel to (p component) and perpendicular to (s component) the plane of incidence. Each of these reflection coefficients is a complex quantity which is an expression of the fact that it contains both amplitude and phase information. The ellipsometer measures two angular quantities Δ and ψ which are related to ρ by the equation

$$\rho = \tan \psi \, e^{i\Delta}$$

The possible range of Δ is 0°-360°, and of ψ is 0°-90°. Oxide films on aluminum are transparent, and the theory

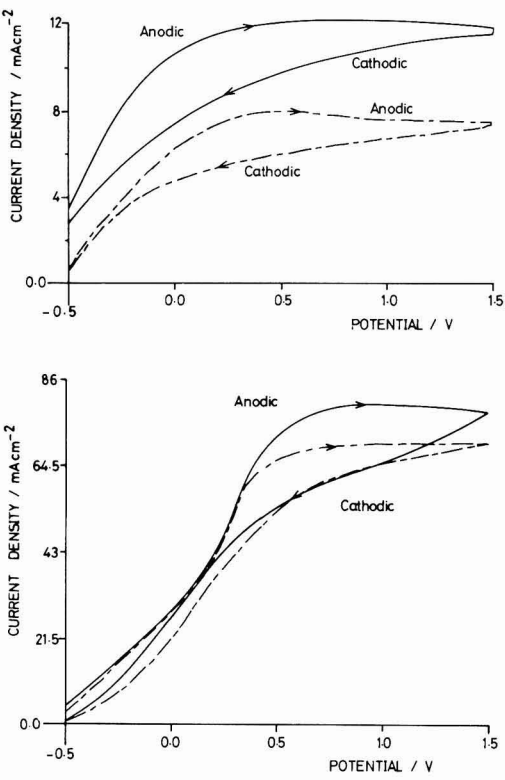

Fig. 1. a, top: Cyclic voltammetry of super pure aluminum in 0.1M NaOH, sweep rates 40 mV-s^{-1} (bold line) and 25 mV-s^{-1} (dashed line). Potentials throughout are against the reversible hydrogen electrode in the same solution. b, bottom: Cyclic voltammetry as in 1a in 1.0M NaOH.

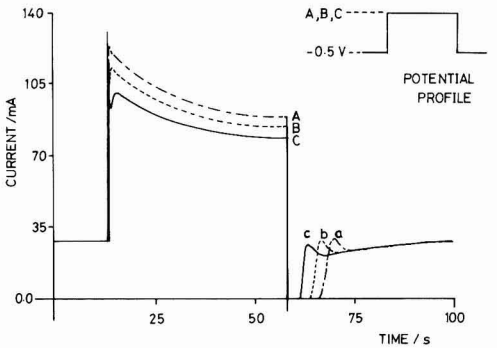

Fig. 2. Current-time transients for the potential program shown. Anodic potentials +1.5V (A), +1.0V (B), and +0.5V (C). a,b, and c are recovery currents corresponding to A, B, and C, respectively.

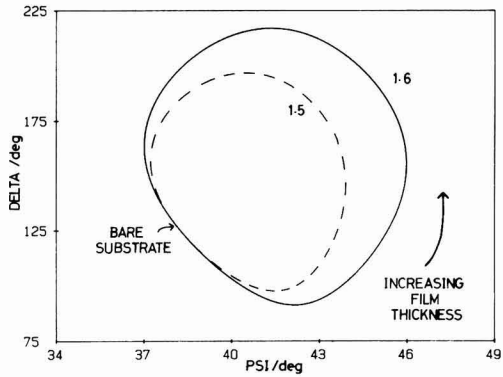

Fig. 3. Optical signals Δ and ψ for an idealized uniform film growth model on a smooth substrate. The refractive index is indicated for each curve.

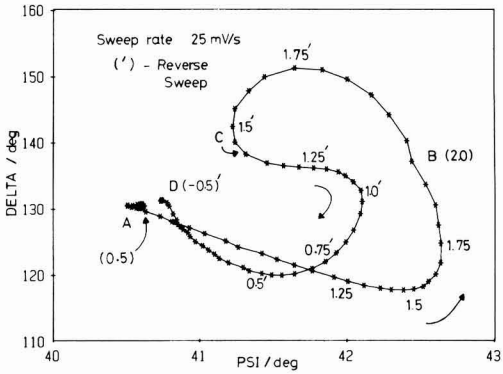

Fig. 5. Optical signals Δ and ψ during cyclic voltammetry as shown in Fig. 1a, covering potential range −0.5V (point A) to +2.0V (point B) and returning to −0.5V (point D). The time interval between each data point is 2s.

for an idealized uniform film model shows that as the film grows, a cyclic change in both Δ and ψ is traced, (see Fig. 3) the size of which depends upon the refractive index of the oxide.

Pretreatment and growth potentials.—On immersing the electrode in the electrolyte, the potential was quickly adjusted to −1.0V in the hydrogen evolution region to cathodically protect the polished surface. After 10s, the potential was shifted to −0.5V, where the optical signal is steady. A pipette was used to disperse the remaining hydrogen bubbles before the potential was stepped to the higher anodic growth potential. A diagram of this potential cycle is shown in Fig. 4.

Optical measurements during cyclic voltammetry.—Figure 5 shows the Δ-ψ signature obtained during a cyclic sweep of potential at 25 mV/s in 0.1*M* NaOH. The starting point A is at −0.5V, where the optical signal is stable. As the potential was scanned positive, a distorted egg-shaped curve was produced, as shown in section A-B. Point B represents a potential of 2.0V, and section B-D is the return scan to −0.5V.

Only a qualitative interpretation of this result was attempted. The anodic sweep A-B evidently results in the formation of a film, but because of the distorted egg shape of the curve, this cannot be a layer of constant optical properties increasing in thickness. During the negative sweep the film continues to grow for a time, but then as point C is approached the Δ-ψ curve turns back on itself and traverses around an inner curve until a position near the starting point is reached.

The optical signal at A did not move appreciably until a potential of 0.1V was reached. The signal at C corresponds to 1.3V. It is possible that the general shape of the Δ-ψ signature in Fig. 5 could be attributed to two entirely different processes: film growth, which accelerates as the potential increases, and chemical dissolution of the film as the potential is reduced.

This experiment suggests that the refractive index of the film is dependent on potential, so the effect of the formation potential was explored in detail.

Constant potential experiments.—A series of films was formed using the potential profile already described (see Fig. 4), in which the pretreatment at −1.0 and −0.5V was held constant, while formation potentials between 1.5 and 3.5V were applied, until approximately one whole Δ-ψ "egg" had been traced.

The eggs traced out at high potentials tended to form nearly closed curves, characteristic of a uniform transparent film. When plotted on common axes (see Fig. 6), the formation curves form a very striking set or "nest" of eggs, which is strongly suggestive of an oxide film increasing in refractive index very regularly with formation potential. The smoothly variable composition of the film implied by this increasing refractive index is most plausibly explained by a film of varying porosity, which fits well with the electrochemical results of Fig. 2.

Another series of eggs (see Fig. 7) was obtained by keeping the anodic growth potential constant (+2.5V) and varying the concentration of the sodium hydroxide. Increasing the concentration decreased the size of the egg, and this implies that the refractive index of the transparent film also decreases, corresponding to the increasing solubility of Al oxides and hydroxides at higher pH's.

Dissolution at open circuit.—In Fig. 8, two curves are shown for growth at +2.5V in 0.1*M* NaOH. The maximum

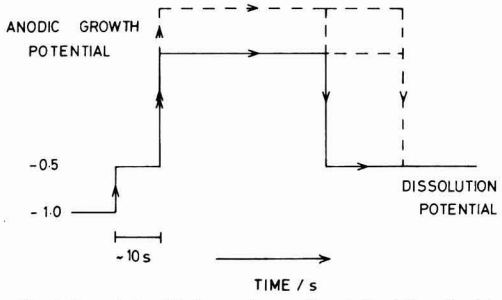

Fig. 4. Potential profile for anodic growth and dissolution of oxide layers.

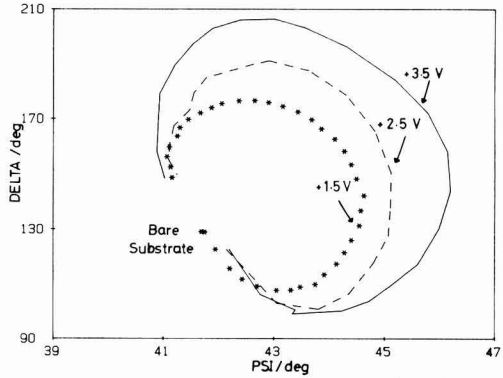

Fig. 6. Family of anodization curves at the indicated growth potentials with data points every 5s. Each run was carried out with a freshly polished electrode.

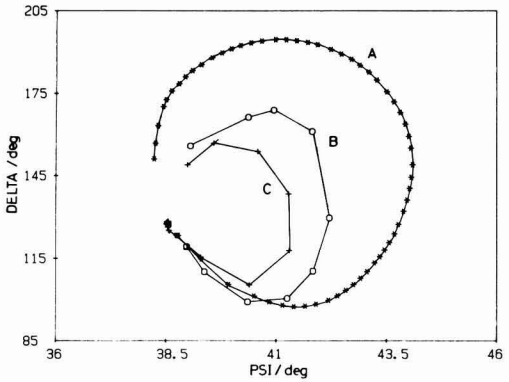

Fig. 7. A family of growth curves at +2.5V, for NaOH concentrations of 0.1M (A), 1.0M (B), and 4.0M (C). Curves B and C have points at intervals of 1s; the time interval between points for curve A is 2s.

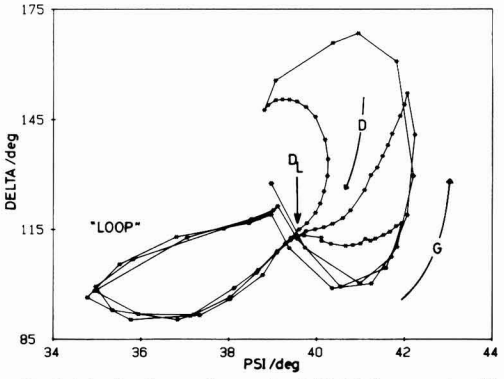

Fig. 9. A family of curves for growth +2.5V (G), interrupted at different stages to show the dissolution signal at −0.5V (D). D_L corresponds to the dissolution limit in the text. The time interval between points is 1s.

current density for this electrolyte is about 50 mA/cm². When a certain film thickness was obtained, the film was allowed to dissolve at open circuit. The potential decreased quickly at first until it reached −0.9V at a position close to the starting position. The potential approached E_{corr}, but in the duration of the experiment never completely stabilized.

During the dissolution phase, the optical signal did not even begin to retrace the formation curve but departed immediately on a totally different path, which nevertheless brought the curve back closely to the starting point.

Dissolution at −0.5V.—A family of curves is shown in Fig. 9 for growth at 2.5V but with interruption of the growth at different stages to show the dissolution signal at −0.5V. All of these curves were obtained with the same electrode, the oxidation potential being reapplied as soon as the dissolution process had brought the Δ-ψ values closely to the starting position. Each point was recorded at a time interval of 1s.

It is convenient to reduce this rather complex picture into three main regions: (*i*) the film growth region, (*ii*) the dissolution pathway until the point D_L (D_L = dissolution limit) is reached, and (*iii*) the remaining part, which we will call the "loop," which finally returns the optical signal to the starting point.

The corresponding current-time transients are identical in structure compared with those in Fig. 2. Examination in three stages shows, first, the falling transient after the anodic pulse which indicates porous film formation; second, a region where after stepping the potential back to −0.5V negligible current flows and the process occurring is attributed to chemical dissolution of the film by the electrolyte; and last, the rising current when the recovery time is complete, the onset of which coincides with the point marked D_L in Fig. 9. The return of the net anodic current accompanies the optical signal which traverses the loop before returning to the starting position.

The formation of the loop is very reproducible even after three growth-dissolution cycles and is fast, taking only about 8s from the point marked D_L to the starting position.

Dissolution at other potentials.—The result of the open-circuit dissolution and the dissolution at −0.5V seem to indicate that the behavior of the loop region of the dissolution process is potential controlled. Further experiments where the dissolution potential was varied can be seen in Fig. 10 and 11. In Fig. 10, the potentials −1.0 and −0.8V were very close to the open-circuit potential (see Fig. 8) and the dissolution behaviors are very similar. Increasing the dissolution potential (Fig. 11) to more anodic potentials than −0.8V leads to the appearance of the loop, which increases in size with an increase of dissolution potential up to about 0.0V where, as seen in Fig. 5, at this potential the rate of film growth exceeds that of film dissolution. Therefore, at this potential no net film dissolution would be expected.

Discussion

It is possible to make qualitative conclusions based purely upon the general shape of the Δ-ψ signatures. It is

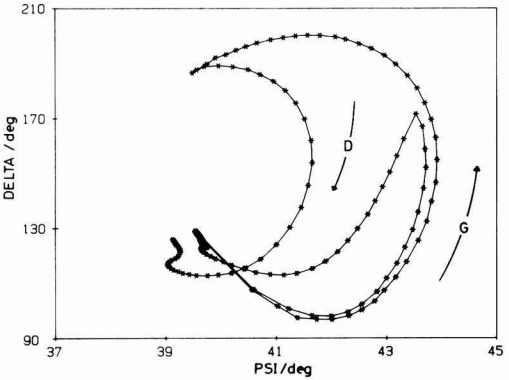

Fig. 8. Growth curves for +2.5V in 0.1M NaOH interrupted at different film thicknesses (G), and their resultant dissolution curves at open circuit (D). The time interval between points is 4.5s.

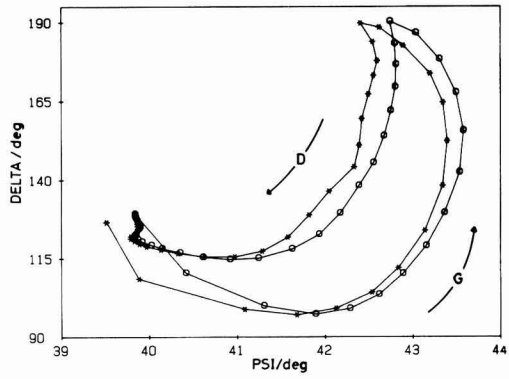

Fig. 10. Optical signal for film growth at +2.5V (G), with dissolution at −1.0V (asterisks) and −0.8V (open circles) (D). The time interval between points is 5.5s.

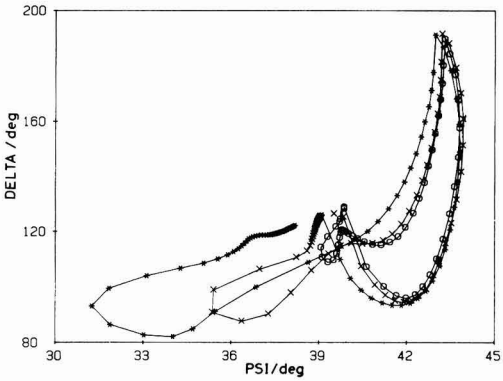

Fig. 11. Growth curves as in Fig. 10, with dissolution at −0.6V (open circles), −0.4V (X's) and −0.2V (asterisks). The time interval between points is 5.5s.

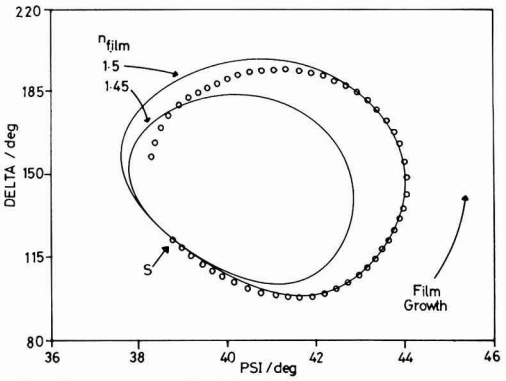

Fig. 12. Comparison of calculated uniform film models (value for the oxide refractive index as indicated), with an experimental growth curve +2.0V in 0.1M NaOH (open circles). S corresponds to the initial experimental point, with further points taken at 2s intervals.

clear that a porous film grows (see Fig. 5) on the aluminum substrate above potentials of about 0.1V and that the refractive index of the film, and hence its density, increases regularly with increasing formation potential and decreasing electrolytic concentration. Films formed in this way dissolve to leave a clean surface which is still smooth even after several growth-dissolution cycles.

The conclusions can be tested in a quantitative way by calculating the Δ-ψ response, using a single-film or multi-film model, measured or estimated values of the various optical constants, and a computer program such as that of McCrackin and Colson (22).

Optical constants of the substrate.—The condition of the surface at −0.5V before anodization is stable and has been used as a reference state. It is not a film-free surface, however, as a film of oxide formed in air during the polishing process is not removed even at −1.0V. Values of n and k for bare, pure aluminum surfaces are available (11, 12, 15, 23, 25), but not for the polished aluminum substrate immersed in a caustic electrolyte. The values of the bare surface optical constants were therefore estimated by assuming that a thin layer (0-5 nm) of oxide of refractive index 1.65 exists initially on the aluminum. The effect of "removing" this layer in the calculations is to increase Δ and decrease ψ. Using this new starting point in the film calculation does give a noticeable change in the Δ-ψ signatures predicted, but none of the conclusions is changed by using the initial measured Δ-ψ values as if they represented a clean surface. Using this and the fact that the surfaces are mechanically polished and are never exactly reproducible, approximate optical constants of the aluminum used were $n = 1.5 \pm 0.15$ and $k = 5.5 \pm 0.4$. These values can be compared with those for aluminum deposited under UHV conditions (23) of $n = 1.43$ and $k = 7.28$. Under our conditions these values correspond to "bare surface" Δ and ψ values of 131.08° and 40.90°, which lie close to the observed starting points.

Film growth models.—The simplest model is the single-film model Fig. 3, in which a uniform oxide film lies between the alloy substrate and the immersion medium. This model suffices for films grown on pure aluminum under certain conditions (14, 15). When the model is applied to these results, however, it is obvious from Fig. 12 that a uniform film model is inadequate (25). Initially, the experimental data indicate a constant refractive index, but as the film thickens the refractive index seems to decrease, implying that the film is increasing in porosity.

Two multilayer models were therefore explored (26), having a linear and an exponential fall in the refractive index with distance from the electrode. Neither model yielded Δ-ψ signatures that fitted any substantial part of the experimental curves.

A two-film model similar to that used by Dell'Oca and Fleming(11) was then tried in which there was a dense oxide layer next to the electrode and a more porous layer in contact with the electrolyte. The model was refined by proposing a smooth transition between the two refractive indexes rather than a sudden step (see Fig. 13). This was done by dividing the film up into many thin slices and generating a function with which to define the refractive index of each slice. The function used was

$$n = n_{min} + (n_{max} - n_{min}) \exp(-x)/[\exp(-x) + \exp(-x_{max}/f)]$$

where n_{min} and n_{max} are the values of refractive index in contact with the electrolyte and metal, respectively, and x_{max} is an arbitrary number which controls the sharpness of the refractive index transition between the two extreme values. The value of x varies from 0 to x_{max} in equal increments for each slice from the metal to the outer film boundary. The fraction $1/f$ determines the distance at which the step from n_{max} to n_{min} is half complete. So for Fig.13, the theoretical parameters are film thickness = 420 nm, slice thickness = 4 nm, $n_{min} = 1.45$, $n_{max} = 1.50$, $x_{max} = 60$, and $f = 2.2$, which implies the dense part of the film is 190 nm thick.

The calculation of the Δ-ψ response is started with a bare surface, and the slices are added one at a time until the total film has been assembled. The result shown in Fig. 13 is a set of Δ-ψ points tracing out the simulated characteristics.

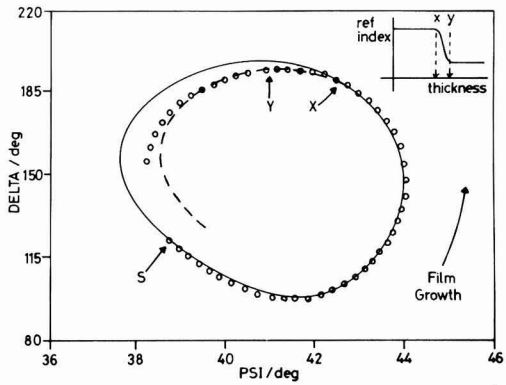

Fig. 13. Comparison of the refined duplex model for film growth (dashed line) superimposed upon the experimental curve from Fig. 12 (open circles) and the uniform film model curve in Fig. 12 (bold line). Theoretical parameters: film thickness = 420 nm, $n_{min} = 1.45$, $n_{max} = 1.50$, $x_{max} = 60$, and $f = 2.2$. The inset shows the smooth transition for the refined model; the start and end of the transition between the two layers are indicated by X and Y, respectively.

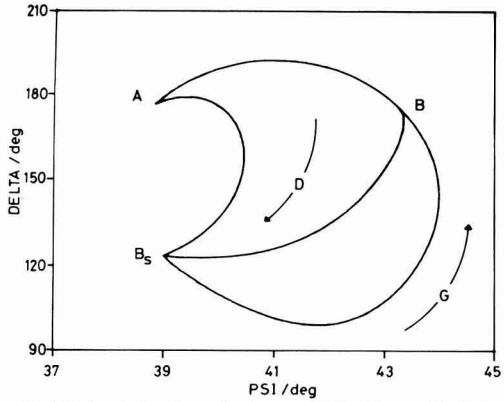

Fig. 14. A calculated anodization curve (G) with two dissolution curves (D), x_{max} = 60, film thicknesses 320 nm (point A) and 210 nm (point B). B_s corresponds to the bare surface.

Film dissolution models.—Accepting that the growth curves can only be explained by a graded-film model, it is clear that a dissolution process quite different from the reverse of the formation process is needed to explain the dissolution trajectory in the Δ-ψ plane. A model in which all of the oxide layers begin to relax toward a lower refractive index at the end of the growth phase was found to give the correct kind of shape. Out of many curves produced by trial and error, Fig. 14 shows the main features seen in the open-circuit dissolution experiment (see Fig. 8).

It therefore seems clear that the outer layers of the oxide are porous enough to allow attack of the inner, dense layers to start immediately upon cessation of the anodization process.

Figure 15 shows a three-dimensional plot indicating how the refractive index of the film changes with thickness and time. At the point marked A, the potential is pulsed anodically and a film of uniform refractive index starts to form. At B, the film becomes duplex in nature and as the thickness increases so the refractive index profile through the film changes until the lower refractive index limit is reached. At C, the potential is stepped back to its initial value and the film chemically dissolves. Note that the thickness remains constant but the refractive index diminishes until at D the whole of the film reaches a predetermined refractive index which represents the point D_L in Fig. 9.

This simple dissolution model is capable of reproducing qualitatively the open-circuit dissolution curve in Fig. 8. However, from Fig. 9 and 11 it is obvious that the model is insufficient in explaining the complete dissolution process which contains the loop phenomenon. A more complex model is therefore required.

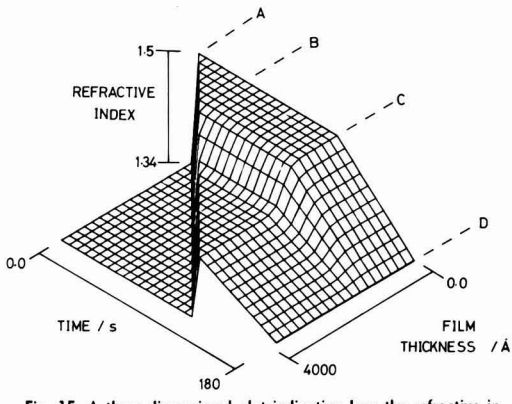

Fig. 15. A three-dimensional plot indicating how the refractive index of the film varies from *A* (the initial anodic pulse) to *D* (the dissolution limit D_L in Fig. 9), with both time and film thickness.

At the position D_L (see Fig. 9), the Δ-ψ value(s) corresponding to this portion clearly indicates that a film of finite thickness still remains on the substrate. At this position, subsequent dissolution causes the current to rise (see Fig. 2) and the Δ-ψ response to depart from the dissolution curve and traverse the loop before returning close to the starting position.

The net anodic recovery current must be due to the chemical breakdown of the film at random sites, thus exposing bare metal and allowing preferential metal dissolution. The metal dissolution process would result in appreciable roughening of the metal surface.

The large Δ-ψ excursion from the dissolution curve cannot be explained by a continuation of the dissolution process alone, nor by the growth of another transparent film or by a mixture of both. The optical constants of the transparent system cannot produce any Δ-ψ values for any film thickness in this region of the Δ-ψ plane, where $\Delta < \Delta_{\text{starting position}}$ and $\psi < \psi_{\text{starting position}}$, assuming reasonable values for the refractive index of the film ($1.4 \leq n \leq 4.0$). This region is therefore "out of bounds" for a transparent film on a smooth aluminum substrate. It very quickly becomes obvious that we must introduce a k (extinction coefficient) value into the optical constants of the system to force the Δ-ψ response into this region. The appreciable roughening caused by the aluminum dissolution reaction must now be taken into account.

The model used so far has assumed a perfectly smooth interface between the substrate and the film (9), such that the reflection from which can be described by the Fresnel complex reflection coefficients and the Drude equation. The problem of microscopically rough surfaces can be treated however by using simple models to characterize the roughness of the surface. The simplest optical model that approximates to a rough substrate is to represent the rough layer as an effective medium of intermediate optical properties, sandwiched between a perfect substrate and a perfect ambient (27). There are several effective-medium models that represent a heterogeneous dielectric mixture by a single parameter. The Maxwell-Garnett (MG) and the Bruggeman effective-medium approximation (EMA) are two of the most popular theories used.

Aspnes *et. al.* (27) have shown that the MG treatment is inconsistent in its definition of the volume fractions of the substrate and ambient media, and they recommend as being self-consistent the Bruggeman theory (EMA). The equation that relates the volume fraction of the inclusions (V_2) in the ambient medium (film) (1) can be written as

$$(1 - V_2)\frac{\epsilon_1 - \langle\epsilon\rangle}{\epsilon_1 + 2\langle\epsilon\rangle} = -V_2\frac{\epsilon_2 - \langle\epsilon\rangle}{\epsilon_2 + 2\langle\epsilon\rangle}$$

where $\langle\epsilon\rangle$ is the effective dielectric function of the rough layer and ϵ_1 and ϵ_2 are the dielectric functions of the film material and bulk substrate, respectively. The effective dielectric function is a complex quantity.

The rough layer was divided into a number of slices of equal thickness, and various structural models (27) describing the inclusion of the substrate into the film were employed. These models were triangular ridges (model 1), close-packed cones (model 2), hemispheres (model 3), inverse cones (model 4), and inverse hemispheres (model 5). Figure 16 shows a section through a rough layer structure using model 1 as the geometric shape with the layer divided into equal slices. From this geometric shape, it is easy to calculate the volume fraction of the base material in each slice of the rough layer. The EMA theory allows the calculation of the optical constants of each slice, knowing the volume fraction of the inclusions, and from these values a new curve is produced in the Δ-ψ plane.

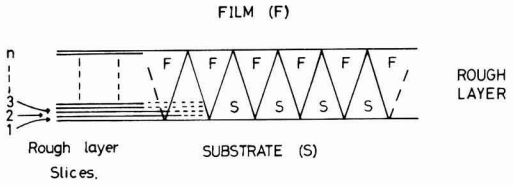

Fig. 16. A schematic diagram showing the rough layer section using rough model 1 (triangular ridges) to describe the inclusion of substrate into the film, and the division of the rough layer into slices of equal thickness.

In Figure 17, the simulated dissolution reaction is stopped at D_L and the rough layer for model 1 is grown for two different rough layer thicknesses. Both curves move into the out-of-bounds region, and increasing the thickness of the rough layer causes the curve to deviate further from the point D_L.

From the Δ-ψ curves in Fig. 9, the Δ-ψ response, having traversed the loop, returns very close to the starting position. Here the film will be very thin, and the optical constants of the system will approach the initial values of the substrate before the first anodic pulse. This can only be explained by the roughened substrate becoming smooth again. With the chemical dissolution of the film near completion, a preferential "leveling off" process of the rough layer, via the aluminum dissolution reaction, would seem to occur. This process may be akin to the leveling and brightening effects observed in electropolishing (28).

The leveling-off process is a simple process to model, as one slice at a time in the rough layer starting from the film boundary has its optical constants changed to those of the medium (1.34, 0) until the underlying substrate boundary is reached. Figure 18 shows how the extinction coefficient varies with time and the rough layer thickness. Initially k = 5.5 and is representative of the substrate, whereas at B, when the rough layer is completely grown, k tends to 0, representing the transparent film. From B, the removal shows k progressively made equal to 0 from the outermost slices at the film boundary until at C the removal of the rough layer is complete.

To allow the film dissolution to continue while the roughening process is occurring, the computer program was adapted so that a suitable constant could be included which represents the ratio of roughening to dissolution in the system. So for example, if the constant was equal to 3, the computer simulation would represent the growth of three slices in the rough layer for every one small reduction in the refractive index of the film (representing film

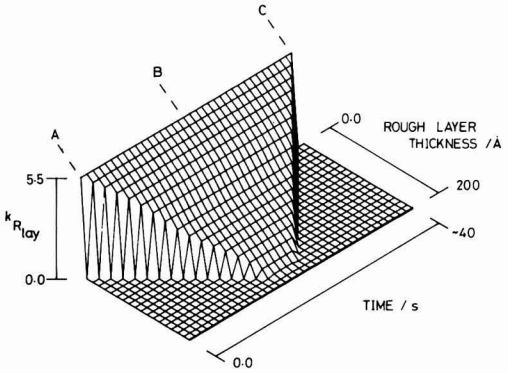

Fig. 18. A three-dimensional plot showing how the extinction coefficient varies with time and the rough layer thickness during the processes of growth (A to B) and dissolution (B to C) of the rough layer.

dissolution). When the rough layer was completely grown, its removal via the leveling-off process was simulated. The initial rate was still used, and three rough layer slices were removed for every one step in the reduction in the refractive index of the film. The best results for all five models used were found when the roughening occurs quickly compared to the film dissolution.

Figure 19 shows a theoretical response for model 1. The saw tooth appearance to the shape of the loop is present to show the two separate parts of the calculation, although this curve could be made smooth by modeling both processes in the same step of the calculation.

All five of the models have a theoretical Δ-ψ response which moved into the out-of-bounds region when the rough layer was grown and produced a loop when coupled to the film dissolution and the smoothing process. However, models 1 and 2 produced loops that showed the greater resemblance to the experimental curves in Fig. 9. Experimentally, film breakdown leading to the substrate roughening would occur at random sites across the substrate and the highly structured rough layer models used here would only be an approximation to the real system.

Finally, another result that can now be explained is the dependence of the loop size upon potential (see Fig. 11). In Fig. 1a and 1b the cyclic voltammograms show that as the potential is raised from −1.0 to −0.2V the current also increases. Therefore, when film breakdown occurs at a more anodic potential in this range, the aluminum disso-

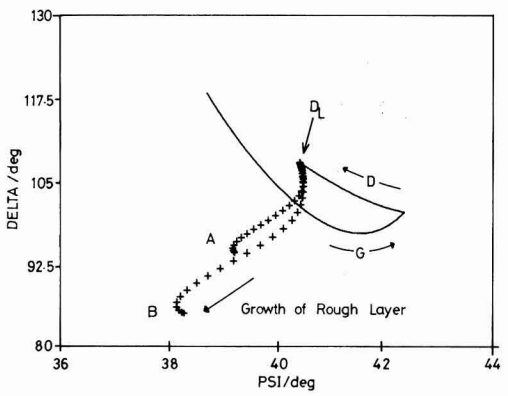

Fig. 17. A calculated growth (G) and dissolution curve (D); parameters are refractive index of film = 1.5, film thickness = 100 nm, and slice thickness = 10 nm. The calculation is stopped when the film refractive index reaches 1.4 (D_L). Simulated roughening using model 1 is then calculated with different rough layer thickness, 10 nm (A) and 20 nm (B).

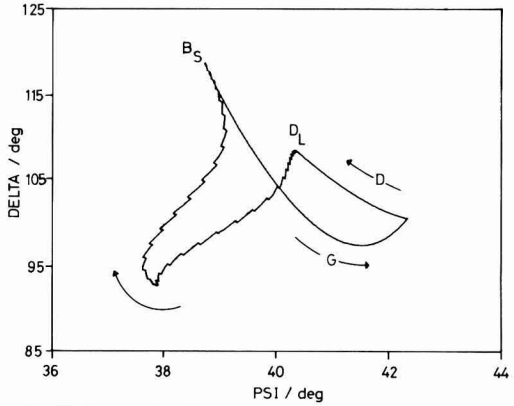

Fig. 19. The complete theoretical model depicting film growth and dissolution to D_L, and the growth and dissolution of the rough layer together with the continued dissolution of the film until point B_S is reached (bare surface). Parameters for the film as in Fig. 17, with rough layer parameters of model = 1, thickness = 20 nm, slice thickness = 0.33 nm.

lution reaction can occur at a faster rate and the effect of the roughening will be greater. Figure 17 shows that an increase in the rough layer thickness, possibly caused by more vigorous aluminum dissolution reaction at higher anodic potentials, would lead to an increase in the size of the loop.

Conclusions

1. The density of anodic oxide films on aluminum in alkaline conditions depends upon the potential of formation and the electrolyte concentration. The films increase in porosity toward low formation potentials and high electrolytic concentrations.

2. The films are not of uniform density throughout their thickness, being denser at the metal surface. A model consisting of a duplex film with a smooth transition in refractive index between the two layers produced a good fit with the experimental results.

3. The dissolution process is not the reverse of the formation process. The oxide layer begins to dissolve throughout its thickness upon cessation of anodization until a critical point is reached where the underlying metal is preferentially dissolved due to film breakdown.

4. Dissolution of the underlying metal and the incomplete oxide layer proceed in parallel, giving a Δ-ψ signal that departs from the dissolution curve and moves into a region in the Δ-ψ plane that is "forbidden" for any reasonable transparent film system.

5. The preferential dissolution of the underlying metal leads to appreciable roughening which has been modeled by constructing a layer between the substrate and the film where inclusions of metal into the film (and vice versa) are used to represent the rough layer.

6. Having now moved into this forbidden region, the Δ-ψ response traverses a loop and returns close to the starting position. The optical constants of the system are now very similar to those before the initial anodic pulse. This implies that the anodic oxide film has been removed and that the rough substrate has become smooth again via some form of leveling-off process.

Acknowledgments

We thank S.E.R.C. and Alcan International Limited for financial support.

Manuscript submitted Feb. 5, 1985; revised manuscript received June 24, 1985.

REFERENCES

1. A. R. Despic and P. D. Milanovic, *Recueil Des Travaux de l'institut des sciences techniques de l'academie serbe des sciences et arts*, **12**, 1 (1979).
2. J. Ruch, *Prog. Batt. Solar Cells*, **3**, 227 (1980).
3. T. Valand, O. Mollestad, and G. Nilsson, Paper 34 presented at the 12th International Power Sources Symposium, Brighton, England (1980).
4. A. R. Despic, D. M. Drazic, M. M. Purenovic, and N. Cikovic, *J. Appl. Electrochem.*, **6**, 527 (1976).
5. D. S. Keir, M. J. Pryor, and P. R. Sperry, *This Journal*, **114**, 777 (1967).
6. D. S. Keir, M. J. Pryor, and P. R. Sperry, *ibid.*, **116**, 319 (1969).
7. W. Bohnstedt, *J. Power Sources*, **5**, 245 (1980).
8. R. Greef and C. Norman, "Control and Exploitation of the Corrosion of Aluminium Alloys," Cranfield, England, April 1983. To be published by Alcan Aluminium, Banbury, England.
9. R. H. Muller, in "Advanced Electrochemistry and Electrochemical Engineering," Vol. 9, R. H. Muller, Editor, p. 167, Wiley, New York (1973).
10. W. E. J. Neal, *Appl. Surf. Sci.*, **2**, 445 (1979).
11. C. J. Dell'Oca and P. J. Fleming, *This Journal*, **123**, 1487 (1976).
12. C. J. Dell'Oca, *Thin Solid Films*, **26**, 371 (1975).
13. C. K. Dyer and R. S. Alwitt, *Electrochim. Acta*, **23**, 347 (1978).
14. R. M. Goldstein, R. J. Lederich, and F. W. Leonhard, *This Journal*, **117**, 503 (1970).
15. M. A. Barrett and A. B. Winterbottom, in "First International Congress on Metallic Corrosion," p. 657, Butterworths, London (1961).
16. A. C. Lowe, *Surf. Sci.*, **56**, 134 (1976).
17. T. Hurlen and A. T. Haug, *Electrochim. Acta.*, **29**, 1133 (1984).
18. J. F. Murphy and C. E. Michelson, in "Proceedings of the Symposium on Aluminium Anodizing," Nottingham, 1961, p. 83, Aluminium Development Association, London (1961).
19. J. F. Murphy, in "Proceedings of the Symposium of Aluminium Anodizing," Birmingham, 1967, p. 3, Aluminium Development Association, London (1967).
20. J. P. O'Sullivan and G. C. Wood, *Proc. R. Soc. London, Ser. A*, **317**, 511 (1970).
21. H. Takahashi, M. Nagayama, H. Akahori, and A. Kitahara, *J. Electron Microsc.*, **22**, 149 (1973).
22. F. L. McCrackin and J. P. Colson, National Bureau of Standards Technical Note 479, Washington, DC, April 1969.
23. A. C. Nyce and L. P. Skolnick, *J. Opt. Soc. Am.*, **65**, 792 (1975).
24. J. E. Norman, *Corros. Sci.*, **17**, 39 (1975).
25. C. J. Dell'Oca and L. Young, *Surf. Sci.*, **16**, 331 (1969).
26. F. L. McCrackin and J. P. Colson, National Bureau of Standards Miscellaneous Publication 256, p. 61, Washington, DC (1963).
27. D. E. Aspnes, J. B. Theeten, and F. Hottier, *Phys. Rev. B*, **20**, 3292 (1979).
28. A. K. Vijh, "Electrochemistry of Metals and Semiconductors," p. 200, Marcel Dekker Inc., New York (1973).

Electrochemical Formation of Graphite-Sulfuric Acid Intercalation Compounds on Carbon Fibers

Yasuhisa Maeda,* Yasuo Okemoto, and Michio Inagaki

Department of Materials Science, Toyohashi University of Technology, Tempaku-cho, Toyohashi 440, Japan

ABSTRACT

The cyclic voltammograms in 98% H_2SO_4 were measured on the mesophase-pitch-based carbon fibers heat-treated at various temperatures. They showed a marked dependence on the heat-treatment temperature of the carbon fibers. The electrochemical formation of graphite-sulfuric acid intercalation compounds was confirmed by x-ray diffraction. The change of graphite layer planes in the carbon fibers due to electrolysis was examined by Raman spectra.

Graphite forms intercalation compounds by the insertion of various ions, atoms, and molecules into its interplanar space. Recently, graphite intercalation compounds (GIC's) have attracted attention because of their unique properties. For a number of new GIC's synthesized by different methods, their structure, physicochemical properties, and applications have been studied actively (1-3).

Graphite is electrochemically oxidized in a concentrated sulfuric acid to form graphite-sulfuric acid intercalation compounds as follows

* Electrochemical Society Active Member.

$$C_x + 3H_2SO_4 \rightarrow C_x^+ HSO_4^- 2H_2SO_4 + H^+ + e^-$$

A bisulfate ion and sulfuric acid molecules are inserted between graphite layers. The positive charge of the oxidized graphite network is balanced by the negative charge of the intercalated ions. In this case, intercalation occurs in the anodic process and deintercalation in the cathodic process.

There are several papers (4-8) reporting electrochemical formation of graphite-sulfuric acid intercalation compounds on the graphite electrodes with high crystallinity, natural graphite, and highly oriented pyrolytic graphite. However, extensive studies on carbon electrodes are uncommon, although carbon materials have wide varieties in structure, in texture, and in shape. Carbon fibers have different textures and different degrees of perfection in structure according to their precursor and heat-treatment (9-11). Therefore, carbon fibers are interesting host materials of GIC because they may give much information on the GIC formation behavior in relation to crystallinity of host materials and also on the development of applications.

In this paper, the electrochemical formation behavior of graphite-sulfuric acid intercalation compounds was examined on the mesophase-pitch-based carbon fibers (11) heat-treated at various temperatures.

Experimental

The electrode materials were the mesophase-pitch-based carbon fibers (Kureha Chemical Industry Company) heat-treated at temperatures of 1800°, 2100°, 2400°, 2700°, and 3000°C for 30 min in argon atmosphere. Figure 1 shows the SEM micrograph of a cross section of the 3000°C treated carbon fibers. It is well known that the degree of graphitization of carbon materials is higher with the rise of heat-treatment temperature (HTT). The average interlayer spacing $\bar{d}(002)$ determined from 002 x-ray diffraction line by using inner standard of silicon is usually used as graphitization degree. The $\bar{d}(002)$ values of the heat-treated carbon fibers are summarized in Table I. The value decreases to the value for the natural graphite, 3.354Å, with the rise of HTT as has been found in various carbon materials.

A bundle of carbon fibers (weight of about 40 mg) attached to a copper lead wire with conducting silver epoxy was prepared as a working electrode. A platinum wire and a saturated calomel electrode were used as a counter and a reference electrode, respectively. An electrolyte was 98% sulfuric acid. Cyclic voltammograms were measured by using a potentiostat (Hokuto Denko, Model HA-501) and a function generator (same company, Model HB-104).

Fig. 1. SEM micrograph of cross section of the 3000°C treatea mesophase-pitch-based carbon fiber.

Table I. Interlayer spacing of the mesophase-pitch-based carbon fibers heat-treated at various temperatures

HTT (°C)	$d(002)$ (Å)
3000	3.361
2700	3.362
2400	3.383
2100	3.405
1800	3.426

The x-ray diffraction pattern of the carbon fibers electrolyzed at a certain potential was measured in order to confirm the formation of graphite-sulfuric acid intercalation compounds. Because of instability of intercalation compounds in air, the electrolyzed carbon fibers were taken out from the electrolyte in nitrogen atmosphere and mounted to the x-ray sample holder with a cover of 0.5 mm thick polyethylene film. The x-ray diffraction measurement was made with a diffractometer (Rigaku Denki, Model Geigerflex-2028).

Raman spectra were measured in order to examine the change of graphite layer planes in the carbon fibers due to electrolysis. In this case, the electrolyzed carbon fibers were taken out from the electrolyte, rinsed repeatedly with pure water, and dried in air. The Raman measurement was made with a Raman spectrometer (JRS, Model 400D) using 4880Å line (150 mW) of Ar-ion laser (NEC, Model GLG-3200). The angle between the incident beam and the fiber axis was 45°, and the scattered light was collected under 90° with the fiber axis. The slit widths at entrance, intermediate, and exit were 500, 600, and 500 μm, respectively.

Results and Discussion

Figure 2 shows the cyclic voltammograms (CV's) on the mesophase-pitch-based carbon fibers heat-treated at

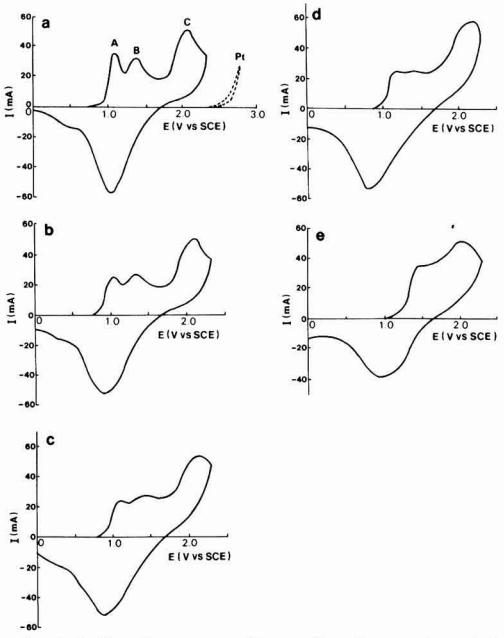

Fig. 2. Cyclic voltammograms (first scan) on the mesophase-pitch-based carbon fibers in 98% H_2SO_4. a, b, c, d, and e: The carbon fibers heat-treated at 3000°, 2700°, 2400°, 2100°, and 1800°C, respectively. Scan rate: 10 mV-s^{-1}. Pt: Platinum.

3000°, 2700°, 2400°, 2100°, and 1800°C. The CV's in a concentrated sulfuric acid showed a remarkable dependence on HTT. In Fig. 2a on the 3000°C treated carbon fibers, three anodic current peaks A, B, and C were observed at potentials of about 1.1, 1,4, and 2.1V, respectively. A cathodic peak appeared at about 1.0V. A platinum working electrode gave no anodic and cathodic peaks in the potential range of 0.0-2.3V in 98% H_2SO_4. The CV on the 2700°C treated carbon fibers (Fig. 2b) is similar to that on the 3000°C treated carbon fibers. From the CV's on the 2400°C and the 2100°C treated carbon fibers (Fig. 2c and 2d), it is indicated that both the anodic current peaks corresponding to A and B peaks in Fig. 2a become broad with the decrease in HTT. In contrast with peaks A and B, peak C seems to be almost independent of HTT. In the CV on the 1800°C treated carbon fibers (Fig. 2e), only two anodic current peaks were observed.

Figure 3 shows the x-ray diffraction patterns of the 3000°C treated carbon fibers for original (a) and 60 min electrolysis at the potential of 1.1, 1.4, and 2.1V (b, c, and d, respectively). On the electrolyzed carbon fibers, 001 diffraction lines from graphite layer planes disappear and new lines due to the formation of GIC are observed. The diffraction lines in Fig. 3b can be indexed by the stage 2 graphite-sulfuric acid intercalation compound with the identity period along the c-axis I_c of 11.33Å, as shown in the figure, and those in Fig. 3c by the stage 1 compound with I_c of 7.98Å. Therefore, anodic current peaks A at the potential of 1.1V and B at 1.4V observed in the CV (Fig. 2a) are attributed to the formation of the stage 2 and the stage 1 compounds, respectively. As shown in Fig. 3d, the product obtained by the anodic oxidation up to the potential of 2.1V has two diffraction lines at almost the same

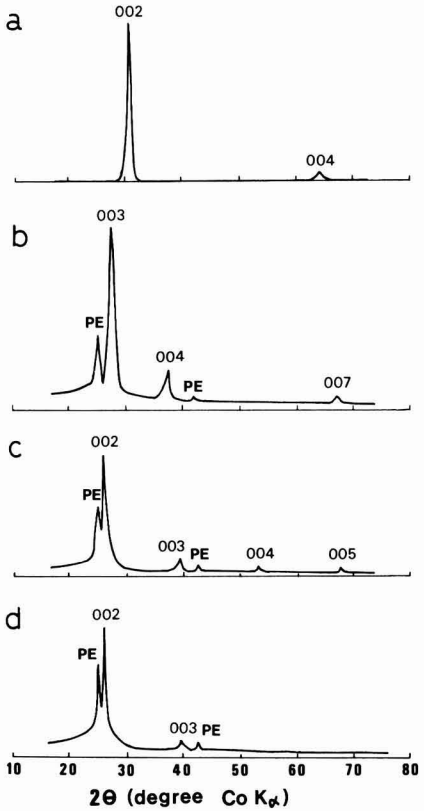

Fig. 3. X-ray diffraction patterns of the 3000°C treated carbon fibers. a: Original. b, c, and d: After electrolysis for 60 min at the potential of 1.1, 1.4, and 2.1V, respectively. PE: Polyethylene.

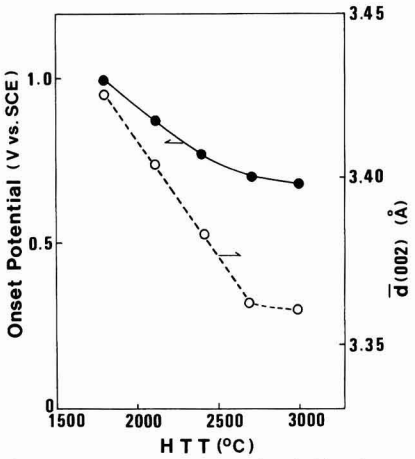

Fig. 4. Dependences of onset potential and of interlayer spacing $\bar{d}(002)$ on heat-treatment temperature.

diffraction angles as the stage 1, but two higher-order diffraction lines are missing. Since the stage 1 GIC which has the maximum content of intercalant is already formed at the potential of 1.4V, anodic current peak C is supposed to be due to the formation of graphite oxide (12, 13). Besenhard *et al.* (8) mentioned the formation of graphite oxide following that of the stage 1 compound on the highly oriented pyrolytic graphite electrode in 96% H_2SO_4. In the CV's on the carbon fibers, the anodic current peak C is quite different from the peaks A and B with regard to HTT dependence. The broadening of the peaks A and B with the decrease in HTT suggests that a distinction in staging of GIC formed gets obscure on the carbon fibers with lower degree of graphitization.

Figure 4 shows the dependences of the onset potential (OP) and of the interlayer spacing $\bar{d}(002)$ on HTT of the carbon fibers. The OP is denoted as the threshold potential which shows the beginning of the anodic current flow in the first scan. The OP value of the carbon fibers treated at the higher HTT is less positive. A striking similarity between the HTT dependences of OP value and $\bar{d}(002)$ suggests that the OP value is closely related to the crystallinity of the host carbon fibers, the higher degree of graphitization facilitating the formation of GIC.

Figure 5 shows the CV on the 3000°C treated carbon fibers in the range of 0.0-1.4V. In this potential range, only the formation of GIC occurs, as shown by two anodic current peaks at 1.1 and 1.4V, but not the forma-

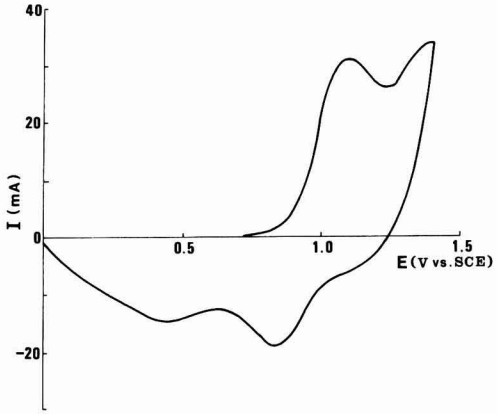

Fig. 5. Cyclic voltammogram (first scan) on the 3000°C treated carbon fibers in 98% H_2SO_4. Scan rate: 10 mV-s^{-1}.

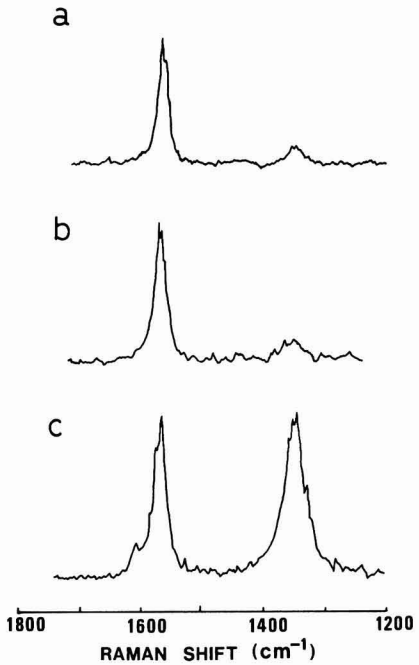

Fig. 6. Raman spectra of the 3000°C treated carbon fibers. a: Original. b and c: After ten times cyclic electrolysis in the range of 0.0-1.4V and 0.0-2.3V, respectively.

tion of graphite oxide. This CV characteristically shows two cathodic peaks at the potential of about 0.4 and 0.8V, which correspond to the reduction of the stage 2 and the stage 1 graphite-sulfuric acid intercalation compounds, respectively. These waves are not clearly detected with scans up to the potential of 2.3V, as shown in Fig. 2a. The CV's (0.0-1.4V range) on the 2700°, 2400°, and 2100°C treated carbon fibers also showed two cathodic current peaks. The potential of these peaks shifted to less positive values with the decrease in HTT. This dependency seems to imply a relation between the deintercalation process and the crystallinity of the carbon fibers.

Figure 6 shows Raman spectra of the 3000°C treated carbon fibers before and after electrolysis. It has been known that carbon materials have two Raman bands at 1580 and 1360 cm^{-1} (14-16), the former being due to the in-plane motion of carbon atoms in the hexagonal graphite layers, and the latter being related to the presence of structural defects in the graphite layer planes. As shown in Fig. 6a, the original carbon fibers without electrolysis give a strong sharp band at 1580 cm^{-1} but only a weak one at 1360 cm^{-1}. The ten times cyclic electrolysis in the range of 0.0-1.4V did not affect the spectrum (Fig. 6b). This suggests that graphite layer planes of the original carbon fibers retain their perfection after the electrochemical formation of the stage 1 graphite-sulfuric acid intercalation compound. In the spectrum of the carbon fibers after the ten times cyclic electrolysis in the range of 0.0-2.3V (Fig. 6c), however, a marked increase in the relative intensity of 1360 cm^{-1} band is observed. Thus the formation of graphite oxide seems to give rise to various defects in graphite layer planes, which may be related to puckering of layer planes due to the carbon-oxygen bond in graphite oxide (12, 13). The introduction of the defects in layer planes by the formation of graphite oxide may cause the disappearance of the higher-order diffraction lines of the stage 1 intercalation compound, as shown in Fig. 3d.

Summary

The results obtained can be summarized as follows. The CV's in 98% H_2SO_4 were measured on the mesophase-pitch-based carbon fibers heat-treated at the various temperatures. Three anodic current peaks at the potential of about 1.1, 1.4, and 2.1V in the CV's were attributed to the formation of the stage 2 and the stage 1 graphite-sulfuric acid intercalation compounds and of the graphite oxide from the measurements of x-ray diffraction patterns and Raman spectra. The CV depended strongly on HTT of the carbon fibers; the onset potential shifting to the positive value, and the anodic current peaks due to the formation of GIC becoming broad with the decrease in HTT. Thus the electrochemical behavior showed a marked dependence of the GIC formation on the crystallinity of the host carbon fibers. For the Raman spectra of the 3000°C treated carbon fibers, the graphite layer planes of the original fibers were found to retain their perfection even after ten times cyclic electrolysis up to 1.4V, that is, ten times repetition of formation and decomposition of the stage 1 compound, but various defects were introduced in the layer planes by the formation of graphite oxide.

Acknowledgment

The authors wish to thank Dr. M. Nakamizo of Government Industrial Research Institute, Kyushu, for Raman spectra measurement. A part of this work was supported by Grant-in-Aid for Scientific Research (A) of the Ministry of Education, Science and Culture, Japan.

Manuscript submitted Feb. 12, 1985; revised manuscript received June 3, 1985.

Toyohashi University of Technology assisted in meeting the publication costs of this article.

REFERENCES

1. L. B. Ebert, *Ann. Rev. Mater. Sci.*, **6,** 181 (1976).
2. M. S. Dresselhause and G. Dresselhause, *Adv. Phys.*, **30,** 139 (1981).
3. M. Inagaki, *Hyomen*, **20,** 130 (1982).
4. M. J. Bottomley, G. S. Parry, A. R. Ubbelohde, and D. A. Young, *J. Chem. Soc.*, 5674 (1963).
5. S. Aronson, S. Lemont, and J. Weiner, *Inorg. Chem.*, **10,** 1296 (1971).
6. R. Fujii, *Denki Kagaku*, **41,** 52 (1973).
7. F. Beck, H. Junge, and H. Krohn, *Electrochim. Acta*, **26,** 799 (1981).
8. J. O. Besenhard, E. Wudy, H. Möhwald, J. J. Nickl, W. Biberacher, and W. Foag, *Synth. Met.*, **7,** 185 (1983).
9. S. C. Bennett and D. J. Johnson, *Carbon*, **17,** 25 (1979).
10. D. J. Johnson, I. Tomizuka, and O. Watanabe, *ibid.*, **13,** 321 (1975).
11. M. Inagaki, M. Endo, A. Oberlin, S. Kimura, M. Nakamizo, Y. Hishiyama, and H. Fujimaki, *Tanso*, **99,** 130 (1979).
12. W. Rüdorff, *Adv. Inorg. Chem. Radiochem.*, **1,** 223 (1959).
13. R. C. Croft, *Quat. Rev.*, **14,** 1 (1960).
14. F. Tuinstra and J. L. Koenig, *J. Chem. Phys.*, **53,** 1126 (1970).
15. M. Nakamizo, R. Kammereck, and P. L. Walker, Jr., *Carbon*, **12,** 259 (1974).
16. M. Nakamizo, H. Honda, M. Inagaki, and Y. Hishiyama, *ibid.*, **15,** 295 (1977).

Open-Circuit Reduction of Oxygen Coverage on Au by Allyl Alcohol in Aqueous Electrolytes

R. Celdrán and J. González-Velasco

Departamento de Electroquímica, Facultad de Ciencias, Universidad Autónoma de Madrid, 28049 Madrid, Spain

ABSTRACT

An open-circuit study of the reduction of oxygen coverage on Au by allyl alcohol was made. The experimental results have been interpreted using Christov's scheme (15). The gold oxide coverage appears to be removed via a chemical, an electrochemical, or a mixed mechanism, depending on different potential values which characterize the diverse zones appearing in the *E-t* curves. Gold oxide reduction seems to take place through two steps in acidic electrolytes and through three in neutral ones. The first step appears to be the reduction of Au_2O_3 to Au_2O, the second a reduction of Au_2O to Au, while the third has been interpreted as a reduction of an aged form of Au_2O.

In previous papers, (1, 2), we have reported on the oxidation mechanism of allyl alcohol on gold in aqueous solutions. The oxidation of the organic substance would interfere with that of the electrode itself. The oxide coverage can then interact with the organic molecules giving rise to a fairly rapid oxygen coverage removal, depending on oxidation level, structure, and stability of the oxide layers. The aim of the present study is to clarify the mechanism of the interaction between the organic reducing agent and the oxide coverage. The study could also provide indirect evidence for the composition and structure of superficial oxygen coverage on gold.

The open-circuit potential decay technique was applied. In this way, it is possible to follow the changes in potential under null net current conditions. The *E-t* curves recorded after anodic polarization of a gold electrode in the bulk electrolyte and in the presence of allyl alcohol give information on the interaction mechanism between electrolyte and oxide layer.

Various authors have used this method to study the development and evolution of oxide coverage on metal electrodes (3-10). The influence of stirring (6, 7) and of diverse reducing agents (6-12) was also investigated. Few papers have appeared on the reduction of oxygen coverage on gold by organic reducing agents (13, 14).

Experimental

Procedures.—Cell, electrodes, apparatus, and activation method have been described elsewhere (1, 2). The reactants were NaOH, K_2SO_4, H_2SO_4 (Merck, P.A.). Allyl alcohol (Fluka, P.A.), was also used. Experiments were carried out under N_2 atmosphere and in unstirred solutions. Temperature (except in experiments for determination of the activation energy) was kept constant at 25.0° ± 0.1°C. Two series of experiments were carried out under the following conditions.

In the first series, a potential E_a = 1.15 V_{SCE} was applied to the working electrode (WE) in the bulk solution for a given time t_a. The circuit was then opened and the *E-t* curve recorded. The electrode was then activated (1) in the bulk solution and the *I/E* curve was recorded and compared with a standard *I/E* curve in order to check its catalytic activity. Thereafter, the electrode was polarized at E_a and allyl alcohol was added in N_2 atmosphere, immediately prior to opening the circuit. The resulting *E-t* relationship was recorded. Measurements were made in unbuffered solutions (H_2SO_4, NaOH, and $10^{-1}M$ and 5 × $10^{-1}M$ K_2SO_4), and in buffer solutions (Britton-Robinson) for the complete *p*H range. The allyl alcohol concentration was varied from $c = 10^{-2}$ to 5 × $10^{-2}M$. The time during which the polarization was applied, t_a, was changed from 5 to 20 min.

In the second series, the WE was activated in the bulk solution (0.1*M* H_2SO_4: μ = 1 with K_2SO_4) then introduced into a second, previously deoxygenated cell containing a solution of allyl alcohol. The solution was stirred with N_2 for 2 min and then left for 30s. Finally, a potential E_a was applied to the WE for a time, t_a, before opening the circuit and recording the *E-t* curve. For this series, the allyl alcohol concentration, *c*, was varied from 10^{-3} to $10^{-1}M$, and t_a was varied from 4 to 45s. The catalytic activity of the WE was checked after each experiment as described (1). All potential values are expressed *vs.* SCE.

Both series of experiments gave rise to similar *E-t* responses. In acidic medium, the different values of the transition times which can be deduced from Fig. 2 and 5 are due to the different t_a and E_a applied.

The experimental determination of τ according to Ref. (15) was made, either as the time corresponding to the intersection of the tangents to AB and CD (Fig. 1) or as the time at which characteristic potential is reached. This po-

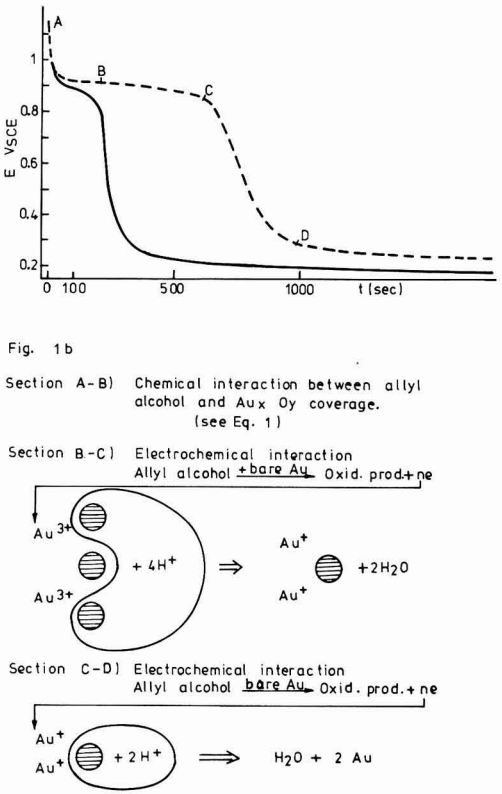

Fig. 1. Open-circuit *E-t* curve of 0.1M H_2SO_4 + 10^{-2} allyl alcohol. (E_a = 1.16 V_{SCE}. t_a = 5 seconds. T = 25°C) showing the different gold oxide reduction zones (9), and a description of the processes supposed to be implied in every section (b).

tential, which corresponds to zero oxygen coverage is given by $E = 0.62$ V_{SCE} for Au in acidic medium (1, 18, 26). In this case, the potential value corresponding to the tangent intersection point is 0.86 ± 0.01 V_{SCE} and the values of τ obtained from both methods do not differ by more than 5%.

Results.—Figures 2, 3, and 4 show *E-t* curves obtained in different media: acid, neutral, and basic (18). In all media, a marked decrease in τ is brought about by the presence of allyl alcohol. The decrease is larger in unbuffered than buffered solutions for all pH values. In alkaline medium, at $t = \tau$ the potential drops sharply to values close to that for H_2 evolution and then increases. Similar behavior is observed for allyl alcohol on other metals (1).

The theoretical treatment (15-17) was applied to the *E-t* curves obtained in the second series of experiments. Table I summarizes the results for the different sections of the *E-t* curves (see Fig. 1) in the second series of experiments. In addition to the results summarized in Table I, the following were determined. The dependence of τ on the different experimental parameters is as follows. τ decreases with increasing allyl alcohol concentration [plots of $(\log \tau/\log c)_{E_a,t_a}$ are linear and show a slope value of $b' = -0.48 \pm 0.02$ ($E_a = 1.22$ V_{SCE}, $t_a = 45$s, and an intercept of +0.90]. τ shows an exponential increase with increasing E_a and a linear increase with increasing intermediate values of t_a (Fig. 6). τ decreases with increasing temperature values. From the slope of the $(\log \tau/T^{-1})_{t_a,E_a}$ plot, the value of the apparent activation energy (E_A) of the overall process can be obtained: $E_A = 73.6$ kJ-mol^{-1} (Fig. 6).

In general, it can be said that the results are similar to those obtained by Christov (15) for the interaction between organic substances and the platinum oxides.

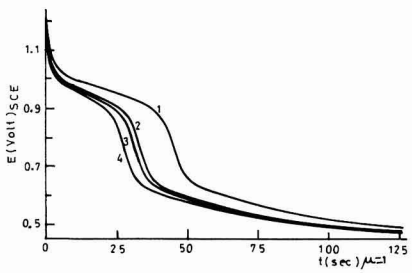

Fig. 2. Open-circuit *E-t* curves in acidic medium at different adsorption times (t_a). Solution = 0.1M H_2SO_4 (μ = 1) + 10^{-2}M allyl alcohol. 1: t_a = 45s. 2: t_a = 30s. 3: t_a = 25s. 4: t_a = 20s; E_a = 1.20 V_{SCE}.

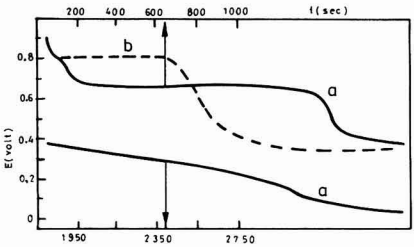

Fig. 3. Open-circuit *E-t* curve in (a) 0.1M K_2SO_4 + 10^{-2}M allyl alcohol (t_a = 5 min, E_a = 0.91 V_{SCE}), (b) 0.1M K_2SO_4 and the values for t_a and E_a given in (a).

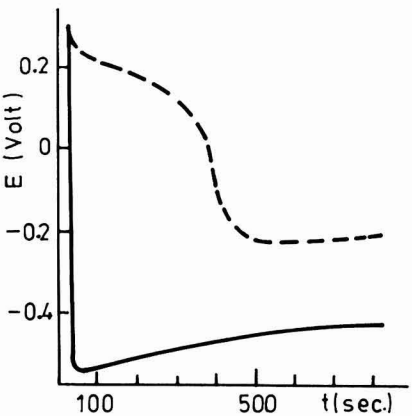

Fig. 4. Open-circuit *E-t* curves in (1) 0.1M OHNa, (2) 0.1M NaOH + 10^{-2}M allyl alcohol. t_a = 20 min. E_a = 0.3 V_{SCE}.

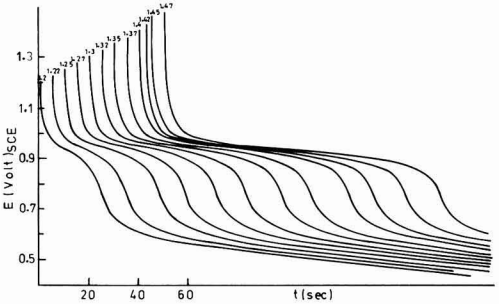

Fig. 5. Open-circuit *E-t* curves for different E_a values. Solution: 0.1M H_2SO_4 + 10^{-2}M allyl alcohol. EdS = 10s. T = 25°C.

Theoretical Treatment of Data

Christov *et al.* (15-17) have proposed a general mechanism to interpret the complete open-circuit reduction of oxygen coverage on Pt by organic reducing agents. It was assumed that two parallel processes take place at the electrodes, and this assumption can be essentially kept for the case of the gold oxides, considering the following equations for the interaction between allyl alcohol and the gold oxides

$$Au_xO_y + \text{allyl alcohol} \xrightarrow{k_1} Au + \text{oxidation products} \quad [1]$$

$$\text{allyl alcohol} \xrightarrow{k_2} \text{oxidation products} + 2ye^- \quad [2a]$$

$$x\text{Au} + y\text{H}_2\text{O} \underset{k_3}{\overset{k_4}{\rightleftarrows}} Au_xO_y + 2y\text{H}^+ + 2ye^- \quad [2b]$$

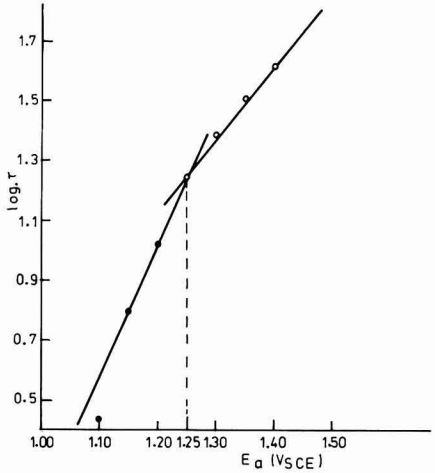

Fig. 6. Plot of log τ vs. E_a. T = 39.8°C; t_a = 10s. 0.1M H_2SO_4 + 10^{-2}M allyl alcohol. (E_a) critical = 1.25 V_{SCE}.

Table I. Results obtained for the second series of experiments

Section A-B	c_{allyl} (mol-liter^{-1})	a $(\delta E/\delta \log t)_c$	b $(\delta \log t/\delta \log c)_E$
	10^{-3}-10^{-2}	-0.120 ± 0.002	-0.30 ± 0.02
	5×10^{-2}-10^{-1}	-0.138 ± 0.002	-0.50 ± 0.02
Section B-C	c_{allyl} (mol-liter^{-1})	$E_i/\log c$	$[\log(-dE/dt)/\log \tau]_{E=E_i}$ $[\log(dE/dt)/\log c]_{E=E_i}$
	10^{-3}-10^{-1}	0.95 ± 0.02	-1.10 ± 0.05 (slope) -0.72 ± 0.05 (intercept) 0.42 ± 0.02
Section C-D	c_{allyl} (mol-liter^{-1})	$m[\partial \log(\tau - t)/\partial \log c]$	$(\partial E/\partial \log(\tau - t))_c$ α
	5×10^{-2}-10^{-1}	$-1/2$	0.244 ± 0.005 0.48 ± 0.01

The partial reactions [1], [2a], and [2b] correspond to chemical oxidation of the reducing agent by the oxygen coverage, electro-oxidation of the reducing agent on the free electrode surface, and electrochemical oxidation and reduction of the electrode, respectively. The e^- produced in reaction [2a] take part in reaction [2b]. k_1, k_2, k_3, and k_4 represent the rate constants of the respective processes.

Although both the structure and the composition of the oxide layers are different for Au and Pt, the kinetic assumptions upon which Cristov (15) based his theory apply to both metals.

The dependence of E on t in every region of Fig. 1 can be theoretically deduced on the assumption that the chemical interaction of the reducing agent and the oxygen coverage is rate determining and the adsorption can be described by a Temkin isotherm. On this basis, a general analytical E-t dependence is derived for the overall process. In order to achieve the direct determination of the kinetic parameters, some particular cases are examined.

High coverage (section A-B of Fig. 1).—The theoretical treatment (16) gives rise to the following relations for a chemical mechanism

$$(\partial E/\partial \log t)_c = \frac{-2 \times 2.303}{f} \simeq 0.12\text{V} \quad \left.\begin{array}{l} \\ \\ \end{array}\right\} \text{for } k_2 c << k_4 \exp(\alpha f E) \quad [3]$$

$$(\partial t/\partial \log c)_E = -1 \quad [4]$$

where $f = \mathbf{F}/RT$, t = time after opening the circuit, E the electrode potential, c the bulk concentration of reducing agent (allyl alcohol), and α the transfer coefficient

$$(\partial E/\partial \log t)_c = -2 \times 2.303/f(1 - \alpha) \simeq 0.24\text{V} \quad \left.\begin{array}{l} \\ \\ \end{array}\right\} \text{when } k_2 c << k_4 \exp(\alpha f E) \quad [5]$$

$$(\partial t/\partial \log c)_E = -3/2 \quad [6]$$

For high coverage and an electrochemical mechanism, the following values should be obtained

$$(\partial E/\partial \log t)_c = -2.303/\alpha f \simeq 0.12\text{V} \quad [7]$$

$$(\partial t/\partial \log c)_E = 0 \quad [8]$$

Low coverage (section C-D of Fig. 1).—The resulting equations (16) take the form

$$(\partial E/\partial \log(\tau - t))_c = 2 \times 2.3/(1 - \alpha)f \simeq 0.24\text{V when } k_2 c >> k_4 \exp(\mathbf{F}E) \quad [9]$$

$$(\partial E/\partial \log(\tau - t))_c = 2 \times 2.3/f \simeq 0.12\text{V when } k_2 c << k_4 \exp(\mathbf{F}E) \quad [10]$$

where τ = time required for the complete reduction of oxygen coverage. The concentration interval over which [9] or [10] is valid, is determined by the slope of the plot $(\log(\tau - t)/\log c)_E$. This slope gives values of $-1/2$ and -1 for Eq. [9] and Eq. [10], respectively.

Medium coverage (section B-C of Fig. 1).—According to Ref. (17), the mathematical analysis predicts the appearance of one or more inflections in the E-t curves, depending on the value of α. This case can be characterized by the concentration dependency of the potential in the region of the inflection

$$E_i = (2.3/f) \log(k_2 k_3/k_1 k_4) \text{ when } (1 - \alpha)k_2 c << k_4 \exp(\alpha/E_i) \quad [11]$$

$$E_i = (2.3/(1 - \alpha)f) \log(k_3/k_1) - (2.3/(1 - \alpha)f) \log c \text{ when } (1 - \alpha)k_2 c >> k_4 \exp(\alpha \mathbf{F} E_i) \quad [12]$$

and by the slope of the plateau in the E-t curve

$$\log(-dE/dt)_{E=E_i} = \log[4g(k_1 k_2)^{1/2}/qf] + \log c \text{ when } (1 - \alpha)k_2 c << k_4 \exp(\alpha f E_i) \quad [13]$$

$$\log(-dE/dt)_{E=E_i} = \log[4g(k_1 k_2)^{1/2}/(1 - \alpha)qf] + \log c \text{ if } (1 - \alpha)k_2 c >> k_4 \exp(\alpha f E_i) \quad [14]$$

where g is inhomogeneity factor from Temkin's isotherm and q the charge required for the formation of a monolayer of oxygen coverage on gold. An additional relation between $(-dE/dt)_{E=E_i}$ and $\log \tau$ can be obtained. The resulting slope and intercept are predicted to be independent of the kinetic parameters. The effect of various factors (t_a, E_a, c, . . .) on τ is also considered (17).

Discussion

The results obtained in the first series of experiments confirm the existence of alcohol-gold oxide interaction observed in other studies (1, 2). Under experimental conditions that differ slightly from those described before, the E-t curves show that the reduction occurs in more than one step (more than one plateau from which more than one transition time can be measured) or show the coexistence of more than one type of adsorbed species. In alkaline medium, results suggest that only one type of oxide [possibly $Au(OH)_3$] is present at sufficiently high anodic potentials.

As said above, the second series of experiments leads to results similar to the first. This can be explained on the basis of the results (1, 2) obtained for the direct oxidation of allyl alcohol on gold. In that case, an inhibition of the oxidation of the organic substance at the potentials at

which gold oxides were formed was observed (E_p, peak potential for the allyl alcohol oxidation appears at 1.03 V_{SCE} and E_p for gold oxide at 1.15 V_{SCE}). It could be argued that a part of allyl alcohol can be oxidized and reduced by electron tunneling through the Au oxide film, analogous to electron tunneling in the case of oxygen evolution at Pt oxide covered Pt electrodes. This contribution could take place at more anodic potentials (E_a) than those applied in this work. At these potentials the electron tunneling contribution should be too small to be considered. A chemical interaction between allyl alcohol and the gold oxides can take place during anodic polarization, but the initial conditions at the moment of open circuit seem to be similar to those obtained for the first series.

The results for this second series show a slow change in the slope in the section C-D of the E-t curve (Fig. 1). This suggests that the removal of the oxide layer occurs in steps. This has also been observed by other authors (4), and attributed to changes occurring in the nature of the adsorbed species. At $E = 0.86$ V_{SCE} the same oxygen coverage is achieved for any value of c, while at $E = 0.62$V, the whole oxide layer is removed.

In order to evaluate the E-t curves, the diagnostic criteria derived from Christov's treatment (15, 17) were used.

The first section (A-B) of the E-t curve is characterized by high potential values and high oxygen coverages. High anodic potentials would enhance the electro-oxidation of the alcohol. High oxygen coverages would hinder its adsorption on the bare metal surface, and hence electro-oxidation, while it would facilitate the chemical interaction between the oxide layer and the alcohol in solution.

The values of the slope $a = (\partial E/\partial \log t)_c$ (Table I) tend to increase with increasing c and this result, similar to that for Pt (20), suggests a chemical interaction between the gold oxide and the alcohol which requires that $k_2 c << k_4 \exp(\alpha f E)$ be satisfied (Eq. [3]). This condition does appear to hold, since at high anodic potentials the electro-oxidation of the electrode surface predominates over that of the alcohol. Moreover, Eq. [11] predicts that for low c values, $E_i \neq f(c)$, while for higher c, E_i would decrease with increasing c, according to Eq. [12]. The E_i values obtained from the experimental E-t curves, show that for $c < 10^{-2}M$, $E_i \neq f(c)$, while a slight decrease in E_i is observed for $c > 5 \times 10^{-2}M$. Moreover, the value of the slope a is the same as that obtained for a purely electrochemical mechanism (Eq. [7]). To choose between chemical or electrochemical interaction, it is necessary to resort to the value of b (Table I). A purely electrochemical mechanism would give $b = 0$ (Eq. [8]), while a chemical one would give $b = -1$ (Eq. [4]).

Table I gives two values of b for section A-B of the curve, depending on the c concentration range. For $c \simeq 10^{-3}$-$10^{-2}M$ $b = -0.30$, but -0.50 when c varies between 5×10^{-2} and $10^{-1}M$. Both values are intermediate between 0 and -1, which suggests that the reduction proceeds through a mixed mechanism with approximately 30% of the reduction being chemical. The higher relative contribution of chemical reduction with increasing c could be expected. The above interpretation is in agreement with previously observed potentiodynamic curves (1, 2). These show that, if c is increased, the electroreduction oxide peak decreases until it disappears at sufficiently high c. At the same time, the allyl alcohol oxidation peak in the cathodic sweep increases with c. This is due not only to its direct oxidation but also to the faster appearance of bare gold surface enhanced by the direct chemical reaction between alcohol (in higher concentrations) and the most oxidizing oxide form. It can be seen in Ref. (21) that a species possibly implied in the process, Au_2O_3, can chemically oxidize the alcohols.

When the section B-C is reached, the oxygen coverage on the electrode has decreased. Thus, chemical oxidation of the alcohol is expected to be slower than in section A-B. Also, the allyl alcohol might encounter a larger bare metal surface, which would increase its electro-oxidation rate. The theory predicts the appearance of an inflection point when both chemical and electrochemical oxidation rates become of the same order.

The experimental potential, E_i, corresponding to the inflection point is independent of c (Table I), for low c values. Equation [11]-[12] predict that, for low values of c, $E_i \neq f(c)$ (Eq. [11] is followed), while for higher values of c, E_i decreases with increasing c according to Eq. [12]. A slight decrease in E_i is observed for $c > 5 \times 10^{-2}M$.

The electro-oxidation of the alcohol should make the electrode potential more negative. The potential value, however, shows only a very slight decrease in this section of the decay curve.

Thus, another mechanism for the elimination of negative charge from the electrode must accompany e^- transfer from the alcohol. The only negative species on the electrode would be the $O^=$ ions, which can react with the H^+ ions in solution. This elimination would yield zero net current and explains why the potential value remains almost unchanged.

The proposed electrochemical mechanism should be responsible for the elimination of the oxide coverage, as suggested by the similarity between the experimental values in Table I—−1.10 and −0.72 (slope and intercept, respectively, of the log $[(-dE/dt/\log \tau]_{E=E_i}$ plot)—and the theoretically predicted—−1.00 (slope) and −0.81 (intercept) (20).

Furthermore, if this mechanism is correct, influence of H^+ concentration on the reaction rate and, consequently on the E-t curves, should be observed. It is to be expected that the elimination rate of $O^=$ would decrease with decreasing H^+ concentration, giving rise to an increase in τ. This is the result obtained (Fig. 3) for E-t curves recorded at near-neutral pH values.

There is a disagreement between the theoretically (20) predicted slope of the plot of $(-dE/dt)$ *vs.* log c (at $E = E_i$) and the experimental ones (1.00 and 0.42, respectively).

It should be pointed out that for oxygen coverage reduction of PtO by organic substances it has been assumed (22) that both chemical and electrochemical reactions follow the same path, *i.e.*, via dehydrogenation of α-H atoms. For gold oxide-alcohol interaction (1, 2), the reaction may follow different paths, giving rise to different reaction rates.

In the section C-D, the theoretical treatment supposes that the electro-oxidation of the organic substance is much faster than its chemical oxidation. The low oxygen coverage makes the chemical oxidation rate too low to be considered. The decreasing potential values in this section are due to electrochemical oxidation of the alcohol.

The experimental values for this section are summarized in Table I. The experimental value for $(\partial \log (\tau - t)/\partial \log c)_E$ coincides with the theoretically predicted (-0.5) when $C_{allyl} >> 5 \times 10^{-2}M$, and shows that Eq. [9] should be valid. The plot of Eq. [9] gives in fact a value for $[\partial E/\partial \log (\tau - t)]_c$ of 0.224 ± 0.005V, in a very good agreement with the theoretical value 0.220V. The derived value of α should be 0.48 ± 0.01.

The observed discrepancy between experimental and theoretical values for low values of c is similar to that obtained for the reduction of PtO by organic substances (20). This fact could be explained if the condition $k_2 c >> k_4 \exp(\alpha f E)$ in Eq. [9] is no longer satisfied due to the decrease of c.

The variation of τ with the different experimental parameters (c, t_a, E_a, T, . . .) is similar to that for Pt and agrees with the proposed interaction mechanism. The decrease in τ with increasing c implies an alcohol-gold oxide interaction whose rate increases with c, according to potentiodynamic studies (1, 2). This decrease of c cannot be attributed to a smaller oxygen coverage due to the presence of the alcohol during anodic polarization (in the second series of experiments), because the same result is obtained in the first series of experiments, in which the WE was polarized before the addition of the alcohol. The linear relation between log τ and E, as well as between τ and t_a, can be deduced by supposing a mixed chemical and electrochemical reduction mechanism of the oxygen cov-

erage. At sufficiently positive potentials but not too high coverage, the rate of oxygen coverage formation will be much greater than the reduction rate. Assuming that the oxygen coverage increase can be described by means of a Temkin isotherm, the linear terms in θ can be neglected. In this way the following equation (17) can be derived

$$[1 - 2g(k_1k_2)^{1/2}c\,\tau/\pi q]^{-1} = 1 + (k_1/k_2)^{1/2}(\pi g k_4 t a/2q)\exp(\alpha f E a) \qquad [15]$$

where g represents the interaction coefficient in the Temkin isotherm and q is the charge required for the formation of a monolayer of oxygen coverage.

In order to obtain an idea about the value of the $2g(k_1k_2)^{1/2}$ factor, plots of Eq. [13] and [14] were made. From the slope value it was deduced that $4g(k_1k_2)^{1/2}/qf = 0.01778$, and taking (27, 28) $q = 850\ \mu$C-cm^{-2}, gives $g(k_1k_2)^{1/2} = 1.47 \times 10^{-4}$. This value is very similar to that deduced from the intercept of the (log τ/log $c)_E$ plot (17). In this case, log $(\pi q/2(k_1k_2)^{1/2}g)$ = intercept = 0.9, and $g(k_1k_2)^{1/2} = 1.68 \times 10^{-4}$. [Incidentally, this value provides an additional test for the validity of Christov's treatment for the case of gold oxides, since it is very similar to that obtained for that case (15).]

A rearrangement of Eq. [15] can be easily made by supposing that $\pi q >> 2g(k_1k_2)^{1/2}c\tau$, as is obtained from the value for $2g(k_1k_2)^{1/2}$ formerly deduced. Finally, the following expression can be obtained for the relation between τ and t_a and E_a

$$\tau = (\pi^2 k_4/2ck_2)\exp(\alpha f E_a)t_a \qquad [16]$$

Plots of log τ *vs.* E_a at different temperatures were made (Fig. 6). At 25.2°C and t_a = 10s the intercept[1] value leads to a k_4/k_2 ratio of 7×10^{-6}, *i.e.*, the oxidation reaction of allyl alcohol is faster than the gold oxide formation. At 39.8°C, the intercept gives a value of 3.5×10^{-6} for this ratio. It seems that with an increase in the temperature k_2 increases more rapidly than k_4. The exponential increase of τ with E_a could be in agreement with the idea of the differential characteristics of the adsorbed species, supposedly formed at different potential values.

Figure 7 gives the τ *vs.* t_a plots at T = 25.0°C and E_a = 1.22 V_{SCE}. The result indicates that, the higher the allyl alcohol concentration, the faster would be the oxide layer elimination. The rate of change of τ with t_a is also dependent on c and can be attributed to a change in the value of α in Ref. (16) induced by the different participation of chemical and electrochemical reactions in the mixed mechanism proposed. These changes of α can be followed by substituting the k_4/k_2 values obtained from the plots of Fig. 6.

Substituting the k_4/k_2 ratio obtained in Eq. [11], (E_i = 0.95 V_{SCE}), one obtains a value of $k_3/k_1 = 5.86 \times 10^{12}$, the same order of magnitude as found in the PtO study (15). This would mean that the chemical interaction [1] between allyl alcohol and gold oxide would be much slower than the electrochemical one (Eq. [2a] and [2b]).

The decrease of τ with stirring for $c < 10^{-2}M$ (Fig. 10) shows the influence of convective diffusion on the process. Faster transport of the alcohol to the surface would accelerate the chemical and electrochemical reduction rates. For $c > 10^{-2}M$, the slightly higher values of τ can be explained supposing the formation of adsorbed intermediates, which would be partly eliminated by stirring, thus making slower the rate of production of electrons (by oxidation of the allyl alcohol molecules initially present). This fact is reflected in potentiodynamic curves taken in almost neutral solutions (Fig. 10). Under stirring, a second reduction peak is recorded which can be attributed to the reduction of a gold oxide produced in a first reduction step. When stirring is stopped, only a reduction peak (Fig. 11b) is obtained. The allyl alcohol molecules keep in contact with the electrode surface and supply electrons for the complete reduction of the oxide layer in a single step.

[1]We take the intercept as the value of log τ at the critical potential point in which the oxygen coverage takes intermediate values ($E \simeq 1.2$ V_{SCE}).

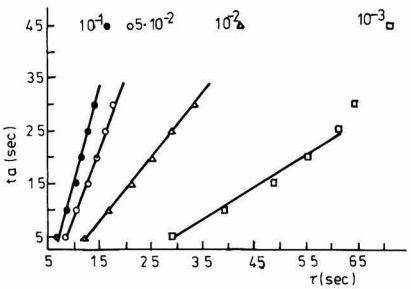

Fig. 7. Plots of t_a *vs.* τ in 0.1M H_2SO_4 at different allyl alcohol concentrations. E_a = 1.20V. T = 25°C.

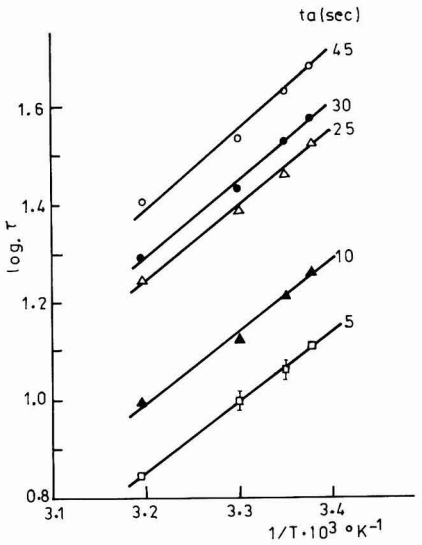

Fig. 8. Plots of log τ *vs.* $1/T$ at different t_a values. 0.1M H_2SO_4 + 10^{-2}M allyl alcohol. E_a = 1.20 V_{SCE}.

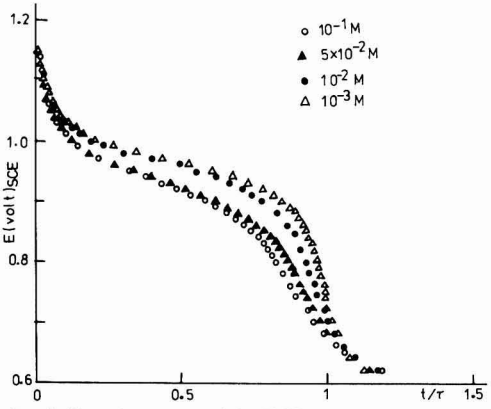

Fig. 9. Plots of E *vs.* t/τ in 0.1M H_2SO_4 at different allyl alcohol concentrations. t_a = 45s. E_a = 1.20 V_{SCE}.

Section A-B is hardly influenced by stirring. This suggests that the chemical process is not transport dependent. In this range, the rate-determining step should be the adsorption of the organic substance as predicted by the assumed mechanism.

Finally, an interpretation of the Au-electrode open-circuit potential decay in absence of alcohol can also be given.

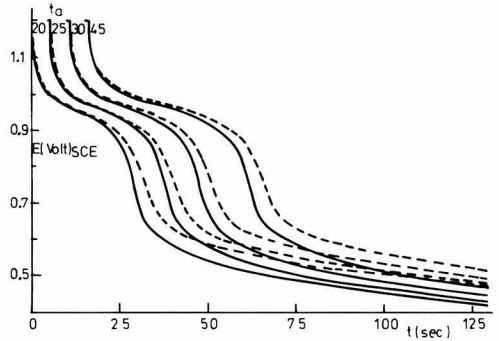

Fig. 10. Influence of stirring on the *E-t* curves taken after different t_a values. E_a = 1.20 V_{SCE}. 0.1M H_2SO_4 + 10^{-2}M allyl alcohol. Dashed line: without stirring. Solid line: with stirring.

In basic medium the reaction mechanism would be initiated by the oxidation of OH^- species

$$2yOH^- \rightarrow 2yOH\cdot + 2ye^- \qquad [16]$$

and

$$Au_xO_y + 2ye^- \rightarrow xAu + yO^= \qquad yO^= + 2yH^+ \rightarrow yH_2O \qquad [17]$$

The $OH\cdot$ radicals can then react with each other and produce H_2O_2. In acidic medium, the H_2O molecules could play the role of the reduced species which can be oxidized and induce the reduction of the oxides

$$2yHOH \rightarrow 2yHO\cdot + 2yH^+ + 2ye^- \qquad [18]$$

$$Au_xO_y + 2ye^- \rightarrow xAu + yO^= \qquad yO^= + 2yH^+ \rightarrow yH_2O \qquad [19]$$

giving rise to $OH\cdot$ radicals which can produce H_2O_2.

The fact that $\tau_{\text{basic medium}} < \tau_{\text{acid medium}}$ seems to predict a reaction [18] slower than reaction [16]. It can be said that the transition times in acid as well as in basic solutions are much longer without, than with, allyl alcohol present in the solution.

Conclusions

On the basis of the experimental data, a mixed mechanism (chemical-electrochemical) can be postulated for the reduction of gold oxide layers (23-26). The following equations give a summarized view of the process described in Fig. 1

allyl alcohol → oxidation products + $6e^-$

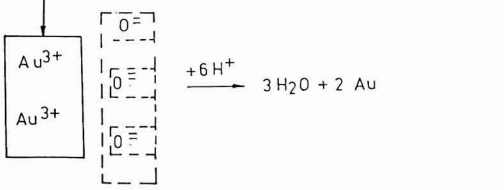

On the surface, after reduction of Au^{+3} ions, the uncompensated charges of $O^=$ make them to repel each other. If the proposed mechanism should take place, the rate of the third step would be dependent on the $(H^+)_{aq}$ according to

$$O^=_{(\text{lattice})} + 2H^+_{aq} \rightarrow H_2O_{(\text{sol})}$$

and

$$v = -\frac{(d\theta_{O^=})}{dt} = K(\theta_{O^=})^n \cdot (H^+)_{aq}{}^h \cdot f(E)$$

where $K = (1/\tau)$, and $f(E)$ is a function of the potential

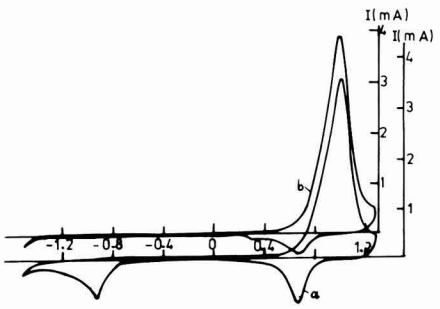

Fig. 11. Voltammograms of 0.1M K_2SO_4 + 10^{-2}M allyl alcohol solutions. a: Without stirring. b: With stirring.

value, decreasing from the first to the third step. Thus, at $(H^+)_{aq} = 10^{-7}M$, the third step could become rate determining. Both *E-t* curves and *i-E* potentiodynamic diagrams seem to agree with such supposition: The *E-t* curves obtained in neutral electrolytes show three different plateaus (Fig. 3). The first one corresponds to the peak potential value obtained for the oxide reduction in voltammograms taken in acidic electrolytes. This process is then attributed to the reduction of Au_2O_3. The second one appears at a potential value similar to the one of a second reduction peak obtained maintaining the electrode at oxide formation potentials values for a given time. This peak is attributed to the reduction of Au_2O, formed by reduction of Au_2O_3. The third one is attributed to the reduction of a more stable form of Au_2O, directly formed during the gold oxidation, and after having undergone the so-called aging process (23-25). This process seems to stabilize such oxide species and that can explain why its reduction occurs only at more negative potentials. In summary, the following equations could describe the processes supposed to be taking place at the potentials of the different plateaus

Step 1:

$$Au_2O_3 + 4H^+ + 4e^- \rightarrow Au_2O + 2H_2O \quad \text{Plateau 1}$$

Step 2:

$$Au_2O + 2H^+ + 2e^- \rightarrow 2Au + H_2O \quad \text{Plateau 2}$$

Step 3:

$$(Au_2O)_{\text{aged}} + 2H^+ + 2e^- \rightarrow 2Au + H_2O \quad \text{Plateau 3}$$

Thus, the Au_2O coverage would be formed in the following way

$$(\theta_{Au_2O})_{\text{total}} = (\theta_{Au_2O})_{\text{initial}} + (\theta_{Au_2O})_{(\text{from step 1})}$$

supposing

$$(\theta_{Au_2O})_{\text{initial}} << \theta_{Au_2O_3}, \text{ then } (\theta_{Au_2O})_{\text{step1}} \simeq \theta_{Au_2O_3}$$

The higher values of τ for the second and the third plateaus reflect not only the higher stability of both Au_2O species, but also the lower electro-oxidation rate of allyl alcohol with decreasingly positive potentials. The decrease of $\theta_{O^=}$ gives rise to a lower electrostatic repulsion between neighboring O , influencing in this way also, the rate of the third step. The influence of $(H^+)_{aq}$ is confirmed since in very acidic solutions, the second plateau almost disappears.

Likewise, the potentiodynamic *i-E* curves in the same neutral solutions (Fig. 8) show two cathodic reduction peaks. Only the second one appears under stirring. Stirring carries away from the electrode the intermediates produced in the allyl alcohol oxidation before that process occurs completely. Thus, a partial reduction of Au^{+3} would take place, giving rise to Au_2O, which, in turn, reduces, giving a second peak. Without stirring the alcohol, oxidation continues and produces the e^- for the direct reduction from Au^{+3} to Au (one single peak).

In summary, it has been shown that an interaction between gold oxides and organic substances takes place and that the interaction follows a similar pattern to the process occurring between the same type of substances and Pt-oxides. The differences observed must be a consequence of the more complex oxidation processes occurring on gold electrodes.

Acknowledgment

This study was supported by the Comision Asesora de Investigación Cientifica y Técnica (Madrid).

Manuscript submitted Jan. 7, 1985; revised manuscript received June 17, 1985.

REFERENCES

1. R. Celdrán and J. González-Velasco, *Electrochim. Acta*, **26,** 525 (1981); *ibid.*, **26,** 763 (1981).
2. R. Celdrán and J. González-Velasco, *Ann. Quim*, **77,** 88 (1981); *ibid.*, **77,** 328 (1981).
3. D. W. Shoesmith, T. E. Rummery, and D. Owen, *Electrochim. Acta*, **22,** 1403 (1977).
4. H. Dietz and H. Göhr, *Electrochim. Acta*, **8,** 343 (1963).
5. B. MacDougall and M. Cohen, *ibid.*, **23,** 145 (1978).
6. J. E. Oxley, G. K. Johnson, and B. T. Buzalski, *ibid.*, **9,** 89 (1964).
7. M. D. Drazic and V. Drazic, *ibid.*, **11,** 1235 (1966).
8. M. W. Breiter, *This Journal*, **109,** 425 (1962).
9. E. I. Sokolova, *Izv. Otd. Him. Nauki Ban*, **8,** 524 (1975).
10. G. Vertés, G. Horanyi, and F. Nagy, *Acta Chim. Acad. Sci. Hung.*, **67,** 145 (1971); *ibid.*, **68,** 217 (1971).
11. L. D. Burke and A. Moynihan, *Electrochim. Acta*, **16,** 167 (1971); *ibid.*, **15,** 1437 (1970).
12. G. Bianchi and P. Longhi, *Chim. Ind.*, **46,** 1286 (1964).
13. M. Betowska-Brescsinska, *Electrochim. Acta*, **24,** 409 (1979).
14. W. Hauffe and J. Heitbaum, *Ber. Bunsenges. Phys. Chem.*, **82,** 487 (1978).
15. M. V. Christov and S. N. Raicheva, *J. Electroanal. Chem.*, **73,** 43 (1976).
16. M. V. Christov and S. N. Raicheva, *ibid.*, **73,** 55 (1976).
17. M. V. Christov, *ibid.*, **73,** 63 (1976).
18. R. Celdrán, Tesis Doctoral, Universidad Autónoma de Madrid, Madrid, Spain (1979).
19. G. A. Bogdanovskii, *Elektrokhimiya*, **4,** 1196 (1968); *ibid.*, **5,** 472 (1969); *ibid.*, **6,** 909 (1970).
20. M. V. Christov and S. N. Raicheva, *J. Electroanal. Chem.*, **73,** 71 (1976).
21. M. P. Pourbaix, "Atlas of Electrochemical Equilibria in Aqueous Solutions," Pergamon Press, New York (1966).
22. M. V. Christov, *J. Electroanal. Chem.*, **76,** 147 (1977).
23. C. M. Ferro, A. J. Calandra, and A. J. Arvia, *ibid.*, **65,** 963 (1975).
24. J. W. Schultze and M. M. Lohrengel, *Ber. Bunsenges. Phys. Chem.*, **80,** 552 (1976).
25. M. M. Lohrengel and J. W. Schultze, *Electrochim. Acta*, **21,** 957 (1976).
26. A. C. Chialvo, W. E. Triaca, and A. J. Arvia, *J. Electroanal. Chem.*, **171,** 303 (1984).
27. R. C. Newman and G. T. Burstein, *ibid.*, **129,** 343 (1981).
28. J. Ganon, G. Nguyen van Huong, and J. Clavilier, *Surf. Sci.*, **79,** 245 (1979).

Electron-Transfer Rates on Chemically Modified Conducting Polypyrrole Film Electrodes

Miguel Saloma and Martha Aguilar

Facultad de Química, Universidad Nacional Autónoma de México, Ciudad Universitaria, Coyoacán 04510, México, D.F.

Manuel Salmón*

Instituto de Química, Universidad Nacional Autónoma de México, Circuito Exterior, Ciudad Universitaria, Coyoacán 04510, México, D.F.

ABSTRACT

A cyclic voltammetric study of the ferrocene redox reaction was used to evaluate the substituent effect in various *para*-substituted poly-N-phenylpyrrole films used as electrodes. To determine the film electrode substituent effect on the ferrocene couple reaction, the heterogeneous standard rate constant values were determined. The observed changes in the film electron-transport rate are the result of the structure monomer variation. Electronic interaction between the polypyrrole nucleus and the *para* substituents on the N-phenyl ring affects the electron-transfer rate of polymer electrodes.

A new class of organic electrodes has become available through the electropolymerization of aromatic compounds such as pyrrole (1). Electrochemically grown thin films of highly conductive polypyrrole, doped with BF_4^-, are insoluble and have long-term stability.

Conductive films of polypyrrole can be modified by introducing substituents into the cationic pyrrole polymer or varying the accompanying anion (2). The fact that the polypyrrole films are prepared electrochemically facilitates these modifications since the variations are made in the selection of the electrolyte or the monomer. We have now made a study of polypyrrole films modified by placing phenyl substituents in the N position of the pyrrole ring; the phenyl substituent assumes a particularly important role because it provides a means of introducing a wide selection of functional groups into the polymer structure as substituents on the phenyl ring.

In polymeric coatings on electrodes, the rate of charge and electron transport across the layer defines the usefulness of these films in devices. This paper deals with a cyclic voltammetric study of the quasi-reversible redox behavior of ferrocene on some poly-N-*para*-substituted phenylpyrrole films used as electrodes. We found that the electron transfer rate constant (k_s) of the ferrocene couple reaction depends on the film electrodes.

* Electrochemical Society Active Member.

Experimental

The polymeric films of poly-N-*para*-substituted phenylpyrrole were prepared by electropolymerization of the corresponding N-*para*-substituted phenylpyrrole monomer with p-H, p-CH_3, p-OCH_3, p-Cl, p-Br, and p-NO_2.

All N-*para*-substituted phenylpyrroles were synthesized from 2,5-dimethoxytetrahydrofuran and the appropriate amine (3). The pure pyrrole monomers were identified by H^1-NMR, IR, and MS and compared with reported data (4).

The film preparations were performed in a one-compartment cell using Pt as the working electrode, a similar counterelectrode, and a saturated calomel reference electrode (SCE). Each electrolytic solution contained $10^{-3}M$ of the corresponding pyrrole monomer, plus $0.1M$ of tetra-

ethylammonium tetrafluoroborate in distilled acetonitrile. The films were grown on 0.5 cm^2 Pt electrode surface, passing 20 mC-cm^{-2} of charge to control the film thickness, estimated as *ca.* 50 nm considering the area of the electrode, density of the film, and the apparent n value for the reaction (5).

The electro-oxidation of the N-*para*-substituted phenylpyrroles conducted at a constant potential of 1.50V for p-H and p-NO_2, 1.12V for p-CH_3 and p-OCH_3, and 1.19V for p-Cl and p-Br, proceeds with the formation of insoluble polymer film on the electrode, as was previously reported (6). Films of these polymers, when mounted in acetonitrile/Et_4NBF_4 solution, can be electrochemically driven between the oxidized and the neutral forms. The films are stable to this reaction and can be cycled repeatedly without evidence of decomposition.

The cyclic voltammetric study of ferrocene ($1 \times 10^{-3}M$ in acetonitrile/Et_4NBF_4 solution) was accomplished using thin films of N-phenyl-pyrroles on a Pt working electrode. All the measurements were prepared with IR compensation.

Electrochemical measurements were performed with a Princeton Applied Research Model 173 Potentiostat, a Model 175 Programmer, and a Hewlett-Packard 7004B X-Y recorder.

Results and Discussion

As can be seen in Table I, the formal potentials, $E°$, for the redox reaction of the dissolved ferrocene using [Pt] poly-N-*para*-substituted-phenylpyrrole-BF_4 electrodes are not significantly different from those measured with a Pt bare electrode. Peak heights vary linearly with the square root of the sweep rate, $\nu^{1/2}$, from 10 to 100 mV/s, as expected for a diffusion-limited process, and the ratio of the peak heights i_{pa}/i_{pc} is always close to unity. There is no evidence of absorption or adsorption on the polymer surface, indicated by the fact that $i/AC\nu^{1/2}$ values (A is the electrode area, C, mol/cm^3) remains constant in the potential sweep range tested. The cyclic voltammograms produced using thicker films (70 nm) provide the same $i/AC\nu^{1/2}$ values, indicating that the signal amplitudes do not depend on film thickness. Moreover, the $E°$ for ferrocene do not superimpose on the $E°$ of the polymer films (6). Representative cyclic voltammograms are displayed in Fig. 1.

The potential difference between the peaks E_{pa} and E_{pc} (ΔE) is greater than 59 mV and increases with the sweep rate. Nicholson's treatment (7) for determining k_s values was used to evaluate the effect of the electrode on the redox reaction. Values for the Ψ parameter were obtained from the ΔE values. For a quasi-reversible reaction, Nicholson's empirical equation is

$$\Psi = k_s (RT/n\mathbf{F}\pi D\nu)^{1/2}$$

where n = 1 electron/molecule for this reaction, D is the diffusion coefficient [$D = 2.76 \times 10^{-5}$ cm^2/s, ferrocene in CH_3CN, measured chronocoulometrically (8)], $\mathbf{F}$ the Faraday, R gas constant, and T absolute temperature.

Table I. Electrochemical data activity from cyclic voltammetry of [Pt] poly-N-*para*-substituted phenylpyrrole film electrodes. Redox electrolyte: $10^{-3}M$ ferrocene in acetonitrile/Et_4NBF_4

Poly-N-*para*-substituted phenylpyrrole electrode	Peak separation ΔE (mV)[a]	$E°$ (mV)[b]	$10^3 k_s$ (cm-s^{-1})
—NO_2	90	400	14.70
—Br	92	417	13.14
—Cl	95	412	12.35
—H	95	412	12.35
—CH_3	97	410	11.16
—OCH_3	100	408	10.47
Bare platinum electrode	60	440	—

[a] Scan rate 100 mV-s^{-1}.
[b] *vs.* SCE.

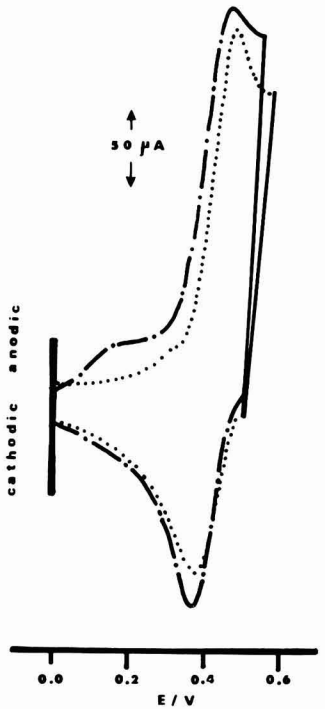

Fig. 1. Cyclic voltammograms of $1 \times 10^{-3}M$ ferrocene using 20 mC of [Pt]-coated electrodes with poly-N-*para*-methylpyrrole (dot-dash line) and poly-N-*para*-chlorophenylpyrrole (dotted line) at 100 mV/s in CH_3CN containing 0.1M Et_4NBF_4.

All these polypyrroles, PPy, polymers, are produced by an electrochemical oxidative coupling process which yields an acceptor-doped conducting complex directly, such as $PPy^+BF_4^-$ (9, 11). With acceptor doping, Hall coefficient measurements (12) clearly showed that the conduction is p-type, *i.e.*, positively charged carriers. It demonstrates that the majority of the carriers move through the organic material and not through the dopant array (13). Then the modification of the monomer should affect the charge transfer rate of the polymer, as can be observed in Table I.

In an earlier communication (14), it was proposed, on a qualitative basis, that a poor interaction between the pyrrole and the phenyl ring was produced by an orthogonal conformation through both rings. Further studies showed that in the N-orthophenylpyrrole series electroactive substituents exhibit electronic and steric effects (15), whereas in the N-*para*-phenylpyrroles only electromeric effects were observed (6). Therefore, the electron-attractive or electron-repulsive induction of *para* groups involve interannular conjugation as well as inductive effects.

In the first study of this series (14), the electroactive behavior of the nitro phenyl group in the poly-N-*para*-nitrophenylpyrrole was analyzed by cyclic voltammetry. Although the nitrophenyl group is independently electroactive, the electron-transfer process between the platinum and the film for the reduction reaction involves an electron exchange between the unsaturated pyrrole matrix and the pendent nitrophenyl groups rather than a hopping process between the groups.

Consequently, the electronic interaction between the polypyrrole nucleus and *para*-substituents on the N-phenyl ring affects the electron-transfer rate of polymer electrodes (16). In effect, when the log of k_s are plotted against their respective Hammett-Brown substituent constants, a linear correlation is obtained (Fig. 2); the resonance and inductive interaction effects are undoubtedly

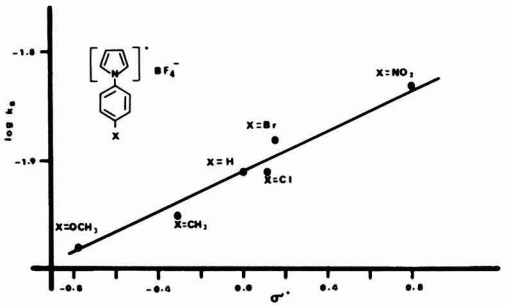

Fig. 2. Electron-transfer rate constant of the ferrocene couple reaction on the poly-N-*para*-substituted phenylpyrrole *vs.* their respective Hammett-Brown substituent constants.

the principal effects involved in the $\rho_\pi\sigma'$ relationship. The positive sign for the substituent constant ρ_π reveals that as the substituents take on more electrophilic character the electron-transfer rate becomes faster.

We can conclude that changes in the electron-transfer rate of the series of polypyrroles is dependent on electronic interaction between the electroactive pyrrole ring of the polymer and the *para*-substituent through the phenyl ring. This electronic interaction has also been observed in the oxidation of the corresponding monomer, due to the fact that, as the substituent takes on more electrophilic character, the oxidation of the N-substituted phenylpyrrole proceeds with more difficulty (6). The mobility of the carriers will be determined by a variety of effects, including chain perfection, crystallinity, etc. (17); however, a delocalized π-system with relatively broad energy bands is certainly an advantage for effective electron transport.

Acknowledgment

The authors would like to thank M. Rosales Hoz for critically reviewing the manuscript.

Manuscript submitted Feb. 25, 1985; revised manuscript received June 10, 1985.

Universidad Nacional Autónoma de México assisted in meeting the publication costs of this article.

REFERENCES

1. A. F. Díaz, K. K. Kanazawa, and G. P. Gardini, *J. Chem. Soc., Chem. Commun.*, 635 (1979); A. F. Díaz and J. I. Castillo, *ibid.*, 397 (1980).
2. M. Salmón, A. F. Díaz, A. J. Logan, M. Krounbi, and J. Bargon, *Mol. Cryst. Liq. Cryst.*, **83**, 265 (1982).
3. H. Gross, *Chem. Ber.*, **95**, 2270 (1962).
4. N. Clauson-Kass and Z. Tyle, *Acta Chim. Scand.*, **6**, 67 (1952); M. Elming and N. Clauson-Kass, *ibid.*, **6**, 867 (1952).
5. A. F. Díaz, J. I. Castillo, J. A. Logan, and W. Y. Lee, *J. Electroanal. Chem.*, **129**, 115 (1981).
6. M. Salmón, Ma. E. Carbajal, J. C. Juárez, A. Díaz, and M. C. Rock, *This Journal*, **131**, 1802 (1984).
7. R. S. Nicholson, *Anal. Chem.*, **37**, 1351 (1965).
8. A. F. Díaz, F. A. Orosco Rosales, J. Paredón Rosales, and K. K. Kanazawa, *J. Electroanal. Chem.*, **103**, 233 (1979).
9. K. K. Kanazawa, A. F. Díaz, G. P. Gardini, W. O. Gill, P. M. Grant, J. F. Kwak, and G. B. Street, *Synth. Met.*, **1**, 329 (1980).
10. W. R. Salaneck, R. Erlandsson, J. Prejza, I. Lundström, and O. Inganas, *ibid.*, **5**, 125 (1983).
11. J. Prejza, I. Lundström, and T. Skotheim, *This Journal*, **129**, 1685 (1982).
12. L. W. Shacklette, R. R. Chance, D. M. Ivory, G. G. Miller, and R. H. Baughman, *Synth. Met.*, **1**, 307 (1979).
13. R. R. Chance, D. S. Boudreaux. H. Eckhardt, R. L. Elsenbaumer, J. E. Frommer, J. L. Bredas, and R. Silbey in "Quantum Chemistry of Polymers—Solid State Aspects," J. Ladik *et al.*, Editors, D. Reidel (1984).
14. M. Salmón, A. Díaz, and J. Goitia, in "Chemically Modified Surfaces in Catalysis and Electrocatalysis," J. S. Miller, Editor, p. 65, ACS Symposium Series 192, American Chemical Society, Washington, DC (1982).
15. M. Salmón, Ma. E. Carbajal, M. Aguilar. M. Saloma, and J. C. Juárez, *J. Chem. Soc., Chem. Commun.*, 1532 (1983).
16. M. Salmón, M. Aguilar, and M. Saloma, *ibid.*, 570 (1983).
17. W. Dietz, P. Cukor, M. F. Rubnes, and H. Jonson, *J. Electron Mater.*, **10**, 683 (1981).

Oxygen Reduction in Tetrafluoroethane-1,2-Disulfonic Acid

K. A. Striebel, P. C. Andricacos,*,[1] E. J. Cairns,* P. N. Ross,* and F. R. McLarnon*

Lawrence Berkeley Laboratory, University of California, Berkeley, California 94720

ABSTRACT

The kinetics of oxygen reduction on platinum in tetrafluoroethane-1,2-disulfonic acid (TFEDSA) and trifluoromethane sulfonic acid (TFMSA) have been studied with the rotating disk electrode technique at pH 1. The resulting Tafel plots coincide within the error of the experiment, indicating similar kinetics in the two electrolytes. The reaction order with respect to oxygen concentration was studied by varying the partial pressure of oxygen above the electrolyte. The rotation-independent currents at 0.90V *vs.* DHE were used to calculate a reaction order equal to one. A first-order analysis of the rotation-dependent currents was then used to extract kinetic currents at lower potentials. These kinetic currents also exhibited first-order dependence on oxygen concentration.

Trifluoromethane sulfonic acid (TFMSA) has been considered for low temperature (< 110°C) fuel cell applications due to the favorable oxygen reduction rate observed in this electrolyte compared with phosphoric acid (1). The use of the less-volatile, higher homolog of TFMSA, tetrafluoroethane-1,2-disulfonic acid (TFEDSA), was suggested by Baker *et al.* (2) to overcome the problems of high acid vapor pressure and low contact angle with PTFE observed with concentrated TFMSA. Preliminary investigations with TFEDSA (3) show insignificant acid vapor pressure and acceptable water vapor pressure at 60-70 weight percent acid, as well as high (nonwetting) contact angles with PTFE. In this work, the kinetics of oxygen reduction in TFEDSA and TFMSA on smooth Pt have been studied with the rotating disk electrode (RDE) technique. Kinetic measurements were made in each of the acids at pH = 1. The dependence of the reduction current on oxygen concentration was determined by varying the partial pressure of oxygen in contact with the electrolyte. This reaction order has been shown to be unity in perchloric, sulfuric, and phosphoric acid electrolytes (4-6). However, in "superacid" electrolytes (TFEDSA and TFMSA) the analysis of RDE data according to a first-order model has not been conclusive. Deviations from first-order analysis have previously been attributed to

*Electrochemical Society Active Member.

[1]Present address: IBM Thomas J. Watson Research Center, Yorktown Heights, New York 10598.

impurity effects (7, 8) and a nonunity reaction order with respect to oxygen (9). We varied the bulk concentration of oxygen in the electrolyte in order to have an independent method for determining reaction order.

Experimental

Experiments were performed in a Pyrex cell with a surrounding water jacket. Circulation of thermostatically controlled water was used to maintain the cell temperature of 25° ± 0.5°C. The rotating disk platinum working electrode had an area of 0.458 cm^2 and was polished with a succession of alumina papers, followed by 6 μm and then 1 μm diamond paste. Rotation was achieved with a Pine Instruments analytical rotator. A dynamic hydrogen electrode (DHE) (10) was held in a separate compartment which was connected to the main cell through a Luggin capillary. The DHE held a constant potential of 3 mV negative of an RHE at the same *p*H. A 1 cm^2 Pt-foil counterelectrode was used directly in the cell, placed as shown in Fig. 1. Premixed cylinders of oxygen and nitrogen (4.31-58.66% ± 0.01% oxygen), pure oxygen, and pure nitrogen were further purified by passing through three molecular-sieve beds (9). All gases were humidified by bubbling through doubly distilled water at room temperature before entering the cell.

The potential of the working electrode was controlled with a PAR Model 173 potentiostat and a PAR Model 175 universal programmer. Current-potential data could be recorded simultaneously with a Nicolet digital oscilloscope and an HP7046B X-Y recorder.

All glassware and electrodes (except the DHE) were cleaned by soaking in a mixture of concentrated sulfuric and 70% nitric acids for two days. This was followed by rinsing and soaking in freshly distilled water at least four times.

TFMSA (from 3M Corporation) was purified by distillation and hydrogen peroxide treatment as reported earlier (8). Tetrafluoroethane-disulfonate was received as the potassium salt from KOR, and it was converted to the acid via ion exchange with prepurified resin (11). Complete conversion to the acid was checked by titration. Water was removed by vacuum distillation, leaving the acid dihydrate. The hygroscopic nature of this solid prevented exact knowledge of the water content. Solutions were prepared by dilution with ultrapure water[2] to *p*H 1. TFMSA solutions were prepared in a similar manner. Both solutions were pre-electrolyzed in the cell for at least 72h at a current of 1 mA.

Results and Discussion

Two single-sweep cyclic voltammograms recorded in TFEDSA at *p*H = 1 are shown in Fig. 2. Curve A was recorded for the stationary disk following the pretreatment potential profile shown in the inset of Fig. 2. For an indication of electrolyte purity, curve B was recorded following the same pretreatment profile with the addition of a 1 min hold at 0.4V *vs.* DHE while rotating the working electrode at 1600 rpm before recording the voltammogram on the stationary electrode.

[2]Harleco Company, Gibbstown, New Jersey.

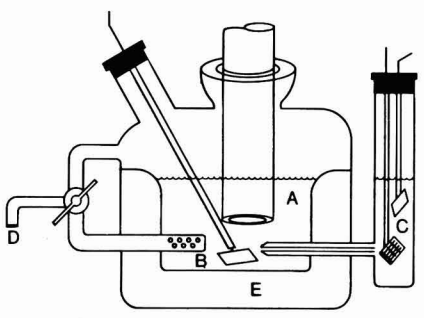

Fig. 1. Electrochemical cell. A: Rotating disk electrode. B: Counterelectrode. C: Dynamic hydrogen reference electrode. D: Gas inlet. E: Water jacket.

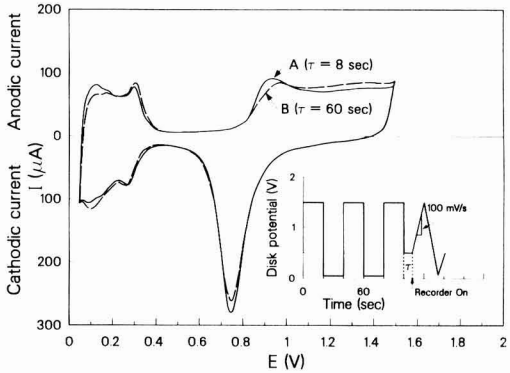

Fig. 2. First-sweep cyclic voltammetry in TFEDSA, *p*H = 1, 25°C, Ar atmosphere. A: Recorded after pretreatment. B: Recorded after pretreatment and holding 60s at 0.4V while rotating at 1600 rpm.

Several voltammograms were recorded in both electrolytes without repolishing the working electrode. The charge associated with the hydrogen adsorption region of the curves increased chronologically. The relative increase in this charge was used to quantify the increase in active electrode area caused by repeated cycling (roughening). All kinetic currents were adjusted downward to an effective roughness factor of 1.5. However, current densities were computed using the projected electrode area.

Similar voltammograms were recorded at a sweep rate of 10 mV/s in order to quantify the anodic currents associated with platinum oxidation. These anodic currents were added to the reduction currents recorded with low pressures of oxygen to adjust for the nonzero base line observed in those experiments.

Current-potential sweeps at rotation speeds of 100-1600 rpm for TFEDSA in contact with pure oxygen are shown in Fig. 3. The potential profile used for electrode pretreatment is shown in the inset in Fig. 3. The reduction currents were found to depend somewhat on sweep rate and sweep direction because of the changing oxidation state of the electrode. Therefore, for the purpose of comparing TFEDSA and TFMSA, positive going sweeps at 10 mV/s were used in all cases. Uncompensated solution resistances of 15-20Ω were accounted for by reading constant-potential data along lines of constant surface potential (with slopes of $1/R_\Omega$), as is indicated in Fig. 3.

The current-potential relationship

$$I = n\mathbf{F}Ak_c\,(C^\circ_{O_2})^m \exp\left(\frac{-\alpha V\mathbf{F}}{RT}\right) \qquad [1]$$

where A is the electrode area, k_c is the reaction rate constant for the cathodic reaction and includes the *p*H dependence, $C^\circ_{O_2}$ is the concentration of oxygen at the electrode surface, m is the reaction order for oxygen, α is the fraction of the overvoltage aiding the reduction reaction, and V is the electrode potential, is expected to apply for oxygen reduction on platinum. Because of the large overpotentials in this reaction, the anodic term has been neglected.

During cathodic reduction, the concentration of oxygen at the electrode surface is lower than that in the bulk. For transport to the rotating disk, it can be shown that

$$C^\circ_{O_2} = \left(\frac{I_L - I}{I_L}\right) C^*_{O_2} \qquad [2]$$

where I_L is the limiting current and $C^*_{O_2}$ is the bulk concentration of oxygen in the electrolyte. Since, in general,

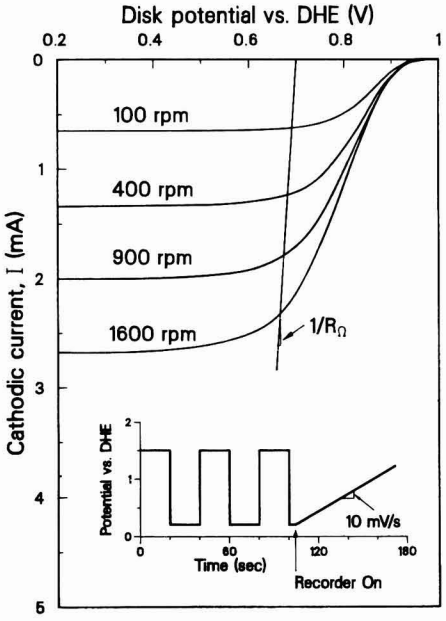

Fig. 3. Current-potential sweeps in TFEDSA, pH = 1, 25°C

$C^{\circ}_{O_2}$ is not known, but $C^{*}_{O_2}$ can be known or controlled, a more useful expression is obtained by substitution of Eq. [2] into Eq. [1], dropping the last term of Eq. [1], with the result

$$I = n\mathbf{F}Ak_c (C^{*}_{O_2})^m \left(\frac{I_L - I}{I_L}\right)^m \exp\left(\frac{-\alpha \mathbf{F}V}{RT}\right) \quad [3]$$

When I is small compared to I_L, then the reaction order m can be determined from the slope of a plot of log I *vs.* log C_{O_2} for constant V. For other conditions, the determination of m is more complicated.

Before reaction order m can be determined, it is necessary to establish the relationship between p_{O_2}, the controlled variable, and $C^{*}_{O_2}$. This was done by use of the Levich equation

$$I_L = 0.62n\mathbf{F}C^{*}_{O_2}D^{2/3}\nu^{-1/6}\omega^{1/2} \quad [4]$$

The slope of a plot of I_L *vs.* $\omega^{1/2}$ is therefore proportional to $C^{*}_{O_2}$. If Henry's law is obeyed

$$C^{*}_{O_2} = K_H p_{O_2} \quad [5]$$

the Levich slope $B = 0.62n\mathbf{F}C^{*}_{O_2}D^{2/3}\nu^{-1/6}$ should be proportional to p_{O_2}.

The applicability of Eq. [4] to the results of Fig. 3 is shown in Fig. 4. All of the lines are straight and pass through the origin, as they should. Figure 5 shows a plot of log B *vs.* log p_{O_2}, which has a slope of unity, demonstrating that Henry's law holds for O_2 in both TFMSA and TFEDSA at pH = 1 and 25°C.

Equation [5] now may be substituted into Eq. [3], yielding

$$I = n\mathbf{F}Ak_c K_H{}^m p_{O_2}{}^m \left(\frac{I_L - I}{I_L}\right)^m \exp\left(\frac{-\alpha \mathbf{F}V}{RT}\right) \quad [6]$$

For potentials near 0.9V, the currents are insensitive to rotation speed above about 400 rpm, as shown in Fig. 3. Under these conditions $I << I_L$, so that $(I_L - I/I_L)$ approaches unity, and, according to Eq. [6], a plot of log I *vs.* log p_{O_2} for constant V should be a straight line of slope m. This plot for TFMSA and TFEDSA (see Fig. 6, part A) indicates that the reaction order m is 1.0 ± 0.05.

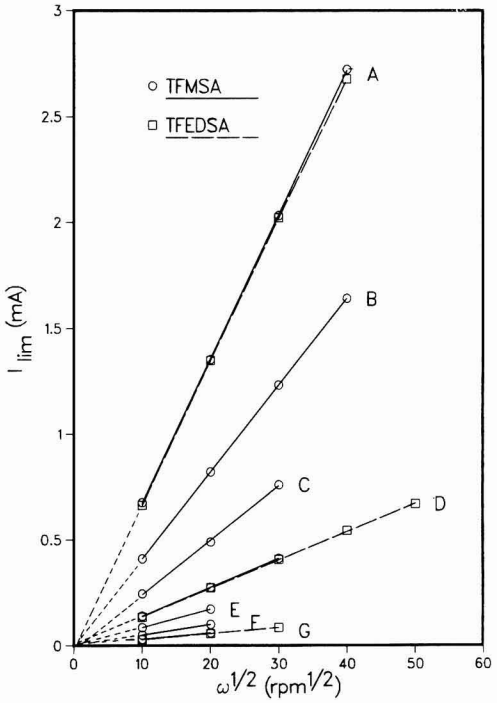

Fig. 4. Levich plots for TFEDSA and TFMSA at various oxygen partial pressures. A: 1.0 atm. B: 0.5866 atm. C: 0.3503 atm. D: 0.2028 atm. E: 0.1258 atm. F: 0.0753 atm. G: 0.043 atm.

The result that m is unity (at 0.90V) allows a simplification of further analysis for higher currents and overvoltages. Even though Eq. [6] is difficult to apply when I is not very small relative to I_L, it can be rearranged as follows. First, define the kinetic current I_K (for m = 1)

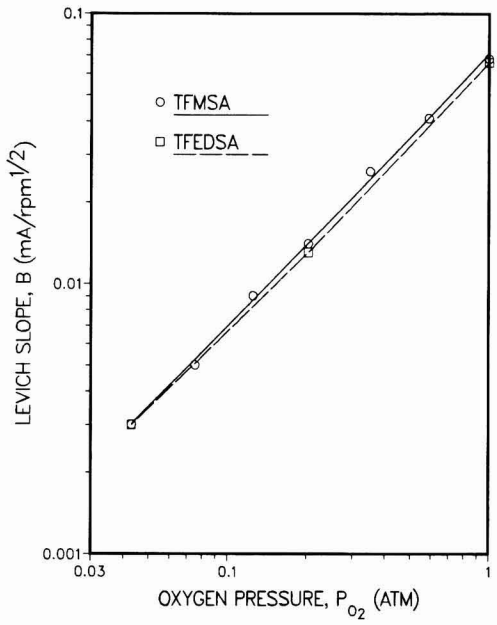

Fig. 5. Levich slopes from Fig. 4

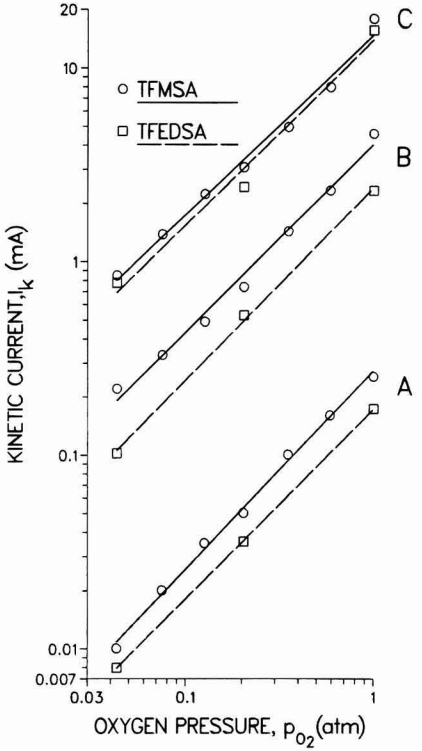

Fig. 6. Kinetic current dependence on oxygen pressure in TFEDSA and TFMSA. A: 0.90V *vs.* DHE. B: 0.80V *vs.* DHE. C: 0.70V *vs.* DHE.

$$I_k = n\mathbf{F}Ak_cC^{\infty}{}_{O_2} \exp\left(\frac{-\alpha\mathbf{F}V}{RT}\right) \quad [7]$$

Substituting Eq. [7] into Eq. [6], setting $m = 1$, and rearranging yields the familiar relation (11)

$$\frac{1}{I} = \frac{1}{I_k} + \frac{1}{I_L} \quad [8]$$

Equation [8] shows that I_k may be obtained from a plot of I^{-1} *vs.* $I_L{}^{-1}$, or since $I_L = B\omega^{1/2}$, a plot of I^{-1} *vs.* $\omega^{-1/2}$ for constant V and p_{O_2} yields I_k from the intercept. The values of I_k may then be used with Eq. [5] and [7] to test the value of m, by plotting log I_k *vs.* log p_{O_2} for a given voltage. This is shown in Fig. 6 for 0.8 (lines B) and 0.7V (lines C), and m is seen to be unity within experimental error.

A direct comparison of the kinetic current densities for TFEDSA and TFMSA was made by first multiplying the currents in TFEDSA by the ratio of the roughness factors (calculated from the hydrogen oxidation peaks observed in the voltage-sweep experiments of the type shown in Fig. 2): $[(RF)_{TFMSA}]/[(RF)_{TFEDSA}] = 0.83$. These currents were then divided by the geometric area of the rotating disk electrode, 0.458 cm². No correction for solubility or diffusivity differences was made, since $B = 0.46$ and 0.44 mA/cm²-s$^{1/2}$ for TFMSA and TFEDSA, respectively, at $p_{O_2} = 1.0$. The potential-log current density curves for 1 atm oxygen pressure are shown in Fig. 7. Over the potential range 0.67-1.0V *vs.* DHE, the kinetic currents are very similar. The familiar change of slope is observed at 0.8V, as is the case in other acids. This change in Tafel slope occurs at the potential below which the electrode surface is oxide free. Exchange current densities calculated by extrapolation of the results obtained at higher potentials are 4×10^{-6} and 6×10^{-6} mA/cm² for TFMSA and TFEDSA, respectively. These can be compared with the exchange current density of 9×10^{-8} mA/cm² reported for 1.1*N* TFMSA, 25°C, by Appleby and Baker (7).

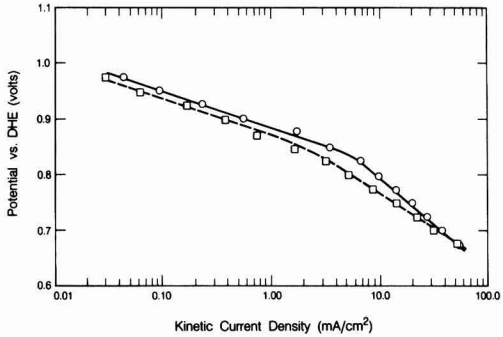

Fig. 7. Tafel plot for oxygen reduction in TFEDSA (squares) and TFMSA (circles) at 1 atm oxygen; pH = 1.0; 25°C.

Conclusions

From the experiments reported above and the analysis of the data, it is concluded that the reaction order of the electrochemical reduction of oxygen on platinum in TFEDSA and TFMSA with respect to oxygen concentration is unity, over the full potential range studied (1-0.65V *vs.* DHE). The kinetics of oxygen reduction on platinum in TFEDSA are very similar to those for TFMSA, the currents being very closely comparable at pH = 1 for identical overvoltages.

These results offer some promise for the use of fluorinated organic acids in high performance fuel cells, while avoiding the high vapor pressure of TFMSA and its undesirable wetting of PTFE. Furthermore, pressurization is expected to improve significantly the performance of cathodes in fuel cells using TFEDSA and TFMSA.

Acknowledgments

This work was supported by the Assistant Secretary for Conservation and Renewable Energy, Office of Energy Systems Research, Energy Storage Division of the U.S. Department of Energy under Contract no. DE-AC03-76SF00098.

Manuscript submitted Jan. 26, 1985; revised manuscript received May 21, 1985. This was Paper 410 presented at the Cincinnati, Ohio, Meeting of the Society, May 6-11, 1984.

The University of California assisted in meeting the publication costs of this article.

REFERENCES

1. A. J. Appleby, in "Proceedings of the Symposium on Renewable Fuels and Advanced Power Sources for Transportation Workshop," H. L. Chum and S. Srinivasan, Editors, p. 55, Solar Energy Research Institute, Golden, CO (1982).
2. B. Baker, Final Technical Report, U.S. Army Mobility Equipment Research and Development Command, Contract no. DAAK02-73-C-0084 (1975).
3. P. N. Ross, *This Journal*, **130,** 882 (1983).
4. A. Damjanovic and V. Brusic, *Electrochim. Acta*, **12,** 615 (1967).
5. A. J. Appleby, *This Journal*, **117,** 328 (1970).
6. Y. Ya. Shepelev, M. R. Tarasevich, and R. L. Burshstein, *Elektrokhimiya*, **7,** 999 (1971).
7. A. J. Appleby and B. S. Baker, *This Journal*, **125,** 404 (1978).
8. P. N. Ross and P. C. Andricacos, *J. Electroanal. Chem.*, **154,** 205 (1983).
9. K-L Hseuh, H. H. Chang, D-T. Chin, and S. Srinivasan, Abstract 730, p. 1074, The Electrochemical Society Extended Abstracts, Vol. 83-1, San Francisco, CA, May 8-13, 1983.
10. J. Giner, *This Journal*, **111,** 376 (1964).
11. P. C. Andricacos and P. N. Ross, EPRI Report no. 1676-02, Palo Alto, CA, June 1982.
12. Yu. V. Pleskov and V. Yu. Filinovskii, "The Rotating Disk Electrode," p. 90, Consultants Bureau, New York (1976).

Irreversible Voltammetric Behavior of the (100) IrO_2 Single-Crystal Electrodes in Sulfuric Acid Medium

Tadeusz Hepel*,[1]

Department of Physics, Brooklyn College, City University of New York, Brooklyn, New York 11210

Fred H. Pollak*

Department of Physics, Brooklyn College, City University of New York, Brooklyn, New York 11210 and Department of Physics, Graduate School and University Center of City University of New York, New York, New York 10036

William E. O'Grady*

Brookhaven National Laboratory, Department of Applied Science, Upton, New York 11973

ABSTRACT

The electrochemical behavior of (100) IrO_2 single-crystal electrodes in 0.5 mol/dm^3 H_2SO_4 has been studied using linear potential scan cyclic voltammetry. A highly irreversible behavior of the main electrochemical process of hydrogen or hydronium ion injection/ejection has been found in the potential range 360-580 mV (*vs.* Ag/AgCl reference). The obtained voltammograms have been compared with those for RuO_2 single crystals possessing similar electrocatalytic properties and the same crystallographic structure and also with the behavior of sputtered and anodic IrO_2 films. It has been found that the energy of major interaction of hydrogen species with the IrO_2 single-crystal structure is close to that observed for sputtered IrO_2 films but differs by *ca.* 29 kJ/mol (corresponding to 300 mV in the potential scale) from that for the anodic IrO_2 films. The penetration depth for hydrogen is highly minimized in the case of single-crystal IrO_2 electrodes and involves at most one or two monolayers. Thus, the coloration/bleaching process described for the IROX films cannot develop on nonhydrated single-crystal IrO_2 electrodes unless their crystallographic structure is damaged by cycling in a wide potential range.

Anodic films of iridium dioxide have recently been the subject of numerous studies on account of their interesting electrocatalytic and electrochromic behavior. Both the oxygen and chlorine evolution reaction proceed on the IrO_2 electrodes with extremely low overvoltages (1-5). In contrast to RuO_2 possessing similar electrocatalytic properties (6-10), the IrO_2 films undergo dissolution at higher positive potentials ($E > 1600$ mV *vs.* Ag/AgCl) and can be removed from the electrode surface (2, 11-13). The hydrous, amorphous IrO_2 films on Ir metal electrodes show electrochromic properties (13-22) sensitive to the change in the electrode potential. The mechanism proposed for the rapid coloration/bleaching process (about 40 ms) is based on the proton injection/ejection mechanism (13). It has been found that the electrochemical processes of anodic formation and cathodic reduction of a thick porous IrO_2 film are highly reversible (12-14).

The initial stages of IrO_2 film growth on Ir electrodes have recently been studied by Mozota and Conway (11), Capon and Parsons (23), and other authors (24-26). The mechanism of interaction of the IrO_2 surface with aqueous solutions has also been discussed from the point of view of the surface acid-base properties (27-31). The latter works have been done using thermal IrO_2 powders.

The behavior of the anodic oxide on Ir electrodes during oxygen evolution in acidic solutions has also been studied by *ex situ*, x-ray photoelectron spectroscopy (XPS) by Kotz *et al.* (32). These authors demonstrate conclusively that a thin oxide (or hydroxide) is formed on iridium surface during O_2 evolution and no higher than IV oxidation states of Ir are present in the film. The composition profiles within the amorphous anodic IrO_2 films have been determined by McIntyre and co-workers (13) using nuclear reactions. The thickness of the hydrated IrO_2 films has been measured by Kim *et al.* (33) using XPS technique.

As regards single crystals, the electrical-transport properties of IrO_2 have been reported by Ryden *et al.* (34) and conduction electron screening effects have been demonstrated in IrO_2 by Wertheim and Guggenheim (35). The optical properties of a single-crystal IrO_2 have been described by Goel *et al.* (36). The latter authors, measuring a near-normal incidence reflectivity in the photon energy range 0.5-9.5 eV, have determined the spectral dependence of the complex dielectric function and refractive index. This in turn allowed making a direct comparison with recent band structure and density-of-states calculations performed by Mattheiss (37).

In this paper, the voltammetric characteristics of the IrO_2 single-crystal electrodes with the exposed (100) surface are presented and discussed in terms of the hydrogen and hydronium ion injection/ejection processes. The observed significant differences between the electrochemical behavior of the IrO_2 (100) electrodes and that of the anodic IrO_2 films on Ir substrates (IROX films) are discussed in detail. A comparison is also made with the RuO_2 and TiO_2 single-crystal electrodes having the same crystallographic structure.

Experimental

The electrochemical cell was of a conventional three electrode design. A coiled Pt wire counterelectrode was separated from the working electrode compartment by a sintered glass joint. A double-junction Ag/AgCl electrode with a saturated KCl internal solution was used as a reference electrode.

The working electrodes were prepared from the oriented IrO_2 single crystals using silver epoxy resin for low resistance contacts and Epoxide (Buehler) for body insulating. The IrO_2 single crystals were grown in this laboratory by a chemical vapor transport in a flowing gas system at 1300°C under 2 atm of the oxygen partial pressure. This procedure was similar to the growth of large RuO_2 single crystals (38, 39). The source materials were the Ir powder of the electronic-grade purity and oxygen. The exposed surface area of the IrO_2 (100) electrode was approximately 0.01 cm^2. The crystal was oriented by x-ray Laue backscattering to within 1°.

A PAR Model 173 potentiostat and PAR Model 175 universal programmer were used for cyclic voltammetry (CV) measurements. The experimental curves were recorded using a Hewett-Packard 7044 X-Y recorder.

*Electrochemical Society Active Member.

[1]Present address: Department of Chemistry and Institute of Colloid and Surface Science, Clarkson University, Potsdam, New York 13676.

Results

Typical cyclic voltammetry characteristics for the IrO_2 single-crystal electrode with the exposed crystallographic face (100) are shown in Fig. 1 and 2. One major pair of anodic/cathodic peaks is observed in the potential range 360-600 mV *vs.* Ag/AgCl in 0.5 mol/dm^3 H_2SO_4 at 298 K. Several other small features are clearly seen or can be inferred both on the anodic and cathodic half-cycles. They are labeled from A_1 to A_4 for anodic processes and C_2 to C_4 for cathodic ones. The sharp current increase A_5 at E = 1300 mV is due to the oxygen evolution reaction. The hydrogen evolution C_0 starts at E = −370 mV.

It is informative to discuss the voltammetric behavior of the IrO_2 (100) electrodes comparing the obtained characteristics with published voltammograms for another transition metal dioxide RuO_2 [single crystals with several orientations (9)] and for iridium metal electrodes covered with anodic IrO_2 films (11, 13, 23-26). There are significant differences in CV characteristics for these electrodes in the whole accessible "structure" window from HER (hydrogen evolution reaction) to OER (oxygen evolution reaction). They are discussed separately for the hydrogen deposition/ionization region and the oxide rearrangement region, although, in case of the IrO_2 single-crystal electrodes, presumably all the processes are based on the injection/ejection of hydrogen or hydronium ions (13). The observed results are reported in the same order.

Hydrogen deposition/ionization region.—In the cathodic half-cycle of the voltammograms for the IrO_2 (100) electrodes, two small features C'_2 and C''_2 are resolvable on the expanded scale curves as illustrated in Fig. 3. The peak potentials are −70 and +25 mV, respectively. On the anodic side of the voltammograms a peak A_2 is observed at E = +170 and may be considered as a counterpart of one or both the cathodic peaks C'_2 and C''_2. Another anodic peak A_1 appears at E = −180 mV (Fig. 2), when the cathodic inversion potential is well shifted into HER region.

The oxide rearrangement region.—The anodic IrO_2 films formed on Ir electrodes contain large amounts of water, and they are porous and amorphous (11-26). These properties result in a high degree of reversibility of the process involved in the oxide rearrangement region.

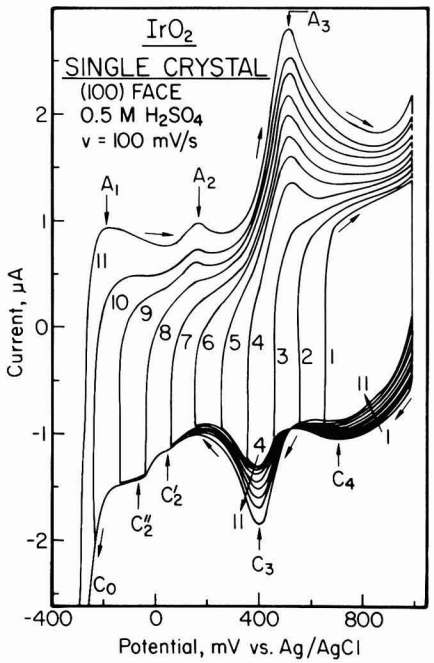

Fig. 2. Dependence of the CV characteristics for the IrO_2 (100) electrode in 0.5 mol/dm^3 H_2SO_4 upon the cathodic inversion potential $E_{i,c}$ [mV]: (1) 650, (2) 550, (3) 450, (4) 350, (5) 250, (6) 150, (7) 50, (8) −50, (9) −150, (10) −250, (11) −350. Potential scan rate v = 100 mV/s.

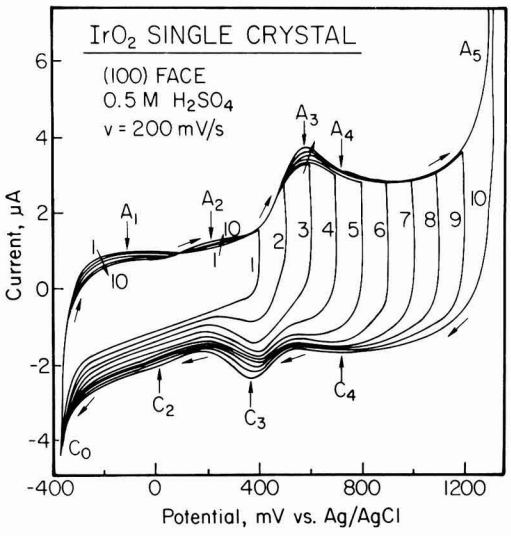

Fig. 1. Dependence of the CV characteristics for the IrO_2 (100) electrode in 0.5 mol/dm^3 H_2SO_4 upon the anodic inversion potential $E_{i,a}$ [mV]: (1) 400, (2) 500, (3) 600, (4) 700, (5) 800, (6) 900, (7) 1000, (8) 1100, (9) 1200, (10) 1300. Potential scan rate v = 200 mV/s.

However, the oxide rearrangement processes we observed on the well-defined, water-free IrO_2 (100) substrates exhibit significant retardation due to the compact structure of the electrode material. The appearance of the main pair of peaks A_3-C_3 is illustrated in Fig. 1 and 2 and in a narrow potential scale in Fig. 4. The peak potentials at scan rate v = 200 mV/s are 580 and 350 mV for the peaks A_3 and C_3, respectively. A small increase in the peak height is observed after prolonged cycling in the po-

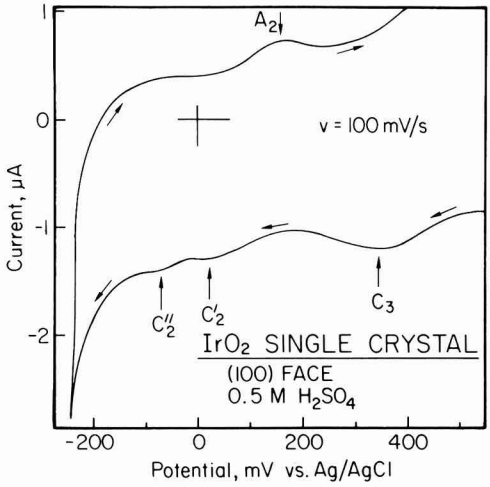

Fig. 3. Part of a cyclic voltammogram for the IrO_2 (100) electrode in 0.5 mol/dm^3 H_2SO_4, showing cathodic features C'_2 and C''_2. Cycling between −250 and +1300 mV. Scan rate v = 100 mV/s.

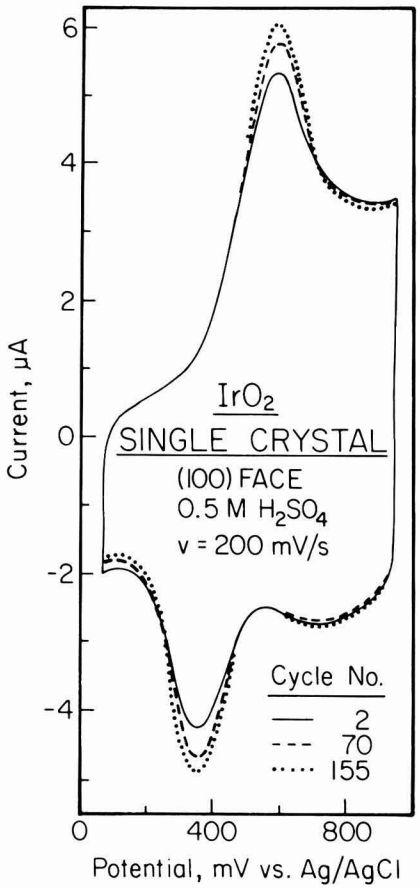

Fig. 4. Cyclic voltammograms for the IrO_2 (100) electrode in 0.5 mol/dm³ H_2SO_4 solution. Effect of the prolonged cycling between +50 and +950 mV at v = 200 mV/s. Cycle numbers are indicated in figure.

tential range 50-950 mV. In Fig. 4, curves are presented for cycles number 2, 70, and 155. The electrode was previously used in cycling experiments, so that some amount of disordered surface monolayers could eventually exist on the electrode surface. However, the pronounced observed irreversibility, as evidenced by the peak separation, remains all the time unchanged. At more positive potentials, there is seen a second pair of peaks labeled A_4-C_4 (the peak A_4 is seen in Fig. 1 when the anodic inversion potential does not exceed 1100 mV). The peak potentials are both equal to 715 mV and are independent of the scan rate v. In contrast to the process A_3-C_3, this is a reversible reaction. The broadness of the peak C_4 suggests repulsive interactions in the presumably hydrated monolayer of the rearranged oxide.

Another pair of peaks labeled A'_3-C'_3 in Fig. 5 appears rather unexpectedly during the long term experiments with changing scan rates from 1 up to 200 mV/s. The peak potentials of this irreversible process change with v and at v = 110 mV/s are 740 and 160 mV for A'_3 and C'_3, respectively. The peaks are situated on the falling branches of the main peaks, A_3 and C_3. The peaks A'_3 and C'_3 disappear after 15 min conditioning of the electrode at E = 550 mV, as shown in Fig. 6. Note that the peaks A'_3-C'_3 were not observed after prolonged cycling in the range 50-950 mV (Fig. 4). Therefore, the only possible reason for the observed change in voltammetric behavior of the IrO_2 electrode is a difference (300 mV) in the cathodic inversion potential (E_c = −250 mV in the reported slow scan rate experiments (see also Fig. 5). A possible explanation of this behavior and a comparison with the behavior of the anodic oxides on the Ir electrodes are given in the next section.

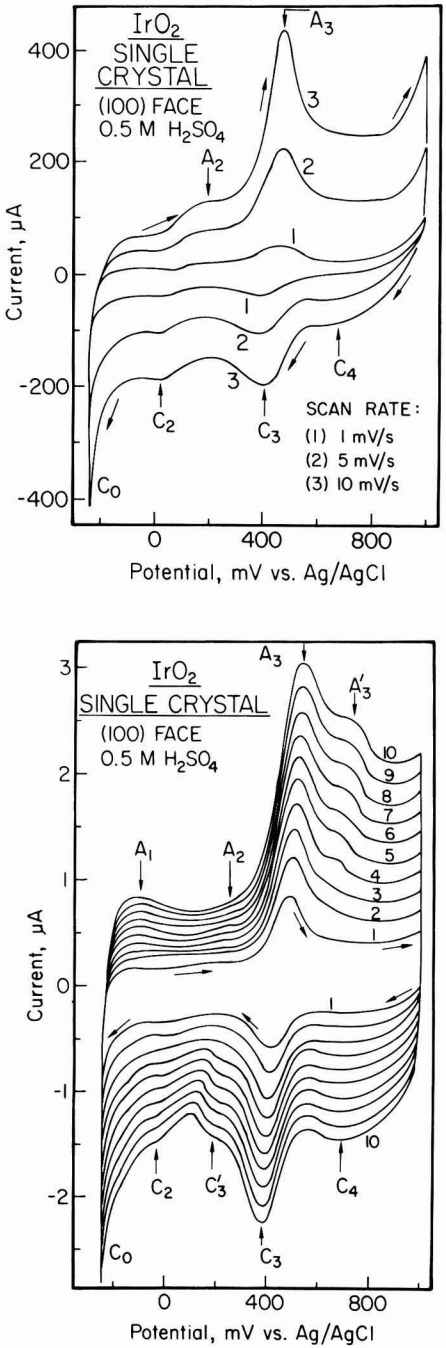

Fig. 5. Scan rate dependence of the CV characteristics for the IrO_2 (100) electrode in 0.5 mol/dm³ H_2SO_4 for slower (a, top) and faster (b, bottom) scan rates. v [mV/s]: (1) 1, (2) 5, (3) 10, (4) 20, (5) 30, (6) 40, (7) 50, (8) 60, (9) 70, (10) 80, (11) 90, (12) 100, (13) 110.

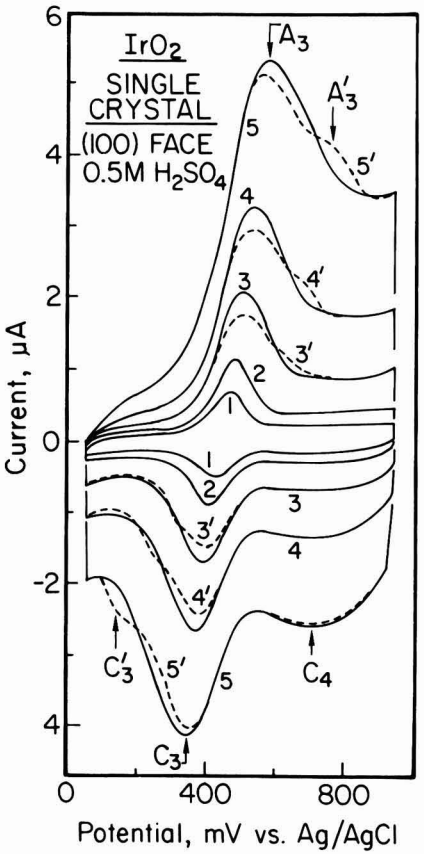

Fig. 6. The CV characteristics for the IrO_2 (100) electrode in 0.5 mol/dm^3 H_2SO_4 solution obtained after prolonged experiments at very slow scan rates (dashed curves) and after additional stirring deoxygenation and conditioning at +550 mV (solid curves). v [mV/s]: (1) 10, (2) 20, (3,3') 50, (4,4') 100, (5,5') 200.

Discussion

Most of the 4d and 5d transition-metal dioxides crystallize with a distorted rutile-type structure with a monoclinic or orthorhombic symmetry (37). Among the almost undistorted materials are IrO_2, RuO_2, and OsO_2. The lattice parameters, a, c, and c/a for IrO_2 are as follows: a = 4.4983Å, c = 3.1544Å, and c/a = 0.701, which can be compared with data for the RuO_2 single crystals whose voltammetric behavior for several crystallographic orientations we have presented elsewhere (9): a = 4.4919Å, c = 3.1066Å, and c/a = 0.696. The parameter c/a serves as a measure of the distortion from the ideal rutile structure, which has $(c/a)_{ideal}$ = 0.586. We see that the lattice parameters for both the IrO_2 and RuO_2 crystals are almost identical. However, the Fermi surface cross sections as calculated (37) or derived from the experimental magneto thermal-oscillation data obtained by Graebner *et al.* (40) are entirely different for IrO_2 and RuO_2 since the Ir atoms are in a $5d^5$ state while the Ru atoms are in $4d^4$ state. It is of a considerable interest to compare the electrochemical characteristics for these two oxides, and also for the n-TiO_2 semiconductor electrode, to gain our understanding of the electrocatalytical properties of these materials. The generalized electrode reaction which can be considered for the above materials is the reduction-oxidation process involving injection/ejection of hydrogen and change in the apparent oxidation state of the metal M

$$MO_n + xH^+ + xe^- = H_xMO_n \quad [1]$$

There are many possible ways for hydrogen to interact with MO_n structure. In the limiting case, the hydration water can be formed. However, hydrogen can also penetrate through the lattice channels and create intercalation structures. The apparent oxidation state of the metal changes, but charge is not localized at any particular metal atom because of the electron band structure, which in the case of IrO_2 and RuO_2 consists of a partially filled E_{2g} band. The oxidation state of the trapped hydrogen may be different. In TiO_2, hydrogen can be considered as a highly ionized neutral donor (41). In anodic IrO_2 films, hydrogen is mainly in the form of hydronium ions near the electrode/electrolyte interface (13), so the net reduction process can be expressed as follows

$$IrO_n \cdot 2H_2O + H_3O^+ + e^- = H_3O^+ \cdot IrO_n^- \cdot 2H_2O \quad [2]$$

where n = 2. The energy of interaction between the hydrogen and the rutile-type oxide structure may also vary with the hydrogen uptake. This is observed, for example, in some lithium intercalation materials. The multiple peak structure in cyclic voltammetry characteristics for transition metal oxide electrodes is therefore not unexpected. At the present stage of our knowledge, we cannot derive any conclusive correlations between the voltammetric peak structure and the localization of the hydrogen interactions. However, it is interesting to compare voltammetric characteristics for different transition metal oxide single crystals having similar crystallographic structure but different electron-band structure and chemical activity. On the other hand, we would like to emphasize significant differences we observed in voltammetric behavior of the same basic compound (IrO_2) synthesized in a different way. Thus, we compare our data for IrO_2 (100) single-crystal electrodes with literature data for anodic IrO_2 films (11-27) and those for IrO_2 sputtered layers (42).

By analyzing voltammograms for the IrO_2 (100) electrode and those for the RuO_2 single crystals with exposed surfaces (110), (001), (111), (101), and (100), we find differences rather than similarities. The behavior of the RuO_2 electrodes is highly reversible in the oxide rearrangement region, and the suggested penetration depth for hydrogen does not exceed one monolayer. In the case of the IrO_2 single crystal, the irreversible character of the major pair of peaks (A_3-C_3) for hydrogen injection/ejection processes [2] remains even at v = 1 mV/s. Moreover, the penetration depth increases upon cycling, especially when cathodic limit is below 0 mV and anodic limit exceeds 1300 mV (OER region).

In the hydrogen region, the voltammetric behavior of the IrO_2 (100) electrode shows some similarities with that of the RuO_2 (100) surface and the n-TiO_2 (001) electrode [there are no electrochemical data for TiO_2 (100) surface]. For all the three crystals, IrO_2 (100), RuO_2 (100), and n-TiO_2 (001), there are seen two cathodic adsorption peaks and only one anodic desorption peak.

In comparison with other single-crystal electrodes, the overvoltage for hydrogen evolution is very low for the IrO_2 (100) electrodes. If the "bleaching" process as described for the hydrated anodic IrO_2 films on the Ir electrodes (13) would take place efficiently on our nonhydrated compact IrO_2 crystals, one would not expect as sharp a current increase at HER potential as we observed. Certainly, the decrease in conductivity and hydrogen diffusion into the crystal bulk is rather inefficient in the case of the IrO_2 (100) electrode. This observation may be compared with the effect of cathodization of the n-TiO_2 single-crystal electrodes (41) resulting in the modification of the doping level by the hydrogen injection into the crystal lattice. An increase in conductivity and the majority carrier concentration is observed in this latter case.

On the basis of the crystallographic structure of IrO_2 single crystals and the experimental observations, we propose a model of the ideal (100) surface being in contact with an aqueous solution. In this model illustrated in Fig. 7, we attempt to correlate the findings of previous authors (12-14) concerning changes in the composition of

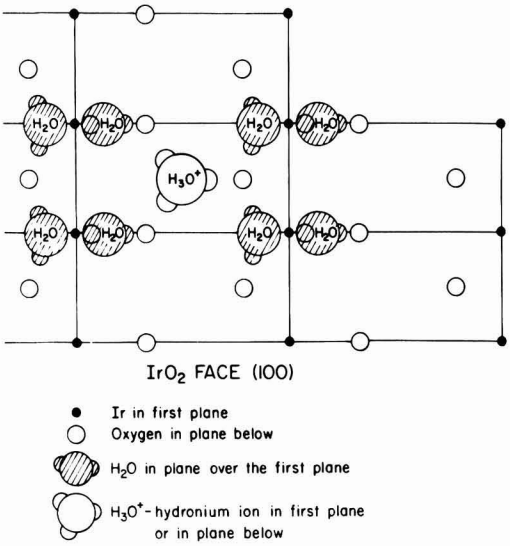

Fig. 7. Schematic representation of the IrO_2 (100) ideal surface after hydration and hydrogenation in first monolayer.

the IROX films upon cathodization ("bleaching") and anodization ("coloration"). The iridium atoms present on the ideal (100) surface have broken bonds with oxygens caused by crystal termination. On contact with an aqueous electrolyte, the iridium atoms will form active centers for the adsorption of water molecules that take an orientation with hydrogens directed toward the electrolyte phase. A dissociation of the hydrogen-oxygen bonds is very probable. It has been found by Trasatti and coworkers (31) that the IrO_2 powders in aqueous solutions are highly negatively charged. The XPS studies revealed (43) that the dissociative adsorption of water molecules always takes place on the iridium metal samples. A negatively charged IrO_2 surface should lead immediately to the attraction of hydronium ions from the solution. The most stable arrangement of the H_3O^+ ion, in the center of the unit cell, is shown in Fig. 7. The composition of the unit cell (two first plane plus surface water) is then $HIrO_2 \cdot 3H_2O$, the same as found by McIntyre *et al.* (13, 14) for "bleached" IROX films. On anodization, this composition should change to $IrO_2 \cdot H_2O$, what can be achieved by withdrawal of H_3O^+ ion. We feel that it would be difficult for hydration and hydrogenation of the next monolayers of a nonhydrated IrO_2 single crystal to proceed without reconstruction of the unit cell. This in turn requires large energies due to the high activation barriers associated with reconstructing process. The single protons can eventually penetrate into the crystal bulk. Cycling in a wide potential range may result in a distortion of the surface lattice and a formation of the next monolayer of the hydrated form of IrO_2 with the expanded unit cell. This process could possibly be manifested by an additional pair of peaks like A'_3-C'_3 in Fig. 5b with a high degree of irreversibility.

Comparing the electrochemical behavior of the anodic hydrated IrO_2 films on the Ir electrodes described by previous workers (11-27) with that of the IrO_2 (100) electrodes presented in this paper, one observes good reversibility of the main, hydrogen injection/ejection process [2] represented by a couple of peaks at 720 mV in the former case and a high degree of irreversibility of this process (peaks A_3-C_3) in the latter case. Also, the reversible potential for this process is lower for single-crystal electrode (E = 410 mV). In the hydrogen region, CV characteristics for the anodic IrO_2 films become sluggish because of the reduced conductivity in the bleached material. This phenomenon is not observed in case of the IrO_2 (100) electrode as the hydrogen penetration depth is highly minimized in the single crystal and does not involve more than perhaps one or two monolayers.

It is characteristic that the sputtered IrO_2 films (42) exhibit a reversible voltammetric behavior similar to the IROX (anodic) films, but in contrast to them the reversible potential for the major process [2] is equal E = 450 mV, *i.e.*, very close to the value E = 410 mV we observed for our single-crystal IrO_2 (100) electrode. Note that the density of the sputtered films decreases on operating in aqueous electrolytes from 10 to 7.8 g/cm^3 due to water uptake. These numbers can be compared with the density for crystalline IrO_2, which is equal to 11.68 g/cm^3 and resembles compact structure of the latter material. On the other hand, the electric conductivity of the IROX films changes by four orders of magnitude during the bleaching/coloration process (from 100 to 0.01 Ω-cm), while that of the sputtered layers changes only by one order of magnitude (from 0.01 to 0.001 Ω-cm). The specific resistivity for crystalline IrO_2 is 10^{-4} Ω-cm, and we did not observe in voltammetric characteristics any significant changes in resistivity of our single-crystal IrO_2 electrodes. Thus, the interatomic distances and water content in IrO_2 samples which are determined by the method of synthesis and pretreatment procedure are directly responsible for both the energy of interaction of hydrogen with IrO_2 structure and the degree of reversibility of the hydrogen injection/ejection process [2]. Also, the electric conductivity and the penetration depth of hydrogen species into the electrode material are directly related to the structural changes caused by preparation conditions.

Conclusion

A highly irreversible behavior of the main electrochemical process of the hydrogen injection/ejection corresponding to Eq. [2] at single-crystal IrO_2 electrodes has been described for the (100) surface. It is manifested by a difference between the voltammetric peak-potentials for the anodic and cathodic half-reactions which approaches 220 mV at v = 200 mV/s. This behavior can be opposed to that of the sputtered and anodic IrO_2 films on the Ir substrates which is reversible. Also, we did not observe characteristic ceasing of the current in the hydrogen region caused in case of the IROX films by a decrease in electrical conductivity associated with the "bleaching" process. Instead, a low overvoltage for the hydrogen evolution reaction has been observed on the IrO_2 (100) electrodes. All these differences can be interpreted by a strong retardation of the hydration and hydrogenation of the compact IrO_2 single crystals in comparison with the favorable compositional changes of the amorphous anodic IrO_2 films. These changes can involve layers 100-200 nm thick in the latter case, while the hydrogen penetration depth for the IrO_2 single crystal electrodes does not exceed one or two monolayers.

Thus, the coloration/bleaching process as described for the IROX films cannot develop on nonhydrated single-crystal IrO_2 electrodes unless their crystallographic structure is damaged by cycling in a wide potential range.

The energy of major interaction of hydrogen species with the IrO_2 single-crystal structure is close to that observed for sputtered IrO_2 films but differs by *ca.* 29 kJ/mol (corresponding to 300 mV difference in the reversible potential for reaction [2]) from that for the anodic IrO_2 films.

Acknowledgment

This work was supported by the United States Department of Energy under Contract no. DE-AC02-80ER10654.

Manuscript submitted April 3, 1984; revised manuscript received *ca.* March 25, 1985.

Brooklyn College assisted in meeting the publication costs of this article.

REFERENCES

1. S. Trasatti and G. Lodi, in "Electrodes of Conductive Metallic Oxides, Part B," S. Trasatti, Editor, Elsevier, Amsterdam (1981).
2. S. Gottesfeld and S. Srinivasan, *J. Electroanal. Chem.*, **86,** 89 (1978).
3. J. Mozota and B. E. Conway, *This Journal*, **128,** 2141 (1981).
4. J. P. Hoare, "The Electrochemistry of Oxygen," Interscience, New York (1968).
5. J. Horkans and M. W. Shafer, *This Journal*, **124,** 1201 (1977).
6. S. Trasatti and W. E. O'Grady, in "Advances in Electrochemistry and Electrochemical Engineering," Vol. 12, H. Gerischer and C. W. Tobias, Editors, pp. 177-261, Wiley and Sons, New York (1981).
7. D. M. Novak, B. V. Tilak, and B. E. Conway, in "Modern Aspects of Electrochemistry," Vol. 14, J. O'M. Bockris and B. E. Conway, Editors, pp. 195-318, Plenum Press, New York (1982).
8. S. Trasatti and G. Buzzanca, *J. Electroanal. Chem.*, **29,** Appl. 1 (1971).
9. T. Hepel, F. H. Pollak, and W. E. O'Grady, in "The Chemistry and Physics of Electrocatalysis," J. D. E. McIntyre, M. J. Weaver, and E. B. Yeager, Editors, p. 512, The Electrochemical Society Softbound Proceedings Series, Pennington, NJ (1985).
10. A. T. Kuhn and C. J. Mortimer, *This Journal*, **120,** 231 (1973).
11. J. Mozota and B. E. Conway, *Electrochim. Acta*, **28,** 1 (1983).
12. B. E. Conway and J. Mozota, *This Journal*, **28,** 9 (1983).
13. J. D. McIntyre, S. Basu, W. F. Peck, W. L. Brown, and W. M. Augustyniak, *Phys. Rev. B*, **25,** 7242 (1982).
14. S. Gottesfeld, J. D. E. McIntyre, G. Beni, and J. L. Shay, *Appl. Phys. Lett.*, **33,** 208 (1978).
15. S. Gottesfeld and J. D. E. McIntyre, *This Journal*, **126,** 742 (1979).
16. G. Beni and J. L. Shay, *Appl. Phys. Lett.*, **33,** 567 (1978).
17. J. D. E. McIntyre, W. F. Peck, and S. Nakahara, *This Journal*, **127,** 1264 (1980).
18. G. Beni, C. E. Rice, and J. L. Shay, *Phys. Rev. B.*, **21,** 364 (1980).
19. G. Beni, C. E. Rice, and J. L. Shay, *This Journal*, **127,** 1342 (1980).
20. C. E. Rice and P. M. Bridenbaugh, *Appl. Phys. Lett.*, **38,** 59 (1981).
21. C. E. Rice, *ibid.*, **35,** 563 (1979).
22. J. L. Shay, G. Beni, and L. M. Schiavone, *ibid.*, **32,** 942 (1978).
23. A. Capon and R. Parsons, *J. Electroanal. Chem.*, **39,** 275 (1972).
24. J. M. Otten and W. Visscher, *ibid.*, **55,** 1 (1974).
25. J. M. Otten and W. Visscher, *ibid.*, **55,** 13 (1974).
26. D. A. J. Rand and R. Woods, *ibid.*, **55,** 375 (1974).
27. L. D. Burke, M. E. Lyons, E. J. M. O'Sullivan, and D. P. Whelan, *ibid.*, **122,** 403 (1981).
28. S. Ardizzone, A. Carugati, and S. Trasatti, *ibid.*, **126,** 287 (1981).
29. G. A. Kokarev, V. A. Kolesnikov, A. F. Gubin, and A. A. Korobanov, *Elektrokhimiya*, **18,** 466 (1982).
30. M. A. Butler and D. S. Ginley, *This Journal*, **125,** 228 (1978).
31. S. Ardizzone, D. Lettieri, and S. Trasatti, *J. Electroanal. Chem.*, **146,** 431 (1983).
32. R. Kotz, H. J. Lewerenz, P. Bruesch, and S. Stucki, *ibid.*, **150,** 209 (1983).
33. K. S. Kim, C. D. Sell, and N. Winograd, *Electrocatal.*, 242.
34. W. D. Ryden, A. W. Lawson, and C. C. Sartain, *Phys. Rev. B*, **1,** 1494 (1970).
35. G. K. Wertheim and H. J. Guggenheim, *ibid.*, **22,** 4680 (1980).
36. A. K. Goel, G. Skorinko, and F. H. Pollak, *ibid.*, **24,** 7342 (1981).
37. L. F. Mattheiss, *ibid.*, **13,** 2433 (1976).
38. Y. S. Huang and F. H. Pollak, Private communication.
39. Y. S. Huang, H. L. Park, and F. H. Pollak, *Mater. Res. Bull.*, **17,** 1305 (1982).
40. J. E. Graebner, E. S. Greiner, and W. R. Ryden, *Phys. Rev. B.*, **13,** 2426 (1976).
41. T. Hepel, M. Hepel, and R. A. Osteryoung, *This Journal*, **129,** 2132 (1982).
42. W. C. Dautremont-Smith, L. M. Schiavone, S. Hackwood, G. Beni, and J. L. Shay, *Solid State Ionics*, **2,** 13 (1981).
43. T. S. Wittrig, D. E. Ibbotson, and W. H. Weinberg, *Surf. Sci.*, **102,** 506 (1981).

Finite-Element Method Approach to the Problem of the IR-Potential Drop and Overpotential Measurements by Means of a Luggin-Haber Capillary

Koichi Tokuda,* Tatsuro Gueshi,[1] Koichi Aoki, and Hiroaki Matsuda*

Department of Electronic Chemistry, Graduate School at Nagatsuta, Tokyo Institute of Technology, Nagatsuta, Midori-ku, Yokohama 227, Japan

ABSTRACT

A finite-element method is applied to the problem of potential distribution around a Luggin-Haber capillary placed perpendicularly to the planar working electrode for the cases when overpotential is absent and when there is overpotential which is linear to current density. Approximate equations are presented for the IR-potential drop between the working electrode and the Luggin-Haber capillary as functions of the outer and inner radii of the capillary tip, the distance from the capillary tip to the working electrode, conductivity of the solution, and average current density. Approximate equations which relate the measured overpotential to the true overpotential, the IR-potential drop, and the relevant parameters are also presented. In the presence of overpotential or polarization, it has been shown that the measured potential can be regarded as a sum of the true overpotential and the IR-potential drop, provided that the tip of the Luggin-Haber capillary is placed no closer from the electrode surface than a distance equal to the outer diameter of the capillary tip.

Measurement or control of the potential of a working electrode under current flow is of great importance not only in the studies on electrode kinetics, but also in practical electrolysis. For this purpose, a Luggin-Haber capillary connected to a reference electrode is usually employed. The cell voltage of a galvanic cell composed of the working and reference electrodes is measured or controlled. Minimization of the ohmic potential drop included in the measured or controlled voltage will be achieved by placing the tip of the Luggin-Haber capillary as close to the surface of the working electrode as possible. When the capillary tip is placed very close to the electrode, however, it shields the latter, causing a decrease in current density and distortion of equipotential surfaces near the capillary tip, so that the potential measured or controlled by the capillary corresponds to a spot of the

*Electrochemical Society Active Member.

[1]Present address: Sanyo Electric Company, Limited, Research Center, Hirakata, Oosaka 573, Japan.

electrode at which the current density is much lower than that in the region of electrode surface sufficiently remote from the capillary tip.

Piontelli and co-workers (1, 2) and Barnartt (3, 4) performed potential mapping studies using rather large model electrolysis cells and obtained equipotential maps around the electrode and capillary tip. Barnartt (3, 4) concluded that the potential inside a capillary of diameter $2r_0$ placed $4r_0$ from one of a pair of parallel-plate electrodes is equal to that in the undistorted field a distance $2r_0/3$ closer than the capillary tip position.

From a theoretical viewpoint, the solution of the Laplace equation with appropriate boundary conditions is required in order to obtain the potential or primary and secondary current distributions in electrolytic cells. Since Kasper's work (5), there have been a number of papers on the potential and current distributions in electrolysis cells. Although it is highly desirable to have analytical solutions, they can be given only for simple geometries by the use of conformal or imaging transformations (6-12). The recent development of high speed computers has made it possible to apply various numerical methods to the problems for more complicated electrode geometries. A finite difference method was utilized by Klingert *et al.* (13) for the computation of the primary and secondary current distribution in an L-shaped region. Pierini and Newman (14) employed the superposition technique to calculate the potential distribution around a disk electrode in axisymmetric cylindrical cells. Fedkiw (15) applied a perturbation method to the calculation of the primary current distribution at an electrode with a sinusoidal profile. An orthogonal collocation technique (16) and a variational method (17) have also been applied to current distribution problems. In recent years, the finite-element method (FEM) has been used in various fields of engineering (18-20). It is a powerful numerical procedure for solving the differential equations of physics and engineering. To our knowledge, the first application of FEM to electrochemistry was done by Kawai and coworkers (21-23) for the solution of Fick's equation and that coupled with chemical reaction terms. One of the advantageous properties of FEM is that it allows us to treat boundary value problems for two- or three-dimensional regions with irregularly shaped boundaries to which an analytical approach is usually very difficult. From this viewpoint, the application of FEM to many problems in electrochemistry is expected. Recently, Alkire *et al.* (24) used FEM to predict the shape changes at a cathode during electrodeposition. Sautebin *et al.* (25) applied FEM to the simulation of the leveling of triangular surface during anodic dissolution in electrochemical machining. In our laboratory, FEM has been used for the calculation of primary current distribution in a two-dimensional model cell composed of an electrode with holes (26) and for the calculation of chronopotentiometric i-t curves at the electrodes coated with polymer of uneven thickness (27).

The present paper describes the application of FEM to the calculation of the potential distribution around the Luggin-Haber capillary placed perpendicularly to the working electrode in the cases (i) where overpotential is absent and (ii) where there is overpotential which is assumed to be linear to current density. This assumption may be justified if the current densities do not deviate much from the average current density. Approximate equations with reasonable accuracies are presented for the IR-potential drop as functions of the outer and inner radii of the capillary tip, the distance between the capillary tip and the working electrode, conductivity of the solution, and average current density. Furthermore, approximate equations which relate the measured overpotential to the true overpotential, the IR-potential drop, and the relevant parameters are presented. It has been shown that in the presence of overpotential or polarization the measured potential can be regarded as a sum of true overpotential and the IR-potential drop when the distance between the capillary tip and the electrode surface is no closer than the outer diameter of the capillary tip. A part of this work has been published as a preliminary note (28).

Formulation of the Problem

The electrochemical problem.—Consider an electrolysis cell composed of three electrodes: a working, an auxiliary, and a reference electrode. The variation of electrical potentials in the cell is schematically shown in Fig. 1. For convenience, we assume in what follows that the working electrode acts as a cathode and the auxiliary as an anode. Since the electrode potential is defined as the difference between the inner potential of the electrode phase and that of the solution adjacent to the electrode surface, we have

$$E^c = \psi^c - \phi^c \quad [1]$$

We can assume without any loss of generality that there is no polarization at the auxiliary electrode and the potential of the electrode is constant

$$E^a = \psi^a - \phi^a = \text{const.} \quad [2]$$

We can also assume that the potential of the reference electrode is constant since current passing through it is negligibly small and polarization at the electrode can be ignored. Thus we have

$$E^{ref} = \psi^{ref} - \phi^{ref} = \text{const.} \quad [3]$$

In Fig. 1, the variation of potentials is depicted in reference to the inner potential of the electrolyte solution adjacent to the auxiliary electrode, ϕ^a, which is also assumed to be constant. Under the equilibrium condition where no current flows through the cell, the inner potential of the electrolyte solution is uniform throughout the cell

$$\phi_{eq}{}^c = \phi_{eq}{}^{ref} = \phi^a \quad [4]$$

Since the cell voltage is defined as

$$V = \psi^a - \psi^c \quad [5]$$

the cell voltage under the equilibrium condition is given by

$$V_{eq} = \psi^a - \psi_{eq}{}^c = (\psi^a - \phi^a) - (\psi_{eq}{}^c - \phi_{eq}{}^c) = E^a - E_{eq}{}^c \quad [6]$$

When current flows without any overpotential at the working electrode (cathode), the electrode potential at the

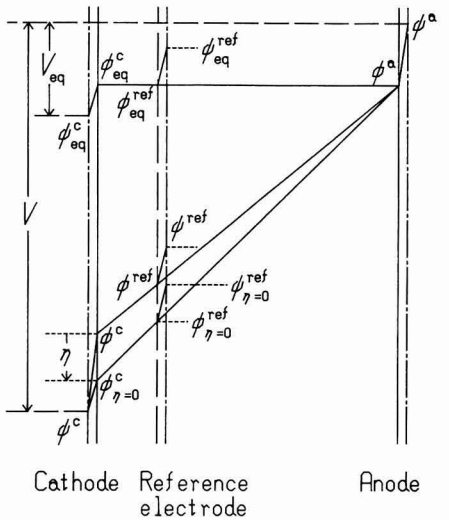

Fig. 1. Schematic diagram of variation of electrical potentials in an electrolysis cell.

cathode is equal to that under the equilibrium condition $E_{\eta=0}{}^{c} = E_{eq}{}^{c}$, *i.e.*

$$\psi^{c} - \phi_{\eta=0}{}^{c} = \psi_{eq}{}^{c} - \phi_{eq}{}^{c} \quad [7]$$

If the electrode reaction occurs at the cathode with overpotential, η, then we have

$$\eta = E^{c} - E_{\eta=0}{}^{c} = E^{c} - E_{eq}{}^{c} = (\psi^{c} - \phi^{c}) - (\psi_{eq}{}^{c} - \phi_{eq}{}^{c}) = (\psi^{c} - \psi^{a}) + (\psi^{a} - \psi_{eq}{}^{c}) + \phi_{eq}{}^{c} - \phi^{c} \quad [8]$$

In terms of Eq. [4]-[6], Eq. [8] can be rewritten as

$$\eta = -(V - V_{eq}) + \phi^{a} - \phi^{c} \quad [9]$$

As stated above, the measured or controlled electrode potential is the potential difference between the terminals of a galvanic cell composed of the working and the reference electrodes; that is, the inner potential of the working electrode against that of the reference electrode

$$(E^{c})_{m} = \psi^{c} - \psi^{ref} \quad [10]$$

Thus, the equilibrium potential of the working electrode is given by

$$(E_{eq}{}^{c})_{m} = \psi_{eq}{}^{c} - \psi_{eq}{}^{ref} = E_{eq}{}^{c} - E^{ref} \quad [11]$$

The IR-potential drop, ΔV_{IR}, due to the solution resistance can be given as the difference between the measured potential of the working electrode when current flows without any overpotential and that at equilibrium

$$-\Delta V_{IR} = (E_{\eta=0}{}^{c})_{m} - (E_{eq}{}^{c})_{m} \quad [12]$$

where ΔV_{IR} is taken to be positive. Equation [12] can be written as

$$-\Delta V_{IR} = (\psi^{c} - \psi_{\eta=0}{}^{ref}) - (E_{eq}{}^{c} - E^{ref}) = \psi^{c} - \phi_{\eta=0}{}^{c} + \phi_{\eta=0}{}^{ref} - \psi_{\eta=0}{}^{ref} - (E_{eq}{}^{c} - E^{ref}) + \phi_{\eta=0}{}^{c} - \phi_{\eta=0}{}^{ref} = \phi_{\eta=0}{}^{c} - \phi_{\eta=0}{}^{ref} \quad [13]$$

where the last expression is obvious from Fig. 1. On the other hand, the measurable overpotential is given by

$$(\eta)_{m} = (E^{c})_{m} - (E_{eq}{}^{c})_{m} = \psi^{c} - \psi^{ref} - (\psi_{eq}{}^{c} - \psi_{eq}{}^{ref}) = (\psi^{a} - \psi_{eq}{}^{c}) - (\psi^{a} - \psi^{c}) + (\psi_{eq}{}^{ref} - \psi^{ref}) = -(V - V_{eq}) + (\phi^{a} - \phi^{ref}) \quad [14]$$

The electrolytic cell model.—Figure 2 shows the schematic diagram of the axisymmetric cylindrical cell together with the cylindrical coordinates employed for the analysis. The cathode (working electrode) and the anode, facing each other, are located in the planes $z = 0$ and $z = 25r_0$, respectively, where r_0 denotes the outer radius of the Luggin capillary. The cell has a cylindrical insulator wall at $r = 15r_0$. The following two cases are treated: (*i*) the Luggin capillary is placed in front of the cathode, the tip of the capillary is at $z = d$, and (*ii*) the capillary is placed through the back of the cathode, its tip being flush with the front surface of the cathode. In either case, z-axis is taken as the center axis of the capillary. Although the choice of the distance between the cathode and the anode ($25r_0$) and the position of the insulator wall ($15r_0$) is arbitrary, these are chosen so that the presence of the capillary does not affect the potential or current distributions in the vicinities of the anode or the insulator wall. It has been confirmed that the use of the values larger than $25r_0$ and $15r_0$ has little effect on the calculated results.

The boundary value problem.—Inner potential in the solution satisfies the Laplace equation

$$\nabla^{2}\phi = \partial^{2}\phi/\partial r^{2} + r^{-1}\partial\phi/\partial r + \partial^{2}\phi/\partial z^{2} = 0 \quad [15]$$

The boundary conditions are as follows: at anode (Γ^{a})

$$\phi = \phi^{a} \quad [16]$$

at cathode (Γ^{c})

$$\phi = 0 \quad [17]$$

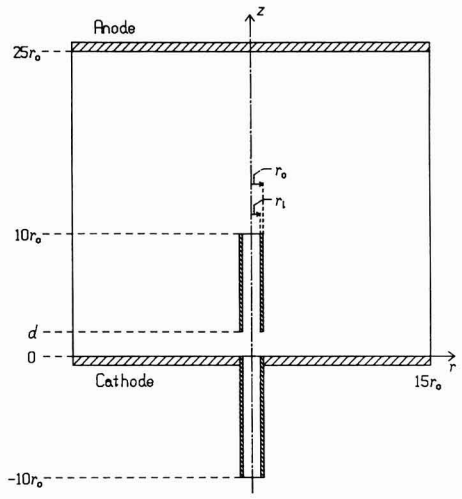

Fig. 2. Schematic diagram of axisymmetric cylindrical model cell and the cylindrical coordinates employed for the analysis. The Lugging-Haber capillary is placed along the center axis either in front of the cathode or through the back of the cathode.

when there is no overpotential, or

$$f(\phi_{re}, [\partial\phi/\partial n]_{re}) = 0 \quad [18]$$

when there is overpotential, and at insulator surface or symmetric axis (Γ^{i})

$$\partial\phi/\partial n = 0 \quad [19]$$

where n is the outward normal and the function f defines the potential-current density relationship.

In this paper, we assume that the overpotential is given as a linear function of current density (29)

$$\eta = \eta_0 + hj \quad [20]$$

where η_0 and h are constants. Although, in general, such a relation does not hold over a wide range of current densities, this approximation may be adequate so far as the current densities do not deviate too much from the average current density. Since the current density at the cathode is given by

$$j = -\kappa(\partial\phi/\partial z)_{z=0} \quad [21]$$

where the sign of cathodic current is taken to be negative and κ is conductivity of the solution, we have in place of Eq. [18]

$$\eta = \eta_0 - h\kappa(\partial\phi/\partial z)_{z=0} \quad [22]$$

or, by the use of Eq. [9]

$$\phi^{a} - \phi^{c} - (V - V_{eq}) = \eta_0 - h\kappa(\partial\phi/\partial z)_{z=0} \quad [23]$$

With the transformation of the variables

$$\Phi = \Phi^{a}[1 - (\phi^{a} - \phi)/(V - V_{eq} + \eta_0)] \quad [24]$$

$$R = r/r_0 \quad [25]$$

$$Z = z/r_0 \quad [26]$$

and

$$n^{*} = n/r_0 \quad [27]$$

our boundary value problem is given as

$$\partial^{2}\Phi/\partial R^{2} + R^{-1}\partial\Phi/\partial R + \partial^{2}\Phi/\partial Z^{2} = 0 \quad [28]$$

at Γ^{a}

$$\Phi = \Phi^{a} \quad [29]$$

at Γ^e

$$\Phi = 0 \text{ or } \Phi = (h\kappa/r_0)(\partial\Phi/\partial Z) \quad [30]$$

at Γ^i

$$\partial\Phi/\partial n^* = 0 \quad [31]$$

The FEM representation of the problem.—Now divide the domain Ω to be analyzed into a number of finite elements and let the potential Φ at any point within a finite element (e) be approximated by

$$\Phi = [N^{(e)}]\{\Phi^{(e)}\} \quad [32]$$

where $[N^{(e)}]$ is a row vector of interpolation (or shape) function of element (e), and $\{\Phi^{(e)}\}$ is a column vector composed of nodal values. Using $[N^{(e)}]$ as weighting functions, applying the Galerkin method to Eq. [28], we have

$$\int_\Omega [N^{(e)}]^T(\partial^2\Phi^{(e)}/\partial R^2 + R^{-1}\partial\Phi^{(e)}/\partial R + \partial^2\Phi^{(e)}/\partial Z^2)\, d\Omega = 0 \quad [33]$$

where superscript T denotes a transpose and $d\Omega = Rd\theta dRdZ$ because of axisymmetry. Performing the integration in Eq. [33] by parts and using the Green Gauss theorem yields local finite-element equations

$$[k^{(e)}]\{\Phi^{(e)}\} = \{f^{(e)}\} \quad [34]$$

where

$$[k^{(e)}] = 2\pi\int_{\Omega^e} \{(\partial[N^{(e)}]^T/\partial R)(\partial[N^{(e)}]/\partial R) + (\partial[N^{(e)}]^T/\partial Z)(\partial[N^{(e)}]/\partial Z)\}RdRdZ + 2\pi(r_0/h\kappa)\int_{\Gamma^e}[N^{(e)}]^T[N^{(e)}]RdR \quad [35]$$

$$\{f^{(e)}\} = 2\pi\int_{(\Gamma^e+\Gamma^a)}[N^{(e)}]^T(\partial[N^{(e)}]/\partial Z)RdR \quad [36]$$

In the derivation of Eq. [35] and [36], boundary conditions [30] and [31] have been taken into account. The global finite-element equations are obtained by assembling the contributions of each element equation

$$[K]\{\Phi\} = \{F\} \quad [37]$$

where

$$\{\Phi\} = \sum_e \{\Phi^{(e)}\};\ [K] = \sum_e [k^{(e)}];\ \{F\} = \sum_e \{f^{(e)}\} \quad [38]$$

Procedure of computation.—Since our problem is axisymmetric, the region Ω was divided into a number of ring elements obtained by revolving quadrilaterals. Quadratic elements were employed. Division of Ω into isoparametric quadratic quadrilateral elements and numbering of nodes were carried out semiautomatically by use of a FORTRAN program which is a modified version of one proposed by Cohen (30). The region Ω was usually divided into *ca.* 200 elements and thus had 1000 ~ 1200 nodes. Automatic renumbering of nodes was employed to minimize the bandwidth of the global matrix $[K]$ (31). Examples of the parts of element grid thus divided are shown in Fig. 3 and 7. The region where sharp potential change is considered to occur was divided into smaller elements than other region. It is well known that the boundary between the electrode and the insulator wall (*e.g.*, the point at $Z = 0$ and $R = 1$ in Fig. 7) is a mathematical singular boundary where the derivative of potential is discontinuous. For the elements including such a singular point, singular elements introduced by Henshell and Shaw were employed (32). The global matrix was assembled by the stiffness method and then altered according to the boundary conditions given by Eq. [29] and [30]. The set of simultaneous equations was solved by the Gauss elimination method.

Calculations were carried out for various values of parameters, r_i/r_0 (0.0 ~ 1.0), d/r_0 (0.1 ~ 4.0), and $h\kappa/r_0$ (0.0 ~ 20.0). Φ^a was taken to be 25.0.

Results and Discussion

Primary potential distribution and the IR potential drop.—Figure 4 shows, as an example, the potential distribution around the Luggin-Haber capillary calculated for geometry $d/r_0 = 0.5$ and $r_i/r_0 = 0.75$ based on the element grid, part of which is shown in Fig. 3, and for $h = 0$ and $\eta_0 = 0$, *i.e.*, when there is no overpotential. It can be seen that the presence of the capillary causes distortion of equipotential surfaces only in the vicinity of the capillary tip and that the potential distribution in the solution region farther than $2r_0$ from the capillary tip is almost equal to that in the absence of the capillary. The value of potential in the capillary becomes constant in the region about

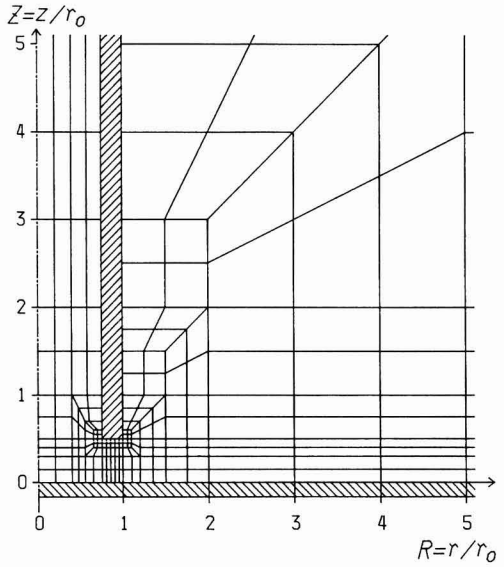

Fig. 3. Example of quadrilateral element grid used in the analysis for the geometry $d/r_0 = 0.5$ and $r_i/r_0 = 0.75$. Shaded part for $Z \geq 0.5$ indicates the cross section of the capillary wall, and that for $Z \leq 0$ denotes the cathode.

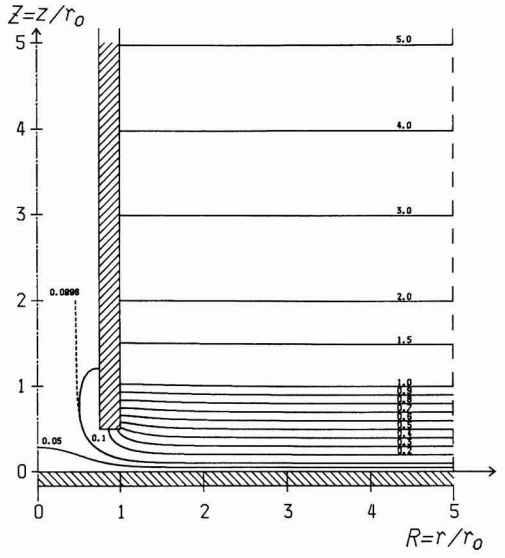

Fig. 4. Primary potential distribution around the capillary tip for the electrode geometry shown in Fig. 3. Numerals on the curves indicate values of function Φ.

$2r_0$ inside from the tip. The difference between this potential and that of the working electrode surface corresponds to the IR-drop involved in the measured electrode potential. Although the equipotential surfaces in Fig. 4 are given not in ϕ but in Φ, it can be seen from Eq. [24] that the real potential distribution is similar to that in Fig. 4.

The current density at the cathode is given by Eq. [21]. By use of Eq. [21], [24], and [26] and condition $\eta_0 = 0$, we have

$$j = -(V - V_{eq})(\kappa/r_0\Phi^a)(\partial\Phi/\partial Z)_{Z=0} \quad [39]$$

Thus the current density at the place sufficiently remote from the capillary is given by

$$j^\infty = -(V - V_{eq})(\kappa/r_0\Phi^a)(\partial\Phi/\partial Z)_{Z=0,R\to\infty} \quad [40]$$

Then we have

$$j/j^\infty = (\partial\Phi/\partial Z)_{Z=0}/(\partial\Phi/\partial Z)_{Z=0,R\to\infty} \quad [41]$$

Variations of relative current distribution j/j^∞ near the capillary tip with the distance from the center axis are shown in Fig. 5 for $r_i/r_0 = 0.75$ when d/r_0 is changed. As a matter of fact, one can see that the more remotely the capillary tip is placed from the electrode surface, the less distortion of the current distribution there is. This figure also reveals that only the part of the electrode just below the capillary tip is shielded and that the current density becomes almost uniform in the region $r \geq 3r_0$. In addition, it has been found that the thinner the capillary wall, the less the distortion of the current distribution, although this is not shown in the figure.

Now we consider the IR-potential drop, ΔV_{IR}, due to the solution resistance under the effect of the presence of the capillary. This can be given by Eq. [13]. Eliminating ϕ from Eq. [13] and [24] and using the condition, $\Phi_{\eta=0}{}^c = 0$ yields

$$\Delta V_{IR} = (V - V_{eq})\Phi_{\eta=0}{}^{ref}/\Phi^a \quad [42]$$

Dividing Eq. [42] by Eq. [40] and rearranging the resulting equation gives

$$\Delta V_{IR} = (-j^\infty r_0/\kappa)\Phi_{\eta=0}{}^{ref}/(\partial\Phi/\partial Z)_{Z=0,R\to\infty} \quad [43]$$

Values of $(-\kappa/r_0 j^\infty)\Delta V_{IR}$ are plotted in Fig. 6 against d/r_0 for several values of r_i/r_0. The straight dot-dashed line corresponds to the uniform potential distribution when there is no capillary. It can be seen from Fig. 6 that the IR-potential drop measured with the capillary is a function of both d/r_0 and r_i/r_0 and that when d/r_0 is larger than 2, the measured value of ΔV_{IR} is smaller by a constant value than the value which would be observed in the absence of the capillary. We tried to express this dependence of ΔV_{IR}

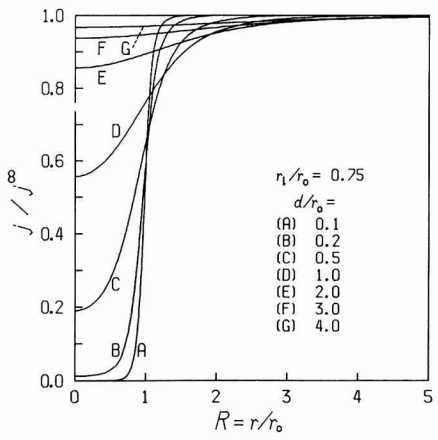

Fig. 5. Effect of the distance between the capillary tip and the cathode on the relative primary current density distribution at the cathode near the capillary tip.

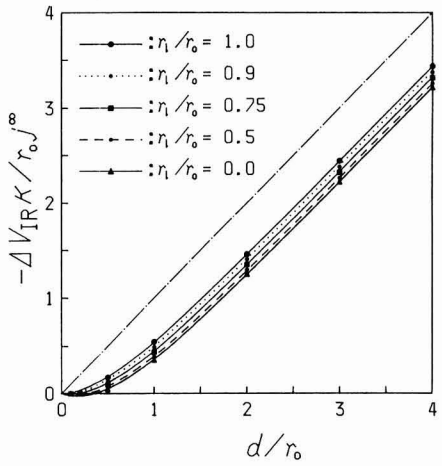

Fig. 6. Dependence of IR-potential drop measured with Luggin-Haber capillary on the distance between capillary tip and the cathode and on the thickness of capillary wall.

on d/r_0 and r_i/r_0 in terms of elementary functions and obtained the following approximate equation with reasonable accuracy

$$\Delta V_{IR} = (-j^\infty/\kappa)[d - r_0\sigma\{1 - 0.1898\exp(-1.51d/r_0) - 0.8102\exp(-1.757d/r_0)\}] \quad [44]$$

where σ is a function of r_i/r_0 given by

$$\sigma = 0.780\{1 - 0.01896(r_i/r_0) - 0.08812(r_i/r_0)^2 - 0.1739(r_i/r_0)^3\} \quad [45]$$

The curved lines in Fig. 6 are those calculated from Eq. [44] and [45]. Equation [45] indicates that the effect of the thickness of the capillary wall is rather small since the value of σ changes only from 0.78 to 0.56 when r_i is changed from 0 to r_0. If the value of d/r_0 exceeds 2.8, then the exponential terms in Eq. [44] are negligible within an error of 1%, and hence Eq. [44] reduces to

$$\Delta V_{IR} = (-j^\infty/\kappa)(d - r_0\sigma) \quad [46]$$

Barnartt (3) proposed 2/3 as a value of σ for $d/r_0 \geq 4$ from his experiment using a model capillary of $r_i/r_0 = 2/3$. Introducing this value into Eq. [45] yields $\sigma = 0.699$, which is 5% higher than the value 2/3 proposed by Barnartt. It can be said that these values are in good agreement if we consider that the experimental value might have some contribution of polarization. Piontelli *et al.* (2) concluded from the experiment with capillaries of varied wall thickness from $r_i/r_0 = 0.08$-1 that $\sigma = 0.6$ for $d/r_0 \geq 6$ and that the approximate equation can be used practically even for $d/r_0 \geq 2$. They also demonstrated that σ is dependent on the ratio r_i/r_0 and varies from 0.714 to 0.476 when r_i/r_0 changes from 0.08 to 1 for $d/r_0 >> 1$. The discrepancy between these values and those calculated from Eq. [45] may result from their semicylindrical model cell, the diameter of which is 200 mm, being too small for the model capillary of 63 mm diam.

The primary potential and current distributions were also calculated for the electrode geometry where the capillary is placed through the back of the working electrode. Figure 7 shows an example of the element grid for the geometry $r_i/r_0 = 0.75$ employed in the FEM calculation. The primary potential distribution is depicted in Fig. 8, which reveals that the equipotential surfaces are almost parallel to the cathode surface if $r \leq 2r_0$ or $z \leq 2.5r_0$. The potential measured by the Luggin-Haber capillary depends on the inner radius of the capillary; the thinner the capillary wall, the higher the measured potential value. The relative primary current density distribution at such an elec-

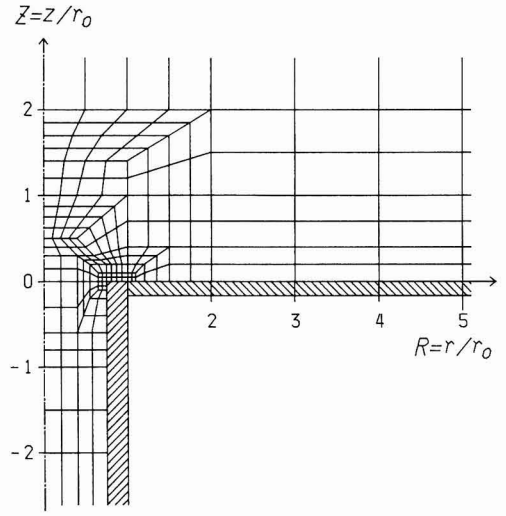

Fig. 7. Part of the quadrilateral element grid used in the analysis for the electrode geometry where the capillary is placed through the back of the cathode. r_i/r_o = 0.75. Shaded part for $0.5 \leq R \leq 1.0$ indicates the cross section of the capillary, and that for $R \geq 1.0$ does the cathode.

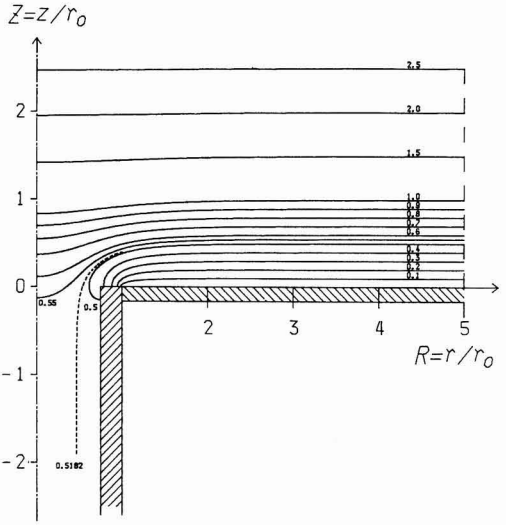

Fig. 8. Primary potential distribution around the capillary tip for the electrode geometry shown in Fig. 7. Numerals on the curves indicate values of function Φ.

trode geometry is shown in Fig. 9. It will be seen that the current density becomes infinity at the boundary between the cathode and the Luggin-Haber capillary wall. Variation of the IR-potential drop calculated from Eq. [41] with the ratio r_i/r_o is depicted in Fig. 10. It was found that the potential drop ΔV_{IR} can be approximated as a function of r_i/r_o by

$$\Delta V_{IR}(\kappa/r_o|j^\infty|) = 0.64 \exp[-0.018(r_i/r_o) - 0.159(r_i/r_o)^2 - 0.24(r_i/r_o)^3] - 0.082(r_i/r_o)^{10} \quad [47]$$

This equation is valid within an error of 0.01 or a relative error of 2.2%.

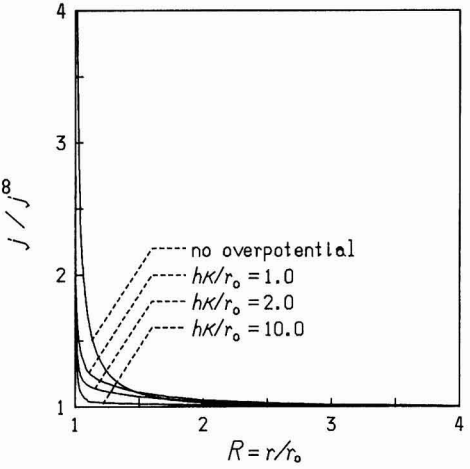

Fig. 9. Relative primary and secondary current density distributions at the cathode for the geometry shown in Fig. 7.

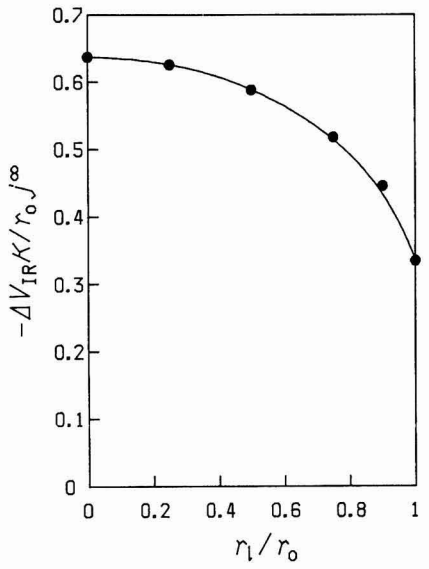

Fig. 10. IR-potential drop measured with the capillary placed through the back of the electrode as a function of r_i/r_o.

Secondary potential distribution and overpotential measured by Luggin-Haber capillary.—In the presence of overpotential, the electrode potential of the cathode is a function of position or $R = r/r_o$. On the assumption of the linear relation between the overpotential and the current density given by Eq. [22], we can use a quantity $h\kappa/r_o$ as a single parameter expressing the effect of overpotential on the potential distribution in the electrolytic cell as can be seen from the foregoing derivation in the Theoretical section. The parameter is known as the Wagner number (12), and is defined by

$$\mathrm{Wa} = (d\eta/dj)(\kappa/L) = h\kappa/r_o \quad [48]$$

where L is the characteristic length and is taken to be equal to r_o. If the current density-overpotential relation is given by the Tafel equation and is approximated by the linear relation [20], then h is given by b/j^∞, where b is the Tafel coefficient.

The potential distributions for the electrode geometries shown in Fig. 3 and 7 are depicted in Fig. 11 and 12, respectively, for $h\kappa/r_0 = 1.0$. Contrary to the case in the absence of overpotential shown in Fig. 4 and 8, the potential at the cathode surface is a function of position in the presence of overpotential, which is manifested in Fig. 11 and 12 by the equipotential surfaces intersecting with the cathode surface. One can see, however, that the distortion of equipotential surfaces are confined only to the region close to the capillary tip. Current density in the presence of overpotential is written in terms of Φ by

$$j = -(V - V_{eq} + \eta_0)(\kappa/r_0\Phi^a)(\partial\Phi/\partial Z)_{Z=0} \quad [49]$$

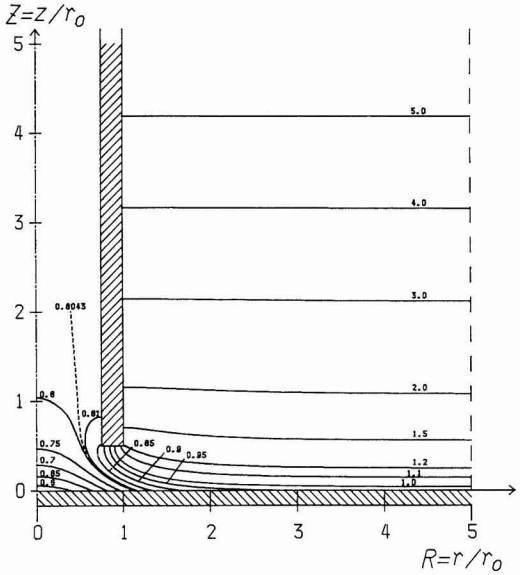

Fig. 11. Secondary potential distribution around the capillary tip for the electrode geometry shown in Fig. 3 for $h\kappa/r_0 = 1.0$. Numerals on the curves show values of function Φ.

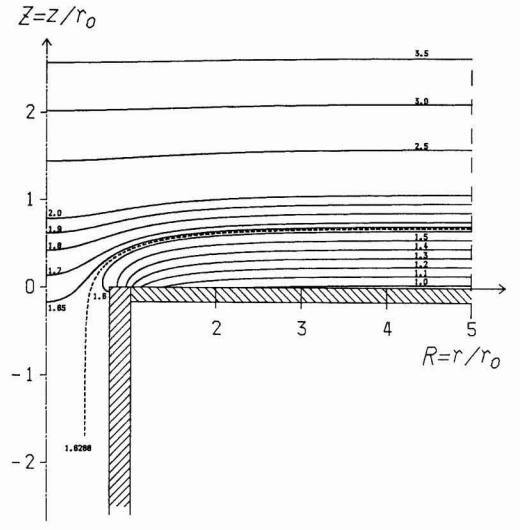

Fig. 12. Secondary potential distribution around the capillary tip for the electrode geometry shown in Fig. 7 for $h\kappa/r_0 = 1.0$. Numerals on the curves show values of function Φ.

The relative current density distribution is calculated from Eq. [41] which is also obtained from Eq. [49] or directly from

$$j/j^\infty = \Phi_{Z=0}/\Phi_{Z=0,R\to\infty} \quad [50]$$

This equation is obtained from Eq. [41] and [30]. In Fig. 13, variations of the relative current density distribution with the distance from the center axis are shown for the geometry of $r_1/r_0 = 0.75$ and $d/r_0 = 1.0$ and for the various values of the Wagner number $h\kappa/r_0$. For the electrode geometry depicted in Fig. 7, the effect of $h\kappa/r_0$ on the current density distribution is shown in Fig. 9. Figures 13 and 9 indicate that the more uniform current density distribution is obtained as the $h\kappa/r_0$ value becomes higher, *i.e.*, the higher the overpotential or the conductivity of the solution, and that the presence of the capillary has little effect on the current density distribution of the electrode region $r \geq 3r_0$.

Evaluation of true overpotential.—It is of interest to examine the significance of the measured overpotential, $(\eta)_m$. We have, from Eq. [14], [24], and [49]

$$(\eta)_m = \eta_0 + (j^\infty r_0/\kappa)\Phi^{ref}/(\partial\Phi/\partial Z)_{Z=0,R\to\infty} \quad [51]$$

From Eq. [51] and [43] it follows

$$(\kappa/j^\infty r_0)\{(\eta)_m + \Delta V_{IR} - \eta_0\} = \Phi^{ref}/(\partial\Phi/\partial Z)_{Z=0,R\to\infty} - \Phi_{\eta=0}{}^{ref}/(\partial\Phi/\partial Z)_{Z=0,R\to\infty} \quad [52]$$

Values of $(\kappa/j^\infty r_0)\{(\eta)_m + \Delta V_{IR} - \eta_0\}$ calculated from the right-hand side of Eq. [52] are plotted against $h\kappa/r_0$ in Fig. 14 for varied values of d/r_0. One can see the plot is almost linear and has unity slope when $d/r_0 \geq 2$. We tried to find an approximate equation which expresses the term $\{(\eta)_m - (\eta_0 + hj^\infty) + \Delta V_{IR}\}$ as a simple function of $h\kappa/r_0$ and obtained the following relation

$$(\eta)_m = (\eta_0 + hj^\infty) - \Delta V_{IR} - (j^\infty r_0/\kappa)\{c_1(h\kappa/r_0)/(c_2 + h\kappa/r_0)\} \quad [53]$$

where c_1 and c_2 are coefficients which depend on d/r_0 and r_1/r_0 and can be expressed by

$$c_1 = 0.402 \exp[-0.709(d/r_0)] + [2.5 - 1.3(r_1/r_0)] \exp[-2.8(d/r_0)] \quad [54]$$

and

$$c_2 = -0.963 + 2.93(d/r_0)^{0.278} \quad [55]$$

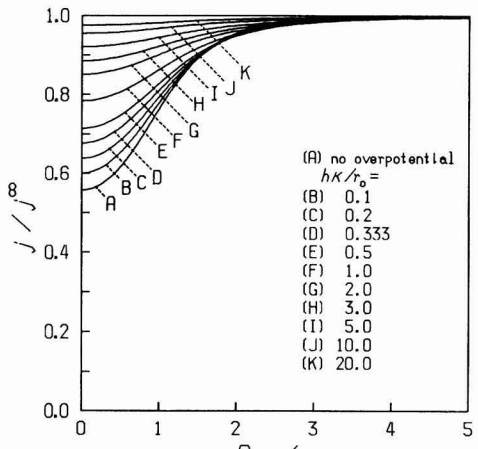

Fig. 13. Dependence of relative current density distribution around the capillary tip upon the parameter $h\kappa/r_0$ for the electrode geometry of $r_1/r_0 = 0.75$ and $d/r_0 = 1.0$. Curve A is identical with curve D in Fig. 5.

respectively. Equations [53]-[55] are valid for $d/r_0 \geq 0.5$ and $0.5 \leq r_1/r_0 < 1.0$ within the relative error of 2%. Although the error involved in Eq. [53]-[55] becomes larger for values of d/r_0 less than 0.5 and these equations cannot be used, it is not recommended that one place the tip of the Luggin-Haber capillary closer than $0.5r_0$ from the electrode surface as will be seen from the discussion below. Figure 15 shows the plots of $(\kappa/r_0 j^\infty)\{(\eta)_m - (\eta_0 + hj^\infty) + \Delta V_{IR}\}$, which is equivalent to $-c_1(h\kappa/r_0)/(c_2 + h\kappa/r_0)$, against d/r_0 for three values of $h\kappa/r_0$. One can see from Eq. [54] that the values of c_1 are small when $d/r_0 \geq 2$, and also see from Fig. 15 that the values of $-(\kappa/r_0 j^\infty)\{(\eta)_m - (\eta_0 + hj^\infty) + \Delta V_{IR}\}$ are very small irrespective of the value of $h\kappa/r_0$ when $d/r_0 \geq 2$. It has also been found that values of $(\kappa/r_0 j^\infty)\{(\eta)_m - (\eta_0 + hj^\infty) + \Delta V_{IR}\}$ scarcely depend on r_1/r_0. These facts indicate that the last term on the right-hand side of Eq. [53] can be neglected and the following approximate equation

$$(\eta)_m = (\eta_0 + hj^\infty) - \Delta V_{IR} \quad [56]$$

is valid under the condition $d \geq 2r_0$. This means that as far as the distance between the capillary tip and the electrode surface is larger than the outer diameter of the capillary tip, the measured overpotential can be regarded as a sum of the true overpotential $(\eta_0 + hj^\infty)$ and the potential drop due to the solution resistance, $(-\Delta V_{IR})$. In other words, if the capillary tip is located at a distance from the electrode surface closer than its diameter, the effect of the shielding of the electrode surface by the capillary can no more be neglected. One can see from Fig. 15 that the measured overpotential is always equal to or larger than the sum of the true overpotential and the IR-potential drop.

For the electrode geometry where the capillary is placed through the back of cathode, Fig. 16 shows plots similar to those in Fig. 14 and 15. It has been established that the following approximate equation holds

$$(\eta)_m = (\eta_0 + hj^\infty) - \Delta V_{IR} + (j^\infty r_0/\kappa)[c_3(h\kappa/r_0)^p/\{c_4 + (h\kappa/r_0)^p\}] \quad [57]$$

where c_3, c_4, and p are coefficients which are functions of r_1/r_0. We obtained simple approximate equations for these coefficients

$$c_3 = 0.338 + 0.0691(r_1/r_0)^4 + 0.0377(r_1/r_0)^8 \quad [58]$$

$$c_4 = 1.138 + 0.229(r_1/r_0)^4 - 0.633(r_1/r_0)^8 \quad [59]$$

$$p = 0.719 - 0.0281(r_1/r_0) \quad [60]$$

Using Eq. [57]-[60], $(\eta)_m$ can be calculated within 3% relative error. Although there occurs no shielding of the electrode surface in this case, one can note that the absolute value of the measured potential is always larger than the sum of the values of true overpotential and the IR-potential drop, It can be said that although this electrode geometry looks sophisticated, it is not recommended for practical use in view of the above fact and the difficulty in fabrication except for the case where the disturbance of electrolyte solution flow due to the presence of the Luggin-Haber capillary should be avoided.

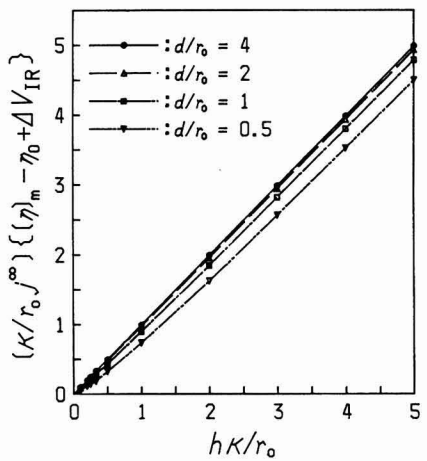

Fig. 14. Variation of the difference between the measured overpotential and IR-potential drop with the value of the parameter $h\kappa/r_0$ for the electrode geometries of $r_1/r_0 = 0.75$ and varied values of d/r_0.

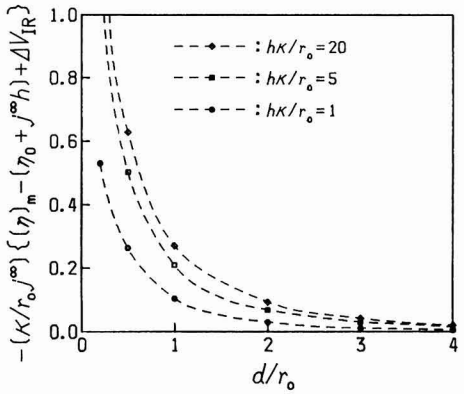

Fig. 15. Dependence of the difference between the measured overpotential and the sum of true overpotential and IR-potential drop on the position of the capillary tip.

Conclusion

Potential and current distributions around the Luggin-Haber capillary placed perpendicularly to the plane electrode surface have been obtained by solving Laplace equation with a finite element method. Approximate equations with reasonable accuracy have been presented for the IR-potential drop as functions of the outer and inner radii of the capillary tip, distance between the capillary tip and the working electrode, conductivity of the solution, and average current density. Approximate equations which relate the measured overpotential to the true overpotential, the IR-potential drop, and the relevant parameters have also been presented. In the presence of overpotential, it has been confirmed that the measured potential can be regarded as a sum of the true overpoten-

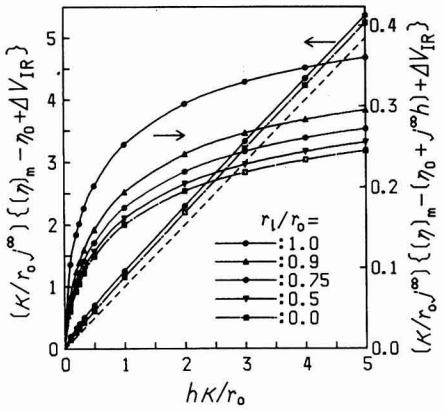

Fig. 16. Plots of the difference between the measured overpotential and IR-potential drop, and the difference between the measured overpotential and the sum of true overpotential and IR-potential drop against the parameter $h\kappa/r_0$ for the electrode geometry where the Luggin capillary is placed through the back of the electrode.

tial and the IR-potential drop provided that the tip of the capillary is placed not closer from the electrode surface than the distance equal to the diameter of the capillary tip.

Manuscript submitted Dec. 26, 1984; revised manuscript received *ca.* March 28, 1985.

Tokyo Institute of Technology assisted in meeting the publication costs of this article.

LIST OF SYMBOLS

c_1, c_2, c_3, c_4 coefficients in Eq. [53] and [57]
d distance between the capillary tip and the cathode (m)
E electrode potential (V)
$\{f^{(e)}\}$ element flux vector
$\{F\}$ global flux vector
h constant (see Eq. [18]) (Ω-m^2)
j current density (A-m^{-2})
j^{∞} current density at the place sufficiently distant from the capillary (A-m^{-2})
$[k^{(e)}]$ element coefficient matrix
$[K]$ global coefficient matrix
L characteristic length (m)
n normal boundary coordinate (m)
n^* transformed normal boundary coordinate
$[N^{(e)}]$ row matrix of interpolation functions
p coefficient in Eq. [57]
r radial coordinate (m)
r_i inner radius of the Luggin-Haber capillary (m)
r_o outer radius of the Luggin-Haber capillary (m)
R transformed radial coordinate
V cell voltage (V)
ΔV_{IR} IR-potential drop (V)
Wa Wagner number
z axial coordinate (m)
Z transformed axial coordinate

Greek characters

Γ boundary or surface of the region analyzed
η overpotential (V)
η_0 constant (see Eq. [18]) (V)
θ angular coordinate
κ conductivity of solution (S-m^{-1})
ϕ inner potential of solution (V)
Φ transformed potential function
ψ inner potential of electrode (V)
Ω region to be analyzed

Superscripts

a anode
c cathode
(e) element
i insulator
ref reference electrode
T transpose of matrix

Subscripts

eq at equilibrium
$\eta=0$ without overpotential
m measured or measurable

REFERENCES

1. R. Piontelli, G. Bianchi, and R. Aletti, *Z. Elektrochem.*, **56,** 86 (1952).
2. R. Piontelli, G. Bianchi, U. Bertocci, C. Guerci, and B. Rivolta, *ibid.*, **58,** 54 (1954).
3. S. Barnartt, *This Journal*, **99,** 549 (1952).
4. S. Barnartt, *ibid.*, **108,** 102 (1961).
5. C. Kasper, *Trans. Electrochem. Soc.*, **77,** 353 (1940); *ibid.*, **78,** 131 (1940); *ibid.*, **82,** 153 (1942).
6. C. Wagner, *Plating*, **48,** 997 (1961).
7. S. Ishizaka and H. Matsuda, *Denki Kagaku*, **19,** 89 (1951); *ibid.*, **20,** 38 (1952); *ibid.*, **20,** 84 (1952); *ibid.*, **22,** 420 (1954).
8. F. Hine, S. Yoshizawa, and S. Okada, *This Journal*, **103,** 186 (1959).
9. J. Newman, *ibid.*, **113,** 501, 1235 (1966).
10. J. Newman, in "Electroanalytical Chemistry," Vol. 6, A. J. Bard, Editor, p. 187, Marcel Dekker, New York (1973).
11. J. Newman, "Electrochemical Systems," Chap. 18, Prentice-Hall, Englewood Cliffs, NJ (1973).
12. N. Ibl, in "Comprehensive Treatise of Electrochemistry," Vol. 6, E. Yeager, J. O'M. Bockris, B. E. Conway, and S. Sarangapani, Editors, Chap. 4, Plenum Press, New York (1983).
13. J. A. Klingert, S. Lynn, and C. W. Tobias, *Electrochim. Acta*, **9,** 297 (1964).
14. P. Pierini and J. Newman, *This Journal*, **126,** 1348 (1979).
15. P. Fedkiw, *ibid.*, **127,** 1304 (1980).
16. R. Caban and T. W. Chapman, *ibid.*, **123,** 1036 (1976).
17. S. H. Glarum, *ibid.*, **124,** 518 (1977).
18. O. C. Zienkiewich, "The Finite Element Method," McGraw-Hill (UK), London (1977).
19. L. J. Segerlind, "Applied Finite Element Analysis," John Wiley and Sons, New York (1976).
20. T. J. Chung, "Finite Element Analysis in Fluid Dynamics," McGraw-Hill, New York (1978).
21. Y. Fujitani, T. Kihara, K. Honda, and T. Kawai, *Seisan Kenkyu*, **24,** 248 (1972).
22. K. Honda, T. Kihara, T. Watanabe, T. Kawai, Y. Fujitani, and S. Shiina, *ibid.*, **24,** 410 (1972).
23. T. Kawai, Y. Fujitani, K. Honda, T. Kihara, and T. Watanabe, *ibid.*, **25,** 113 (1973).
24. R. Alkire, T. Bergh, and R. L. Sani, *This Journal*, **125,** 1981 (1978).
25. R. Sautebin, H. Froidevaux, and D. Landolt, *ibid.*, **127.** 1096 (1980).
26. Y. Nishiki, K. Aoki, K. Tokuda, and H. Matsuda, *J. Appl. Electrochem.*, **14,** 653 (1984).
27. K. Aoki, K. Tokuda, H. Matsuda, and N. Oyama, *J. Electroanal. Chem.*, **176,** 139 (1984).
28. T. Gueshi, K. Tokuda, and H. Matsuda, *Denki Kagaku*, **51,** 107 (1983).
29. C. Wagner, *This Journal*, **98,** 116 (1951).
30. H. D. Cohen, *Int. J. Num. Meth. Eng.*, **15,** 470 (1980).
31. R. J. Collins, *ibid.*, **6,** 345 (1973).
32. R. D. Henshell and K. G. Show, *ibid.*, **11,** 180 (1977).

Electrochemistry of Molten Calcium Nitrate Tetrahydrate

Keith E. Johnson* and F. Wayne Yerhoff

Department of Chemistry, University of Regina, Regina, Saskatchewan, Canada S4S 0A2

ABSTRACT

The electrochemical properties of calcium nitrate tetrahydrate were studied by voltammetry, coulometry, and chemical analysis. The electrolyte anode reaction was oxidation of water to oxygen on either gold or platinum. The major reaction at a gold cathode was reduction of nitrate to nitrite and a solid calcium hydroxide electrode film. Small amounts of oxygen and more than the theoretically predicted quantity of nitrite were detected, suggesting a secondary chemical reaction. The reduction reaction at platinum gave 50-75% of the theoretical yield of nitrite. The voltammetric behavior of OH^-, NO_2, and HNO_3 in this system were studied.

Molten calcium nitrate tetrahydrate and similar molten hydrates are of considerable interest as solvents with properties intermediate between those of aqueous solutions and ionic melts. Conductance measurements (1), additivity of molar volumes (2), PMR studies (3), entropies of solution (4), diffusion coefficients [(5, 6) but see Ref. (7)], acoustic velocity measurements (8), and x-ray diffraction measurements (9) all indicate that the water molecules in calcium nitrate tetrahydrate melts are strongly coordinated to the calcium ion. The result is a liquid with the properties of an ionic melt composed of bulky $(Ca(H_2O)_4)^{+2}$ cations and nitrate anions. The low melting point of this compound (42.7°C), together with a metastable supercooled phase extending to room temperature, thus allows the direct comparison of an "ionic" solvent with dilute aqueous solutions.

Calcium nitrate tetrahydrate has been used as a supporting electrolyte in the electrochemical investigation of a number of cations (5-7, 10-15). Courgnaud and Tremillion (16) have investigated the electrochemistry of the molten hydrate itself at gold and platinum electrodes using bulk electrolysis followed by chemical analysis and single sweep voltammetry. The anode reaction was found to give oxygen and protons, as expected for water electrolysis, but at a potential almost 0.7V more negative for Au than for Pt. The authors concluded, on the basis of their finding no detectable concentration of nitrite ion after electrolysis with a platinum cathode, that the electrolytic reduction of this melt also involved only water. Like the anode reaction, reduction appeared to occur at a more negative potential (by 0.3V) at gold than at platinum.

These solvent electrolysis properties, as described, appeared useful for a coal electrogasification study we had undertaken, since only water was electrolyzed and some control over initial decomposition potentials appeared to be available simply by changing electrode materials. Our preliminary results, however, did not correspond to those reported, and we therefore reexamined in detail the electrochemical properties of calcium nitrate tetrahydrate.

Experimental

Calcium nitrate tetrahydrate (Fisher certified ACS or BDH analytical reagent) was used without further purification. Dehydration *in vacuo* at room temperature, then at 150°C, gave a hydration number of 4.00 ± 0.01. Certified ACS sodium nitrite (Fisher), calcium hydroxide Fisher), and nitric acid (CIL) were also used without purification. Electrodes were of 99.999% Pt or Au (Johnson, Matthey, and Mallory) sealed in soft glass. Microelectrodes were ground to a flat surface with a Bethlehem 7a7 CW12 glass grinding wheel; electrode areas, measured by optical micrometry, were 0.018 mm^2 for Pt and 0.066 mm^2 for Au.

Cyclic voltammograms were obtained using a Metrohm E626 Polarecord and E612 VA Scanner plus a Houston Instruments RE0074 X-Y recorder. All electrochemical measurements were made relative to a 0.05*m* Ag^+/Ag in $Ca(NO_3)_2 \cdot 4H_2O$ reference electrode consisting of a 0.8 mm diam silver wire dipped in the silver ion solution contained in a narrow glass tube ending in a porous ceramic plug. This system has been shown to be well behaved in calcium nitrate tetrahydrate melts (4). The microelectrode, reference electrode, and a spiral Pt wire counterelectrode were mounted in a rubber stopper which was fitted tightly into the cell containing the solution in $Ca(NO_3)_2 \cdot 4H_2O$ to prevent loss of water. Voltammograms of electrolytes in this solvent were made first upon a weighed amount of the most concentrated solution. Weighed amounts of pure solvent were then added with thorough mixing to give the lower concentrations measured. Solutions were maintained at 70.0 ± 0.1°C using a Polyscience Polytemp bath thermostat. No inert gasses were passed through the solution once it had been confirmed that oxygen was too insoluble to be detected in this system (6, 16).

Bulk electrolysis was performed using a Fisher controlled potential electroanalyzer; current was measured using a Weston Instruments milliammeter, and total charge calculated by graphical analysis of the current-time curve. The cell was equipped with a cathode compartment, consisting of a 2.5 cm diam glass tube ending in a fine sintered glass frit, which was suspended from the rubber cell cover so as to be easily removed. After electrolysis, the cathode compartment plus the Au (16 cm^2) or Pt (19 cm^2) plate cathode was removed, rinsed off with water, dried, and weighed. The catholyte was thoroughly mixed, and then weighed samples taken for analysis. Finally, the cathode cell components were washed, dried, and weighed to give the total weight of catholyte (25-30g). After the longer electrolyses, nitrite was also detectable in the anolyte, presumably because of leakage through the fritted disk; this quantity was included in the nitrite total.

A weighed sample of electrolyzed material in aqueous solution was tested for nitrite by addition of sulfanilamide and N(1-naphythyl)-ethylenediamine dihydrochloride (Marshall's reagent), followed by comparison of the 550 nm absorption of the diazo compound thus formed with external standards. The total concentration of reducing agents formed by electrolysis was measured by adding a weighed sample of electrolyzed melt to water or cold saturated H_3BO_3 solution, adding a measured quantity of standard Ce(IV) solution sufficient to oxidize all reducing agents, and backtitrating with standard Fe(II) using "ferroin" indicator.

Gas analysis was run in cells with a sealed anode or cathode compartment connected to a "Tedlar" gas sampling bag and arranged to allow flushing of the system with purified nitrogen. Two plates were arranged to allow complete emptying of the gas bag by squeezing. The system was flushed with nitrogen, and the gas bag was emptied, after which the electrolysis was run. After electrolysis, gas was transferred from the sampling bag to a gas measuring apparatus to give the total quantity of gas produced. Gas analysis was performed using a Carle AGC-311 gas chromatograph, with a thermistor detector calibrated to allow quantitative determination of the gas composition.

* Electrochemical Society Active Member.

Results

The products of oxidation of pure calcium nitrate tetrahydrate (90°-95°C, +1.3V *vs.* Ag/Ag$^+$ reference) at a platinum anode were oxygen and nitric acid, as reported (16). The nitric acid concentration in the gases above the electrolyte was substantial, and resulted in chemical attack on the gas sampling bag used in the apparatus, as well as any rubber or tygon seals or connectors used. The measured quantity of oxygen produced in such cases was somewhat variable. In a glass apparatus plus sampling bag with relatively short contact times or in runs where the theoretical amount of $Ca(OH)_2$ had been added to neutralize HNO_3, oxygen production was 100± 5% of theoretical.

The major product of reduction at a gold cathode (90°-95°C, −1.2 to −1.3V) was nitrite, detected both by specific analysis for nitrite and by quantitative analysis for reducing agents (methods agreed within 1%). Figure 1 shows the total amount of NO_2^- as a percentage of the theoretical yield relative to the total number of coulombs passed. The amount of nitrite detected in excess of 100% (8% at 68C) was well above the total estimated error. The only significant gaseous cathode product was a small amount of oxygen observed after extensive electrolysis (100-350C), amounting to 5-10% of the theoretical nitrite value. After the most extensive electrolysis, traces of hydrogen and nitrous oxide were also detected by GC.

The major product of reduction of calcium nitrate tetrahydrate at a platinum cathode (90°-95°C, −1.2 to −1.3V) was again nitrite ion, although in considerably lower yield. Figure 1 shows nitrite produced at a Pt electrode, cleaned in concentrated nitric acid before each run, as a function of total coulombs passed. Electrodes not cleaned in a systematic manner before use gave less regular nitrite/coulomb relationships. A white, water-insoluble film was again formed on the electrode. Gas bubble formation on the electrode was sometimes observed to a slight extent. No measurable volume of gaseous products could be detected. Electrolysis under a propane atmosphere showed no significant production of nitrogen. The possibility that water was being reduced at the cathode to hydrogen, which then reacted chemically with nitrate or nitrite, was tested: no sign of reaction between hydrogen gas and calcium nitrate tetrahydrate with or without added nitrite ion could be detected after contact with stirring at 95°C for 3 days. The possibility of further reduction of nitrite ion at the electrode was also considered: no significant quantities of the gaseous reduction products NO, N_2O, or N_2 were detected by GC, nor was any trace of the characteristic color of NO_2 or the characteristic smell of NH_3 observed at any time. In two cases the catholyte was analyzed both for reducing substances [by Ce(IV)/Fe(II) redox titration] and spectrophotometrically for nitrite. The reducing capacity of the catholyte was found to be equivalent to the quantity of nitrite present, indicating that no other soluble oxidizable products of NO_3^- reduction had been formed.

Calcium nitrate tetrahydrate electrochemistry was also examined by means of linear sweep and cyclic voltammetry. Figure 2 shows full range (+2.0 to −2.5V) and partial range (+1.4 to −1.2V) cyclic voltammograms obtained for this electrolyte using both gold and platinum electrodes relative to 0.05*m* Ag$^+$/Ag in calcium nitrate tetrahydrate. Table I summarizes the peak current potentials observed, along with the reactions represented and the symbols identifying these peaks in Fig. 2. The electrolyte oxidation potentials were found to be similar (1.1-1.3V) for both Au and Pt, in contrast to the previously reported (16) difference of 0.7V. The major cathodic process was attributed, from the chemical evidence, to reduction of nitrate to nitrite with concommitant formation of an insulating film on the electrode. The apparent peak A in Fig. 2, which occurred consistently at −1.5V with both Au and Pt electrodes at 50 mV/s, was an artifact of film formation. If the reverse sweep potential was not taken above 0.7-0.8V, all current flow ceased. Increasing the sweep rate resulted in large cathodic shifts in the "peak" position as well as large increases in the maximum current.

The electrode film produced during reduction of nitrate was removed by the oxidative process giving rise to

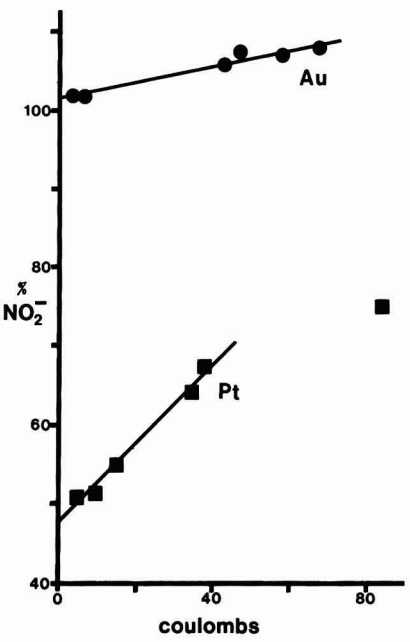

Fig. 1. Total amount of nitrite produced as a percentage of the theoretical yield by electrolysis of calcium nitrate tetrahydrate melt at 90°-95°C using a platinum (19 cm²) or a gold (16 cm²) plate cathode.

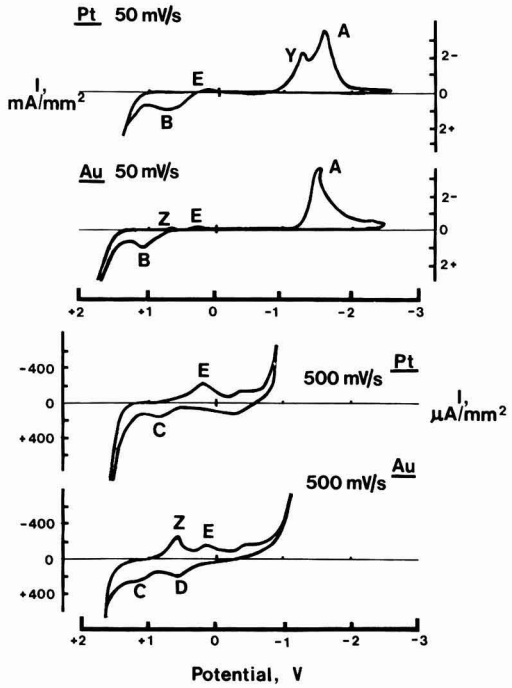

Fig. 2. Cyclic voltammograms of calcium nitrate tetrahydrate at 70.0°C using a platinum or a gold microelectrode. a: +2.0 to −2.5V b: +1.5 to −1.1V.

Table I. Cyclic voltammetry peak potential values *vs.* Ag^+/Ag for $Ca(NO_3)_2 \cdot 4H_2O$ melt

Electrode reaction	Peak potential (V) Au	Pt	$[E_p - E_p/2]$ (V) Au	Pt	Fig. 2 Symbol
Anodic sweep					
NO_2^- oxidation	+0.4	+0.5	0.15	0.15	Peak D
OH^- oxidation	+1.0	+0.9	0.10	0.14	Peak C
$Ca(OH_2)$ solid film	$\geq$ +0.9	$\geq$ +0.8	$\simeq$ 0.5	$\simeq$ 0.3	Peak B
H_2O oxidation	> +1.2	> +1.2	—	—	—
Cathodic sweep					
Oxide film reduction	+0.6	—	0.03	—	Peak Z
HNO_3 reduction	+0.1	+0.1	0.07	0.08	Peak E
Unidentified reduction	—	−1.2	—	0.1	Peak X
NO_3^- reduction	"−1.5"	"−1.5"	—	—	Peak A

anodic peak B of Fig. 2 in the area of 0.8-1.3V. This peak was not observed where the cathodic sweep did not go beyond −1.0V. The cyclic voltammogram of calcium hydroxide solution in calcium nitrate tetrahydrate between +0.5 and +1.3V showed a single broad anodic peak with no cathodic peak, rapidly decreasing on subsequent cycles. Peak voltages were similar for Au and Pt electrodes (Table II). The single sweep peak current varied linearly with concentration for both electrodes up to approximately 0.02*m*, giving lines with similar slopes. A linear relationship between peak current and the square root of scan rate was found for scan rates from 10 to 300 mV/s for both metals, with a similar slope and small negative current intercept for each. A corresponding peak (peak C, Fig. 2) is observed for pure solvent only in the limited range sweeps, where film formation is not extensive enough to block all current flow.

Voltammetry cycles between +1.3 and −1.3V in the pure melt gave rise to an additional anodic peak at approximately +0.5V on a gold electrode (peak D, Fig. 2). This was identified as the oxidation peak of nitrite ion by studies of dilute solutions of sodium nitrite. Cyclic voltammograms of such solutions showed a broad peak near +0.5V (Table II) with both Au and Pt electrodes; peak currents decreased rapidly on subsequent cycles. Both metals also gave a small shoulder about 0.2V less anodic, which disappeared on subsequent cycles. The gold electrode gave a small additional anodic peak near +0.75V. Single-sweep voltammetry anodic peak currents were shown to vary linearly with concentration for both metals (similar slopes, intercepts near 0) up to about 0.015*m* $NaNO_2$. The peak current *vs.* (sweep rate)$^{1/2}$ relationship was linear from 10 to 300 mV/s, with a small positive intercept and a slope slightly greater for Au than Pt. This relationship was also roughly linear for the small +0.75V peak on gold.

Cyclic voltammetry of $NaNO_2$ solutions with either Au or Pt gave, on the cathodic sweep, a broad cathodic peak at 0.1-0.3V, also seen in the voltammograms of pure calcium nitrate tetrahydrate (peak E, Fig. 2), and identified as characteristic of nitric acid (below). An additional sharp cathodic peak was also seen with a gold electrode (peak Z, Fig. 2), and was investigated further. Cyclic sweeps in 0.01*m* $NaNO_2$ at 100 mV/s were run from −0.2V to positive potentials beginning at +0.6V and incremented by +0.1V. The sharp cathodic peak Z was just detectable (at +0.66V) on the return from a sweep to +0.8V. The peak grew and shifted to +0.56V over the next three cycles (to +1.1V), after which it stayed approximately constant. A similar experiment run with pure calcium nitrate tetrahydrate, however, showed no trace of this peak until anodic sweeps to 1.3-1.4V were run, *i.e.*, until some nitric acid had been generated by solvent electrolysis. In addition, cycles run as far as +1.3V in circumstances where an oxidizable species (NO_2^-, OH^-, film) was present but nitric acid could not persist [*e.g.*, sat. $Ca(OH)_2$] did not produce a +0.56V peak on the cathodic return, but rather led to a new cathodic peak at −0.2V. This indicated that the formation of the electroactive species responsible for the +0.56V peak required both a potential greater than +0.7V and the presence of nitric acid.

The electrochemistry of nitric acid in calcium nitrate tetrahydrate gave considerably different voltammograms with gold and platinum microelectrodes. With gold, a sweep from +1.0 to −0.5V gave two cathodic peaks (Fig. 3, Table II), one at about +0.2V and a sharp peak at about +0.6V. The first, at +0.2V, gave a peak current varying linearly with added HNO_3 concentrations up to 0.025*m* at a sweep rate of 50 mV/s (Fig. 4). The second, corresponding to peak Z in Fig. 2, showed an approximately constant current at all HNO_3 concentrations. The peak current *vs.* (sweep rate)$^{1/2}$ relationship for the +0.2V peak due to 0.010*m* HNO_3 was composed of two linear portions with a distinct break between 100 and 150 mV/s, also observable in the peak potential values (Fig. 5). The anodic sweep of the cycle was consistent with nitrite oxidation.

The shape of the voltammetric curve due to nitric acid on a platinum electrode (Fig. 3) was dependent upon both the nitric acid concentration and the sweep rate. At low concentrations or high sweep rates the cathodic sweep gave a single peak near 0.0 V (Table II). The return anodic sweep gave a broad peak at +0.6*V* characteristic of nitrite oxidation. At low sweep rates or high concentrations the voltammograms had the complex form shown in Fig. 3. The anodic return sweep, starting from 0 current, produced a strong cathodic current. The relationship observed between cathodic peak currents and HNO_3 concentration at a 50 mV/s sweep rate is shown in Fig. 4; the transition between simple peaks and the type shown in Fig. 3 occurred between 0.005 and 0.010*m*. Figure 5 shows the dependence of cathodic peak currents on (sweep rate)$^{1/2}$ for 0.010*m* HNO_3. Voltammograms of the type shown in Fig. 3 occurred at sweep rates of 50 mV/s or less, simple voltammograms were observed at 200 mV/s or greater, and transitional shapes were observed at intermediate sweep rates. This transition was a function of both sweep rate and concentration.

Aside from nitric acid reduction, the most marked difference between calcium nitrate tetrahydrate voltammograms using Au and Pt microelectrodes was the appearance of a large cathodic peak at −1.25V (peak Y, Fig. 2) only with platinum. This peak, which partly overlapped the nitrate reduction "peak," was presumed to represent the process which did not lead to nitrite production during coulometric analysis using a Pt cathode at −1.2 to 1.3V. Cyclic voltammograms were run from various positive potentials to −1.35V. Those run from +0.7V or less deteriorated rapidly to 0 current flow. However, cycles from +1.25 to −1.35V gave a stable system which showed the −1.25V peak on the cathodic sweep. On the anodic sweep, a cathodic current peak appeared at approximately the same potential (Fig. 6). The only other current observed was an anodic peak at +1.0V, as expected for hydroxide film removal. Table III shows the results obtained from cyclic voltammetry at various sweep rates; as rate increased the cathodic peak current stayed almost constant, while the anodic sweep cathodic current increased until it was the greater of the two. Peak potentials were almost constant throughout. In order to determine if the reaction producing peak Y was responsible for film formation on Pt, 500 mV/s cyclic voltammograms were run from 0.0 V to negative potentials starting at −1.20V

Table II. Peak potential values of electroactive solutes in $Ca(NO_3)_2 \cdot 4H_2O$, 70°C

	I variable concentration 50 mV/s				II variable scan rate, 0.010*m*			
	0.005*m*		0.025*m*		25 mV/s		300 mV/s	
Solute	Au	Pt	Au	Pt	Au	Pt	Au	Pt
$Ca(OH)_2$	+1.03	+0.84	+0.99	+0.88	+1.01	+0.83	+1.08	+0.86
$NaNO_2$	+0.42	+0.55	+0.44	+0.47	+0.44	+0.45	+0.45	+0.55
HNO_3	+0.17	+0.03	+0.31	+0.28[a]	+0.23	+0.23[a]	−0.03	+0.05

[a] Leading peak.

and incremented by −0.05V. Runs to −1.20 and −1.25V showed no significant change in the maximum (edge) current after ten cycles. Runs to −1.30, −1.35, and −1.40V showed a drop in maximum current of 10, 20, and 40%, respectively, after ten cycles. Thus, film formation appeared much more closely related to the nitrate reduction "peak" A than to peak Y.

Full +2.0 to −2.5V cycles at 50 mV/s with a gold electrode and added water (1-10*m*) showed no additional peaks. A general increase in peak current beyond −1.5V was observed. The platinum electrode behaved similarly, but the unique peak Y appeared to decrease slightly in size and shift to a slightly more anodic value. Peak current values for Y obtained from 50 mV/s cyclic voltammetry between +1.4 and −1.4V are shown in Table IV as a function of added water concentration. The cathodic peak potential became slightly more positive with increasing water content, while the anodic sweep cathodic current increased. These peak current changes may be related to electrode film dissolution by water.

Attempts to detect a number of other species in calcium nitrate tetrahydrate solution by voltammetry were not successful. Bubbling of oxygen, hydrogen, or nitrous oxide for up to 1/2 h gave no detectable peaks in this solvent or in solvent saturated with $Ca(OH)_2$. The lack of reactivity of oxygen had been observed previously (6, 16) and attributed to the low solubility of oxygen in the melt.

Discussion

The solvent oxidation reaction in calcium nitrate tetrahydrate appears to be a straightforward oxidation of water

$$H_2O - 2e^- \rightarrow 2H^+ + 1/2\ O_2$$

$$2H^+ + 2NO_3^- \rightleftharpoons 2HNO_3$$

We have not been able to reproduce the 0.7V difference in oxidation potential previously observed (16) between gold and platinum electrodes in this electrolyte. Both voltammetry and the potentials observed during bulk electrolysis indicate similar oxidation potentials at both electrode materials.

The major solvent reaction at a gold cathode is clearly reduction of nitrate to nitrite ion

$$NO_3^- + 2e^- \rightarrow NO_2^- + O^{-2}$$

$$O^{-2} + H_2O \rightarrow 2\ OH^-$$

The excess of nitrite observed coupled with the observation of oxygen as a cathode product suggests the results observed in the reduction of alkali nitrate melts (17), where oxide dianions produced in the electrochemical reduction of nitrate react chemically with nitrate ion to give additional nitrite and peroxide ions

$$NO_3^- + O^{-2} \rightarrow NO_2^- + O_2^{-2}$$

$$O_2^{-2} + H_2O \rightarrow 2\ OH^- + 1/2\ O_2$$

The existence of oxide ions in a hydrate melt appears unlikely, but in this system an insoluble basic film, as shown by cyclic voltammetry, forms rapidly on the cathode. Similar films occur at the cathode during the reduction of $Ca(NO_3)_2/KNO_3$ melts (18). Local depletion of water could occur near the electrode surface, allowing oxide ions to exist long enough to react with nitrate. The concentration of free water in this system is low, and the rate of diffusion of bulky $(Ca(H_2O)_4)^{+2}$ into the film should be

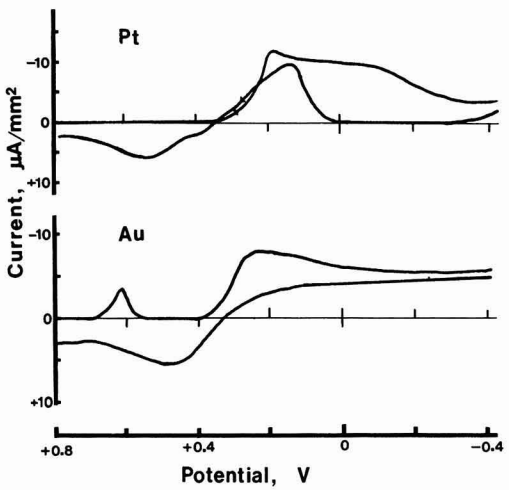

Fig. 3. Cyclic voltammograms of 0.01*m* nitric acid in calcium nitrate tetrahydrate at 70.0°C using a platinum or a gold microelectrode.

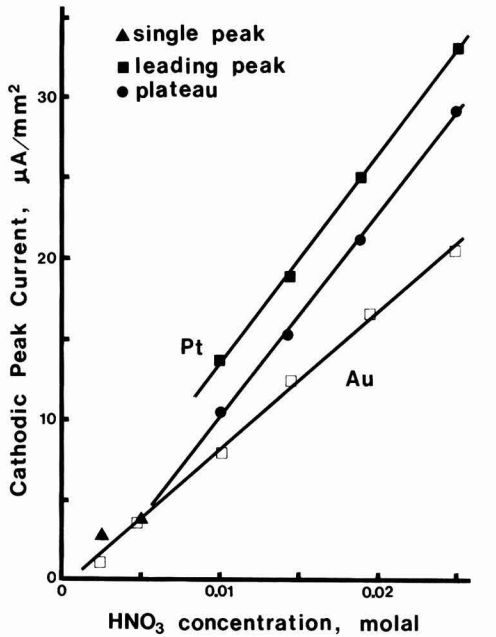

Fig. 4. Cyclic voltammetric cathodic peak current as a function of concentration of nitric acid in calcium nitrate tetrahydrate at 70.0°C and 50 mV/s using a platinum or a gold microelectrode.

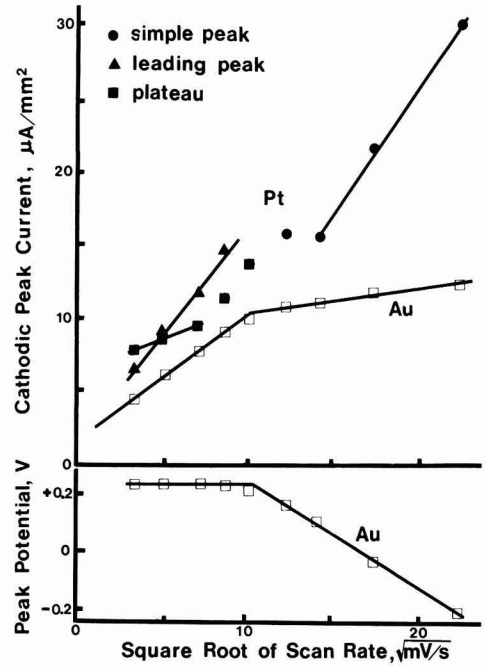

Fig. 5. Cyclic voltammetric cathodic peak current and peak potential as a function of the square root of scan rate for 0.01*m* nitric acid in calcium nitrate tetrahydrate at 70.0°C using a platinum or a gold microelectrode.

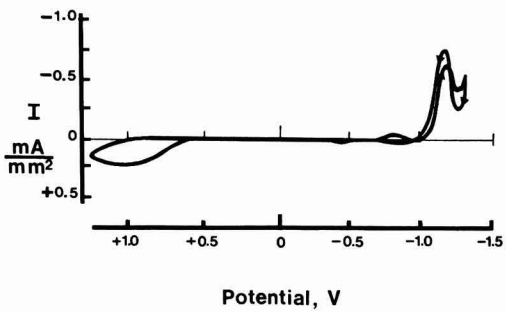

Fig. 6. Cyclic voltammogram of calcium nitrate tetrahydrate at 70.0°C and 50 mV/s using a platinum electrode.

relatively slow. Peroxide ions produced by the oxide/nitrate reaction would diffuse out and produce oxygen after reaction with water. This evidence for the production of oxide dianion suggests that water is not involved in the initial electrochemical reduction reaction on gold.

The previously reported 0.3V difference in solvent reduction potential between Au and Pt appears to be due to the identification of the slope of peak Y (Fig. 2) as due to solvent reduction; a peak in this position was in fact observed in voltammetry of the 2.6 H_2O hydrate melt (16). The fact that the reaction represented by peak Y does not give nitrite as a reduction product explains why the authors concluded that water reduction was the major solvent reaction in this system.

The reaction represented by peak Y appears, both from the chemical evidence and from the absence of nitrite oxidation peaks in the anodic sweep (Fig. 2 and 6), to produce a product other than nitrite. This peak may represent reduction of water to hydrogen, but if so then all the hydrogen must be adsorbed on the electrode, since none is detected by GC and hydrogen has been shown to be neither reactive nor soluble in the melt. A second possibility is reduction of a previously formed platinum oxide film. The possibility that peak Y represents a further reduction of nitrite cannot be excluded, although no plausible products of such a reaction could be detected.

We have observed that a cyclic voltammogram of $Ca(NO_3)_2 \cdot 4H_2O$ run using a freshly ground Pt microelectrode surface does not show peak Y, although it appears as soon as an electrochemical reaction occurs at the electrode or if the electrode is soaked in concentrated nitric acid. This result supports the "PtO" reduction hypothesis, since concentrated HNO_3 is known to produce such films (23-25). The observed reaction, however, represents a very large quantity of material. If one assumes that the roughly linear increase in bulk nitrite production represents a linear decrease in peak Y material, the percentage NO_2^-/coulomb data in Fig. 1 can be used to estimate that 0.65 C/cm² are required for complete reduction of this material. The surface area of bright platinum has been estimated to be 1.5-2.5 times the theoretical value by hydrogen charging experiments, which imply that the total charge required to reduce one "monolayer" of "PtO" will be 400-650 μC/cm² (19-21). It has been demonstrated that more than one monolayer may be deposited on a Pt electrode, but, although the exact nature of this oxide/oxygen film was controversial, there was a general belief that it amounted to no more than two to five additional "monolayers," whether deposited by anodization (19-22) or chemically (23-25). This gives an estimated charge required for complete film removal of 1-3 mC/cm², or approximately 300 times less than the estimated charge consumed here. The large charge capacity of the reaction is confirmed by the peak current observed in voltammetry, where the estimated area of peak Y in Fig. 2 represents a value of about 0.7 C/cm².

The reaction represented by peak Y also exhibits unusual behavior during cyclic voltammetry, in that a cathodic peak is observed during the anodic sweep of the cycle (Fig. 6). This type of anomaly has been reported in a few other cases (11-13, 26-28) and attributed to adsorption or other surface phenomena. The observation of an adsorption/desorption phenomenon is more easily associated with the hypothesis that this peak is due to production of adsorbed hydrogen, since a similar result is reported for the neutral molecule N_2O in alkaline aqueous solution (26). There was, however, no detectable effect on the electrochemistry of this system resulting from hydrogen (or N_2O or O_2) being bubbled through the melt. Water did cause both a change in peak current and a small positive shift in peak potential, but this may be attributable to a solvent effect on the electrode film. An important difference in the *I vs.* (scan rate)$^{1/2}$ relationship was also observed: with the N_2O reduction peak, these values were found to be directly proportional, while in this work such a relation was not found. The explanation involving trace organic impurities (28) may be relevant to this system: reagent-grade calcium nitrate tetrahydrate shipped in plastic bottles was used without further purification and may well have contained trace organics.

The overall cyclic voltammogram of calcium nitrate tetrahydrate indicates no reversible electrochemical reactions for any of the solvent oxidation or reduction products. Of the three major products, soluble hydroxide, presumably in the form $(CaOH(H_2O)_3)^+$, behaves in the simplest manner on both gold and platinum electrodes

$$(CaOH(H_2O)_3)^+ - 2e \rightarrow (Ca(H_2O)_3)^{+2} + H^+ + 1/2\ O_2$$

$$H^+ + (CaOH(H_2O)_3)^+ \rightleftharpoons (Ca(H_2O)_4)^{+2}$$

Linear relationships with near-zero intercepts are seen for both metals between peak current values and both the concentration up to 15-20 m*m* and the square root of scan rate up to 300 mV/s. Peak potentials show a small increase with increasing scan rate. The peak potential on Pt

Table III. Peak current and potential values, $Ca(NO_3)_2 \cdot 4H_2O$, 70°C, Pt electrode +1.25 to −1.35V, variable scan rate

Scan rate (mV/s)	Cathodic scan V_p (V)	I (mA/mm²)	Anodic scan V_p (V)	I (mA/mm²)	V_p (V)	I (mA/mm²)
50	−1.21	−0.94	−1.17	−0.31	+0.9	0.19
100	−1.22	−1.25	−1.20	−0.86	+1.0	0.31
250	−1.22	−1.31	−1.21	−1.42	+1.0	0.47
500	−1.22	−1.31	−1.20	−1.53	+1.0	0.58
1000	−1.21	−1.31	−1.20	−1.53	+1.0	0.69

Table IV. Peak current and potential values, $H_2O/Ca(NO_3)_2 \cdot 4H_2O$, 70°C, Pt electrode +1.4 to −1.4V, 50 mV/s

[H_2O] (m)	Cathodic scan V_p (V)	I (mA/mm²)	Anodic scan V_p (V)	I (mA/mm²)	V_p (V)	I (mA/mm²)
0	−1.27	−3.05	−1.22	−1.35	+1.12	0.75
1	−1.24	−2.80	−1.21	−1.35	+1.05	0.95
2.5	−1.23	−2.55	−1.20	−1.40	+1.00	0.65
5	−1.20	−2.25	−1.19	−1.45	+0.95	1.05
7.5	−1.19	−2.15	−1.17	−1.70	+0.90	0.85
10	−1.19	−2.35	−1.19	−2.35	+0.86	1.15

is in reasonable agreement with a single-scan value derived previously (16).

The oxidation of nitrite also appears reasonably straightforward. Variations of peak current with concentration are again linear up to 15-20 m*m*, as is the relationship with (scan rate)$^{1/2}$ up to 300 mV/s. The detection of HNO_3 on the reverse sweep indicates the overall reaction

$$NO_2^- + H_2O \rightarrow HNO_3 + H^+ + 2e^-$$

$$H^+ + NO_3^- \rightleftharpoons HNO_3$$

An additional cathodic peak (peak Z) is seen only with a gold electrode, and appears to be a gold oxide film reduction peak. It is observed only in the presence of nitric acid and when the potential is more positive than +0.7V, but the peak current is independent of nitric acid concentration. The peak is narrow ($E_p - E_p/2 = 30$ mV) and symmetrical; there is no detectable diffusion current due to this peak. A small secondary peak on the nitrite diffusion current is also observed at +0.75V at high nitrite concentrations. In the absence of nitric acid but in the presence of oxidizable substances, this peak is not observed; rather, a peak with similar characteristics appears at −0.2V.

The reduction mechanism of nitric acid appears complex, with substantial differences between gold and platinum electrodes. The reduction peak shape on gold is simple (Fig. 3), and the relationship between peak height and concentration is linear at 50 mV/s to at least 25 m*m* (Fig. 4). The I *vs.* (scan rate)$^{1/2}$ relationship, however, shows a sharp break to a lower slope at approximately 100 mV/s (Fig. 5). Changes in slope of this kind are characteristic of a change from reversible (fast electrode kinetics) to irreversible (slow electrode kinetics) systems, as is the simultaneous change from constant peak potential to decreasing peak potential observed here. In simple cases of this kind, however, there is a substantial, nonlinear, "quasi-reversible" zone not seen here. Additionally, the low slope and high slope linear portions of the relationship both extrapolate to the origin in the simple system (29), whereas in this case the low slope line extrapolates to a large positive current. Behavior of this type implies a more complex reduction mechanism. Switches from high to low slope roughly similar to that observed are predicted in systems where reversible or quasi-reversible electrode kinetics are followed by irreversible chemical reaction. The present system will be still more complex since reduction here will produce two molecules, one of which will be a basic anion which should react irreversibly with an additional molecule of the starting material, HNO_3

$$HNO_3 + 2e^- \rightarrow NO_2^- + OH^-$$

$$OH^- + HNO_3 \rightarrow NO_3^- + H_2O$$

$$HNO_3 + NO_2^- \rightleftharpoons NO_3^- + HNO_2$$

The situation at the platinum electrode appears even more complex. Two entirely different peak shapes are observed, depending upon both HNO_3 concentration and scan rate. The low sweep rate/high concentration form (Fig. 3) features, on the cathodic sweep, a leading peak which trails into a level plateau region terminating in a drop to near zero current over only 150 mV. This is accompanied on the reverse anodic sweep by a cathodic current peak, also of complex shape. Other instances of reverse current peaks have already been described with reference to peak Y. In this case, the observation that continuation of the sweep beyond −0.6V gives rise to a new peak with concommitant loss of the return cathodic current suggests that an adsorbed insulating film is responsible for the current drop at −0.2V in the anodic sweep. Presumably, the anodic sweep cathodic current results from desorption of the film allowing further reduction, while the −0.6V peak represents reductive destruction of the film and renewed reduction of HNO_3. The correlation of this peak system with HNO_3 concentration suggests that the adsorbed material is a product of HNO_3 reduction (or chemical reaction). The shape of the cathodic peak/plateau is of a type predicted for either a reversible chemical reaction followed by reversible reduction or reversible reduction followed by irreversible catalytic chemical reaction (29). Neither of these simple situations is likely to describe the system fully.

At high sweep rates or low concentrations, the peak shapes simplify to a single cathodic peak on the cathodic sweep with no detectable cathodic peak on the anodic return sweep. The simple cathodic peak has, however, an exceptionally low trailing diffusion current relative to that observed with a gold electrode, while the I_p *vs.* (scan rate)$^{1/2}$ relationship (Fig. 5), although apparently linear, has a large negative current intercept. Both observations suggest a continuing effect due to adsorbed material. The reason for the change in peak shape with scan rate, which is not of the type predicted for simple systems, is unclear. The disappearance of the cathodic peak on the anodic sweep shows that the role of adsorption has changed; the rate of formation of adsorbable material, the total quantity of adsorbable material, and the rate of desorption at potentials less than −0.2V may all be involved. A complex equilibrium network involving NO_3^-, NO_2^-, HNO_3, HNO_2, and H_2O is likely associated with reductions at both Pt and Au electrodes.

Acknowledgment

The authors wish to thank the National Science and Engineering Research Council of Canada for financial support of this work.

Manuscript submitted Jan. 24, 1984; revised manuscript received June 7, 1985. This was paper 794 presented at the

San Francisco, California, Meeting of the Society, May 8-13, 1983.

The University of Regina assisted in meeting the publication costs of this article.

REFERENCES

1. C. A. Angell, *This Journal*, **112**, 1224, (1965); C. A. Angell, *J. Chem. Phys.*, **70**, 3988 (1966).
2. J. Braunstein, L. Orr, and W. MacDonald, *J. Chem. Eng. Data*, **12**, 415 (1967).
3. C. T. Moynihan and A. Fratiello, *J. Am. Chem. Soc.*, **89**, 5546 (1967).
4. B. Burrows and S. Noersjamsi, *J. Phys. Chem.*, **76**, 2759 (1972).
5. J. Braunstein *et al.*, *J. Electroanal. Chem.*, **15**, 337 (1968).
6. C. T. Moynihan and C. A. Angell, *J. Phys. Chem.*, **74**, 736 (1970).
7. D. G. Lovering, *J. Electroanal. Chem.*, **50**, 91 (1974).
8. R. Carpio, M. Mehmed, F. Borsay, C. Petrovic, and E. Yeager, *J. Phys. Chem.*, **86**, 4980 (1982).
9. R. Caminiti, A. Musinu, G. Paschina, G. Piccaluga, and G. Pinna, *Z. Naturforsch.*, **36A**, 831 (1981).
10. D. G. Lovering, *Collect. Czech. Chem. Commun.*, **37**, 3697 (1972); *ibid.*, **38**, 1719 (1973).
11. C. Nanjundiah and R. Narayan, *Electrochim. Acta*, **26**, 203 (1981); *ibid*, **26**, 367 (1981).
12. R. Narayan and K. T. Valsaraj, *ibid.*, **27**, 153 (1982).
13. R. Narayan and C. Nanjundiah, *J. Electroanal. Chem.*, **136**, 159 (1982).
14. N. P. Bansal and J. A. Plambeck, *This Journal*, **124**, 1036 (1977).
15. N. P. Bansal and J. A. Plambeck, *Electrochim. Acta.*, **23**, 1053 (1978).
16. R. P. Courgnaud and B. Tremillion, *Bull. Soc. Chim. Fr.*, 758 (1965).
17. P. G. Zambonin, *J. Electroanal. Chem.*, **24**, 365 (1970); K. E. Johnson and P. Zacharias, *This Journal*, **124**, 448 (1977).
18. V. D. Prisyazhnyi, D. A. Tkalenko, and N. A. Chmilenko, *Elektrokhimiya*, **16**, 115 (1980).
19. D. Gilroy and B. E. Conway, *Can. J. Chem.*, **46**, 875 (1968).
20. R. Thacker and J. P. Hoare, *J. Electroanal. Chem.*, **30**, 1 (1971).
21. A. J. Appleby, *ibid.*, **24**, 97 (1970).
22. T. Biegler and R. Woods, *ibid.*, **20**, 73 (1969).
23. J. P. Hoare, *This Journal*, **110**, 1019 (1963).
24. J. P. Hoare, R. Thacker, and C. R. Wise, *J. Electroanal. Chem.*, **30**, 15 (1971).
25. J. P. Hoare, *This Journal*, **126**, 1502 (1979).
26. K. E. Jonson and D. T. Sawyer, *J. Electroanal. Chem.*, **49**, 95 (1974).
27. P. Margaretha and P. Tissot, *ibid.*, **99**, 127 (1979).
28. A. Damjanovic, M. A. Genshaw, and J. O'M. Bockris, *This Journal*, **114**, 446 (1967).
29. D. D. MacDonald, "Transient Techniques in Electrochemistry," Chap. 6, Plenum Press, New York (1977).

A Capacitance and Electrolyte Electroreflectance Study of the ZnSe/Electrolyte Interface

P. Lemasson,* C. Hinnen, N. R. de Tacconi,[1] and C. Nguyen Van Huong

Laboratoire d'Electrochimie Interfaciale du CNRS, 92195 Meudon Principal Cedex, France

ABSTRACT

The semiconductor-electrolyte junction is studied in the particular case of n-ZnSe/indifferent electrolytes by means of capacitance and electrolyte electroreflectance measurements. In comparing both kinds of results obtained for two extreme pH conditions (pH = 0 and 14), we need to define a reference state for the clean electrode in each medium. A basic solution acts as a more able etching solution than an acidic one creating fast acceptor interface states in the vicinity of the valence band maximum tending to fix the Fermi level. The evolution of these reference states with controlled perturbations of the interface confirm that the characteristics of the junction remains governed mainly by the presence of interface states at the semiconductor electrode. Such an analysis of combined electrical and spectroscopic data constitutes a promising way for a better understanding of the semiconductor/electrolyte junction in connection with the physical models developed for metal/semiconductor junctions.

During the last 30 years, the semiconductor-electrolyte junction has received much attention. This attraction was mainly due to the simple preparation procedure and the versatility of this junction as compared to the classical solid Schottky barriers, although such an important parameter as temperature cannot be easily varied in a large range.

The models used in the description of the semiconductor-electrolyte interface (1) are generally based on those already elaborated for solid-state junctions, especially metal-semiconductor junction (2). However, this analogy necessitates the definition of a proper Fermi level in the electrolyte. Such a requirement can be easily fulfilled in the case of a redox electrolyte, but it presents much more difficulty for an electrolyte without an explicit redox couple (3). Due to its fundamental interest as well as its use in physical measurements (electroreflectance) and semiconductor technology, the latter case necessitates more insight, and it is the aim of the present article to deal with some physical and electrochemical aspects of semiconductor-indifferent electrolyte junctions.

The semiconductor used as an electrode in such investigations must fulfill two requirements: (*i*) its physical properties are clearly established and can be accounted for unambiguously by a band model; (*ii*) its electrochemical behavior has already received attention and can be considered as simple. For this purpose, we selected n-ZnSe, a II-VI compound with wide energy gap (2.7 eV) whose electrochemical behavior (5, 6) and EER investigations have been previously described (6c).

By analyzing mainly two types of measurements, capacity and electrolyte electroreflectance (EER), which bring complementary information, we attempt in this article to give more insight into the formation of the semiconductor-electrolyte (indifferent) junction. The description of such a junction necessitates the use of many different physical parameters. The various data obtained can then be accounted for by a model similar to that of metal-semiconductor junctions, provided that the existence of different types of interface states is taken into account.

Experimental

The zinc selenide single crystals were grown and donated by Professor Lozykowski.[2] They were In doped

*Electrochemical Society Active Member

[1]Permanent address: Instituto de Investigaciones Fisicoquimicas Teoricas y Aplicadas (INIFTA), 1900 LaPlata, Argentina.

[2]H. Lozykowski, Institute of Physics, Nicholas Copernicus University, Torun, Poland

with a free carrier density of $\sim 2 \times 10^{17}$ cm^{-3} as determined by Hall effect measurement. Prior to their mounting as electrodes, an ohmic contact was realized with In-Hg amalgam by heating at ~300°C in argon atmosphere for 1-2 min. A gold wire was then soldered to these contacts. The back and sides of the crystals were insulated from the electrolyte by means of an epoxy resin (Scotch Cast, 3M Company) and then mounted on the electrode holder. The exposed face was carefully polished with diamond paste (0.25 μm) and, when necessary, etched in a 1% bromine in methanol solution at ~5°C. The best etching time was found to be 20s (see Discussion section).

The cell was of the classical three-electrode type with quartz windows for light passage and a gold counterelectrode. The reference electrode was a mecury-mercurous sulfate immersed in saturated potassium sulfate aqueous solution (0 V *vs.* MSE = +0.65V *vs.* NHE).

Electrolytes were prepared by dissolving Merck-Suprapur grade chemicals in Millipore purified water. The following solutions were used: 1*M* $HClO_4$, 1*M* NaOH, and 10^{-2}*M* $K_3Fe(CN)_6$ + 1*M* $HClO_4$, and 10^{-2}*M* $K_3Fe(CN)_6$ + 1*M* NaOH. In order to saturate or to eliminate oxygen, either an oxygen or an argon bubbling of the electrolytes was undertaken prior to electrochemical experiments.

As a light source, a 400W tungsten-halogen lamp was used together with electrochemical and electroreflectance equipment which have been described previously (6a, 7).

The capacity measurements are achieved at 15 Hz and 100 kHz. The EER spectra are recorded at almost normal incidence for the light beam, and with an electrical perturbation whose characteristics are 15 Hz and 0.5V_{eff}.

Results

Etched Electrode Surface and Definition of a Reference State

The changes in voltammograms, capacity curves, and EER spectra are studied simultaneously as a function of the semiconductor surface preparation. The characteristics are reported in Fig. 1 in the case of 1*M* NaOH electrolyte. During the electrochemical investigations, the potential range was limited negatively to hydrogen evolution and positively at +2.0V *vs.* MSE, *i.e.*, in a range where no anodic current is detectable within the limit of 10^{-9} A-cm^{-2}. The EER spectra are reported for a dc potential of 0 V *vs.* MSE; thus, the possibility of anodic current even for large ac modulation (1V_{eff}) can be excluded.

In the case of a freshly polished electrode surface, without etching treatment (Fig. 1) the Mott-Schottky plot (C^{-2} *vs.* V, where C is capacity and V is potential) is far from linear and the EER signal is small and without distinct structure in the vicinity of the fundamental transition E_0 at about 2.72 eV.

The influence of a further chemical etching in bromine-methanol solution is clearly evidenced in Fig. 1 for two different etching times (10 and 20s). In both cases, the C^{-2}-V plots now present an acceptable linearity, but the flatband potential V_{FB} as well as the free carrier density N_D deduced from these plots differ noticeably (V_{FB} = −2.6V *vs.* MSE and $N_D = 3.6 \times 10^{17}$ cm^{-3} for 10s; V_{FB} = −3.1V and $N_D = 8 \times 10^{17}$ cm^{-3} for 20s). We have to emphasize that these values are deduced from measurements with a 15 Hz perturbation. At 100 kHz, in the second case (etching time 20s) we obtain V_{FB} = −3.1V *vs.* MSE and $N_D = 2.7 \times 10^{17}$ cm^{-3}. The EER spectrum shows more clearly the influence of the etching (Fig. 1b), and it is only in the second case that it becomes acceptable, with a large signal enabling a precise determination of the peak energies. This typical spectrum and the corresponding capacity values being reproducible are proposed to characterize the reference state for this junction.

Equivalent observations are made in acidic medium (1*M* $HClO_4$, pH 0) (Fig. 2). We notice, however, that the C^{-2}-V plots as well as the EER spectra differ in some aspects, when the so-called reference state is reached. Excluding the variation of V_{FB} with pH, the slopes of the C^{-2}-V plots are larger and lead to a unique value of $N_D \simeq 2 \times 10^{17}$ cm^{-3} at 15 Hz and 100 kHz; the EER spectrum presents oscillations of slightly lower amplitude. As will be discussed in the Discussion section, these observations may certainly be correlated with physical differences during the formation of the semiconductor-electrolyte interface.

At both pH values, there was no noticeable influence of the presence of oxygen in the electrolyte.

Modifications of the Reference State

Influence of a positive polarization.—The electrochemical treatment is achieved in order to induce a modification of the semiconductor-electrolyte interface when studied under the same conditions as described in the previous section, allowing a comparison with the reference state. The treatment is strictly dependent on the pH of the solution.

pH 0.—In this case, a positive polarization at a potential value where a detectable current crosses the junction induces a remanent effect only if the solution is saturated in oxygen and if the electrode is illuminated during the process. The particular conditions used here are (*i*) polarization value of +8.0V *vs.* MSE, (*ii*) electrolyte saturated in oxygen, and (*iii*) illumination with white light.

The main results obtained in capacity and EER measurements are reported in Fig. 3. During the whole treatment, the current density is small (~1.5 μA-cm^{-2}) and constant. We observe that at 15 Hz, the C^{-2}-V plot differs from that obtained in the reference state (the slope and the linear portion decrease), whereas at 100 kHz the C^{-2}-V plot remains identical to that of the reference state. The EER spectra at a dc voltage of 0 V diminish in amplitude, mainly for the negative part of the oscillation, and after 1h of such a treatment present the perturbed shape indicated in the lower part of Fig. 3b.

pH 14.—In that case, the perturbation of the junction is obtained with a positive polarization only (no noticeable influence of either oxygen or light). Our experimental conditions are then (*i*) polarization at +4.0V *vs.* MSE up to 15 min, and (*ii*) presence of oxygen and illumination or not.

We already noticed that a treatment lasting more than 15 min does not further influence the behavior of the semiconductor-electrolyte interface. The net result of the electrochemical treatment on both C^{-2} *vs.* V plot and EER spectra is presented in Fig. 4. Whereas an enhancement of the EER signal together with an improvement of the signal/noise ratio is noticeable, the C^{-2}-V plots at 15 Hz are strongly modified: the linearity range and the slope decrease together.

Influence of oxidizing species.—The Ox species is $K_3Fe(CN)_6$. The treatment is achieved in an electrochemical cell devoted exclusively to this purpose; the characterization is then realized in a separate cell containing the supporting electrolyte.

pH 0.—The electrode treatment is achieved in a 1*M* $HClO_4$ solution containing 10^{-2} $K_3Fe(CN)_6$. The complete cycle is eight voltage sweeps between −2.0 and +2.0V *vs.* MSE at a sweep rate of 50 mV-s^{-1}.

The result of this treatment is presented in Fig. 5. We notice that the C^{-2}-V plot is slightly modified at high frequency as well as at low frequency, whereas the EER signal decreases progressively in a way analogous to that observed with an electrochemical treatment (see the positive polarization pH 0 section).

Furthermore, we mention that at the end of the treatment the electrode surface presents a slightly modified aspect (green-gray) easily detectable with naked eye.

pH 14.—During the treatment, which consists of six voltage sweeps between −2.0 and +2.0V *vs.* MSE at a sweep rate of 50 mV-s^{-1}, the electrolyte is 1*M* NaOH + 10^{-2}*M* $K_3Fe(CN)_6$ solution.

Under further investigation in 1*M* NaOH electrolyte, the behavior of the ZnSe-electrolyte interface changes slightly for Mott-Schottky plots (at high and low frequency) but drastically for the EER spectra, which pres-

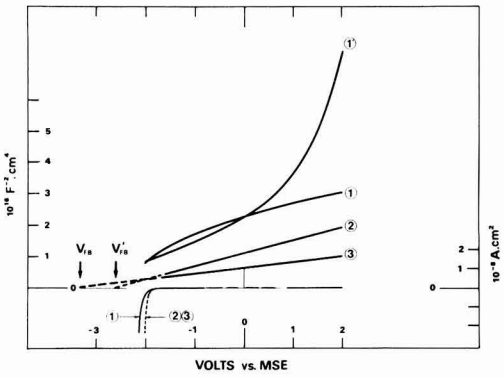

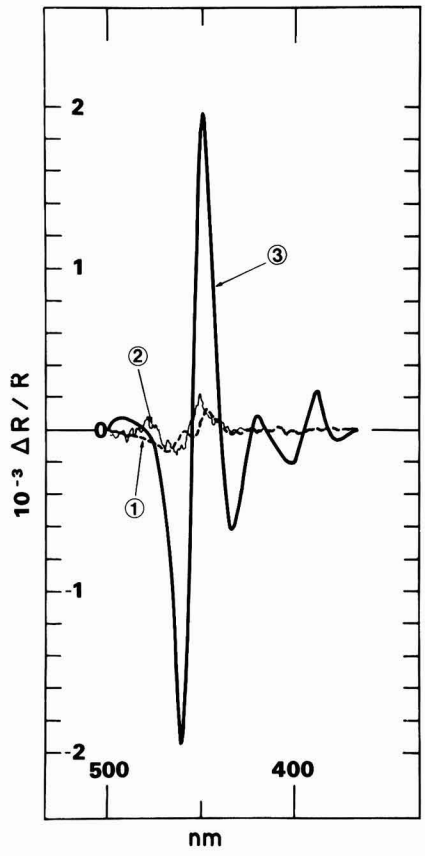

Fig. 1. Electrical and electro-optical characteristics of the n-ZnSe-1M NaOH junction for different semiconductor surface preparations. 1 and 1′: Just polished with 0.25 μm diamond paste. 2: Etched 10s in 1% bromine-methanol solution. 3: Etched 20s in 1% bromine-methanol solution. a(above): Dark current and C^{-2} *vs.* V characteristics. In the latter case, the perturbation frequency is 15 Hz. For clarity's sake, the Schottky plot at 100 kHz is not represented. b(right): EER spectra.

ent a complete rotation of phase together with an important attenuation (Fig. 6).

The semiconductor surface becomes reddish as the treatment is completed. The red layer formed is dissolved easily in CS_2, thus indicating that it is a selenium layer.

Discussion

Reference State: Electrical and Electro-optical Characterization

Prior to electrochemical investigations, the semiconductor electrode is mechanically polished and chemically etched. Such a preparation plays a major role in the subsequent electrode behavior. Results presented in the Results section allow a definition of quality for the semiconductor surface, based upon electrical (capacity) and electro-optical (electroreflectance) measurements. More precisely, the criteria are twofold.

First, the differential capacity *vs.* potential measurement must lead to linear Mott-Schottky plots (C^{-2}-V) for high as well as low frequency perturbation. Furthermore, in a large potential range ($\geq$ 1V), a correct Mott-Schottky plot enables calculation of free carrier density analogous to that determined by physical techniques such as Hall effect measurement. This requirement is generally obeyed only at high frequency, but, in some cases, it can be verified even at low frequency (a few hertz).

Second, the electroreflectance signal must be sufficiently large in the vicinity of the fundamental E_0 transition ($\sim 10^{-3}$ in absolute value in our case).

Third, nevertheless, this latter criterion must be adequately adapted due to the influence of the free carrier density on the amplitude of the EER signal as outlined by Aspnes (8).

In addition to the large signal amplitude, the broadening parameter, Γ, must be sufficiently small (~50 meV in the present case).

When the first two conditions are fulfilled, it becomes possible to (*i*) fix the energy position of the semiconductor Fermi level in an electrochemical scale by means of the flatband potential value V_{FB} and (*ii*) determine a precise value of the fundamental transition energy E_0 (and of the higher transition energies).

Results reported in Fig. 1 indicate that the damaged layer produced by the mechanical polishing must be removed by an adequate chemical etching which depends on the semiconductor. Thus, in the case of ZnSe, a satisfying surface preparation consists in a mechanical polishing with diamond paste 1/4 μm followed by a chemical etching in 1% bromine in methanol solution at ~5°C for ~15s.

The parameter values corresponding to the reference state are reported in Table I. We must notice first that an open-circuit barrier height or band bending, V_S, can be deduced from rest and flatband potentials. The rest potential is accurately determined using an electrometer. From one experiment to another, fluctuations are very small and V_R can be considered as really fixed. This band bending is pH dependent

$$V_S = 1.65\text{V at pH} = 0$$

$$V_S = 2.3\text{V at pH} = 14$$

Such values are large as compared to those obtained for ZnSe in the metal-semiconductor configuration (9). However, they seem to be fairly explained by the existence of acceptor interface states, located in the range 0.5-1.0 eV

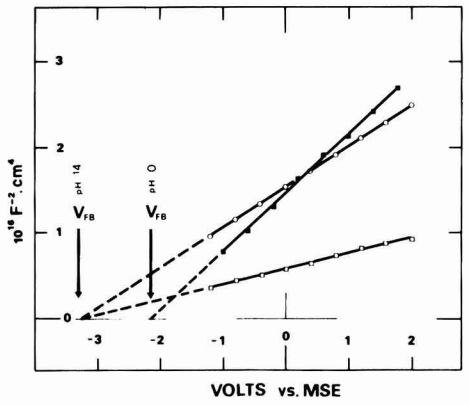

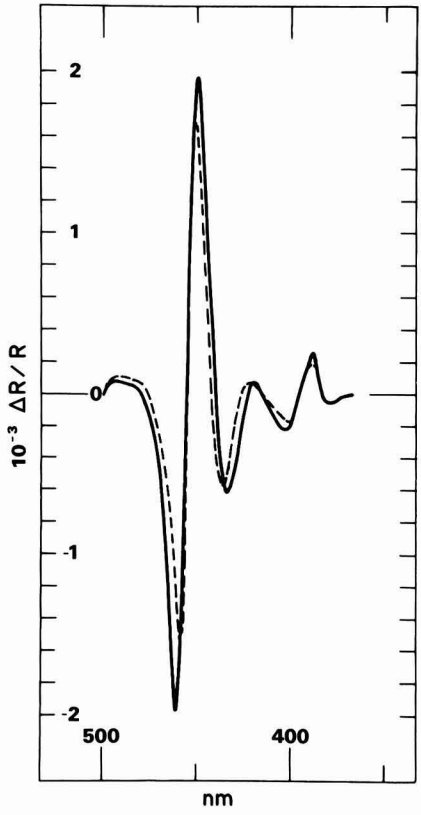

Fig. 2. Comparison of electrical and electro-optical characteristics of the n-ZnSe-indifferent electrolyte junction in the reference states (see the text for the definition) at pH 0 and 14. a(above): C^{-2} vs. V. Filled squares: pH 0, 15 Hz, and 100 kHz. Open squares: pH 14, 15 Hz. Circles: pH 14, 100 kHz. b(right): EER spectra. Solid line: pH 14. Dashed line: pH 0.

higher than the valence-band maximum, which tend to fix the Fermi level. The existence of such acceptor states has already been demonstrated for semiconductor-vacuum interfaces by photoemission measurements, especially in the case of n-GaAs, which is isoelectronic to ZnSe (10), and also for ZnSe (11). They may be explained by the penetration in the gap of the empty surface-state band associated with Se atoms upon removal of the "clean" surface reconstruction. In contact with an electrolyte this removal is more pronounced when the solution is an etchant for ZnSe, which is the case for NaOH. The higher value of V_S at pH 14 agrees well with these considerations. Further discussion is possible together with an analysis of capacity and EER measurements in the reference state of the electrode.

Differential capacity.—At high frequency (100 kHz), the reference states are slightly different at pH 0 and 14 (N_D calculated from the Mott-Schottky slope changes from 2×10^{17} cm^{-3} to 2.7×10^{17} cm^{-3}) and differ noticeably at low frequency (N_D changes from 2×10^{17} to 8×10^{17} cm^{-3}). The flatband potential value is here insensitive to the perturbation frequency (Table I). These observations may likely be correlated with the above considerations on the existence of acceptor surface states in the vicinity of the valence-band maximum

We attempt now to estimate the density of surface states analyzing the capacity measurements. This estimation is made assuming that the models established in the case of the metal-semiconductor junctions can be used for electrolyte-semiconductor junctions and the analysis is different according to the possibility or impossibility for the interface states to follow the perturbation (2a, 12).

At 100 kHz, we may assume that the interface states do not follow the perturbation. This hypothesis corresponds to a linear C^{-2}-V plot in a large potential range for band bendings greater than 2V. If the interface states followed the ac perturbation at 100 kHz, no such linear plots could exist. In that case and provided that the occupation of these states is governed by the semiconductor Fermi level, the slope of the Mott-Schottky plot is no longer proportional to N_D^{-1} but to $[(1 + \alpha)N_D]^{-1}$ (12), where

$$\alpha = \frac{e\delta D_{ss}}{\epsilon_i} \qquad [1]$$

and δ is the thickness of the interfacial layer, D_{ss} the density of states per surface unit, ϵ_i the dielectric constant of the interfacial layer, and e the electron charge. Therefore, due to the similarity between $(N_D)_{Hall}$ and $(N_D)_{Schottky}$ at pH 0, we may assume that D_{ss} is smaller than that at pH 14, a statement which matches well the etching character of basic solutions. From the slope value at 100 kHz in the electrolyte of pH 14, we calculate

$$\alpha = 0.35 \qquad [2]$$

It seems reasonable to assume δ of the order of some angstroms and ϵ_i slightly lower than ϵ_s ($8.7\epsilon_0$). This leads to the estimation of D_{ss}

$$D_{ss} \sim 5 \times 10^{13} \text{ cm}^{-2} \qquad [3]$$

a value which is compatible with the barrier height of 2.3 eV.

At low frequency, it is no longer valid to assume that the interface states do not follow the perturbation and the above analysis is no longer possible. However, Fonash (12) has recently proposed a detailed treatment of that case, and we applied it to our results. Without giving more details, it is sufficient to say that the amount of very slow surface states, as deduced from this treatment, is low, on the order of 10^{11} cm^{-2}.

The D_{ss} value, as computed from relation [1], seems to be in the limits for Fermi level pinning, as established re-

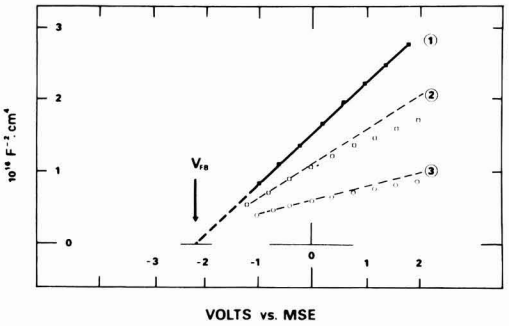

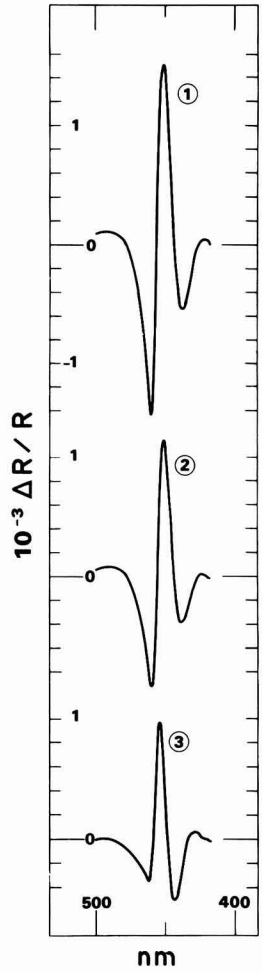

Fig. 3. Characteristics of the n-ZnSe-1M $HClO_4$ junction before and after electrochemical perturbation (positive polarization + 8V vs. MSE and illumination in the presence of oxygen). 1. Reference state. 2 and 3: After, respectively, 30 min and 1h of perturbation. a(above): C^{-2} vs. V (15 Hz). b(right): EER spectra.

cently by Zur *et al.* (13), in the case of submonolayer metal coverage. The influence of the very slow surface states is therefore negligible on this phenomenon irrespective of their influence on the frequency dispersion of Mott-Schottky plots.

Electrolyte electroreflectance.—Provided that the low field approximation can be made, the EER spectra can be fairly analyzed using the three-point method (14). The validity of this method depends on the existence of a fully depleted layer at the surface of the semiconductor and on the assumption that the electro-optical energy $\hbar\,\Omega$ and the broadening parameter obey the relation

$$3\hbar\,\Omega < \Gamma \qquad [4]$$

Consequences of relation [4] are (*i*) the proportionality between the EER signal amplitude and that of the alternating modulation and (*ii*) the constancy of the transition energy when the dc potential changes.

In the present case, we have

$$\hbar\,\Omega \simeq 24 \text{ meV}$$

$$\Gamma \simeq 50 \text{ meV}$$

and condition [4] is clearly not fulfilled. However, the two main consequences are verified and it seems reasonable to assume that the low field limit approximation is valid. The E_0 and Γ values deduced are reported in Table I and we remark that they differ slightly between pH 0 and 14. The smaller value of Γ at pH = 0 seems to be consistent with the above remarks about the lower density of interface states at this pH than at pH 14. Another feature, not reported in Table I, consists in the larger signal amplitude at pH 14 than at pH 0. If we follow a treatment proposed recently by Tomkiewicz *et al.* (15), the general expression for $\Delta R/R$ (8)

$$\frac{\Delta R}{R} = -\frac{2eN_D V_{ac}}{\epsilon_s} L(\hbar\omega) \qquad [5]$$

[where $L(\hbar\omega)$ is the spectral lineshape function] can be rewritten

$$\frac{\Delta R}{R} = A\left(1 - \frac{e}{C_H}\frac{dD_{ss}}{dV}\right)dV \qquad [6]$$

with $A = -\dfrac{2eN_D}{\epsilon_s} L(\hbar\omega)$ and C_H the capacity of the electrolyte Helmholtz layer. Changing expression [5] to expression [6] is possible assuming that the variations in potential are divided between the space-charge layer and the Helmholtz layer by means of interface states. If the dc potential is fixed, an interface which presents acceptor states must correspond to larger signals than an interface

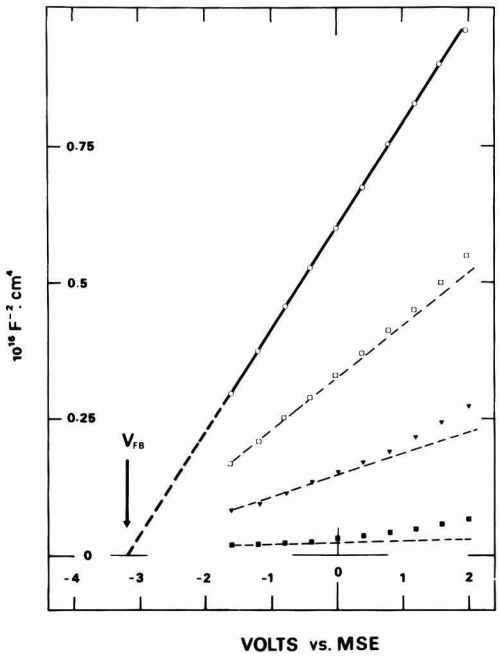

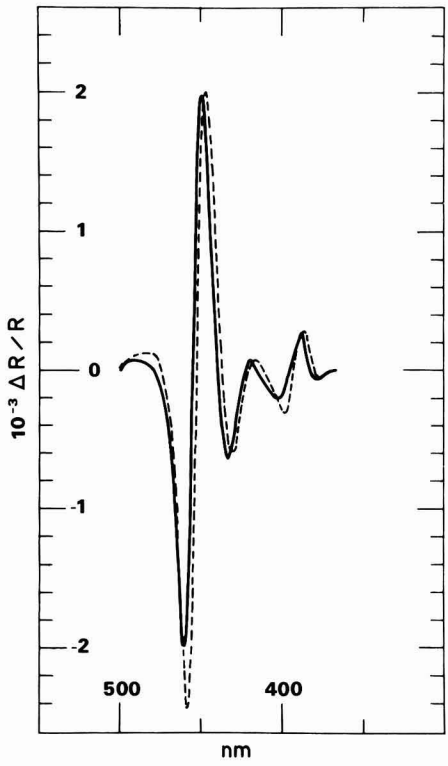

Fig. 4. Characteristics of the n-ZnSe-1M NaOH junction before and after electrochemical perturbation (polarization + 4V vs. MSE). a(above): C^{-2} vs. V (15 Hz). Circles: Reference state. Open squares: 5 mn treatment. Triangles: 10 mn treatment. Closed squares: 15 mn treatment. The C vs. V (100 kHz) plots do not differ noticeably and are not represented. b(right): EER spectra. Solid line: Reference state. Dashed line: After 15 min electrochemical perturbation.

without states: in the first case dD_{sa}/dV is negative and in the second $dD_{sa}/dV = 0$. We have to notice that the treatment which leads to expression [6] is independent of the nature of the interface states, and will be used in the following when the existence of donor interface states can be assumed.

Expression [6] accounts for the difference observed in $\Delta R/R$ amplitude between pH 0 and 14 and is consistent with the existence of acceptor interface states in greater amount at pH 14.

A conclusion deduced from both capacity and EER data analysis concerning the reference state can already be pointed out: the interface ZnSe-electrolyte (and this is certainly not limited to ZnSe) behaves more ideally at pH 0 than at pH 14.

The Perturbed Reference State

Electrochemical perturbation.—This type of perturbation corresponds to that induced by the various treatments achieved in supporting electrolyte under positive polarization of the electrode. According to the remarks about the experimental results (Results section), we can ascertain that the charge transfer mechanism at pH 14 differs from that at pH 0. In the former case, there is no influence of both dissolved oxygen and illumination, whereas in the latter the situation is completely reversed. It appears that at pH 14 the transfer step must be associated with majority carriers (electrons) and at pH 0 with minority carriers generated by illumination. Such an analysis has already been proposed by one of us (6b), but, nevertheless, needs to be made more precise. The main results are reported in Table I.

pH 0.—At pH 0, the transfer step is associated with holes and induces a modification of the electrode behavior only in the presence of oxygen. Therefore, the complete reaction is not specifically limited by the potential value, provided that the electric field in the space-charge layer is large enough to confine the holes in the immediate vicinity of the semiconductor surface. The exact reaction occurring is difficult to determine, but a comparison with results obtained about the oxidation of ZnSe exposed to oxygen and light (16) allows the assumptions of (*i*) the formation of both Zn excess and ZnO and (*ii*) the transformation of Se into soluble products (H_2SeO_3, presumably).

After such a treatment, the differential capacity measured at 100 kHz remains unchanged, whereas at 15 Hz it leads to noticeably different apparent values of N_D (8.6×10^{17} cm^{-3}) and to a diminution of the potential range where a Mott-Schottky behavior is observed. This observation may be accounted for by the statement that the fast interface states remain unaffected, whereas new slow states are created in an amount of approximately 10^{11} cm^{-2} (this result is obtained by arguments similar to those developed in the Differential capacity section).

More striking are the variations with respect to the reference state observed in the EER oscillations in the vicinity of E_0. In this energy range, the absorption coefficient, α, is $10^3 < \alpha < 10^4$ cm^{-1} (17) and the penetration depth of light is at least one order of magnitude larger than the space-charge layer thickness. We conclude from this observation that EER spectra would account mainly for the bulk properties of the semiconductor. Such a statement contradicts clearly our experimental results. We observe an important spectrum shape modification, a slight shift of E_0 towards lower values, and an important attenuation of the spectrum amplitude. By reference to Eq. [6], these results imply the formation of new interface states (already deduced from capacity measurements) and we can ascertain that these states are of the donor type ($dD_{sa}/dV > 0$). Such observations may be correlated with those made by photoemission during the formation of metal-semiconductor junctions where such donor states have been evidenced (18, 19).

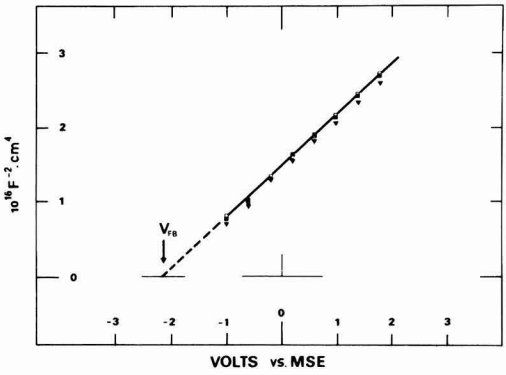

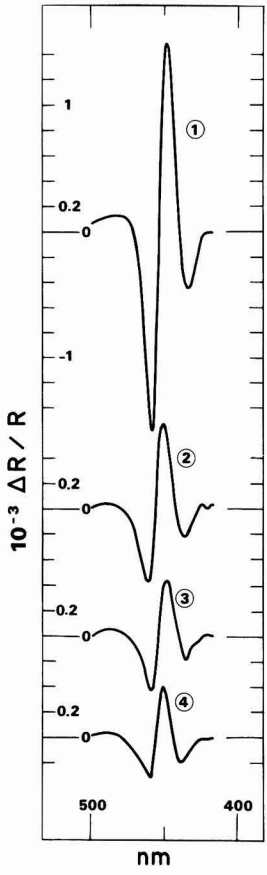

Fig. 5. Behavior of the n-ZnSe-1M $HClO_4$ junction before and after chemical perturbation [cycling between −2.0 and + 2.0V vs. MSE in 1M $HClO_4$ + 10^{-2}M $Fe(CN)_6^{3-}$ for eight cycles at a sweep rate of 50 mV-s^{-1}]. a(above): C^{-2} vs. V plots. Closed squares: Reference state at 15 Hz and 100 kHz. Triangles: Perturbed state at 15 Hz. Open squares: Perturbed at 100 kHz. b(right): EER spectra. 1: Reference state. 2: After two cycles. 3: After four cycles. 4: After eight cycles.

pH 14.—The transfer step is associated with electrons, and the resulting modifications to the reference state are independent of both oxygen and light. It seems reasonable to assume that electrons are injected by OH^- adsorbed at the electrode surface into the semiconductor conduction band. The control of this process by the electrode potential indicates that the transfer occurs via a tunneling process. By analogy with the metal-semiconductor case, we can attempt to determine the present transfer mechanism more precisely.

Calculating the probability P of a triangular barrier being penetrated by an electron with energy ΔE less than the height of the barrier, it is found that

$$P = \exp\left[-\frac{2}{3}(\Delta E)^{3/2}/E_{00}V_S^{1/2}\right] \quad [7]$$

where the parameter

$$E_{00} = \frac{\hbar}{2}\left[\frac{N_D}{m_e^*\epsilon_s}\right]^{1/2} \quad [8]$$

(m_e^* is the effective mass of the electron in the semiconductor) plays a major role. In the present case ($m_e^* = 0.17\ m_o$; $\epsilon_s = 8.7\epsilon_o$, and $N_D = 2 \times 10^{17}$ cm^{-3}), we have

$$E_{00} = 6.8 \times 10^{-3}\ eV$$

Using the expression developed by Padovani and Stratton (20), we can define the band bending values delimiting the various charge transfer processes: thermionic, thermionic-field, and field emission (the two latter refer to tunneling processes). Details of the calculations are beyond the scope of the present paper, and the results are

$V_S \leq 0.6V$	thermionic emission
$0.6 < V_S \leq 29.4V$	thermionic-field emission
$V_S > 29.4V$	field emission

Obviously, the band bending value during the electrochemical treatment (~10 eV) implies that the transfer process we observe is analogous to thermionic-field emission. A consequence of these considerations is that ΔE must be rather small (*ca.* 0.1 eV), thus leading to the location of the OH^- adsorbed groups which donate their electrons in the vicinity of the conduction bandedge (−3.1V *vs.* MSE) in an energy position very different from that they occupy in the electrolyte bulk.

The electrochemical treatment analyzed above induces some particular features in the differential capacity as well as the EER signal. The high frequency capacity remains unchanged, whereas the low frequency capacity is strongly modified and the "pseudo" Mott-Schottky slope increases up to 2×10^{19} (Table II). This variation can be interpreted in terms of slow interfacial energy states (*cf.* the Differential capacity section) and leads to a density of states of *ca.* 2×10^{12} cm^{-2}. This density of states can be related to the increase of the EER signal, which, by means of relation [6], indicates that dD_{sa}/dV is more negative than in the reference state at pH 14.

The electrochemical treatment can then be considered as a strong etching process which, like the etching by

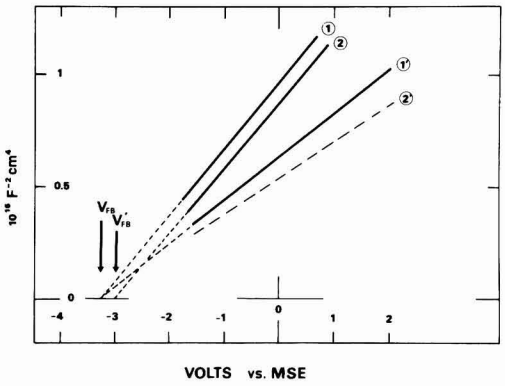

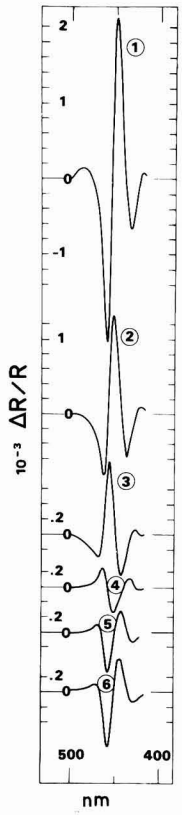

Fig. 6. Characteristics of the ZnSe-1M NaOH junction before and after chemical perturbation [cycling between −2.0 and +2.0V vs. MSE in 1M NaOH + 10^{-2}M $Fe(CN)_6^{3-}$ for six cycles at a sweep rate of 50 mV-s^{-1}]. a(above): C^{-2} vs. V plots. 1 and 1′: Reference states at 100 kHz and 15 Hz, respectively. 2 and 2′: Perturbed states at 100 kHz and 15 Hz, respectively, at the end of the six cycles. b(right): EER spectra. 1: Reference state. 2: After two cycles. 3: After three cycles. 4: After four cycles. 5: After five cycles. 6: After six cycles. Notice that the phase rotation appears to be complete after four cycles and after six cycles, and that the spectrum is restored in phase but strongly attenuated as compared to the reference state.

NaOH, preserves the surface stoichiometry (Zn and Se are involved in final soluble products) and increases the density of interfacial acceptor energy states.

Chemical perturbation.—By chemical perturbation, we mean that the chemical composition of the semiconductor surface is severely perturbed. The use of the oxidizing species $Fe(CN)_6^{3-}$ seems especially adequate for this purpose (6b). The exact process by which this species produces the modified semiconductor surface is not yet clear and depends on the pH of the solution. At pH 0, the reaction seems to be chemical, whereas at pH 14 it seems to be a mixture of electrochemical and chemical processes. At each pH value, the resulting surface is different and behaves specifically when studied in supporting electrolyte of equivalent pH value.

pH 0.—The modified interface behaves like that produced by electrochemical perturbation at pH 0 both in capacity and EER.

It seems reasonable to assume that the semiconductor surface produced by the ferricyanide treatment is similar to that produced by the former electrochemical treatment and, therefore, we do not emphasize it.

pH 14.—The final result of the treatment is to create a selenium layer on the top of the ZnSe electrode. This layer induces a specific behavior of the modified electrode when immersed further in an electrolyte of pH 14. The EER signal is strongly attenuated and rotates in phase. The slope of the Mott-Schottky plot changes at low frequency, but does not at high frequency. In the latter case, in addition, the flatband potential shifts towards a slightly more positive value. This observation seems in good agreement with that already made on CdSe electrodes upon deposition of a Se layer (21). By analogy with the observation made during the formation of Ge-GaAs interfaces (22), it seems appropriate to assume the creation of donor interface states with large relaxation time due to the interaction between Se atoms and the ZnSe surface. The strong attenuation of the EER signal is in part accounted for by the absorption of light in the Se layer, whose fundamental energy gap is *ca.* 2 eV, and the absorption coefficient larger than 10^5 cm^{-1} in the region

Table I. The reference state parameters at pH 0 and 14. The steady-state barrier height V_S(open circuit) can be deduced from V_R and V_{FB} determinations using the relation $V_S = |V_{FB} - V_R|$. The free carrier density as determined by Hall effect is ~ 2×10^{17} cm^{-3} and serves as a reference value

Electrolyte	Rest potential V_R (V *vs.* MSE)	Capacity V_{FB} (V *vs.* MSE)		Capacity N_D (cm^{-3})		N_D (cm^{-3}) Hall effect	Electroreflectance E_o (eV)	Electroreflectance Γ (meV)
		15 Hz	100 kHz	15 Hz	100 kHz			
$HClO_4$ (pH = 0)	−0.65	−2.2	−2.3	2×10^{17}	2×10^{17}	2×10^{17}	2.724	43
NaOH (pH = 14)	−0.8	−3.2	−3.1	8×10^{17}	2.7×10^{17}	2×10^{17}	2.711	57

Table II. The question mark indicates that the experimental results cannot be interpreted using a simple model. The Schottky plots are not clearly linear in a large potential range, and the phase rotation of the EER signals excludes the use of the three-point method

Electrolyte	Treatment	Capacity				EER	
		V_{FB} (V)		N_D (cm^{-3})		E_0 (eV)	(meV)
		15 Hz	100 kHz	15 Hz	100 kHz		
$HClO_4$	Positive polarization + Oxygen + Light	?	−2.3	8.6×10^{17} (?)	2×10^{17}	2.714	35
	$Fe(CN)_6^{3-}$	?	−2.2	2.4×10^{17}	2.1×10^{17}	2.728 (?)	43
NaOH	Positive polarization	−3.1 (?)	−3.1	2×10^{19}	3.0×10^{17}	2.732	61
	$Fe(CN)_6^{3-}$	−3.2 (?)	−3.0	1.5×10^{18} (?)	2.8×10^{17}	?	?

of 2.7 eV (23). The phenomenon of phase rotation of the EER signal has already been described by other authors and has been accounted for similarly by the existence of interface energy states induced by an electrochemical treatment (15) and by the formation of a heterojunction (24).

Conclusion

By coupling electrochemical and *in situ* electroreflectance measurements and by applying controlled perturbations at the interface, we tried to infer a description of the ZnSe-electrolyte interface by analogy with the models used for the metal-semiconductor junctions.

The above discussion establishes that the ZnSe-supporting electrolyte junction behaves like a metal-semiconductor junction. However, the main interface properties are governed not by the bulk properties of the semiconductor-electrode, but by its surface states. These surface states can be either intrinsic to the semiconductor surface or resulting from a specific interaction with the electrolyte.

Summing up, we can say that an electrolyte with no etching properties (acidic medium) leads to the formation of an interface with a low density of interface states, whereas a basic electrolyte with etchant character leads to a pinning of the semiconductor Fermi level by acceptor surface states located *ca.* 0.5 eV above the valence band maximum.

Perturbing the reference state defined above induces particular effects which differ according to the nature and intensity of the perturbation. The simple model with acceptor interface states governing the junction properties must be made more sophisticated to incorporate a relatively large density of donor interface states located in the upper part of the semiconductor gap.

Provided that these considerations are taken into account, an electrolyte-semiconductor junction can be described, at least qualitatively, like a metal-semiconductor interface.

Manuscript submitted Jan. 22, 1985, revised manuscript received April 25, 1985.

REFERENCES

1. See, *e.g.*, J. F. Dewald, *Bell Syst. Tech. J.*, **39,** 615 (1960); H. Gerischer, *Z. Phys. Chem. (N. F.)*, **26,** 223 (1960); V. A. Myamlin and Yu. V. Pleskov, "Electrochemistry of Semiconductors," Plenum Press, New York (1967); S. R. Morrison, "Electrochemistry at Semiconductor and Oxidized Metal Electrodes," Plenum Press, New York (1981).
2. See, *e.g.*, (a) E. H. Rhoderick, "Metal-semiconductor contacts," Oxford University Press, Oxford, England (1978); (b) L. J. Brillson, *Surf. Sci. Rpt.*, **2,** (2) (1982).
3. D. Haneman, *Surf. Sci.*, **86,** 462 (1979).
4. See, *e.g.*, A. J. Bard, A. B. Bocarsly, F-R. F. Fan, E. G. Walton, and M. S. Wrighton, *J. Am. Chem. Soc.*, **102,** 3671 (1980).
5. R. Williams, *This Journal*, **114,** 1173 (1967); P. M. Smiley, R. N. Biagioni, and A. B. Ellis, *ibid.*, **131,** 1068 (1984).
6. (a) J. Gautron, P. Lemasson, F. Rabago, and R. Triboulet, *ibid.*, **126,** 1868 (1979); (b) P. Lemasson and J. Gautron, *J. Electroanal. Chem.*, **119,** 289 (1981), (c) P. Lemasson, J. Gautron, and J. P. Dalbéra, *Ber. Bunsenges. Phys. Chem.*, **84,** 796 (1980).
7. J. P. Dalbéra, C. Hinnen, and A. Rousseau, *J. Phys. C. (Paris)*, **38,** 185 (1977).
8. D. E. Aspnes, *Phys. Rev. Lett.*, **28,** 913 (1972).
9. S. G. Lorrie, J. R. Chelikowsky, and M. L. Cohen, *Phys. Rev. B*, **15,** 2154 (1977).
10. D. Bolmont, V. Mercier, P. Chen, H. Lüth, and C. A. Sébenne, *Surf. Sci.*, **126,** 509 (1983).
11. A. Ebina, T. Anno, Y. Suda, H. Koinuma, and T. Takahashi, *J. Vac. Sci. Technol.*, **19,** 301 (1981).
12. S. J. Fonash, *J. Appl. Phys.*, **54,** 1966 (1983).
13. A. Zur, T. C. McGill, and D. L. Smith, *Phys. Rev. B*, **28,** 2060 (1983).
14. D. E. Aspnes and J. E. Rowe, *Phys. Rev. Lett.*, **27,** 188 (1971).
15. M. Tomkiewicz, W. Siripala, and R. Tenne, *This Journal*, **131,** 736 (1984).
16. A. Ebina, K. Asano, Y. Suda, and T. Takahashi, *J. Vac. Sci. Technol*, **17,** 1074 (1980).
17. J. Gautron, C. Raisin, and P. Lemasson, *J. Phys. D: Appl. Phys.*, **15,** 153 (1982).
18. D. Bolmont, P. Chen, and C. A. Sébenne, *Surf. Sci.*, **117,** 417 (1982).
19. W. E. Spicer, P. W. Chye, P. R. Skeath, C. Y. Su, and I. Lindau, *J. Vac. Sci. Technol.*, **16,** 1422 (1979).
20. F. A. Padovani and R. Stratton, *Solid-State Electron.*, **9,** 695 (1966).
21. K. W. Frese, Jr., *J. Appl. Phys.*, **53,** 1571 (1982).
22. P. Chen, D. Bolmont, and C. A. Sébenne, *J. Phys. C: Solid State Phys.*, **15,** 6101 (1982).
23. J. Stuke, *J. Non-Cryst. Solids*, **4,** 1 (1970).
24. R. L. Brown, L. Schoonveld, L. L. Abels, S. Sundaram, and P. M. Raccah, *J. Appl. Phys.*, **52,** 2950 (1981).

Photoelectrochromic Properties of Polypyrrole-Coated Silicon Electrodes

Hiroshi Yoneyama,* Koichi Wakamoto, and Hideo Tamura

Department of Applied Chemistry, Faculty of Engineering, Osaka University, Yamada-oka 2-1, Suita, Osaka 565, Japan

ABSTRACT

Photoelectrochromic properties of polypyrrole-coated Si electrodes in propyrene carbonate solutions were investigated to obtain fundamental information on optical image formation. It took about 1s or more for a coated film ca. 90 nm thick to complete its color change when the entire surface of the film was illuminated with a 500W xenon lamp, an observation of which indicates diffusion limitation of electrolyte anions in the film. In contrast, different image forming behaviors were seen when the film was illuminated with a He-Ne laser. Illumination of the film on n-type Si substrates with the laser for 1s gave an optical image of about ten times of the illuminated area, while an optical image comparable with the illuminated area was obtained for p-type Si substrates for the same illumination time. In either case, continuous irradiation caused peripheral growth of the optical image in the film.

One of recent interests in polymer-coated electrodes concerns their electrochromic properties (1-14). A polymer film is usually deposited on a metallic conductive substrate, such as a thin Pt film, and highly conducting SnO_2 and In_2O_3. A color change of the coated film occurs when it is stimulated by a large current pulse that causes oxidation of a reduced film or reduction of an oxidized film. If a semiconductor is used in place of the metallic conductive substrates, different features in electrochromism will appear with the assistance of illumination. Since semiconductor electrodes have a photosensitized action, illumination of polymer-coated semiconductor electrodes should spontaneously cause the color change without a change in the applied bias if the electrodes are properly biased in advance. Several interesting features of photoelectrochromism have recently been reported by Inganaes and Lundström for polymethylpyrrole-coated n-type Si (15). In this paper, we wish to report detailed characteristic features concerned with optical image formation and its storage. The polymer chosen was electropolymerized polypyrrole, which was deposited onto n- and p-type single-crystal wafers. It will be shown that behavior of the color change caused by illumination shows little difference between the conductivity type of the semiconductor substrate.

Experimental

Silicon single-crystal wafers manufactured by Osaka Titanium Company were used. They were polished with 0.06 μm alumina to give a mirror finish, then etched in 46% HF for 15 min, and finally rinsed with methanol. Electrodeposition of polypyrrole was made at 0.3 mA-cm^{-2} in 0.1*M* pyrrole dissolved in propyrene carbonate. The electrolysis charge usually employed was 36 mC-cm^{-2}, which gave *ca.* 90 nm thickness (14).

The polymer deposition on n-type Si electrodes was carried out by illuminating the electrode with light of wavelengths longer than 390 nm, obtained from a 500W xenon lamp in combination with a colored glass filter (Toshiba UV-390), while the deposition onto p-type Si was conducted without illumination. The illumination intensity was *ca.* 2.3W, as determined by a power meter (Coherent Radiation, Model 201).

For *in situ* measurements of the color change associated with the redox reaction of the polymer film, the electrode was set in an electrolytic cell in such a way that the incident light path was *ca.* 45° with respect to the perpendicular from the surface. The illuminating light in this case was the same as that described above. The light reflected from the electrode surface was passed through a monochrometer (JASCO, Model CT-25), a chopper (Nikon, Model M205), and introduced to a PbS detector (Hamamatsu Photonics, Model P397). The signal from the detector was measured by a electrophotometer (Nikon, Model SP 104). The monochrometer was used to isolate the 400 nm light from the reflected light. According to the published optical properties of oxidized and neutral polypyrrole films (14, 16, 17), the latter film has large absorptivity at this wavelength, but this is not so for the oxidized film. In order to obtain optical image formation, a 1.3 mm diam area of the film on Si was illuminated with a He-Ne laser (NEC, Model GLG 5700). The intensity of the laser beam was 24.5 mW.

A potentiogalvanostat (Hokuto Denko, Model HA 101), a function generator (Hokuto Denko, Model HB 104), and a X-Y recorder (Yokogawa Electric, Model 3077) were used for conventional electrochemical measurements. A saturated calomel electrode (SCE) served as a reference electrode, and the counterelectrode was a Pt plate. The potential cited in this paper is referred to this reference electrode. Polypropyrene carbonate was purified by distillation (18), and lithium perchlorate was dried *in vacuo* at 150°C overnight. Other chemicals were reagent grade.

Results and Discussion

Current-potential curves taken under illumination of polypyrrole-coated Si at 100 mV-s^{-1} are shown in Fig. 1 and 2 for the cases of n- and p-type Si substrates, respectively, together with the reflectance change associated with photoelectrochemical reactions of the coated elec-

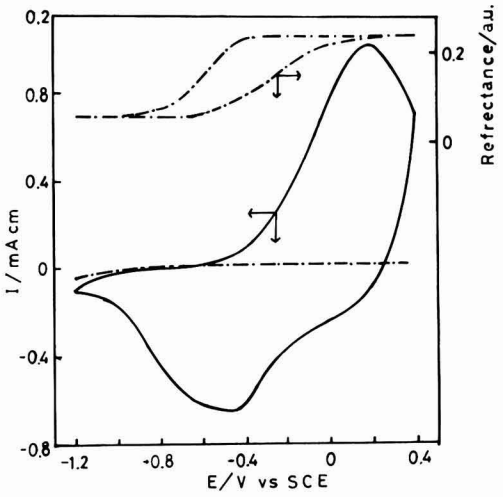

Fig. 1. Steady current-potential curves of a polypyrrole-coated n-type Si electrode under illumination (solid line) and in the dark (dot-dash line), and the top curve is for reflectance of the film measured *in situ*. Film thickness: *ca.* 90 nm. Solution: 0.1M $LiClO_4$ in propyrene carbonate. dE/dt = 100 mV-s^{-1}.

*Electrochemical Society Active Member.

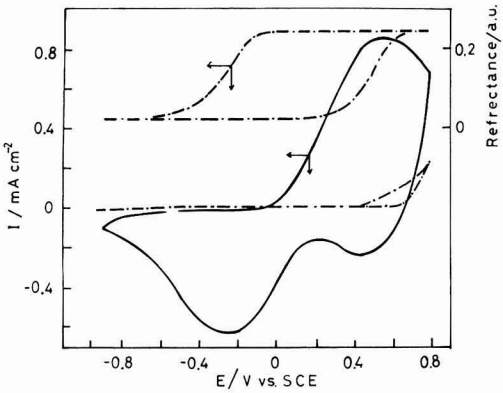

Fig. 2. As in Fig. 1, but for a p-type Si substrate.

trodes. Also given in the figures are the dark currents. In the case of using the n-type Si substrate, some reduction of the oxidized polymer occurred in the dark at 0.4V (not shown in the figure). This potential was chosen as the anodic limit of the potential sweep in Fig. 1, since the oxidized polymer on Pt is reduced a little at this potential. Appreciable reduction of the oxidized polymer in the dark occurred, however, at potentials where a large cathodic wave appeared under illumination. The polymer-coated p-type Si did not show appreciable reactivities in the dark unless the film was in a neutral state. The neutral film shows voltammograms similar to those shown in Fig. 2 during the anodic scan.

The color of polypyrrole in the neutral state is yellow. In the oxidized state it is dark brown. The film on Si electrodes was, however, green in the neutral state and dark brown in the oxidized state to the naked eye, owing to interference of the black Si substrate.

The oxidized film on p-type Si was not reduced in the dark, and, similarly, the neutral film on n-type Si was not oxidized in the dark at potentials similar to those shown in Fig. 1 and 2. Thus, the electrode potentials of −0.9V for p-type Si and 0.4V for n-type Si were chosen in the following experiments to cause photosensitized reactions of the coated polymer film. As Fig. 1 and 2 demonstrate, these potentials are sufficiently large to reduce the film on p-type Si and to oxidize the film on n-type Si electrodes, respectively.

The transient photocurrent behavior and reflectance change of the film-coated electrode are shown in Fig. 3 together with the imposed electrode potential profiles; in each case, the entire electrode surfaces were illuminated. Upon illumination of the neutral film-coated n-type Si electrode at 0.4V, anodic photocurrents flowed until the film was completely oxidized, as seen in the reflectance change (Fig. 3a). Additional illumination had no significant effect. When the electrode potential was switched to −1.2V, cathodic currents flowed, as shown in the figure, and simultaneously the film was reduced to give the original reflectance. The reduction behavior of the film at −1.2V was not greatly affected by the illumination. Similar results were obtained for the p-type Si substrate except that illumination was required to reduce the film. A long time was required to complete the color change of the films for both n- and p-type Si electrodes; it took about 1s or more. The diffusion of electrolyte anions in the polymer film seems to control the rate of the color change (6).

The film color at p-type Si produced by photosensitized reduction of the oxidized film was stable after interruption of illumination, provided that the electrode bias was not interrupted (Fig. 4a). Under open-circuit condition, however, the color of the reduced film gradually changed, indicating that oxidation occurred. Residual oxygen in the electrolyte solution must be responsible for

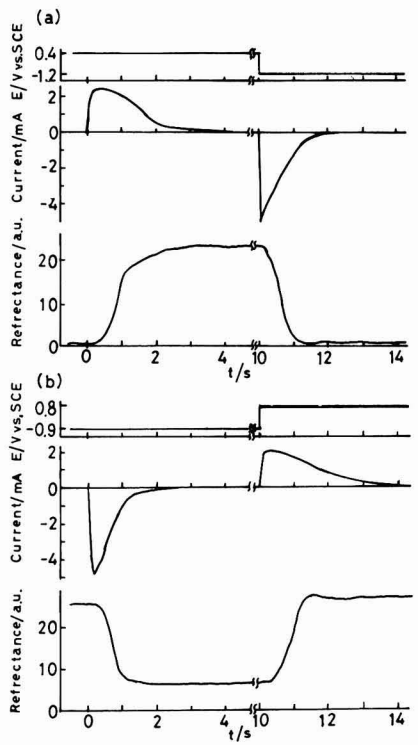

Fig. 3. Transient behavior of current and reflectance at 400 nm of polypyrrole-coated Si electrodes during an imposed potential step. a: n-Type Si electrode coated initially with neutral polypyrrole film. b: p-Type Si electrode coated initially with oxidized polypyrrole film. The entire surfaces of the electrodes were illuminated during the measurements.

the observed color change. In the case of the oxidized film on n-type Si, the interruption of illumination at 0.4V caused small instantaneous cathodic current flow, as described above. The initial value of this cathodic current was *ca.* 1/15 of the initial current observed when the electrode potential was switched from 0.4 to −1.2V under illumination (Fig. 3a).

This current, however, soon decayed to zero. As a result, the cathodic charge due to this dark current did not result in any significant fading of the film color. The color produced by the photosensitized oxidation of the neutral film was stable irrespective of whether or not the electrode bias was interrupted, possibly because the residual oxygen has no effect on the oxidized state of the film.

The durability of the color change to repeated potential step pulses was investigated under illumination of the

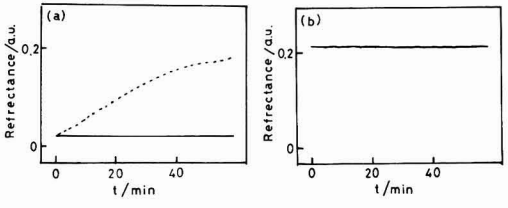

Fig. 4. Stability of the film color produced by illumination during its interruption. a: Polymer-coated p-type Si polarized at −0.9V in the dark (solid line) and under open circuit (dashed line). b: Polymer-coated n-type Si in the dark with and without polarization at 0.4V.

coated film. The voltage pulse chosen had a 10s interval and ranged from 0.8 to −0.9V for p-type Si and from −1.2 to 0.4V for n-type Si. The response characteristics during the initial stage are those shown in Fig. 3. It was found that with repeated potential step cycles, reduction of the film decreased. If the ratio of the difference in reflectance of the film between the oxidized and the reduced state at extended potential pulse cycles (ΔR) to that at the first cycle ($\Delta R_{initial}$) is plotted as a function of the cycle number, Fig. 5 is obtained.

We speculated that the decrease of $\Delta R/\Delta R_{initial}$ with the cycles might have been brought about by oxidative decomposition of the coated film (19). The effect of the anodic potential on the durability of the film was then investigated. The results showed, however, that the decrease in the anodic potential from 0.4 to 0V for the case of n-type Si and from 0.8 to 0.3V for p-type Si did not make any appreciable improvements. Furthermore, the decrease in the anodic potential also produced a slowdown in the response of the color change. Additional studies are required to clarify detailed chemistry related to the decrease of $\Delta R/\Delta R_{initial}$ with the potential step cycles.

In order to obtain information on optical image formation, the film was irradiated with a laser beam to produce an image pattern in a spot on the coated film. The same anodic potential was used as that employed in obtaining Fig. 3: 0.4V for n-type Si and −0.9V for p-type Si. While an image could be formed, the area of the spot gradually increased on continuous irradiation of the film. The peripheral growth of the image occurred more rapidly at the n-type Si electrode than at the p-type one. Photographs of image patterns were taken at different illumination time, and the patterned area of the spot to the total filmed area was determined. This ratio was compared with the ratio of the charge consumed in the image formation to that required in the conversion of all the film to the same color as the image. The results are shown in Table I. The area of the laser beam was 0.013 cm², and the total area of the electrode surface was 0.95 cm².

As may be seen in Table I, the illumination for 1s of p-type Si coated with the oxidized polymer produced an image of the laser beam. In the case of the n-type material, the image pattern was ten times larger than the area of the laser beam. The charge consumed during the image formation was larger for all illumination times for the p-type electrode compared to that at the n-type one. As described below, such difference in the image formation behavior must be closely related to the mechanism by which the color change initially propagates.

When the image is formed in the film on the n-type Si electrodes, electrolyte anions are incorporated into the illuminated part of the film in its outermost part, to change there from a reduced state of high electrical resistivity to an oxidized state of low electrical resistivity. Once the outermost part of the film becomes highly conductive, the peripheral growth of the optical image pattern will easily occur at the film/solution interface, as illustrated in Fig. 6a. However, the growth of the optical image in the p-type Si electrode is associated with exclusion of the incorporated anions to give an insulating polymer film. The image pattern formation in this case must occur initially from the film/semiconductor interface as a result of diffusion of the incorporated anions towards the solution side of the film, as illustrated in Fig. 6b.

As already reported (20-23), adhesion of the polymer to Si is rather poor, so that the existence of electrolyte solu-

Table I. Growth of the optical image pattern with continuous irradiation of a fixed area of the electrode surface[a]

Illumination time (s)	n-Type Si		p-Type Si	
	Colored area[b] (%)	Fraction of charge consumed[c] (%)	Colored area (%)	Fraction of charge consumed (%)
1	15	0.92	1.2	4.2
2	22	1.8	4.9	16
3	35	2.7	7.7	19
4	42	3.5	15	27
5	68	4.3	31	31

[a] The semiconductor electrodes coated with polypyrrole of ca. 90 nm thickness were illuminated with a He-Ne laser beam of 24.5 mW. The n-type Si coated initially with a neutral film was polarized at 0.4V, and the p-type one with an oxidized film was polarized at −0.9V.
[b] The colored area to the entire electrode surface is given.
[c] The ratio of charge consumed in the formation of the colored image to that required for the complete coloring of the entire surfaces.

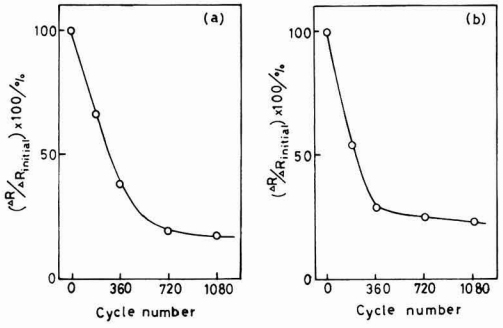

Fig. 5. The ratio of the difference in reflectance between the oxidized and neutral states at extended potential pulse cycles to that at the first cycle vs. the cycle number of the potential pulse. a: n-Type Si substrate. b: p-Type substrate. Potential pulse: −0.9 to 0.8V for a, and −1.2 to 0.4 V for b. The interval of the pulse: 10s.

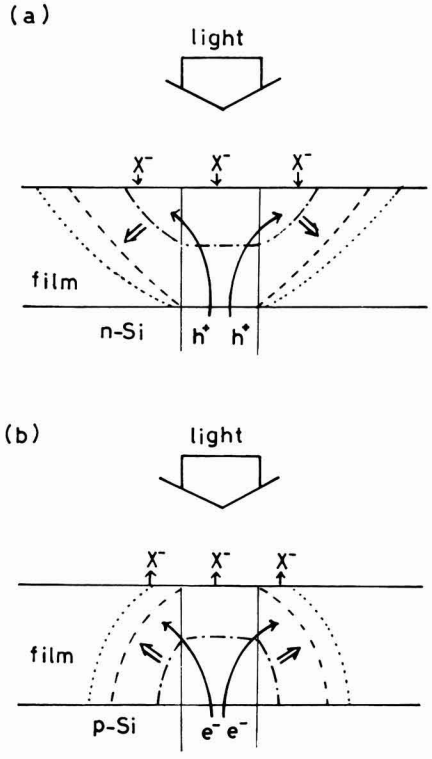

Fig. 6. Schematic illustration of the growth of the domain where the color change of the coated film occurs. a: n-Type Si substrate. b: p-Type substrate. X^- denotes an electrolyte anion.

tions in the film as well as at the film/Si interface is highly probable. If so, the distance for photogenerated charge carriers to travel an insulating layer zone will be short compared with the apparent film thickness, and the real situations encountered in the image forming process will be more complicated than that discussed above. Nevertheless, the different behavior of the propagation of the image pattern with illumination time between the n-type and p-type S substrate (Table I) can be explained well by the above described discussion with use of Fig. 6.

Conclusion

In this study, we employed polypyrrole films as photoelectrochromic material. The durability of the coated film and its response behavior are unsatisfactory from the view point of practical application, but improvements in the properties might be made by suitable choice of another kind of electrically conductive polymer. The resolution of the optical image formed, however, will be controlled by similar manner, as shown in Table I and schematically illustrated in Fig. 6. In this sense, the exposure of patterned light for well-controlled time is said to be important for the formation of good optical images.

Manuscript submitted Dec. 26, 1984; revised manuscript received May 1, 1985.

Osaka University assisted in meeting the publication costs of this article.

REFERENCES

1. F. B. Kaufman, A. H. Schraeder, M. Edward, and V. V. Patel, *Appl. Phys. Lett.*, **36,** 422 (1980).
2. H. Akaboshi, S. Toshima, and K. Itaya, *J. Phys. Chem.*, **85,** 818 (1981).
3. G. C. S. Collins and D. J. Schiffrin, *J. Electroanal. Chem. Interfacial Electrochem.*, **139,** 335 (1982).
4. K. Itaya, H. Akaboshi, and S. Toshima, *This Journal*, **129,** 762 (1982).
5. P. C. Bookbinder and M. S. Wrighton, *ibid.*, **130,** 1080 (1982).
6. A. F. Diaz, J. I. Castillo, J. A. Logan, and E-Y. Lee, *J. Electroanal. Chem. Interfacial Electrochem.*, **129,** 389 (1983).
7. P. C. Lacaze, J. E. Dubois, A. Desebene-Monvernay, P. L. Desbene, J. J. Bassetier, and D. Richard, *ibid.*, **147,** 107 (1983).
8. F. Garnier, G. Tourillon, M. Gazard, and J. E. Dubois, *ibid.*, **148,** 299 (1983).
9. A. Desbene-Monvernay, P. C. Lacaze, J. E. Dubois, and P. L. Desbene, *ibid.*, **152,** 87 (1983).
10. R. N. Dominey, T. J. Lewis, and M. S. Wrighton, *J. Phys. Chem.*, **87,** 5345 (1983).
11. K. Kaneto, S. Ura, K. Yoshino, and Y. Inuishi, *Jpn. J. Appl. Phys.*, **23,** L189 (1984).
12. G. Tourillon and F. Gardiner, *J. Phys. Chem.*, **87,** 2289 (1983).
13. T. Kobayashi, H. Yoneyama, and H. Tamura, *J. Electroanal. Chem. Interfacial Electrochem.*, **161,** 419 (1984).
14. S. Kuwabata, H. Yoneyama, and H. Tamura, *Bull. Chem. Soc. Jpn.*, **57,** 2247 (1984).
15. O. Ingnaes and I. Lundstrom, *This Journal*, **131,** 1129 (1984).
16. K. Yakushi, L. J. Lauchlan, T. C. Clarke, and G. B. Street, *J. Chem. Phys.*, **79,** 4774 (1983).
17. J. L. Bredas, J. C. Scott, K. Yakushi, and G. B. Street, *Phys. Rev. B.*, **30,** 1023 (1984).
18. C. K. Mann, in "Electroanalytical Chemistry," Vol. 3, A. J. Bard, Editor, p. 119, Dekker, New York (1968).
19. R. A. Bull, F-R. F. Fan, and A. J. Bard, *This Journal*, **127,** 1009 (1982).
20. R. N. Noufi, A. J. Frank, and A. J. Nozik, *J. Am. Chem. Soc.*, **103,** 1849 (1981).
21. T. Skotheim, I. Lundström, and J. Prejza, *This Journal*, **128,** 1625 (1981).
22. F-R. F. Fan, B. L. Wheeler, A. J. Bard, and R. N. Noufi, *ibid.*, **128,** 2042 (1981).
23. T. Skotheim, L.-G. Petersen, O. Inganäs, and I. Lundström, *ibid.*, **129,** 1737 (1982).

Technical Notes

Performance of Suspension-Impregnated Sintered Nickel Composite Electrodes

W. A. Ferrando*

Naval Surface Weapons Center, Materials Division, White Oak, Silver Spring, Maryland 20903-5000

Low cost, high performance nickel electrodes will be required for improved Ni-H_2, Ni-Zn, Ni-Fe cells. Several years of effort have been directed to the development of a porous sintered, nickel-plated graphite fiber plaque impregnated by the electrochemical method (1, 2). Plaques were successfully fabricated by compression sintering of electroless nickel-plated graphite mat (3). In the course of optimization, it was found that plaques produced using chopped electroplated graphite fiber exhibited more uniform porosity, durability, and other properties.

Concurrently, an effort was undertaken to find an alternative method of active material [$Ni(OH)_2$] impregnation suitable for these composite plaques. The electrochemical method had been observed to produce good results. Although simpler and quicker than the older chemical methods, the electrochemical method requires batch processing in tanks with temperature, pH, time, and current control, as well as time-consuming rinsing. There is also some concern over bath concentration depletion and chemical attack on the plaque.

The Suspension Impregnation Method

It was found that the pore size (~50 μm) and open pore structure of the composite plaque allowed it to accept direct impregnation by fine particulate $Ni(OH)_2$. To accomplish this, commercial battery-grade $Ni(OH)_2$ was ground by ball milling to particle diameters (~1-20 μm). The powder was mixed with ethylene glycol (b.p. 198°C) to the consistency of a heavy cream (about 1:2 by weight). The inert semiviscous glycol fluid served to hold the fine active material particles in suspension and provided the lubrication necessary for direct infiltration into the pores.

The impregnation procedure consists of several simple steps. The plaque is placed on a level, nonporous surface. A quantity of the freshly mixed suspension fluid is ap-

*Electrochemical Society Active Member.

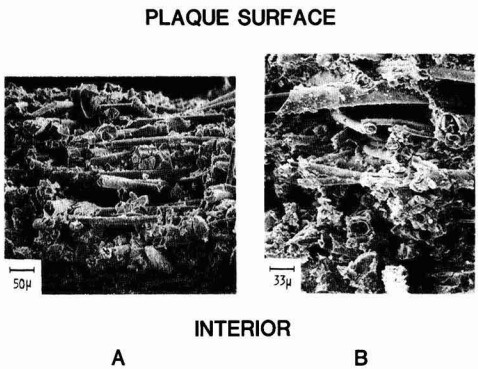

Fig. 1. SEM micrographs, composite plaque cross sections (as cut surfaces). Active material deposition by electrochemical impregnation (A), and by suspension impregnation (B).

plied on and gently rubbed into the plaque surface. The operation is repeated from the reverse side. The plaque is heated (~150°C) to evaporate the glycol carrier fluid. Finally, it is brushed lightly to remove surface material and weighed to determine electrode capacity. The operation is repeated, if necessary, to achieve the desired loading level. The entire process can be carried out in a few minutes. Figure 1 shows SEM photographs of the cut edges of suspension-impregnated (A) and electrochemically impregnated (B) composite plaques. Cut ends of the nickel-plated graphite fibers are visible. The pictures enable one to make a rough visual comparison of the initial active material distribution through the cross section by the two methods.

Cobalt Additive Addition

Cobalt additive has long been used to improve utilization and cycle life of nickel electrodes. Recent investigation (4) has revealed that cobalt additive is most efficiently utilized when it is applied to the active material surfaces within the pores, rather than as a volume constituent. The cobalt apparently facilitates proton charge transfer across the active material-electrolyte interface. This addition may be accomplished chemically by soaking the impregnated plaque in an aqueous cobalt compound solution followed by conversion to $Co(OH)_2$. Cobalt may be added also by a very brief electrochemical deposition from a cobalt impregnation bath. Cobalt added by either method constitutes about 1-4 weight percent of the active mass. Surface deposition of the additive allows the suspension-impregnated electrode to achieve 90% utilization within five to ten discharge cycles.

Test cells were fabricated using a single composite nickel electrode sandwiched between two commercial negatives in 31% KOH with no electrolyte additives and under flooded conditions. Electrochemically impregnated electrode capacities were determined from the postformation weight gain of active material. Capacities of the suspension-impregnated electrodes were determined by the total weight increase measured after cobalt treatment.

Results

Continuous cycling tests were performed on the cells. The imposed regime included charging at the *C* rate (125%), 10 min rest, followed by discharge at the *C*/2 rate to 0.75V cutoff (> 95% DOD). Table I lists several important parameters for representative composite electrodes tested according to this regime. The reported utilizations were measured after the initial rise in capacity. Since an objective of this effort was to maximize the usable energy density, several electrodes (no. 83, 85, 95) were electrochemically reimpregnated after initial formation in order to augment loading levels. The high theoretical loadings achieved were of little advantage, however, since reduced utilizations were observed for these electrodes. Working energy densities of 150-170 Ah/kg (0.27-0.35 Ah/cm^3) were realized generally for the electrochemically impregnated electrodes. The inability to effect a usable increase in energy density by repeated electrochemical impregnation was due probably to the difficulty of maintaining proper conditions within the pores for compact deposition at high loading levels.

Suspension-impregnated electrodes did not suffer this drawback to high loading levels. Entries to Table I indicate that a combination of high active material loading and good utilization could be attained. Operating energy densities in the range of 175-192 Ah/kg (0.24-0.325 Ah/cm^3) were observed in the cycling tests. Utilization of active material rarely failed to achieve 90% and sometimes exceeded 100% of theoretical capacity. Table I includes several 2.5 mm thick electrodes, which were rapidly and efficiently impregnated by the suspension method. Thick plaques normally present a challenge for any impregnation method. Microgrinding or special precipitation techniques might be able to produce a finer $Ni(OH)_2$ powder for use in the suspension. In such case, better filling of small pores might allow somewhat higher useful energy densities to be attained.

Several electrodes without current collector grids were fabricated and tested. These are represented by entry no. 44 of Table I and in the data of Fig. 2. The limited test (80 cycles) yielded good utilization and verified the inherent integrity and electrical conductivity of the composite structure. This result indicates that successful composite electrodes might be fabricated without a current collector grid.

Table I. Test electrode parameters

Electrode[a]	Plaque porosity (%)	Nominal thickness (mm)	Theoretical capacity (Ah/kg)	(Ah/cm^3)	Ultimate utilization (%)
83-A[b]	89	1.0	190	0.345	82
85-A	85	1.0	191	0.380	83
95-A	82	1.0	208	0.448	78
97-A	82	1.0	205	0.410	74
101-A	71	1.0	169	0.363	86
44-B	83	1.0	183	0.321	95
65-B	91	1.5	189	0.248	93
73-B	73	2.5	193	0.256	95
74-B	73	2.5	208	0.327	91
70-B	73	2.5	169	0.219	113
75-B	82	1.0	183	0.308	105
Powder sinter (commercial) 8/81	—	0.84	86	0.323	—

[a] Electrode dimensions: 2.4 × 4.5 cm.
[b] A indicates electrochemical impregnation; B indicates for suspension impregnation.

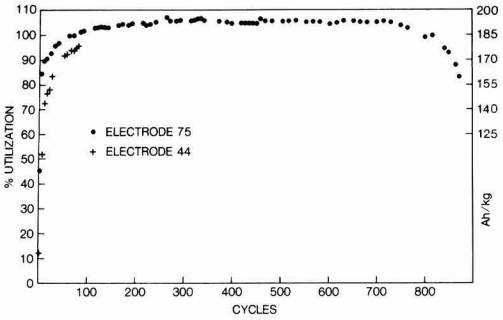

Fig. 2. Active material utilization and volumetric energy density vs. charge-discharge cycles for suspension-impregnated electrodes. No. 75 with current collection grid. No. 44 without current collection grid.

Figure 2 shows the excellent life-cycle durability results obtained with the suspension-impregnated composite electrode. Electrode no. 75 yielded very constant utilization in excess of 100% throughout its lifetime of 800 cycles under the aforementioned test regime. This performance level was typical of the test electrodes with cobalt surface treatment, although most tests were not carried beyond 80-100 cycles.

In order to provide a meaningful life-cycle base line, a commercial positive was tested under substantially identical conditions. Its capacity was determined from the manufacturer's specified cell rating. This capacity, however, apparently underestimated its true capacity somewhat from the observed extended discharge period. This, in turn, implied correspondingly lighter cycling conditions than the specified charge (C) and discharge (C/2). Figure 3 shows the test results. The utilization, normalized here to the maximum observed value, remained reasonably constant over most of the test period. A (gravimetric) energy density of about 115 Ah/kg was achieved. A useful life of about 900 cycles was observed. Cycle-life durability is a major consideration in any secondary battery system. Thus, the main intention in presenting Fig. 2 and 3 is to show the comparability of cycle life between the composite electrode and a powder sintered electrode under the same demanding cycling regime.

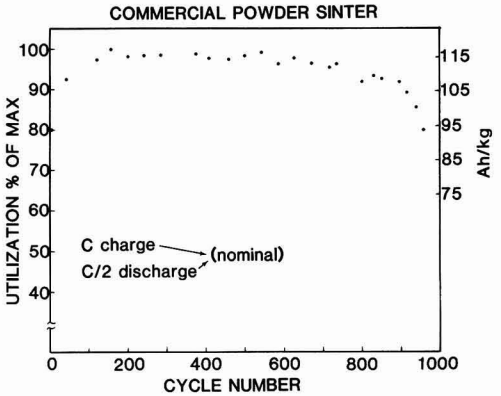

Fig. 3. Normalized active material utilization and volumetric energy density vs. charge-discharge cycles for commercial powder sintered electrode.

In conclusion, this work shows the potential for a successful high energy density, electrically durable, lightweight nickel composite electrode fabricated by a relatively simple suspension method of active material impregnation.

Manuscript received Jan. 18, 1985.

The Naval Surface Weapons Center assisted in meeting the publication costs of this article.

REFERENCES

1. D. F. Pickett, "Fabrication and Investigation of Nickel-Alkaline Cells. Part I: Fabrication of Nickel Hydroxide Electrodes Using Electrochemical Impregnation Techniques," AFAPL-TR-75-34, Air Force Wright Aeronautical Laboratories, WPAFB, OH (1975).
2. W. A. Ferrando and R. A. Sutula, in "The Nickel Electrode," R. G. Gunther and S. Gross, Editors, pp. 271-285, The Electrochemical Society Softbound Proceedings Series, Pennington, NJ (1982).
3. W. Ferrando, W. W. Lee, and R. A. Sutula, *J. Power Sources*, **12**, 249 (1984).
4. W. W. Lee and W. A. Ferrando, NSWC Technical Report, TR 84-122, Naval Surface Weapons Center, White Oak, MD, Defence Technical Information Center, Alexandria, VA.

Electroless and Immersion Plating of Palladium on Zirconium

Cheazone Hsu and Robert E. Buxbaum

Department of Chemical Engineering, Michigan State University, East Lansing, Michigan 48824-1226

Zirconium is an important metal which is widely used in nuclear and chemical industries. In some applications, the zirconium surface is coated with a thin metal film to prevent corrosion or to change the surface properties. A thin coating of copper, nickel, or iron on zirconium is reported to prevent corrosion of cladding material in nuclear reactors (1, 2). Also, Dini *et al.* (3) studied plating nickel, silver, or chromium on zirconium in order to join zirconium to stainless steel.

Palladium is a particularly attractive coating for zirconium. Buxbaum (4) describes the advantages of using a coated palladium window of zirconium for separating tritium from the breeder blanket of a fusion reactor. Also, Stokes and Buxbaum (5) have suggested using a palladium coating to allow the removal of H isotopes from zirconium pressure tubes in CANDU-PHW reactors.

Currently, the following metals can be plated on zirconium: Ni, Fe, Cu, Sn, Cr, and Ag. Schicker *et al.* (6, 7) describe nickel and iron electrodeposition on zirconium following pretreatment by mechanical descaling, alkaline cleaning, and chemical etching. After electrodeposition, the sample is baked at 200°C to prevent blistering. Kohan (8) describes immersion plating of nickel, copper, and tin on Zircaloy 2 using a pretreatment of vapor blasting, cathodic alkaline cleaning, and pickling. Thicknesses up to 7 μm are deposited by this method. Saubestre (9) describes nickel and copper electroplating on zirconium using a cathodic pretreatment in a suitable electrolyte. Wax *et al.* (10) describe the electroplating of copper, nickel, and chromium on zirconium using an activation solution of ammonium bifluoride and sulfuric acid; and Donaghy (1, 2) holds two patents on processes for electroplating and electroless plating of these same metals. Recently, Dini *et al.* (3) described electroplating nickel, silver, and chromium on zirconium, and showed that adhesion was improved by a postplating heat-treatment at 700°C in constrained geometry or by mechanical treatments such as surface threading or knurling.

At least two dozen formulations for palladium plating baths have been suggested or patented. However, no

technique has been published for either electroplating or nonelectrolytic plating palladium on zirconium.

Experiments

The following two palladium bath formulations were selected for this study. First, we used the immersion plating solution that Johnson (11) used to plate palladium on copper, brass, beryllium-copper, phosphor-bronze, and nickel-silver. The composition was $PdCl_2$, 5 g/liter; HCl (38%), 200 ml/liter. The temperature was 25°C. Second, we used the electroless palladium bath solution of Pearlstein and Weightman (12). The composition was $PdCl_2$, 2 g/liter; HCl (38%), 4 ml/liter; NH_4OH (28%), 160 ml/liter; NH_4Cl, 27 g/liter; $NaH_2PO_2 \cdot H_2O$, 10 g/liter. The temperature was 50°C. The *p*H was 9.8.

The surface pretreatment was as follows.

1. The sample, zirconium disk with surface area of 10 cm^2, was machined from a zirconium bar of 99.8% purity.
2. Surface grinding and polishing were used to remove some surface scale and oxide.
3. Detergent washing and solvent cleaning with trichloroethylene were used to remove surface oil and grease.
4. The sample was given a cathodic alkaline cleaning. (Composition: NaOH, 35 g/liter; Na_3PO_4, 10 g/liter. *p*H: 12. Temperature: 90°C. Time: 3 min. Cathodic current density: 0.1 A/cm^2. Voltage: 4V.)
5. The sample was given a water rinse.
6. The sample was given an "acid pickling" (13). (Composition: HNO_3 70%, 10 parts; HF 49%, 1 part; H_2O, 10 parts. Temperature: 25°C. Time: 0.5 min.)
7. Another water rinse was given.
8. The sample was given an activation etching. (Composition: NH_4HF_2, 15 g/liter: H_2SO_4, 1 g/liter. Temperature: 25°C. Time: 1, 2, 3, 6, or 10 min.)
9. A final water rinse was applied.
10. Then, the palladium plating was applied. Immersion plating was tried with and without activation etching step in the surface pretreatment.

Immersion Plating Results

Because the positive potential of zirconium is higher than that of palladium, the palladium ions can theoretically replace atoms of the zirconium substrate in solution by immersion plating. For this process, zirconium atoms must be simultaneously oxidized and dissolved as ions into the solution while palladium ions in solution deposit onto the zirconium substrate. We find, however, that immersion plating (using a $PdCl_2$-HCl solution) does not give good results: the palladium did not coat the zirconium surface. Without the activation etching prior to immersion plating, a possible explanation is that an oxide film stopped the replacement reaction. Zirconium, being a reactive metal, quickly forms a stable film of surface oxide when the pickled surface is exposed to air or water. Although the thickness of surface oxide is less than 0.0025 μm (14), it may be thick enough to stop atomic replacement. With activation etching in the surface pretreatment, a thin film of zirconium hydride was formed on the surface and there was still no replacement reaction.

Electroless Plating Results

The surface was activated for electroless plating of palladium on zirconium by forming an adherent, electrically conducting film of black zirconium hydride using a solution containing 15 g/liter NH_4HF_2 and 1 g/liter H_2SO_4. Zirconium hydride provides an improved surface for palladium deposition because it, like palladium, is a face-centered cubic structure (15). Activation etching times of 1, 2, 3, 6, and 10 min were tested at 25°C, and it was found that at least 3 min is necessary to form an adherent palladium deposit. About 9 μm of zirconium was etched off after 3 min of activation at 25°C.

Adhesion was determined by scratching through the coating with a sharp blade; the surface showed no lifting or peeling when viewed under a microscope. Adhesion was also evaluated by a heat quenching test (16): the sample was heated in a vacuum oven to 200°C at a rate of 30°C/h, and was then immersed in room temperature water. No flaking, peeling, or blistering was observed. An adherent palladium coating 5 μm thick was achieved after 3h plating at 50°C.

Acknowledgment

The authors are grateful to the National Science Foundation, who supported this research through Grant no. CPE 8205021.

Manuscript submitted Feb. 4, 1985; revised manuscript received June 10, 1985.

Michigan State University assisted in meeting the publication costs of this article.

REFERENCES

1. R. E. Donaghy, U.S. Pat. 4,093,756 (1978).
2. R. E. Donaghy, U.S. Pat. 4,137,131 (1979).
3. J. W. Dini, H. R. Johnson, and A. Jones, *J. Less-Common Met.*, **79**, 261 (1981).
4. R. E. Buxbaum, *Sep. Sci. Technol.*, **18**, 1251 (1983).
5. C. L. Stokes and R. E. Buxbaum, "Paper presented at the AIChE North Central Student Conference, April, 1984.
6. W. C. Schickner, J. G. Beach, and C. L. Faust, *This Journal*, **100**, 289 (1953).
7. W. C. Schickner, J. G. Beach, and C. L. Faust, *Met. Finish.*, **52** (7), 57 (1954).
8. L. R. Kohan, *ibid.*, **57** (11), 68 (1959).
9. E. B. Saubestre, *This Journal*, **106**, 305 (1959).
10. D. E. Wax and R. L. Cowan, U.S. Pat. 4,017,368 (1977).
11. R. W. Johnson, *This Journal*, **108**, 632 (1961).
12. F. Pearlstein and R. F. Weightman, *Plating*, **56**, 1151 (1969).
13. "Metal Finishing Guidebook Directory," p. 168, Metals and Plastics Publications, Hackensack, NJ (1984).
14. T. L. Barr, *J. Vac. Sci. Technol.*, **14**, 660 (1977).
15. J. Fitzwilliam, A. Kaufmann, and C. Squire, *J. Chem. Phys.*, **9**, 678 (1941).
16. Standard Test Methods for Adhesion of Metallic Coatings, ASTM B571-79, American Society for Testing and Materials, Philadelphia (1984).

Effect of Active Layer Composition on the Service Life of (SnO_2 and RuO_2)-Coated Ti Electrodes in Sulfuric Acid Solution

Chiaki Iwakura and Kenji Sakamoto

Department of Applied Chemistry, Faculty of Engineering, Osaka University, Suita, Osaka, Japan

Although RuO_2- and IrO_2-coated Ti electrodes (Ti/RuO_2 and Ti/IrO_2) have been known to possess high catalytic activity, not only for chlorine evolution, but also for oxygen evolution, they lack the stability required for practical use as an oxygen anode, and therefore many researchers have been trying to prolong their service lives by different means (1). In general, the addition of *ca.* 70 mole percent (m/o) TiO_2 to the RuO_2 layer produces the bene-

ficial properties for chlorine evolution (2), but the service life as well as catalytic activity of the (TiO_2 and RuO_2)-coated Ti electrodes (Ti/TiO_2-RuO_2) for oxygen evolution decreases monotonously with increasing TiO_2 content (3). Recently, Burke and McCarthy (4) have reported that the addition of 20 m/o ZrO_2 to the RuO_2 layer increased the service life of the Ti/RuO_2 electrode for oxygen evolution in 6*M* KOH at 80°C by a factor of 5.3. Noguchi *et al.* (5) have also reported that the addition of *ca.* 33 m/o Co oxide to the IrO_2 layer increased the service life of the Ti/IrO_2 electrode for oxygen evolution in 4*M* H_2SO_4 at 60°C by a factor of 12.5. In both cases, however, it is not clear why such compositions are optimum for the active layers.

In this work, the effect of active layer composition on the service life of (SnO_2 and RuO_2)-coated Ti electrodes (Ti/SnO_2-RuO_2) in sulfuric acid solution was investigated in connection with the electrodes physicochemical properties from a fundamental viewpoint rather than a practical viewpoint. Both fundamental and practical investigations on the Ti/SnO_2-RuO_2 and related electrodes are still active, as can be seen from recent papers (6-9), although the idea of the use of SnO_2 in RuO_2-based anodes for industrial brine electrolysis goes back to earlier patents (10-12). The electrocatalysis of such electrodes for oxygen and chlorine has already been studied by Chertykovtseva *et al.* (13) and the present authors (14).

Experimental

The test electrodes (Ti/SnO_2-RuO_2) were prepared by a thermal decomposition method in the following way. First, a Ti plate (2.5 cm^2) was mechanically polished with emery paper (~ no. 1000) and then chemically etched with a boiling aqueous solution of 0.2*M* oxalic acid for 10 min. Next, an appropriate amount of a mixture of 0.1*M* $SnCl_4$- and 0.1*M* $RuCl_3$-20 weight percent (w/o) HCl aqueous solutions was applied to one side of the cleaned Ti plate. It was dried at 50°C and then placed in a preheated furnace at 350°C for 10 min. Such operations were repeated four times. Finally, the fifth coating was made and then the plate was dried at 50°C, followed by heating at 450°C for 1h to complete the thermal decomposition. The total loading amount of SnO_2 and RuO_2 was kept constant at 1×10^{-5} mol/cm^2. The amount of each metal oxide will be indicated in parentheses in mole percent.

All the electrochemical measurements were done in 0.5*M* H_2SO_4 at 30°C by conventional means. An all-Pyrex glass H-type cell with Teflon stoppers was used as an electrolytic cell and a Pt sheet as a counterelectrode. The reference electrode used was a mercury (I) sulfate electrode (Hg/Hg_2SO_4, 0.5*M* H_2SO_4).

The other experimental procedures and conditions will be given in the next section when necessary.

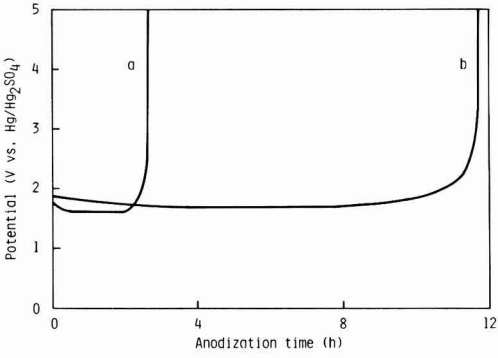

Fig. 1. Typical potential-time curves for Ti/RuO_2 (a) and Ti/SnO_2(70)-RuO_2(30) (b) electrodes under anodization at 500 mA/cm^2 in 0.5*M* H_2SO_4.

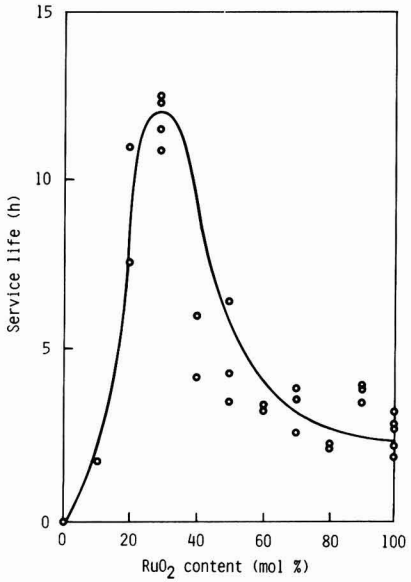

Fig. 2. Plot of service life against RuO_2 content for Ti/SnO_2-RuO_2 electrodes.

Results and Discussion

The accelerated life tests of the Ti/SnO_2-RuO_2 electrodes with different RuO_2 contents were carried out by anodization at 500 mA/cm^2. Typical potential-time curves are shown in Fig. 1. In any case, the potential remains almost unchanged for a certain time and then increases rapidly. Hereinafter, the service life will be defined as the time of operation before the anode potential increases significantly, say 5V *vs.* Hg/Hg_2SO_4 (iR included). Figure 2 shows the plot of service life against RuO_2 content. It is clear that the service life *vs.* RuO_2 content plot has a maximum at around 30 m/o RuO_2. This happened to coincide in Sn/Ru ratio with the reported Sn-Ru binary alloys, *i.e.*, Ru_3Sn_7, $RuSn_2$, and Ru_2Sn_3 (15). The service life of the Ti/SnO_2(70)-RuO_2(30) electrode is longer than that of the Ti/RuO_2 electrode by a factor of 4.5-5. This is in a marked contrast to the result obtained with a series of Ti/TiO_2-RuO_2 electrodes for oxygen evolution (3).

The anodic polarization curves of some Ti/SnO_2-RuO_2 electrodes are shown in Fig. 3. All the electrodes shown, except for the Ti/SnO_2(90)-RuO_2(10) electrode, have the dual Tafel slopes of 0.06 and 0.12 V/decade, suggesting that the mechanism of the oxygen evolution reaction is

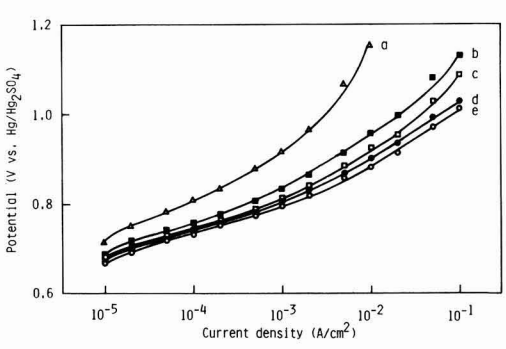

Fig. 3. Galvanostatic polarization curves of Ti/SnO_2(90)-RuO_2(10) (a), Ti/SnO_2(70)-RuO_2(30) (b), Ti/SnO_2(50)-RuO_2(50) (c), Ti/SnO_2(30)-RuO_2(70) (d), and Ti/RuO_2 (e) electrodes.

unchanged. Furthermore, the current-potential curves of these electrodes can almost completely be superposed upon each other when they are replotted on the basis of the current density per given amount of RuO_2 (*e.g.*, 1×10^{-5} mol/cm²). This indicates that the active center for the oxygen evolution reaction is on the Ru sites, which is in agreement with the view reported previously (14).

Figure 4 shows SEM microphotographs of the surfaces of the Ti/RuO_2 and Ti/SnO_2(70)-RuO_2(30) electrodes. Evidently, the surface of the latter electrode is much more smooth and compact, with smaller cracks and pores than those of the former electrode. Thus, the result of Fig. 2 cannot be explained simply on the basis of an increase of effective surface area in the usual way (8). The increased smoothness and compactness of the electrode surface are considered to lead to the prolonged service life because they depress the penetration of electrolyte through cracks or pores in the active layer and thereby the formation of a resistive TiO_2 film on the Ti substrate (3).

The coloring of the solution straw-yellow during the life tests indicates clearly the occurrence of the anodic dissolution of the active layer, which can also lead to the formation of a resistive TiO_2 film on the Ti substrate (3). So, the dissolution rate of the active layer during anodization was determined by fluorescent x-ray analysis for both the Ti/RuO_2 and Ti/SnO_2(70)-RuO_2(30) electrodes. Many test electrodes were used in the measurements, so that one electrode corresponds to each point in Fig. 5 as well as in Fig. 2. Figure 5 shows the variation of the normalized residual amounts of Ru and Sn species with the anodization time. In either case, the Ru species dissolve fast at the first stage, quite slowly in the middle period, and again rapidly at the final stage. From a detailed comparison of these data with the data shown in Fig. 1, one can notice that the potential change is almost paralleled by the dissolution of RuO_2. In addition, the charges, determined by cyclic voltammetry between 0.1 and 0.3V *vs.* Hg/Hg_2SO_4, was also found to change correspondingly with the anodization time; *i.e.*, it increased and decreased at the first and final stages, respectively. Though the reason why a period of constancy in overpotential, as well as charges, with no dissolution exists is unclear at the present stage, it is evident from Fig. 5 that the RuO_2 dissolution is depressed to a great extent by the coexistence of SnO_2 and RuO_2 and that not only RuO_2 but also SnO_2 dissolve anodically, as was already confirmed by means of SIMS (14). Besides these facts, it is worth noting that both RuO_2 and SnO_2 dissolve almost in the same manner, suggesting the interaction between them.

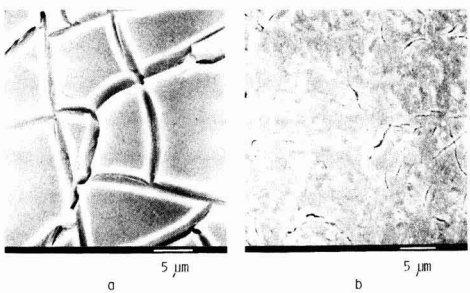

Fig. 4. Microphotographs taken by SEM of the surfaces of Ti/RuO_2 (a) and Ti/SnO_2(70)-RuO_2(30) (b) electrodes.

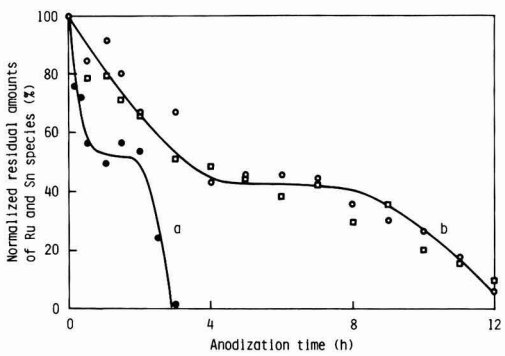

Fig. 5. Variation of normalized residual amounts of Ru (circle) and Sn (square) species with anodization time for Ti/RuO_2 (a) and Ti/SnO_2(70)-RuO_2(30) (b) electrodes.

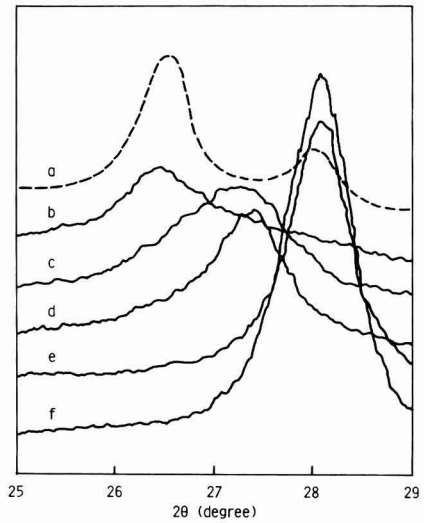

Fig. 6. X-ray diffraction patterns of SnO_2(70)-RuO_2(30) mixed powders (a), Ti/SnO_2 (b), Ti/SnO_2(90)-RuO_2(10) (c), Ti/SnO_2(70)-RuO_2(30) (d), Ti/SnO_2(50)-RuO_2(50) (e), and Ti/RuO_2 (f) electrodes.

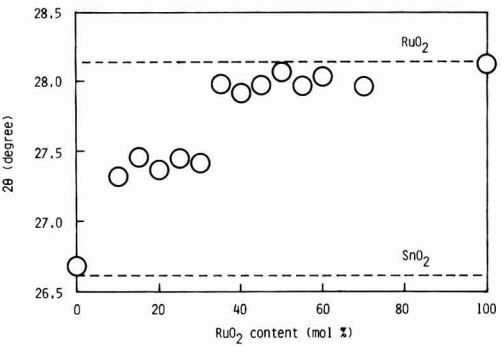

Fig. 7. Plot of x-ray diffraction angle against RuO_2 content for Ti/SnO_2-RuO_2 electrodes.

The x-ray diffraction measurement was carried out for different electrode samples under the following conditions: a counterelectrode of Cu; tube voltage of 30 kV; tube current of 10 mA, time constant of 4s, scan rate of 0.5°(2θ)/min; and a slit width of 0.3 mm. Figure 6 shows the x-ray diffraction patterns of some Ti/SnO_2-RuO_2 electrodes together with the mixed powders of SnO_2(70) and RuO_2(30). In this figure, only the patterns for each main peak in a (110) plane are shown since the patterns for the subpeaks in the other planes such as (101) and (211) were quite similar to those for the main peaks. As shown typically for the Ti/SnO_2(50)-RuO_2(50) electrode, the peaks of the electrodes with relatively high RuO_2 contents coin-

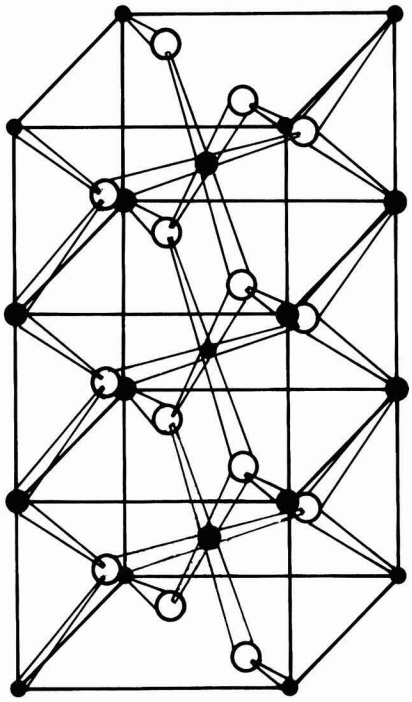

Fig. 8. Probable triple-rutile structure of $RuSn_2O_6$. Small filled circles: Ru. Large filled circles: Sn. Open circles: O.

cided in diffraction angle with the peak of the Ti/RuO_2 electrode though they were somewhat broader, probably because of the replacement of Ru site by Sn species without change of the RuO_2 crystal structure. However, the $Ti/SnO_2(70)$-$RuO_2(30)$ electrode exhibits a specific diffraction peak which lies between the two peaks of SnO_2 and RuO_2. The change of the diffraction angle of the main peak with the composition is more clearly shown in Fig. 7. No diffraction peak was observed for the $Ti/SnO_2(95)$-$RuO_2(5)$ electrode, indicating the destruction of the SnO_2 crystal structure. The alternative broad diffraction peaks appeared at the $Ti/SnO_2(90)$-$RuO_2(10)$ electrode, and they became sharp gradually with increasing RuO_2 content up to 30 m/o. These suggest strongly that a new, somewhat distorted, crystalline structure, probably $RuSn_2O_6$, is formed at the electrode with the composition of around $SnO_2(70)$-$RuO_2(30)$ during the electrode preparation. From the analogy to triple-rutile structure of mossite $FeNb_2O_6$ (16), the new crystal may be represented by the structure shown in Fig. 8, though further detailed studies are necessary.

In conclusion, the service life of the Ti/RuO_2 electrode can be prolonged by the presence of SnO_2 in the active layer with the optimal composition of around 70 m/o SnO_2 and 30 m/o RuO_2. This is probably due to the formation of a new crystalline but somewhat disordered $RuSn_2O_6$, which leads to the depression of the anodic dissolution of the active layer, in addition to the increased smoothness and compactness of the active layer.

Acknowledgments

Financial support of a part of this work by Toyo Soda Manufacturing Company, Limited, is gratefully acknowledged. The authors are greatly indebted to Professor Nobutami Kasai, Osaka University, for helpful comments on the interpretation of the x-ray diffraction data.

Manuscript submitted Feb. 20, 1985; revised manuscript received June 4, 1985.

Osaka University assisted in meeting the publication costs of this article.

REFERENCES

1. A. Nidola, in "Electrodes of Conductive Metallic Oxides," S. Trasatti, Editor, Part B, 627, Elsevier, Amsterdam (1981).
2. F. Hine, M. Yasuda, and T. Yoshida, *This Journal*, **124,** 500 (1977); F. Hine, M. Yasuda, T. Noda, T. Yoshida, and J. Okuda, *ibid.*, **126,** 1439 (1979).
3. C. Iwakura, M. Inai, M. Manabe, and H. Tamura, *Denki Kagaku*, **48,** 91 (1980).
4. L. D. Burke and M. McCarthy, *Electrochim. Acta*, **29,** 211 (1984).
5. F. Noguchi, S. Matsumura, T. Iida, T. Mitamura, Y. Arai, and Y. Kamegaya, *Denki Kagaku*, **51,** 713 (1983).
6. W. Badawy, K. Doblhofer, I. Eiselt, H. Gerischer, S. Krause, and J. Melsheimer, *Electrochim. Acta*, **29,** 1617 (1984).
7. N. Krastajic, M. Spasojevic, and M. Jaksic, *J. Res. Inst. Catal. Hokkaido Univ.*, **32,** 19, 29 (1984).
8. A. Bandi, I. Vartires, A. Mihelis, and C. Hainarosie, *J. Electroanal. Chem.*, **157,** 241 (1983).
9. R. U. Bondar, E. A. Kalinovskii, I. V. Kunpan, and V. S. Sorokendya, *Elektrokhimiya*, **19,** 1104 (1983).
10. G. Bianchi, V. De Nora, P. Gallone, and A. Nidola, South African Pat. 68/7371, 68/7482 (1968).
11. J. H. Etwisle, D. Lee, and A. Scrutton, Ger. Offen. 1,952,484 (1970); *C.A.*, **73,** 491 (1970).
12. K. J. O'Leary, U.S. Pat. 3,776,834 (1983); *C.A.*, **80,** 450 (1974).
13. T. A. Chertykovtseva, D. M. Shub, and V. I. Veselovskii, *Elektrokhimiya*, **14,** 275, 1260 (1978); T. A. Chertykovtseva, Z. D. Škuridina, D. M. Shub, and V. I. Veselovskii, *ibid.*, **14,** 1412 (1978).
14. C. Iwakura, M. Inai, and H. Tamura, *Chem. Lett.*, 225 (1979); C. Iwakura, M. Inai, T. Uemura, and H. Tamura, *Electrochim. Acta*, **26,** 579 (1981); C. Iwakura, Y. Taniguchi, and H. Tamura, *Chem. Lett.*, 689 (1981).
15. F. A. Shunk, "Constitution of Binary Alloys, Second Supplement," p. 650, McGraw-Hill, New York (1969).
16. R. Kiriyama, in "Kessho Kogaku Handobukku," Henshu Iinkai, Editor, p. 57, Kyoritsu Shuppan, Tokyo (1975).

Application of Electrochemical Fluorination to the Synthesis of Perfluoroalkane Sulfonic Acid Electrolytes

Preparation of $F_2C(SO_3H)_2$

E. J. M. O'Sullivan*,[1]

Department of Chemistry, Case Center for Electrochemical Sciences, Case Western Reserve University, Cleveland, Ohio 44106

F. W. Klink, ** **C. C. Liu,*** **and E. B. Yeager***

Department of Chemical Engineering, Case Center for Electrochemical Sciences, Case Western Reserve University, Cleveland, Ohio 44106

Perfluorinated alkane sulfonic acids have been receiving attention in the last few years as potential fuel cell electrolytes (1, 2). However, except for trifluoromethane sulfonic acid, acids of this class are not widely available, particularly the multifunctional compounds. Consequently, progress in the evaluation of the electrolyte properties of these acids has been impeded. Effective methods for the synthesis of attractive perfluorinated sulfonic acids are therefore needed which can generate appreciable quantities of these acids in a highly pure form.

Synthetic routes based on electrochemical fluorination (ECF) (3-7) in anhydrous hydrogen fluoride (AHF) are attractive for the preparation of perfluoroalkane sulfonic acids. Although the fluorination of alkane sulfonic acids cannot be carried out directly by ECF (3), Brice and Trott (8) and Gramstad and Haszeldine (9) showed that alkane sulfonyl halides (chlorides and fluorides) could be successfully fluorinated by this method to give perfluoroalkane sulfonyl fluoride products in fairly high yields. The perfluorinated sulfonyl fluoride products were converted to the corresponding acid salt by alkaline hydrolysis, the free acid then being obtained either by distillation from a solution of concentrated sulfuric acid and sulfonic acid salt, or by ion exchanging solutions of the salt (10).

In this paper, the electrochemical fluorination of methanedisulfonyl fluoride, $H_2C(SO_2F)_2$, to produce difluoromethanedisulfonyl fluoride, $F_2C(SO_2F)_2$, in high yields is described, along with the conversion of the latter compound to the disulfonic acid form. The formation of $F_2C(SO_2F)_2$ from $H_2C(SO_2F)_2$ via ECF has been reported previously (11). Methanedisulfonyl fluoride was selected as a substrate for ECF rather than the corresponding disulfonyl chloride since it has been established (9) that substrates containing the $-SO_2F$ group rather than the $-SO_2Cl$ group give higher yields of the perfluoroalkane sulfonyl fluoride compounds. Also, in the case of substrates containing a high ratio of $-SO_2Cl$ groups to C-H bonds there is the possibility of formation of undesirable C-Cl bonds in the course of electrolysis.

Experimental

The methanedisulfonyl fluoride reactant used in the electrochemical fluorination reaction was synthesized via a two-step process. In the first step, methanedisulfonyl chloride, $H_2C(SO_2Cl)_2$, was synthesized by a reaction involving acetic acid (Fisher, Reagent), chlorosulfonic acid (Pfaltz and Bauer, 99%), and phosphorous oxychloride (Fisher, Purified) as described by Fild and Rieck (12). In the second step, the $H_2C(SO_2Cl)_2$ was converted to $H_2C(SO_2F)_2$ by the action of potassium bifluoride (Harshaw, 97%) in acetonitrile (Fisher, 99%). Following removal of the precipitated KCl product by filtration, the $H_2C(SO_2F)_2$ was recovered by vacuum distillation. Typically, chemical yields of 70-75% were obtained by each of these two reactions. Elemental analysis and proton and fluorine NMR confirmed the identification of $H_2C(SO_2F)_2$. This material was purified by further vacuum distillation, and its purity was found to be in excess of 98% by gas chromatography. The major impurities in the $H_2C(SO_2F)_2$ were $H_2C(SO_2Cl)_2$ and $H_2C(SO_2Cl)SO_2F$.

The electrochemical fluorination reaction was conducted in a Simon-type reactor (3) with a volume of 500 ml. The details of the cell design and support system have been reported previously (13). In a typical experiment, the reactor temperature was maintained at 10° ± 1°C with the condenser kept at −50° to −60°C. A 20 ml/min flow rate of nitrogen was maintained throughout the experiment in order to sweep away hazardous gaseous products. Typically, 450 ml of anhydrous hydrogen fluoride (AHF) was added directly to the cell and purified by pre-electrolysis at a constant cell voltage at 5.5V until the current decayed to a constant base-line value of ~0.2 A/dm². The purpose of this pre-electrolysis step, which was typically conducted for 12-18h, was to form the anodic nickel fluoride film and remove any water present in the AHF.

After the pre-electrolysis of the AHF, approximately 30g of $H_2C(SO_2F)_2$ was added to the cell, bringing the reactant concentration to 5% by weight. The cell was operated at a constant cell voltage of 5.5V with an average current density of ~0.5 A/dm². The electrolysis current remained relatively constant as long as the reactant was present and rapidly decayed when the last amount of reactant was consumed. New reactant was then added when the current decayed to the base-line value. A typical run duration was 150h. The fluorination product formed a separate heavy phase, which could be observed along with some solid corrosion products, at the bottom of the reactor when the agitation was turned off. A greenish-white corrosion product, presumably nickel difluoride (9), could also be observed loosely coating the anodes.

One of the methods employed for carrying out salt-to-acid conversions in the present work was electrodialysis. A three-compartment PTFE cell was employed which used Nafion 117 membranes as separators. The Nafion membranes (proton version, 1100 eq weight, 0.007 in. thick) were cleaned in hot water, which was frequently changed, for at least two weeks prior to use. A solution of the sulfonate salt, $F_2C(SO_3Li)_2$ rather than the Ba salt, was placed in the central compartment. Solutions of LiOH (0.5*M*) and trifluoromethane sulfonic acid (1.0*M*) were placed in the cathode and anode compartments, respectively. Platinum gauze was used for the anode and cathode. Current densities of 10 A/dm² with respect to the Nafion membranes were employed. In view of the rather high electric fields present across the membrane at such high current densities, diffusion of the bulky $F_3CSO_3^-$ ion from the anode compartment should be negligible. Similarly, back-diffusion of Li^+ ion from the cathode compartment should also be minimal.

Results and Discussion

At the completion of the electrolysis experiment, the cell and cell condenser were warmed to room tempera-

*Electrochemical Society Active Member.
**Electrochemical Society Student Member.
[1]Present address: IBM Thomas J. Watson Research Center, Yorktown Heights, New York 10598.

ture. To facilitate recovery of volatile products from the cell, which included the $F_2C(SO_2F)_2$, a cold trap consisting of coiled Monel tubing immersed in a Dry Ice/isopropanol mixture (temperature ~ −73°C) was incorporated in the outlet gas stream from the condenser. HF and product material were simultaneously carried over from the warmed cell and condenser in a stream of N_2 gas and were collected in a flask of ice water placed at the outlet of the cold trap. The HF dissolved in the water, while the $F_2C(SO_2F)_2$ product was insoluble, forming a second, transparent layer at the bottom of the flask. Only a trace quantity of organic material remained with the corrosion products in the cell. The product recovered in the ice water trap was separated from the aqueous phase and washed further with water to remove traces of HF. No traces of color were exhibited by this product at any time.

Fractional distillation of the ECF product initiated at 56.5°C and rose rapidly to a steady temperature of 57.2°C. A 250 ml round-bottom glass distillation flask was employed and operated at ambient pressure. In order to avoid any introduction of contaminants, no stopcock grease was used for the glass joints. Thermometers with ground glass joints were placed in both the still flask and at the entrance of the condenser. Only the product recovered at 57.2°C was employed for the conversion to $F_2C(SO_3H)_2$. Fluorine NMR confirmed the structure of $F_2C(SO_2F)_2$ showing two triplets, one centered at −36.6 ppm relative to $CFCl_3$ and the other at 96.8 ppm. Proton NMR confirmed the absence of C-H bonds in the product, indicating the maximum C-H material presented was less than 5%.

The chemical yield of the ECF step was approximately 70%, with a product-recovered-based current efficiency averaging 44%.

Preparation of $F_2C(SO_3H)_2$ from $F_2C(SO_2F)_2$.—Various methods were explored for converting $F_2C(SO_2F)_2$ to the acid form. In general, perfluorinated alkane sulfonyl fluorides are readily hydrolyzed under alkaline conditions only (9). The hydrolysis of $F_2C(SO_2F)_2$ was found to be most effectively carried out using concentrated aqueous solutions of either $Ba(OH)_2$ or LiOH since the relatively insoluble fluoride salt by-products, BaF_2 and LiF, respectively, could be separated from the hydrolysis mixtures by filtration. The stoichiometric equation for the $Ba(OH)_2$ hydrolysis reaction, for example, may be written as follows

$$F_2C(SO_2F)_2 + 2Ba(OH)_2 = F_2C(SO_3)_2Ba + BaF_2 + 2H_2O \quad [1]$$

The hydrolysis reactions were conducted at room temperature over periods of 1-2 days. In this step, the $F_2C(SO_2F)_2$ was added in a batchwise manner to the alkali solutions in FEP bottles. The additions were carried out in such a manner that the reaction temperature did not exceed 35°C. A slight excess of alkali was employed in order to insure complete conversion of sulfonyl fluoride functional groups to sulfonate groups. At the completion of the reaction, the insoluble fluoride salts were removed by filtration. The Ba or Li disulfonic acid salts were recovered from the filtrate after removal of the water using an aspirator.

Sulfate anion was detected in the hydrolysis solutions utilizing LiOH as the hydrolyzing base. The odor of sulfur dioxide from the hydrolysis solutions has also been detected at the completion of the hydrolysis reaction. The sulfate was removed as $BaSO_4$ by the addition of barium hydroxide. The amount of sulfate formed during the hydrolysis reaction has been found to be 0.001-0.002 mol per mole of $F_2C(SO_2F)_2$. Sulfate was not present in the original $F_2C(SO_2F)_2$ and only to a very minor extent as an impurity in the LiOH. The sulfate is evidently generated by hydrolysis of the $F_2C(SO_3^-)_2$ anion.

Fabes and Swaddl (14) have reported that $F_3CSO_3^-$ oxidatively hydrolyzes quantitatively in alkaline solutions at 297°C, and suggested the following equation for the process

$$F_3CSO_3^- + 6\ OH^- = 3F^- + SO_4^{=} + CO_3^{=} + H_2 + 2H_2O \quad [2]$$

Perhaps a process similar to reaction [2] leads to the instability of the difluoromethane disulfonate even though the temperature did not exceed 35°C. A more likely process, however, is the oxidation of the disulfonate in alkaline solution by O_2 from the air. The disulfonate may be more susceptable to oxidative hydrolysis than the monosulfonate because the presence of two $-SO_3^-$ groups on one carbon leads to lower stability.

Various methods were explored for converting the disulfonic acid salts to the acid form, principally ion exchange and electrodialysis. A disadvantage of the electrodialysis method is the relatively long periods required (several days) to reduce the Li^+ content to very low levels (*e.g.*, 2-3%) in the disulfonic acid material. Furthermore, despite extensive cleaning of the Nafion 117 membranes employed in the cell, cyclic voltammograms of smooth Pt electrodes recorded in $F_2C(SO_3H)_2$ solutions (*e.g.*, 1.0*M*) prepared by this method indicated the presence of impurities, particularly in the hydrogen adsorption/desorption region. These impurities were also found to interfere severely with rotating ring-disk electrode measurements of O_2 reduction in these electrolytes. These impurities were not removed by pre-electrolysis methods or by treatment with hydrogen peroxide. Since the $F_2C(SO_2F)_2$ was highly purified prior to hydrolysis by multiple fractional distillations, it seems likely that a major portion of these impurities were generated during the further hydrolysis of $F_2C(SO_3^-)_2$. The $F_2C(SO_3Li)_2$ salt cannot be purified readily by recrystallization from aqueous solutions prior to being submitted to electrodialysis owing to its extremely high solubility. In general, the most effective method for purifying the newly prepared $F_2C(SO_3H)_2$ was found to be distillation of its dihydrate under reduced pressure (~0.3 torr air). Distillation also served to remove traces of salt remaining after electrodialysis.

Ion exchange was also investigated as a convenient method for converting $F_2C(SO_3Li)_2$ to the acid form. Amberlite IR 120 resin was employed after being washed extensively with ultrapure water. The ion exchange resin did not appear to degrade while it was in contact with the disulfonic acid, and essentially quantitative conversion of the salt to the acid was achieved. The disulfonic acid prepared by ion exchange was also subsequently purified by vacuum distillation of its dihydrate, and its composition was confirmed by elemental analysis. In the case of perfluoroalkane sulfonic acid salts, which can be purified by recrystallization, *e.g.*, the potassium salts of tetrafluoroethane-1,2- and hexafluoropropane-1,3-disulfonic acids, the method of electrodialysis would be one of the methods which should produce purer acid than ion exchange methods (15), since the resin is a potential source of organic impurities.

Voltammetry of platinum.—Linear potential sweep voltammetry of smooth Pt in a N_2 (Matheson, 99.9995%) saturated solution provides a convenient qualitative check of electrolyte purity. Cyclic voltammograms of 0.5*M* $F_2C(SO_3H)_2$ and 1.0*M* H_3PO_4 are shown in Fig. 1. The disulfonic acid was purified by twice distilling the dihydrate under reduce pressure, while the phosphoric acid was carefully purified as described elsewhere (16). The voltammogram of the $F_2C(SO_3H)_2$ exhibits reasonably well-defined hydrogen and oxide film regions. The minor peak present at ~0.75V *vs.* RHE (1 atm) in the anodic sweep increases slightly with sweep rate and becomes less pronounced at lower concentrations. It is probably an impurity peak. Overall, however, the voltammogram of $F_2C(SO_3H)_2$ indicates that this acid is reasonably pure.

There are some differences between the hydrogen and oxide regions of the voltammetric profiles of Pt recorded in the 0.5*M* $F_2C(SO_3H)_2$ and H_3PO_4 electrolytes. The onset of oxide formation in the anodic sweep occurs at ~70 mV more negative in the case of the sulfonic acid electrolyte relative to phosphoric acid. This is an indication of weaker adsorption on Pt by the sulfonic acid electrolyte relative to phosphoric acid. Also, as observed in the case

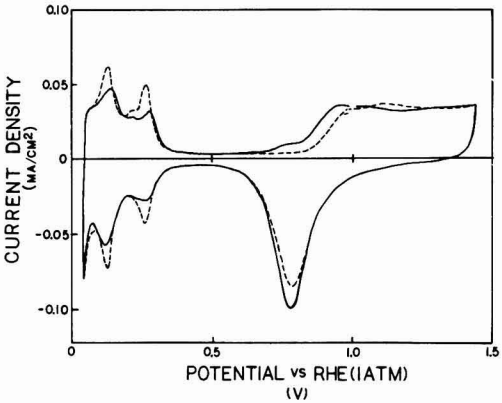

Fig. 1. Voltammograms of platinum in purified 0.5M $F_2C(SO_3H)_2$ (solid line) 1.0M H_3PO_4 (dashed line) at 25°C, N_2 saturated, sweep rate = 25 mV/s.

of weakly adsorbing acids (17), *e.g.*, $HClO_4$, the peak current for the strongly adsorbed form of hydrogen on Pt at *ca.* 0.25V is lower for the $F_2C(SO_3H)_2$ than for the H_3PO_4. The absence of significant adsorption behavior on electrode surfaces such as platinum is a desirable property for acid fuel cell electrolytes.

Conclusions and Future Works

Electrochemical fluorination of methanedisulfonyl fluoride in AHF is a viable route for the production of difluoromethanedisulfonyl fluoride. High yields are obtained by this method, and it is anticipated that a variety of other perfluoroalkane sulfonyl fluorides may be prepared in this manner. We have recently constructed a new electrochemical reactor system with a three-electrode configuration, improved agitation, and a more uniform current density distribution. We believe these improvements will increase the yield and permit use of higher current densities.

The physicochemical properties of $F_2C(SO_3H)_2$, *e.g.*, conductivity and vapor pressure, are being characterized. The dihydrate does not wet Teflon above its melting point (~70°C). Studies of O_2 electroreduction on platinum using rotating ring-disk and gas-diffusion electrode techniques are also in progress and will be reported. The stability of $F_2C(SO_3H)_2$ will also be checked, particularly at elevated temperatures.

Acknowledgments

This research has been supported by NSF, by NASA through a fellowship to one of the authors (F. W. K.), and by the Electric Power Research Institute.

Manuscript submitted Feb. 18, 1985; revised manuscript received May 13, 1985.

Case Western Reserve University assisted in meeting the publication costs of this article.

REFERENCES

1. A. J. Appleby and B. S. Baker, *This Journal*, **125,** 404 (1978).
2. P. N. Ross, *ibid.*, **130,** 882 (1983).
3. J. H. Simons, "Fluorine Chemistry," Academic Press, New York (1950).
4. J. Burdon and J. C. Tatlow, in "Advances in Fluorine Chemistry," Vol. 1, M. Stacey, J. C. Tatlow and A. G. Sharpe, Editors, pp. 129-165, Butterworth's Scientific Publications, London (1960).
5. S. Nagase, in "Industrial Electrochemical Processes," A. T. Kuhn, Editor, pp. 71-88, Marcel Dekker, New York (1967).
6. A. P. Tomilov, S. G. Mairanovskii, M. Y. Fioshin, and V. A. Smirnov, "Electrochemistry of Organic Compounds," J. Schmorak, Translator, pp. 417-441, Wiley, New York (1972).
7. N. L. Weinburg, in "Technique of Electroorganic Synthesis," N. L. Weinburg, Editor, pp. 1-82, in "Techniques of Chemistry," John Wiley and Sons, New York (1975).
8. T. J. Brice and P. W. Trott, U.S. Pat. 2,732,398 (1956).
9. T. Gramstad and R. N. Haszeldine, *J. Chem. Soc.*, 173 (1956); *ibid.*, 2460 (1957).
10. F. E. Behr, U.S. Pat. 4,329,478 (1982).
11. F. E. Behr and R. J. Koslar, Paper 5 presented at the Fifth Winter Fluorine Conference, Daytona Beach, FL, Feb. 1-6, 1981.
12. V. M. Fild and H. Rieck, *Chem. Z.*, **100,** 391 (1976).
13. C. Pelisena, C. C. Liu, and R. F. Savinell, *This Journal*, **129,** 2720 (1982).
14. L. Fabes and T. W. Swaddle, *Can. J. Chem.*, **53,** 3053 (1975).
15. B. E. Conway, H. Angerstein-Kozlowska, W. B. A. Sharp, and E. E. Criddle, *Anal. Chem.*, **45,** 1331 (1973).
16. J. C. Huang, R. K. Sen, and E. Yeager, *This Journal*, **126,** 786 (1979).
17. J. C. Huang, W. E. O'Grady, and E. Yeager, *ibid.*, **124,** 1732 (1977).

In Situ Spectra of Intermediate Species Recorded during Electrochemical Reduction of p-Benzoquinone

Chong-Hong Pyun* and Su-Moon Park**

Department of Chemistry, University of New Mexico, Albuquerque, NM 87131

p-Benzoquinone has been studied extensively photochemically and/or electrochemically due to its importance as an electron acceptor in many chemical as well as biological reactions. It is generally recognized to undergo an electrochemical-chemical-electrochemical (ECE) reaction when reduced in nonaqueous media (1-6), *i.e.*

$$BQ + e^- \rightarrow BQ^{\bullet -} \quad [1]$$

$$BQ^{\bullet -} + H^+ \rightarrow BQH^{\bullet} \quad [2]$$

$$BQH^{\bullet} + e^- \rightarrow BQH^- \quad [3]$$

$$BQH^- + H^+ \rightarrow BQH_2 \quad [4]$$

where BQ represents p-benzoquinone. Rates of chemical steps, *i.e.*, reactions [2] and [4] have not been reported in nonaqueous solutions, but are slow enough for a nearly complete reoxidation peak for the anion radical to be observed on cyclic voltammetric scales. The apparent decay rate of $BQ^{\bullet}$ was reported by Fukuzumi *et al.* (7) to be 5.7×10^{-3} min^{-1} in neutral water at room temperature with first-order kinetics. The second-order disproportionation rate of $BQ^{\bullet -}$, *i.e.*

$$2BQ^{\bullet -} + 2H^+ \rightarrow BQ + BQH_2$$

is, however, reported to be 1.7×10^8 and 1.1×10^9 $M^{-1}\text{-}s^{-1}$ at pH = 7.2 and 2, respectively, in water by Adams and Michael (8). This disparity indicates the complexity of the

* Electrochemical Society Student Member.
** Electrochemical Society Active Member.

chemistry of p-benzoquinone anion radicals. We believed that a half-life of about 2h for $BQ^{\bullet}$ in water as reported by Fujuzumi *et al.* (7) was excessively long.

Spectra of intermediate species including BQ• and BQH• have been studied using either pulse radiolysis (8-12) or by oxidation of hydroquinone (BQH_2) with solid oxidants such as MnO_2 in water (7). The medium was either water (pure or buffered) or a water-isopropylalcohol (up to 3*M*) mixture. These media are often saturated with N_2O to scavenge radical species produced upon pulse radiolysis, which may lead to some unknown side reactions. Iso-propylalcohol was used to remove any intermediate radical species other than OH•. Attempts at recording transient spectra *in situ* in an electrochemical cell under well-controlled conditions have been made (5, 6), but to the best of our knowledge no such spectra have been recorded using spectroelectrochemical methods with controlled amounts of proton donors.

In this communication, we report the spectra of intermediate species electrogenerated in dimethylsulfoxide (DMSO) solution using near-normal incidence reflectance spectroelectrochemistry (NMIRS). We believe we recorded spectra for all the intermediate species, *i.e.*, $BQ^{\bullet}$, BQH•, and BQH^{-}.

Eastman Organic's reagent-grade p-benzoquinone was used after recrystallization from water. Mallinckrodt's reagent-grade DMSO was used after fractional distillation with a reflux ratio of 5:1 under the reduced pressure. *Tetra*-n-butylammonium perchlorate (TBAP; Southwestern Analytical, Incorporated, Austin, Texas) was used as a supporting electrolyte after drying for 24h at about 100°C. The spectra were recorded at a reflective platinum disk electrode (Sargent Welch S-30101-20A) using a bifurcated optical fiber probe. The spectroelectrochemical system was controlled by an Apple II+ microcomputer. Details of the instrumentation are described elsewhere (13). Cyclic voltammograms were recorded with a Princeton Applied Research (PAR) Model 173 potentiostat-galvanostat along with a PAR Model 175 universal programmer.

Cyclic voltammograms (CV's) shown in Fig. 1 indicate that the anion radical produced upon negative potential sweep is very stable. When water is added to this electrochemical system, practically the same reversible CV is obtained with a prewave due to the enhanced adsorption at the electrode surface. The adsorbed species is stripped off with one scan, leaving the following electron transfer practically reversible (Fig. 1b). This illustrates that the electrogenerated anion radical is fairly stable, even at a reasonably high concentration of the proton donor. Similarly, one can conclude from the CV's shown that the rate of protonation is fairly slow even in solutions containing water.

The spectrum of the anion radical, $BQ^{\bullet}$, recorded after 11 min of electrolysis in "dry" DMSO, is shown in Fig. 2a. This spectrum was recorded while electrolysis was proceeding. To compensate the amount of the $BQ^{\bullet}$ building up in the probe path, the wavelengths were scanned up and down, and the average value of the two was used. The data acquisition time was approximately 5 min.

The spectrum shown in Fig. 2a has exactly the same features as in those recorded in water (7-12), except that the absorption bands are red shifted by about 30 nm in DMSO. We believe that the spectral blue shift observed in the aqueous medium is due to the hydrogen bonding to the benzoquinone carbonyl groups, as was observed in the 9,10-anthraquinone system (14). To confirm this, we ran an experiment in water with 0.20*M* $NaClO_4$ as a supporting electrolyte; exactly the same spectrum as shown in Fig. 2a was observed. The spectrum in water, however, showed about 32 nm of blue shifts. Furthermore, the anion radical was reasonably stable. To our surprise, the anion radical spectra were observed even after more than 30 min after its generation by controlled potential electrolysis. The absorption maxima are believed to arise from the π-π^* transition, and spectral features are due to the C—O stretching vibration in the excited state (15).

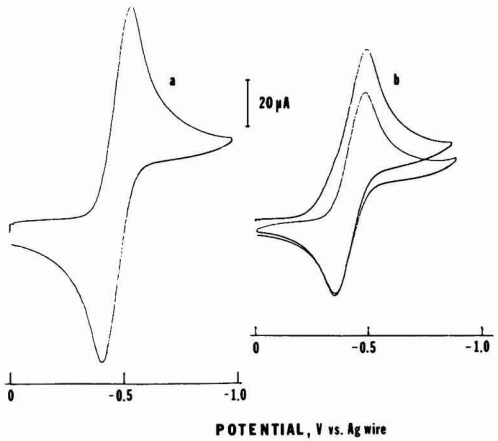

Fig. 1a: Cyclic voltammogram (CV) recorded in a solution containing 1.87 mM p-benzoquinone and 0.10M TBAP in "dry" DMSO. b: CV recorded in a solution containing 1.21 mM p-benzoquinone, 0.10M TBAP, and 10.0% H_2O in DMSO. The reference electrode was a Ag wire, and the scan rate was 100 mV/s for both experiments.

When further electrolysis is performed under the same condition, the spectrum shown in Fig. 2b is obtained. One can notice in this spectrum that the absorption bands at 427 nm and at about 670 nm are growing. This effect is more pronounced when the electrolysis is carried out in DMSO containing 10.0% H_2O even at a much shorter electrolysis time. Note also that the spectral bands show 4 ~ 5

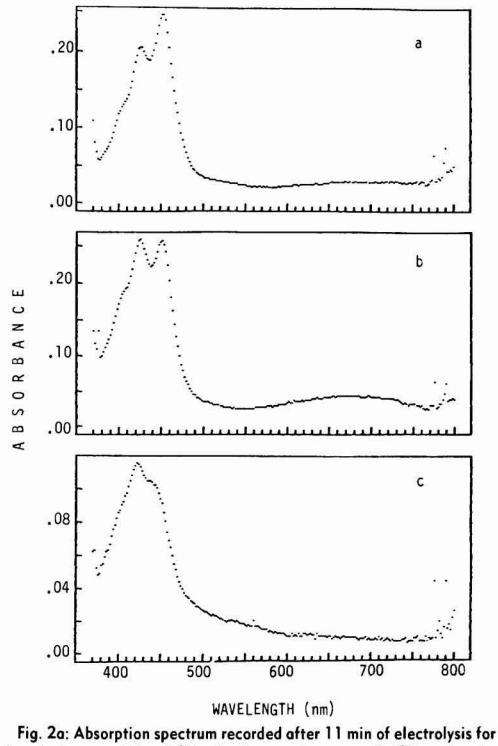

Fig. 2a: Absorption spectrum recorded after 11 min of electrolysis for the solution containing 1.87 mM p-benzoquinone at −0.68V vs. Ag wire electrode. b: Absorption spectrum recorded after 36 min of electrolysis for the same solution as in a. c: Absorption spectrum recorded after 3 min of electrolysis for the solution containing 1.21 mM p-benzoquinone and 10.0% H_2O at −0.62V.

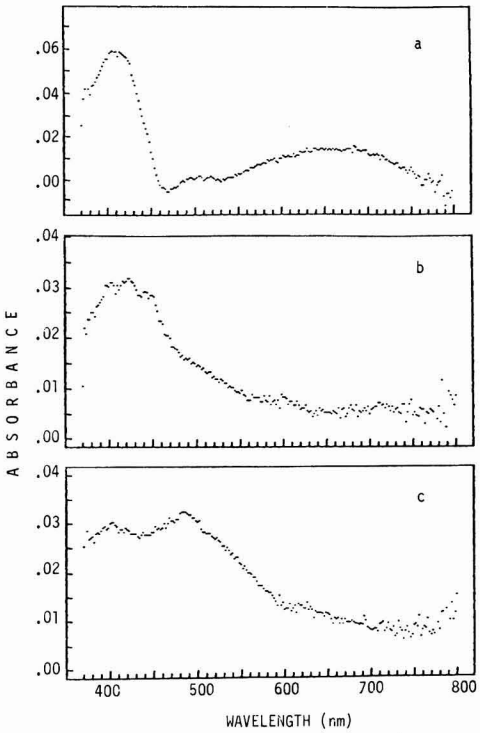

Fig. 3a: Difference spectrum obtained from those shown in Fig. 2b and 2a. b: Difference spectrum obtained from the solution containing 1.21 mM p-benzoquinone and 10.0% H_2O for electrolysis times of 8 and 19 min, respectively. c: Spectrum recorded with the circuit open after 30 min of electrolysis for the solution used in Fig. 3b.

nm blue shifts in Fig. 2c compared to those shown in Fig. 2a due to the addition of water. When the difference between the spectra shown in Fig. 2b and 2a is taken, a spectrum shown in Fig. 3a is obtained. The same spectra as in Fig. 3a are also obtained when differences are calculated from those shown in Fig. 2c and 2a. This indicates that the process producing a species responsible for the spectrum in Fig. 3a is facilitated by the presence of water. Note that this process is already occurring in "dry" DMSO but the rate is much slower. Thus, we attribute the spectrum in Fig. 3a to the free radical generated upon protonation of the anion radical, which is formed at the top of the diffusion layer. We believe that the broad band at about 670 nm is perhaps also from the free radical. For several spectra that we obtained, almost constant ratios of the absorbance at 410 nm to that at 670 nm were observed, indicating that both absorption peaks came from the same source. One may speculate, however, that the absorption band at 670 nm may have resulted from the intermediate dimer formed from the free radical. The presence of such a dimer was speculated by Eggins and Chambers from their cyclic voltammetric studies (5).

The absorption spectrum of the free radical, BQH•, was reported by Adams and Michael (8). They produced this species by generating anion radicals in water of pH = 2.0. The assumption was that anion radicals produced protonate quickly to produce free radicals at low pH's. The spectrum recorded at pH = 2.0 had similar spectral features to the one recorded at a neutral pH, but had its absorption maximum at about 410 nm. In our spectrum, the blue shift of the free radical with respect to that of the anion radical is more extensive than in Adams and Michael's observation. This could perhaps be due to the solvent/supporting electrolyte effects. The transition of the benzoquinone anion radical should be affected by the solvent polarity more than that of the free radical, which does not carry any charges on it.

Also noticed in this spectrum (Fig. 3a) is the presence of an absorption band at about 500 nm. This band grows significantly enough to give a band broadening as shown in Fig. 3b, when the water content becomes high. When the electrical circuit is open, we notice that the absorption peak at about 500 nm grows at the expense of the one at 410 nm, as shown in Fig. 3c. Eventually, all the transient absorption peaks disappear, and the final solution is dominated by the absorption peaks attributable to the final product, hydroquinone (BQH_2). Of course, this happens only when the exhaustive electrolysis is performed. This series of spectroscopic observations indicate that there are no final products detectable other than hydroquinone. Thus, we believe that the absorption band observed at about 500 nm is due to the protonated anion (BQH^-) in reaction [3]. An attempt to obtain the spectrum of BQH^- by deprotonating BQH_2 in strong alkaline medium was not successful; the deprotonation reaction was accompanied by the oxidation of BQH_2 as well. Although the spectra of intermediate species were assigned mostly from the sequence of reactions summarized by [1]-[4], they are in good agreement with those reported for BQ• and BQH• obtained under quite different experimental conditions. The spectrum for BQH^- has not been reported to the best of our knowledge.

We conclude from the current spectroelectrochemical study that we observed transient spectra corresponding to the anion radical ($BQ^{\bullet-}$), protonated free radical (BQH•), and protonated anion (BQH^-) species. Surprisingly, as already pointed out, the electrogenerated $BQ^{\bullet-}$ is reasonably stable even in neutral water as was originally observed by Fukuzumi *et al.* (7). Perhaps the benzoquinone anion radical generated by pulse radiolysis (8-12) may not be stable due to the host of other reactive intermediate species produced along with the desired product. Particles of very high energies are employed in pulse radiolysis. Further work on the solvent effect on the spectra, effect of water, and the rate of decay of each intermediate species is in progress in our laboratory.

Manuscript submitted March 11, 1985; revised manuscript received May 8, 1985.

REFERENCES

1. S. Wawzonek, R. Berkey, E. W. Blaha, and M. E. Runner, *This Journal*. **103,** 456 (1956).
2. I. M. Kolthoff and T. B. Reddy, *ibid.*, **108,** 980 (1961).
3. R. Jones and T. M. Spotswood, *Aust. J. Chem.*, **15,** 492 (1962).
4. W. R. Turner and P. J. Elving, *This Journal*, **112,** 1215 (1965).
5. B. R. Eggins and J. Q. Chambers, *ibid.*, **117,** 186 (1970).
6. V. J. Koshy, V. Sawayambunathan, and N. Periasamy, *ibid.*, **127,** 2761 (1980).
7. S.-I. Fukuzumi, Y. Ono, and T. Keii, *Bull. Chem. Soc. Jpn.*, **46,** 3353 (1973).
8. G. E. Adams and B. D. Michael, *Trans. Faraday Soc.*, **63,** 1171 (1967).
9. P. S. Rao and E. Hayon, *J. Phys. Chem.*, **19,** 2274 (1973).
10. G. N. R. Tripathi, *J. Chem. Phys.*, **74,** 6044 (1981).
11. G. N. R. Tripathi and R. H. Schuler, *ibid.*, **76,** 2139 (1982).
12. G. N. R. Tripathi and R. H. Schuler, *J. Phys. Chem.*, **87,** 3101 (1983).
13. C.-H. Pyun and S.-M. Park, *Anal. Chem*, To be published.
14. M. Fujihara and S. Hayano, *Bull. Chem. Soc. Jpn.*, **45,** 644 (1972).
15. Y. Harada, *Molec. Phys.*, **8,** 273 (1964).

Investigation of Photoelectrode Redox Polymer Junctions

Ronald L. Cook* and Anthony F. Sammells*

Eltron Research, Incorporated, Aurora, Illinois 60505

There are several incentives for the characterization of semiconductor junctions with redox containing solid polymer electrolytes (SPE). An understanding of such junctions can be expected to have important implications on the design of solid-state photoelectrochemically rechargeable galvanic devices possessing charge capacity. In addition, the presence of polymer-incorporated redox species in close proximity to the semiconductor surface may act as an antenna probe for measuring perturbations in interbandgap surface states when the junction is exposed to selected chemical species.

We have previously shown the viability of such junctions for the storage of photogenerated electrochemical energy (1, 2). Here, solid-state cells based upon both poly(ethylene oxide) and Nafion[1] as SPE's have been shown to be potentially attractive for energy storage. A recent example discussed by us is the two photoelectrode cell

$$p/InP/Fe^{+3}\ porphine/Nafion\ 117/Ru^{2+}\ (bpy)_3/n\text{-}CdS$$

which has been shown to generate photopotentials in excess of 1V upon simultaneous AM1 illumination of both photoelectrodes, using the above electrochemically reversible redox couples (2). In addition, semiconductor films deposited onto appropriate substrates have been found promising, via the use of impedance techniques, for the detection of gases such as CO (3-5).

For electrochemical energy storage, the redox polymer phase should, in principal, possess the following properties: (*i*) the redox species must be fixed into a relatively immobile polymer site so that any self-diffusion resulting in spontaneous self-discharge would be eliminated; (*ii*) the immobilized redox species must retain some electrochemical reversibility; and (*iii*) an excess concentration of mobile conducting species should be present in the vicinity of the redox couple, over and above that normally necessary for ionic conduction, to preserve electroneutrality in the proximity of the immobilized redox species during redox electrochemistry. The perfluorinated cation exchange material Nafion was selected as a candidate SPE material whose properties may address these criteria (6-9).

Photoelectrochemical (PEC) cells using n-CdS as a photoanode and Nafion 117 as the SPE were prepared and doped with a variety of transition metal complexes of varying redox potentials and overall molecular charge (+2, 0, −1). The role of such introduced redox species for perturbing photoelectrode properties was of interest both for understanding conditions which promote electron transfer for charge (or discharge) in solid-state PEC storage devices, and also for understanding their role in changing semiconductor properties which might facilitate the use of this junction for various detector applications.

Experimental

n-CdS single crystals were obtained from Cleveland Crystals, Incorporated, and were initially polished with 600 grit emery paper, followed by 5 μm alumina on a Texmet polishing cloth and finally with 0.3 μm alumina on a Microcloth polishing cloth. The ohmic contact area was initially etched with a solution of HNO_3:H_2SO_4:HOAc:HCl (30:20:10:0.1) for 20s. Ohmic contact was achieved by introduction of a gallium-indium eutectic onto the etched CdS face. Current collection was achieved via a Nichrome wire using a silver epoxy, which was cured at 150°C for 1h. Immediately prior to fabrication of the cell, the front face was polished with 5 and 0.3 μm alumina, rinsed, and the face etched with HNO_3:H_2SO_4:HOAc:HCl solution as above.

Electrochemical measurements were performed using potentiostatic control provided by either a Stonehart Associates BC 1200 or a Wenking LT 78 potentiostat. Differential capacitance measurements for Mott-Schottky plots were performed using a H-P 4276A digital LCZ meter at 1000 and 10,000 Hz. Thin film coatings of gold and silver were vacuum-deposited on glass slides with an Edwards 306A evaporator. Photoelectrode illumination was achieved via a Sylvania 300W ELH bulb. Light intensities were measured with an Eppley 8-48 pyranometer. Cyclic voltammograms on the redox couples were run in acetonitrile (Burdick and Jackson) with tetrabutylammonium hexafluorophosphate (Southwestern Analytical Chemicals, Incorporated) as supporting electrolyte. A three-electrode configuration consisting of a platinum working electrode, a platinum counterelectrode, and a Ag/Ag^+ reference electrode was used for the cyclic voltammetry scans.

Results and Discussion

Cell preparation.—Solid-state PEC cells were fabricated by introducing 0.05 ml of a solution containing 50 mg/ml of Nafion 117 and 0.5 mg/ml of the appropriate redox couple in a solution of lower aliphatic alcohols onto the surface of a n-CdS photoanode and a glass slide possessing both an evaporated gold counterelectrode and silver quasi-reference electrode. The Nafion was allowed to dry partially for 15 min on each of these surfaces, after which the two half-cells were pressed together and allowed to dry for an additional 2h. The cell configuration used in this work is shown in Fig. 1. The transition metal complexes selected for introduction into the Nafion polymer included $FeCp_2$, $Ru(bpy)_3^{2+}$, $Fe(bpy)_3^{2+}$, $Fe(CN)_6^{4-}$, and $Fe(acac)_3$. These complexes were selected to provide for both a variation in overall molecular charge and chemical potential at localized sites within the Nafion polymer. Several films were initially cast onto Teflon substrates and allowed to dry. Upon removal and visual examination of these films (40× magnification), the polymer con-

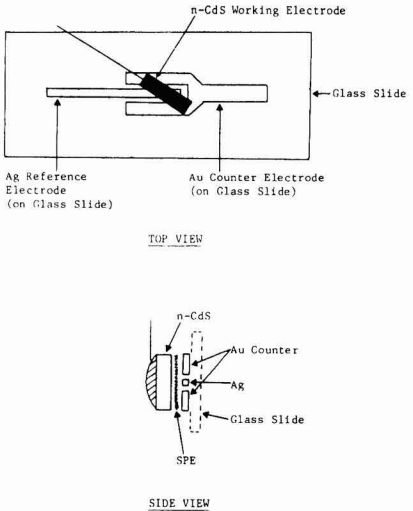

Fig. 1. Schematic diagram of cell configuration used in this work

* Electrochemical Society Active Member.

[1] Nafion is the registered trademark for a family of perfluorsulfonic acid ion-exchange membranes manufactured by E. I. du Pont de Nemours and Company.

taining $Ru(bpy)_3^{2+}$ was yellow and homogeneous. For concentrations of $Ru(bpy)_3^{2+}$ up to 20 mg/ml SPE, the polymer remained homogeneous in appearance. Similar observations were made when $Fe(bpy)_3^{2+}$ was introduced into the polymer.

In comparison, ferrocene, was in fact insoluble at concentrations greater than 1 mg/ml of the SPE, as manifested by its appearance as microcrystalline needles upon solvent removal from the polymer. Similar observations were made when $Fe(acac)_3$ was introduced into the polymer. The anionic complex $Fe(CN)_6^{4-}$ remained homogeneous at concentrations up to 2 mg/ml SPE.

Photoelectrochemical measurements.—To gain some preliminary insight into the respective PEC characteristics of the SPE cell when the redox species $FeCp_2$, $Ru(bpy)_3^{2+}$, $Fe(CN)_6^{4-}$, and $Fe(acac)_3$ are present in the proximity of semiconductor/SPE junctions, cells possessing the general configuration n-CdS/SPE + redox species/Au were prepared using the procedures discussed above. The initial photopotentials realized from these cells under simulated AM1 illumination conditions are compared in Table I. As can be seen, these photopotentials (which are mainly around 200 mV) appear to be relatively invariant when compared to, for example, $E_{1/2}$ values for the same redox species in acetonitrile using a platinum electrode, *e.g.*, $FeCp_2$ (0.285V *vs.* Ag/Ag^+), $Ru(bpy)_3^{2+/3+}$ (1.25V *vs.* Ag/Ag^+).

Although this was initially thought explainable by the presence of Fermi level pinning by the n-CdS, it was later observed that photopotentials for $Ru(bpy)_3^{2+}$-modified SPE-PEC cells were in the −500 to −600 mV range when SnO_2 conducting glass was used as the counterelectrode. This result suggests that the photopotentials observed in the CdS/Nafion + redox couple/Au system may have been limited by inadequate interfacial contact between the Nafion polymer and the gold counterelectrode. Such interfacial contact limitations have previously been reported using Nafion/WO_3-based SPE electrochromic devices (10). SnO_2, however, shows significant adhesive strength attributable to covalent bonding between the sulfonic acid groups in the SPE and receptive functional groups on the SnO_2 substrate electrode (11). Thus, the increased photopotentials observed for n-CdS/SPE cells using SnO_2 conducting glass counterelectrodes can, in part, be explained by improved interfacial contact with the Nafion polymer at the counterelectrode.

In order to determine the dependency of the SPE-incorporated redox species concentration on the photopotential of n-CdS/Nafion + $Ru(bpy)_3^{2+}$/conducting glass, SPE cells, $Ru(bpy)_3^{2+}$ concentrations were varied between 0.0004g and 0.006 g/ml/SPE and their photopotentials under 100 mW/cm^2 illumination compared. As can be seen from Table II, the photopotentials for this system were not dependent on the concentration of the incorporated redox species over the concentration range studied, thereby indicating that the double layer present at the semiconductor/SPE junction was invariant under these experimental conditions. If significant perturbation of the double-layer region were to have occurred, however, this might have influenced the photopotential observed by changing the space charge region width and the corresponding barrier height.

For cells based upon the proton conducting SPE, generally low currents were observed which were attributed to the poor conductivity of this polymer when used in solid-state cells. However, substitution of Na^+ for H^+ conductivity in the SPE/alcohol mixture before polymer formation on the semiconductor substrate was found to enhance overall ionic conductivity of the final solid-state cell. Figure 2 shows a current-voltage PEC curve for the cell n-CdS/SPE:$FeCp_2$:NaCl/Au. Overall cell resistance was found to be 14 kΩ, and a current density of 25 $\mu A/cm^2$ could be obtained by applying a 300 mV anodic overpotential to the photoanode.

Table I. Photopotential values for the PEC cells CdS/Nafion + redox species/Au

Redox species introduced into H^+ conducting Nafion 117	Photopotential under AM1 illumination at n-CdS (mV)
$Ru(bpy)_3^{2+}$	−200
$Fe(bpy)_3^{2+}$	−190
$Fe(CN)_6^{4-}$	−220
$FeCp_2$	−270
H^+ conducting Nafion	−200

Table II. Photopotential measurements on n-CdS/Nafion 117 + $Ru(bpy)_3^{2+}$/conducting glass as a function of $Ru(bpy)_3^{2+}$ concentration

$Ru(bpy)_3^{2+}$ (mg/ml/SPE[a])	Photopotential (mV)
0.375	−485
0.75	−488
1.5	−490
3.0	−480
6.3	−500

[a] 1 ml SPE solution contains 50 mg/ml Nafion 117.

Capacitance measurements.—For cells prepared in this work, differential capacitance measurements were performed on n-CdS/redox SPE junctions, to determine if there was any sensitivity of the measured n-CdS flatband potential to the redox species introduced into the Nafion polymer. Figure 3 compares differential capacitance measurements performed on n-CdS junctions with the proton conducting SPE, (*i.e.*, no introduced redox species) and the SPE's containing $Ru(bpy)_3^{2+}$ and $Ru(bpy)_3^{2+}$ + $FeCp_2$, performed at 1000 Hz. These C_{sc}^{-2} *vs.* *V* plots show good linearity even though some of the cells possessed a relatively high resistance. Some frequency dispersion was noted at higher frequencies. Deviations from linearity for such plots might be expected if there is a high electrolyte resistance in series with the semiconductor space charge region or if a high population of surface states is present at the semiconductor/electrolyte interface (12). Results obtained from both current-voltage curves and the application of an ac signal to the cell suggested that some degree of rectification may be present at the semiconductor/SPE interface. Here, the ac signal from a signal generator was introduced through the cell and a measuring resistor. The output current as measured across the resistor was fed into an oscilloscope. The negative half of the sine wave was only two thirds the height of the positive half of the sine wave. This suggested that

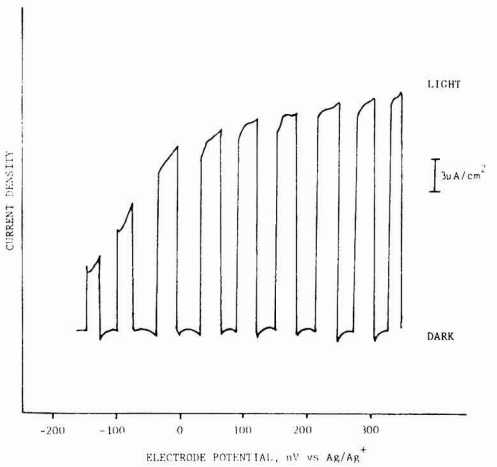

Fig. 2. Current-voltage relationship for the cell n-CdS/Nafion:$FeCp_2$:NaCl/Au

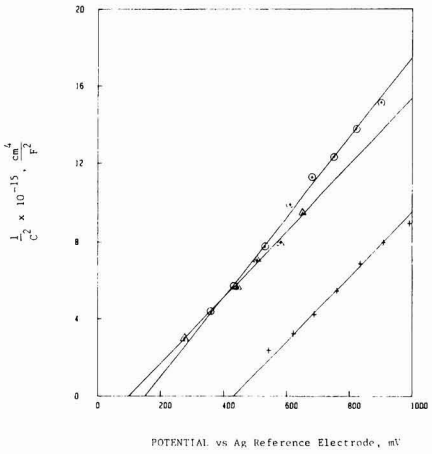

Fig. 3. Mott-Schottky plots for CdS/SPE/Au (crosses), CdS/SPE + $Ru(bpy)_3^{2+}$/Au (circles), and CdS/SPE + $Ru(bpy)_3^{2+}$ + $FeCp_2$/Au (triangles).

about 30% rectification was present in the cell. It should be noted that for semiconductor/metal oxide solid-state junctions where current rectification is seen, linear Mott-Schottky plots have been obtained (12).

Since good linearity and reproducibility were obtained from C_{sc}^{-2} *vs.* V plots in work reported here, it was of interest to compare measured n-CdS flatband potentials (V_{FB}) as a function of the introduced redox species. For the undoped proton, conducting SPE, V_{FB} was -0.43V *vs.* the silver reference electrode. Upon the introduction of $Ru(bpy)_3^{2+}$ or $FeCp_2$ into the SPE, the n-CdS flatband potential was shifted progressively in a cathodic direction [V_{FB} = 0.151V, $Ru(bpy)_3^{2+}$, V_{FB} = 0.097V, $(FeCp)_2$]. This cathodic shift is consistent with that for the oxidation potentials seen for $Ru(bpy)_3^{2+}$ ($E_{1/2}$ = 1.25V *vs.* SCE) and $FeCp_2$ (0.285V *vs.* SCE) in acetonitrile. Similar cathodic shifts have also been observed in the cells n-TiO_2/Nafion + redox couple/SnO_2 conducting glass and n-TiO_2/polyamps[2] + redox couple/SnO_2 conducting glass.

Such changes in V_{FB} may be due to modifications at the electrode surface induced either by direct adsorption of the redox couple or to variations in the capacitance associated with the polymer itself upon changing the redox species. Currently experiments are being performed by us to identify the origin of such observed V_{FB} shifts upon varying the introduced redox couple. If, in fact, the shift in V_{FB} is directly dependent in part on the redox potential of the introduced redox couple, then such semiconductor/SPE junctions might form the basis of a detector technology. For example, an introduced gas or chemical species might be expected to modify the immediate chemical environment of the SPE-incorporated redox couple and thus give detectable parametric changes (*e.g.*, V_{FB}) at the semiconductor surface.

For the n-CdS/redox SPE solid-state junctions considered here, changes occurring in the Helmholtz double-layer voltage V_H as a result of varying redox species can result in perturbation of the semiconductor bandedge energy. This can be expected by consideration of the relationship

$$V_{FB} = E_{sc}^{\circ} - \mu + V_H$$

where μ is the difference in energy between the bulk conduction bandedge and the Fermi level, and V_H is the Helmholtz double-layer voltage. When a redox-containing surface is introduced onto a semiconductor, three possibilities can be envisioned for perturbing V_H: (*i*) the presence of interface states at the junction may induce a voltage drop across the polymer that may be indistinguishable from a Helmholtz voltage; (*ii*) if the polymer is insulating, the point of zero charge (PZC) will be different than that for the bare semiconductor resulting in perturbation of V_H; and (*iii*) if electron exchange can occur between semiconductor surface states and polymer-incorporated redox species, then the former will define V_H and thus V_{FB}.

Donor surface states are expected near the valence band and acceptor states near the conduction band. If the E_{redox} for a redox species is below the donor state, or above the acceptor state, then the energetics will promote charging of surface states and thus change V_{FB}. Work is currently being performed directed towards clarifying which of these effects influences V_{FB} at n-CdS/SPE interface. It is not clear at this time, however, which of these mechanisms is responsible for the observed shift in the n-CdS flatband potential.

In conclusion, (*i*) it has been observed that the measured flatband potential in the described cells can be modified by introduction of selected redox species into the SPE, (*ii*) photopotentials in the range 500-600 mV can be obtained if good interfacial contact is maintained at both the working and counterelectrode, and (*iii*) the photopotentials obtained in the n-CdS/Nafion 117 + $Ru(bpy)_3^{2+}$ conducting glass SPE cells are not dependent on the concentration of the incorporated redox species.

[2] Polyamps is poly(2-acrylamido-2-methyl-propane sulfonic acid).

Acknowledgment

This work was supported in part by the Office of Naval Research.

Manuscript submitted Jan. 8, 1985; revised manuscript received *ca.* March 15, 1985.

Eltron Research, Incorporated, assisted in meeting the publication costs of this article.

REFERENCES

1. A. F. Sammells and P. G. P. Ang, *This Journal*, **131,** 617 (1984).
2. A. F. Sammells and S. K. Schmidt, *ibid.*, **132,** 520 (1985).
3. R. R. Hooker, U.S. Pat. 3,933,433 (1974).
4. V. W. Brown, in "Proceedings of the Second West Virginia University Conference on Coal Mine Electrotechnology, 22-1/22-17 (1974).
5. J. G. Firth, A. Jones, and T. A. Jones, *Ann. Occup. Hyg.*, **18,** 63 (1975).
6. R. S. Yeo, *This Journal*, **130,** 533 (1983).
7. H. L. Yeager, B. Kipling, and R. L. Dotson, *ibid.*, **127,** 303 (1980).
8. H. L. Yeager, Z. Twardowski, and L. Miclarke, *ibid.*, **129,** 324 (1982).
9. N. E. Prieto and C. R. Martin, *ibid.*, **131,** 751 (1984).
10. J. P. Randin, *ibid.*, **129,** 1215 (1982).
11. D. A. Buttry and F. C. Anson, *J. Am. Chem. Soc.*, **104,** 4824 (1982).
12. S. R. Morrison, "Electrochemistry at Semiconductor and Oxidized Metal Electrode," Chap. 8, Plenum Press, New York (1980).

JOURNAL OF THE ELECTROCHEMICAL SOCIETY

SOLID-STATE SCIENCE AND TECHNOLOGY

OCTOBER 1985

Rapid Isothermal Fusion of PSG Films

J. S. Mercier,* I. D. Calder, R. P. Beerkens,[1] and H. M. Naguib*,[2]

Northern Telecom Electronics Limited, Semiconductor Components Group, Ottawa, Ontario, Canada K1Y 4H7

ABSTRACT

This paper presents results on rapid isothermal fusion (RIF) characteristics of phosphosilicate glass (PSG) obtained using an incoherent lamp annealer in a N_2 ambient. The effects of varying the temperature (1000°-1200°C), the cycle duration (10-60s), and the phosphorus concentration in the glass (2.5-8.0 w/o) were investigated. The out-diffusion of phosphorus from the PSG films during RIF cycles were also studied. In conjunction with these experiments, dopant redistribution induced by typical RIF cycles in a boron-implanted silicon substrate was measured to assess the practicality of the RIF technique for VLSI applications and to identify a process window. The results for the boron profile redistribution were used as a basis of comparison between RIF and conventional furnace treatments. Although restricted to VLSI applications where a relatively high phosphorus content of approximately 8 w/o is acceptable in PSG films, it is concluded that RIF in a N_2 ambient is nevertheless much more effective for the fusion of PSG films than conventional furnace processing and thus much more compatible with VLSI processing.

As a part of the fabrication sequence for integrated circuits, a layer of phosphosilicate glass (PSG) is deposited to provide passivation and electrical insulation between metal interconnects and underlying structures. Before the subsequent deposition of metal takes place, it is necessary to smooth the surface topography to ensure continuity of the overlying metallization. At present, this treatment is typically a furnace glass fusion cycle at 1000°C for 30 min or more (1-5) and is the last high temperature process step in the fabrication of LSIC's. This heavy thermal load will be unacceptable for processing new generations of VLSI circuits because it will induce appreciative lateral and vertical dopant redistribution in small geometry devices.

Thermal processing requirements can be eased by using different materials or ambients during the fusion cycle. Although increasing the phosphorus concentration does lead to a lower fusion temperature for PSG films, excessive concentrations eventually promote the formation of phosphoric acid in the presence of moisture (2, 4), thereby causing reliability problems due to corrosion of overlying aluminum interconnect lines. As an alternative solution, rapid isothermal fusion (RIF) has been shown in limited studies to improve PSG step coverage, while causing less junction diffusion than conventional furnace processing cycles because of its lower time-temperature product (6-9).

In this work, we have studied the effect of RIF on PSG films having a practical range of phosphorus concentrations, namely, 2.5, 4.0, 6.6, and 8.0 w/o. The RIF experiments were performed in a N_2 ambient using a tungsten halogen lamp system.[3] In addition, the out-diffusion of phosphorus from the PSG films during RIF was examined.

The amount of dopant diffusion induced by RIF in underlying device junction areas will largely determine its range of usefulness for VLSI applications (6-12). Therefore, boron-implanted silicon wafers were also processed separately and junction depths were measured after undergoing typical RIF cycles. Finally, fusion and dopant redistribution experiments were carried out in a conventional furnace and the results were compared with the RIF data to assess the relative applicability of each technique to VLSI processing.

Experimental Procedures

Sample preparation.—The test structure used to observe PSG fusion is illustrated in Fig. 1. A thermal SiO_2 layer was first grown on a Si(100) substrate to a thickness of 100 nm, at a temperature of 1000°C. A 1.0 μm LPCVD polysilicon film was deposited at 625°C and phosphorus-doped with a $POCl_3$ cycle at 900°C. The polysilicon was then patterned into sharp steps using a dry etching technique. Finally, 1.0 μm thick PSG films were deposited in a horizontal, hot-wall LPCVD system at a temperature of 410°C using the silane and phosphine oxidation process.

Samples for studying dopant redistribution in silicon were formed by first growing a 40 nm thermal oxide on (100) n-type Si substrates. Boron was then implanted through this oxide layer with a dose of 3×10^{15} B^+/cm^2 at an energy of 25 keV.

Rapid isothermal fusion.—The fusion cycles were carried out in a commercially available tungsten halogen lamp systems. Cycle durations were varied from 10 to 60s and temperatures from 1000° to 1200°C. The RIF experi-

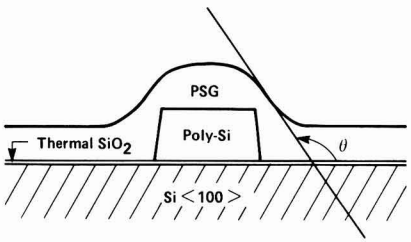

Fig. 1. Test structure for RIF studies, showing the step coverage angle θ. The PSG film is 1.0 μm thick, the polysilicon step is 1.0 μm high, and the thermal oxide thickness is 100 nm.

* Electrochemical Society Active Member.

[1] Present address: Department of Electrical Engineering, University of Waterloo, Waterloo, Ontario, Canada N2L 3G1.

[2] Present address: Fairchild Camera and Instrument Corporation, Mountain View, California 94039.

[3] A Heatpulse 210T™ tungsten halogen lamp annealing system was used. It was manufactured by A. G. Associates, Palo Alto, California.

ments were performed in a N_2 ambient. The temperature was controlled using feedback from a Chromel-Alumel thermocouple attached to a silicon test piece situated to the side of the wafer.

Junction dopant redistribution.—Boron-implanted silicon wafers were subjected separately to rapid isothermal annealing (RIA) cycles identical to some of those used in the RIF experiments. Other implanted samples were subjected to an 80 min, 900°C annealing cycle in 1 atm of N_2, performed in a conventional furnace.

Analysis.—To quantify the extent of the fusion, SEM cross-sectional micrographs were used to measure the change in the PSG step coverage angle θ, with an accuracy of ±5°. In order to measure the angle θ with the SEM, the samples were cleaved and given a decorative etch for 1 min in 50:1 buffered HF to delineate the underlying polysilicon/PSG interface. The phosphorus concentration of the PSG films was determined with energy dispersive x-ray (EDX) electron microprobe analysis to within ±0.2 w/o.[4] For an electron-beam energy of 6 keV, a value of 600 (±60) nm was calculated for the probing depth.

The dopant redistribution in the implanted silicon samples was evaluated using secondary ion mass spectroscopy (SIMS) and a "bevel-and-etch" (B&E) technique. The B&E method relies on the larger etch rate of doped silicon relative to undoped silicon in certain etchants. By using this property on a beveled (~1°-2°) implanted silicon substrate, the junction area can be delineated interferometrically and related back to the actual junction depth. SIMS measures both active and inactive impurity concentrations, *i.e.*, the metallurgical junction depth, while the B&E technique yields a measure of the depth of active dopants, *i.e.*, the electrical junction depth.

Results and Discussions

Rapid isothermal fusion.—A summary of the complete RIF results is given in Table I. For all phosphorus concentrations investigated, the control (*i.e.*, as-deposited) PSG samples showed a typical step coverage angle θ of approximately 80°. Representative results obtained after RIF for a range of initial phosphorus concentrations $[P]_0$ are shown in the SEM micrographs of Fig. 2. For all but the 8.0 w/o PSG films, a temperature of 1200°C and/or a 60s cycle duration is needed to obtain substantial PSG fusion (*i.e.*, $\theta \gtrsim 110°$).

Results for 8.0 and 6.6 w/o PSG films are shown in Fig. 3 and 4, respectively. For these films, an 1100°C/10s RIF cycle is sufficient to obtain a value of 113° for θ (Fig. 3c). It would seem quite plausible that by increasing either the RIF cycle duration to 60s or the temperature to 1200°C, further fusion will be obtained. Unfortunately, the SEM micrograph of Fig. 3d shows that large voids form on each side of the step as a consequence of these extreme RIF treatments. For the 6.6 w/o films, the SEM micrographs of Fig. 4 show similar results, except under more severe RIF conditions.

The formation of voids has been observed previously, although their presence was largely attributed to the use of a H_2 ambient (13). In that study, it is argued that the presence of phosphorus in the glass, in the form of phosphorus pentoxide (P_2O_5), is also directly responsible for

[4] Calibration was obtained using colorometric analysis performed at Balazs Laboratory, Mountain View, California.

Table I. Summary of RIF results listing, for given temperatures, the minimum cycle duration for which fusion occurs and eventually voids form

P content (w/o)	Onset of fusion ($\theta > 90°$C) T (°C)	t (s)	Void formation T (°C)	t (s)
2.5	1200	≳ 40	—	—
3.9	1150	≳ 60	—	—
3.9	1200	≳ 20	—	—
6.6	1100	≳ 20	—	—
6.6	1150	≳ 10	1200	≳ 40
8.0	1050	≳ 60	1100	≳ 60
8.0	1100	≳ 10	1200	≳ 10

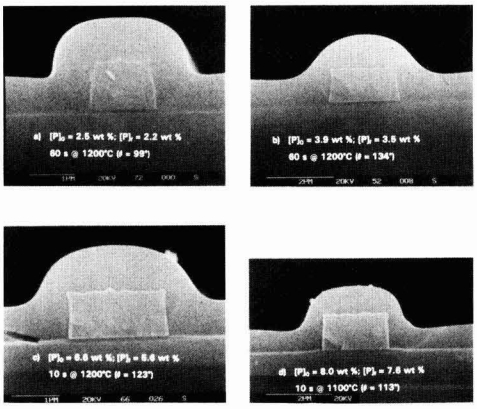

Fig. 2. SEM micrographs showing the best RIF results obtained at four different phosphorus concentrations. $[P]_0$ and $[P]_f$ are the initial and the final phosphorus concentrations, respectively.

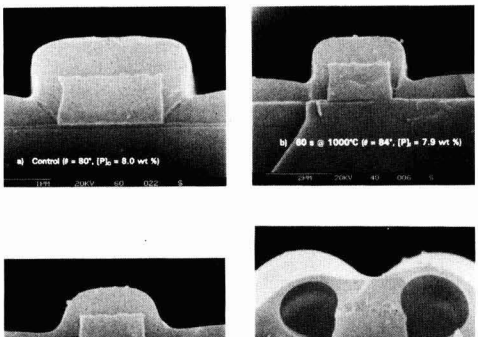

Fig. 3. SEM micrographs showing $[P]_0$ and $[P]_f$ fusion results for 8.0 w/o PSG films are the initial and final phosphorus concentrations, respectively.

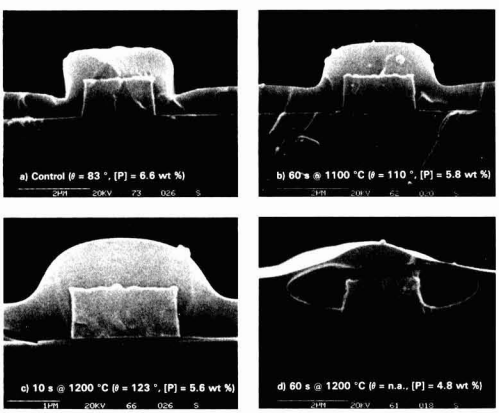

Fig. 4. SEM micrographs showing fusion results for 6.6 w/o PSG films. The phosphorus concentrations given under micrographs 3b to 3d were measured after the RIF cycles.

the formation of voids. This conclusion is supported by our findings, since an enhancement in void formation was observed with an increase in the phosphorus content of the PSG films.

Because P_2O_5 sublimes at a temperature of about 300°C, a sufficient local concentration of P_2O_5 could, under the right conditions, lead to the formation of cavities in the glass. In the case of RIF, accelerated sublimation of the P_2O_5 may result from the rapid heat-treatment which would not allow sufficient time for the P_2O_5 to diffuse slowly out of the film without creating a permanent deformation of the softened PSG. The reasons for which the conditions favoring the formation of voids are found only on the sides of steps are not clear. To our knowledge, the only experimental evidence suggesting different glass properties in these regions comes from the faster etch rate observed on each side of steps for as-deposited oxide films, after the cross-sectional decorative etch of cleaved samples has been performed for the SEM examination. As a result, diagonal etch lines, visible in the SEM micrograph of Fig. 3a, are formed in the glass on each side of the polysilicon steps. RIF inhibit the occurrence of these etch lines, as seen in the micrographs of Fig. 3. Although the severity of these etch lines is observed to decrease proportionally with the nominal phosphorus content in the layer, they still remain for undoped glass films. Therefore, a localized structural property which does not depend entirely on the presence of phosphorus, such as a different glass density or stress level, could also be involved in the formation of voids. More work is needed to understand the mechanisms of such localized void formation.

Phosphorus out-diffusion.—Some loss of phosphorus from the PSG films occurs during RIF treatments, as can be inferred from the initial phosphorus concentrations $[P]_0$ and the final concentrations $[P]_f$ detailed in Fig. 2 and 3. Since only the top half of each PSG film was probed with EDX during the phosphorus analysis, it can be concluded that the observed changes in phosphorus concentration were likely caused by out-diffusion to the ambient. These results can be plotted to extract useful information on the diffusion of phosphorus in PSG during RIF.

If we assume that the probing depth d_p (600 ± 60 nm) for the EDX electron microprobe analysis of phosphorus in the PSG films is much larger than the diffusion length $(Dt)^{1/2}$, the reduction in phosphorus concentration $\Delta[P]$, lost to the ambient out of the original concentration $[P]_0$, is given by (14)

$$\Delta[P]/[P]_0 \simeq (2/d_p)(Dt/\pi)^{1/2} \quad [1]$$

where D is the diffusion coefficient for phosphorus in SiO_2 and t is the time. In Fig. 5, we plot the expression $\Delta[P]/[P]_0 t^{1/2}$ against $1/T$, which should also vary with $D^{1/2}$, to find an Arrhenius relationship, described by $D = D_0 \exp(-E_D/kT)$. Only data for $[P]_0$ = 6.6 and 8.0 w/o were used, since for these cases alone was the loss $\Delta[P]$ sufficiently greater than the experimental error. An activation energy E_D = 2.24 ± 0.28 eV, which is twice the slope of the line fit in the plot shown in Fig. 5, was determined. For example, a value of $D = 8.5 \pm 2.3 \times 10^{-13}$ cm²/s is calculated at 1100°C. These values obtained for both E_D and D are comparable to results reported elsewhere (15, 16) for studies performed in a conventional furnace at similar phosphorus concentrations (~10^{21} cm^{-3}). Values for D which are several orders of magnitude lower than the above result have also been published, although lower phosphorus concentrations were involved (15, 17).

Dopant redistribution.—Figure 6 shows the effect of various RIA cycles on the diffusion of boron in implanted silicon test samples, as determined by SIMS (closed symbols) and by the B&E techniques (open symbols). The as-implanted values of junction depth measured with these two techniques were 0.35 and 0.2 μm, respectively. It must be noted that, although the absolute results obtained from the two measurement techniques

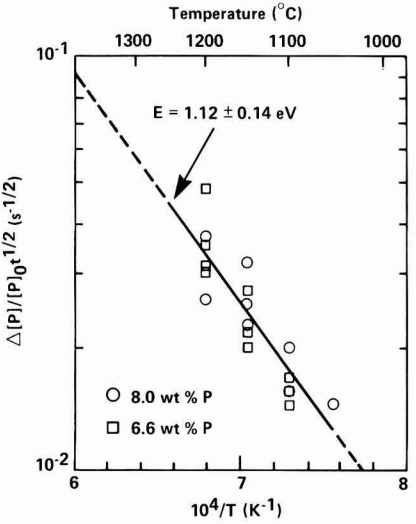

Fig. 5. Arrhenius plot for the out-diffusion of phosphorus during RIF treatments, for two concentrations and various RIF conditions. $\Delta[P] = [P]_f - [P]_0$ is the amount of phosphorus lost to the ambient during RIF. The slope of the linear fit yields $E_D/2$, where E_D is the activation energy for phosphorus diffusion in glass.

are different, the measurements of the junction depth increases Δx_j agree quite closely. The SIMS results from the 900°C, 80 min furnace annealing cycle in N_2 are also included in Fig. 6.

Example of VLSI process window for RIF.—In order to establish the upper bound of a process window for the application of RIF of PSG films to VLSI processing, the issue of dopant redistribution induced by rapid isothermal processing in underlying device shallow junctions must be addressed (7-12). For VLSI applications, a somewhat arbitrary upper limit of 0.1 μm could be placed on the acceptable junction depth increase resulting from a fusion cycle. This would correspond to, for example, a 50% displacement of a typical 0.2 μm shallow junction. As a consequence, the results from Fig. 6 indicate upper limits to RIF conditions of 1000°C/60s or 1100°C/10s.

The dopant redistribution results also show that any 1200°C RIF cycle would be too extreme. Also, on the basis of the RIF results alone (Table I), a 1200°C cycle should be

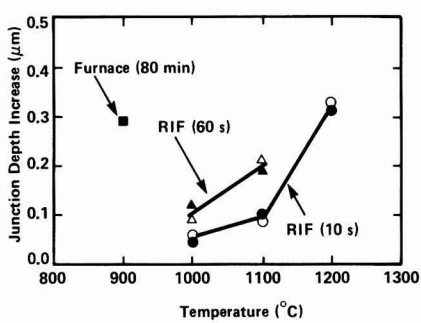

Fig. 6. Graph showing the temperature dependence of the junction depth increase in a boron-implanted Si substrate induced by various heating cycles. The results shown were obtained with both the B&E method (open symbols) and SIMS (closed symbols). The implantation conditions are given in the text. The junction depth for the as-implanted Si samples was 0.20 μm, as measured with the B&E method, and 0.35 μm, as measured with SIMS. The result for the 60s/1200°C was Δx_j = 1.4 μm (B&E) and thus was not included in the figure.

avoided in any case since undesirable fusion characteristics are observed, namely, void formation in high phosphorus content PSG and insufficient fusion in low phosphorus content PSG. In addition, the use of a long fusion period (> 20s) could be economically impractical in a serial processing system.

It must be emphasized that the discussion for the given example applies to silicon substrates implanted with boron, which is one of the fastest diffusing species of the commonly used dopants in IC fabrication (18). If a slower diffusing species is used, such as arsenic, larger and/or hotter RIF cycles could be acceptable. However, if even shallower junctions are required, more stringent restrictions would be imposed on the RIF conditions.

The RIF results summarized in Table I can be used to determine the lower bound for the process window which is defined as the point when the reentrant profile is eliminated (*i.e.*, $\theta > 90°$). From Table I, it is clear that the 1100°C/10s RIF cycle can only induce acceptable fusion in 8.0 w/o PSG films. It has also been reported that an 1100°C/10s RIA cycle would be sufficient for the dopant activation of shallow junctions (10). Furthermore, experiments conducted in our laboratories and elsewhere (19) have shown that wafer warpage induced by RIA cycles of up to 1100°C is negligible; in some cases, wafer flatness is even improved. For the 1000°C/60s case, which is really too long for practical applications, as discussed above, satisfactory fusion was not obtained for any of the phosphorus concentrations investigated.

RIF vs. conventional furnace processing.—A comparison between RIF results and conventional furnace fusion (FF) results in a N_2 ambient is shown in Table II. In this experiment, the same boron implant used above to define a process window was the basis of comparison between RIF and FF. The results for the optimum 1100°C/10s RIF cycle ($\Delta x_j \simeq 0.1$ μm and $\theta \simeq 113°$) are compared with FF results obtained with the 900°C, 80 min furnace annealing cycle. The dopant redistribution result for the boron-implanted silicon substrate during the FF cycle ($\Delta x_j \simeq 0.3$ μm) is much larger than for the RIF result ($\Delta x_j \simeq 0.1$ μm), as also shown in Fig. 6. Nevertheless, absolutely no fusion was obtained during the FF cycle, for all phosphorus concentrations investigated. Similar fusion results were also obtained elsewhere (1). This comparison demonstrates quite convincingly that, for equivalent redistribution of a typical boron dopant profile in silicon, RIF is much more effective than FF for the fusion of PSG films.

Table II. Comparison of rapid isothermal processing and conventional furnace processing, giving the increase in junction depth Δx_j in an implanted silicon substrate, for a dose of 3×10^{15} B^+/cm^2 implanted at 25 keV through a 40 nm thermal SiO_2 layer, and the change in step coverage angle θ (initially at 80°) of a reflowed PSG film

Process (N_2 ambient)	Heating cycle	Δx_j (μm)	Fusion for 8 w/o PSG
Furnace	80 min at 900°C	0.3	None
RIF	10s at 1100°C	0.1	$\theta = 113°$

Conclusion

We have proved that, for equivalent dopant redistribution of junction profiles in silicon, rapid isothermal processing in a N_2 ambient is much more effective than conventional furnace processing for the fusion of PSG films.

A process window has been identified for typical VLSI applications. It consists of an 1100°C/10s RIF treatment of PSG films containing approximately 8 w/o phosphorus. These conditions increased an initial reentrant step coverage angle of 80° to a final value of more than 110°. A typical boron profile implanted in a silicon substrate and subjected to the same conditions underwent only a 0.1 μm increase in junction depth, making RIF compatible with VLSI applications where a relatively high phosphorus content is acceptable in PSG films.

Acknowledgments

The authors would like to thank B. Tait, J. Saeki, M. Brown, T. Abraham, A. Loro, and B. Theriault for their technical assistance and V. Ho for helpful discussions.

Manuscript submitted Feb. 26, 1985; revised manuscript received June 12, 1985. This was Paper 420 presented at the New Orleans, Louisiana, Meeting of the Society, Oct. 7-12, 1984.

Northern Telecom Electronics Limited assisted in meeting the publication costs of this article.

REFERENCES

1. J. B. Price and E. Reed, Abstract 372, p. 571, The Electrochemical Society Extended Abstracts, Vol. 83-1, San Francisco, CA, May 8-13, 1983.
2. R. A. Bowling and G. B. Larrabee, *This Journal*, **132,** 141 (1985).
3. N. Hashimoto, Y. Yatsuda, and S. Mutoh, *Jpn. J. Appl. Phys.*, **16,** 73 (1977).
4. W. E. Armstrong and D. L. Tolliver, *This Journal*, **121,** 307 (1974).
5. A. Naumaan and J. T. Boyd, *J. Vac. Sci. Technol.*, **17,** 529 (1980).
6. D. F. Downey, C. F. Russo, and J. T. White, *Solid State Technol.*, **25,** 87 (1982).
7. J. Kato and S. Iwamatsu, *This Journal*, **131,** 1145 (1984).
8. H. Nishimura, Y. Suizu, and T. Tsujimaru, Abstract 519, p. 760, The Electrochemical Society Extended Abstracts, Vol. 84-2, New Orleans, LA, Oct. 7-12, 1984.
9. T. Hara, H. Suzuki, and M. Furukawa, *Jpn. J. Appl. Phys.*, **23,** L453 (1984).
10. J. Narayan, O. W. Holland, R. E. Eby, J. J. Wortman, V. Ozguz, and G. A. Rozgonyi, *Appl. Phys. Lett.*, **43,** 957 (1983).
11. R. B. Fair, J. J. Wortman, and J. Liu, *IEDM Tech. Dig.*, 658 (1983).
12. T. E. Seidel, *IEEE Electron Dev. Lett.*, **edl-4,** 354 (1983).
13. H. Takeuchi and J. Murota, *This Journal*, **131,** 403 (1984).
14. B. I. Boltaks, "Diffusion in Semiconductors," Chap. IV, Academic Press, New York (1963).
15. M. Ghezzo and D. M. Brown, *This Journal*, **120,** 146 (1973).
16. C. T. Sah, H. Sello, and D. A. Tremere, *J. Phys. Chem. Solids*, **11,** 288 (1959).
17. R. N. Ghoshtagore, *Thin Solid Films*, **25,** 501 (1975).
18. R. B. Fair in "Impurity Doping Processes in Silicon," F. F. Y. Wang, Editor, Chap. 7, Elsevier, North-Holland, New York (1981).
19. M. Current and A. Yee, *Solid State Technol.*, **26,** 197 (1983).

Effects of Wet Cleaning on Si Contaminated with Heavy Metals during Reactive Ion Etching

Tetsuo Hosoya, Yoshiharu Ozaki, and Kazuo Hirata

Nippon Telegraph and Telephone Corporation, Atsugi Electrical Communication Laboratory, 1839, Ono, Atsugi-shi, Kanagawa Prefecture 243-01, Japan

ABSTRACT

Heavy metal removal from Si wafers contaminated during reactive ion etching (RIE) is studied using wet cleaning techniques. Si wafers are intentionally contaminated during RIE with Fe, Cr, or Ni, which are atomic components of stainless steel, the material used in dry etching apparatus. The Si wafers are washed with several reagents, and heavy metal removal results are estimated using secondary ion mass spectrometry and stacking fault observation. The results show that Fe and Cr are removed by wet etching the Si wafers to approximately a 30 nm depth but that Ni cannot be removed. The results indicate that to protect Si wafers against heavy metal contamination during RIE, Ni-free materials should be used for fixtures in the dry etching chamber.

In fabrication processes for high density LSI's, dry etching techniques are essential in producing fine patterns with high accuracy. Reactive ion etching (RIE) is especially useful in etching fine patterns because of its anisotropic etching features. However, RIE results in more contamination and damage to etched Si wafers than plasma etching. This is due to the sputtering and bombardment action of energetic ions generated during RIE. Many studies have been done on relationships between RIE conditions and device characteristics (1-3). It has been found that heavy metal contamination in a reactor during RIE causes a decrease in Si wafer minority carrier lifetime in silicon wafers subsequently subjected to high temperature heat-treatment.

To avoid heavy metal contamination in Si wafers, RIE reactor design improvement is required to prevent stainless steel used in the etching chamber from coming into contact with the plasma, or materials containing heavy metals should not be used in the etching chamber. Another approach, to eliminate the influence of heavy metal contamination, is to develop effective methods for removing the contaminated layer in the LSI fabrication process. This paper concerns Si wafer heavy metal-contaminated layer removal by wet cleaning methods, focusing on the behavior of Fe, Cr, and Ni, stainless steel's constituent elements.

In this study, Si wafers were intentionally contaminated with heavy metals during RIE. Pure metals, Fe, Cr, and Ni, are used as contamination sources, and wet cleaning procedures are developed so as to be applicable to LSI processes. The Fe and Cr removal and Ni nonremoval results are obtained through examination using secondary ion mass spectrometry (SIMS) and stacking fault (SF) observation.

The following sections describe the experimental procedures and results, the reason for Ni nonremoval, and application of findings to RIE apparatus design.

Experimental

Si wafer heavy metal contamination was carried out using RIE. The RIE reactor used in this work is shown schematically in Fig. 1. The RF power (13.56 MHz) was applied to the cathode electrode. Si wafers , which were 3 Ω-cm boron-doped (100) slices with a diameter of 3 in., were loaded on a stainless steel cathode electrode (Fe 74%, Cr 18%, Ni 18%). CF_4 was used as the etching gas at a pressure of 2 Pa. The RF power density and the etching time were set to 0.18 W/cm^2 and 30 min, respectively. Etching rates for Si were 9 ~ 13 nm/min. The wafers were contaminated with heavy metals sputtered from the cathode electrode. When using pure metals as a source of contamination, metal plates with a high purity (99.9%), *i.e.*, Fe, Cr, and Ni, were set on the cathode electrode. The wafers were then placed on the plates. A 50 μm thick Teflon sheet was placed between the plates and the cathode electrode. This sheet was replaced with a new sheet after every plate change to avoid Si wafer contamination from other plate metals which may have adhered to the sheet.

Cleaning procedures following the contamination step in RIE consisted of the following steps: (*i*) ashing in O_2 glow discharge, (*ii*) washing in $H_2SO_4 + H_2O_2$ solution and rinsing in deionized water, (*iii*) cleaning by RCA treatment (4) (washing in $NH_4OH + H_2O_2$ and $HCl + H_2O_2$ solution) followed by diluted HF washing after each step. The reagents used were IC-grade EL-class reagents. In this paper, the authors call these three treatment steps the basic cleaning procedure. Steps *i* and *ii* are for removal of the plasma polymerized film and resists after dry etching, and step *iii* is for final Si wafer cleaning. As a result, the Si surface was etched off to an 8 nm depth in the basic cleaning procedure. When heavy metal contamination was not sufficiently removed from the Si wafers by the basic cleaning procedure, additional cleaning treatments using various liquid reagents were tried between steps *ii* and *iii*.

SIMS and SF observation were used to evaluate the degree of heavy metal removal. SIMS analysis was carried out using both Hitachi IMA-2 for estimating the heavy metal amounts remaining on the Si surface and Cameca ims-3f for the depth profile analysis. Hitachi IMA-2 was used under 10 kV Ar^+ ion beam acceleration voltage conditions with a 1300 μm spot diameter. Cameca ims-3 was used under 15 kV O_2^+ ion beam acceleration voltage conditions with a 150 μm spot diameter. Evaluation was carried out using the peak height ratio of each secondary ion spectrum intensity to that of $^{28}Si^+$. It is desirable to detect isotopes with the highest existence ratio for each metal in order to detect the secondary ions in high sensitivities. In this work, $^{54}Fe^+$, $^{52}Cr^+$, and $^{60}Ni^+$ were picked to detect each heavy metal. This was done to avoid an S/N ratio reduction due to the secondary ion settling on Si. The SF occurrence was observed as follows. Contaminated Si wafers were treated using the above-mentioned cleaning procedure. Next, they were oxidized at 1100°C in a wet O_2 atmosphere for 2h. After the SiO_2 was etched off with an HF solution, SF was visualized by etching the wafers to a

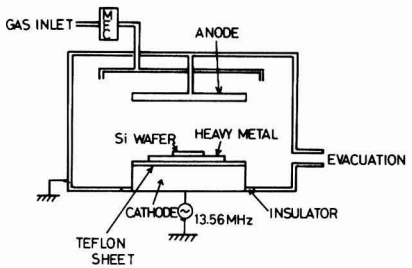

Fig. 1. RIE reactor diagram

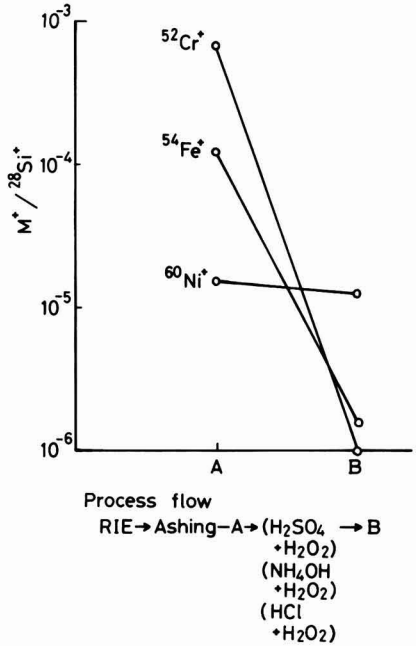

Fig. 2. Relation between remaining Fe, Cr, and Ni amounts and cleaning steps, using stainless steel as the contamination source, expressed by SIMS spectrum intensity ratios, $M^+/^{28}Si^+$. SIMS measurement was done at A and B steps.

1 μm depth by Wright etching (5) and observed with a microscope.

Results

Removal of heavy metal contamination originating from stainless steel.—SIMS analysis was carried out on stainless steel-contaminated samples and cleaned using the basic cleaning procedure. Fe, Cr, and Ni, which compose stainless steel, were detected on the Si surface, as shown in Fig. 2. Heavy metal mass peak intensities on the Si surface after the basic cleaning procedure were high for Ni, Fe, and Cr in descending order. Cr was removed to the SIMS detection limit level after cleaning. These results indicate that Ni is the most difficult material to remove from Si.

Removal of heavy metal contamination originating from pure metals.—Si wafers contaminated with Fe, Cr, or Ni pure metals were prepared using RIE and SF observation. After applying the basic cleaning procedure, SF's were not observed on the Cr-contaminated Si wafers but were observed on those contaminated with Fe and Ni, as shown in Fig. 3. No SF's were observed on the Fe-contaminated Si wafers when the wafers were etched to a 20 nm depth with an HNO_3 + HF + CH_3COOH solution before RCA treatment as shown in Fig. 4A. However, on the Ni-contaminated wafers, SF's were observed, as shown in Fig. 4B. In the wet etching process, used in Fig. 4, Si was etched off to an 8 nm depth using the basic cleaning procedure and to 20 nm depth with the mixed solution. Consequently, the Si etched depth was estimated to be about 30 nm.

The relation between remaining Fe, Cr, or Ni amounts and the cleaning steps was investigated by SIMS, using the ratio of mass intensities to $^{28}Si^+$. Remaining amounts of the three elements decreased with each step in the cleaning procedure, as shown in Fig. 5. The amount of Cr was below the SIMS detection limit level after the basic cleaning steps with no Si wet etching. For Fe, the amount was the same as for Cr if the Si wet etch procedure was employed before RCA treatment. However, Ni remained

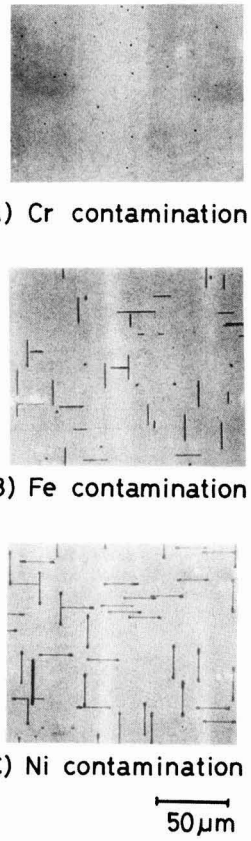

Fig. 3. SF observation results after basic cleaning procedure. SF's were made visible by Wright etching method.

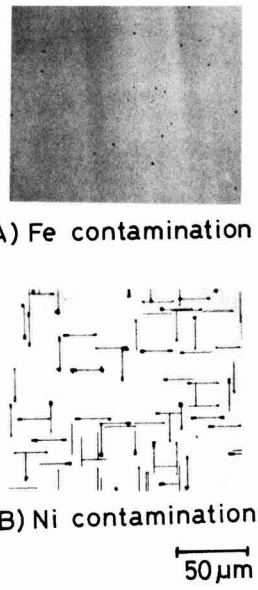

Fig. 4. SF observation results after adding 20 nm Si wet etching to basic cleaning procedure. SF's were made visible by Wright etching method.

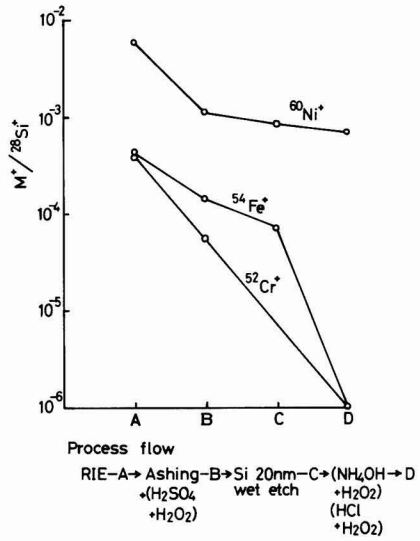

Fig. 5. Relation between remaining Fe, Cr, and Ni amounts and cleaning steps, using pure metals as the contamination source, expressed by SIMS spectrum intensity ratios, $M^+/^{28}Si^+$. SIMS measurement was done at A, B, C, and D steps.

high even after all cleaning steps were carried out. These results support the SF observation.

Metal plate wet etching rates were investigated using the solutions employed in the basic cleaning procedure. Ni was etched in considerable quantity, as much as Fe, with the HCl + H_2O_2 solution, as shown in Table I.

Thus, the etching of metals in Si is different from that of metal itself. The chemical state of the Ni atom added to Si wafers during RIE was of concern and was investigated by XPS analysis.

XPS analysis of the Ni-contaminated wafer.—Possible Ni atom chemical states were considered to be either of a metallic state, a compound with Si, or a compound with the etching gas element. The compound with Si, nickel silicide, is known to be formed at 200° ~ 300°C (6) and to be insoluble in acids except for hydrofluoric acid (7). XPS analysis was carried out on the Si surface immediately after Ni contamination. A Ni and a nickel oxide were detected, while nickel silicide was not, as shown in Fig. 6. Nickel oxide formation is considered to be caused by the Ni oxidation during ashing treatment.

On the basis of XPS analysis results mentioned above, nickel removal investigations were carried out using wet cleaning methods.

Ni-contaminated layer removal.—Several kinds of wet etching solutions were applied before the RCA treatment in the basic cleaning procedure. These are summarized in Table II. The treatments were aimed at accomplishing the following: treatments a, b, and c were for Ni removal. Treatment d was to remove nickel oxide with HCl and nickel with HNO_3. Treatment e was for Ni removal and was carried out in diluted HCl using a 5 mA dc current between the Ni-contaminated sample and a Si cathode

Table I. Etching rates for heavy metals by the solutions used in the basic cleaning procedure

Solutions	Etching rates for metals (at./cm²-min) Ni	Fe
$H_2SO_4 + H_2O_2$	2×10^{18}	1×10^{18}
Diluted HF	2×10^{17}	2×10^{16}
$NH_4OH + H_2O_2$	1×10^{16}	1×10^{16}
$HCl + H_2O_2$	5×10^{20}	5×10^{21}

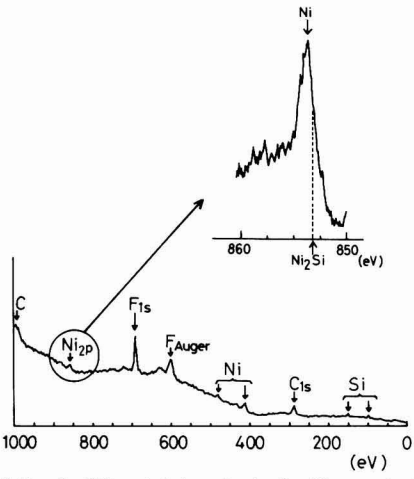

Fig. 6. Si wafer XPS analysis immediately after Ni contamination

electrode. The results obtained indicate SF occurrence in all the samples and that Ni was impossible to remove from the Si surface.

Discussion

The experimental results are summarized as follows: (*i*) Cr is removed using the basic cleaning procedure; (*ii*) Fe is removed by adding 20 nm Si wet etching to the cleaning procedure; and (*iii*) Ni is not removed despite the application of several cleaning procedures. The reason Ni cannot be removed is discussed below.

Consider a simple model in which metal atoms sputtered from metal plates are ionized in glow discharge and impinge on the Si wafer surface with an acceleration energy equivalent to the cathode fall potential. Metal ions such as Fe^+, Cr^+, and Ni^+ are implanted at a finite depth from the Si surface. Here, the metal atom depth profiles become important in interpreting wet cleaning characteristics.

The Ni depth profile in Si wafers was measured using SIMS profile analysis. It is found that Fe and Ni were introduced to 50 and 60 nm depths, respectively, as shown in Fig. 7. The SIMS profile analysis generally presents a deeper profile due to a tailing phenomenon in highly concentrated impurity analysis (8). Thus, the impurity profile depth shown in Fig. 7 must be slightly exaggerated. For example, as already mentioned, Fe was removed by etching the Si to approximately a 30 nm depth, while Fig. 7 shows that Fe exists to 50 nm. The Fe depth in the wafer is shown to be 20 nm larger using SIMS profile analysis than that found in actual wet etching. Considering the Fe case, Ni is inferred to etch at most 40 nm in the Si wafer. This inference also comes from Ni ion's small acceleration energy of 700 eV for the 0.2 W/cm² power condition. It thus follows that Ni could be removed by etching the Si to approximately 40 nm.

Fe and Ni profiles were estimated using the "step etch" method. Namely, metal-contaminated Si wafers were

Table II. Treatments for Ni removal applied before RCA treatment in the basic cleaning procedure

Treatment	
a	Stir in a $(NH_4)_2S_2O_8$ 200g, HCl 10 cm³ and H_2O 1000 cm³ solution at 70°C
b	Stir in a $K_2Cr_2O_7$ 13g, H_2SO_4 50 cm³ and H_2O 100 cm³ solution at 70°C
c	Stir in an HCl 300 cm³ and HNO_3 100 cm³ (aqua regia) solution at 70°C
d	Stir in HNO_3 after stirrred in HCl at 70°C
e	Electrolytic etching in 12% HCl

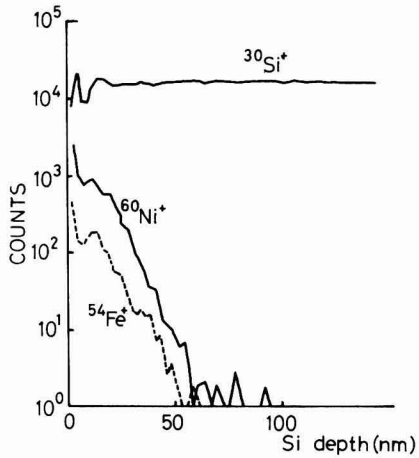

Fig. 7. Ni and Fe depth profiles in Si wafers estimated by SIMS profile analysis, expressed by counts of each metal isotope detected by SIMS.

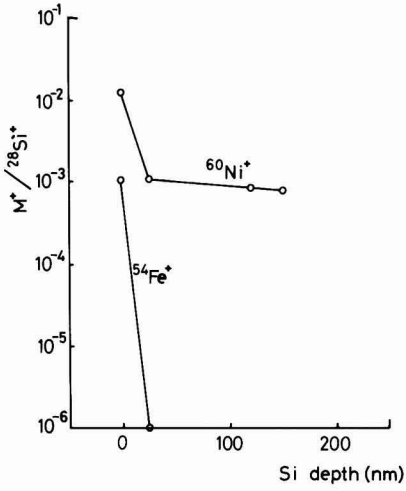

Fig. 8. Heavy metal depth profile in Si wafers estimated by step etch method, expressed by SIMS spectrum intensity ratios, $M^+/^{28}Si^+$.

etched to a certain depth using a HNO_3 + HF + CH_3COOH solution after ashing followed by diluted HF etching. SIMS analysis was performed after these steps. Results are the same as if Ni is penetrated to a depth of 150 nm, while they show that Fe was below the SIMS detection limit level at 30 nm. This is shown in Fig. 8. Etching of the Ni-contaminated Si wafer using the mixed solution stopped at 150 nm depth. It was necessary to dip the Ni-contaminated wafer into an HF solution to restart etching. Some layer seemed to prevent the etching.

Thus, the fact that Ni in Ni-contaminated Si wafers, contaminated during RIE, cannot be removed is believed to be caused by Ni redeposition onto the Si wafers in the wet cleaning procedure. High Ni metal etching rates, and discrepancy in Ni depth profiles between the SIMS profile analysis and step etching, would be explained by this readhesion concept.

These results indicate that one means of protecting Si wafers against heavy metal contamination during RIE is to select Ni-free materials for the fixtures in the dry etching chamber.

Conclusion

Wet cleaning effects on Si wafers have been investigated for removing heavy metal-contaminated layers introduced during RIE. Si wafers were intentionally contaminated with stainless steel constituent elements, *i.e.*, Fe, Cr, and Ni, during RIE. Wet cleaning procedures were designed to combine washing in NH_4OH + H_2O_2 solution and HCl + H_2O_2 solution with etching employing a HNO_3 + HF + CH_3COOH solution. The amount of heavy metal removed was estimated by SIMS and SF observation in the Si wafers after wet cleaning. The results show that Fe and Cr are removed by etching the Si wafers to approximately 30 nm using wet cleaning procedures. However, Ni cannot be removed, even though Ni-contaminated Si wafers were etched to 150 nm. This failure to remove Ni is probably due to Ni redeposition to the Si surface during wet etching. Usage of Ni-free materials for fixtures in the dry etching chamber will be one way to avoid heavy metals contamination in Si wafers.

Acknowledgment

The authors wish to thank Toyoki Kitayama for his valuable suggestions and encouragement and Izumi Kawashima for carrying out the SIMS analysis.

Manuscript submitted June 25, 1984; revised manuscript received April 11, 1985.

Nippon Telegraph and Telephone Public Corporation assisted in meeting the publication costs of this article.

REFERENCES

1. H. R. Deppe, B. Hasler, and J. Hopfner, *Solid State Electron.*, **20,** 51 (1977).
2. Y. Ozaki, K. Hirata, S. Yabumoto, and M. Oshima, "Proceedings of the 2nd Symposium on Dry Processes," p. 55, Institute of Electrical Engineering, Tokyo (1980).
3. L. M. Ephrath and R. S. Bennett, *This Journal*, **129,** 1822 (1982).
4. W. Kern and D. A. Puotinen, *RCA Rev.*, **31,** 187 (1970).
5. M. W. Jenkins, *This Journal*, **124,** 757 (1977).
6. I. Ohdomari and K. Suguro, *J. Vac. Soc. Jpn.*, **22,** 411 (1979).
7. S. P. Murarka, *J. Vac. Sci. Technol.*, **17,** 775 (1980).
8. C. W. Magee, R. E. Honig, and C. A. Evans, Jr., "Depth Profile by SIMS: Depth Resolution, Dynamic Range and Sensitivity," p. 172, Springer Series in Chemical Physics 19, Springer-Verlag, Berlin (1982).

Deep-UV Contact Lithography Using a Trilevel Resist System for Magnetic Bubble Devices with Submicron Minimum Feature

H. Umezaki, N. Koyama, Y. Maruyama, Y. Sugita, and R. Suzuki

Hitachi Limited, Central Research Laboratory, Kokubunji, Tokyo 185, Japan

ABSTRACT

Deep UV lithography using a trilevel resist system has been developed to delineate submicron patterns for magnetic bubble memory devices. The trilevel resist system consists of PIQ® as a bottom polymer layer, spin-coated TiO_x as an intermediate layer, and MRS as a top imaging resist. All these layers can be spun and baked sequentially. MRS resist patterns are defined by deep-UV contact printing and transferred to TiO_x layer and PIQ layer sequentially using reactive ion etching with CF_4 gas for TiO_x and O_2 gas for PIQ. Using this trilevel resist process, 0.4 μm lines and spaces were fabricated and contiguous disk patterns of 2 μm bit period for bubble memory devices of 16 Mb/cm^2 were also fabricated successfully.

Magnetic bubble memory devices with the bit capacity of 1 and 4 Mb are now in volume production(1). These devices are all Permalloy devices in which track patterns for bubbles consist of Permalloy patterns. These patterns have gaps between neighboring bits. The minimum feature of these patterns is 1 μm, and the patterns are fabricated using contact printer or 10× projection printer with conventional UV light. High density ion-implanted bubble memory devices of 4-16 Mb in memory capacity are now under development (2, 3). Bubble propagation tracks of these devices are fabricated by implanting H_2 or Ne ions into bubble garnet through mask patterns. Since the mask patterns, named contiguous disks, have no gaps between neighboring bits, the requirement for lithography can be relaxed compared with Permalloy devices. However, for higher density devices of 4-16 Mb/cm^2, the delineation of patterns with the minimum feature of 0.5-1.0 μm is required even using this approach to fabricate 4-16 Mb/cm^2 devices.

Conventional UV lithography, however, is insufficient for this purpose because of its lack of practical resolution. Deep-UV lithography is known to be superior to UV lithography and has the high resolution capability in submicron range (4). Deep-UV contact lithography uses the same technique as the conventional UV lithography, except for light source and resist. A Xe-Hg lamp is well known to be the deep UV-light source. As deep-UV resist, we employ the negative-type MRS[1] resist, which is composed of poly(p-vinylphenol) and 3,3′-diazidodiphenyl sulfone (5, 6, 7). The MRS resist has properties of high sensitivity to 200-300 nm radiation, high resolution, and good resistance to dry etching.

The mask patterns for ion-implanted bubble devices should satisfy the following requirements: (*i*) the thickness is large enough to stop incident ions; (*ii*) the material is highly heat resistant not to be deformed during implantation; and (*iii*) the edge profile is steep and smooth to obtain a clearly defined propagation track. To satisfy these requirements, we employ the polyimide resin PIQ(8)[2] with the thickness of 1.5 μm as a mask material and transfer MRS patterns to PIQ layer using trilevel resist technique (9).

In this paper, the characteristics of MRS resist such as resolution capability and process latitude in resist profile control and linewidth control are reported. The trilevel resist process using the MRS resist as top imaging resist, the spin-coated TiO_x as an intermediate layer, and the PIQ as a bottom polymer layer is presented. Experimental results demonstrating the performance of the process are also included.

Experimental

The MRS resist films were spin-coated on substrates to thickness of 0.3-0.6 μm and prebaked at 80°C for 20 min. The thickness was changed for the purpose of the experiment and adjusted by diluting the resist solution with cyclohexanone. Exposure was carried out using the contact aligner Cobilt CA800 equipped with a 500W Xe-Hg lamp (Ushio Electric, Incorporated) and an aluminum mirror. Since the spectral photosensitivity of the MRS resist is restricted to 200-300 nm wavelength, a cold mirror is not necessary to expose the MRS resist. The photomask used in the experiment consisted of a quartz substrate and a thin layer of chromium patterns which were delineated by electron-beam writing. The thickness of the quartz substrate was 2.4 mm. After exposure, the MRS resist was developed in MF312 developer (Shipley) diluted with water at 1:4 and rinsed in deionized water.

In order to compare the resolution capability of MRS with conventional UV resist, the resolution of AZ1350J (Shipley) was also investigated. To perform the experiment under the same condition, the same photomask and the same aligner were used, except for a light source, *i.e.*, a Xe-Hg lamp for MRS and a Hg lamp for AZ1350J. The AZ1350J resist was developed in the AZ developer (Shipley), diluted with water at 1:1, and rinsed in deionized water.

The trilevel resist system studied here consists of MRS/TiO_x/PIQ. A schematic diagram of the process is shown in Fig. 1. A substrate was coated successively with the thick polymer layer of PIQ (1.5 μm), the thin layer of spin-coated TiO_x (0.1 μm), and the thin MRS resist layer (0.3 μm). The TiO_x film was obtained by spin-coating and baking an organotitanium solution which will be described in detail later. The top imaging resist MRS was defined by the deep-UV contact printing. Transfer of the resist patterns to TiO_x layer was performed by reactive ion etching (RIE) in CF_4 plasma. The patterns in TiO_x layer were then replicated in thick PIQ layer by RIE in pure O_2 plasma.

Results and Discussion

Characteristics of MRS.—The resolution of MRS was compared with the conventional UV resist AZ1350J. The results are shown in Fig. 2. Both resist patterns were defined by the same contact aligner using the same photomask patterns of lines and spaces. The thicknesses of these two types of resist were both 0.6 μm. It can be seen from the figure that the resolution of AZ1350J is about 0.5 μm and that of MRS is less than 0.4 μm. The resolution of MRS is thus superior to that of AZ1350J. As for AZ-type resist, Smith *et al.* demonstrated the linewidth of 0.4 μm using a contact printer and conformable photomask (10). In our experiment, however, the resolution is about 0.5 μm. This is presumably due to the difference of photomask structures. In our experiment, a hard mask plate was used and this should cause the degradation of resolution.

The MRS resist thus exhibits a high resolution. But this resist is also known to have such a property that the cross-sectional profile varies sensitively according to de-

[1]MRS stands for micro resist for shorter wavelength, and is commercially available from Hitachi Chemical Company Limited under the trade name RD2000N.

[2]PIQ stands for Polyimide Iso-indroquinazolinedione, and is a trade name of Hitachi Chemical Company Limited.

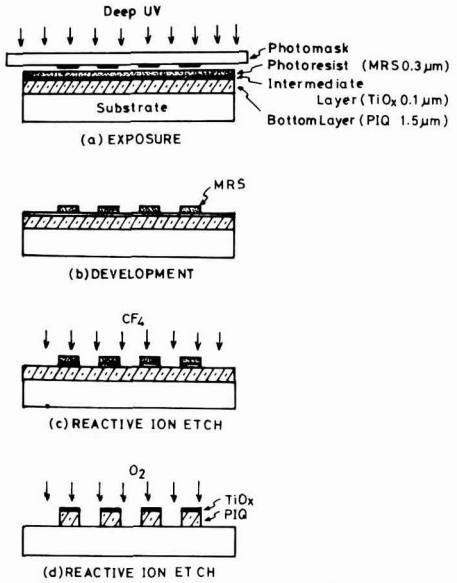

Fig. 1. Schematic diagram of the trilevel resist process

velopment conditions (5). Examples of this phenomenon are shown in Fig. 3. The resist thickness is 0.6 μm for the left-hand samples and 0.25 μm for the right-hand samples. A development time was changed by 15s from the minimum time required to delineate a pattern. In the case of 0.6 μm thick resist, the profile changes with increasing a development time and results in the undercut profile. On the other hand, for the resist with the thickness of 0.25 μm, the profile does not change and is always steep in all development conditions.

The undercut profile shown here is caused by a strong absorption of deep-UV light by MRS resist (5). In the case of 0.6 μm thick resist, the deep-UV light cannot reach at the lower layer, owing to a strong absorption, and the resists at the lower part are removed by prolonged development. In the case of 0.25 μm thick resist, however, the thickness is so small that the deep-UV light can penetrate all through the resist. Therefore, the resist profile is always steep at every development condition. This property is desirable, since the steep profile ensures that the good linewidth control and the restriction on development condition can be relaxed compared with the case of thick MRS resist.

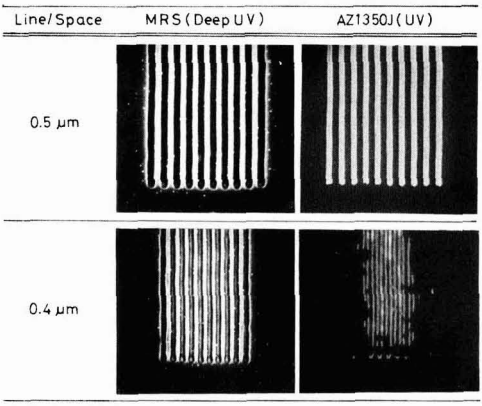

Fig. 2. Comparison of the resolution of MRS resist (deep UV) and AZ1350J resist (UV) delineated by contact printing.

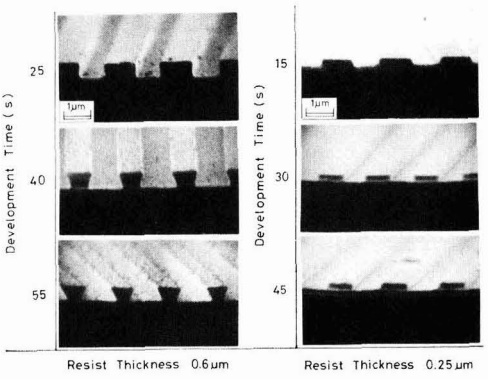

Fig. 3. MRS resist profiles as a function of development time. The thicknesses are 0.6 μm for the left-hand samples and 0.25 μm for the right-hand samples.

Figure 4 shows the linewidth variation of thin MRS resist patterns as functions of exposure and development time. The results of UV resist AZ1350J are also shown in the figure. The thicknesses of MRS and AZ1350J are 0.27 and 0.26 μm, respectively. The test patterns used in the experiment were lines and spaces with the widths of 1.0, 0.75, and 0.5 μm, respectively. The patterns on the photomask were transferred to the resists with each exposure and development condition. The exposure time was changed from the minimum time to delineate a pattern to about eight times the minimum time. The development time was changed from 5 to 160s. Under these exposure and development conditions, linewidth for MRS resist and spacewidth for AZ1350J resist were measured by scanning electron microscope (SEM) observation.[3]

The contour lines shown in the figure were obtained from the values of measurement points and indicate the exposure and development conditions where the same linewidth is obtained. Therefore, as the density of contour lines is small, the latitude of exposure and development condition becomes large. It can be seen that the density of contour lines for MRS resist is smaller than that for AZ1350J resist. That is, the linewidth variation of MRS caused by a fluctuation of exposure or development condition is smaller than that of AZ1350J resist. The rectangular regions in the figure correspond to the latitude of linewidth control ±20%, that is, 1 ± 0.2, 0.75 ± 0.15, and 0.5 ± 1 μm, respectively. As shown in the figure, the rectangular region of MRS resist is larger than that of AZ1350J resist for each linewidth. The rectangular region of 0.75 μm patterns for MRS resist is almost the same as that of 1.0 μm patterns for AZ1350J resist. This indicates that the 0.75 μm pattern can be fabricated with the same

[3]Since the types of these two resists are different, *i.e.*, MRS is the negative-type resist and AZ1350J is the positive-type resist, the line pattern for MRS resist corresponds to the space pattern for AZ resist when the same photomask pattern is used.

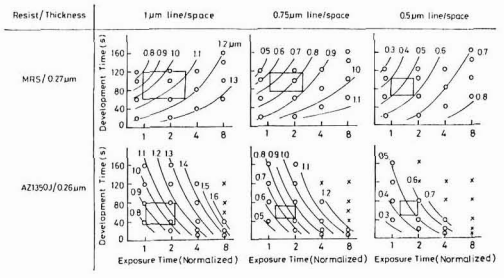

Fig. 4. Linewidth variations of MRS resist and AZ1350J resist patterns as functions of exposure and development times.

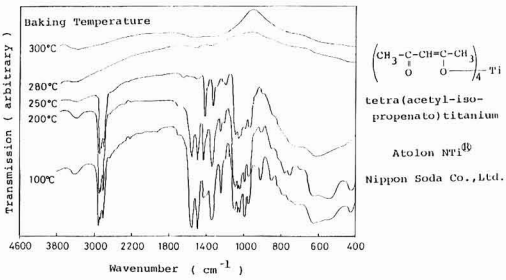

Fig. 5. Fourier transform infrared spectra for Atolon NTi films which were baked at temperatures from 100° to 300°C.

tolerance as that for 1 μm pattern of AZ1350J resist. As for 0.5 μm pattern, the MRS pattern can be obtained at every exposure and development condition. The condition for AZ1350J resist is restricted, as can be seen in the figure.

Here it should be noticed that the thin resist cannot be used in itself as a mask pattern for etching or ion implantation. Therefore, we introduced the trilevel resist process where thin MRS resist was used as the top imaging resist.

Trilevel resist process.—The present trilevel resist system is composed of PIQ, TiO_x, and MRS as already indicated in Fig. 1. An intermetidate layer TiO_x was obtained from the organometal solution of tetra(acetyl-isopropenato)titanium (Atolon NTi®; Nippon Soda Company Limited). Figure 5 shows the Fourier transform infrared spectra for Atolon NTi films which were baked at temperatures from 100° to 300°C. The baking treatment was performed in the air atmosphere for 30 min in all cases. The strong absorptions due to organic compounds are observed for the samples baked at less than 250°C, but they disappear when the baking temperature is greater than 280°C. From these results, it can be said that the inorganic TiO_x is obtained by baking Atolon NTi at temperature higher than 280°C.

The TiO_x films thus obtained have some advantages compared with spin-on glass (SOG) (11) or SiO_2 films deposited by plasma enhanced chemical vapor deposition (PECVD) (9). These materials are widely used as an intermediate layer for trilevel resist process. Table I shows the comparison of these materials. A deposition process of TiO_x and SOG is simple because there is no need of evacuation process, which is necessary for PECVD. The adhesion of MRS or AZ resist to the TiO_x film is excellent, and the adhesion promoter such as hexamethyl disilazane (HMDS) is not needed here. On the other hand, the adhesion promoter is necessary for SOG and SiO_2. The stability of Atolon NTi solution is good compared with the SOG solution. In the case of SOG solution, proper storage is required since the silicate material can easily be hydrolyzed by moisture in the air to form SiO_2-like crystals. These crystals cause defects in a spin-on film. The TiO_x films obtained from Atolon NTi solution pose no such problem, because the hydrolysis in this case hardly occurs and defects in the films are few. The defects in PECVD SiO_2 film are usually caused by particles which eventually flake off from the surrounding wall of PECVD chamber. Therefore, careful cleaning procedures are required to decrease defects in a film.

Table I. Comparison of intermediate layers for trilevel resist process.

Material	TiOx (Spin-On)	SOG (Spin-On)	SiO_2 (Plasma CVD)
Process Simplicity	○	○	X
Adhesion of MRS or AZ	○	X	X
Defect	○	△	△

Linewidth control.—Linewidth control of the patterns delineated by the trilevel resist process depends on three factors, i.e., image transfers of photomask patterns to resist layer, resist patterns to intermediate layer, and intermediate patterns to bottom layer. As described previously, the accuracy of image transfer to MRS resist is superior to that of AZ resist. In the present case, the MRS patterns are transferred to TiO_x and PIQ layer successively. Therefore, these etching processes must be controlled precisely. The TiO_x etching process is especially critical since the thin (0.3 μm thick) MRS resist must be used to etch TiO_x layer using reactive ion etching. To control a linewidth precisely in TiO_x etching, therefore, the sufficient etching selectivity is required. For this purpose, we investigated etching conditions, that is, an etching gas and RF power. The results are shown in Fig. 6. The etching gases studied here were CF_4, CF_4/O_2, CHF_3, and CHF_3/Ar, and the RF power was changed from 100 to 400W. The vacuum pressure was 5 Pa in every case. It can be seen that the etching rate of TiO_x in CF_4 plasma is relatively high and the etching rate ratio of TiO_x to MRS is also high. When O_2 gas is mixed in CF_4 gas, the etching rate of TiO_x increases. However, the etching rate of MRS also increases and the ratio becomes smaller. In the case of CHF_3 plasma, a deposition process occurs when an RF power is small (100-200W). At high RF power (400W), the etching becomes possible and the etching rate ratio is high. CHF_3/Ar plasma etching behavior is almost the same as the case of CHF_3 plasma.

In order to obtain the high etching rate ratio, the CHF_3 or CHF_3/Ar plasma with 400W RF power is most favora-

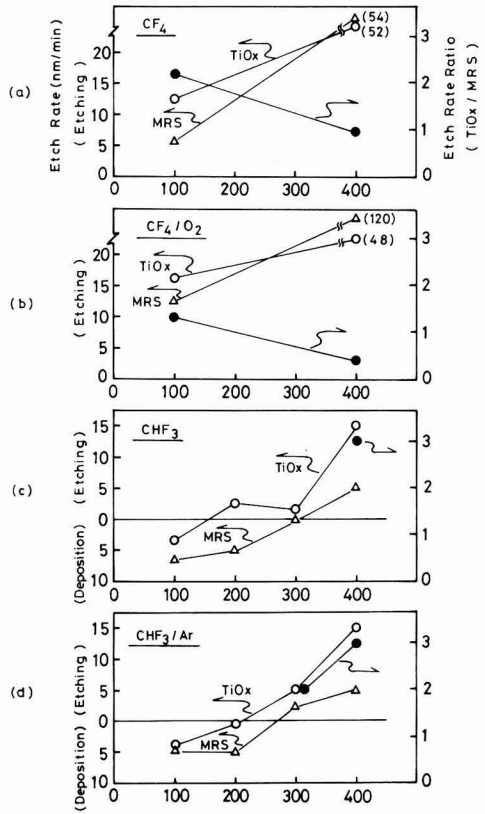

Fig. 6. Etching rate of TiO_x and MRS resist and etching rate ratio of TiO_x/MRS as a function of RF power. a: CF_4 50 sccm. b: CF_4 50 sccm + O_2 5 sccm. c: CHF_3 50 sccm. d: CHF_3 50 sccm + Ar 15 sccm. Vacuum pressure was 5 Pa in every case. The substrate on which wafers were placed was SiO_2 for CF_4 and CF_4 + O_2 gases and Teflon for CHF_3 and CHF_3 + Ar gases.

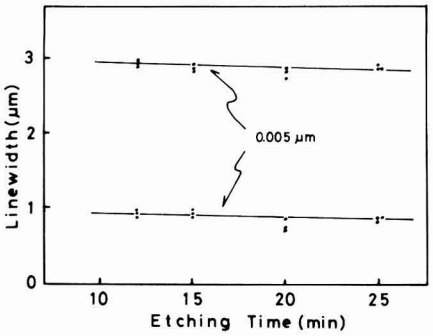

Fig. 7. Linewidth variations of TiO_x patterns as a function of etching time. Etching gas was CF_4 with the flow rate of 50 sccm. Vacuum pressure was 5 Pa, and RF power was 100W.

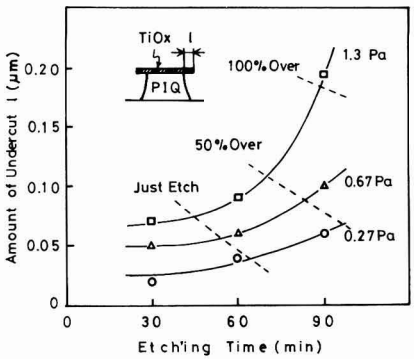

Fig. 9. Amounts of undercut as a function of etching time. Vacuum pressure was changed from 0.27 to 1.3 Pa. RF power was 100W.

ble. However, the plasma discharge is unstable at that condition and the reproducibility of etching becomes poor. The stability of plasma discharge was improved when the vacuum pressure was increased (to 10 Pa). But, at the high vacuum pressure, the deposition process again occurred.

From these results, we selected the CF_4 as an etching gas and the RF power to be 100W. Under these conditions, the linewidth variation was measured as a function of etching time. The results are shown in Fig. 7. The linewidth decreases linearly with increasing the etching time, and the decreasing rate is 0.005 μm/min. The rate is so small that the linewidth can be controlled precisely. The linewidth variation is only ±0.025 μm when the etching time was changed from the standard time (for example at 15 min) by ±5 min.

Figure 8 shows the etching rates of PIQ, MRS, and Atolon NTi films in O_2 RIE. The Atolon NTi film was baked at 200° or 300°C. The RF power was 100W, and the vacuum pressure was 0.27 Pa. It can be seen that the etching rates of PIQ and MRS are almost the same: 23 nm/min. The Atolon NTi baked at 200°C is etched slightly, and the etching rate is 0.7 nm/min. However, the Atolon NTi baked at 300°C is not etched in this measurement time. As mentioned previously, the Atolon NTi baked at 200°C still contains organic contents and is, therefore, slightly etched by O_2 RIE. On the other hand, the Atolon NTi baked at 300°C changes to the inorganic material TiO_x and remains intact during O_2 RIE. From these results, it can be concluded that the Atolon NTi film baked at 300°C serves as a good mask material for an etching of PIQ by O_2 RIE.

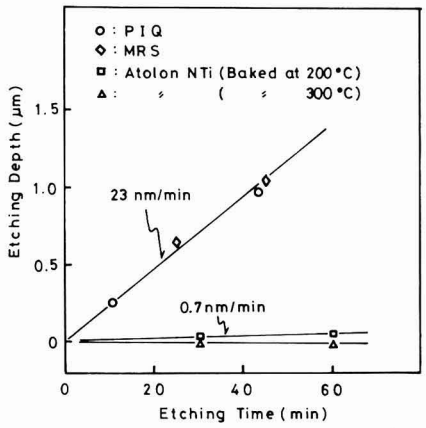

Fig. 8. Etching rates of PIQ, MRS, and Atolon NTi by O_2 reactive ion etching. Atolon NTi films were baked at 200° and 300°C. RF power was 100W, and vacuum pressure was 0.27 Pa.

The vacuum pressure in O_2 RIE is a key parameter for linewidth control (12). When the vacuum pressure is too high, an undercut profile occurs. On the other hand, the plasma discharge becomes unstable as the vacuum pressure is too low. To obtain the practical condition, we investigated the amount of undercut of the PIQ pattern under the protective TiO_x layer as a function of vacuum pressure. The results are shown in Fig. 9. The vacuum pressure was changed from 0.27 to 1.3 Pa. The amounts of undercut were measured by an SEM observation. When the pressure is 1.3 Pa, the amount of undercut increases rapidly with increasing the etching time and reaches 0.2 μm at the etching time of 90 min, which is about twice the time required to eliminate 1.5 μm thick PIQ layer. The amount of undercut decreases when the vacuum pressure is low. At the pressure of 0.27 Pa, the undercut becomes very small and the amount is 0.06 μm even at the etching time of 90 min, which is about 50% greater than the time required to eliminate PIQ layer. With our RIE apparatus, the lowest pressure above which the plasma discharge is stable is about 0.13 Pa. Therefore, the vacuum pressure of 0.27 Pa was selected.

Applications.—Figure 10 is an SEM photograph of lines and spaces patterns delineated by the trilevel resist process with the deep UV contact printing. Linewidths are 0.75 and 0.4 μm, respectively. The patterns consist of 1.5 mm thick PIQ with 0.1 μm thick TiO_x on the top surface.

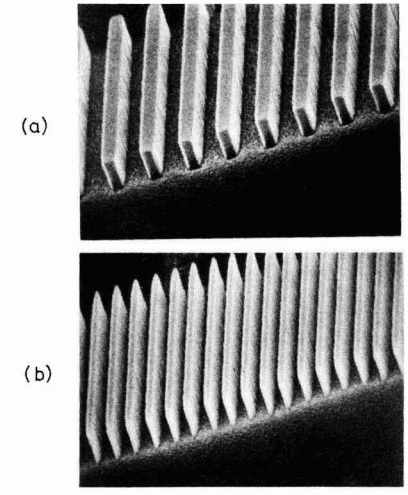

Fig. 10. SEM photographs of lines and spaces patterns delineated by the trilevel resist process with a deep-UV contact printing. Linewidths are 0.75 (a) and 0.4 (b) μm.

SEM Photograph	Bit Period (μm)	Minimum Feature	
		Design (μm)	Measurement (μm)
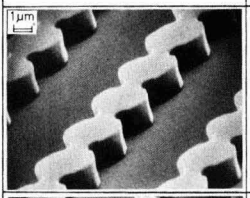	3	0.75	0.75
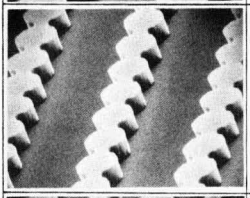	2	0.6	0.65
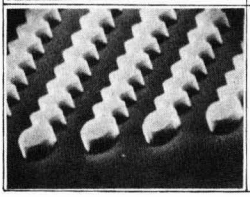	1.5	0.5	0.65

Fig. 11. Contiguous disk patterns for ion-implanted bubble memory devices delineated by the trilevel resist process with deep-UV contact printing.

As can be seen in the figure, the undercut of PIQ layer is very small and submicron patterns of 0.75 and 0.4 μm are delineated successfully.

Figure 11 shows the contiguous disk patterns for ion-implanted bubble memory devices. Bit periods of these patterns are 3, 2, and 1.5 μm and the minimum features are designed to be 0.75, 0.6, and 0.5 μm, respectively. The thicknesses of PIQ are 1.5 μm thick for 3 and 2 μm period patterns and 1.0 μm thick for a 1.5 μm period pattern. These thicknesses are necessary to stop accelerated ions used in each ion implantation. It can be seen that the edge profiles of these patterns are steep and smooth, which are the characteristics necessary for the mask pattern against an ion implantation, as mentioned previously. Patterns of 0.75 μm minimum feature for 3 μm period pattern are defined precisely, and that for 2 μm period pattern is also allowable. However, the discrepancy between a design and measurement value becomes large in the case of 1.5 μm bit period pattern. Therefore, the practical resolution limit of deep-UV contact printing is seen to be about 0.6 μm, and the minimum bit period is about 2 μm. The result is different from that for lines and spaces test patterns. The difference is caused by a diffraction effect. Since a contiguous disk pattern contains a cusp shape at the minimum feature part, the corner of the cusp is rounded by a diffraction effect and the width of the neck, which is the minimum feature, becomes large. That is, a diffraction in practical pattern is not so simple as in lines and spaces pattern and causes a degradation of resolution limit.

From the results obtained here, it can be said that deep-UV contact lithography can be applicable to 2 μm period ion-implanted bubble devices of 16 Mb/cm² in storage density.

Conclusion

Deep-UV contact lithography using trilevel resist system has been developed for magnetic bubble devices with submicron minimum feature. The trilevel resist system consists of MRS resist, TiO_x, and PIQ. The MRS resist patterns were delineated by deep-UV contact printing and the patterns were then transferred into TiO_x and PIQ sequentially using reactive ion etching in CF_4 plasma and in O_2 plasma, respectively. The thickness of MRS is 0.3 μm. The thin MRS resist like this can provide a submicron pattern with a greater process latitude than that of UV printing with AZ resist. The TiO_x film was obtained by spin coating and baking an organotitanium solution. Therefore, the three layers of the present process can all be formed by spin coating method. The adhesion of MRS resist to TiO_x film is good and etching selectivities of TiO_x to MRS (CF_4 RIE) and PIQ to TiO_x (O_2 RIE) are also good. Using the present trilevel resist process, 0.4 μm lines and spaces were delineated and the 2 μm period contiguous disk patterns with the minimum feature of 0.6 μm for bubble memory devices of 16 Mb/cm² were also fabricated successfully.

Acknowledgments

The authors wish to thank S. Nonogaki, T. Iwayanagi, and T. Matsuzawa of Hitachi Central Research Laboratories for their technical advice about MRS resist, and S. Yoshimoto, H. Kanai, H. Nishida, and H. Nozawa of Hitachi Mobara Works for their helpful discussions during this work. Thanks are also due to N. Koiso, A. Tanzawa, K. Asai, and M. Kanou of Hitachi Central Research Laboratories for their technical support.

Manuscript submitted March 22, 1985; revised manuscript received June 17, 1985. This was Paper 529 presented at the New Orleans, Louisiana, Meeting of the Society, Oct. 8-12, 1984.

Hitachi Limited assisted in meeting the publication costs of this article.

REFERENCES

1. S. Matsumoto, M. Hiroshima, and S. Yoshimoto, Paper FA-3 presented at Intermag '83, Philadelphia, April 5-8, 1983.
2. R. Wolf, J. C. North, W. A. Johnson, R. R. Spiwak, L. J. Varnerin, and R. F. Fischer, *AIP Proc. Conf. 10*, 339 (1972).
3. Y. Sugita, R. Suzuki, T. Ikeda, T. Takeuchi, N. Kodama, M. Takeshita, R. Imura, T. Satoh, H. Umezaki, and N. Koyama, Submitted to *IEEE Trans. Magn.*
4. B. J. Lin, *J. Vac. Sci. Technol.*, **12,** 1317 (1975).
5. T. Iwayanagi, T. Kohashi, S. Nonogaki, T. Matsuzawa, K. Douta, and H. Yanazawa, *IEEE Trans. Electron Devices*, **ed-28,** 1306 (1981).
6. T. Matsuzawa and H. Tomioka, *IEEE Electron Device Lett.*, **edl-2,** 90 (1981).
7. T. Matsuzawa and H. Tomioka, *IEEE Trans Electron Devices*, **ed-29,** 1284 (1981).
8. K. Sato, S. Harada, A. Saiki, T. Kimura, T. Okubo, and K. Mukai, *IEEE Trans. Parts, Hybrids, Packag.*, **php-9,** 176 (1973).
9. J. M. Moran and D. Maydan, *J. Vac. Sci. Technol.*, **16,** 1620 (1979).
10. H. I. Smith, N. Efremow, and P. L. Kelley, *This Journal*, **121,** 1502 (1974).
11. G. W. Ray, S. Peng, D. Burriesci, M. M. O'Toole, and E.-D. Liu, *ibid.*, **129,** 2152 (1982).
12. C. H. Ting and K. L. Liauw, *J. Vac. Sci. Technol. B*, **1,** 1225 (1983).

Lateral Growth Process of GaAs over Tungsten Gratings by Metalorganic Chemical Vapor Deposition

Hiromitsu Asai and Seigo Ando

Nippon Telegraph and Telephone Corporation, Musashino Electrical Communication Laboratory, Musashino-shi, Tokyo 180, Japan

ABSTRACT

Lateral epitaxial growth of GaAs over tungsten gratings with 5 μm wide lines and spaces on (001) GaAs substrates is performed using metalorganic chemical vapor deposition. A study is made of the dependence of facet shapes and growth rates of the overgrown layers on grating direction, growth temperature, and arsine (AsH_3) and trimethylgallium (TMG) flow rates. From the perspective of crystallography, all the facets observed in the overgrown layers were found to be classified into four individual groups: {110}, {$\bar{1}$11}As, {112}As, and {113}Ga faces. The GaAs opening direction on the (001) substrate surface is found to be the most essential parameter for determining the crystallographic planes of the facets. Other important controlling parameters for the facet formation are the growth temperature and partial pressure of AsH_3. The partial pressure of TMG has no influence on the faceting growth. On the other hand, the overall growth rate of the overgrown layer is limited only by the TMG flow rate. These results can be qualitatively explained by the Langmuir-Rideal model.

Lateral epitaxial growth over oxide or metal mask films formed on crystal substrates has recently developed into an attractive technique for fabricating such new devices as permeable base transistors (PBT's) (1-3) and optical wave guides (4). To date, many reports on the lateral growth of GaAs (1-9), Si (10, 11), and InP (12) over metal or oxide mask films have been published.

Halide vapor phase epitaxy (VPE) has been employed as the most general method for overgrowth purposes, because it has several advantages for successfully accomplishing the overgrowth as will be mentioned below. In the VPE growth, there is a thermal equilibrium between the solid and vapor phases. The dependence of surface kinetics on substrate orientation makes an important contribution to the large ratio of lateral to vertical growth rates. In addition, polycrystalline solids, which prevent the lateral overgrowth, do not deposit over large areas of the mask films, because of the desorption or etching processes of source species. In this case, HCl, which is produced or introduced intentionally during the VPE growth, plays an important role in the etching process. In fact, Jastrzebski *et al.* (11) added HCl vapor etching steps intentionally to the Si overgrowth procedure using SiH_2Cl_2, reporting that the nucleation of poly-Si over SiO_2 was eliminated. However, there are serious problems with the HCl introduction. For example, some kinds of chloride reactants generated during the deposition process react with a quartz reactor or substrates, and, consequently, cause unintentional doping, the so-called "autodoping." Additionally, abrupt interfaces in composition and doping or epitaxial layers containing Al cannot be readily obtained by this method.

For metalorganic chemical vapor deposition (MOCVD), on the other hand, such problems do not exist because of the growth system, which excludes HCl. Moreover, MOCVD is well known to have such advantages as allowing precise control of composition and doping in multicomponent structures. However, lateral overgrowth has been difficult to successfully accomplish using MOCVD, because polycrystalline GaAs can be readily deposited over mask films (13) due to the lack of etching process in this growth mechanism.

Recently, Gale *et al.* (14) and Asai *et al.* (3) demonstrated that the MOCVD lateral GaAs growth can be accomplished without polycrystalline deposits over mask films by optimizing the growth conditions. Lateral overgrowth using MOCVD has developed into an applicable technique for fabricating PBT's. However, the details regarding the GaAs overgrowth process in MOCVD have not yet been made clear.

In this paper, we report on the lateral GaAs growth over a tungsten grating with 5 μm wide lines and spaces on a (001) GaAs substrate using MOCVD. To study the overgrowth process, our attention has been focused on the facet shapes formed at GaAs overgrown film edges and the vertical growth rates of the overgrown films. The dependencies of geometrical shapes of the facets and growth rates on the tungsten grating direction, growth temperature, and source gas flow rates are examined. The tungsten grating direction on the (001) substrate surface is found to be the most essential parameter to determine the geometrical shape of the overgrowth layer. The other controlling parameters are the growth temperature and the partial pressure of arsine (AsH_3). However, the partial pressure of trimethylgallium (TMG) has no influence on the facet formation, though an overall growth rate of the overgrown layer is controlled by mass transport. On the basis of the obtained results, the MOCVD overgrowth mechanism is discussed.

Experimental Procedure

The MOCVD system used for GaAs overgrowth in this work was a conventional horizontal quartz reactor with an RF induction heater. The upper surface of a graphite susceptor was tilted about 7° from the gas flow. The growth temperature was monitored by a thermocouple inserted into the susceptor. An electronic-grade, 10% mixture of AsH_3 in hydrogen was used as an arsenic source. TMG vapor was provided by bubbling hydrogen through this liquid, which was held at 0°C in a stainless steel bubbler. A main impurity in the TMG was Si, whose concentration was nominally 1 ppm. A purified H_2 carrier gas having a 4 liter/min flow rate was introduced with the TMG and AsH_3 into the reactor. The overgrowth was performed under atmospheric pressure.

In order to examine the overgrowth processes, we used the patterned substrates having tungsten gratings, as shown in Fig. 1. After etching Si-doped (2×10^{18} cm^{-3}), GaAs (001) ± 0.5° wafers with a $3H_2SO_4$-$1H_2O_2$-$1H_2O$ solution, a 400Å sputter tungsten grating of 5 μm wide lines and spaces was made as a masking pattern on the wafer with a conventional lift-off technique. A stripe direction of the tungsten grating oriented on the substrate is a very important factor for affecting facet shapes of the overgrown layers, as will be described later.

In this paper, the grating direction is defined as an angle from the <$\bar{1}$10> direction on the (001) GaAs surface called the "grating angle." The grating angle was varied from 0° to 90° to examine the dependence of the overgrowth on the grating direction. Taking the crystallographic symmetry of a zinc blende structure into account, this angle region can cover all grating directions on the (001) surface. The determination of the <$\bar{1}$10> and <110> directions on the (001) GaAs wafer was made by means of the etching profile test with a $1H_2SO_4$-$1H_2O_2$-$1H_2O$ solution (15).

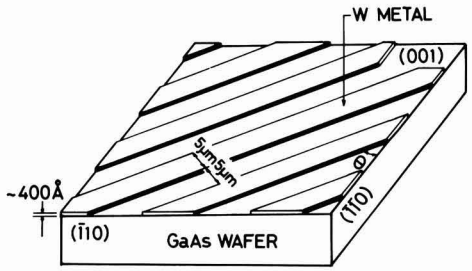

Fig. 1. Schematic picture of a substrate used for overgrowth.

The growth procedure began with substrates having tungsten gratings being loaded into the reactor, after being washed sequentially in trichloroethylene, acetone, and methanol. To compare layer thicknesses, substrates having no grating were also used. The reactor was purged with a purified H_2 gas for about 2h. An AsH_3 gas was introduced when the susceptor temperature reached 400°C to protect the substrate from thermal damage. Typical growth time was 2h. Growth conditions were varied widely, as summarized in Table I. When one condition was varied, the others were fixed at standard conditions in order to clarify the effects of the varied condition. This is indicated by the parentheses in Table I.

Our attention in this work focuses specifically on the facet shapes and layer thicknesses formed during overgrowth. In order to determine the crystallographic planes of the facets, (1̄10) and (110) cleavage planes of the overgrown layers were observed for 0°-45° and 45°-90° grating directions, respectively, with an optical microscope. All grown layers were stain etched with a $10H_2O$-$1H_2O_2$-1HF solution for 15s. Consequently, buried tungsten stripes could be clearly seen as dark lines in the cross-sectional views. The thickness of a selectively grown layer was measured from the step height between the top surface of the layer and the tungsten grating in the cross-sectional view of the sample.

Overgrowth on Various Directional Gratings

In this section, we describe the effects of grating direction on lateral overgrowth from three perspectives. First, for typical grating directions, the relationship between surface morphology and facet formation of overgrown layers is examined. Second, the inclination of the facet with respect to a (001) substrate surface is studied as a function of the grating angle from <1̄10>. Third, on the basis of the results, a model for the overgrowth process is discussed.

Cleaved cross sections of the GaAs layers simultaneously grown over tungsten gratings with various directions were observed by an optical microscope. Figures 2a, 2b, and 2c present the cross-sectional photographs of the grown layers over the tungsten gratings oriented at 0°, 30°, and 90° directions from the <1̄10>, respectively. These samples were grown under the conditions of 630°C and [TMG] and [AsH_3] mole fractions of 3.2×10^{-5} and 1.7×10^{-3}, respectively. Note that Fig. 2a and 2b indicate (1̄10) cleavage planes, while Fig. 2c represents a (110) cleavage plane. It is clear from this figure that the lateral overgrowth strongly depends on the grating direction.

Table I. Growth conditions

Growth temperature (°C)	400-800	(630)[a]
[TMG] (mole fraction)	$2.3\text{-}12.8 \times 10^{-5}$	(3.2×10^{-5})
[AsH_3] (mole fraction)	$0.2\text{-}7 \times 10^{-3}$	(1.7×10^{-3})
[AsH_3]/[TMG]	6-220	(53)
Total flow rate (liter/min)	4	
Grating direction from the <1̄10> (°)	0-90	

[a] Parentheses mean standard growth conditions (see text).

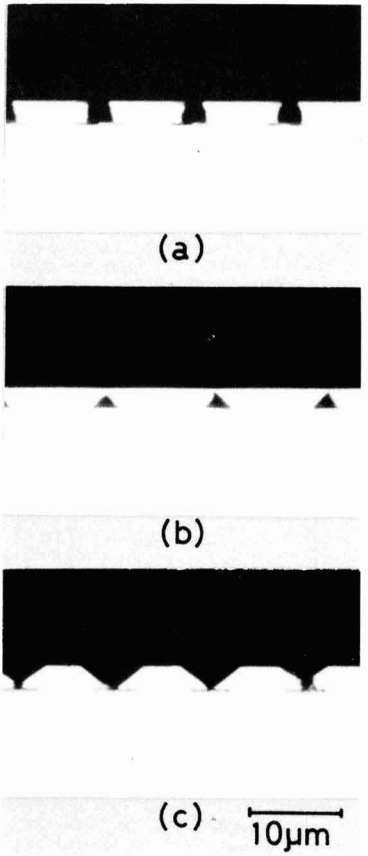

Fig. 2. Photomicrographs of cleaved cross sections of grown layers over tungsten gratings oriented at 0° (a), 30° (b), and 90° (c) from the <1̄10> direction. Note that the a and b show the (1̄10) cleavage planes and that the c represents the (110) plane.

For the 0° grating direction, which corresponds to the <1̄10> direction, the lateral overgrowth facets exhibited planes shaped perpendicularly to the (001) surface (Fig. 2a). For the 30° gratings, the facets had reverse-mesa-shaped planes at the initial overgrowth stage. As the overgrowth continued, the reverse-mesa-shaped GaAs stripes laterally developed and finally joined at the reverse-mesa top to form continuous, flat, specular layers. In the top view of such a sample, one could not observe any disturbance due to the presence of the 5 μm width-and-space tungsten grating. In the cross-sectional view, however, triangular voids were seen near the centers of the tungsten stripes as a result of reverse-mesa formation during initial overgrowth (see Fig. 2b).

For the 90° grating direction, which corresponds to the <110> direction, the overgrowth profile indicated ordinary mesa-shaped planes (Fig. 2c). When the overgrowth exhibiting this facet type continued, the top surface of the ordinary mesa became narrower as growth proceeded until the overgrown layer was finally composed of only inclined surfaces. The inclined plane was identified with {1̄12}As faces from the facet angle of 37° with respect to the (001) surface. The overgrowth continued further, and if the V-shaped grooves left on the layer surface were filled up one could then expect to obtain an overgrown layer free of voids near the center of the tungsten stripes. In contrast to this expectation, anomalous faceting growth took place actually as shown in Fig. 3. The facets could not be characterized by specific planes.

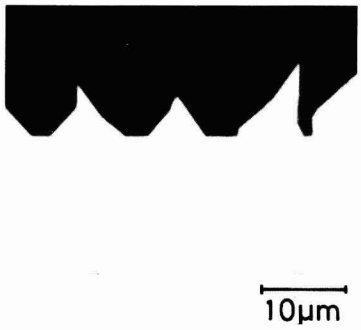

Fig. 3. Photomicrograph of a (110) cleaved plane of an overgrown layer for the 90° tungsten stripe direction which corresponds to <$\bar{1}$10>.

Surface morphology of MOCVD layers is well known to depend strongly on substrate orientation (16). The layer surface on the ($\bar{1}\bar{1}\bar{1}$)As substrate indicated very defective morphology, including many poly-like hillocks (17). Since ($\bar{1}$12)As and ($\bar{1}\bar{1}\bar{1}$)As surfaces are composed of a relatively large number of As atoms, the defective growth is considered to take place on the ($\bar{1}$12)As, similarly to that on the ($\bar{1}\bar{1}\bar{1}$)As. Since the growing surface for the 90° grating direction is only the inclined {$\bar{1}$12}As face, anomalous faceting growth such as is shown in Fig. 3 is believed to occur.

The overgrown layers are characterized by the facet shapes, as shown in Fig. 2. To determine the crystallographic plane for the facet, the angle of the facet with respect to the (001) surface was measured from cross-sectional photographs of the layers. The facet angle for the tungsten grating direction from 0° to 90° is presented in Fig. 4. All the samples were simultaneously grown under the conditions of 630°C and [TMG] and [AsH_3] of 3.2×10^{-5} and 1.7×10^{-3} mole fraction, respectively. From this figure, the facet angle can be clearly classified into three regions.

In the 0°-10° grating direction region, the facet angle was perpendicular to the substrate surface, which corresponds to the {110} crystallographic plane. For the substrates with 10°-45° grating orientations, the sidewalls of the overgrowth layers had an angle of 130° with respect to the (001) surface. This angle coincided with the one of the {$\bar{1}\bar{1}\bar{1}$}As plane with respect to the (001) surface. For the 45°-90° GaAs opening directions from <$\bar{1}$10>, the overgrowth profile observed on a (110) cleavage plane indicated the inclined plane forming an angle of 37°. The angle coincided with the one of the {$\bar{1}$12}As face with respect to the (001) surface.

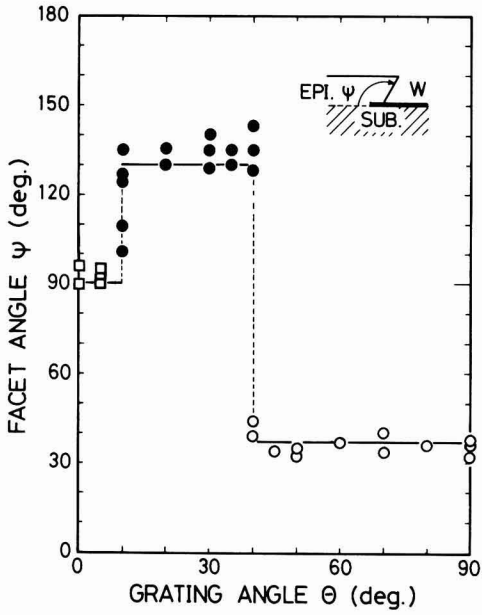

Fig. 4. Facet angle (see inset) with respect to the (001) surface plane as a function of the tungsten grating angle from <$\bar{1}$10>.

In each region of the grating angle, the sidewalls of the overgrown layers were found to retain the same angle with respect to the (001) surface planes as mentioned above. This suggests the following overgrowth process. Lateral overgrowth is seeded from the edges of the masking tungsten stripes by selective epitaxial deposits initially formed only on the exposed regions. However, the lateral growth fronts do not proceed perpendicularly toward the stripe direction.

Microscopically, the lateral growth fronts are composed of two small specific planes formed perpendicularly to the cleavage planes, as shown in Fig. 5. The specific plane can be determined by observation of the cleavage plane. For example, for the 30° grating directions, a small plane observed on the ($\bar{1}$10) cleavage plane corresponds to the {$\bar{1}\bar{1}\bar{1}$}As crystallographic plane forming an angle of 125.3°, in principle, with respect to (001) surface plane.

This overgrowth process is also supported by the observation of the overgrowth layer surface shown in Fig. 6. In this figure, although almost all growth fronts are parallel to the tungsten stripe, anomalous growth is observed in some areas. The anomalous growth areas are very similar to the zigzag growth process portrayed in Fig. 5. The areas of the films with parallel growth fronts are also believed to be composed of a number of facets, as previously reported by Vohl *et al.* (11). This overgrowth process, therefore, generally occurs in growth over the misoriented masking stripes, whose direction is not parallel to low indexes such as the <$\bar{1}$10> and <110> directions.

Dependency of Overgrowth on Growth Parameters

Growth parameters in MOCVD control facet formation as well as layer quality, such as surface morphology and electron mobility. In this section, we describe the dependence of the overgrowth on growth temperature and AsH_3 and TMG mole fractions. Since a smooth surface of an overgrown film was found to be obtainable for the 30° grating direction, as mentioned in the preceding section, the main focus is on the dependency of the lateral growth over the 30° tungsten grating.

Growth temperature.—Growth temperature affects facet formation in overgrowth in conjunction with surface morphology. For typical growth temperatures, we have conducted a study on the relationship between the surface morphology and the facet formation of the overgrown layers. Figures 7a, 7b, 7c, and 7d present the overgrowth layers obtained at 710°, 630°, 600°, and 510°C, respectively, with all other growth conditions being the same, that is, [TMG] = 3.2×10^{-5} mole fraction and [AsH_3] = 1.7×10^{-3} mole fraction. All the specimens shown in

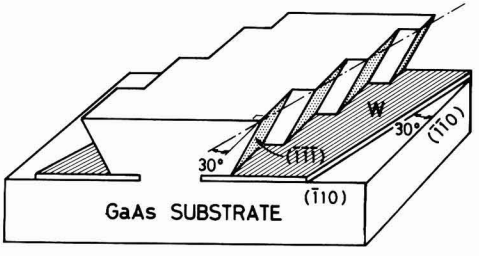

Fig. 5. Schematic picture of overgrowth process onto 30° GaAs stripe openings.

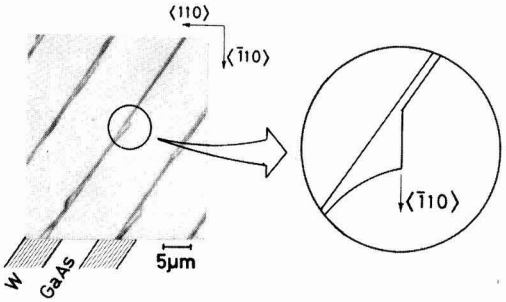

Fig. 6. Photomicrograph of the surface of the overgrown layer just before joining lateral growth fronts seeded from the edges of tungsten stripes.

these figures were grown over 30° gratings from the <1̄10> direction. Note that the cross-sectional views were observed on the (1̄10) cleavage planes.

The sidewall of an overgrown layer at the high temperature of 710°C consists of reverse-mesa- and ordinary mesa-shaped planes as shown in Fig. 7a. At a growth temperature above this value, only the ordinary mesa-shaped planes formed on the exposed GaAs stripes. The cross-sectional views of the samples at 630° and 600°C indicate the same reverse-mesa-shaped planes (see Fig. 7b and 7c). Though the triangular voids are also seen in the layer at 600°C, they were slightly smaller in size than those at 630°C. Therefore, the ratio of lateral to vertical growth rates tends to slightly increase with a decrease in the growth temperature. This tendency demonstrated qualitative agreement with the results using (011) GaAs substrates (12).

The surface of the films obtained at 630°C is flat and smooth (Fig. 7b) On the other hand, the surface of the film grown at 600°C represents defective morphology, which exhibits a rough-patterned structure reflecting the underlying tungsten grating, as shown in Fig. 7c.

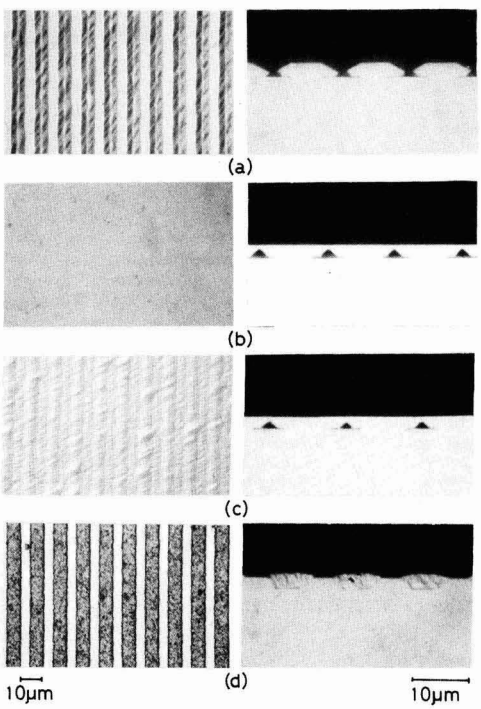

Fig. 7. Photomicrographs of surfaces and (1̄10) cleavage planes of layers grown over 30° tungsten gratings at 710°C (a), 630°C (b), 600°C (c), and 510°C (d).

At a growth temperature lower than 530°C, GaAs deposition occurred not only on the exposed GaAs surface but also on the masking tungsten stripes. The deposition of polycrystalline GaAs on the tungsten stripes prevented the lateral epitaxial growth from the edges of the tungsten stripes (see Fig. 7d). Consequently, the well-defined facets cannot be observed for the overgrown layers at the lower growth temperature.

The formation of polycrystalline GaAs over the mask surface, as shown in Fig. 7d, is the major problem encountered during lateral overgrowth. In MOCVD growth in particular, the poly-GaAs deposits readily over the tungsten mask, because the sticking coefficient for Ga is unity. For a growth temperature above 530°C, however, GaAs growth is initiated only on the exposed area. This suggests that Ga adatoms on the tungsten are transferred to the growing GaAs surface. The driving force behind transferring the Ga adatoms is produced by atomic surface diffusion and by the difference between the nucleation probabilities for the GaAs and the tungsten. The atomic surface diffusion length decreases with a decrease in the growth temperature. Nucleation of polycrystalline GaAs, therefore, takes place on the tungsten stripes at low growth temperature.

In addition to the growth temperature, the polycrystalline deposit onto the tungsten surface is very sensitive to the tungsten mask characteristics. For example, the poly-GaAs nuclei form around the defects present on the tungsten surface such as pinholes, topological irregularities, and contaminated regions. These defects considerably increase the nucleation probability on the tungsten surface. Furthermore, the intrinsic properties of a mask surface, such as its surface free energy and number of free surface sites where source species are incorporated (18, 19), also have influence on the nucleation probability for the mask.

The facets of films grown over 30° gratings are affected by the growth temperature, as shown in Fig. 7. To examine the facet shapes in detail, the angle of the facet was measured with respect to the (001) substrate surface. The facet angle for the growth temperature from 550° to 810°C is presented in Fig. 8. Other growth parameters remain the same, that is, $[TMG] = 3.2 \times 10^{-5}$ mole fraction and $[AsH_3] = 1.7 \times 10^{-3}$ mole fraction. It is remarkable that the growth temperature of 710°C represents the critical point in change from the reverse mesa to the ordinary mesa geometric shape of the overgrowth layers. The sidewalls of these geometric shapes indicate the facet forming angles of 130° and 27°, respectively. From these angles, the faces constituting the sidewalls of the overgrown layer are identified with the {1̄11}As and the {113}Ga crystallographic planes.

On the other hand, with the decrease in the growth temperature, the sidewall inclination of the overgrowth layer changed gradually from 130° to 105° with respect to the (001) substrates. The gradual change is attributed to the reduction in the surface diffusion length of source species with the decrease in the growth temperature. A well-defined facet is not formed due to the reduction of atomic diffusion along the top and side surfaces of the growing layers.

The temperature dependence of the facet formation mentioned above was not observed for all of the grating directions. For example, for the tungsten grating directions of 0° and 90°, which correspond to <1̄10> and <110>, respectively, the facet angle with respect to the (001) surface plane is independent of the growth temperature, as shown in Fig. 9. For the 0° grating direction, the sidewall of the layer observed on the (110) cleavage plane indicates a plane perpendicular to the (001) surface, which corresponds to the {110} crystallographic plane. For the 90° grating direction, the overgrowth profile on the (110) cleavage planes exhibits the inclined plane forming an angle of 37° with respect to the (001) surface plane. This

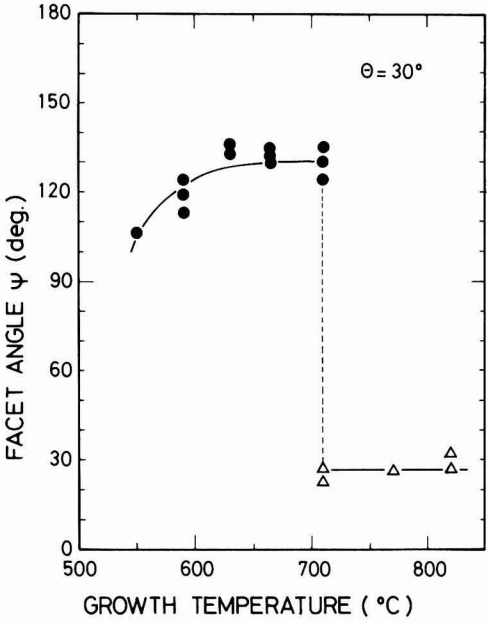

Fig. 8. Facet angle with respect to the (001) surface plane as a function of the growth temperature. Grating direction was 30° from <$\bar{1}$10>. Other growth parameters: [TMG] = 3.2 × 10^{-5} mole fraction, and [AsH_3] = 1.7 × 10^{-3} mole fraction.

angle coincides with that of the {$\bar{1}$12}As crystallographic plane. With respect to the facet formation, the relationship between the grating angle and the growth temperature is more complex. The details of this will be described below.

AsH_3 and TMG mole fractions.—AsH_3 and TMG mole fractions ([AsH_3] and [TMG]) are key parameters in controlling the MOCVD film characteristics, such as p-n conversion. One can expect that the faceting growth onto the GaAs stripe openings is also affected by the [AsH_3] and [TMG] conditions. This represents our final experiment on facet dependence. In order to properly separate the [AsH_3] and [TMG] effects, the [AsH_3] condition was varied under a constant [TMG] and vice versa.

Figures 10a, 10b, and 10c are photomicrographs of the (110) cleaved planes of films grown at 6.8 × 10^{-3}, 1.7 × 10^{-3}, and 0.4 × 10^{-3} AsH_3 mole fractions, respectively. For all of the specimens, the tungsten grating directions were 30° from the <$\bar{1}$10>, [TMG] was 3.2 × 10^{-5} mole fraction, and the growth temperature was 630°C. The geometrical shape of the layer grown at [AsH_3] = 1.7 × 10^{-3} mole fraction was the reverse mesa, as shown in Fig. 10b. This condition of [AsH_3] was optimal for obtaining the smooth surface of the layer. Even though the AsH_3 mole fraction was increased, the films exhibited the same reverse-mesa-shaped planes. The layer surface, however, became wavy and defective (see Fig. 10a). On the other hand, when the AsH_3 mole fraction was decreased, the ordinary mesa-shaped planes were formed in addition to the reverse-mesa-shaped planes as the sidewalls of the overgrown layer (Fig. 10c). This geometrical shape is very similar to that of the 710°C growth temperature (*cf.* Fig. 7a).

From the cross-sectional photographs shown in Fig. 10, the [AsH_3] dependence of a facet angle with respect to the (001) surface was examined. The facet-angle variation for [AsH_3] of 0.2-7 × 10^{-3} mole fractions is represented in Fig. 11. The observed geometrical shapes of the overgrown layers are shown in the two insets. Up to a mole fraction of [AsH_3] = 0.8 × 10^{-3}, which corresponds to [AsH_3]/[TMG] = 25, the sidewalls consisting of ordinary mesa- and reverse-mesa-shaped planes were formed,

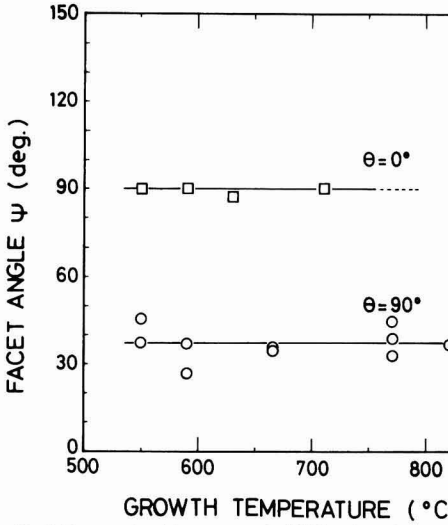

Fig. 9. Facet angle with respect to the (001) surface plane as a function of the growth temperature. Grating directions were 0° and 90°, corresponding to the <$\bar{1}$10> and <110> directions, respectively.

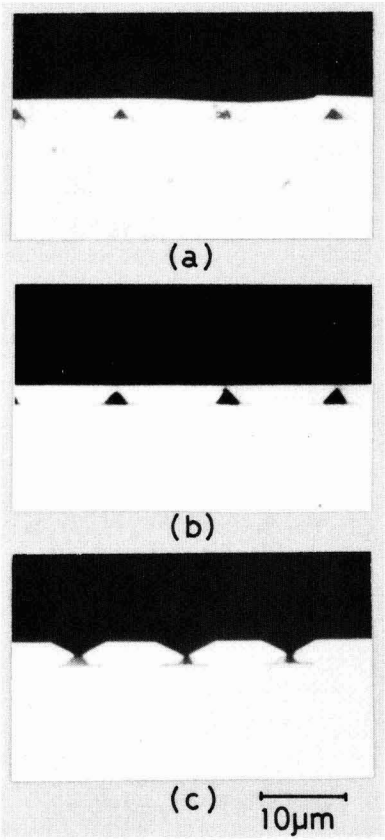

Fig. 10. Photomicrographs of ($\bar{1}$10) cleavage plans of layers grown at [AsH_3] of 6.8 × 10^{-3} (a), 1.7 × 10^{-3} (b), and 0.4 × 10^{-3} (c) mole fractions. All the layers were grown on the tungsten gratings oriented 30° from <$\bar{1}$10>.

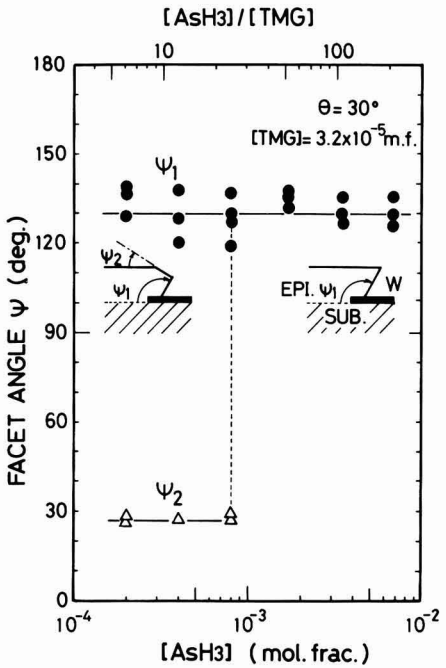

Fig. 11. Facet angle with respect to the (001) surface plane as a function of $[AsH_3]$. Growth temperature was 630°C.

whose angles with respect to the (001) surface were 130° and 27°, respectively (see the left inset of Fig. 11). From these angles, the facets were found to correspond to the $\{\bar{1}\bar{1}1\}$As and {113}Ga faces. Above a mole fraction of $[AsH_3] = 0.8 \times 10^{-3}$, the sidewall indicated only the $\{\bar{1}\bar{1}1\}$As.

From this result only, however, one cannot know whether the growth parameter causing the facet variation is $[AsH_3]$ or $[AsH_3]/[TMG]$. Therefore, we studied the effects of the [TMG] variation on the overgrowth under $[AsH_3] = 1.7 \times 10^{-3}$ mole fraction. The facet angle with respect to the (001) surface as a function of [TMG] is presented in Fig. 12. Under the conditions of [TMG] = 2.3-12.8 $\times$ 10^{-5} mole fraction corresponding to

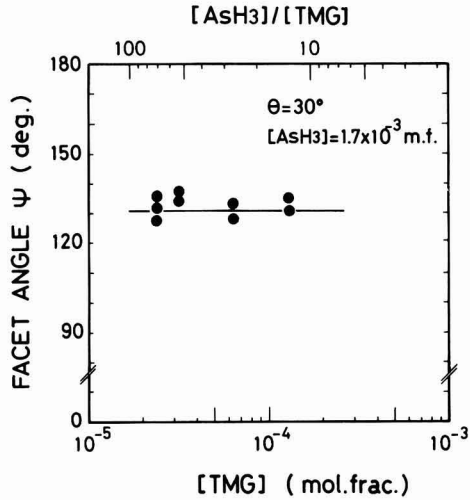

Fig. 12. Facet angle with respect to the (001) surface plane as a function of [TMG]. Growth temperature was 630°C.

$[AsH_3]/[TMG]$ = 13-74, the sidewall of the overgrown layer indicates only the facet forming an angle of 130° with respect to the (001) surface. Even below $[AsH_3]/[TMG] = 25$, no plane other than the $\{\bar{1}\bar{1}1\}$As face was formed regarding the sidewalls of the overgrown layers. On the other hand, when $[AsH_3]/[TMG]$ was reduced below 25 through a decrease in $[AsH_3]$ with a constant [TMG], the {113}Ga face was formed in additional to the $\{\bar{1}\bar{1}1\}$As face (see Fig. 11). Therefore, the facet formed during the selective growth on the tungsten gratings is concluded to depend on $[AsH_3]$ rather than $[AsH_3]/[TMG]$.

Vertical Growth Rate of Overgrown Layer

Studies of growth rate provide us with basic information on growth mechanisms. For selective growth without poly-GaAs deposition over a tungsten surface, reacting species which arrived from the gas phase to the tungsten surface should be (*i*) released again into the gas phase, or (*ii*) transferred to a growing GaAs surface. In case (*i*), the vertical growth rate on the limited area can be predicted as being essentially the same as the growth rate on the substrate without the tungsten grating. On the other hand, in case (*ii*), the vertical growth rate in the limited region is apparently enhanced compared to that on the surface without the tungsten grating.

The vertical growth rate was determined from the height of a top side of the overgrown layer on the limited GaAs area. The vertical growth thickness, t, *vs.* the grating angle is given as the closed circles in Fig. 13, where the growth time was 2h. The layer thickness on the substrate without the tungsten grating is also shown as an open triangle. From this figure, the thickness of the overgrown layer is found to strongly depend on the grating direction. Moreover, the vertical growth rates of the overgrown layers shown in Fig. 13 were larger than the layer thickness on a substrate without the tungsten grating. The vertical growth rate on a limited area is only apparently enhanced. Therefore, the arrival species at the tungsten surface are not released again into the gas phase but are transferred to the growing GaAs surface.

To clarify this situation further, let us consider an average layer thickness, $\bar{t}$, which is calibrated by filling up the V grooves or the triangular voids as shown in the inset of Fig. 13. The calibrated layer thicknesses are represented as open circles in the figure. The average layer thickness was found to coincide with the layer thickness on the substrate without the tungsten pattern in all the grating directions. Therefore, an amount of the reacting species which lead to the GaAs growth is basically the same. The difference in the heights of the top sides of the layers on the limited areas is only apparent.

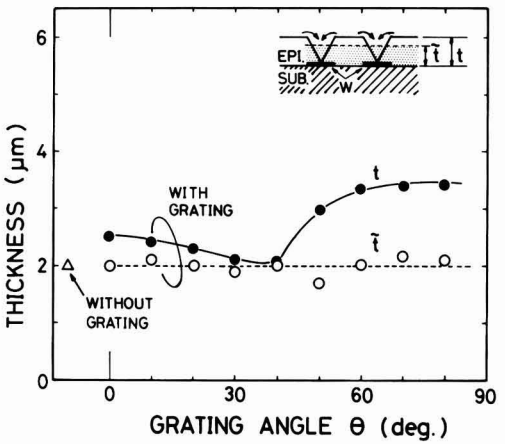

Fig. 13. Layer thicknesses for 2h growth time as a function of grating direction.

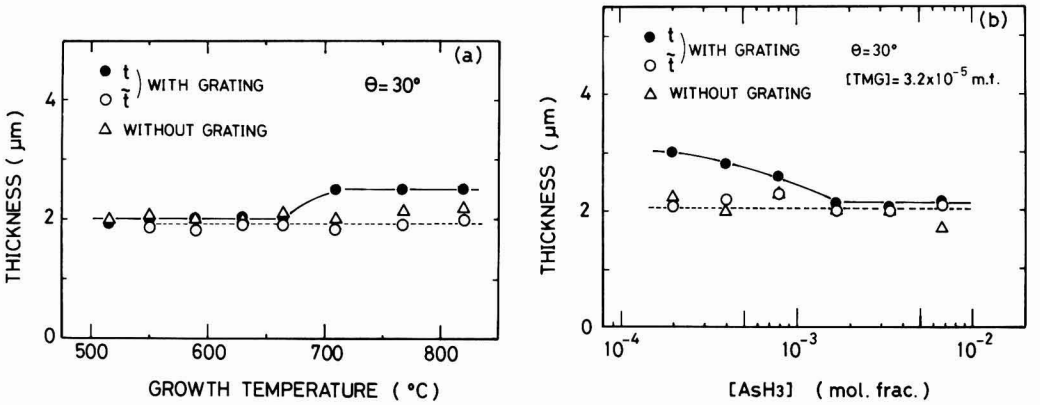

Fig. 14. Layer thicknesses for 2h growth time as functions of growth temperature (a) and [AsH_3] (b). The layers were grown over the 30° tungsten gratings at 630°C.

Vertical growth rates on the limited area are also studied with respect to growth temperature and [AsH_3]. Figures 14a and 14b plot film thickness at a growth time of 2h as functions of the growth temperature and [AsH_3], respectively. All of the films were grown over the 30° tungsten gratings. The apparent and average thicknesses of the selectively grown layers are indicated as the closed and open circles, respectively. The layer thickness on the substrate without the grating is also represented as open triangles. Though the apparent thickness on the GaAs opening varied with the growth temperature and [AsH_3], the average thickness was independent of the growth conditions. This was similar to the layer thickness on the substrate without the grating.

Moreover, the average thickness coincided with the thickness on the substrate without the grating. From the results of the average thickness, it can be concluded that the overall growth rate under this range of growth conditions is essentially limited by mass transport through the stagnant layer in the gas phase. However, surface kinetics cannot be ruled out as an MOCVD growth mechanism, because the various crystallographic faces form with a dependence on the tungsten stripe direction, the growth temperature, and [AsH_3].

Crystallographic Aspect and Overgrowth Mechanism

In this section, we discuss the facets of the overgrown layers on the tungsten gratings demonstrated in Fig. 2, 7, and 10 from a crystallographic aspect. With respect to the crystallograhic planes of the formed facets, the relationship between the grating direction and growth condition is studied. On the basis of these discussions, the overgrowth mechanism is examined.

Facet identification.—The facets of the overgrown layers on the tungsten gratings are studied from the crystallographic point of view. From the facet angle of the overgrown layers, the geometric shapes of the layers can be classified into four individual groups, as shown in Fig. 15.

The overgrown facet forming an angle of 90° with respect to the (001) surface plane was observed on ($\bar{1}10$) cleavage planes for the near <$\bar{1}10$> grating directions. This result was independent of the growth conditions. From this facet angle, these formed planes correspond to the {110} crystallographic planes (see Fig. 15I). In the region of 10°-45° tungsten opening directions, two types of facet shapes were observed on the ($\bar{1}10$) cleavage planes. One is represented by the inclined planes forming an angle of 130° with respect to the (001) surface, which corresponds to the {$\bar{1}\bar{1}\bar{1}$}As planes (Fig. 15II). The other is represented by the planes forming an angle of 27° with respect to the (001) surface planes, which corresponds to the {113}Ga (Fig. 15III).

The {$\bar{1}\bar{1}\bar{1}$}As and {113}Ga planes, in principle, form angles of 125.3° and 25.2°, respectively, with respect to the (001) surface planes. One of these types was changed into the other by the growth temperature or [AsH_3] conditions. For the 45°-90° tungsten grating directions from <$\bar{1}10$>, only the plane forming an angle of 37° with respect to the (001) surface was observed on the (110) cleavage plane independent of the growth conditions (Fig. 15IV). From the angle of the inclined plane observed on the (110) cleaved plane, the facet corresponds to the {$\bar{1}12$}As, which, in principle, forms an angle of 35.3° with respect to the (001) surface plane.

These facet types shown in Fig. 15 are summarized with respect to the grating direction and growth conditions. The classification of these facet types is plotted out for the growth temperature and grating angle in Fig. 16. Below the growth temperature of 440°C, no GaAs nuclei are deposited on the exposed GaAs regions nor on the tungsten surface. In the 530°-440°C region, poly-GaAs is deposited on the tungsten surface. Though monocrystalline GaAs was grown onto the exposed GaAs area, the facets could not be observed, owing to the deposition of poly-GaAs on the tungsten surface. Therefore, the temperature range above 530°C is a subject of some discussion concerning the facet types.

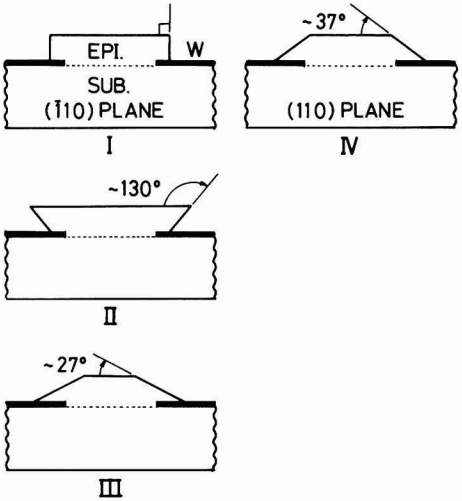

Fig. 15. Schematic diagrams of the overgrowth profiles produced on the (001) GaAs plane under the various growth conditions (see text).

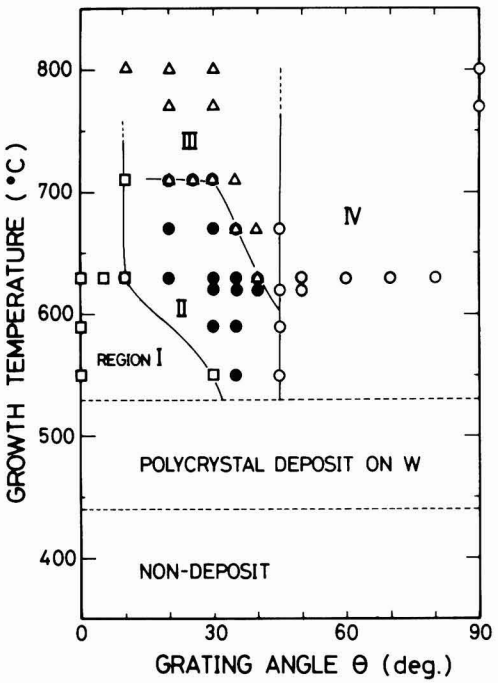

Fig. 16. Classification of facet types for growth temperatures and grating angles.

A similar classification is also mapped for [AsH_3] and the grating angle in Fig. 17. Regions I, II, III, and IV in Fig. 16 and 17 mean the extent of growth parameters and grating direction, where the overgrowth profiles indicate types I, II, III, and IV as presented in Fig. 15. In these plots, for example, the region II+III means a conditional extent which produces the side wall consisting of the {$\bar{1}\bar{1}\bar{1}$}As and {113}Ga planes, as shown in Fig. 10c.

It is clear from these figures that the GaAs opening direction on the (001) substrate surface is the most essential parameter for the overgrowth. This is because the facet shape is controlled by the grating direction, except in the

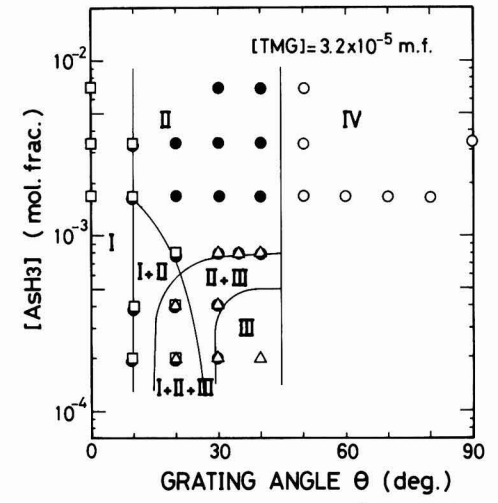

Fig. 17. Classification of face types for [AsH_3] and grating angle. Growth temperature was 630°C.

10°-45° region. This reason is not well understood at present, but it is considered to relate to the atomic arrangements, atomic bond directions, and crystallographic polarity on the defined stripe opening of the (001)GaAs substrate surface. The other limitations for the faceting growth are growth temperature and [AsH_3].

It is noteworthy that the {$\bar{1}\bar{1}\bar{1}$}As sidewall plane of the selectively grown layer changes to the {113}Ga at the growth temperature of more than 710°C. Additionally important is the fact that the {113}Ga side plane is formed together with the {$\bar{1}\bar{1}\bar{1}$}As plane at less than a 0.8×10^{-3} mole fraction of [AsH_3]. In short, an increase in the growth temperature and a decrease in [AsH_3] have a similar influence on facet formation.

Overgrowth mechanism.—We will now discuss our experimental results in terms of the Langmuir-Rideal mechanism, where gas phase gallium species react with surface-adsorbed arsenic (20). Although the reacting species are written as Ga and As for the sake of simplicity, the actual surface species which lead to GaAs growth are considerably more complex in MOCVD (21).

In the Langmuir-Rideal model, the growth rate, R, is given by

$$R = K\Theta_{As}P_{Ga} \quad [1]$$

where K is a rate constant, P_{Ga} is the initial partial pressure of the Ga species in the gas phase, and Θ_{As} is the surface coverage of the As species. The Θ_{As} is written as

$$\Theta_{As} = \frac{\beta_{As}P_{As}}{1 + \beta_{As}P_{As}} \quad [2]$$

where P_{As} is the partial pressure of the As species in the gas phase and β_{As} is the Langmuir adsorption constant for the As species, that is, the ratio of the rate constant for the adsorption of the As species to the rate constant for desorption.

Assuming that TMG is completely decomposed by the homogenous reaction in the gas phase (22), $P_{Ga} \approx P_{TMG}$, where P_{TMG} is the inlet partial pressure of TMG in the gas phase, such that Eq. [1] can be rewritten into

$$R = K\Theta_{As}P_{TMG} \quad [3]$$

From this equation, one can expect that the slight difference in growth rate is caused by the Θ_{As} dependence on the surface orientation. However, the dependence of the growth rate on the orientation is not measurable by an experiment using individual substrates with various orientations because $\Theta_{As} \approx 1$, *i.e.*, $\beta_{As}P_{As} >> 1$, in almost all cases (20). Consequently, Eq. [3] is reduced to

$$R = KP_{TMG} \quad [4]$$

Therefore, the predicted growth rate demonstrates a linear dependence on the partial pressure of TMG, and is independent of the AsH_3 overpressure.

Let us consider the case where various crystallographic faces are arranged within the surface diffusion length of the reacting species. The growth rate dependence on the orientation predicted from Eq. [3] is enhanced by the diffusion of the reacting species from the face where the growth rate is relatively low to the face with the relatively high growth rate. As a consequence, the growth rate is considered to depend significantly on the surface orientation. The faceting growth is also dominated by this mechanism.

The planes where the growth rate is relatively small are believed to be formed as facets of the overgrowth layer. The Θ_{As} is dependent on the growth temperature and the AsH_3 partial pressure while being independent of the TMG partial pressure. Therefore, the faceting growth is strongly dependent on the temperature and the partial pressure of AsH_3, while being independent of the partial pressure of TMG. However, the overall average growth rate of the overgrown layer depends only on the partial pressure of TMG.

Conclusion

Lateral epitaxial growth of GaAs over tungsten gratings with 5 μm wide lines and spaces on (001) GaAs substrates was performed using MOCVD. Lateral overgrowth was seeded from the edges of the masking tungsten stripes by selective epitaxial deposits initially formed only on the exposed regions. The facets were formed at the GaAs-overgrown film edges. From crystallographic aspect, all the facets observed in the overgrown layers were found to be classified into four individual groups of {110}, {$\bar{1}\bar{1}\bar{1}$}As, {$\bar{1}$12}As, and {113}Ga faces. The GaAs opening direction on the (001) substrate surface was found to be the most essential parameter for determining the geometric shape of the overgrowth layer. The other controlling parameters were the growth temperature and the partial pressure of AsH_3. The partial pressure of TMG had no influence on the facet formation, although the average growth rate of the overgrown layer was controlled by the mass transport of the reacting species including Ga atoms. These results could be qualitatively explained by the Langmuir-Rideal model.

Acknowledgments

The authors wish to thank Dr. Kenji Kumabe for his encouragement throughout this work. They also would like to thank Dr. Nobuhiko Susa, Dr. Hideo Sugiura, and Dr. Kunishige Oe for their useful comments.

Manuscript submitted March 11, 1985; revised manuscript received *ca.* June 19, 1985.

Nippon Telegraph and Telephone Corporation assisted in meeting the publication costs of the article.

REFERENCES

1. C. O. Bozler and G. D. Alley, *IEEE Trans. Electron Devices*, **ed-17,** 1128 (1980).
2. B. A. Vojak, R. W. McClelland, G. A. Lincoln, A. R. Calawa, D. C. Flanders, and M. W. Geis, *IEEE Electron Device Lett.*, **edl-5,** 270 (1984).
3. H. Asai, S. Adachi, S. Ando, and K. Oe, *J. Appl. Phys.*, **55,** 3868 (1984).
4. F. J. Leonberger, C. O. Bozler, R. W. McClelland, and I. Melngailis, *Appl. Phys. Lett.*, **38,** 313 (1981).
5. F. W. Tausch, Jr., and A. G. Lapierre III, *This Journal*, **112,** 706 (1965).
6. D. W. Shaw, *ibid.*, **113,** 904 (1966).
7. S. Iida and K. Ito, *J. Cryst. Growth*, **13/14,** 336 (1972).
8. C. O. Bozler, R. W. McClelland, J. P. Salerno, and J. C. C. Fan, *J. Vac. Sci. Technol.*, **20,** 720 (1982).
9. N. Kondo, M. Kawashima, S. Ando, and K. Oe, *Appl. Phys. Lett.*, **45,** 1070 (1984).
10. P. Rai-Choudhury and D. K. Schroder, *This Journal*, **120,** 664 (1973).
11. L. Jastrzebski, J. F. Corboy, J. T. McGinn, and R. Pagliaro, Jr., *ibid.*, **130,** 1571 (1983).
12. P. Vohl, C. O. Bozler, R. W. McClelland, A. Chu, and A. J. Strauss, *J. Cryst. Growth*, **56,** 410 (1982).
13. R. Azoulay, N. Bouadma, J. C. Bouley, and L. Dugrand, *ibid.*, **55,** 229 (1981).
14. R. P. Gale, R. W. McClelland, J. C. C. Fan, and C. O. Bozler, *Appl. Phys. Lett.*, **41,** 545 (1982).
15. S. Adachi and K. Oe, *This Journal*, **130,** 2427 (1983).
16. D. H. Reep and S. K. Ghandhi, *J. Cryst. Growth*, **61,** 449 (1983).
17. H. Heinecke, E. Veuhoff, N. Pütz, M. Heyen, and P. Balk, *J. Electron. Mater.*, **13,** 815 (1984).
18. W. A. P. Claassen and J. Bloem, *This Journal*, **127,** 194 (1980).
19. W. A. P. Claassen and J. Bloem, *ibid.*, **128,** 1353 (1981).
20. W. H. Petzke, V. Gottschalch, and E. Butter, *Krist. Tech.*, **9,** 763 (1974).
21. D. H. Reep and S. K. Ghandhi, *This Journal*, **130,** 675 (1983).
22. M. R. Leys and H. Veenvliet, *J. Cryst. Growth*, **55,** 145 (1981).

An Alternative Approach to the Calculation of Four-Probe Resistances on Nonuniform Structures

John Albers

National Bureau of Standards, Semiconductor Devices and Circuits Division, Gaithersburg, Maryland 20899

H. L. Berkowitz*

U.S. Army Electronics Technology and Devices Laboratory, ERADCOM, Fort Monmouth, New Jersey 07703

ABSTRACT

An alternative approach to the calculation of the four-probe resistance of nonuniform resistivity structures is presented. This approach is based upon two simplifications in the form of the four-probe resistance integral. The first arises from the integral's being independent of the probe current density as well as the probe radius. The second simplification involves the rewriting of the integral as one involving only the kernel (without any Bessel functions) and with finite limits which depend only upon the probe spacing. The form of these limits is determined by the analytic calculation of the four-probe resistance for the case of a semi-infinite slab. For the case of a uniform layer over an insulating or conducting boundary, the simplified integral leads to analytic expressions for the four-probe resistance which are compared with the more extensive technique and are also investigated as a function of the probe spacing. For nonuniform resistivity structures, the simplified integral can be easily evaluated by means of the Newton-Cotes numerical procedure. For general multilayer cases, the results obtained from the Newton-Cotes method are compared with those obtained from more extensive numerical techniques and are shown to be in excellent agreement. This allows for a vastly simplified implementation of the previously proposed spreading resistance calibration technique.

Recently, a multilayer expression for the in-line four-probe resistance, $Z(x, S)$, has been derived in the form (1)

$$Z(x, S) = 2\rho(x) \int_0^\infty A(x, \lambda)\{J_0(\lambda S) - J_0(2\lambda S)\}I_\nu(\lambda a)\, d\lambda \quad [1]$$

where $\rho(x)$ is the resistivity, $J_0(\lambda S)$ is the first-order Bessel function, $A(x, \lambda)$ is the kernel of the integral and is related to the resistivity structure, $I_\nu(\lambda a)$ is the Hankel transform of the generalized probe-current density normalized to unit current (2), ν is an index which refers to the specific form of the current density, a is the probe radius, and λ is the integration variable. It was shown that the four-probe resistance could always be obtained from the two-probe spreading resistance, $R(x, S)$, from the general expression

$$Z(x, S) = R(x, 2S) - R(x, S) \quad [2]$$

*Electrochemical Society Active Member.

The four-probe resistance was also numerically shown to be (*i*) independent of the probe radius and the probe-current density, and (*ii*) simply related to the sheet resistance, $\Re(x)$, when the distance to an insulating boundary is small compared with the probe spacing. The former observation provided the basis for a calibration procedure for determining the value of the probe radius to be used in spreading resistance profile analysis. The use of the four-probe resistance in the calibration procedure requires the evaluation of the integral in Eq. [1]. This evaluation can be greatly simplified, and it is the purpose of the present work to derive a simplified expression for $Z(x, S)$ and hence greatly facilitate the use of the calibration procedure.

Derivation

As the four-probe resistance is independent of the probe current density and the probe radius, Eq. [1] may be rewritten as

$$Z(x, S) = \frac{\rho(x)}{\pi} \int_0^\infty A(x, \lambda)\{J_0(\lambda S) - J_0(2\lambda S)\}\, d\lambda \qquad [3]$$

This particular simplification of the integral has been numerically verified for a range of structures. The thrust of the present work is to further simplify the integral by finding a function, $f(1/S)$, such that Eq. [3] can be written as

$$Z(x, S) = \frac{\rho(x)}{\pi} \int_{f(1/2S)}^{f(1/S)} A(x, \lambda)\, d\lambda \qquad [4]$$

In going from Eq. [3] to Eq. [4], the Bessel functions have been removed from the integrand and their effect on the integral has been preserved by the replacement of the limits in Eq. [3] by finite limits which depend only upon S. This particular choice for the limits of the integral is not arbitrary but was motivated by the substitution of the Berkowitz-Lux (3) form of the spreading resistance in both terms in the right-hand side of Eq. [2]. The resulting expression contains the integral of $A(x, \lambda)$ where the lower limit depends upon $1/2S$ and the upper limit depends upon $1/S$. The particular form obtained from this substitution does not adequately represent the results for a wide class of structures. However, this observation provided the insight into the general form which the simplification of the integral would take.

The search for the function, $f(1/S)$, is aided by the calculation of Eq. [3] and [4] for the case of a semi-infinite slab. In this case, $A(x, \lambda) = 1$, and the integral in Eq. [3] can be evaluated analytically (4) to give

$$Z(x, S) = \frac{\rho}{\pi} \int_0^\infty \{J_0(\lambda S) - J_0(2\lambda S)\}\, d\lambda = \frac{\rho}{2\pi S} \qquad [5]$$

This indicates that $f(1/S) = 1/S$, as can be verified by direct substitution into Eq. [4]. If this choice is generally correct, then the four-probe resistance will be represented by the equation

$$Z(x, S) = \frac{\rho(x)}{\pi} \int_{1/2S}^{1/S} A(x, \lambda)\, d\lambda \qquad [6]$$

which is far simpler to evaluate and analyze than Eq. [1]. The validity of Eq. [6] was investigated for uniform layers over insulating or conducting boundaries, for a wide class of two-layer structures, and for general nonuniform multilayer structures. The results of these investigations are contained in the next three sections.

Uniform Resistivity Layers over Perfectly Insulating or Conducting Boundaries

The kernel for a uniform resistivity layer over an insulating or a conducting boundary, *i.e.*, coth (λx), tanh (λx), may be used to analytically evaluate the integral in Eq. [6] for these cases. Specifically

$$Z(x, S) = \frac{\rho(x)}{\pi} \int_{1/2S}^{1/S} \coth(\lambda x)\, d\lambda = \frac{\rho}{\pi x} \ln\left\{\frac{\sinh(x/S)}{\sinh(x/2S)}\right\} \qquad [7]$$

for an insulating boundary and

$$Z(x, S) = \frac{\rho(x)}{\pi} \int_{1/2S}^{1/S} \tanh(\lambda x)\, d\lambda = \frac{\rho}{\pi x} \ln\left\{\frac{\cosh(x/S)}{\cosh(x/2S)}\right\} \qquad [8]$$

for a conducting boundary. It is important to note in both cases that the probe spacing and the distance to the boundary appear as the ratio x/S. It is this ratio which determines the behavior of the functions.

For the situation where the distance to the boundary is small compared to the probe spacing, *i.e.*, $x/S < 1$, the sinh function may be replaced by its argument whereas the cosh function approaches unity. By making use of these limiting values for small x/S, it is straightforward to show that

$$\lim_{x/S < 1} Z(x, S) = \frac{\rho \ln(2)}{\pi x} \qquad [9]$$

for an insulating boundary and

$$\lim_{x/S < 1} Z(x, S) = 0 \qquad [10]$$

for a conducting boundary. From Eq. [9], it is clear that the idea of a "thin" isolated layer must be phrased in terms of the ratio of the thickness of the layer and the probe spacing. As the probe spacing becomes large compared to the distance to the boundary, the uniform layer may be considered to be "thin." This is important as it places an objective criterion on the use of the idea of thin layers. Equation [10] states for the case of a uniform layer over a conducting boundary that the four-probe resistance approaches zero as the probe separation becomes large compared to the distance to the conducting boundary.

For the situation where $x/S > 1$, the hyperbolic functions contained in Eq. [7] and [8] may be replaced by exponentials of the same argument. Then

$$\lim_{x/S > 1} Z(x, S) = \frac{\rho}{2\pi S} \qquad [11]$$

for both the insulating and conducting boundary conditions. Hence, for $x/S > 1$, the results for both the insulating and conducting boundaries approach the semi-infinite slab result given by Eq. [5]. These results are summarized in Fig. 1, where the scaled four-probe function, $(\pi x/\rho)Z(x, S)$, is plotted for a wide range of x/S for each of the three boundary conditions. For $x/S < 1$, the three functions appear as three separate curves. The conducting boundary result decreases rapidly to zero, while the semi-infinite slab result decreases slowly to zero. In this same region, the insulating boundary result has reached its asymptotic value of ln (2). When x/S is approximately 0.5, the insulating boundary and conducting boundary results begin curving toward the semi-infinite slab results. This curving and merging is finally complete once x/S is approximately 2-3. Beyond this point, all three curves lie on top of each other, as indicated by Eq. [11]. These indicate, once x/S is approximately 2 or greater, that the effects of any boundary (especially an insulating boundary) have been completely removed. This would mean that four-probe resistance measurements made on thick layers, $x/S > 1$, should not be associated with a sheet resistance interpreted in terms of a parallel conduction model, *i.e.*, in terms of a sheet resistance $\Re(x)$, defined by

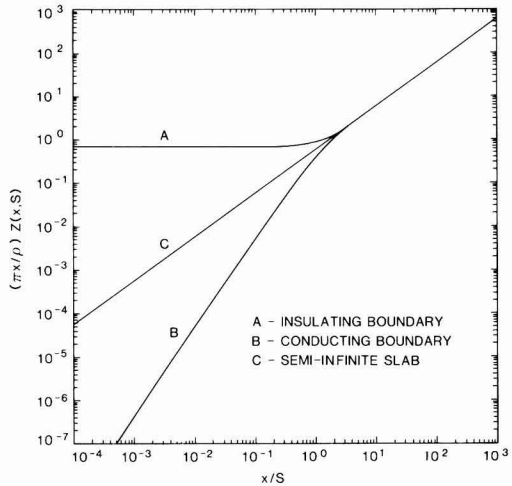

Fig. 1. The four-probe resistance scaled by $(\pi x/\rho)$, *i.e.*, $(\pi x/\rho)Z(x, S)$, is presented for a large range of x/S for several boundary conditions. The curve denoted by A represents the result for an insulating boundary, while the curves denoted by B and C represent the results for a conducting boundary and no boundary (semi-infinite slab), respectively.

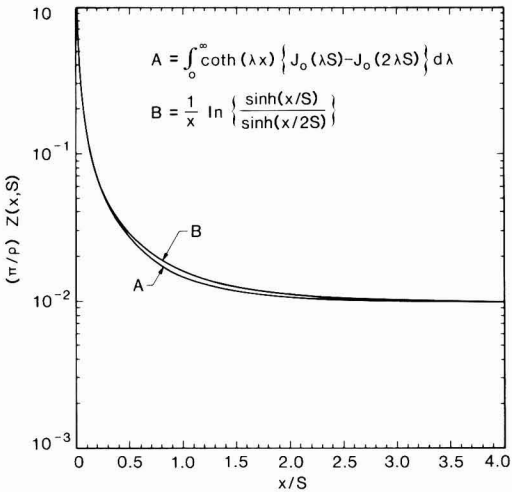

Fig. 2. The four-probe resistance scaled by (π/ρ), $(\pi/\rho)Z(x, S)$, calculated from Eq. [1] and [7], are presented for the case of a uniform resistivity layer over an insulating boundary condition.

$$\Re(x) = \frac{1}{\int_0^x \sigma(x')\,dx'} \qquad [12]$$

Having established the analytical results from the cases of semi-infinite slabs, uniform layers over insulating, or conducting, boundary conditions, what remains to be shown in this section is how well these results agree with the "exact" results obtained from Eq. [1]. Figure 2 contains the results of this comparison for a uniform layer over an insulator. In general, the agreement is very good. In the middle region of x/S values (from about 0.5 up to about 2.0), the maximum difference between the two results is about 10%.

A Two-Layer Structure

A particular example where the equations can be worked out exactly is the two-layer case where the top layer has a larger resistivity than the bottom layer. The resistivities of the bottom and top layers are ρ_1 and ρ_2, respectively. The form of the kernel of the integral is given by

$$A_2(x, \lambda) = \frac{\rho_1 A_1 + \rho_2 \tanh(\lambda x)}{\rho_2 + \rho_1 A_1 \tanh(\lambda x)} \qquad [13]$$

where x is the position of the surface of the top layer and A_1 is the kernel evaluated at the surface of the bottom layer. Introducing the variable q defined as $q = \rho_1/\rho_2$ and expanding the right-hand side of Eq. [13] to terms of order q, leads to the expression

$$A_2(x, \lambda) = (qA_1 + \tanh(\lambda x))(1 - qA_1 \tanh(\lambda x))$$
$$A_2(x, \lambda) = \tanh(\lambda x) + qA_1(1 - \tanh(\lambda x)) + \ldots \qquad [14]$$

Substituting this form for the kernel into Eq. [6] and evaluating the integral leads to the following expression of the four-probe resistance for this particular two-layer structure

$$Z(x, S) = \frac{\rho_2}{\pi x} \ln\left\{\frac{\cosh(x/S)}{\cosh(x/2S)}\right\} + \frac{\rho_1}{\pi x} \ln\{\tanh(x/S) - \tanh(x/2S)\} \qquad [15]$$

Equation [15] represents the four-probe resistance of a two-layer structure and reduces to Eq. [9] and [11] under the appropriate conditions.

Numerical Evaluation of $Z(x, S)$

A numerical integration scheme is required for the evaluation of the $Z(x, S)$ integral in Eq. [6] for the case of a general nonuniform resistivity structure. Two general techniques were used in the evaluation of the integral in Eq. [6]. The first makes use of the trapezoidal-Romberg technique with a 0.005% convergence criterion on the evaluation of the integral. This integration technique was the one which was used previously (5) to evaluate the spreading resistance correction factor integral. The second technique makes use of the nine-point Newton-Cotes method (6) in the evaluation of the integral. In particular, the logarithmic spacing used in Eq. [12] of Ref. (3) was employed. The purpose of using the first technique was to provide for an "exact" evaluation of the $Z(x, S)$ integral in Eq. [6]. The Newton-Cotes technique was investigated as a faster, more efficient, method. For the Newton-Cotes method of evaluation, the four-probe resistance was calculated using the expression

$$Z(x, S) = \frac{\rho(x)}{\pi} \ln(2) \sum_{i=0}^{8} w_{8,i} \lambda_i A(x\lambda_i) \qquad [16]$$

where

$$\lambda_i = \frac{2^{i/8}}{2S} \quad (0 \le i \le 8) \qquad [17]$$

$w_{8,i} = C_i/8$, and where C_i are the Newton-Cotes weighting factors (6). A comparison of the results of the integration performed with the trapezoidal-Romberg technique and with the nine-point Newton-Cotes method indicates that the latter method gives an excellent representation of the integral of Eq. [6]. Hence, for all subsequent analysis, the Newton-Cotes method will be used. The remaining item to be considered focuses upon the comparison of the four-probe resistances as calculated by Eq. [1] and by Eq. [6] (using the Newton-Cotes method).

The purpose of this section is to present the salient features of the calculation of the function $Z(x, S)$ for both "thin" and "thick" layers. As indicated previously, the concepts of "thin" and "thick" do not refer to the absolute layer thicknesses, but depend rather upon the ratio of the layer thickness (or distance to the insulating boundary) to the probe separation. Obviously, for almost all

practical applications, an isolated layer of up to approximately 10 μm may always be considered to be thin. However, the distinction between thin and thick becomes important for the case of a nonuniformly doped layer over a substrate of the same conductivity type. Here, the total thickness of the wafer must be considered to be the depth to the insulating boundary, *i.e.*, the back of the wafer. Typically, this thickness can be several hundred microns and here the ratio x/S may be on the order of or greater than unity.

A number of implant-type resistivity structures were used with an insulating boundary placed up to several microns below the implanted region. This situation was used to simulate the implant into a junction isolating substrate. In these cases, x/S is always much less than unity and the junction-isolated layer formed by the implant is clearly thin in the sense described above. These structures were used to calculate $Z(x, S)$ using Eq. [1] and [6]. The probe spacings used ranged from 25 up to 1000 μm. In all cases, the results of the two techniques were found to be in agreement to within less than 1%. Also, direct evaluation of the sheet resistance showed that the relation between $Z(x, S)$ and the sheet resistance, $\Re(x)$, *i.e.*

$$Z(x, S) = \frac{\ln (2)}{\pi} \Re(x) \qquad [18]$$

was satisfied. This would indicate that the Newton-Cotes technique for the evaluation of $Z(x, S)$ as given by Eq. [6] yields the correct result for a thin, *i.e.*, $x/S < 1$, layer.

The same gaussian-type implant structures were used with the insulating boundary placed at 350 μm below the end of the implant structure. This was meant to simulate the situation which would arise from an implant structure into a substrate of the same conductivity type. As discussed above, the back surface of the wafer is now the insulating boundary condition. For the total thicknesses involved, the calculation should probe the results from the region where $x/S > 1$ down to the region where $x/S < 1$. In addition, the substrate resistivity was changed to emulate the approach to junction-type isolation at the end of the implant distribution. When the Newton-Cotes evaluation of $Z(x, S)$ was used and compared with the results of Ref. (1), the maximum deviation was found to be on the order of 10%. However, deviations of this magnitude were not typical of all structures, nor were they typical of any one structure. In general, deviations of about 1-2% were typical. In particular, deviations of this size were found in the surface region of nearly all the structures considered. Typical comparisons of the four-probe resistance integrals are contained in Fig. 3 for illustrative purposes. The overall quality of the Newton-Cotes results indicates that this computationally simpler form of $Z(x, S)$ presented in Eq. [16] and [17] can be used with confidence and at a substantial reduction in computation time. To illustrate the reduction in computation time, the calculations performed in Ref. (1) (using Eq. [1]) usually took several CPU minutes on a minicomputer (equivalent to at least an hour on a microcomputer). The same calculations using the Newton-Cotes method (Eq. [16] and [17]) take several CPU seconds on a minicomputer and on the order of 15-30s on a microcomputer. In addition, the calibration procedure proposed in Ref. (1) is now accessible as a simple add-on to any spreading resistance correction factor algorithm. This calibration procedure is described in detail in Ref. (1) and is implemented exactly as described there. The important difference resulting from the present work is that the calculation of the four-probe resistance for each value of the probe radius (used in the multilayer analysis of the spreading resistance data) can be performed very quickly even on a microcomputer system.

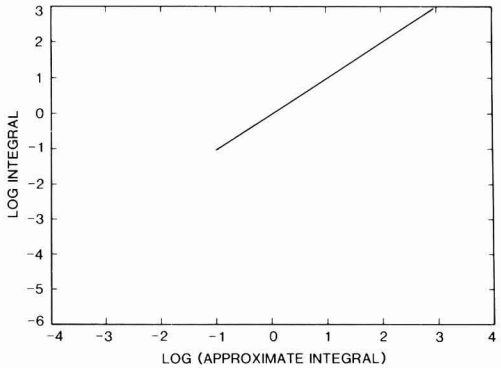

Fig. 3. The four-probe resistance integral as evaluated by the trapezoidal-Romberg method (Eq. [1]) and as evaluated by means of the Newton-Cotes evaluation (Eq. [16]) are plotted against each other in this figure. The data represent a wide range of structures. The data at the lower end represent deviations due to shorting substrates where the four-probe resistance does not provide any useful information.

A listing of the Newton-Cotes evaluation of $Z(x, S)$, written in FORTRAN (but easily translated to other languages), may be obtained from the authors upon request.

Results and Conclusions

A simplified method for evaluating the four-probe resistance has been presented and discussed. The resulting equation for the four-probe resistance involves an integral of $A(x, \lambda)$ over a small interval dictated by the probe spacing. In particular, the larger the value of the probe spacing, the closer the interval is to the origin. In a sense, this signals the importance of the substrate resistivity and the boundary condition as the small λ behavior of the kernel function is dominated by the ratio of the substrate resistivity and the resistivity of the point in question. Analytic expressions have been derived for the cases of a uniform layer over an insulating boundary or a conducting boundary. These expressions have been investigated as a function of x/S. For small values of x/S, the sheet resistance of a uniform layer has been shown to arise for the case of an insulating boundary. For large values of x/S, all three cases have been shown to merge together and provide a caveat in the interpretation of four-probe resistance measurements in terms of a sheet resistance obtained from a laminar conduction model.

A nine-point Newton-Cotes integration scheme has been presented and discussed for the evaluation of the simplified four-probe resistance integral and have been compared with the more complicated methods presented in Ref. (1). Typical differences between the two methods are in the 1-2% range with maximum values on the order of 10%. However, the Newton-Cotes method produces a reduction in computation time down into the region of seconds for both minicomputers and microcomputers. Consequently, the Newton-Cotes technique for evaluating the four-probe resistance can now be readily used in the calibration procedure which was proposed in Ref. (1).

REFERENCES

1. J. Albers and H. L. Berkowitz, *This Journal*, **131,** 392 (1984).
2. H. L. Berkowitz and R. A. Lux, *ibid.*, **126,** 1479 (1979).
3. H. L. Berkowitz and R. A. Lux, *ibid.*, **128,** 1137 (1981).
4. A. D. Wheelon, "Tables of Summable Series and Integrals Involving Bessel Functions," Holden-Day, San Francisco, CA (1968).
5. J. Albers, *Solid-State Electron.*, **23,** 1187 (1980).
6. F. Scheid, "Numerical Analysis," pp. 109-110, McGraw-Hill, New York (1968).

Complete Process Modeling for VLSI Multilayer Structures

Kouichi Sakamoto, Kenji Nishi, Tetsuo Yamaji, Tatsuro Miyoshi, and Shintaro Ushio

Oki Electric Industry Company, Limited, 550-1 Higashiasakawa, Hachioji, Tokyo 193, Japan

ABSTRACT

A new one-dimensional process simulator, ASPREM or advanced SUPREM, has been developed. ASPREM features the capability for multilayer structures and the incorporation of many up-to-date models. In this paper, general features of ASPREM are first described. Then details of many up-to-date models, such as oxidation-enhanced diffusion with or without polysilicon, impurity diffusion in polysilicon and SiO_2, and stress effects to phosphorus diffusion after high dose ion implantation are reported with experimental results. Finally, applications to base-emitter self-aligned technology (BEST) transistors are described, followed by brief concluding remarks.

More than half a decade has already passed since the first process simulators, SUPREM and its extended version, SUPREM-II, were introduced from Stanford University (1, 2). Several process simulators have since been developed from different organizations (3-6). Most of them are designed for simulating two-dimensional impurity profiles, since the lateral diffusion is becoming more important with shrinking minimum pattern size. However, because of mathematical complexities of moving boundary problems, major efforts have been made to solve efficiently the diffusion equation for simplified structures. No great efforts have been made to develop more accurate physical models for multilayer structures. We currently need process simulators for mulitlayer structures which always appear in VLSI devices.

The authors introduced the prototype of multilayer process simulator as early as 1981 (7). Many process models have since been developed and incorporated in this simulator which is currently called advanced SUPREM or ASPREM. Some of the newly developed models are oxidation-enhanced diffusion models of impurities under high concentration or with polysilicon on top of the substrate, diffusion models within silicon dioxide and polysilicon, and stress effects to phosphorus diffusion under various ambients.

Recently, SUPREM-III has been developed by Stanford University as a one-dimensional process simulator to handle multilayer structures (8).Though basic features of ASPREM are similar to those of SUPREM-III, ASPREM excels in such models as impurity diffusion within polysilicon and SiO_2.

In this article, general features of ASPREM are first described. Then, some of the up-to-date process models are reported in detail. Finally, applications to base-emitter self-aligned technology (BEST) transistors (9) are described.

Process Models in ASPREM

General features.—ASPREM can handle multilayer structures including SiO_2, Si_3N_4, and polysilicon. Thickness, dopant profiles, and, in the case of the silicon substrate and polysilicon, sheet resistances can be calculated after each process step. In the case of MOS transistors, threshold voltage can also be calculated with varying back bias voltages.

Basic models for impurity diffusion are based on a vacancy mechanism formulation (10), except that impurities can diffuse by interstitialcy mechansim during oxidation. According to this model, increased charged vacancies account for enhanced diffusion under high concentration of impurities. In the case of phosphorus diffusion, the model developed by Fair *et al.* (11) is used with some modification on the evaluation of stress, which is described later. Recent developments on high concentration diffusion of phosphorus have shown that not vacancies, but self-interstitials or both, account for enhanced diffusion (12, 13). At this stage, however, Fair and co-workers' model is still the only quantitative model which can handle high concentration diffusion of phosphorus.

The oxidation process uses the Deal-Grove model (14). For the heavily doped silicon substrate, the model developed by Ho *et al.* (15, 16) has been implemented in ASPREM to account for the enhanced oxidation rate. Ho and co-workers' model is also used for the oxidation of heavily doped polysilicon, where carrier concentration is replaced by impurity concentration within grains. The ambient-pressure dependence of the oxidation rate is also included. The parabolic growth rate depends linearly on the ambient pressure, whereas the linear growth rate depends on the power of ambient pressure, with the power being less than unity (17). The possible explanation for the nonlinear relationship of the linear growth rate on ambient pressure may exist in atomic-level reaction of oxidants with silicon atoms in the substrate. Details can be found elsewhere (17).

As-implanted impurity profiles are assumed to be a joint-half gaussian distribution for arsenic, phosphorus, and antimony, and a modified Pearson IV distribution for boron in all materials including SiO_2 and Si_3N_4 (10). An exponentially decaying tail is assumed only within the silicon substrate because channeling could occur only within the single cyrstal. In addition to basic elements, ASPREM can handle implantation of compounds such as BF and BF_2 which have gained increasing importance in applications to the formation of a shallow junction in CMOS devices. Here, we assumed that a resulting boron profile is the same as the one in which boron ions are implanted with the artificial energy calculated by mulitplying the mass ratio of boron in the compound to the original implant energy (18). This is reasonable when we assume that, upon entering the substrate, the implanted compound immediately decomposes into its constituting elements, while conserving kinetic energy and momentum.

In the following, some of the process models including oxidation-enhanced diffusion, and impurity diffusion in polysilicon and SiO_2, are described in detail.

Oxidation-enhanced diffusion.—The impurities such as boron and phosphorus diffuse faster in the silicon substrate during oxidation. This phenomenon, called oxidation-enhanced diffusion (OED), has been explained by the excess silicon self-interstitials generated at the oxidizing silicon surface, and depends on generation, recombination, and diffusion of interstitials. Taniguchi *et al.* (19) already reported the practical model of OED in which the increment of the diffusivity due to oxidation, ΔD, is proportional to the power of oxidation rate and decreases exponentially with the depth from the silicon surface. Some of the authors also reached the similar equation for ΔD, except that ΔD depends on the impurity concentration at the oxidizing silicon surface (20), as seen in Fig. 1. Thus, ΔD is expressed as follows

$$\Delta D = \frac{D_0}{1 + a \cdot C_s/n_i} V_{ox}{}^{0.3} \exp\left(-\frac{E_0}{kT}\right) \exp\left(-\frac{x}{L_1}\right) \quad [1]$$

where V_{ox} is the oxidation rate, C_s is the surface impurity concentration, n_i is the intrinsic carrier concentration, E_0 is the activation energy, T is the temperature, k is the Boltzmann constant, x is the depth from the silicon sur-

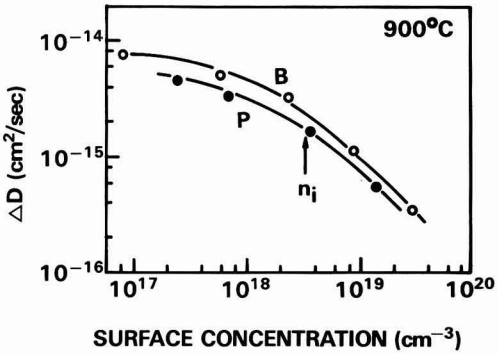

Fig. 1. *D vs.* surface impurity concentration for boron and phosphorus at 900°C.

face, L_1 is the characteristic length, D_0 is the fitting parameter which depends on impurity species, and a is also a fitting parameter which is fixed to 1.8. When C_s is much lower than n_i, Eq. [1] reduces to the one in Taniguchi's model. On the other hand, when C_s is much higher than n_i, ΔD in Eq. [1] becomes zero, indicating that no oxidation-enhanced diffusion occurs.

Oxidation-enhanced diffusion with polysilicon.—When there is a polysilicon layer on top of the silicon substrate, we must take the effects characteristic of polysilicon into account. Since the oxidation rate of polysilicon is similar to that of the silicon substrate, except for the difference in crystal orientation, we can expect that the amount of silicon self-interstitials generated by oxidation at the polysilicon surface is also similar to the one at the single-crystalline silicon surface. However, when silicon self-interstitials diffuse into the substrate through a polysilicon film, they may be easily trapped at polysilicon grain boundaries.

Some of the authors already reported (20) that ΔD of boron and phosphorus in the silicon substrate during oxidation of a polysilicon film on top of substrate is exponentially dependent on the polysilicon thickness, as shown in Fig. 2. Similar results were also obtained by Swaminathan (21). Hence, the complete expression for the impurity diffusion in the substrate during oxidation of polysilicon on top of it can be written as

$$\Delta D = \frac{D_0}{1 + a \cdot C_s/n_i} V_{ox}^{0.3} \exp\left(-\frac{E_0}{kT}\right) \exp\left(-\frac{x}{L_1}\right) \exp\left(-\frac{z}{L_2}\right) \quad [2]$$

where z is the polysilicon thickness and L_2 is the characteristic absorption length of interstitials in polysilicon.

Since the parameter, L_2, depends on the annihilation of silicon self-interstitials at grain boundaries, it depends on the area of grain boundaries and, thus, on the grain size. From Fig. 2, in which the grain size is about 0.1 μm, the obtained length for L_2 is 1100Å, independent of impurity species. We note that this value is similar to Swaminathan's results (1000Å). As for the L_2 dependence on the grain size, g, the following equation is used

$$L_2 = (g'/g \cdot (1/L'^2 - 1/L_1^2) + 1/L_1^2)^{-1/2} \quad [3]$$

where g' is 0.1 μm and L' is the absorption length when $g = g'$ and is 1100Å as already stated. Usually, g is smaller than 10 μm. In that case, it is easy to check whether or not L_2 is linearly dependent on g. Since g is linearly dependent on the reciprocal of grain boundary area and L_2 is expressed as $\sqrt{D_{int}\tau}$ where D_{int} is interstitial diffusivity and τ is a lifetime, linear dependence of L_2 on $\sqrt{g}$ implies that τ is linearly dependent on the reciprocal of grain bondary area. When g approaches infinity, *i.e.*, the polysilicon approaches single-crystalline silicon, L_2 reduces to L_1.

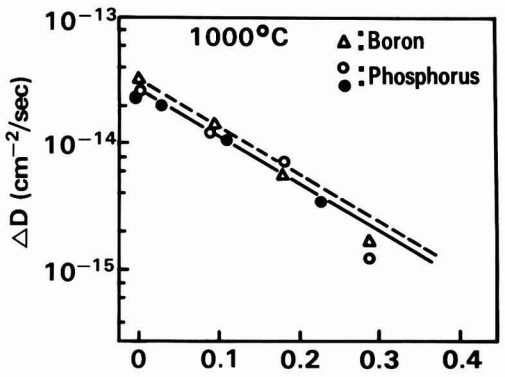

Fig. 2. *D vs.* polysilicon thickness for boron and phosphorus at 1000°C. The data are taken from Ref. (20).

This model has been implemented in ASPREM and has contributed to accurately simulate impurity profiles for polysilicon-source such as a base and an emitter region with doped polysilicon in conventional bipolar devices and BEST.

Stress effects on phosphorus diffuison.—Phosphorus diffusivity usually increases with increasing phosphorus concentration. However, when the phosphorus concentration exceeds several 10^{20} cm^{-3}, the enhancement factor decreases. Fair attributed this to the decrease of vacancy concentration caused by reduced bandgap, ΔE_g, due to the strain (22). However, he did not try to measure the values of strain experimentally, but rather obtained the relationship between ΔE_g and phosphorus concentration by fitting the calculated results to the experimental junction depths.

Using his relationship for the simulation of implanted phosphorus diffusion, we became aware that his estimates of E_g are too large. Sakamoto, one of the authors, and Sasaki tried x-ray double-crystal diffractometry in order to obtain the actual strain values in the phosphorus-implanted wafers after annealing in nitrogen or oxygen ambient (23). Figure 3 shows the actual maximum strain, s_m, *vs.* peak concentration of unprecipitated phosphorus. Also shown is the strain calculated from Fair's relationship by using Wortmann and co-workers' equation between ΔE_g and stress (24) and also the well-established relation of stress and strain. The strain calculated from Fair is larger than actual strain, as expected. It should be noted that the maximum strain depends on annealing ambients. As a best fit equation for s_m in the substrate and peak concentration of unprecipitated phosphorus, C_p, after annealing in nitrogen, the following equation is obtained

$$s_m = 1.9 \times 10^{-24} C_p + 4.2 \times 10^{-14} \sqrt{C_p - 1.3 \times 10^{20}}\ (\text{cm}^{-3}) \quad [4]$$

The first term of the right-hand side alone is the strain after annealing in oxygen. The second term is added when the samples are annealed in nitrogen. More detailed experiments have revealed that the second term decreases inversely proportional to oxygen partial pressure when the samples are annealed in a mixture of nitrogen and oxygen (23). It is beyond the scope of this paper to discuss the difference in the strain after annealing in various ambients. We only note that this could be due to the difference in the type of residual lattice defects in implanted layers after annealing (25).

Equation [4] is used in ASPREM to calculate ΔE_g, which is used to obtain the reduced vacancy concentration and, thus, phosphorus diffusivity. In Fig. 4, we show examples of phosphorus diffusion in nitrogen or oxygen ambients.

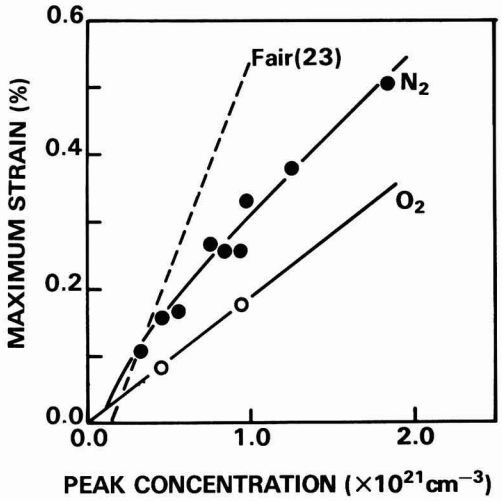

Fig. 3. Maximum strain vs. phosphorus peak concentration after ion implantation and subsequent annealing in nitrogen or oxygen.

Si(100) wafers were implanted with phosphorus at 40 keV with a dose of 1×10^{16} cm^{-2} and were annealed at 900°C for 20 min in nitrogen. After these wafers were subsequently annealed at 900°C for 100 min in nitrogen or oxygen, phosphorus profiles were obtained by secondary ion mass spectroscopy (SIMS). Phosphorus tails extend deeper when annealed in oxygen, showing enhanced diffusion. Oxidation-enhanced diffusion expressed by Eq. [1] alone cannot account for this large enhancement, since ΔD in Eq. [1] is much smaller than phosphorus diffusivity in nitrogen when surface concentration is as high as that shown in Fig. 4. On the other hand, simulation results using ASPREM, which includes strain effects from phosphorus diffusion, are in good agreement with SIMS profiles. Thus, it is concluded that enhanced diffusivity of high concentration phosphorus in oxygen is mainly due to the smaller strain compared with that in nitrogen.

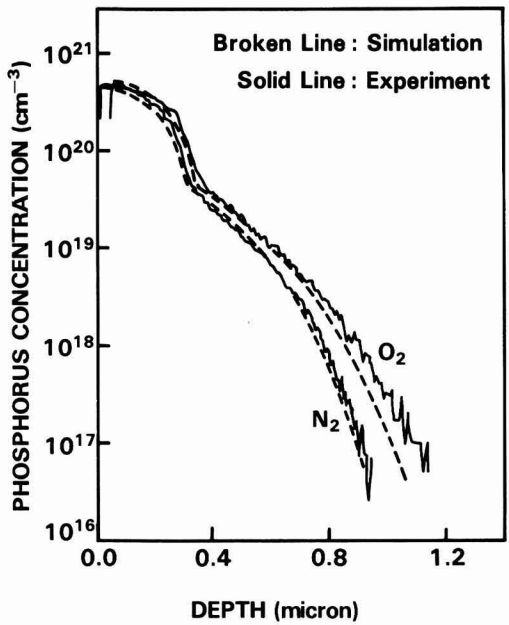

Fig. 4. Experimental and simulated phosphorus profiles after ion implantation and subsequent annealing in nitrogen or oxygen.

Diffusion model in polysilicon.—The polysilicon layer has been found increasingly important in the fabrication of VLSI. The polysilicon layer is used for interconnects, gate electrodes, high valued resistance, and as a diffusion source for shallow junctions. Although several papers have been published for impurity diffusion in polysilicon, there has not been an effective diffusion model (8, 26, 27).

Difficulties in dealing with impurity diffusion in polysilicon arise from the fact that impurities can exist in two regions: within grains and at grain boundaries (21, 26). Another multilayer simulator, SUPREM-III, does not distinguish these two regions for diffusion analysis, although it includes segregation effects for the calculation of carrier concentration. In order to understand the diffusion mechanism in polysilicon, however, it is essential to include the effects of impurity segregation at grain boundaries. We have tried to model impurity diffusion in polysilicon including these effects.

Figure 5 shows a schematic cross section and impurity concentration in polysilicon. In the proposed model, we specify impurity concentration within grains and at grain boundaries independently. The sum of these concentrations gives the total impurity concentration. Impurities in each region can diffuse independently along the X-axis (depth direction). Diffusion along the Y-axis is also taken into account for impurities within grain boundaries by estimating the diffusion length within grains. Impurities in the two regions transport to each other through the interface of grains and their boundaries.

The model is summarized in the equations

$$C = C_i + C_b \quad [5]$$

$$\frac{\partial C_i}{\partial t} = \frac{\partial}{\partial x}\left(D_i \frac{\partial C_i}{\partial x}\right) - h'(mC_{is} - C_b) \quad [6]$$

$$\frac{\partial C_b}{\partial t} = \frac{\partial}{\partial x}\left(D_b \frac{\partial C_b}{\partial x}\right) + h'(mC_{is} - C_b) \quad [7]$$

where t is time, C is total impurity concentration, $C_i(C_b)$ is impurity concentration within grains (at grain boundaries), $D_i(D_b)$ is impurity diffusivity within grains (at grain boundaries), C_{is} is impurity concentration within grains near boundaries, h' is the coefficient for impurity transport through the interface of grains and their boundaries, and m is the segregation coefficient in thermal equilibrium. The value for m is taken from Mei and co-workers model (28) by taking the grain size into account. Equations [6] and [7] show impurity diffusion within grains and at their boundaries, respectively. The impurities at each region can diffuse independently except that they transport each other at the interface of grains and their boundaries. The amount of impurity transport is expressed by the second term of the right-hand side in Eq. [6] and [7]. Since the magnitude of m, which depends on the grain size, affects which of the impurities within

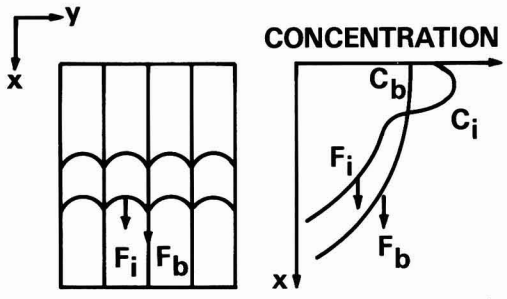

Fig. 5. Schematic model for impurity diffusion in polysilicon. F_i (F_b) and $C_i(C_b)$ are impurity flow and impurity concentration within grains (at grain boundaries), respectively.

Table I. Impurity diffusivities at polysilicon grain boundaries

	Pre-exponential factor (cm^2/s)	Activation energy (eV)
Boron	0.82	2.74
Phosphorus	5.1	2.91
Arsenic	1100	3.53

grains or at grain boundaries is dominant in polysilicon, it is necessary to analyze impurity diffusion independently at each region.

Because of slower diffusion within grains, C_{is} may be different from C_i, which is the average impurity concentration within grains. We use d^*C_i for C_{is} where d is g/minimum (g, $\sqrt{4D_i t}$). d reflects the effects of impurity diffusion within grains along the Y-axis and approaches unity for longer annealing. As the value for h', we usually use a transport coefficient, h, which depends on temperature and impurity species. However, when C_{is} exceeds solid solubility of impurities within grains, impurity flow from grain boundaries into grain insides can be neglected. This is accomplished by equating $h' = 0$ when C_{is} is greater than solid solubility.

D_i is taken as impurity diffusivity within the silicon substrate, since grain insides are single crystalline. On the other hand, we have obtained D_h by fitting the simulated results to the experimental profiles by SIMS. D_h for boron, phosphorus, and arsenic through the temperature range 800°-900°C is shown in Table I, and is three orders of magnitude higher than D_i.

Figure 6 shows simulated and experimental profiles of boron and phosphorus. The samples are ion implanted with a dose of 10^{16} cm^{-2} to the 0.5 μm thick polysilicon with grain size of 0.1 μm, grown on (100) silicon. They are subsequently annealed at 800°C in nitrogen for 46 and 10 min for boron and phosphorus, respectively. In these profiles, we can distinguish surface and tail regions. In the surface region, impurities retain as-implanted profiles, indicating that no significant diffusion occurred. This slower diffusion is limited by impurity diffusion within grains. In the tail region, the profiles shows a gentle slope indicating faster diffusion. This is due to very fast impurity diffusion through grain boundaries. It is noted that impurities at grain boundaries cannot be transported into grain insides, since C_{is} in the tail region exceeds solid solubility. On the other hand, at the diffusion front, the profile shows a relatively steep slope indicating slower diffusion. This is caused by a significant amount of impurities at grain boundaries transported into grain insides. Good agreements between simulated profiles and SIMS profiles show that the proposed model works effectively for impurity diffusion in polysilicon.

It should be pointed out here that simulation of oxidation of heavily doped polysilicon is also significantly improved by employing the proposed model for impurity diffusion in polysilicon. We use Ho and co-workers' oxidation model (15, 16) for polysilicon as well as for the silicon substrate. In their model, the oxidation rate depends on the surface carrier concentration. By assuming that surface carrier concentration is equal to surface impurity concentration within grains, simulated SiO_2 thickness after oxidation of polysilicon agrees well with the experimental result, which also confirms the effectiveness of the proposed model in polysilicon.

Phosphorus diffusion in SiO_2.—While phosphorus diffusion in SiO_2 is important for MOS gate region, its mechanism has remained one of the least-known fields in VLSI processes. There have been a few reports on phosphorus diffusivity in SiO_2 (29, 30), but their values spread by several orders of magnitude. We have extensively studied phosphorus diffusion in SiO_2, and obtained the diffusivity in relation to local phosphorus concentration.

Phosphorus with different doses was implanted to a thick oxide film thermally grown on (100) silicon. The wafers were subsequently annealed in dry oxygen at various temperatures. Figure 7 shows examples of phosphorus profiles measured by SIMS. A flat profile where phosphorus concentration is higher than 10^{20} cm^{-3} indicates that very fast diffusion occurred in this region. On the other hand, a steep slope in the lower phosphorus concentration region indicates slower diffusion. An assumption that phosphorus diffusivity, D_{ox}, depends only on the local phosphorus concentration has led to the following expression for the phosphorus diffusivity

$$D_{ox} = D_{i,ox} + bC_{ox}^n \quad [8]$$

where $D_{i,ox}$ is phosphorus diffusivity in low concentra-

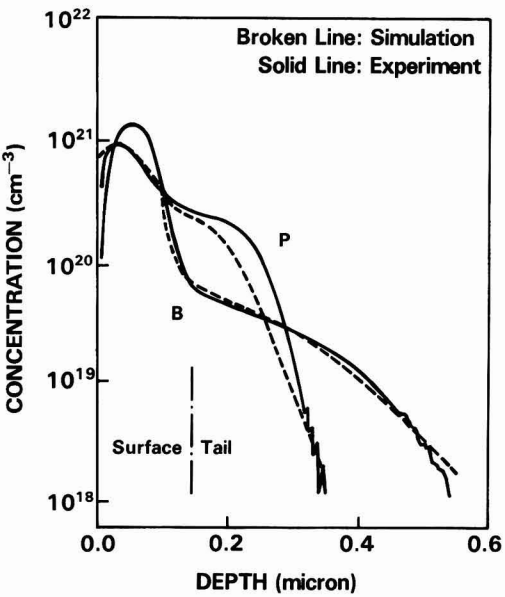

Fig. 6. Boron and phosphorus profiles in polysilicon after ion implantation and subsequent annealing in nitrogen.

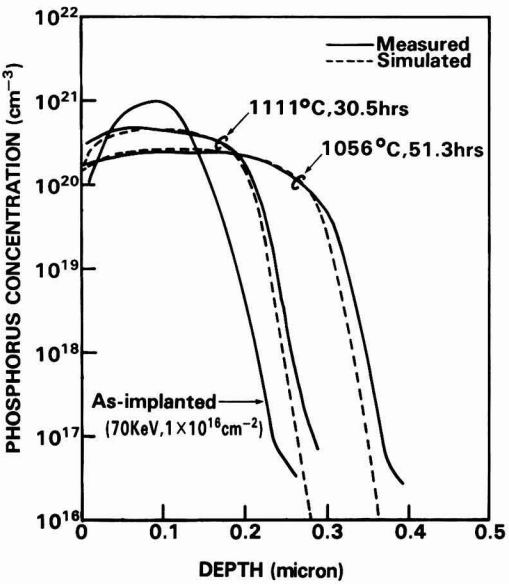

Fig. 7. Experimental and simulated phosphorus profiles in SiO_2 after ion implantation and subsequent annealing in nitrogen.

tion, C_{0X} is phosphorus concentration, and both b and n are fitting parameters. Best fit values for $D_{i,0X}$, b, and n are

$$D_{i,0X} = 3.22 \times 10^{-2} \exp[-4.1 \text{ (eV)}/kT] \text{ cm}^2/\text{s} \quad [9]$$

$$b = 1.13 \times 10^{-20} \exp[-7.1 \text{ (eV)}/kT] \text{ cm}^{6.5}/\text{s} \quad [10]$$

$$n = 1.5 \quad [11]$$

In Fig. 7, simulated results are also shown with experimental profiles. We can see good agreement between simulations and experiments.

The tendency of increasing phosphorus diffusivity with phosphorus concentration in the high concentration region is similar to Ghoshtagore's experiments (30) in which phosphorus was diffused from PSG. The obtained phosphorus diffusivity in thermal SiO_2 in our experiments is also similar to his results. This may indicate that Eq. [8] is generally applicable to phosphorus diffusion in SiO_2.

Examples

In order to demonstrate the capabilities of ASPREM, we show here an example of simulated impurity profiles from a bipolar process called BEST, which was first introduced from OKI as a high performance bipolar technology with extensive use of polysilicon (9).

The schematic cross section of BEST transistors is shown in Fig. 8. The simulated region is at a cross section through emitter and active base region, which constitutes an essential part of BEST transistors. Two different fabrication processes, named A and B, were simulated. A detailed description of process sequence A is as follows: epitaxy, oxidation in oxygen at 900°C for 20 min, BF_2 ion implantation with dose of 1×10^{14} cm^{-2} at 40 keV for base formation, annealing in nitrogen at 900°C for 30 min, SiO_2 etching, polysilicon deposition with thickness of 3000Å, polysilicon oxidation in oxygen at 900°C for 30 min, Si_3N_4 deposition with thickness of 2000Å, annealing in nitrogen at 900°C for 30 min and at 950°C for 50 min, Si_3N_4 and SiO_2 etching, oxidation in dry O_2 at 900°C for 30 min, arsenic implantation for emitter with dose of 1.2×10^{16} cm^{-2} at 60 keV, oxidation in steam at 950°C for 40 min at 0.67 atm, and annealing in nitrogen at 1000°C for 35 min.

Process B is intended to form shallower emitter and base regions, and boron was implanted after polysilicon was deposited. The process sequence is as follows: epitaxy, polysilicon deposition with thickness of 3000Å, oxidation in oxygen at 900°C for 30 min, Si_3N_4 deposition with thickness of 2000Å, annealing in nitrogen at 900°C for 30 min and at 950°C for 50 min, Si_3N_4 and SiO_2 removal, polysilicon oxidation in steam at 950°C for 40 min at 0.67 atm, annealing in nitrogen at 1000°C for 15 min, boron implantation with dose of 4.5×10^{14} cm^{-2} at 70 keV, SiO_2 removal, oxidation in oxygen at 900°C for 30 min, annealing in nitrogen at 950°C for 30 min, arsenic implantation with dose of 1.2×10^{16} cm^{-2} at 60 keV, followed by annealing in nitrogen at 950°C for 60 min.

Figures 9a and b show simulated and experimental impurity profiles for processes A and B, respectively. First of all, it should be pointed out that overall agreement between simulated and measured impurity profiles are satisfactory for both the processes. A kink in the boron profile around a base/emitter junction can be attributed to the retarded diffusivity by the electric field generated from a steep profile of high concentration arsenic and is also simulated well. The electric field also affects the diffusion of phosphorus, which piles up around the base/emitter junction. This is caused by electric-field-driven phosphorus flow against the gradient of phosphorus concentration. Although it is not clear from Fig. 9, we note that the simulated SiO_2 thickness after oxidation of heavily arsenic-doped polysilicon agrees well with the actual thickness, which is a by-product of distinguishing impurities within grains from those at grain boundaries in the polysilicon diffusion model as discussed.

Measured profiles show a pile-up of arsenic at the polysilicon/Si interface. Although this phenomenon needs more study, the effect on the overall arsenic profile can be negligible. We can see a discontinuity of phosphorus profile at the polysilicon/Si interface. This is due to the use of a relatively large segregation coefficient, which

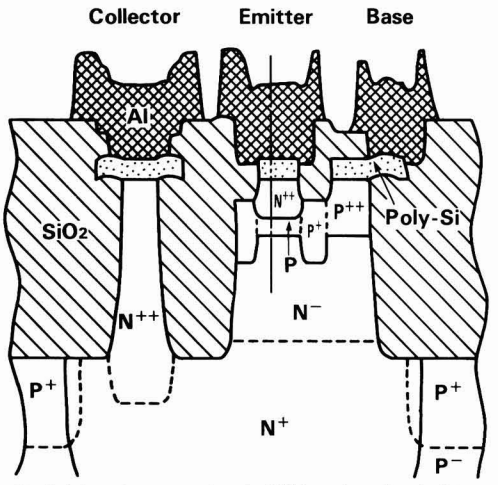

Fig. 8. Schematic cross section of a BEST transistor. Base/emitter region (indicated by a vertical line) is simulated by ASPREM as an example.

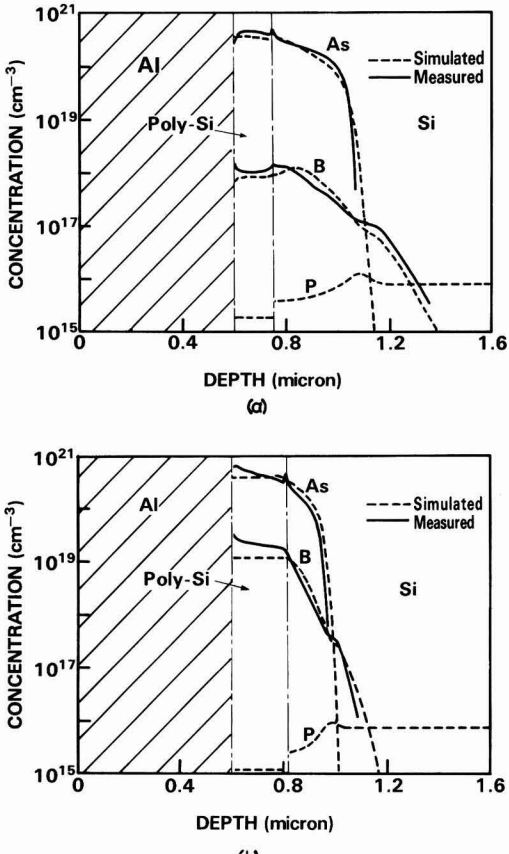

Fig. 9. Experimental and simulated impurity profiles at base/emitter region of a BEST transistor for (a) process A and (b) process B.

has been determined from another experiment on diffusion from a heavily phosphorus-doped polysilicon. Since, in ASPREM, the segregation coefficient is defined as the ratio of impurity concentration in Si to that within grains in polysilicon, interface discontinuity could appear for different process conditions. Further study is necessary for interface phenomena.

Conclusions

A multilayer simulator, ASPREM, has been developed. ASPREM features many up-to-date process models, which include an oxidation-enhanced model with or without polysilicon, strain effects to high concentration phosphorus diffusion, a diffusion model in polysilicon, and a phosphorus diffusion model in SiO_2. The details of these models have been discussed. As a multilayer simulator, ASPREM can be applied to the complete VLSI processes including bipolar and MOS transistors. The effectiveness of ASPREM has been demonstrated by BEST transistors. Especially, accurate simulation of diffusion and oxidation for polysilicon source emitter is worth noting, since similar processes are important for MOS transistors as well.

In addition to being applicable to current processes, ASPREM will serve as an effective tool in developing new multilayer models. This is significant, since multilayer structures are becoming more important, while few established models for multilayers exist.

Acknowledgment

We acknowledge Mr. Kawakatsu for sample preparation of BEST transistors and Mr. Ichikawa for SIMS measurements. We also acknowledge Mr. Higashi and Mr. Mizokami for their encouragement to complete this work.

Manuscript submitted Feb. 19, 1985; revised manuscript received June 4, 1985. This was Paper 411 presented at the Denver, Colorado, Meeting of the Society, Oct. 11-16, 1981.

OKI Electric Industry Company Limited assisted in meeting the publication costs of this article.

REFERENCES

1. D. A. Antoniadis, S. E. Hansen, R. W. Dutton, and A. G. Gonzalez, Stanford Electronics Laboratory Technical Report No. 5019-1, Stanford Electronics Laboratory, Stanford, CA, May 1977.
2. D. A. Antoniadis, S. E. Hansen, and R. W. Dutton, Stanford Electroncis Laboratory Technical Report No. 5019-2, Stanford Electronics Laboratory, Stanford, CA, June 1978.
3. K. Taniguchi, M. Kashiwagi, and H. Iwai, *IEEE Trans. Electron Devices*, **ed-28,** 575 (1981).
4. D. J. Chin, M. K. Kump, H. G. Lee, and R. W. Dutton, *ibid.*, **ed-29,** 336 (1982).
5. C. D. Maldonado, F. Z. Custode, S. A. Louis, and R. Pancholy, *ibid.*, **ed-30,** 1462 (1983).
6. K. A. Salsburg and H. H. Hansen, *ibid.*, **ed-30,** 1004 (1983).
7. K. Nishi, K. Sakamoto, and S. Ushio, Abstract 411, p. 998, The Electrochemical Society Extended Abstracts, Vol. 81-2, Denver, CO, Oct. 11-16, 1981.
8. C. P. Ho, J. D. Plummer, S. E. Hansen, and D. W. Dutton, *IEEE Trans. Electron Devices*, **ed-30,** 1438 (1983).
9. S. Shimizu and H. Kitabayashi, *IEDM Tech. Dig.*, 332 (1979).
10. D. A. Antoniadis and D. W. Dutton, *IEEE Trans. Electron Devices*, **ed-26,** 490 (1979).
11. R. B. Fair and J. C. C. Tsai, *This Journal*, **124,** 1107 (1983).
12. S. M. Hu, P. Fahey, and R. W. Dutton, *J. Appl. Phys.*, **54,** 6912 (1983).
13. K. Nishi and D. A. Antoniadis, *ibid.*, **56,** 3428 (1984).
14. B. E. Deal and A. S. Grove, *ibid.*, **36,** 3770 (1965).
15. C. P. Ho and J. D. Plummer, *This Journal*, **126,** 1516 (1979).
16. C. P. Ho and J. D. Plummer, *ibid.*, **126,** 1523 (1979).
17. L. N. Lie, R. R. Razouk, and B. E. Deal, *ibid.*, **129,** 2828 (1982).
18. R. G. Wilson, *J. Appl. Phys.*, **54,** 6879 (1983).
19. K. Taniguchi, K. Kurosawa, and M. Kashiwagi, *This Journal*, **127,** 2243 (1979).
20. K. Sakamoto, K. Nishi, and T. Miyoshi, Paper presented at the 1982 Symposium on VLSI Technology, Japan Applied Physics Society and IEEE Electronic Device Society, Oiso, Japan, August 1982.
21. B. Swaminathan, Ph.D. Thesis, Stanford University, Stanford, CA (1983).
22. R. B. Fair, *J. Appl. Phys.*, **50,** 860 (1979).
23. M. Sasaki and K. Sakamoto, in "Semiconductor Processing," ASTM STP 850, Diensh C. Gupta, Editor, American Society for Testing and Materials, Philadelphia (1984).
24. J. J. Wortmann, J. R. Hauser, and R. M. Burger, *J. Appl. Phys.*, **35,** 2122 (1964).
25. S. Prussin, *ibid.*, **45,** 1635 (1974).
26. G. Zaeschmar, *ibid.*, **54,** 2281 (1983).
27. A. D. Buonaquisti, W. Carter, and P. H. Holloway, *Thin Solid Films*, **100,** 235 (1983).
28. L. Mei, M. Rivier, Y. Kwart, and R. Dutton, in "Semiconductor Silicon 1981," H. R. Huff and R. J. Kriegler, Editors, p. 1007, The Electrochemical Society Softbound Proceedings Series, Pennington, NJ (1981).
29. M. Ghezzo and D. M. Brown, *This Journal*, **120,** 146 (1973).
30. R. N. Goshtagore, *Thin Solid Films*, **25,** 501 (1975).

Degradation Mechanism of Lightly Doped Drain (LDD) n-Channel MOSFET's Studied by Ultraviolet Light Irradiation

M. Saitoh, H. Shibata, H. Momose, and J. Matsunaga

Toshiba Corporation, Semiconductor Device Engineering Laboratory, 1, Komukai Toshiba-cho, Saiwai-ku, Kawasaki 210, Japan

ABSTRACT

The degradation of lightly doped drain (LDD) n-channel MOSFET's has been investigated in detail making use of ultraviolet light irradiation, and the following results have been obtained. The degradation of the parasitic MOSFET consisting of the gate, the LDD region, and the insulator in between, which dominates the deterioration of the total performance, can be divided into two phases. In the initial phase, the degradation is rapid compared to that in the succeeding phase. The initial phase degradation is due not to surface-state generation, but to electron capturing of the oxide covering the LDD region which has a large number of traps. The quality of the insulator above the LDD region should be carefully controlled in order to make highly reliable LDD MOSFET's.

As the device dimensions are reduced in VLSI's, hot carrier-induced MOSFET degradation becomes a problem of more importance, and many efforts have been made to solve it. Along with the studies on the degradation mechanism (1-15), explorations of highly reliable MOSFET's have also been made (16-22). Consequently, lightly doped drain (LDD) MOSFET has been proposed and widely believed to have high reliability.

Hsu *et al.* (21, 22), however, reported recently that when the LDD MOSFET's and the conventional MOSFET are compared under the same substrate current during the stress, the former shows two orders of magnitude faster deterioration in transconductance (G_m) than the latter. This fact seems to suggest that the LDD MOSFET's have their own degradation mechanism which makes them of little advantage to the conventional MOSFET.

Thus, in order to make highly reliable LDD MOSFET's, the degradation mechanism of the LDD structure should be made clear. For this purpose, we tried to make use of ultraviolet (UV) light irradiation, in which the energy distribution of generated hot carriers is almost independent of the impurity concentration of the LDD region. This fact makes experimental results easy to interpret.

Experimental

The MOSFET's examined were fabricated in a conventional poly-Si gate N MOS process with and without LDD (N^-) region (conventional MOSFET's were cofabricated as a reference).

After gate patterning, gate oxide over source/drain area was etched off by wet chemical etchant. Phosphorus ions were implanted to form N^- diffusion, while no ion implantation was made for the wafers of conventional MOSFET's. Then, so-called postoxidation was done.

A new type sidewall, self-defined polysilicon sidewall (SEPOS), was used at the sidewall making step for LDD Tr's. The process flow for the SEPOS is shown in Fig. 1. Onto the postoxide, LPCVD polysilicon was uniformly deposited, and then the surface was slightly oxidized. SiO_2 reactive ion etching (RIE) followed to leave oxide frame only at the vertical sides of the polysilicon steps. After subsequent polysilicon RIE, the oxide-framed polysilicon sidewall was completed. Then, arsenic ions were implanted to make N^+ regions. The polysilicon sidewall was removed by plasma etching, and CVD SiO_2 was deposited on it. Passivation was made by depositing BPSG (boro-phosphosilicate glass) onto the CVD SiO_2 film.

Surface impurity concentration of channel (boron) and N^+ (arsenic) regions were 1.5×10^{16} and 2×10^{20} cm^{-3}, respectively. That of N^- (phosphorus) regions was varied from 3.8×10^{17} to 3.2×10^{18} cm^{-2} (ion dose from 5×10^{12} to 4×10^{13} cm^{-2}). The effective channel length was 0.5-0.7 μm, and gate oxide thickness 25 nm. The N^- region length ranged from 0.24 to 0.36 μm, depending upon phosphorus concentration.

Samples were irradiated with UV light of 4.63 eV, as shown in Fig. 2, using a commercial EPROM eraser which can erase EPROM data within 10 min. During the irradiation, all the electrodes were connected to the ground potential. All measurements were carried out at room temperature (21°-25°C).

Results

The changes in the linear region of drain current *vs.* gate voltage characteristics after 4h UV light irradiation are shown in Fig. 3 for low (3.8×10^{17} cm^{-3}) and high (1.7×10^{18} cm^{-3}) N^- LDD samples and, for comparison, for a conventional sample. The low N^- one reveals a drastic increase in threshold voltage and a certain amount of decrease in transconductance G_m, while the high N^- one shows only a small decrease in G_m. No change can be observed for the conventional one. Figure 4 compares their subthreshold characteristics. It is found that the low N^- one shows smaller subthreshold slope than the others, and the curve shows parallel shift in the positive direction after irradiation, while no change is observed for the high N^- and the conventional samples.

Figure 5 shows the time dependencies of (*i*) the increase in V_{th} which is defined as V_G giving rise to I_D of 10^{-7}A for $V_D = 0.1$V and (*ii*) the decrease in I_{to} which is defined as I_D for $V_G = V_{th}$(initial) + 3.5V, for the low N^- sample. Here, errors coming from temperature fluctuation are corrected. Two curves drawn in the same frame are the data

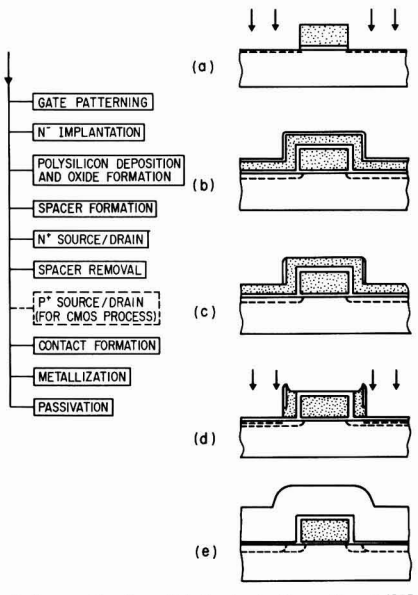

Fig. 1. Process flow for self-defined polysilicon sidewall (SEPOS).

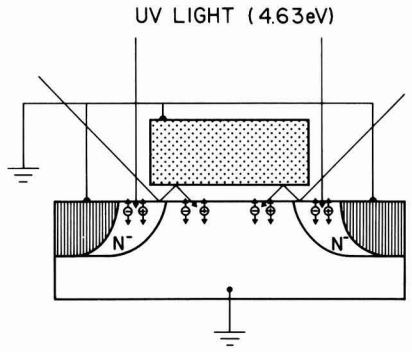

Fig. 2. Ultraviolet (UV) light irradiation using an EPROM eraser

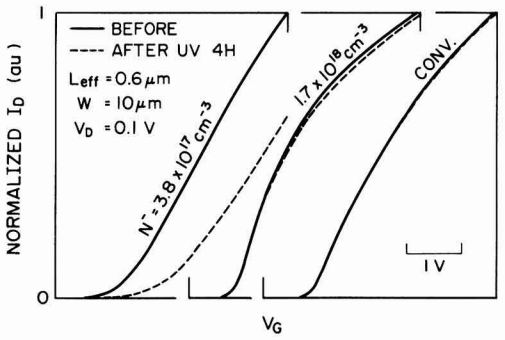

Fig. 3. Changes in the linear region of I_D vs. V_G characteristics caused by 4h UV light irradiation for a 3.8×10^{17} and a 1.7×10^{18} cm^{-3} N^- concentration LDD MOSFET, and a conventional MOSFET.

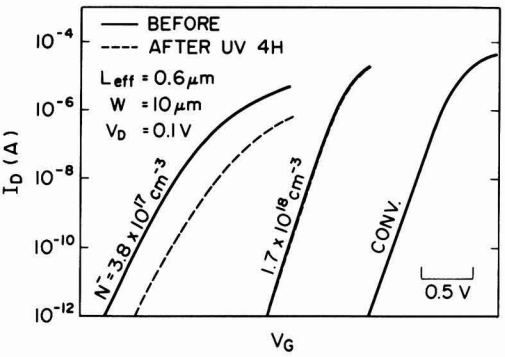

Fig. 4. Replots of the I_D-V_G curves in Fig. 3. Changes in subthreshold characteristics are compared.

for different samples under the same experimental condition. The threshold voltage V_{th} shows rapid increase within 0.5h and comes to clear saturation thereafter, although the saturation values are largely different from sample to sample. On the other hand, I_{to} does not show such clear saturation. Figure 6 shows the results corresponding to Fig. 5 in the case of high N^- sample. The similar behavior is observed, though the V_{th} shift is very small.

Electrical stress was also studied, where the stress condition was $V_D = V_G = 6V$. Transconductance change ΔG_m and threshold voltage shift ΔV_{th} were measured in this case as a function of stress time. Source and drain were reversed during measurements. Samples of 6.9×10^{17}, 1.7×10^{18}, and 3.2×10^{18} cm^{-3} N^- concentrations showed a

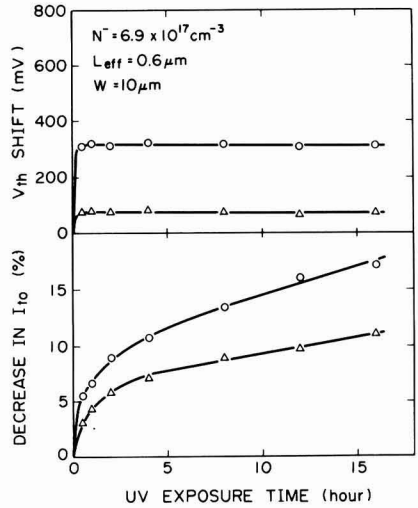

Fig. 5. Increase in V_{th} and decrease in I_{to} as a function of UV exposure time. Here V_{th} is defined as V_G, giving rise to 10^{-7}A of I_D for $V_D = 0.1V$, and I_{to} as I_D for $V_G = V_{th}$(initial) + 3.5V. Concentration of N^- region is 6.9×10^{17} cm^{-3}.

decrease in G_m (which is revealed in Fig. 7) but a negligibly small (< 10 mV) V_{th} shift. In contrast, in the case of 3.8×10^{17} cm^{-3} N^- concentration samples, G_m shows a negligibly small decrease (< 1%) and V_{th} a fairly large increase, as shown in Fig. 8.

In Fig. 9, $\Delta G_m(\Delta I_{to}$ for UV irradiation case) corresponds to the phase 1; initial rapid degradation stages (see Discussion section) are shown as a function of N^- concentration for both UV irradiation and electrical stress cases. In the former case, ΔG_m decreases with N^- concentration, while in the latter case it seems almost independent of the concentration.

Discussion

From the results shown in Fig. 3 and 4, we can derive a model for the LDD MOSFET's and the effect of UV light irradiation (Fig. 10). The features of the model are (i) LDD MOSFET's consist of a main Tr (A in Fig. 10a) and para-

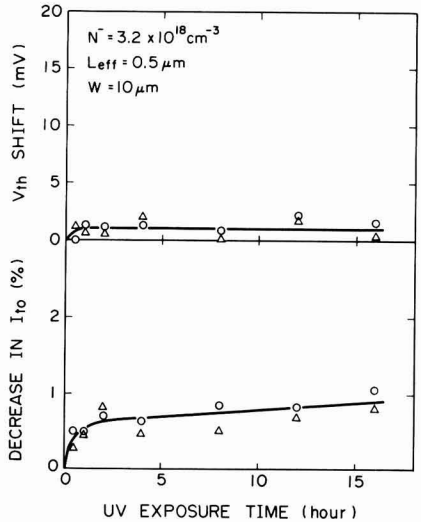

Fig. 6. The same data as in Fig. 5, except for N^- concentration of 3.2×10^{18} cm^{-3}.

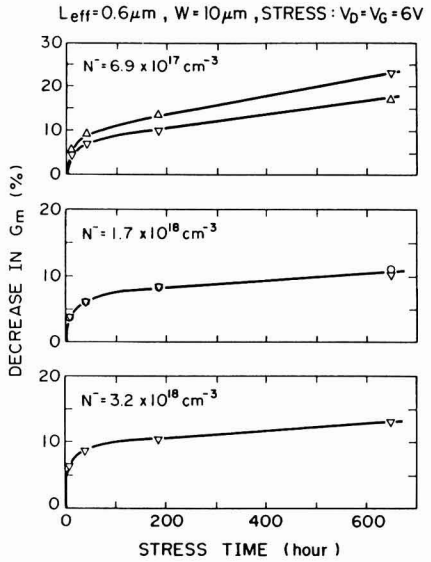

Fig. 7. Decrease in G_m as a function of electrical stress time. Here G_m is defined as $(\partial I_D/\partial V_G)_{max}$. Concentration of N^- region is from 6.9×10^{17} to 3.2×10^{18} cm^{-3}. Threshold voltage shift V_{th} is negligibly small (10 mV) for all cases. Definition of V_{th} is the same as in Fig. 5.

sitic Tr's (B in Fig. 10a) connected in series and (*ii*) UV irradiation brings change only to the parasitic Tr's. This is known from the fact that the conventional sample does not change. It is considered that in the low N^- concentration region (3.8×10^{17} cm^{-3}, for example) the threshold voltage of the parasitic Tr's is higher than that of the main Tr and they dominate the total I_D-V_G characteristics. Therefore, a drastic change including subthreshold curve shift occurs for low N^- sample. In the high N^- concentration region (1.7×10^{18} cm^{-3}, for example), the threshold voltage of the parasitic Tr's is lower than that of the main Tr. So, the expected threshold voltage shift in the parasitic Tr's results only in the transconductance decrease.

The relatively gentle subthreshold slope of the parasitic Tr comes from its depletion-type operation, the process-induced gate oxide thickening there, and/or the relatively large amount of surface states (although the amount does not increase by UV irradiation as shown by the parallel shift of the subthreshold curve). The fact that the parasitic Tr of low N^- concentration before UV irradiation has a threshold voltage higher than that of the main Tr suggests that a certain amount of negative charge (or interface states) exists above the N^- regions when the fabrication process is finished.

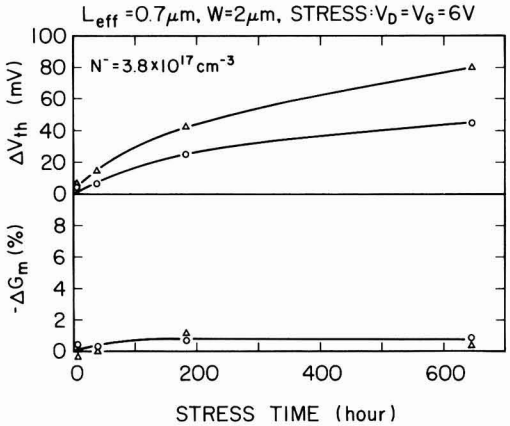

Fig. 8. Threshold voltage shift V_{th} and decrease in G_m as a function of electrical stress time. Concentration of N^- region is 3.8×10^{17} cm^{-3}.

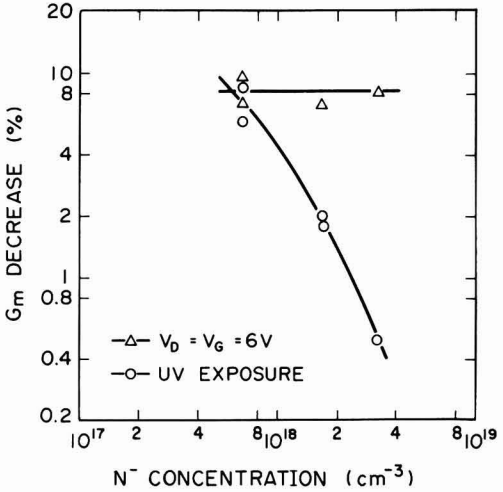

Fig. 9. G_m (for electrical stress) and I_{to} (for UV irradiation) corresponding to phase 1 charge (see text).

As can be seen in Fig. 5, the change in the characteristics of the parasitic Tr can be divided into two phases: phase 1 is the part until the saturation in the V_{th} shift *vs.* UV exposure time curve, and phase 2 is the one after the saturation. Consequently, the total I_D-V_G characteristics of

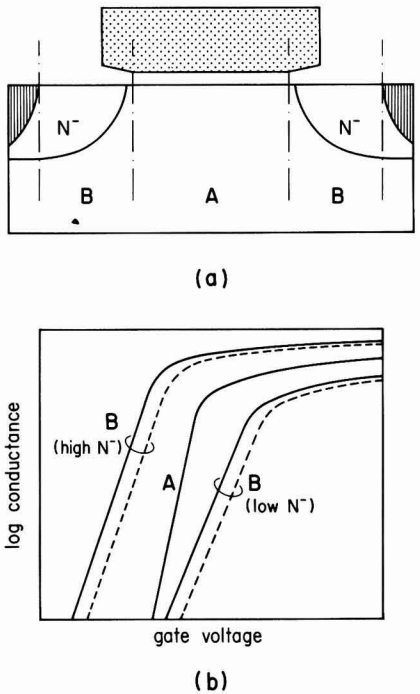

Fig. 10. A model for the LDD MOSFET's and their own degradation mechanism. LDD MOSFET's consist of a main Tr (A) and parasitic Tr's (B). Degradation characteristics of LDD Tr arise from threshold voltage shift of the parasitic Tr('s).

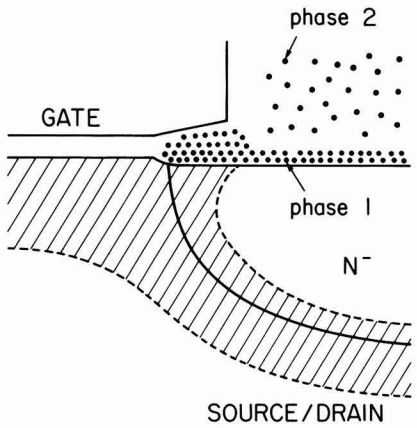

Fig. 11. A model for the location of fixed negative charge which changes the characteristics of parasitic Tr('s).

the LDD Tr in triode operation can be expressed by

$$V_D/I_D = \frac{1}{G_{m1}(V_G - V_{th1})} + \frac{1}{G_{m2}(V_G - V_{th2})} + \frac{1}{G_{m3}(V_G - V_{th3})}$$

where V_{th1}, V_{th2}, and V_{th3} are the threshold voltages of the main Tr, of the parasitic Tr which corresponds to the phase 1 change, and of the parasitic Tr which corresponds to the phase 2 change. By UV light irradiation, V_{th1} does not shift, V_{th2} shifts rapidly and then becomes saturated, and V_{th3} shows relatively slow and long lasting shift. The picture derived from the above discussion is illustrated in Fig. 11. The phase 1 charge may be due to built-in traps in both the oxide grown from Si of N^- region and that grown from phosphorus-doped gate polysilicon during the postoxidation step. On the other hand, the phase 2 charge may be due to those in the LPCVD SiO_2.

Because of the parallel shift of the subthreshold curve (Fig. 4), it is concluded that the V_{th2} shift comes not from surface-states generation, but from increase of trapped negative charges. This is also true for the V_{th3} shift if the barrier height for hot holes is not lowered by the trapped electrons, because the energy of UV light-generated hot holes, 3.51 eV, (4.63 eV photon energy −1.12 eV bandgap of Si) is smaller than the potential barrier of Si-SiO_2 interface for holes (~3.7 eV) (2).

The dependence of ΔG_m on N^- concentration in the UV irradiation case (Fig. 9) is explained by the higher N^- sample's having lower sensitivity to the fixed charge above the N^- region. Here, the amount of the fixed charge is assumed to be the same for all the N^- concentrations, which is reasonable, as the UV light-induced hot carrier injection phenomenon does occur almost equally for all the N^- concentrations. In the electrical stress case, however, the saturation amount of the phase 1 charge seems to increase with the N^- concentration. In other words, it increases with the energy and population of hot carriers injected; higher N^- must lead to higher energy and population (23). This is why ΔG_m for the phase 1 (Fig. 9) seems to have little dependence on N^- concentration. Anyway, essentially the same mechanism seems to dominate the degradation both in the UV irradiation case and the electrical stress case.

Here it should be noted that the 6.9×10^{17} cm^{-3} N^- concentration sample reveals the behavior of low N^- sample (*i.e.*, large V_{th} shift) in UV irradiation case (Fig. 5), while it reveals that of high N^- sample (*i.e.*, negligibly small V_{th} shift) in electrical stress case (Fig. 7). It may come from the difference in the spacial and energetic distribution of hot carriers from UV irradiation to electrical stress. However, we cannot make further comment on this, because the difference from sample to sample is too large, as can be seen in Fig. 5-8.

Finally, we would like to note that the quality of the insulator above the N^- region should be carefully controlled, as well as the impurity profile of the region, in order to make highly reliable LDD MOSFET's.

Conclusions

From a study making use of ultraviolet light irradiation, the following conclusions have been derived.

The LDD n-channel MOSFET has its own degradation mechanism as follows. The oxide covering the LDD (N^-) region, which is grown from the N^- region and the phosphorus-doped gate polysilicon, has a large number of electron traps. Electrons injected into the oxide are captured by these traps and shift the threshold voltage of the parasitic, depletion-type MOSFET in the positive direction. CVD SiO_2 by the side of the gate also has electron traps which play the similar role. The former shift is rapid compared to the latter one and becomes saturated in a certain amount. In contrast, the latter shift is slow and long lasting. This mechanism dominates the degradation of the LDD MOSFET's as far as the energy of hot-carriers is too low to activate another mechanism such as surface-state generation.

Acknowledgments

The authors would like to acknowledge Dr. Y. Nishi and Dr. H. Nozawa for helpful discussion.

Manuscript received April 25, 1985. This was Paper 455 RNP presented at the Cincinnati, OH, Meeting of the Society, May 6-11, 1984.

Toshiba Corporation assisted in meeting the publication costs of this article.

REFERENCES

1. T. H. Ning, P. W. Cook, R. H. Dennard, C. M. Osburn, S. E. Schuster, and H-N. Yu, *IEEE Trans. Electron Devices*, **ed-26,** 346 (1979).
2. P. E. Cottrell, R. R. Troutman, and T. H. Ning, *ibid.*, **ed-26,** 520 (1979).
3. R. B. Fair and R. C. Sun, *ibid.*, **ed-28,** 83 (1981).
4. H. Matsumoto, K. Sawada, S. Asai, M. Hirayama, and K. Nagasawa, *ibid.*, **ed-28,** 923 (1981).
5. Y. Nakagome *et al.*, in "Proceedings of the 14th Conference on Solid State Devices," p. 99, Tokyo (1982).
6. K. K. Ng, G. W. Taylor, and A. K. Sinha, *IEEE Trans. Electron Devices*, **ed-29,** 1323 (1982).
7. E. Takeda and N. Suzuki, *IEEE Trans. Electron Device Lett.*, **edl-4,** 111 (1983).
8. S. Tam, F-C. Hsu, C. Hu, R. S. Muller, and P. K. Ko, *ibid.*, **edl-4,** 249 (1983).
9. E. Takeda *et al.*, *ibid.*, **edl-4,** 329 (1983).
10. K. K. Ng and G. W. Taylor, *IEEE Trans. Electron Devices*, **ed-30,** 871 (1983).
11. S. Horiguchi *et al.*, in "Extended Abstracts, 15th Conference on Solid State Devices and Materials," p. 257, Tokyo (1983).
12. C. Hu, *IEDM Tech. Dig.*, 176 (1983).
13. M-S. Liang *et al.*, *ibid.*, 186 (1983).
14. F.-C. Hsu and S. Tam, *IEEE Trans. Electron Device Lett.*, **edl-5,** 50 (1984).
15. F.-C. Hsu and K.-Y. Chiu, *ibid.*, **edl-5,** 148 (1984).
16. S. Ogura *et al.*, *IEEE Trans. Electron Devices*, **ed-27,** 1359 (1980).
17. P. J. Tsang, S. Ogura, W. W. Walker, J. F. Shepard, and D. L. Critchlow, *ibid.*, **ed-29,** 590 (1982).
18. E. Takeda, H. Kume, T. Toyabe, and S. Asai, *ibid.*, **ed-29,** 611 (1982).
19. E. Takeda, T. Makino, and T. Hagiwara, in "Extended Abstracts, 15th Conference on Solid State Devices and Materials," p. 261, Tokyo (1983).
20. Y. Matsumoto, T. Higuchi, S. Sawada, S. Shinozaki, and O. Ozawa, *IEDM Tech. Dig.*, 392 (1983).
21. F.-C. Hsu and H. R. Grinolds, *ibid.*, 742 (1983).
22. F.-C. Hsu and H. R. Grinolds, *IEEE Trans. Electron Device Lett.*, **edl-5,** 71 (1984).
23. J. M. Pimbley and G. Gildenblat, *ibid.*, **edl-5,** 256 (1984).

Redistribution and Electrical Properties of S Implanted in GaAs

S. S. Chan

Avantek, Incorporated, Santa Clara, California 95051

B. G. Streetman*

Department of Electrical and Computer Engineering, University of Texas at Austin, Austin, Texas 78712

J. E. Baker

Materials Research Laboratory, University of Illinois at Urbana-Champaign, Urbana, Illinois 61801

ABSTRACT

The redistribution and electrical characteristics of ion-implanted S in GaAs have been investigated using secondary ion mass spectrometry (SIMS) and Hall profiling in the dose range of 7×10^{12} to 1×10^{15} cm^{-2}. A significant dose dependence of the redistribution has been observed, with the light dose implants exhibiting the most severe diffusion during annealing. In the presence of a sufficiently high level of Si doping, the redistribution of implanted S is reduced for annealing temperatures up to 800°C, possibly due to the formation of a S-Si complex. Suitably chosen S + Si dual implants show a similar effect and result in a higher activation efficiency than is achievable by Si-only implants of the same total dose. Implantation damage produced by Ar and S dual implants also causes significant redistribution changes. Low levels of damage enhance the S redistribution during annealing, while a high level of damage strongly inhibits it for temperatures up to 900°C. Where the S redistribution is inhibited by damage, however, electrical activity is reduced or lost.

The redistribution of ion-implanted impurities during annealing is often nonfickian, owing to the presence of defects (1-5), self-interstitials (6), or another chemical species which interacts with the implanted impurity (7, 8). Both enhanced and retarded diffusion have been observed as a result. Data from early work show that implanted S in GaAs undergoes considerable redistribution upon annealing, with only fair to poor electrical activation (9-14). More recent studies using capless annealing in an H_2-As_4 atmosphere indicate less redistribution (15, 16), while other reports using dielectric encapsulation (17, 18) continue to describe severe S migration.

The redistribution characteristics of S-only implants for a variety of doses annealed at 900°C with Si_3N_4 encapsulation have been reported by Yeo *et al.* (17). The dose dependence of such redistribution has also been investigated by Wilson *et al.* (19) for a much larger dose range, using SiO_2 encapsulation and a melt-ambient capless technique (20). Some evidence of a possible S-Si interaction which retards the redistribution of S has been pointed out by Yoder (21) in the data of Oakes and Degenford (22). Wilson and Jamba (23) also showed that S redistribution during annealing is much reduced if the GaAs substrate has been preamorphized by equal doses of Ga and As ions before S implantation.

In this work, we examine the possibility of modifying the redistribution of implanted S in the presence of Si and/or excess implantation damage. To that end, the redistribution of implanted S is examined along with its electrical properties as a function of implantation dose and annealing temperature, and Si doping. We study S implants in the presence of implanted Si and Si introduced during crystal growth. An effort is made to isolate the effects of implantation damage by examining Ar coimplants with S which approximate the damage of the corresponding S + Si dual implants.

This study is performed using Si_3N_4 encapsulation, which is the most common encapsulant capable of preventing both Ga and As loss from the sample surface (24, 25).

Experimental Procedures

Redistribution characteristics of S-only implants were studied by performing 250 keV implants into Cr-doped semi-insulating GaAs substrates. Possible S-Si interactions were studied by dual implants of S and Si into Cr-doped GaAs and also by implanting S into Si-doped MBE-grown layers. For studies of the effects of implantation damage on S diffusion, S and Ar dual implants were employed.

The energies of dual implants were chosen such that the projected ranges of the different ion species were approximately the same. All implantations were performed at room temperature with the substrates tilted 7° from the surface normal to avoid channeling effects. Annealing was performed in flowing forming gas using an oxygen-free RF plasma-deposited Si_3N_4 cap (24, 25). The resulting impurity distributions were measured with secondary ion mass spectrometry (SIMS), using a Cs^+ primary beam for S or Si studies, and an O_2^+ beam to detect Cr. Absolute concentrations for implanted species in unannealed samples were obtained by measuring the depths of the sputtered SIMS craters with a Sloan Dektak mechanical stylus and setting the integrated areas of uncalibrated SIMS profiles equal to the implantation doses. These were then used as standards for calibrating the SIMS profiles in annealed samples by comparing matrix and impurity secondary ion counts. Cr concentrations in the GaAs substrates were obtained by comparing with a GaAs sample having a known Cr implant. The accuracies of the depth scales are estimated to be 5-10%, and are limited by the Dektak accuracy, the uniformity of the sputtering rate, and the flatness of the bottom of the craters created. The uncertainties and reproducibility of the impurity concentrations obtained are estimated to be 10-20%, limited by the stability and reproducibility of the impurity ion yields relative to the matrix ion yield, both during a run and between runs. To enhance SIMS sensitivity, S implants were performed in most cases using the ^{34}S isotope to avoid mass interference from O_2 during SIMS analysis, achieving a detection limit of $\sim 10^{15}$ cm^{-3}.

Carrier concentration and mobility profiles were obtained by double ac Hall measurements combined with chemical layer removal (26) using a 1:1:200 mixture of 30% H_2O_2, conc sulfuric acid, and deionized water. The Cr-doped GaAs substrates were first tested for possible type conversion during annealing by implanting with Ar ions and checking for electrical conductivity after a high temperature anneal. No type conversion has been found for these samples after annealing at temperatures up to 800°C. Such conversion does occur at 900°C, however, rendering electrical data for samples annealed at this temperature invalid.

*Electrochemical Society Active Member.

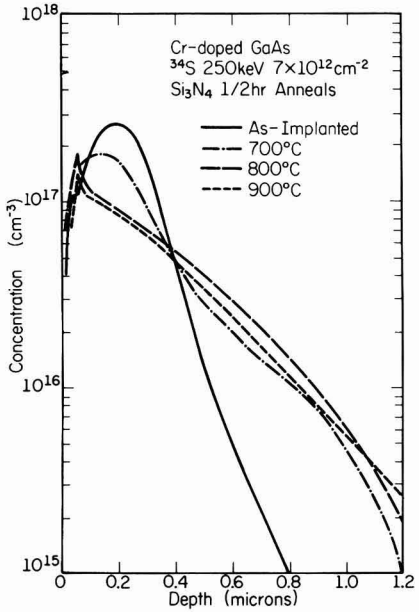

Fig. 1. SIMS profiles of ^{34}S due to a 7×10^{12} cm^{-2} implant and after several anneals.

Results and Discussion

S-only implants.—The redistribution of S-only implants was investigated first as a function of dose and annealing temperature to form a basis for comparison with later dual implants. Shown in Fig. 1 and 2 are the SIMS profiles of S implanted at 250 keV before and after annealing at 700°, 800°, and 900°C for doses of 7×10^{12} and 10^{15} cm^{-2}. The higher dose is above the amorphization threshold of 1.4×10^{14} cm^{-2} as estimated using the critical energy deposition model (27) and Winterbon's energy deposition tables (28). In addition to these doses, data from an intermediate dose (7×10^{13} cm^{-2}) will be discussed.

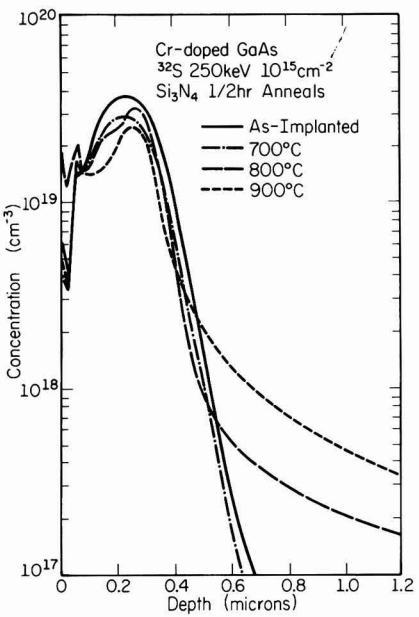

Fig. 2. SIMS profiles of ^{32}S due to a 10^{15} cm^{-2} implant and after annealing.

Two artifacts of SIMS measurements should be noted here and distinguished from the rest of the data. Thin native oxides on the sample surfaces (inevitably formed as a result of atmospheric exposure) usually cause enhancement of secondary ion yields which are quite unrelated to the actual concentrations of the chemical species being monitored (29). Also, a short time is required before the sputtering rate and the rate of primary ion incorporation into the surface reach their steady state. As a result, the matrix and impurity counts have a period of instability corresponding to the first few hundred angstroms of sputtering, and the impurity profiles are discounted in this region.

The unannealed S profiles are skewed for both doses, with peaks occurring at 0.21 ± 0.02 μm. LSS statistics (30, 31) predict a projected range of 0.19 μm and a straggle of 0.07 μm

In the vicinity of their peaks, the unannealed distributions are approximately gaussian with a straggle $\Delta R_p \cong 0.11$ μm. The tail of the distribution is close to gaussian for the high dose case (Fig. 2), but is considerably deeper than gaussian for implants below the amorphization threshold (Fig. 1). Similar observations have been reported for implanted Se in GaAs and have been attributed to interstitial migration in crystalline GaAs during implantation when the total dose does not exceed the amorphization threshold (23).

Upon annealing, dose-dependent redistribution occurs similar to that reported by Wilson *et al* (19). For the low dose implant (Fig. 1), S diffuses significantly at temperatures as low as 700°C. At 800° and 900°C, the as-implanted peak is entirely lost. The tail regions of the profiles (*i.e.*, > 0.9 μm) for all three annealing temperatures are approximately gaussian locally. The diffusion coefficients in these regions are estimated to be 9×10^{-13}, 1×10^{-12}, and 8×10^{-12} cm^2/s for 700°, 800°, and 900°C, respectively. These values are consistent with those reported by Sansbury and Gibbons (10) for implanted S, but are almost an order of magnitude higher than the results of Kendall (32) and two to three orders of magnitude higher than those reported by Young and Pearson (33) for S indiffusion experiments into GaAs substrates. Some S outdiffusion into the Si_3N_4 cap also seems to take place, as evidenced by decreasing integrated areas under the S profiles with increasing annealing temperature. The high dose implant behaves differently (Fig. 2). The as-implanted peak is retained with only minor distortions even after a 900°C anneal. However, penetrating tails are still formed after 800° and 900°C annealing.

Implanted S in the presence of implanted Si.—Possible impurity interactions between S and Si (21, 22) were investigated by using dual implants in which various doses of Si were coimplanted at 220 keV with medium (7×10^{13} cm^{-2}) doses of S at 250 keV. At these ion energies, the range statistics of the two species are approximately the same, and the ratio of S to Si concentrations remains almost constant throughout the as-implanted layer.

Shown in Fig. 3 and 4 are the SIMS profiles of a 7×10^{13} cm^{-2} S implant in the presence of a 3×10^{14} cm^{-2} Si coimplant after annealing at 800° and 900°C, respectively. Shown also for comparison are the corresponding S distributions due to S-only implants and the Cr profiles in the dual implants. It is apparent that the Si coimplant substantially reduces the redistribution of S upon annealing at both temperatures and roughly preserves the as-implanted shape of the S profiles. However, at 900°C a secondary peak appears in the S profile when Si is coimplanted. Little outdiffusion into the cap occurs at either temperature, and SIMS analysis shows that the Si distribution is essentially unchanged by annealing.

Increasing the Si dose in the coimplant experiment to 5×10^{14} cm^{-2} or decreasing it to 1×10^{14} cm^{-2} gives the same general results shown in Fig. 3 and 4. However, further reducing the Si dose to 3.5×10^{13} cm^{-2} brings about

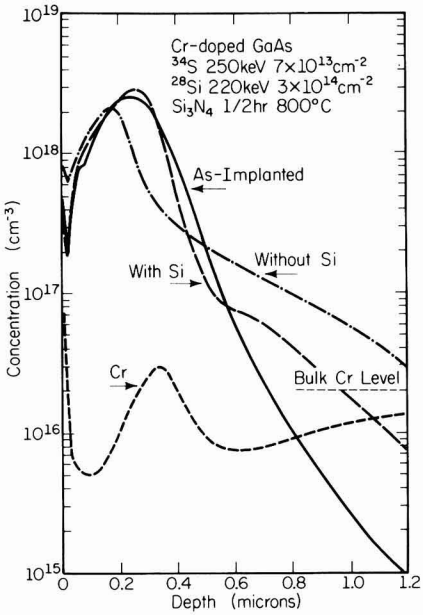

Fig. 3. SIMS profiles of ^{34}S due to a 7×10^{13} cm^{-2}, 250 keV ^{34}S implant in the presence of a 3×10^{14} cm^{-2}, 220 keV ^{28}Si coimplant and annealed at 800°C ("with Si"). Shown also for comparison are the SIMS profile of ^{34}S if the ^{28}Si coimplant is absent ("without Si") and the Cr distribution in the dual implants.

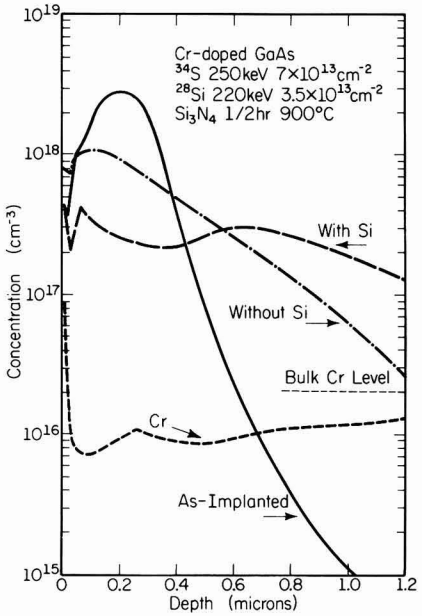

Fig. 5. SIMS profile of ^{34}S due to a 7×10^{13} cm^{-2}, 250 keV ^{34}S implant in the presence of a 3.5×10^{13} cm^{-2}, 220 keV ^{28}Si coimplant and annealed at 900°C ("with Si"). Shown also for comparison are the SIMS profiles of ^{34}S if the ^{28}Si coimplant is absent ("without Si") and the Cr distribution in the dual implants.

an entirely different behavior. With 800°C annealing (not shown), there is somewhat more S redistribution with the Si coimplant than in the case of the S-only implant. At 900°C, however, the Si coimplant causes the implanted S to be largely swept out of the implanted region (Fig. 5).

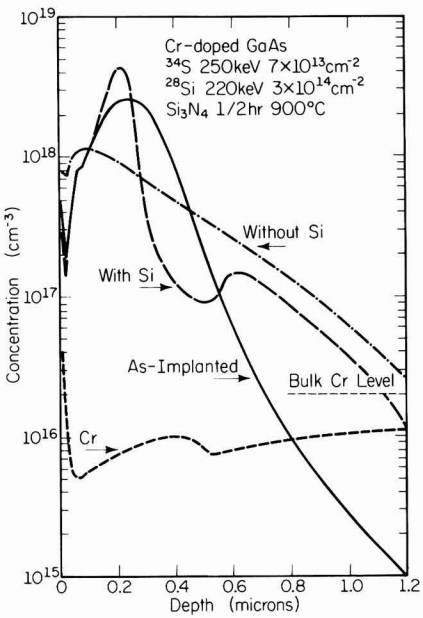

Fig. 4. SIMS profile of ^{34}S due to a 7×10^{13} cm^{-2}, 250 keV ^{34}S implant in the presence of a 3×10^{14} cm^{-2}, 220 keV ^{28}Si coimplant and annealed at 900°C ("with Si"). Shown also for comparison are the SIMS profiles of ^{34}S if the ^{28}Si coimplant is absent ("without Si") and the Cr distribution in the dual implants.

This appears to be a case of very pronounced defect-enhanced redistribution. The Si profile is again found to be little changed by annealing. The as-implanted S profile in Fig. 5 is somewhat narrower and has a peak closer to the surface than the corresponding profile in Fig. 4. The only difference in the implantation conditions is the dose of the Si coimplant, with the lower Si dose (which is not amorphizing) associated with the shallower and narrower as-implanted S profile. We believe that the discrepancy is mostly due to the uncertainties in the depth scale.

The behavior of the Cr originally present in the substrates is found to be quite independent of the dose of the Si coimplant. Annealing at 800°C results in the formation of a local Cr accumulation within a region characterized by extensive Cr depletion (Fig. 3). The local Cr accumulation can be attributed to gettering by residual damage (5), or Cr precipitation at nucleation sites provided by residual damage (4). At 900°C, the local Cr accumulation virtually disappears (Fig. 4 and 5), leaving a broad (~3 μm) Cr depletion region.

S implantation into Si-doped MBE layers.—The above experiments suggest a possible S-Si interaction which slows down the redistribution of S when the Si concentration is sufficiently high. However, to discriminate between the effects of the implanted Si and the additional damage associated with the Si implant, S implants at 250 keV and 7×10^{13} cm^{-2} have been performed into GaAs layers heavily doped with Si ($N_{si} \cong 2.2 \times 10^{18}$ cm^{-3}) during MBE growth. Upon annealing at 800°C (Fig. 6), the S redistribution is clearly less severe than if there is no Si doping, but is still considerable. There is also little outdiffusion of S into the cap (the integrated S concentration is 6×10^{13} cm^{-2}). The diffusion tail in this case is almost exponential, which is consistent with the view that fast diffusing S is slowed by trapping (34, 35) in the presence of Si doping. However, when the annealing temperature is raised to 900°C, the S redistribution is not inhibited by the Si doping.

Influence of Si on the S profile is not observed when the Si doping in the MBE layer is reduced to 1×10^{18}

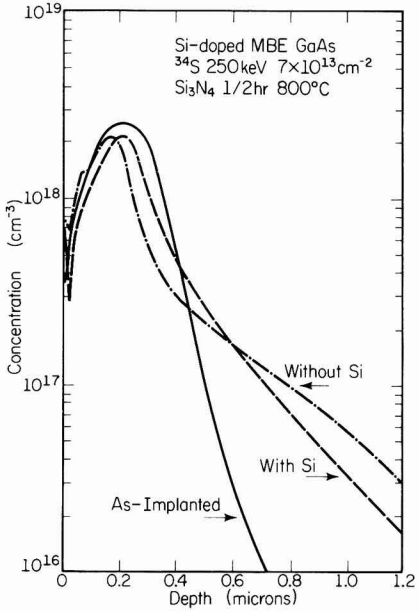

Fig. 6. SIMS profiles of ^{34}S due to a 7×10^{13} cm^{-2} ^{34}S implant into heavily Si-doped ($N_{el} \simeq 2.2 \times 10^{18}$ cm^{-3}) MBE GaAs annealed at 800°C ("with Si"). Shown also for comparison is the SIMS profile of ^{34}S if the Si doping is absent ("without Si").

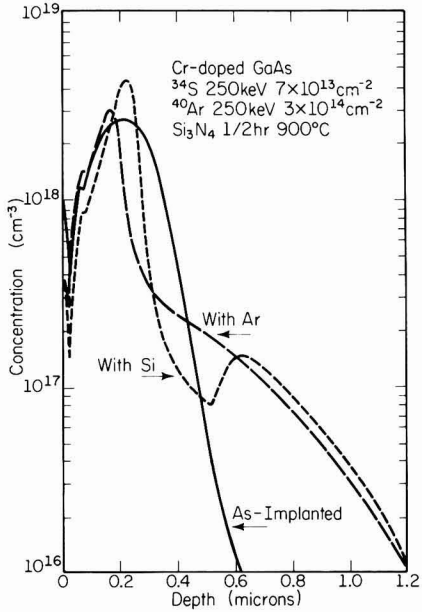

Fig. 7. SIMS profile of ^{34}S due to a 7×10^{13} cm^{-2}, 250 keV ^{34}S implant in the presence of a 3×10^{14} cm^{-2}, 250 keV ^{40}Ar coimplant and annealed at 900°C ("with Ar"). Shown also for comparison is the SIMS profile of ^{34}S due to the same implant in the presence of a 3×10^{14} cm^{-2}, 220 keV ^{28}Si implant annealed at the same temperature ("with Si").

cm^{-3}. This supports the view that the S-Si interaction is a short-ranged one, such as the formation of a nearest neighbor complex as suggested by Yoder (21). Such a S-Si complex may be a slower diffuser than S because of a large physical size or because Si itself has a very low diffusivity in GaAs. At sufficiently high temperatures, such complexes are expected to break up. This is apparently the case for the 900°C anneals observed here, in which S redistribution is not strongly slowed by the presence of Si.

S and Ar dual implants.—The results on S-implanted MBE layers suggest that the reduced redistribution of implanted S at 900°C observed in the case of Si coimplants (Fig. 4) must involve factors other than Si doping. It is therefore useful to investigate the role of implantation damage in such redistribution. To simulate the damage due to the Si implants, Ar was coimplanted with S at 250 keV to the same doses as the Si coimplants discussed above. In the case of a 7×10^{13} cm^{-2} S implant and a 3×10^{14} cm^{-2} Ar coimplant, the extent of S redistribution after 800°C annealing is observed to be somewhat less than if a Si coimplant had been used. When the annealing temperature is raised to 900°C, an approximately gaussian tail appears (Fig. 7) which largely coincides with the Si coimplant case, but without the secondary peak observed in Fig. 4.

For the same S dose (7×10^{13} cm^{-2}), when the dose of the Ar coimplant is raised to 5×10^{14} cm^{-2}, very little S redistribution is observed for 800°C annealing. At 900°C, somewhat more redistribution is observed, but it is much less than in S-only implants and somewhat less than in S + Si dual implants. Again, the secondary peak observed for Si coimplants does not occur. When the dose of the Ar coimplant is lowered to 3.5×10^{13} cm^{-2}, defect-enhanced redistribution is observed, similar to the corresponding low dose Si coimplant (Fig. 5).

Electrical properties.—Unlike Column IV dopants such as Si, S is not amphoteric and may therefore be capable of yielding heavier n-type doping in high dose implantations. Of particular interest are the electrical properties of S-only implants and the combinations of S + Si and S + Ar dual implants where the redistribution of S is inhibited.

Figure 8 shows carrier concentration and mobility profiles due to a 7×10^{13} cm^{-2} (medium dose) S implant at 250 keV into Cr-doped GaAs, annealed at 800°C. Shown also for comparison is the atomic S distribution as measured by SIMS. It is apparent that activation efficiencies and carrier mobilities (~4000 cm^2/V-s) are high in the tail

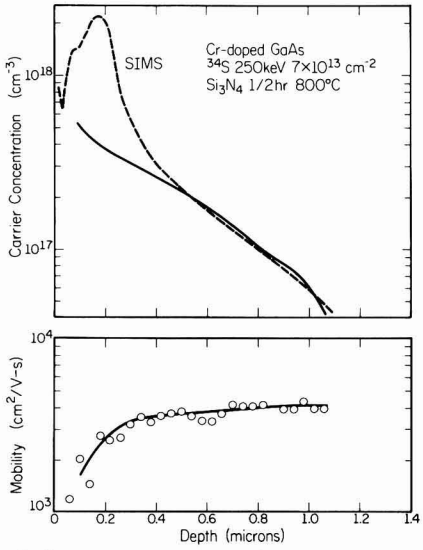

Fig. 8. Carrier concentration and mobility profiles due to a 7×10^{13} cm^{-2} ^{34}S implant at 250 keV, annealed at 800°C. The SIMS profile is also shown for comparison.

of the atomic distribution. However, in the vicinity of the SIMS peak, a substantial fraction of the implanted S is electrically inactive and the carrier mobilities are also low relative to the active electron concentration. While little published data are available concerning the solid solubility of S in GaAs at 800°C, electron concentrations as high as 3×10^{18} cm^{-3} have been obtained by H_2S doping during VPE growth at 750°C (36). Group VIA elements (S, Se, Te) are known to form electrically inactive complexes or precipitates at high concentrations, but this does not happen until the active electron concentration exceeds $\sim 1 \times 10^{18}$ cm^{-3} (37, 38). Apparently, the low activation in the vicinity of the SIMS peak is due to residual damage remaining after the 800°C anneal. The overall doping efficiency after correcting for outdiffusion into the cap is 36%.

When the S dose is lowered to 7×10^{12} cm^{-2}, the carrier concentration profile after an 800°C anneal assumes a shape similar to the corresponding SIMS profile (shown in Fig. 1), and carrier mobilities are relatively high (~3700 cm^2/V-s) throughout. In contrast, raising the S dose to 10^{15} cm^{-2} results in electrical activity only in the tail region of the atomic profile, with a maximum electron concentration of $\sim 4 \times 10^{17}$ cm^{-3}. The overall activation is ony 2.3%. This is consistent with an increasing amount of residual damage in the vicinity of the SIMS peak as the dose is increased. However, other factors may also be involved as discussed below.

Shown in Fig. 9 are the carrier concentration and mobility profiles due to a dual implant of 7×10^{13} cm^{-2} S at 250 keV and 3×10^{14} cm^{-2} Si at 220 keV, annealed at 800°C. Shown also for comparison (dashed line) is the carrier concentration profile due to a 3.7×10^{14} cm^{-2} Si-only implant at 220 keV annealed at the same temperature. SIMS profiles presented in Fig. 3 indicate that the redistribution of S in this case is reduced in the presence of the Si coimplant. Figure 9 shows also that the activation efficiency of the dual implant is higher than that of a Si-only implant of an equivalent dose. The peak electron concentration due to the dual implant is also 45% higher (1.6×10^{18} cm^{-3} *vs* 1.1×10^{18} cm^{-3}). A surface inactive layer of 0.25 μm exists in both cases and is presumably due to incomplete lattice recovery from implantation damage. This dual implant can be used to achieve a higher peak electron concentration and lower sheet resistivity than is obtainable by Si implantation alone, without encountering the problems caused by the high diffusivity of S-only implants. The improved n-type activation may result from S preferentially occupying As sites, thus forcing more of the Si to occupy Ga sites where they act as donors.

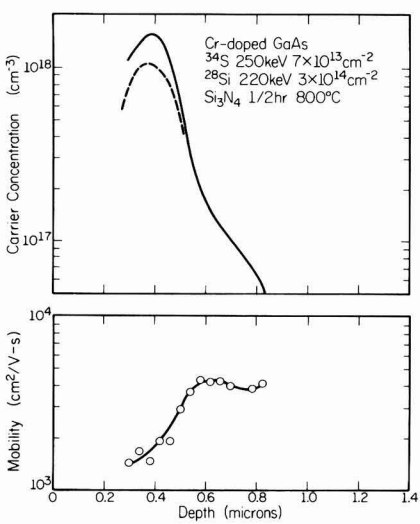

Fig. 9. Carrier concentration and mobility profiles due to a dual implant of 7×10^{13} cm^{-2} ^{34}S at 250 keV and 3×10^{14} cm^{-2} ^{28}Si at 220 keV annealed at 800°C. The dashed line is the carrier concentration profile due to a 3.7×10^{14} cm^{-2} single ^{28}Si implant at 220 keV annealed at the same temperature.

While SIMS profiles indicate that S + Ar dual implants in which the Ar dose in amorphizing are very effective in inhibiting S redistribution, no measurable electrical activity is detected for these dual implants after an 800°C anneal. The redistribution of Cr in these cases is very similar to those shown in Fig. 3 and 4, and is therefore quite insufficient to result in complete compensation of the implanted S. While the degree of recovery of the GaAs lattice achievable after high dose Ar implants is also in question, the following experiment showed that additional factors are involved. The experiment consisted of amorphizing a Cr-doped GaAs substrate with a 5×10^{14} cm^{-2} Ar implant and then annealing it for 15 min (instead of the usual 30 min) with Si_3N_4 encapsulation. The cap was removed and the partially annealed sample implanted with 7×10^{13} cm^{-2} S at 250 keV. Annealing was again performed with a second nitride cap at 800°C for an additional 15 min. The implantation damage associated with the amorphizing Ar implant was therefore annealed for a total time of 30 min, while the damage associated with the S implant was annealed for only 15 min. Electrical profiling showed that in this case the implanted layer recovered sufficiently to give a significant peak carrier concentration ($\sim 5 \times 10^{16}$ cm^{-3}) with a relatively high mobility (2000-4000 cm^2/V-s). It appears, therefore, that the total lack of electrical activity is only associated with annealing implanted S in the presence of a very large density of defects (as found in an amorphized substrate). This may occur through the formation of thermally stable but electrically inactive complexes which are too large to diffuse rapidly. This is also consistent with the observation that, in the case of high dose (1×10^{15} cm^{-2}) S-only implants, very low concentrations of carriers are found in the vicinity of the peak of the S distribution, where a similar mechanism may occur due to the presence of a high density of implantation damage.

Summary and Conclusions

The redistribution characteristics of ion-implanted S in GaAs have been investigated and found to be strongly affected by implantation damage and Si doping. In general, a high density of implantation damage inhibits the redistribution, while a low level of damage enhances it. As a result, implanted S profiles after annealing are characterized by relatively little change in the vicinity of the implant peak (for sufficiently high doses) and the formation of penetrating tails away from the peak due to defect-enhanced redistribution. The presence of Si doping in a sufficiently high concentration slows the redistribution of S for temperatures up to 800°C, possibly by the formation of a S-Si complex. Above 800°C, the complexing effect of Si is no longer sufficient to inhibit S redistribution.

In S + Si dual implants using a medium dose (7×10^{13} cm^{-2}) of S and a larger dose of Si, both the Si and the additional implantation damage due to the Si coimplant have a part in inhibiting redistribution of S during annealing. The secondary peak in the S profile after a 900°C anneal in this case (Fig. 4) is possibly due to a complex interaction between Si trapping, inhibited S redistribution in regions of heavy implantation damage, and enhanced redistribution in regions of lower level damage. Christel and Gibbons (39) have presented calculations which show that local stoichiometric disturbances due to unequal recoil of Ga and As can result in regions of excess As, followed by a deeper region of excess Ga, with a transition region in between. It is clear that Ga and As vacancies affect impurity diffusion; there is also experimental evidence that the Ga divacancy plays a significant role in aiding the diffusion of S in crystalline GaAs (33). Hence, the anomalous redistribution evident in Fig. 4 and 7 may involve such local stoichiometric imbalances. It is conceivable that locally enhanced out-diffusion of S from

a particular region (due to stoichiometric imbalances or otherwise) may result in a local minimum in the S profile and an apparent S buildup in adjacent regions, as is indicated in these figures.

The electrical activation of single S implants after 800°C annealing is fair for low and medium dose implants and poor for high dose implants. Activation is especially low near the peaks of medium and high dose implants where implantation damage is considerable. The level of damage required to prevent significant S redistribution during annealing will also prevent it from becoming electrically active. Apparently, annealing under these conditions produces thermally stable but electrically inactive S-defect complexes which do not diffuse significantly. In contrast, suitably chosen S + Si dual implants both inhibit the redistribution of S (up to 800°C) and result in a higher activation efficiency than is achievable by high dose Si-only implants of the same total dose. In this case, S implantation can be advantageously applied to achieve high donor concentrations without significant S migration. However, the results presented here indicate that such improvements exist in a rather narrow range of coimplant conditions and that residual defects in the surface layer remain after annealing.

Acknowledgment

The authors wish to thank H. Morkoc and T. J. Drummond of the Coordinated Science Laboratory and Department of Electrical Engineering, University of Illinois at Urbana-Champaign, for growing the MBE layers used in this work. This work was supported by the Joint Services Electronics Program under Contract N00014-79-C-0424, the Office of Naval Research under Contract N00014-76-C-0806, and the National Science Foundation under Grant DMR-80-20250.

Manuscript submitted Feb. 22, 1985; revised manuscript received July 2, 1985.

The University of Texas assisted in meeting the publication costs of this article.

REFERENCES

1. C. W. Farley and B. G. Streetman, *J. Electron. Mater.*, **13,** 401 (1984); also, *This Journal*, **131,** 946 (1984).
2. A. Lidow, J. F. Gibbons, V. R. Deline, and C. A. Evans, Jr., *Appl. Phys. Lett.*, **32,** 149 (1978).
3. B. J. Masters and E. F. Gorey, *J. Appl. Phys.*, **49,** 2717 (1978).
4. V. Eu, M. Feng, W. B. Henderson, H.B. Kim, and J. M. Whelan, *Appl. Phys. Lett.*, **37,** 473 (1980).
5. P. K. Vasudev, R. G. Wilson, and C. A. Evans, Jr., *ibid.*, **36,** 837 (1980).
6. E. B. Stoneham and J. F. Gibbons, in "Ion Implantation in Semiconductors," S. Namba, Editor, p. 57, Plenum Press, New York (1975).
7. A. J. N. Houghton and B. Tuck, *Solid-State Electron.*, **25,** 441 (1982).
8. P. N. Favennec, M. Gauneau, H. L'Haridon, B. Deveaud, C. A. Evans, Jr., and R. J. Blattner, *Appl. Phys. Lett.*, **38,** 271 (1981).
9. J. M. Woodcock, J. M. Shannon, and D. J. Clark, *Solid-State Electron.*, **18,** 267 (1975).
10. J. D. Sansbury and J. F. Gibbons, *Rad. Eff.*, **6,** 269 (1970).
11. R. G. Hunsperger and O. J. Marsh, *ibid.*, **6,** 263 (1970).
12. F. H. Eisen and M. B. Welch, in "Ion Implantation in Semiconductors 1976," F. Chernow, J. A. Borders, and D. K. Brice, Editors, p. 97, Plenum Press, New York (1977).
13. M. Fujimoto, H. Yamazaki, and T. Honda, in "Ion Implantation in Semiconductors 1976," F. Chernow, J. A. Borders, and D. K. Brice, Editors, p. 89, Plenum Press. New York (1977).
14. H. Müller, J. Gyulai, J. W. Mayer, F. H. Eisen, and B. Welch, in "Ion Implantation in Semiconductors," S. Namba, Editor, p. 19, Plenum Press, New York (1975).
15. R. M. Malbon, D. H. Lee, and J. M. Whelan, *This Journal*, **123,** 1413 (1976).
16. H. Kanber, M. Feng, V. K. Eu, R. C. Rush, and W. B. Henderson, *J. Electron. Mater.*, **11,** 1083 (1982).
17. Y. K. Yeo, Y. S. Park, and R. Kwor, *J. Appl. Phys.*, **53,** 1815 (1982).
18. R. Kwor, Y. K. Yeo, and Y. S. Park, *ibid.*, **53,** 4786 (1982).
19. R. G. Wilson, D. M. Jamba, V. R. Deline, C. A. Evans, Jr., and Y.S. Park, *ibid.*, **54,** 3849 (1983).
20. C. L. Anderson, K. V. Vaidyanathan, H. L. Dunlap, and G. S. Kamath, *This Journal*, **127,** 925 (1980).
21. M. N. Yoder, in "Semi-Insulating III-V Materials," G. J. Rees, Editor, p. 281, Nottingham, England (1980).
22. J. G. Oakes and J. E. Degenford, GaAs Monolithic Microwave Subsystem Technology Base Report N00014-78-C-0268, Westinghouse Electric, Pittsburgh, PA (1980).
23. R. G. Wilson and D. M. Jamba, *Appl. Phys. Lett.*, **39,** 715 (1981).
24. K. V. Vaidyanathan, M. J. Helix, D. J. Wolford, B. G. Streetman, R. J. Blattner, and C. A. Evans, Jr., *This Journal*, **124,** 1781 (1977).
25. M. J. Helix, K. V. Vaidyanathan, B. G. Streetman, H. B. Dietrich, and P. K. Chatterjee, *Thin Solid Films*, **55,** 143 (1978).
26. W. V. McLevige, P. K. Chatterjee, and B. G. Streetman, *J. Phys. E*, **10,** 335 (1977).
27. M. Lin, *Electron. Lett.*, **14,** 695 (1978).
28. K. B. Winterbon, "Ion Implantation Range and Energy Deposition Distributions," Vol. 2, IFI/Plenum Publishing Corporation, New York (1975).
29. C. A. Andersen, *Int. J. Mass. Spectrom. Ion Phys.*, **2,** 61 (1969).
30. J. Lindhard, M. Scharff, and H. Schiott, *Mat. Fys. Medd. Dan. Vid. Selsk.*, **33,** 1 (1963).
31. J. F. Gibbons, W. S. Johnson, and S. W. Mylroie, "Projected Range Statistics, Semiconductors and Related Materials," 2nd ed. Dowden, Hutchinson and Ross, Stroudsburg, PA (1975).
32. D. L. Kendall, in "Semiconductors and Semimetals," Vol. 4, R. K. Willardson and A. C. Beer, Editors, p. 163, Academic Press, New York (1968).
33. A. B. Y. Young and G. L. Pearson, *J. Phys. Chem. Solids*, **31,** 517 (1970).
34. T. Hirao, K. Inoue, S. Takayanagi, and Y. Yaegashi, in "Ion Implantation in Semiconductors 1976," F. Chernow, J. A. Borders, and D. K. Brice, Editors, p. 1, Plenum Press, New York (1977).
35. J. A. Davies and P. Jespersgard, *Can. J. Phys.*, **44,** 1631 (1966).
36. H. Poth, H. Bruch, M. Heyen, and P. Balk, *J. Appl. Phys.*, **49,** 285 (1978).
37. H. C. Casey, Jr., and M. B. Panish, "Heterostructure Lasers, Part B: Materials and Operating Characteristics," p. 98, Academic Press, New York (1978).
38. L. J. Vieland and I. Kudman, *J. Phys. Chem. Solids*, **24,** 437 (1963).
39. L. A. Christel and J. F. Gibbons, *J. Appl. Phys.*, **52,** 5050 (1981).

Furnace and Rapid Thermal Annealing of P^+/n Junctions in BF_2^+-Implanted Silicon

M. E. Lunnon and J. T. Chen

Philips Research Laboratories, Signetics Corporation, Sunnyvale, California 94086

J. E. Baker

Materials Research Laboratory, University of Illinois, Urbana, Illinois 61801

ABSTRACT

Shallow p-n diodes with junction depths between 0.15 and 0.3 μm have been fabricated by rapid thermal and furnace annealing of boron fluoride implants made into single-crystal wafers. The implants were performed at 30 keV with a dose of 1×10^{15} or 3×10^{15} ion-cm^{-2}. For very shallow junctions, the residual implant damage is found to degrade the reverse bias diode leakage characteristics. The residual damage can be nearly eliminated and shallow junction characteristics can be improved by preamorphizing the wafers with a single 50 keV silicon implant at a dose of 1×10^{15} ion-cm^{-2}.

This report examines methods of obtaining shallow source-drain regions for p-channel devices used in complementary-metal-oxide-semiconductor (CMOS) structures. Shallow junctions (< 0.3 μm) will be required with the scaling down of device dimensions to increase component density. Ion implantation of boron into crystalline silicon, which is used to introduce the dopant into source-drain regions, is accompanied by a channeling effect which leads to increased penetration of the implanted profile. Because of the relatively high diffusion coefficient of boron in silicon, dopant redistribution occurs during furnace annealing.

In this study, boron is replaced by boron fluoride (BF_2) as the implanted species in order to obtain a shallow implanted profile in monocrystalline silicon (1). Rapid thermal annealing is utilized to minimize boron diffusion during dopant activation (2). The electrical carrier profiles and residual implantation damage are compared for rapid thermal and furnace annealing. In this way, the effect of the proximity of residual damage to the p-n junction is investigated by measurement of the p-n diode characteristics. These measurements are also performed on wafers with a surface layer amorphitized by a silicon implant, followed by a boron fluoride implant and a rapid thermal or furnace anneal. Other workers have used multiple silicon (3) or germanium (4) implants to displace the implantation damage from the device regions. It will be shown that a single, low energy silicon implant can be used to eliminate channeling of boron in a subsequent low energy, boron fluoride implantation and that the residual damage is greatly reduced compared to boron fluoride implanted into monocrystalline silicon.

Experimental

Boron fluoride was implanted at 30 keV with a dose of 1×10^{15} or 3×10^{15} ion-cm^{-2} into 10 cm diam, (100) silicon wafers doped with phosphorus to a resistivity of 4-6 Ω-cm. The 30 keV boron fluoride implant is equivalent to a boron implant at 6.7 keV. In some cases the silicon wafers had been preamorphized with a silicon implant at an energy of 50 keV and with a dose of 1×10^{15} ion-cm^{-2}. The silicon and boron fluoride implants were made with the ion beam tilted at an angle of 7° to the wafer normal in a random direction to minimize channeling. The substrates were held at approximately room temperature.

The implanted wafers were annealed either in a standard furnace or an AG21OT Heatpulse™ system using a nitrogen ambient. The temperature control system in the Heatpulse system has a temperature feedback mechanism which enables the wafer to be held at a constant annealing temperature. The duration of the anneal is defined here as the time spent at the constant annealing temperature.

The boron and fluorine concentration profiles were obtained by secondary ion mass spectrometry (SIMS) using O_2^+ primaries and positive secondary ions. The sheet resistance was measured by contour mapping with a four-point probe (5). The electrical carrier concentrations and the p-n junction depths were determined from spreading resistance profiles.[1] The junction depth measurements were reproducible to within ± 0.02 μm. The implantation damage, before and after annealing, was examined by transmission electron microscopy (TEM).

Diode structures were fabricated using the implant and anneal conditions described above to evaluate the electrical characteristics of the p-n junctions. Current-voltage measurements were performed on oxide isolated, circular diodes of 1 mm diam.

Results and Discussion

Figure 1 shows the boron concentration profiles after implantation of boron fluoride into crystalline or into

[1] Measurements made by Solecon Laboratories, Incorporated, Sunnyvale, California 94089-2221.

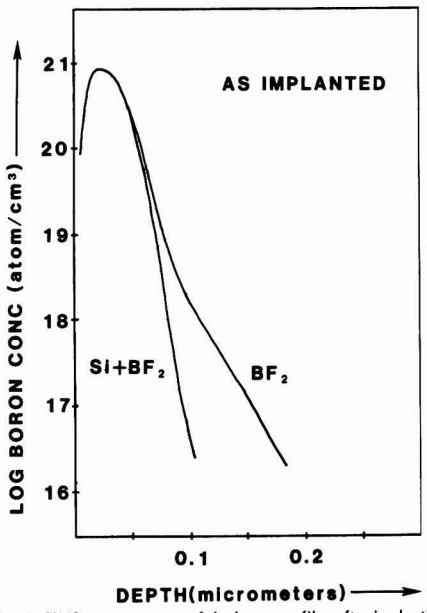

Fig. 1. SIMS measurements of the boron profiles after implanting BF_2 at 30 keV with a dose of 3×10^{15} monocrystalline and amorphous silicon.

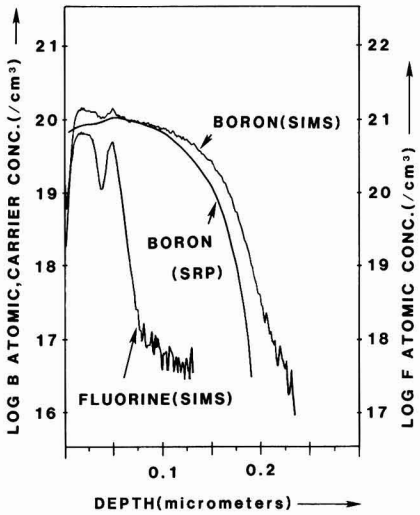

Fig. 2. SIMS and spreading resistance profiles for a BF_2 implant at 30 keV and with a dose of 3×10^{15} after rapid thermal annealing at 1100°C for 5s.

amorphous silicon and illustrates the channeling effect observed with implantation into crystalline silicon. Figure 2 shows the boron and fluorine dopant concentration profiles, together with the boron electrical carrier concentration profile, after rapid thermal annealing of the implant made into crystalline material. The fluorine outdiffuses during the anneal, leaving a broad fluorine peak close to the wafer surface, together with a sharp peak at a depth of 50 nm. It will be shown below that this is the location of the residual implantation damage. However, the retained fluorine does not affect the boron electrical activation because only the tail region of the implanted boron remains inactive. Similar spreading resistance profiles were obtained after each of the implant and anneal conditions described in Table I. The junction depths shown in Table I were measured from the spreading resistance profiles at a carrier concentration of 10^{15} cm^{-3}, which corresponds to the background doping concentration.

The depth of the residual ion implantation damage was measured from TEM cross sections. Figure 3a depicts the initial implantation damage caused by a 30 keV boron fluoride implant with a dose of 3×10^{15} ion-cm^{-2}. An amorphous layer is formed with a heavily damaged crystalline region just below the amorphous-crystalline interface. After rapid thermal annealing, a band of implantation damage remains at this depth (Fig. 3b). The TEM planar section (Fig. 3c) shows this damage to consist of irregularly shaped dislocation loops. The depth from the

Table I. Structural and electrical properties of the p^+/n junctions. The annealing conditions are: A, furnace anneal at 600°C for 30 min and at 950°C for 10 min; B, rapid thermal anneal for 5s at 1100°C

Implant	Si (50 keV) BF_2 (30 keV)	1×10^{15}		3×10^{15}		1×10^{15} 1×10^{15}
Anneal		A	B	A	B	A
Sheet resistance ($\Omega/\square$)		143	130	78	72	181
Defect depth (μm)		0.065	0.063	0.063	0.060	0.080
Junction depth (μm)		0.24	0.15	0.30	0.20	0.20
Reverse bias leakage current density (5V) (nA-cm^{-1})		1	23	1	10	1

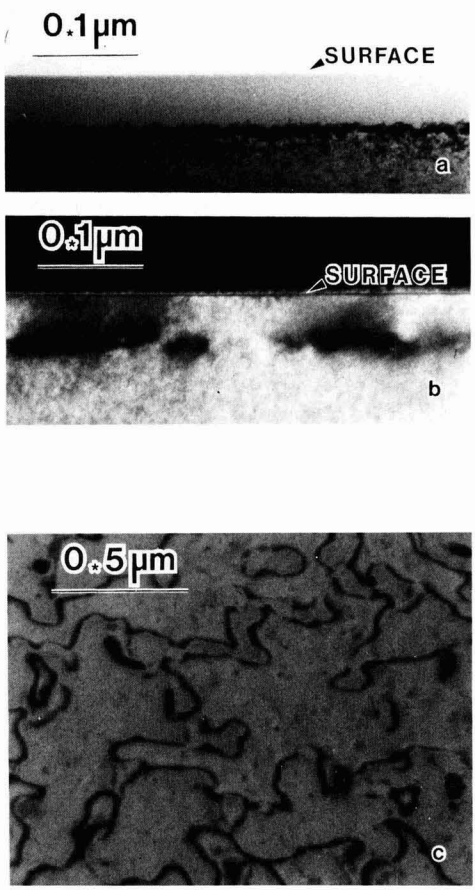

Fig. 3. a: TEM cross section showing the amorphous layer formed after a BF_2 implant at 30 keV with a dose of 3×10^{15}. b: TEM cross section showing the residual implant damage after the structure in a has been rapid annealed at 1100°C for 5s. c: TEM planar section of the residual damage shown in b.

wafer surface to the lower edge of the band of dislocation loops is listed in Table I. A similar defect structure occurs after furnace rather than rapid thermal annealing.

Shown in Fig. 4a is the amorphous layer formed after a silicon implant at 50 keV and a dose of 1×10^{15} ion-cm^{-2} followed by a boron fluoride implant at 30 keV and a dose of 1×10^{15} ion-cm^{-2}. In this case, the silicon implant energy and dose was chosen to produce an amorphous layer (110 nm deep) which would contain the entire boron distribution from the subsequent boron fluoride implant. After the furnace anneal described in Table I, implantation damage is located at a depth of 80 nm but only small dislocation loops remain with an average loop diameter of 200 nm (Fig. 4b). A similar defect structure is observed if the boron fluoride implant is omitted, indicating that the damage is characteristic of the silicon implant. Almost complete elimination of implant damage has been reported for multiple silicon implants followed by a boron implant and furnace annealing (6). It has been shown here that this can be achieved by furnace annealing of dual silicon and boron fluoride implants.

There are several comparisons which can be made from Table I that illustrate the interdependence of residual implant damage, junction depth, diode leakage characteristics, and sheet resistance. First, the values listed in Table I for rapid thermal anneals are compared with those after furnace annealing for boron fluoride implanted into crys-

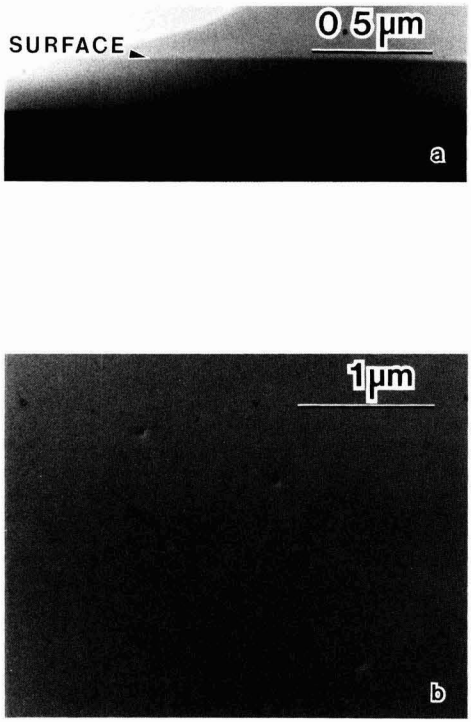

Fig. 4. The TEM cross section (a) shows the amorphous layer formed after a 40 keV silicon implant at a dose of 1×10^{15} followed by a BF_2 implant at 30 keV with a dose of 1×10^{15}. The planar section (b) shows the residual damage after a two-step furnace anneal at 600°C for 30 min and 950°C for 10 min.

talline silicon with a dose of 1×10^{15} or 3×10^{15} ion-cm^{-2}. It can be seen that a lower sheet resistance combined with a shallower junction depth can be achieved with rapid thermal annealing. This is consistent with the ability of rapid thermal annealing to thermally activate the implanted dopant while minimizing dopant diffusion. The higher annealing temperature of the rapid thermal anneal may account for the relatively low values of the sheet resistances. Although low sheet resistance values and shallower junction are obtained, rapid thermally annealed diodes have relatively high leakage current densities. There is a correlation between increased leakage and a smaller separation between the residual damage and the p/n junction depth. This finding is now compared with the equivalent results for the dual silicon and boron fluoride implants. After furnace annealing, a low leakage current density (1 nA-cm^{-2} at -5V) combined with a small separation (0.12 μm) between the implant damage and the p/n junction is found. This suggests that the reverse bias characteristics are improved by a reduction of the residual defect density through use of the dual implant.

Conclusions

Shallow p-n diodes with good leakage characteristics are obtained by rapid thermal annealing or furnace annealing of boron fluoride-implanted, single-crystal silicon wafers. Generally, rapid thermally annealed diodes have shallower junction depths with lower sheet resistances but higher leakage current densities than furnace-annealed diodes. The high leakage current density is attributed to the close proximity of residual implant damage to the p-n junction.

The residual damage can be greatly reduced by preamorphization of the silicon wafers using a single silicon implant at 50 keV with a dose of 1×10^{15} ion-cm^{-2}. In this way, shallow junctions with good leakage characteristics can be obtained.

Acknowledgments

The authors gratefully acknowledge the technical assistance of K. Belton for TEM specimen preparation. Funding for the SIMS analyses was provided by the National Science Foundation under MRL Grant DMR-8-20250.

Manuscript received Feb. 22, 1985.

Philips Research Laboratories assisted in meeting the publication costs of this article.

REFERENCES

1. R. G. Wilson, *J. Appl. Phys.*, **54,** 6879 (1983).
2. J. E. Seidel, *IEEE Electron Devices Lett.*, **edl-4,** 353 (1983).
3. C. Carter, W. Maszara, D. K. Sadana, G. A. Rozgonyi, J. Liu, and J. Wortman, *Appl. Phys. Lett.*, **44,** 459 (1984).
4. D. K. Sadana, W. Maszara, J. J. Wortmann, and G. A. Rozgonyi, *This Journal*, **131,** 943 (1984).
5. D. S. Perloff, F. E. Wahl, and J. Conragan, *ibid.*, **124,** 584 (1977).
6. B-Y. Tsaur and C. H. Anderson, Jr., *J. Appl. Phys.*, **54,** 6336 (1983).

Two-Dimensional Ion Implantation Profiles from One-Dimensional Projections

M. D. Giles

AT&T Bell Laboratories, Murray Hill, New Jersey 07974

J. F. Gibbons

Stanford Electronics Laboratories, Stanford University, Stanford, California 94305

ABSTRACT

Two-dimensional ion implantation profiles can be constructed from one-dimensional projections more quickly than by direct calculation. This method can be applied to many common target structures that can be reduced to an equivalent nonplanar single-layer target. This paper shows how the Boltzmann transport equation method can be extended to calculate two-dimensional effects for the implanted ion, damage distributions, and stoichiometry disturbances. The same approach can also be used with Monte Carlo methods.

The Boltzmann transport equation (BTE) approach (1) has been successfully applied to many ion implantation problems, predicting range and damage distributions, recoil distributions (2), and stoichiometry disturbances in compound semiconductors (3). The effects of ion backscattering can also be included if a multiple-pass scheme is used (4). All of this work has been restricted to one dimension. As device dimensions shrink, the lateral spread of implanted ions can no longer be neglected because of their effect on device behavior, providing the motivation to extend the method to two dimensions. Direct two-dimensional calculation is possible (5), but the computation time can be considerable. This paper describes a simpler method based on construction of two-dimensional information from one-dimensional projections.

Calculation of a two-dimensional profile by any method begins with the calculation of the results of implantation at a single point, yielding the point response function. There are then two levels of complexity possible. The simplest approach is to use the same response function at each point along the surface. A more general solution recomputes the response function at each point across the target. The simpler solution requires that the target have the same structure at each point along the surface, apart from the presence or absence of an opaque mask. This is satisfied exactly by a planar target even if it contains many planar layers. It is also approximately satisfied by a nonplanar single-layer target. The general solution can be used for any target shape and composition at the cost of an extra order in computation. These possibilities are illustrated in Fig. 1. Most cases of practical interest, such as silicon-silicon dioxide-polysilicon structures, are nonplanar multilayer (see Fig. 1f) and so require a general calculation scheme. We would like to treat these cases as a nonplanar single layer (see Fig. 1e) to speed up the calculations. This is made possible by a small scaling of the layers to form an equivalent silicon structure, as has been done previously for one-dimensional calculations. We will therefore concentrate on the single-layer case.

There are several approaches to the calculation of a point response in a single-layer target. The most common is to revert to a moments approach (6, 7) which allows the construction of a two-dimensional gaussian profile or a hybrid Pearson-Gaussian profile, and this has been used in several early two-dimensional simulation programs (8-10). At the other end of the spectrum in complexity, a full two-dimensional Monte Carlo (11) or Boltzmann (5) calculation can be performed. As will be seen, this can represent an unnecessarily large amount of work for this problem. As an intermediate approach, one-dimensional projections of the profile can be calculated and used to reconstruct the two-dimensional response function. It is found that two projections, one vertical and one lateral, are sufficient to do an accurate reconstruction. This method can be applied to both the Monte Carlo and Boltzmann schemes.

Method

Monte Carlo.—The initial result from a program such as TRIM (12) is a three-dimensional histogram of the final ion positions in the target. In a one-dimensional calculation, the histogram is flattened onto one vertical dimension to describe the final profile. The number of ion tracks that is necessary to describe the distribution is governed by the desired statistical error in the distribution; if a histogram box contains N ions, then the error is approximately $\sqrt{N}$. This dictates the use of at least 10^4 ions to maintain roughly 10% accuracy over the first decade of the profile. For a two-dimensional direct calcula-

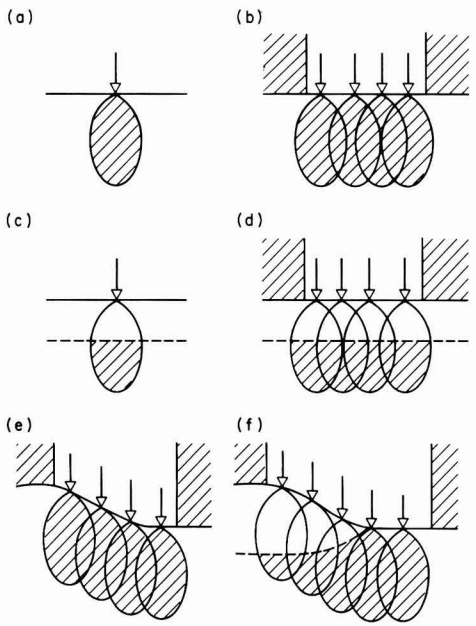

Fig. 1. Examples of point-response functions and corresponding targets. a: Point response for a single-layer target. b: Superposition in a mask window. c: Point response for a multilayer target. d: Superposition for a planar multilayer target. e: Superposition for a nonplanar single-layer target. f: General superposition using different point response functions.

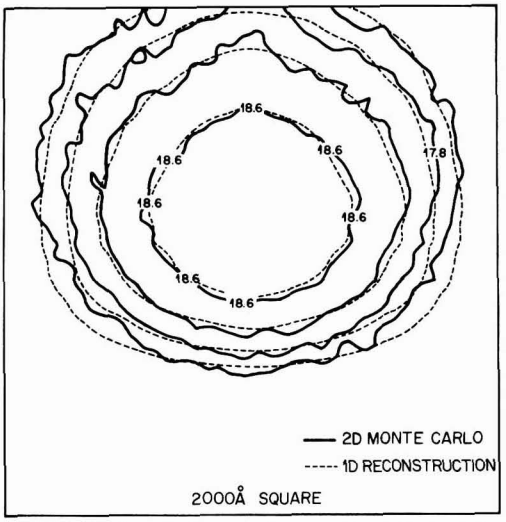

Fig. 2 Comparison of a direct two-dimensional Monte Carlo calculation (10^5 ions) with a reconstruction from projections (10^4 ions) for 20 keV boron implanted into silicon at a dose of 10^{15} cm^{-2}.

tion, the ions are spread over a plane rather than a line, so more ions must be followed to maintain statistical accuracy—between 10^5 and 10^6 ions are necessary, with a corresponding increase in calculation time.

In the alternative method proposed here, lateral information is obtained by flattening the histogram into one dimension laterally. The point response is then taken to be the product of the vertical and lateral projections. Because one-dimensional information is used throughout, 10^4 ion tracks are sufficient to define the result. The statistical error in the lateral projection is actually less than for the vertical profile because the lateral case is symmetric and the half-width is less than the total profile depth, so the histogram is spread over fewer bins. Figure 2 compares direct calculation using 10^5 ions with a reconstruction from 10^4 ions for 20 keV boron implanted into silicon. This comparison shows that the direct calculation is satisfactorily reproduced over the first two decades and justifies reconstruction from only two projections.

Boltzmann.—A one-dimensional Boltzmann vertical calculation does not contain lateral information because projection of the ion motion onto an axis is an integral part of the calculation. However, by changing the initial and boundary conditions, a lateral projected profile may be

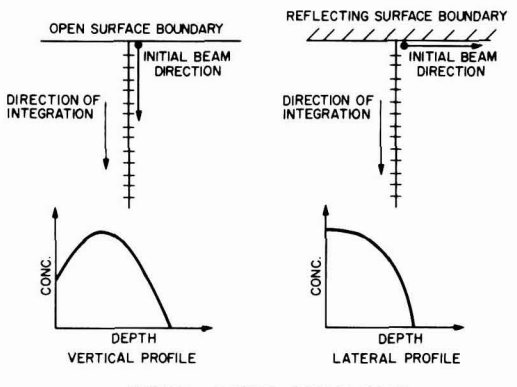

Fig. 3. Comparison of Boltzmann calculation method for vertical and lateral profiles.

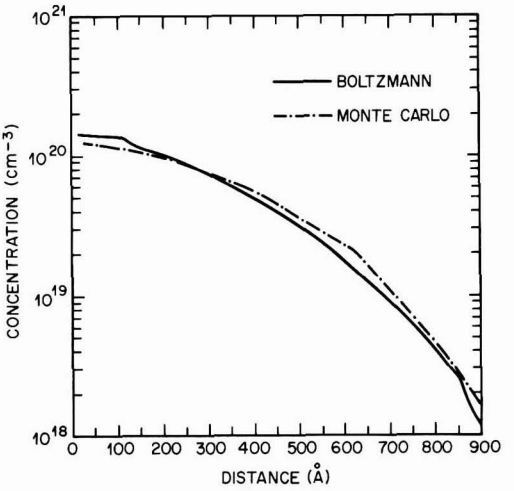

Fig. 4. Comparison of Monte Carlo and Boltzmann methods for lateral profile of 20 keV boron in silicon. Dose: 10^{15} cm^{-2}.

obtained. In a vertical calculation, the direction of integration is parallel to the initial beam direction. At each integration step, the ion motion is projected onto the integration direction so that the final result is a vertical projected profile. The surface is considered as an open boundary so that ions may be ejected out of the target. For a lateral calculation, the direction of integration is perpendicular to the initial beam direction. The same projection operation therefore produces a lateral projected profile. The surface is considered as a reflecting boundary so that only one half of the symmetric lateral distribution need be calculated. The two calculation conditions are compared in Fig. 3. For the lateral calculation, multiple passes (4) are essential because the beam angle causes many ions to be considered as backscattered. The multiple pass approach allows the motion of backscattered ions to be fully considered. Typical calculations require five passes, each of which is much shorter than a vertical calculation, leading to an overall calculation time of roughly twice the vertical time. The time to construct a point response for VLSI applications is in the range of

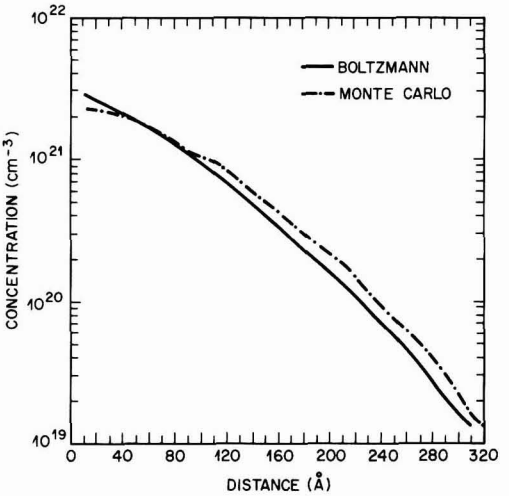

Fig. 5. Comparison of Monte Carlo and Boltzmann methods for lateral profile of 50 keV arsenic in silicon. Dose: 10^{15} cm^{-2}.

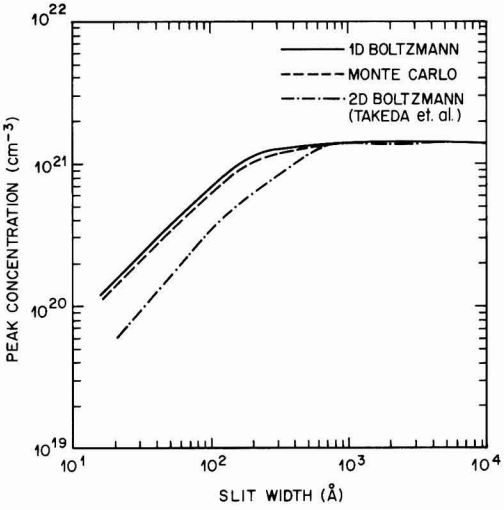

Fig. 6. Comparison of calculations for peak concentration for implantation of 50 keV arsenic through a narrow slit into silicon. Dose: 5×10^{15} cm^{-2}.

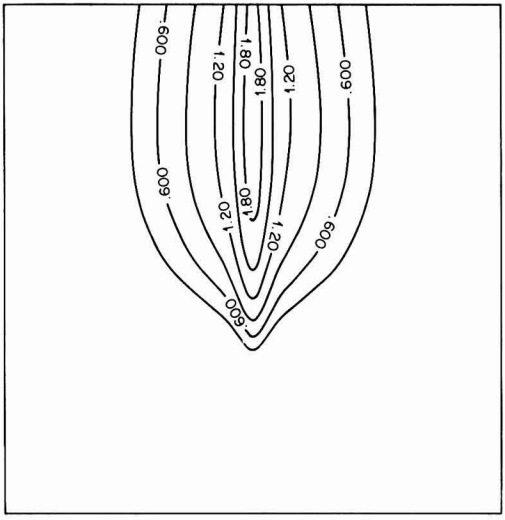

Fig. 8. Damage point response function for 20 keV boron implanted into silicon. Dose: 10^{15} cm^{-2}.

5-50s on a Cray-1 computer, compared with 50-500s for the same calculations using a vectorized Monte Carlo code.

Figures 4 and 5 compare lateral profiles calculated by the Monte Carlo and Boltzmann methods, showing very good agreement, and also confirming the accuracy of the calculations because the methods are independent. Comparison is also possible with the two-dimensional Boltzmann work of Takeda *et al.* (5). Figure 6 shows the change in peak concentration with slit width for implantation of 50 keV arsenic through a narrow window on a silicon substrate. All three methods show the same trends, but the data from Takeda *et al.* indicate a wider spread in the point response for their work.

Direct measurement (13) of true lateral profiles has not yet been achieved to sufficient accuracy for a useful comparison to be made. The closest thing possible to an experimental comparison at this time is to compare with profiles from tilted-beam experiments (14-17). In the BTE approach, this corresponds to tilting the initial beam direction and leaving the surface boundary open. Figure 7 compares calculation with experiment (17) for 60 keV arsenic implanted at various angles, showing the same movement of the peak position with tilt angle. The poor fit to the deeper profiles is believed to be in part due to inaccuracy in the measured profiles. For example, the experimental data for normal incidence seem truncated in comparison with the calculated curve and also in comparison with the other experimental curves and published data (18).

In one dimension, the BTE approach has also been used to calculate damage distributions (1), stoichiometry disturbances (3), and recoils in multilayer targets (2). In

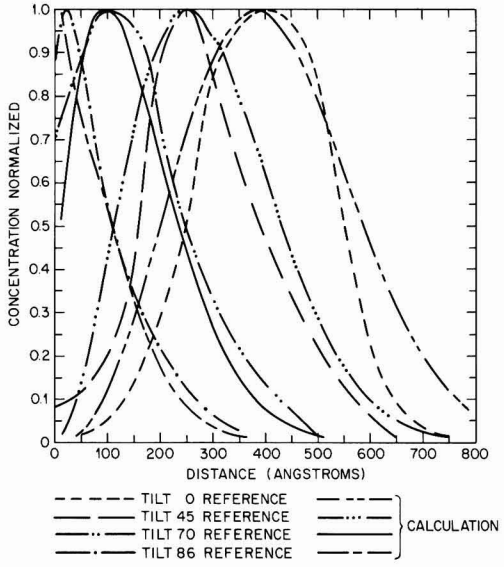

Fig. 7. Comparison of Boltzmann calculation with experiment for 60 keV arsenic implanted into silicon at various beam angles.

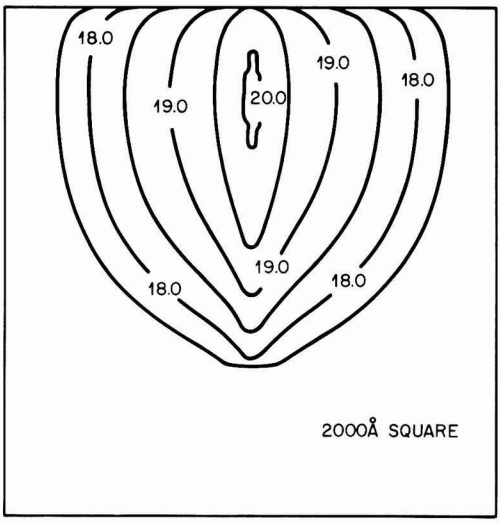

Fig. 9. Recoil atom point response function for 50 keV silicon implanted into gallium arsenide. Dose: 10^{15} cm^{-2}.

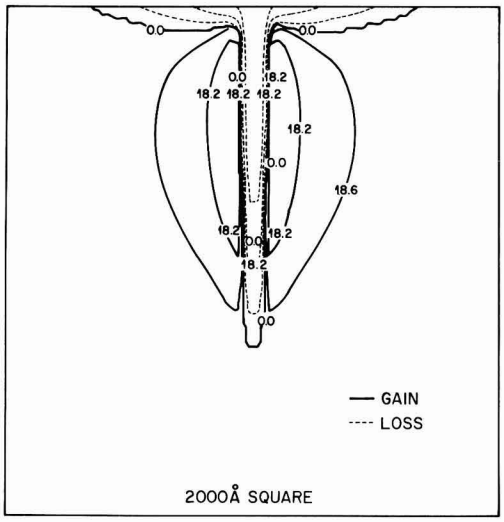

Fig. 10. Net substrate displacement from 50 keV silicon implanted into gallium arsenide. Dose: 10^{15} cm^{-2}.

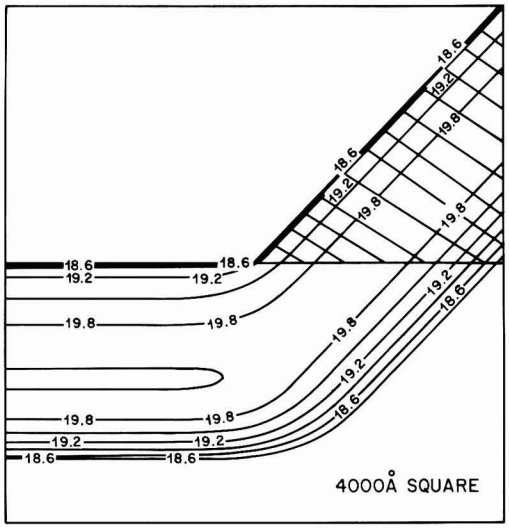

Fig. 12. Concentration profile for 20 keV boron into silicon at a 45° mask edge.

two dimensions, we have restricted ourselves to single-layer targets, but calculation of damage and stoichiometry is still possible by constructing point response functions for the appropriate quantities. Figure 8 shows a calculation for damage from a 20 keV boron implant into silicon. The general shape is similar to that of the concentration profile, although the dynamic range is less. For displacement and stoichiometry calculations, it is necessary to construct responses for displaced atoms and the corresponding vacancies separately. The net disturbance is then the difference in the two response functions. Figure 9 shows the concentration response for recoils from 50 keV silicon implanted into gallium arsenide, considering the substrate atoms together because their masses are so similar. The corresponding profile for vacancies is almost identical. The difference in these two correlated quantities gives the net imbalance, as shown in Fig. 10. This shows some surface loss of recoiled atoms and net displacement of atoms from the beam axis outward.

Example Profiles

Once the point response function has been calculated, it is easy to obtain two-dimensional profiles at various mask edges by convolution. Figures 11 and 12 illustrate calculations for 20 keV boron at an abrupt and a 45° mask edge, respectively. The construction time for each profile, given the one-dimensional sections, is much less than 1s on a Cray-1. Figure 13 shows a similar calculation for a damage distribution at a 45° mask edge. Finally, Fig. 14 shows net substrate atom displacement for a 50 keV silicon implant through a narrow window with abrupt edges into GaAs, which can be compared with the point response of Fig. 11.

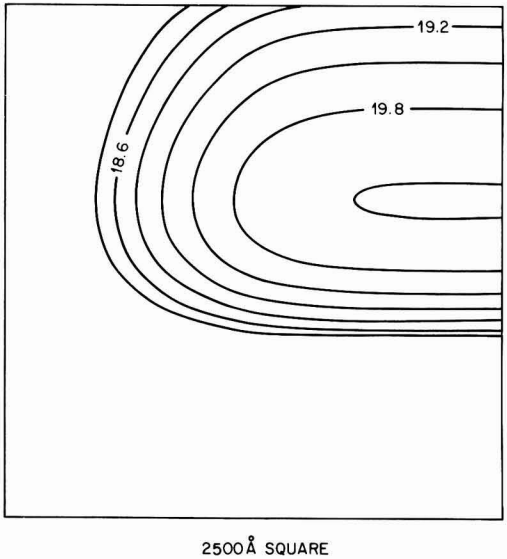

Fig. 11. Concentration profile for 20 keV boron into silicon at an abrupt mask edge.

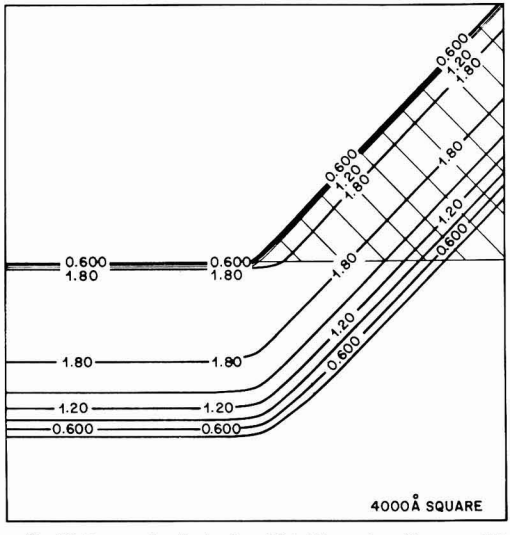

Fig. 13. Damage distribution from 20 keV boron into silicon at a 45° mask edge.

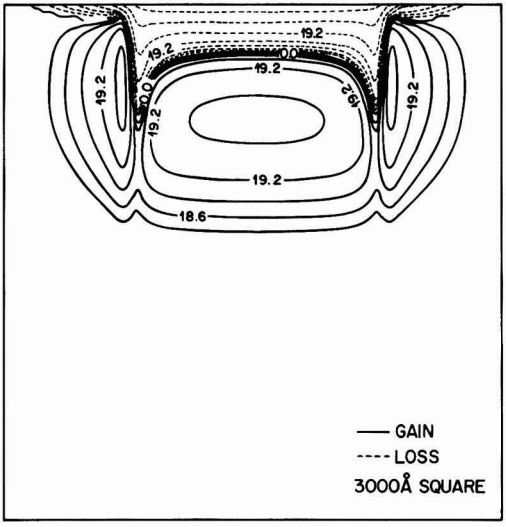

Fig. 14. Net substrate displacement from 50 keV silicon into gallium arsenide at an abrupt mask window.

Conclusions

The method of construction from projections allows two-dimensional implantation profiles to be calculated in the same order of magnitude of time as one-dimensional results, at the loss of some generality. Through scaling, the method can be used for practical useful structures, and it can be applied to both Monte Carlo and Boltzmann schemes. Through appropriate choice of point-response function, damage and stoichiometry effects can also be calculated. There is little advantage in using a more complex method unless a full, general solution is required and the increased computing resources are available.

Acknowledgments

The major portion of this work was funded at Stanford Electronics Laboratories though the support of DARPA (Contract no. MDA903-79-C-0257). Thanks are due to W. Fichtner of AT&T Bell Laboratories for making available the Monte Carlo code and encouraging the presentation and publication of this work.

Manuscript submitted March 25, 1985; revised manuscript received July 8, 1985. This was Paper 489 presented at the New Orleans, Louisiana, Meeting of the Society, Oct. 7-12, 1984.

AT&T Bell Laboratories assisted in meeting the publication costs of this article.

REFERENCES

1. L. A. Christel, J. F. Gibbons, and S. Mylroie, *J. Appl. Phys.*, **51,** 6176 (1980).
2. L. A. Christel and J. F. Gibbons, *Nucl. Instrum. Methods*, **182/183,** 187 (1981).
3. L. A. Christel and J. F. Gibbons, *J. Appl. Phys.*, **52,** 5050 (1981).
4. M. D. Giles and J. F. Gibbons, *Nucl. Instrum. Methods*, **209/210,** 33 (1983).
5. T. Takeda and A. Yoshii, *IEEE Electron Devices Lett.*, **edl-4,** 430 (1983).
6. J. Lindhard, M. Scharff, and H. E. Schiøtt, *Mat. Fys. Medd. K. Dan. Vidensk. Selsk.*, **27,** No. 15 (1963).
7. H. Runge, *Phys. Status Solidi A*, **39,** 595 (1977).
8. D. Chin, M. Kump, and R. W. Dutton, Stanford University Process Analysis Program, July 1981.
9. C. D. Maldonado, *Appl. Phys. A*, **31,** 119 (1983).
10. B. R. Penumalli, *IEEE Trans. Electron Devices*, **ed-30,** 986 (1983).
11. W. P. Petersen, W. Fichtner, and E. H. Grosse, *ibid.*, **ed-30,** 1011 (1983).
12. J. P. Biersack and L. G. Haggmark, *Nucl. Instrum. Methods*, **174,** 257 (1980).
13. P. Roitman, J. Albers, and D. R. Myers, *J. Appl. Phys.*, **55,** 4436 (1984).
14. S. Furukawa and H. Matsumura, *Appl. Phys. Lett.*, **22,** 97 (1973).
15. H. Okabayashi and D. Shinoda, *J. Appl. Phys.*, **44,** 4220 (1973).
16. W. A. Grant, J. S. Williams, and D. Dodds, *Rad. Eff.*, **29,** 189 (1976).
17. L. De Cata, J. S. Williams, and H. B. Harrison, *Nucl. Instrum. Methods B*, **4,** 368 (1984).
18. J. Nakata and K. Kajiyama, *Jpn. J. Appl. Phys.*, **21,** 1363 (1982).

High Speed Integrated Circuit Using Silicon Molecular Beam Epitaxy (Si-MBE)

E. Kasper

AEG-Telefunken Forschungsinstitut, D 7900 Ulm, Germany

K. Wörner

Telefunken electronic GmbH, D 7100 Heilbronn, Germany

ABSTRACT

Si-MBE is a low temperature deposition method for epitaxial silicon layers with thickness and doping profile control on a submicron level. The MBE equipment described in detail is designed for high throughput of round wafers (ten 3 in. wafers per day). The apparatus consists of six subsystems, the reliable and simple operation of which has been proved during a 2 yr test period. For the first time we report on fabrication of high performance integrated circuits using Si-MBE material. Frequency dividers were fabricated using, apart from MBE, a commercial process line. Clock frequencies of up to 2.8 GHz were realized by these dividers with integrated transistors with transit frequencies up to 7 GHz.

Si-MBE promises several advantages which should make it a powerful instrument for future material and device fabrication. Remarkable properties are low process temperature, precise control of thickness and doping profile on a submicron scale, and high flexibility concerning the choice of material combinations and layer numbers.

Up to now, much effort has been directed toward the technological development of the Si-MBE system and toward the fabrication of materials (1, 2) and of basic devices (3) demonstrating the capability of the method; see also, for instance, recent reviews (4, 5) and the excellent bibliography (6). Several groups now are intensively thinking about industrial application of the method, and they are bearing in mind that facts like cost, throughput, and yield are of the same importance as technical feasibility (7, 8).

Si-MBE may influence the fabrication of integrated circuits in an evolutionary or revolutionary way. For near-future applications, the evolutionary way accepting the well-established IC-process sequence has to be chosen. Our experience with this evolutionary way is described in the following report, which covers (*i*) layer growth in high throughput Si-MBE equipment with a ten-wafer cassette within a load-lock chamber; (*ii*) influence of surface treatment, buried layer structures, and postepitaxial processes on crystal perfection and dopant profiles of the MBE-layers; and (*iii*) fabrication of a GHz frequency divider. Apart from MBE all other process steps were taken from a process sequence routinely used for manufacturing these frequency dividers.

Si-MBE apparatus.—Si-MBE systems provide inside of a clean UHV chamber several individually regulated molecular beams (silicon, dopants, alloy materials, metals) which are directed onto the cleaned surface of a heated substrate. Our homemade apparatus (9) has been designed for high throughput fabrication of electronic-grade material. A wafer cassette positioned in a separate UHV-storage chamber which is connected to the growth chamber by a gate valve enhances the throughput. Crystal quality is improved by an extremely clean environment provided by low residual gas content (process pressure) and by the use of silicon as material for components which are in line of sight with the substrate. For simple operation, effusion cells emitting neutral molecular beams are used as dopant sources. Handling of round wafers without contaminating the back side is ensured by a special transport mechanism and by radiation heating of the substrates positioned in an annular holder made from silicon. This equipment, reliably working for two years, consists of the following six subsystems.

1. An ultrahigh vacuum system which allows a clean environment during the total process time. A proper choice of pumps, vacuum parts, materials and their pretreatments, and of the procedure is necessary to obtain a process vacuum not substantially worse than the base vacuum. Our system (see Fig. 1) is pumped down by a turbo-molecular pump getting the gas molecules out of the vacuum chamber and by a high speed titanium-sublimation pump gettering the gas molecules inside the vacuum chamber (9). Materials used for components are copper and stainless steel for cold parts and molybdenum, titanium, boron nitride, graphite, and silicon itself as often as possible for hot parts. All components are preheated 50 K above their operation temperature and scrubbed by electrons. All hot components are heat shielded to reduce thermal load. The heat shieldings of the material sources are water cooled to avoid thermal coupling. Intentionally, we do not use liquid nitrogen-cooled "cold walls" in the line of sight of the substrate, because methane (CH_4) adsorbed on the cold wall can easily be desorbed by electrons. Typical process pressure is 10^{-10} mbar. The main residual gas is hydrogen.

2. The substrate heater should be able to uniformly heat large diameter wafers up to temperatures necessary for thermal cleaning and growth. The most promising type is a radiant heater positioned near the back side of the wafer, where care is taken to reduce thermal stresses on the wafer below the stress level activating slip line generation (10). This is successfully done with our substrate heater by using a graphite meander radiation source and a substrate holder made from silicon avoiding temperature differences at the rim of the wafer by providing equal absorption properties of substrate and ring holder. Crystal

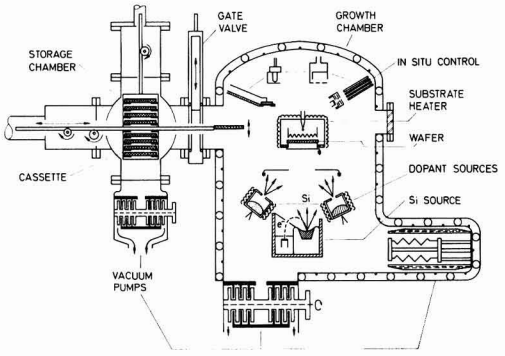

Fig. 1. Sketch of our Si-MBE apparatus. Growth chamber on the right side. Load-lock with cassette on the left side. Both UHV chambers are connected by a gate valve with 150 mm aperture.

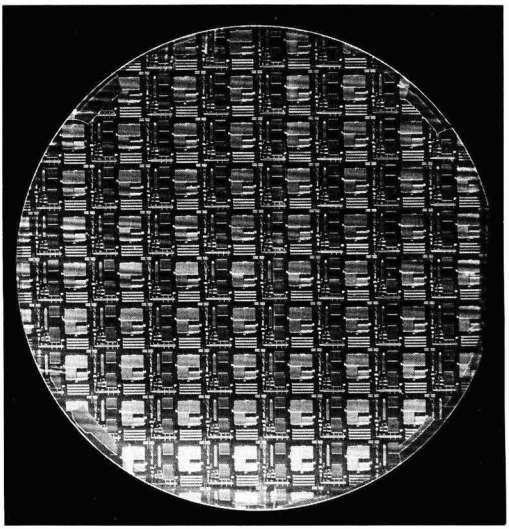

Fig. 2. X-ray topograph of a wafer with a 3 μm film grown on patterned oxide (0.2 μm thick). Slip lines and dislocations were avoided by uniformly heating the substrate. Contrast arises from the strain field of the patterned oxide.

perfection and absence of slip lines are routinely checked by x-ray topography (see Fig. 2). Power consumption for heating a 75 mm Ø wafer at a growth temperature of 750°C amounts to 700W.

3. The silicon molecular beam is generated by E-gun evaporation from pure silicon source material in the central portion melted and heated up to approximately 2000 K. Molten silicon is so reactive as to attack all other known crucible materials. The purity of the Si beam is enhanced by protecting the commercial E-gun from bombardment of backscattered electrons and ions by a silicon shielding. On a 30 cm distant substrate, typical growth rates are in the range of several micrometers per hour. Whereas E-gun evaporation is considered to be a reliable, clean, well-controlled process, it should be mentioned that it is also a source of particle beams (backscattered electrons, secondary electrons, silicon ions) and of electromagnetic radiation (light, x-rays, bremsstrahlung) influencing surface physics (adsorption, desorption, dissociation).

4. Dopant beams are generated by evaporation from effusion cells. For dopant materials we use Sb (for n-doping) and Ga (for p-doping). With Sb as a dopant material, concentrations up to the saturation limit of 2×10^{19}/cm^3 (at a growth temperature of 750°C) can be obtained (10, 11). But, near the saturation limit, incomplete electrical activation and degradation of the crystal perfection occurs. Well below the saturation limit, resistivity, Hall mobility of the layers, and their temperature dependence are similar to P- or As-doped bulk material (10-14). Thermodynamical calculations (15) predict a molecular beam that mainly consists of Sb_4 molecules. We found, by mass spectrometric analysis of the antimony beam, Sb atoms as well as Sb_2 and Sb_4 molecules. Up to now, a quantitative comparison with the calculations (15) has not been performed, because molecules are partly dissociated within the ionization chamber of the mass spectrometer and the sensitivity of the quadrupole mass spectrometer varies with atomic mass.

With Ga as a dopant material, carrier levels up to 2×10^{18}/cm^3 were achieved (16-18). The relatively high ionization energy of the Ga acceptor (70 meV) results in a dependence of resistivity on dopant concentration, quite different from B-doped bulk material. Already at Ga dopant levels above 1×10^{17}/cm^3 the acceptors start to be only partially ionized as proved by Hall effect measurements. The upper Ga-dopant concentration amounts to approximately 1×10^{19}/cm^3 (growth temperature: 550°C). The carrier concentration belonging to this saturation limit amounts to 2×10^{18}/cm^3 at room temperature (2.3×10^{16}/cm^3 at 77 K). With hole levels above 1×10^{17}/cm^3, device designers have to bear in mind the properties of the Ga acceptor.

Dopant atom incorporation can be enhanced and sharpness of interfaces can be improved by a technique we have called doping by secondary implantation during molecular beam epitaxy (DSI-MBE) (19). With this technique, silicon ions which are always produced by E-gun evaporation are accelerated by an electric field (typical potential difference between substrate and E-gun amounts to several hundred volts) toward the substrate. We believe that a main part of the low energy silicon ions implants atoms of the adsorbed dopant layer by impact (secondary implantation) into the growing MBE layer. The effect itself has been confirmed by another group (20), but the mechanism is a subject of controversial opinions.

5. *In situ* measurements of fundamental growth parameters are possible in the UHV environment of the growth chamber. Usually, analysis of the surface, the residual gas composition, the molecular beam intensities, and the temperatures of the substrate and effusion cells is employed. More than usual effort is directed by us toward mass spectrometry of dopant fluxes, absolute calibration of temperatures, and analysis of backscattered electrons.

Mass spectrometry of dopant fluxes is performed by a separate mass spectrometer sensitive to the range of atomic mass numbers 1-500 and by using a multiplier for ion counting. A shielding with properly positioned apertures protects the parts of the crossed-beam ion source of the spectrometer from being contaminated with dopant material or silicon. During operation of the effusion cells the mass numbers of Ga, Sb, Sb_2, and Sb_4 isotopes can be detected. Using this mass spectrometer, we investigated the relation between effusion cell temperature and dopant flux density, the response of flux intensity on power variations of the cell heater, and the thermal cleaning of freshly loaded dopant materials from oxide layers.

Crystal perfection and dopant incorporation are influenced by the substrate temperature and the temperature of the evaporating surface of the dopant material. These temperatures differ from the reference temperatures measured by thermocouples mounted into the substrate heater and the effusion cells. The temperature differences between surface and reference thermocouple depend on design of substrate heater and effusion cell, on substrate doping (different absorption of radiation), on volume of cell load, and in some cases on thermal coupling from E-gun to substrate (significant only at very low growth temperatures) or from substrate heater to effusion cell (significant for wafer diameters greater than 50 mm and antimony effusion cell).

Intensity and energy spectrum of backscattered electrons, secondary electrons, and ions are measured by a Faraday probe with variable grid voltage. The primary source of electrons is the E-gun itself. Because of the magnetic field of the E-gun, the electron path is curved and only fast backscattered electrons can escape from the E-gun. The slow (several electronvolts) secondary electrons are generated by the impact of backscattered electrons onto the chamber wall. One can understand that the intensity and energy spectrum of the electrons scattered to the substrate sensitively depend on the design of the growth chamber. Near the substrate, the flux density of scattered electrons is in the order of 10^{12} electron/cm^{2}s.

6. The wafers are put into the growth chamber and removed through a load-lock chamber also pumped down to ultrahigh vacuum (see Fig. 1). Thereby the clean UHV environment within the growth chamber is maintained during several weeks until material must be reloaded or parts must be replaced. We have installed within the load-lock chamber a wafer cassette, the use of which further reduces the mean time for insertion of a wafer. On a nor-

mal working day, with this equipment, a 1 μm epitaxial layer can be deposited on ten 75 mm diam wafers.

Growth of device quality material.—The procedure consists of chemical cleaning of the substrate surface, insertion of the cassette into the load-lock chamber, pump down of the load-lock during the night, and epitaxy during the following day. One wafer after another is taken up from the cassette and transported by a transfer system to the growth chamber and put back after epitaxy. In the growth chamber, the wafer is inserted into the substrate heater. After a short heat cleaning step (900°C, 5 min), process parameters are adjusted to their proper values and growth is started by opening the main shutter and the cell shutters. Growth temperatures are between 550° and 800°C. The growth process is monitored by the *in-situ* control instruments and finished at the desired layer thickness by closing the shutters.

For establishing the growth of high quality layers one has to consider the importance of a clean environment, the role of surface diffusion of adatoms, the time dependence of dopant incorporation, and the existence of radiation (light, x-rays) and charged particles (electrons, ions) inside the growth chamber.

Models of ideal growth assume a clean surface on which pure beams of silicon and dopant material are impinging. Under real growth conditions, there will be undesired contaminating atoms, radiation, and charged particles. Actually, essential characteristics of Si-MBE are the attempt to suppress the contamination to a level as low as possible and the toleration of the level of electromagnetic and particle radiation inherently connected with the use of an E-gun. There are two principal sources of contamination, namely, the substrate surface itself mainly chemisorbed with oxygen and carbon, and residual gas. The chemisorbed substrate surface must be cleaned *in situ*, otherwise the deposited layer grows as a polycrystal. We use a short (5 min) thermal cleaning step at 900°C to remove the oxide layer. Strongly chemisorbed carbon cannot be removed by this moderate heating step. It is essential, therefore, to use a chemical pretreatment resulting in low carbon chemisorption (12, 21). It seems to us that careful handling, pure materials, and rapid transfer into the UHV chamber are more important than the choice between the different etching procedures. Carbon contaminants in the rising water not detected by electrical resistivity measurement may cause a nonreproducible carbon coverage. Remaining 5h in usual laboratory atmosphere increases the carbon coverage by a tenth of a monolayer as proved by ESCA measurements.

For perfect growth, the pressure and composition of the residual gas must also fulfill severe requirements during the cleaning and growth process. Heavy hydrocarbons must not be detected by a sensitive quadrupole-mass spectrometer. Partial pressures of oxygen, water, and also nitrogen should be well below the 10^{-11} mbar range. Only hydrogen as main component is allowed to be present at a partial pressure of several 10^{-10} mbar (22).

Fast surface diffusion of silicon adatoms was claimed (23) to play a dominant role for low temperature epitaxial growth under MBE conditions. Smooth surface, temperature-independent growth rate, and negligible desorption were explained by vertical growth via lateral motion of monatomic steps generated by the unintentional misorientation of commercial substrates (typically 1/4°). BCF (Burton, Cabrera, Frank) theory (24), assuming steps to be a capture site for diffusing adatoms, predicts negligible desorption only for an adatom diffusion length much higher than the step distance. A low energy barrier of surface diffusion (<1 eV) is compatible with the experimentally observed desorption and growth rates (23). These experiments should be compared with the strongly temperature-dependent growth rate, the desorption, and the moderate surface diffusion (energy of surface diffusion ≈ 1.6 eV) observed with vapor phase epitaxy (25). Possibly, the difference in the energy barrier of surface diffusion is caused by hydrogen adsorption (26) during VPE or by radiation-enhanced motion during MBE.

Surface segregation, low sticking coefficients, and large time constants for incorporation of the dopants Sb and Ga (10, 12, 13, 17) rule out monatomic steps also to be an effective capture site for adsorbed dopant atoms, because during growth a step passes a point on the surface roughly every second. Therefore, BCF theory cannot describe dopant material incorporation during MBE. Other models (27, 28) describe the time dependence of dopant incorporation at least qualitatively.

There are considerable differences about the sticking coefficients of dopant material given in literature. Uncertainty of temperature was believed to be the cause of these differences (27). We have built three MBE equipments with different design but with the same careful calibration of cell and substrate temperatures. The sticking coefficient in every Si-MBE apparatus differs from the other. This experimental fact leads us to consider radiation and charged particle beams influencing the desorption, dissociation, and incorporation of dopant atoms. After every redesign of the apparatus, dopant level adjustment should take place. Electromagnetic and particle radiation also influence adsorption/desorption (29), contamination, and possibly silicon adatom migration as described above.

GHz-frequency divider.—A simple application of Si-MBE is to replace the epitaxial layer on an integrated circuit usually made by conventional vapor phase epitaxy by an MBE layer without changing pre- or postepitaxial processes or circuit layout. Clearly, in doing so the full potential of MBE will not be utilized, but this is an effective way to analyze the compatibility of the MBE process with the other IC manufacturing process steps. Improvements should be based on low growth temperature, reduced autodoping, and precise thickness control.

As a test vehicle, we selected a frequency divider used for television tuners. Initially, this commercial device was developed for an operating frequency up to 900 MHz (ultrahigh-frequency band of European television). Meanwhile, one needs frequency dividers up to X-band frequencies (12 GHz). Of late, Si bipolar IC's entered the lower microwave regime (30). Whereas in 1980 the fastest bipolar LSI circuits were considered to be based on integrated transistors with a transit frequency of f_T = 4 GHz (31), now the frequency limit of integrated bipolar transistors is shifted with laboratory examples toward f_T = 14 GHz (32) using a sidewall base contact structure (SICOS) technology. The highest reported clock frequency of a GHz-frequency divider is 5.5 GHz (33). These authors used a half-micron bipolar technology with advanced super self-aligned processes (SST-1A). Propagation delays for nonthreshold logic (NTL) of 42 ps/gate, power-delay products of 20 fJ/gate, and transit frequencies of 12.4 GHz were obtained with this technique. The highest operation frequency of the divider has been obtained at a high power dissipation of 884 mW. Encouraging results were also obtained with other special laboratory techniques. Using the direct nitride passivated base surface (DNP-II) process (34) resulted in a f_T value of 10 GHz and a clock frequency for the divider of 3.9 GHz at a power dissipation of 316 mW. Using vertically isolated self-aligned transistors (VIST) (35) resulted in a low power consumption of 84 mW at 2.5 GHz (f_T = 6 GHz) for a four-stage frequency divider (1:16).

We used, apart from Si-MBE, a 2 μm linewidth process sequence, which was developed for manufacturing of commercially available frequency dividers (36). Process sequence and circuit design were chosen to allow for the high yield production of a GHz-frequency divider with power dissipation below 100 mW. One layout of the test circuits is shown as a chip photograph (Fig. 3). This test chip contains a preamplifier, a master-slave flip-flop in ECL technique as binary divider, and test devices.

Prior to epitaxy, an As buried layer (RS = 8 Ω/□) was diffused and a B-channel stopper was implanted to avoid inversion layers below the isolation oxide. Thermal processes after epitaxy were diffusion of the collector contact, oxidation of the isolation oxide, and annealing of

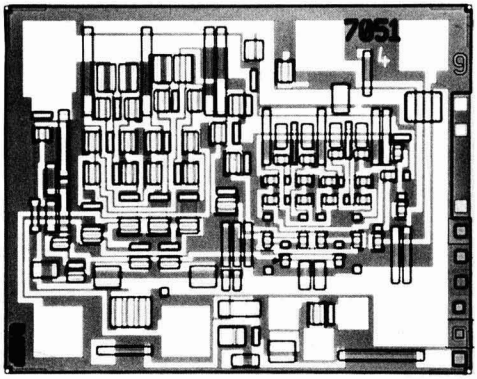

Fig. 3. Chip photo of a frequency divider with test devices. Layout-set number 7051.

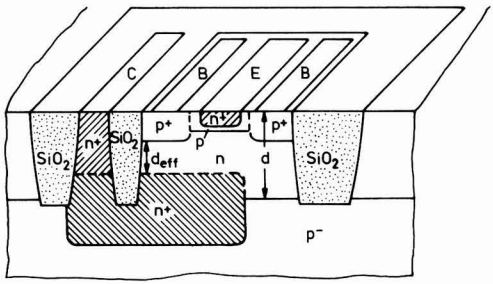

Fig. 4. Frequency divider. Vertical structure of integrated transistors with oxide isolation.

base, base contact, and emitter implantation (Table I). The vertical structure of the integrated transistors is shown in Fig. 4. The effective thickness d_{eff} of the collector is lower than the epitaxial thickness d due to outdiffusion of the buried layer and due to the depth penetration of the base contact. Typical emitter depth amounts to 0.25 μm, typical base width is 0.1 μm, and base contact penetrates 0.55 μm. In this experiment, the thickness d was reduced from 2.5 to 0.9 μm, thereby reducing the effective thickness d_{eff} (see Fig. 4) from 1.6 to 0.2 μm. The differences between d and d_{eff} are larger for thicker layers because of the prolonged time for oxidation of the isolation oxide. Alternatively, another test circuit was used (layout-set number 852) with diffused isolation and diffused emitter. The frequency limit of transistors with oxide isolation is roughly 2 GHz higher than the frequency limit (5 GHz) of transistors with diffused isolation (7).

With these test circuits we investigated yield as a function of the surface treatment, influence of pre- and postepitaxial process steps on the quality of the MBE film, and transit frequency of the frequency divider and of integrated transistors as a function of the epitaxial layer thickness.

All fundamental growth experiments were performed on homogeneous substrates with flat, well-defined surfaces. Epitaxy for IC fabrication, however, starts on the surface of a heat-treated substrate, parts of which are oxidized, diffused, and ion implanted. These processes generate surface steps which are large compared with the monatomic misorientation steps present at flat surfaces. Surface contamination, defect propagation from substrate to layer, and growth mode can be influenced by these varied start conditions. Yield measurements can give general information about the significance of such varied start conditions. We obtained detailed information about causes of yield reduction by several methods for analysis of surfaces and defect structure (ESCA, TEM, x-ray topography, interference microscopy, defect etching). Initially, yield was considerably reduced when we replaced VPE layers by MBE layers. This was caused by residual

Table I. Postepitaxial processes. Heat cycles above 500°C

Aim	Process
Contact to buried collector	P diffusion, diffusion temperature dependent on epitaxial thickness (900°-1000°C)
Oxide isolation	High pressure oxidation (20 bar) at 800°C, duration dependent on epitaxial thickness
Base, base contact, emitter	Room temperature implantation (B and As), furnace annealing at temperatures between 900° and 950°C

contamination at surface steps when applying the usual chemical cleaning treatment immediately before insertion into the magazine of the load-lock chamber. High device yield (up to 90%) was obtained by applying the following cleaning procedure. A modified cleaning solution based on hydrogen peroxide [known as RCA-etch (37)] yields low stacking fault and dislocation densities (1×10^3/cm^2). This etching sequence is preceded by a centrifugal wafer spray. High purity water wets the spinning wafer; N_2 finally dries it for removal.

The buried layer zones themselves with their high As-dopant concentration do not degrade the high crystalline quality of the overlying film. Transmission electron micrographs clearly show that the epilayer grown onto buried layers exhibits the same lattice perfection as the part grown directly on the p-type substrate.

Autodoping is a well-known problem of epitaxy on substrates with buried layers. In order to investigate autodoping we grew layers on p-substrates, half of which were doped with arsenic in the same way as buried layer zones. Then we profiled doping level and junction abruptness on several spots on both halves of the wafer by C-V and spreading resistance measurements (see Fig. 5). We found that (*i*) junctions are abrupt within measurement accuracy (38) and carrier diffusion length (approximately a Debye length) and (*ii*) doping level is not influenced by the underlying substrate doping. That means practically that autodoping should not be considered when layer growth is performed by Si-MBE.

Postepitaxial processes may be influenced by the content of carbon, oxygen, or hydrogen, or by the concentration of interstitials or vacancies. Using the same process sequence as for the fabrication of the commercial devices, we did not find any hint that MBE material behaves other than VPE material with respect to postepitaxial processes.

The frequency limit depends on the thickness of the epilayer. Figure 6 exhibits the frequency limit, f_T, as a function of the emitter current, I_E, for several epitaxial thicknesses. Epitaxial dopant density is 1×10^{16}/cm^3. The emitter area is a single stripe 2.5 μm wide and 25 μm long. Collector-base voltage, U_{CB}, was fixed at 2V. Frequency limit increases with increasing current up to a saturation value obtained at current densities of 1×10^8-2.5×10^8 A/m^2. Frequency limits in excess of 4 GHz are obtained already at current densities above 3×10^7 A/m^2 with epilayers 0.9-2.5 μm thick. The upper frequency limit of 7 GHz is obtained with epilayers about 1.2 μm thick. With thinner epilayers (see no. 192 in Fig. 6) the collector-base capacity increased, due to the reduced effective thickness decreasing the frequency limit (6 GHz for d = 0.9 μm). With thicker layers the collector resistance increases with increased effective thickness, reducing the frequency limit (5.8 GHz for d = 2 μm). The latter effect is more pronounced with lower epidoping level. With a doping level of 3×10^{15}/cm^3 (Sb), we obtained a frequency limit f_T of 6 GHz with d = 1.2 μm, f_T = 4 GHz with d = 2 μm, and f_T = 2.5 GHz with d = 2.5 μm. For low power consumption,

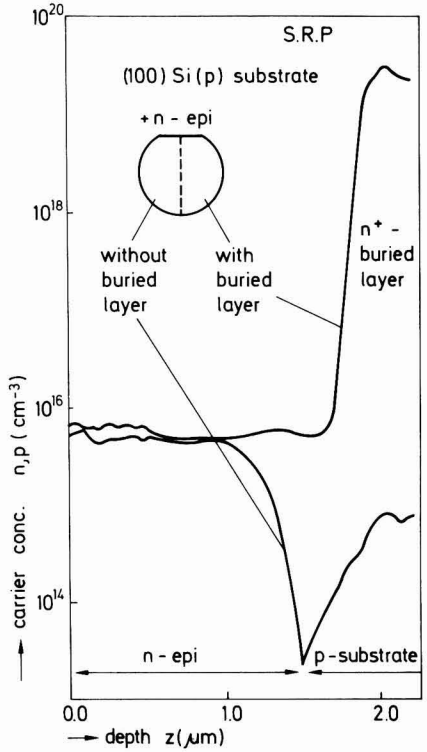

Fig. 5. Spreading resistance measurement of carrier profile of the epilayer on p-substrate with and without buried layer.

high frequency limits should be obtained at low collector-base voltage (U_{CB}) levels. An example is given in Table II. With integrated transistors of these frequency limits, frequency dividers with clock frequencies up to 2.8 GHz could be fabricated.

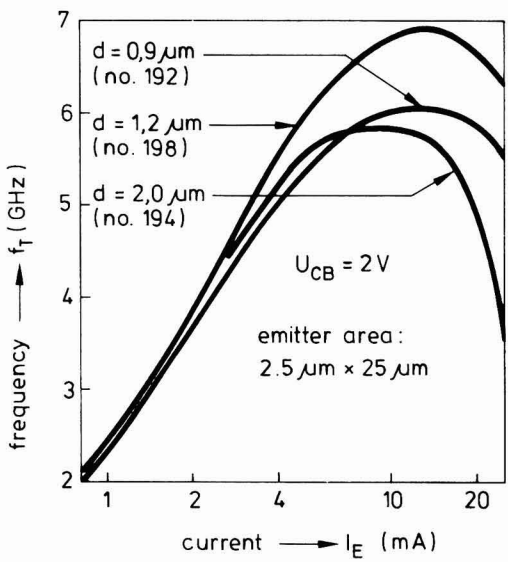

Fig. 6. Transit frequency f_T as a function of emitter current I_E for transistors with different epilayer thickness d.

Table II. Frequency limit f_T as function of the collector-base voltage U_{CB} at an emitter current I_E = 5 mA (no. 179, epilayer thickness 1.35 μm)

U_{CB} (V)	0.5	1	2	4	5	6
f_T (GHz)	5.45	5.75	6.1	6.35	6.45	6.6

Conclusions

We have proved for the first time that use of Si-MBE material enables the fabrication of high speed integrated circuits with excellent performance. Apart from Si-MBE, the process sequence of a commercial frequency divider has been used. High crystal perfection on buried layer substrates, absence of autodoping, and compatibility with postepitaxial processing are offered by this conventional use of an epitaxial layer.

Further improvement should be expected by using the full capability of Si-MBE, including, in addition low process temperatures and precise control of submicron layers, the high flexibility of materials, profiles, and structures.

The layers have been grown in an Si-MBE apparatus which was designed for industrial application. Simple handling, high throughput, and reliable operation were demonstrated since the installation of this equipment in 1982. Based on the principles of this equipment (storage chamber with a cassette, excellent vacuum conditions, low process temperatures, large area wafer heater, high precision *in situ* process control), development of the next generation equipment should also fulfill high requirements with respect to low cost and high throughput production of Si-MBE layers.

Acknowledgments

Technical assistance by Mr. H. Kibbel, layer assessment by Mr. H. J. Herzog and Mr. H. Jorke, and discussion with Dr. U. König and Dr. Th. Ricker are acknowledged. Part of the work was sponsored by the Ministry of Technology of Germany.

Manuscript submitted Oct. 10. 1984; revised manuscript received June 25, 1985.

AEG-Telefunken Forschungsinstitut assisted in meeting the publication costs of this article.

REFERENCES

1. J. C. Bean, L. C. Feldmann, A. T. Fiory, S. Nakahara, and I. K. Robinson, *J. Vac. Sci. Technol. A.*, **2,** 436 (1984).
2. E. Kasper, H. J. Herzog, and H. Kibbel, *Appl. Phys.*, **8,** 199 (1975).
3. J. Freyer, E. Kasper, and H. Barth, *Electron. Lett.*, **16,** 865 (1980).
4. Y. Ota, *Thin Solid Films*, **106,** 1 (1983).
5. F. C. Allen, S. S. Iyer, and R. A. Metzger, in "Proceedings of the SPIE Technology Symposium," p. 2, Los Angeles, January 1982.
6. J. C. Bean and S. R. McAfee, *J. Phys. (Paris)*, **43,** C5-153 (1982).
7. E. Kasper and K. Wörner, Abstract 51, p. 73, The Electrochemical Society Extended Abstracts, Vol. 84-1, Cincinnati, OH, May 6-11, 1984.
8. R. G. Swartz, G. M. Chin, A. M. Voshchenkov, P. Ko, B. A. Wooley, S. N. Finegan, and R. H. Bosworth, *IEEE Electron. Devices Lett.*, **edl-5,** 20 (1984).
9. U. König, H. J. Herzog, H. Jorke, E. Kasper, and H. Kibbel, in "Collected Papers of MBE-CST-2," p. 193, Tokyo (1982).
10. U. König, H. Kibbel, and E. Kasper, *J. Vac. Sci. Technol.*, **16,** 985 (1979).
11. U. König, E. Kasper, and H. J. Herzog, *J. Crys. Growth*, **52,** 151 (1981).
12. Y. Ota, *This Journal*, **124,** 1795 (1977); **126,** 1761 (1979).
13. J. C. Bean, *Appl. Phys. Lett.*, **33,** 654 (1978).
14. Y. Shiraki, in "Collected Paper of MBE-CST-2," p. 179, Japanese Society of Applied Physics, Tokyo (1982).
15. R. R. Hultgren, "Selected Values of Themodynamic Properties of Metals and Alloys," Report of the Minerals Research Laboratory, University of California, Berkeley, CA (1962).

16. U. König, H. Jorke, and H. Kibbel, Paper presented at the 2nd European MBE-workshop, Institute of Physics, Brighton, England (1983).
17. G. E. Becker and J. C. Bean, *J. Appl. Phys.*, **48,** 3395 (1977).
18. S. S. Iyer, R. A. Metzger, and F. G. Allen, *ibid.*, **52,** 5608 (1981).
19. H. Jorke, E. Kasper, and H. Kibbel, Paper presented at the 3rd International MBE-Conference, San Francisco, CA, August 1984.
20. R. A. A. Kubiak, W. Y. Leong, and E. H. C. Parker, Paper presented at the 3rd International MBE-Conference, San Francisco, CA, August 1984.
21. A. Ishizaka, K. Nakagawa and Y. Shiraki, in "Collected Papers of MBE-CST-2," p. 183, Tokyo (1982).
22. E. Kasper and H. Kibbel, *Vak. Tech.*, **33,** 13 (1984).
23. E. Kasper, *Appl. Phys. A*, **28,** 129 (1982); or T. de Jong, Thesis, University of Amsterdam, Amsterdam, The Netherlands (1983).
24. W. K. Burton, N. Cabrera, and F. Frank, *Trans. R. Soc. (London)*, **243A,** 299 (1951).
25. R. C. Henderson and R. F. Helm, *Surf. Sci.*, **30,** 310 (1972); R. F. C. Farrow, *This Journal*, **121,** 899 (1974).
26. A. A. Chernov and M. P. Rusaikin, *J. Cryst. Growth*, **45,** 73 (1978).
27. R. A Metzger and F. G. Allen, *J. Appl. Phys.*, **55,** 931 (1984).
28. M. Tabe and K. Kajiyama, in "Collected Papers of MBE-CST-2," p. 187, Japanese Society of Applied Physics, Tokyo (1982).
29. B. A. Joyce, *Surf. Sci.*, **35,** 1 (1973).
30. C. P. Snapp, *Microwave J.*, **93,** (August 1983).
31. H. Nakashiba, I. Ishida, K. Aomura, and T. Nakamura, *IEEE Trans. Electron Devices*, **ed-27,** 1390 (1980); K. Wörner, H. Caluss, H. M. Rein, and H. Kostka, Dig. Techn. Papers, p. 73, ESCIRC 78, Amsterdam, The Netherlands (1978).
32. T. Nakamura, K. Nakazato, T. Miyazaki, T. Okabe, and M. Naga, 1984 IEEE International Solid-State Circuit Conference, Dig. Techn. Pap., p. 152 (1984).
33. T. Sakai, S. Konaka, Y. Kobayashi, M. Suzuki, and Y. Kawai, *Electron. Lett.*, **19,** 283 (1983).
34. S. Watanabe, S. Shinozaki, N. Kusama, S. Miyazaki, and T. Nakata, IEEE 1984 Monolithic Circuits Symposium, Dig. Pap., p. 24 (1984).
35. T. Fujita, H. Sakai, K. Kawakita, and T. Takamoto, *Jpn. J. Appl. Phys.*, **22-1,** 125 (1983).
36. K. Wörner, *IEEE Trans.*, **ce-30,** 297 (1984); Data sheet U 822 BS /U 824 BS, Telefunken electronic GmbH, Heilbronn, Germany.
37. See, for instance, W. Kern, *Semicond. Int.*, p. 94 (April 1984).
38. L. A. Hing and J. E. Curron, *Electron. Lett.*, **19,** 1091 (1983).

Diffusion of Oxygen in Silicon Thermal Oxides

E. A. Taft*

General Electric Company, Schenectady, New York 12301

ABSTRACT

A method for comparing the oxidation rates of silicon under an initial 1000Å of thermal oxides is described. Ellipsometry is used to measure the thicknesses of a pair of samples before and after a relatively short time of additional oxide growth in dry oxygen. Excluding the known orientation effect, a large variation in growth rate at a given temperature is noted. The rate is directly related to the index of refraction of the initial oxide. As this index is known to depend upon the initial growth temperature, the apparent oxygen diffusion "activation energy" must include this newly documented temperature factor. Parabolic and linear rate constants are presented and are compared with literature values. This study gives further evidence that silicon thermal oxides are metastable structures.

The linear-parabolic model of Deal and Grove (1) is still the generally accepted interpretation of thermal oxide growth on silicon. Though recognized early by, *e.g.*, Hopper *et al.* (2) and Irene and van der Meulen (3, 4) as not an exact model, careful experimental work did not result in much improved interpretation. Additions to the linear-parabolic approach continue to appear (5-9), and new physical possibilities are advanced (10-12), but the basic model remains. (Only a few of many papers are referenced here.)

This paper will present new oxygen diffusion data which should be considered within the linear-parabolic model framework. The experimental approach follows the lead of Taft (13) and of Irene *et al.* (14), who show density differences in silicon thermal oxides. The effect of this oxide structure variation on the diffusion rate of oxygen is examined.

The diffusion of gas through a network is strongly dependent on the relative size of the interstices of the network and diameter of the diffusant molecule (15). If the density of vitreous silicon oxides varies by several percent, the interstitial volume also varies. The diffusion of the oxidant through a silicon thermal oxide might be expected to strongly depend upon changes in this interstitial volume. Hence, as the index of refraction and density does vary with the oxide formation temperature (13), the diffusion constant of the oxidant should not be expected to be the same for all thermal oxides. Rate growth variations have been reported in other multiple oxidation studies (10, 16).

* Electrochemical Society Active Member.

It has been observed that the oxides are metastable in that they can be reheated up to the formation temperature without appreciable change in the index of refraction. Heating to a higher temperature will cause the film structure to relax to the index appropriate to that for a film grown at this higher temperature. Irene *et al.*, (14) have documented this oxide stability. This fact is a necessary part of the diffusion study.

This paper will also present data on the linear and parabolic rate constants of oxide growth in dry oxygen on <111> and <100> silicon wafers. The purpose here is not so much to give new data but to provide an informed starting place for comments on the rate constants and to show that the oxides reported are typical. The effective activation energy of the parabolic rate constant especially is discussed.

Experimental

Oxides were grown in dry oxygen on <100> and <111> single-crystal silicon at various temperatures to about 1000Å thick. The wafers were cleaned in hot H_2SO_4-H_2O_2 and given an HF acid dip to remove native or previously grown oxide. They were then hydrogen fired to 1200°C for 10 min. This high temperature cleaning (2, 17) gave initial ellipsometer readings of about 3Å as found by Claussen and Flower (17). The index of refraction and thickness was carefully checked with a Gaertner L119 ellipsometer. A second measurement was made the following day to test oxide stability. Pairs of wafers of the same orientation from different temperature runs were chosen to be of the same thickness to < 1%. Dilute HF

etching was used on one wafer, when necessary, to obtain a close thickness match. These pairs of wafers were then placed in an oxidation furnace at the lower of the original growth temperatures of the pair. A growth time for adding 5-10% to the original thickness was chosen. This new oxide is now considered as an incremental growth over a small part of the growth curve near 1000Å. The thickness and index of the incremented oxides were carefully remeasured. Again, a second measurement was made the following day to check reproducibility of measurements.

Also, oxide growth-time curves for 700°-1170°C temperature in dry oxygen were developed. <100> and <111> wafers of 1 1/2 in. diam were employed for this work also. The thickness data were taken in the 100-1500Å range with the Gaertner L119 ellipsometer.

Results

The matched thickness wafer pairs did not have matched growth rates. The oxide grown originally at the higher temperature always had a greater incremental growth thickness. The ratio of these new growth thicknesses was at first plotted against the initial growth temperature differences of the pairs. Only a trend was observed. As noted before (13), the index is a better measure of the state of the oxide film than growth temperature. Furnace contamination, generally water vapor, which might occur in our small tube furnace will give an effectively higher temperature to a sample. The incremental thickness ratio was then plotted against the difference in initial index for each pair of samples. This curve is shown in Fig. 1.

A point on this graph is found from the example of the following wafer pair. One wafer had an oxide thickness of 973Å with an index of 1.4686. The oxide was grown at 1000°C. A second wafer oxide grown at about 1170°C was chosen at nearly the same thickness at 975Å. Its index was 1.4623. After 20 min in the oxidation furnace at 1000°C, the first oxide was 57Å thicker at 1030Å with the index unchanged at 1.4685. The second oxide increased slightly in index to 1.4636 and was 107Å thicker at 1082Å. The initial indexes were different by 0.0063 and the ratio of incremental growths was 107/57, or 1.88. This point appears in Fig. 1.

The thickness of the oxide was measured immediately if a dilute HF etch was used. When checked the following day, it was noticed that, invariably, the thickness had increased by several angstroms. Subsequent measurements were unchanged. Wafers from the oxidation furnace which were not etched appeared to have stable thicknesses. (Wafer pairs included samples with neither oxide etched and samples where either the high or the low temperature oxide was adjusted in thickness. No correlation was observed during subsequent measurements.) The thickness chosen for etched oxides was from the later stabilized value; repeatability was closer than ± 1Å. The reproducibility of the index measurement was < ±0.0005. The thickness and index of refraction of the oxide readings taken on subsequent days were generally within these values. Additional readings were sometimes taken to verify the stability of the films, or to check for errors in this manually operated two-zone ellipsometer arrangement. The angle of incidence is the most critical setting. The observed reproducibility is well within the resetability of this angle.

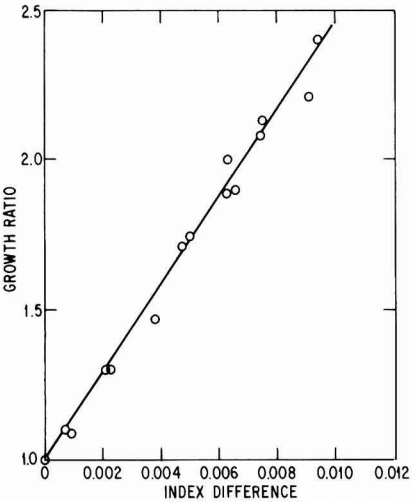

Fig. 1. Incremental growth ratio for pairs of oxidized wafers relative to the initial index of refraction difference in the low and the high temperature oxides.

After the short extended growth of the oxide pairs, it was typically found that the index of the lowest temperature film had not changed. This result might be expected, as the new growth was but a continuation at the temperature of the initial growth. The index of the higher temperature film was typically found to be higher than initially. In this case, the oxide added at the lower temperature would be expected to have a high index. The initial high temperature oxide remains unchanged with the lower temperature exposure. The averaged index of the composite film is then greater than the original index. A calculation from ellipsometer readings using a two film case shows that the agreement of thickness and indexes of refraction is good. One further note—Fig. 1 contains points from both <100> and <111> silicon oxidation pairs.

The thickness-time growth curves of <111> and <100> silicon oxide were analyzed by hand fitting to an equation of the form $t = A(X - 20) + B(X^2 - 20^2)$ (3). Minutes of growth is t; A and B are the reciprocal rate constants; and X is the oxide thickness in angstroms. The rate constants are plotted in Fig. 2 and 3. The points for the lowest temperatures are not reliable, as large corrections were made for initial growth (18). The growth curves of Hopper *et al.* (2) and of Irene and van der Meulen (3), which were carefully analyzed, are not in particularly good agreement with each other. For this reason and the fact that there was some scatter in the 15-30 points making up our growth curves, the hand fitting of the equations seemed adequate.

Discussion

Diffusion.—Figure 1 shows that there are large readily measurable variations in the incremental growth rate of oxide films in the same environment. The variations appear to correlate to the sensitivity of the oxygen diffusion constant to the packing (in amorphous material) of the solid oxides. This conclusion is a restatement of commentary from the introduction. The sequence of the argument goes from our measured index of refraction change to the measured (14) and calculated density change through the Lorenz-Lorentz relation to an inferred interstitial volume change. The 0.43% decrease in index of refraction leads, in our example, to the 88% increase in the diffusion rate of oxygen through a thermal oxide on silicon.

This result indicates that another source for a temperature coefficient for diffusion in silicon thermal oxides has been identified. In the usual linear-parabolic analysis of oxidation, the coefficient for the parabolic rate contains the diffusion term. The temperature variation of this parabolic rate is often compared to the variation of molecular oxygen diffusion found for fused quartz (1). The possible constraint imposed by this comparison has now been removed, and a larger temperature variation may be considered more favorably.

If the incremental thickness differences in the oxide films described were attributed to only the parabolic term in the growth rate, these differences would also apply directly to the diffusion constant change. When the index changes of Fig. 1 are converted to inverse tempera-

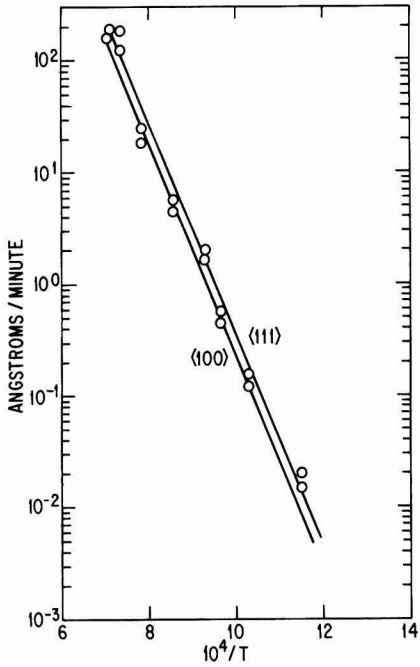

Fig. 2. Linear rate constants for dry oxides on <111> and <100> silicon.

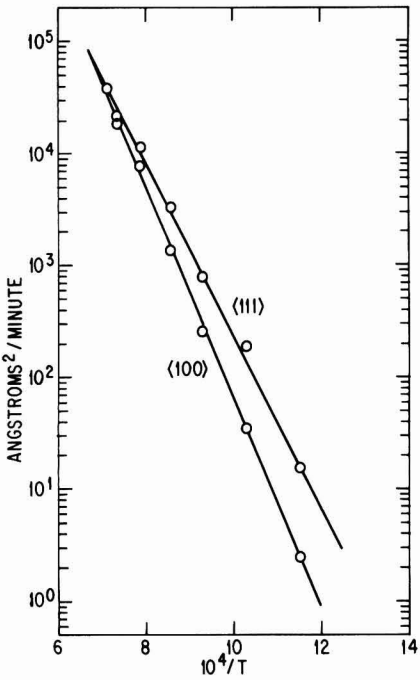

Fig. 3. Parabolic rate constants for dry oxides on <111> and <100> silicon.

ture through Ref. (13) and plotted against the logarithm of incremental thickness, a curve corresponding to an energy of ~0.3 eV is found for <111> silicon.

This structurally dependent diffusion rate of oxygen in silicon oxide is decreasing with decreasing temperature as does the normal temperature dependent diffusion rate for, *e.g.*, fused quartz. In a series of grown oxide films, the net result is a steeper diffusion *vs.* inverse temperature curve or a higher apparent activation energy for diffusion. The activation energy for molecular oxygen in fused quartz according to Norton (19) is 1.17 eV. Adding the temperature effect found here, the net activation energy should be 1.17 + 0.3 or 1.47 eV. This is for oxide formed on <111> silicon in dry oxygen. Taft (13) shows that oxides on <100> silicon have a slightly steeper index-temperature variation than those on <111> material. As the data of Fig. 1 also apply to <100> silicon, the apparent activation energy for diffusion in these oxides could be about 1.6 eV. It should be mentioned that these are minimum corrections. Consideration of the linear rate contribution or of the small effect of the two-layer oxide after regrowth will make for somewhat larger corrections.

The numbers are, of course, approximations, as the added factor is determined from data on a series of structurally different oxides. The data also indicate a T rather than $1/T$ relation with diffusion. It might be expected that the observed Arrhenius plot of the parabolic rate constant for oxide films would be nonlinear over an extended temperature range (8, 20, 21).

Rate constants.—As the major point of this paper is to present the oxygen diffusion effect, the rate constants determined in Fig. 2 and 3 are meant to serve in a corroborative role. The oxides grown here will be shown to be similar to those generally accepted in the literature. In the temperature range 900°-1200°C used for the diffusion measurements, the literature is fairly consistent.

Our activation energy for the linear rate constants is about 1.88 eV. This value is similar to that found by Hopper *et al.* (2), Kamigaki (6), and Lie *et al.* (8). Slightly greater values at ~2.0 eV are found by Deal and Grove (1) and Deal *et al.* (7). Slightly lower values are found by Irene (22, 23), Irene and van der Meulen (3), and Irene and Dong (20). The latter group finds the activation energy for <100> to be slightly higher than for <111> silicon. Also they find that the activation energy is not constant with temperature. Our rate constants for oxide on <111> silicon are slightly higher than those of Lie *et al.* (8) and Hopper *et al.* (2), and considerably higher than those of Deal and Grove (1) and Irene and van der Meulen (3). At 1000°C, the constant agrees with Revesz and Evans (24). The rate constant for oxide grown on <111> silicon appears to be about twice that grown on <100> silicon at the same temperature. This observation has been previously reported by van der Meulen (4), Irene (22), and Kamagaki (6). It appears that the linear rate constants for oxides grown in this experiment compare favorably to those reported in the literature.

Our activation energy for the parabolic rate constants is dependent upon the orientation of the silicon. For <111> silicon, it is ~1.45 eV, and for <100> silicon it is ~1.85 eV. For <111> silicon, our value is close to that of Lie *et al.* (8) and Hopper *et al.* (2), as was also noted for the linear term. Values nearer to 1.2 eV were found by Deal and Grove (1), Deal *et al.* (7), and by Revesz and Evans (24). Irene (22) and Irene and van der Meulen (3) found higher values. A larger activation energy for the <100> orientation is noted by Irene (22). Irene and Dong (20), Lie *et al.* (8), and Han and Helms (21) do not find a constant activation energy. The rate constants for <111> silicon are near those obtained by Lie *et al.* (8) and Hopper *et al.* (2) and smaller than the Deal and Grove (1) values. As with the linear term, our rate constants for the parabolic term are in reasonable agreement with reported values.

The actual oxide growth time for, *e.g.*, a 1000Å oxide on <111> silicon at 1000°C, is found to be in better agreement among the several references given than are the derived rate constants. While our rate constants do not agree as well with those of Deal and Grove (1) as they do with others, the calculated growth times for this oxide are within a few percent of each other. It appears that the dry oxides grown for this diffusion experiment are much like other oxides reported.

Summary

Incremental growth rates in dry oxygen of oxides on silicon in the same furnace are found to differ by more than two. These rates are directly related to the index of refraction of the initial oxide film and thus to the original growth temperature. Therefore, there seems to be a change in diffusion rate because of a change in the oxide structure with growth temperature. This structure factor when added to the activation energy for the diffusion of oxygen through fused quartz could account for the higher effective activation energy of the parabolic rate constants usually observed. The activation energy for growth of oxide on <100> silicon should be higher than that on <111> silicon.

Acknowledgment

I should like to express my thanks to H. R. Philipp for his encouragement in the course of this work.

Manuscript submitted Jan. 28, 1985; revised manuscript received June 20, 1985.

General Electric Company assisted in meeting the publication costs of this article.

REFERENCES

1. B. E. Deal and A. S. Grove, *J. Appl. Phys.*, **36,** 3770 (1965).
2. M. A. Hopper, R. A. Clarke, and L. Young, *This Journal*, **122,** 1216 (1975).
3. E. A. Irene and Y. J. van der Meulen, *ibid.*, **123,** 1380 (1976).
4. Y. J. van der Meulen, *ibid.*, **119,** 530 (1972).
5. D. W. Hess and B. E. Deal, *ibid.*, **122,** 579 (1975).
6. Y. Kamigaki and Y. Itoh, *J. Appl. Phys.*, **48,** 2891 (1977).
7. B. E. Deal, D. W. Hess, J. D. Plummer, and C. P. Ho, *This Journal*, 125, 339 (1978).
8. L. N. Lie, R. R. Razouk, and B. E. Deal, *ibid.*, **129,** 2828 (1982).
9. W. A. Tiller, *ibid.*, **127,** 625 (1980).
10. M. Hamasaki, *Solid-State Electron.*, **25,** 479 (1982).
11. W. A. Tiller, *This Journal*, **130,** 501 (1983).
12. S. M. Hu, *J. Appl. Phys.*, **55,** 4095 (1984).
13. E. A. Taft, *This Journal*, **125,** 968 (1978).
14. E. A. Irene, D. W. Dong, and R. J. Zeto, *ibid.*, **127,** 396 (1980).
15. F. J. Norton, *J. Appl. Phys.*, **28,** 34 (1957).
16. Chien-Jih Han and C. R. Helms, *This Journal*, **132,** 402 (1985).
17. B. H. Claussen and M. Flower, *ibid.*, **110,** 983 (1963).
18. E. A. Taft, *ibid.*, **131,** 2460 (1984).
19. F. J. Norton, *Nature*, **171,** 701 (1961).
20. E. A. Irene and D. W. Dong, *This Journal*, **125,** 1146 (1978).
21. C. J. Han and C. R. Helms, *ibid.*, **132,** 516 (1985).
22. E. A. Irene, *ibid.*, **121,** 1613 (1974).
23. E. A. Irene, *Appl. Phys. Lett.*, **40,** 74 (1981).
24. A. G. Revesz and R. J. Evans, *J. Phys. Chem. Solids*, **30,** 551 (1969).

Oxidation Properties of Nickel in the Temperature Range 1073-1500 K

F. A. Elrefaie,[1] A. Manolescu,[2] and W. W. Smeltzer*

Institute for Materials Research and Department of Metallurgy and Materials Science, McMaster University, Hamilton, Ontario, Canada L8S 4M1

ABSTRACT

Oxidation of nickel after preoxidation at 1473 K was investigated during isothermal stages in oxygen atmospheres, $10^3 \leq P_{O_2} \leq 10^5$ Pa, at temperatures in the range 1073-1500 K. The reaction kinetics were parabolic; the parabolic oxidation rate constant was proportional to $P_{O_2}^{1/n}$ with the value of n varying from 5.5 ± 0.2 at 1073 K to 6.2 ± 0.2 at 1473 K. The activation energy of oxidation was 225 ± 4 kJ/mol NiO. Marker measurements indicated that the polycrystalline columnar NiO scales, which exhibited a preferred (100) texture, grew by predominant outward nickel diffusion. The measured values of the parabolic oxidation rate constants were higher by a factor of ≤ 3 than values calculated using nickel self-diffusion coefficients of single-crystal NiO, due probably to a component of nickel migration along easy diffusion paths developed in the polycrystalline scales.

Oxidation of nickel is expected to follow parabolic kinetics when the kinetics are controlled by lattice diffusion of nickel via cation vacancies in the NiO scale. Application of Wagner's theory for parabolic oxidation (1) to the high temperature scaling of nickel has been examined by several investigators as reviewed in Ref. (2-5). The agreement between experimental and calculated values of the parabolic oxidation rate constant is satisfactory to a first approximation at temperatures higher than 1273 K; at lower temperatures, this agreement breaks down and can attain a discrepancy as high as 5-7 orders of magnitude at 773 K. This discrepancy arises because nickel migration along easy diffusion paths in the polycrystalline NiO layer such as dislocations and subgrain and grain boundaries plays a predominant role in the reaction mechanism. The purpose of this research, accordingly, was to investigate the influence of a preformed thin NiO layer, which was relatively free of easy diffusion paths, on the subsequent morphological development and oxidation mechanism of scales grown during isothermal stages at 1073-1473 K.

*Electrochemical Society Active Member.

[1]Present address: Department of Metallurgical Engineering, Cairo University, El Giza, Egypt.

[2]Present address: Ontario Hydro Research Laboratory, Toronto, Ontario, Canada.

Experimental

Nickel plate specimens, 2 × 1 × 0.05 cm, were prepared from 99.995 atom percent (a/o) purity sheet containing impurity contents as listed in Table I. These specimens after abrasion on 600 and 800 SiC grit paper and ultrasonic cleaning in methanol were annealed in flowing ultrahigh purity argon at 1473 K. An annealed specimen, average grain size ~ 0.1 cm, was polished on napless cloths to 1 μm diamond paste using kerosene and cleaned as above prior to placement in the oxidation apparatus.

Oxidation kinetics were measured gravimetrically using a recording semimicrobalance assembly as described elsewhere (6). The oxidizing atmospheres maintained at 10^5 Pa were static air, flowing oxygen, or oxygen-argon mixtures of oxygen partial pressures ranging from 1×10^3 to 2×10^4 Pa. A specimen was oxidized initially at 1473 K for 120-300s, then the furnace temperature was altered to a lower value, whereupon the specimen was oxidized isothermally and subsequently at several other temperatures in the same atmosphere.

Table I. Impurity contents of nickel, 99.995 a/o pure

Element	B	C	N	O	F	Na	Mg	Al	Si	S	Cl
ppma	0.3	7	0.6	4	0.5	0.04	1	1	10	0.8	0.01
Element	K	Ca	Ti	Cr	Mn	Fe	Cu	Ag	Ba	Pb	
ppma	0.02	0.3	0.05	0.03	0.2	20	3	0.02	0.2	0.02	

Marker studies were carried out by placing platinum wire, 25 μm diam, around a nickel specimen which was sandwiched between two α-Al_2O_3 disks and heated at 1273 K in argon for 10.8 ks to assure the absence of a gap between the wire and specimen surface.

Optical and electron microscopy was used to investigate the morphology of the NiO layers. Preferred orientations of the oxide grains within the polycrystalline scales were determined using an inverse pole figure method (7) whereby the texture coefficient of an (hkl) plane, P_{hkl}, of oxide is given by

$$P_{hkl} = \frac{I_{hkl}/I_{r,hkl}}{\frac{1}{n}\Sigma\, I_{hkl}/I_{r,hkl}} \quad [1]$$

In this expression, I_{hkl} and $I_{r,hkl}$ are integrated intensities from the (hkl) peak of oxide within the scale and of randomly oriented powder, and n is the number of peaks examined.

Results

Oxidation kinetics.—Typical oxidation curves are illustrated by the parabolic-type plots in Fig. 1. In this case, a nickel specimen was initially oxidized in air at 1473 K for 300s before altering the furnace temperature to 1098 K. Although this latter temperature was attained after 5.4 ks, the slope of the kinetic curve plotted in parabolic form continued to decrease and eventually reached a constant value after 30 ks from which the parabolic rate constant was determined. When the temperature was then changed over ~ 50 K ranges, parabolic oxidation behavior was established after 600-1800s from temperature stabilization.

Values of the parabolic oxidation rate constant obtained at specified temperatures are plotted *vs.* oxygen pressure in Fig. 2. This rate constant was proportional to $P_{O_2}^{1/n}$ where n = 5.5, 5.8, 5.4, 6.3, and 6.2 at 1073, 1173, 1273, 1373, and 1473 K, respectively, within an estimated error of ±0.2.

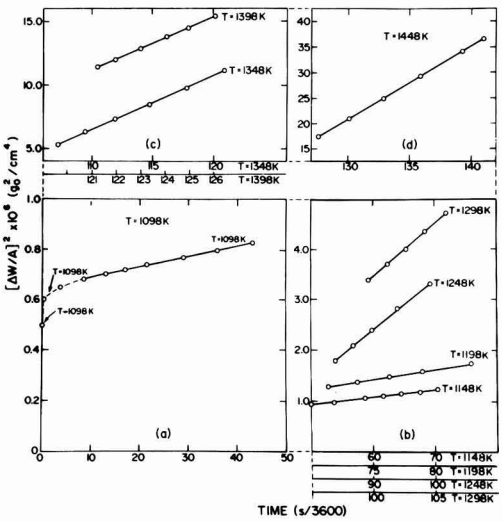

Fig. 1. The parabolic oxidation of nickel in air at temperatures in the range 1098-1448 K. The specimen was preoxidized at 300s at 1498 K before altering temperature to 1098 K, followed by subsequent oxidation at 1098 K (a), 1148, 1198, 1248, and 1298 K (b), 1348 and 1398 K (c), and 1448 K (d).

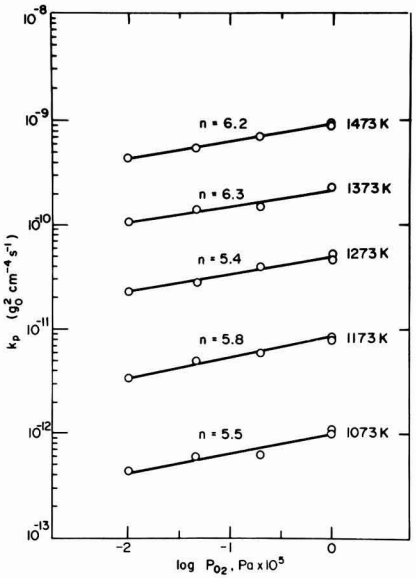

Fig. 2. The dependence of the parabolic oxidation rate constants on oxygen pressure according to the relationship $k_p = k_p^{\circ}(P_{O_2})^{1/n}$.

Arrhenius plots of the parabolic rate constants for oxidation of nickel in the various atmospheres are shown in Fig. 3. The activation energies calculated from the slopes of the least squares linear fits are given in Table II; an average value of 225 ± 4 kJ/mol NiO is estimated at constant oxygen pressure within $10^3 \leq P_{O_2} \leq 10^5$ Pa.

Oxide microstructure.—As illustrated in Fig. 4, a uniformly thick NiO layer was formed at 1473 K upon oxidizing nickel for 300s. One or two oxide grains extended

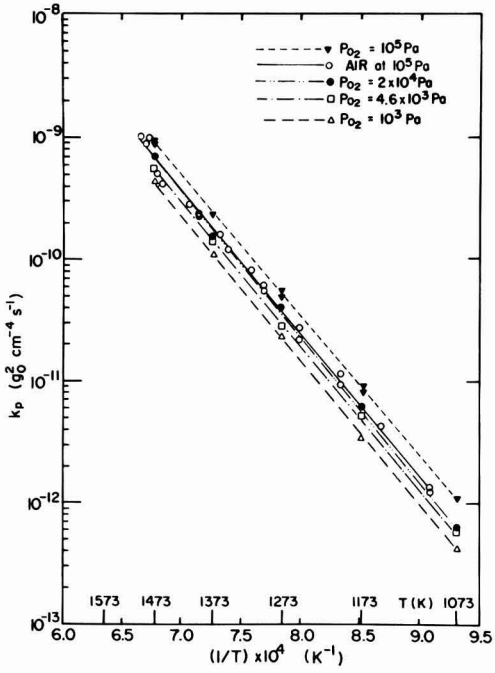

Fig. 3. Arrhenius plots of the parabolic oxidation rate constants in the temperature range 1073-1500 K at different oxygen pressures.

Table II. Activation energies for parabolic oxidation of nickel in various atmospheres

Atmosphere total pressure: 1 atm (1×10^5 Pa)	Temperature range (K)	Activation energy (J/mol NiO)
Oxygen	1073-1473	221,750
Air	1098-1500	223,840
O_2-Ar: $P_{O_2} = 2 \times 10^4$ Pa	1073-1473	228.030
O_2-Ar: $P_{O_2} = 4.6 \times 10^3$ Pa	1073-1473	223,840
O_2-Ar: $P_{O_2} = 10^3$ Pa	1073-1473	228,030

across this layer, and it exhibited a relatively flat outer surface. This scale morphology can be contrasted to that of the NiO layer formed when nickel was directly oxidized at the lower temperature of 1098 K for a long period of 155 ks as shown in Fig. 5. In this latter case, the small grains of ~ 3 μm diam within the NiO layer were encased by oxide ridges, and they exhibited little preferred texture, as indicated by the values of P_{hkl} calculated for (111), (200), (220), and (311) planes, $0.9 < P_{hkl} < 1.1$, using Eq. [1].

A typical morphology of the oxide layers obtained after complete cycles of oxidation over several temperatures is shown in Fig. 6. The photomicrograph shown in Fig. 6a manifests the formation of a compact oxide layer having good adherence to the metal. The fracture cross section, Fig. 6a, illustrates formation of columnar NiO grains extending completely across the scale which are of smaller lateral dimension adjacent to the metal. The external surfaces of these grains, Fig. 6b, are flat even though the intersections of grain boundaries with the external surface were severely faceted. These fully developed scales exhibited a (100) preferred orientation texture as illustrated by the values of P_{hkl} recorded in Table III. The columnar grains in the scales exhibited little lateral growth during the oxidation cycles, as their average lateral diameter was ~ 3 μm as measured along the midpoint line in the scale.

Marker measurements.—The oxidation run on the nickel specimen with markers was carried out in air according to the reaction sequence illustrated in Fig. 1, followed by a prolonged final oxidation state of 252 ks at 1448 K. Figure 7 illustrates the positions of two markers. The marker in Fig. 7a is located directly on the metal/oxide interface, and NiO internal precipitates exist beneath the marker. A thin layer of NiO was formed beneath the marker shown in Fig. 7b, but such markers remained at positions tangent to the main metal/oxide interface. These markers were oxidized with indication of oxide precipitation within the marker matrix. Scale void population was high in the region around a marker and the scale tended to jut out from the marker.

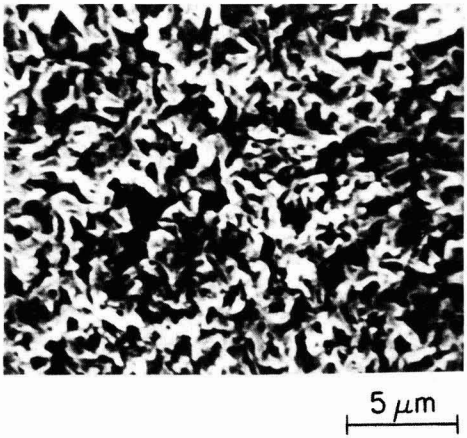

Fig. 5. The topology of NiO layer formed on nickel after direct oxidation in air at 1098 K for 155 ks.

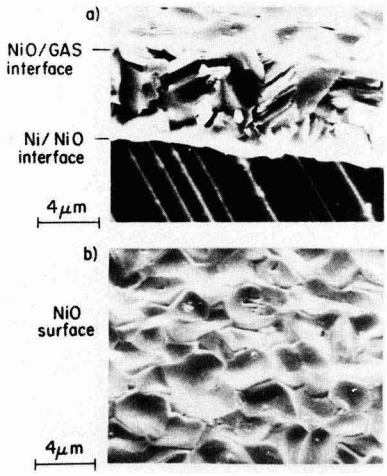

Fig. 6. The NiO layer formed on nickel in air at temperatures in the range 1098-1448 K after the complete oxidation cycle as given in Fig. 1. a: Fracture cross section. b: NiO surface at scale/gas interface.

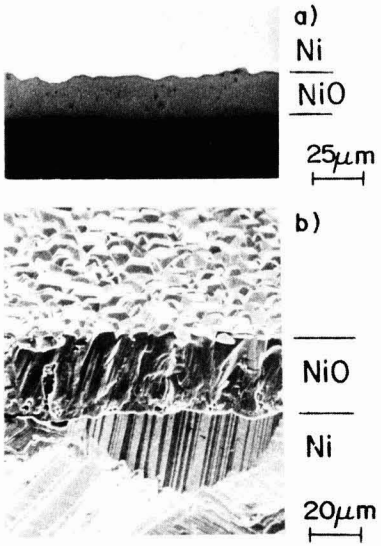

Fig. 4. The NiO layer formed on nickel after oxidation in air at 1473 K. a: Metallographic cross section. b: Fracture cross section.

Discussion and Conclusions

Values of the parabolic oxidation rate constant in oxygen atmospheres, $10^3 \leq P_{O_2} \leq 10^5$ Pa, were obtained at temperatures in the range 1073-1500 K by oxidizing nickel specimens isothermally in stages at several temperatures after brief preoxidation at 1473 K. This rate constant was proportional to $P_{O_2}^{1/n}$ where $5.5 \leq n \leq 6.2$, which is in agreement with the hypothesis that nickel migration

Table III. Texture coefficient of (hkl) planes of NiO in scales formed on nickel as calculated by Eq. [1]

Atmosphere $P = 10^5$ Pa	P_{hkl} (111)	(200)	(220)	(311)
O_2	0.02	2.99	0.06	0.92
Air	0.20	2.00	0.60	1.30
O_2-Ar; $P_{O_2} = 10^3$ Pa	0.00	2.68	0.13	1.18

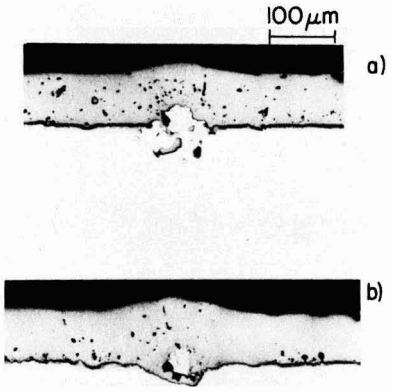

Fig. 7. The positions of platinum markers on a nickel specimen after oxidation according to the reaction cycle given in Fig. 1 followed by prolonged oxidation of 252 ks at 1448 K.

through NiO predominately by doubly charged cation vacancies determined the growth rate of this oxide layer (2-5). An average value of 22 kJ/mol for the activation energy of parabolic oxidation is of approximately the same magnitude, but 225 kJ/mol less than the most recent determination for the activation energy of nickel self-diffusion in single-crystal NiO (8).

The values obtained at different temperatures for the parabolic rate constant at $P_{O_2} = 10^5$ Pa are compared to those from the literature in Fig. 8. Fair agreement exists for all evaluations above 1273 K. The previously reported values at temperatures less than 1273 K are of larger magnitude than those reported in this investigation and they yield Arrhenius plots of smaller slopes. In this lower temperature range extending down to 773 K, oxide growth has been interpreted as being controlled by nickel short-circuit diffusion involving easy diffusion paths in the polycrystalline NiO scales formed on nickel polycrystalline sheet or nickel single-crystal faces (2-5). These easy diffusion paths have been assumed to be largely associated with the oxide grain boundaries since these are decorated by a network of outward extending ridges at the external oxide surface when the metal is directly oxidized as illustrated in Fig. 5.

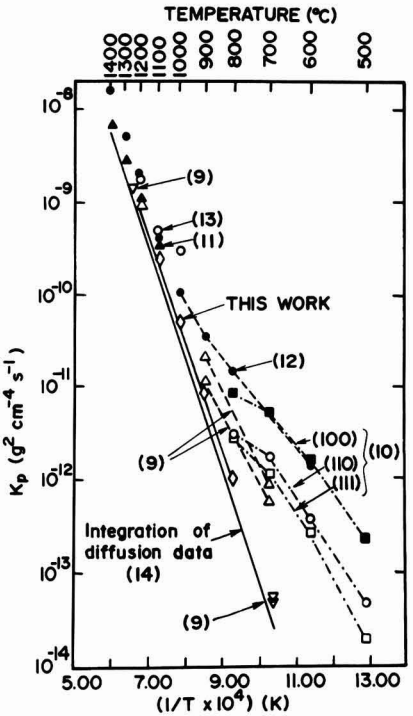

Fig. 8. Arrhenius plots of parabolic oxidation constants at $P_{O_2} = 10^5$ Pa for NiO layer growth on polycrystalline, crystal faces, and pre-oxidized polycrystalline nickel. The numbers on plots are the references. The experimental determinations from Ref. (9) at 973 K are from direct observations of thickening of the NiO grain matrix.

Arrhenius plots of the parabolic rate constants obtained under the condition of preoxidation were linear over the entire temperature range from 1073 to 1500 K, as shown in Fig. 3 and 8. This behavior arose because preoxidation at 1473 K led to formation of a thin oxide layer relatively free of easy diffusion paths. This layer thickened upon subsequent stages of oxidation at lower temperatures into scales containing large columnar oxide grains mainly by nickel lattice diffusion. These conclusions are also consistent with earlier optical measurements on the growth of individual large oxide grains in scales grown at 973 K (9) on polycrystalline nickel as illustrated in Fig. 8.

One can utilize the Wagner theory for parabolic oxidation based upon lattice ambipolar diffusion to quantitatively assess diffusional processes during nickel oxide layer growth. The parabolic rational rate constant (1) is

$$k_r \text{ (eq/cm-s)} = \bar{c} \int_{a'_0}^{a''_0} D \, d \ln a_0 \qquad [2]$$

where $\bar{c}$ is the average equivalent nickel concentration in NiO, D is the self-diffusion coefficient of nickel in NiO, and $a_0 = (P_{O_2})^{1/2} = \{P_{O_2} \text{ (Pa)}/1.013 \times 10^5 \text{ (Pa)}\}^{1/2}$ is the oxygen activity integrated over the limits from the metal/oxide to oxide/oxygen interface. Since D conforms to a $P_{O_2}^{1/n}$ relationship where $4 \leq n \leq 6$ (15), Eq. [2] becomes

$$k_p \text{(g O}^2\text{/cm}^4\text{-s)} = nD^0(P''_{O_2})^{1/n} \left(\frac{M_0 \rho_{NiO}}{M_{NiO}}\right)^2 [1 - (P'_{O_2}/P''_{O_2})^{1/n}] \qquad [3]$$

Here, D^0 is the nickel self-diffusion coefficient at $P_{O_2} = 10^5$ Pa, M_0 and M_{NiO} are the atomic weight and formula weight of oxygen and NiO, respectively, and $\rho = 6.85$ g/cm^3 is the density of NiO.

The tracer diffusion coefficient of nickel in NiO, D^*, was determined (14) recently at $P_{O_2} = 10^5$ Pa and at temperatures in the range 795-1673 K

$$D^* \text{ (cm}^2\text{/s)} = 2.2 \times 10^{-2} \exp - 246.9 \text{ kJ}/RT \qquad [4]$$

Since the diffusion process is controlled by a vacancy mechanism, D^* is related to D by a correlation factor $D^* = fD$, where $f = 0.78$. At $P''_{O_2} = 1$, Eq. [3] becomes

$$k_p \text{(g O}^2\text{/cm}^4\text{-s)} = 2.76nD^*[1 - (P'_{O_2})^{1/n}] \qquad [5]$$

Based on Eq. [5], k_p values were calculated utilizing values of D^* (Eq. [4]) and $n = 6$ for doubly charged nickel vacancies, since $5.5 \leq n \leq 6.2$ from this investigation, and P'_{O_2} for equilibration of NiO with nickel (17). These calculated values are compared to the experimentally obtained values in Table IV and Fig. 8. These values are in fair

Table IV. A comparison of the measured and calculated values, Eq. [5], of the parabolic oxidation rate constants of preoxidized nickel in oxygen, $P_{O_2} = 10^5$ Pa, and over the temperature range 1073-1473 K

T (K)	Measured k_p (g^2/cm^4-s)	Calculated k_p (g^2/cm^4-s)	$\frac{k_p(\text{meas})}{k_p(\text{calc})}$
1473	$9.2 \pm 0.2 \times 10^{-10}$	5.7×10^{-10}	1.6
1373	2.3×10^{-10}	1.3×10^{-10}	1.8
1273	$5.0 \pm 0.3 \times 10^{-11}$	2.5×10^{-11}	2.0
1173	$8.2 \pm 0.2 \times 10^{-12}$	3.4×10^{-12}	2.4
1073	1.0×10^{-12}	3.2×10^{-13}	3.2

agreement, the measured values being two to three times larger than the theoretical values.

It would appear that the difference between the experimental and calculated values of the parabolic rate constant was not associated with oxide formation by inward diffusion of oxygen because its diffusion is at least two orders of magnitude less than that for nickel diffusion in NiO (18). Marker measurements, moreover, wherein the marker remains at the metal/oxide interface, indicate that the NiO layer grew predominantly by outward diffusion of nickel. Nickel and platinum are completely miscible and the platinum marker did not remain completely inert. Consequently, formation of internal oxide and a concaved oxide beneath the main metal/oxide interface and the markers, Fig. 7, was brought about by dissociation of NiO and inward oxygen migration through the marker. In similar reported marker experiments (11), NiO formed beneath a porous platinum film marker, but fine relatively inert Al_2O_3 powder markers remained at the Ni/NiO interface.

Since the NiO layer during growth was not completely free from easy diffusion paths such as dislocations, subgrain boundaries (sgb), and grain boundaries (gb), the nickel flux should be given in terms of an effective diffusion coefficient

$$D_{eff} = D + \Sigma D_i f_i \quad [6]$$

where D_i is a diffusion coefficient for an easy diffusion path and f_i is the fraction of diffusion sites in this path such that $\Sigma f_i << 1$. The comparison between experimental and calculated values of the parabolic oxidation rate constant, Table IV, demonstrates that $D_{eff}/D \sim 1.5$-3.

One can readily demonstrate that preferential nickel diffusion via high angle boundaries characteristic of polycrystalline NiO did not play a role in growth of the columnar grained and textured scales. At 1073 K, $D = 2.8 \times 10^{-14}$ cm²/s (14) and $D_{gb} = 2 \times 10^{-9}$ cm²/s in polycrystalline NiO (16) where the width of the boundaries may be taken as 7×10^{-8} cm (16). The average diameter of the columnar NiO grains was ~ 3 μm. Thus, $D_{gb}f_{gb} = 2(2 \times 10^{-9})(7 \times 10^{-8})/(3 \times 10^{-4}) \simeq 9 \times 10^{-13}$ cm²/s, which is 30 times larger, rather than two to three times larger, than D. Metallography, as shown in Fig. 4 and 6, also illustrated that the boundaries of the columnar grains in the preferentially (100)-textured scales did not exhibit evidence of ridges by enhanced oxide growth as did boundaries of grains in untextured oxide scales formed at 1098 K as shown in Fig. 5.

One therefore concludes that the grain boundaries in the textured columnar grained scale did not permit a rapid rate of nickel diffusion as exhibited by high angle boundaries in polycrystalline NiO. It would appear that any enhanced nickel diffusion by boundaries in the columnar scale is of the same magnitude as to be expected by dislocation arrays throughout the scale acting as subgrain boundaries. Since $D_{sgb} = 6 \times 10^{-11}$ cm²/s at 1073 K (3, 14), $D_{sgb}f_{sgb} = 6 \times 10^{-14}$ cm²/s, yielding $D_{eff}/D = 2$ if each grain of ~ 3 μm diam is assumed to contain two subgrains. This latter consideration involving a small degree of short-circuit nickel diffusion by dislocation arrays at grain and subgrain boundaries is consistent with the findings that uniformly thick columnar grained (100)-textured scales grew on the preoxidized metal specimens.

Acknowledgments

The author appreciated helpful discussions with A. T. Chadwick and A. Atkinson on the subject of this paper. This research was carried out under the auspices of the Natural Sciences and Engineering Research Council of Canada.

Manuscript submitted March 7, 1985; revised manuscript received June 17, 1985.

McMaster University assisted in meeting the publication costs of this article.

REFERENCES

1. C. Wagner, "Atom Movements," p. 153, ASM, Cleveland, OH (1951).
2. W. W. Smeltzer and D. J. Young, *Prog. Solid State Chem.*, **10,** 17 (1975).
3. A. Atkinson, R. I. Taylor, and A. E. Hughes, in "High Temperature Corrosion," R. A. Rapp, Editor, p. 110, NACE-6, National Association of Corrosion Engineers, Houston, TX (1983).
4. P. Kofstad, in "High Temperature Corrosion," R. A. Rapp, Editor, p. 123, NACE-6, National Association of Corrosion Engineers, Houston, TX (1983).
5. R. A. Rapp, *Met. Trans. A*, **15,** 765 (1984).
6. P. Mayer and W. W. Smeltzer, *This Journal*, **121,** 538 (1974).
7. G. B. Harris, *Philos. Mag.*, **43,** 113 (1952).
8. A. Atkinson and R. I. Taylor, *J. Mater. Sci.*, **13,** 427 (1978).
9. D. Caplan, M. J. Graham, and M. Cohen, *This Journal*, **119,** 1205 (1972).
10. R. Herchl, N. N. Khoi, T. Homma, and W. W. Smeltzer, *Oxid. Met.*, **4,** 35 (1972).
11. K. Fueki and J. B. Wagner, Jr., *This Journal*, **112,** 384 (1965).
12. J. Paidassi and L. Berry, *C. R. Acad. Sci. Paris*, **262,** 1553 (1966).
13. D. L. Douglass, *Corros. Sci.*, **8,** 665 (1968).
14. A. Atkinson and R. I. Taylor, *Philos. Mag. A*, **39,** 581 (1979).
15. M. L. Volpe and J. Reddy, *J. Chem. Phys.*, **53,** 1117 (1970).
16. A. Atkinson and R. I. Taylor, *Philos. Mag. A*, **43,** 979 (1981).
17. B. C. H. Steele, "Electromotive Measurements in High Temperature Systems," C. B. Alcock, Editor, p. 3, American Elsevier Publishing Co., New York (1968).
18. A. E. Hughes, A. Atkinson, and A. T. Chadwick, AERE Harwell Report R-11200 (1984).

Growth Mechanism of Silicon Plasma Anodic Nitridation

M. Hirayama, T. Matsukawa, H. Arima, Y. Ohno, and H. Nakata

Mitsubishi Electric Corporation, LSI Research and Development Laboratory, 4-1 Mizuhara, Itami, Hyogo 664, Japan

ABSTRACT

Nitridation of silicon was performed in a temperature range of 680°-920°C by 13.56 MHz RF oscillation in nitrogen-hydrogen plasma. Growth kinetics and activation energy of nitridation were investigated. The relationship between nitridation time (t) and nitrided film thickness (x_n) was found to be $x_n\,(2 - 0.00695V_{dc}) = 0.86 \times 10^{-6}t$. External dc voltage ($V_{dc}$) on plasma nitridation was effective in obtaining a high growth rate of nitrided film on silicon. Activation energy for the plasma anodic nitridation of silicon (0.25 eV) was twice as large as the value of plasma nitridation without an external dc voltage. The role of hydrogen in plasma nitridation was also studied with quadrupole mass spectroscopy.

Progress in MOS VLSI densification requires a large capacitance in a small capacitor area (1). Therefore, the direct nitridation of silicon may be one of the most attractive techniques for the device fabrication process. Compared with the widely used silicon dioxide film, silicon nitride film has a higher dielectric constant. The silicon nitride film is chemically stable and is also much better as a diffusion barrier for impurities and metals. In spite of these advantages, the silicon nitride film deposited on silicon wafers by LPCVD cannot be used for the gate dielectric film of MOSFET because it was interfacial instabilities between the silicon nitride and the silicon substrate. Many attempts at achieving direct nitridation and forming the silicon nitride film have already been made (2, 3). Ito *et al.* reported that uniform amorphous silicon nitride films could be obtained from the reaction of silicon in an ammonia ambient and applied to the LSI device fabrication (4). However, these films were very thin because of the slow diffusion of nitridant species through the nitrided film. To improve the low growth rate, plasma nitridation and plasma anodic nitridation were attempted. A high reaction rate was given by the plasma-exited reactive species compared with the thermal reaction. Plasma anodic nitridation was expected to give an enhanced growth rate, similar to that in the case of the anodic oxidation of silicon (5). Also, the reaction temperature could be decreased below the temperature of the thermodynamical limit beause the plasma reaction forms reactive species.

In this paper, the growth mechanism of plasma anodic nitridation will be investigated. To prevent the contamination of oxygen and hydro-oxygen, we used highly purified hydrogen and nitrogen for our experiment.

Experimental

The vacuum system, gas sources, and experimental arrangements for achieving the plasma anodic nitridation of silicon are shown in Fig. 1. They are the same as those used in the earlier study (6). Nitrogen plasma was generated at a pressure range from 0.5 to 2.0 torr by an RF oscillator whose frequency was 13.56 MHz. Anodization voltage applied between the anode and the ground level was supplied by an external dc supply. The nitridation experiments were performed in a temperature range from 680° to 920°C. Boron-doped n-type (100)-oriented CZ silicon wafers, whose resistivity was about 10 Ω-cm, were used for the nitridation. To remove the native oxide on the silicon surface, hydrogen plasma was generated prior to the nitridation process under a pressure below 0.2 torr. The reaction chamber was first pumped down to less than 4×10^{-5} torr with a turbo molecular pump to minimize the residual gases. Then research-grade nitrogen and hydrogen were admitted to the reaction chamber. After the pressure became stable, glow discharge was initiated by applying RF power. The anodizing voltage applied to the sample was typically 150V. The nitridation time was varied between 10 min and 400 min.

In order to study the nitridation mechanism, quadrupole mass analysis of the reacting plasma in the chamber was performed. Transmission electron microscopy (TEM) was carried out to examine the interface structure of silicon nitride and silicon. Also, characterization of the nitrided film was studied using Auger electron spectroscopy and infrared absorption.

Results and Discussion

Film composition.—The infrared absorption spectrum of Fig. 2 shows the characteristic absorption peak of nitride film at wave number of 865, 895 cm^{-1}. The wafer was nitrided at 920°C for 400 min with an external dc voltage of 150V. A peak at 610 cm^{-1} identified as the phonon absorption of the silicon substrate was observed, but no absorption interpreted as Si-O bonds was found in this spectrum. The 865 and 895 cm^{-1} peaks are due to the stretching vibration of Si-N bonds and seem to be almost the same as the peak described by Frieser (2). However, a peak at 920 cm^{-1}, higher than our measurement, results for Si-N bonds was reported by Ito *et al.* (4).

The chemical composition of films formed by plasma anodic nitridation was examined by Auger electron spectroscopy (AES). The AES analysis revealed the presence of nitrogen and oxygen at the surface of the nitrided samples. Since hydrogen is not detectable with Auger spectroscopy, the hydrogen content of these samples is not known. Carbon peaks were not observed from any AES spectra, so carbon atoms at the sample surface did not exist. Sputter etching was accomplished with a 1.0 keV argon ion to obtain in-depth profiles. A typical Auger spectrum of the plasma anodic nitridation film is shown in Fig. 3. The film was grown for 300 min in a nitrogen-hydrogen mixture with an external dc voltage of 150V. The N_{KLL} and O_{KLL} lines are clearly observed on this spectrum obtained from the surface of the nitrided film. From the results of infrared absorption and the Auger spectrum, it is concluded that the silicon surface was changed to silicon nitride by this plasma anodic nitridation.

Nitridation.—Figure 4 is a cross-sectional view of plasma-anodized silicon and the silicon dioxide boundary using a high resolution transmission electron microscope (TEM). It is observed that the thickness of the nitrided films on the silicon surface is almost the same as it is on the silicon dioxide surface. On the sidewall of the silicon dioxide, the film thickness is small. This nitridation behavior shows anisotropical growth resulting from plasma

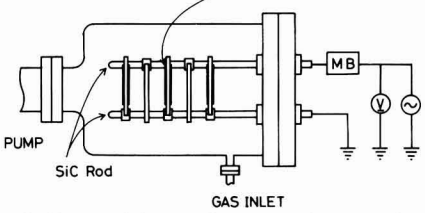

Fig. 1. Schematical diagram of experimental apparatus for plasma anodic nitridation.

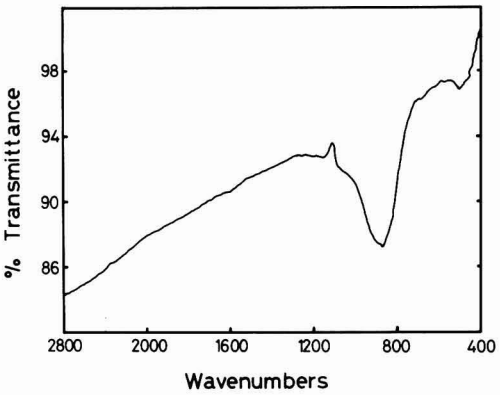

Fig. 2. Infrared transmission curve of nitrided silicon

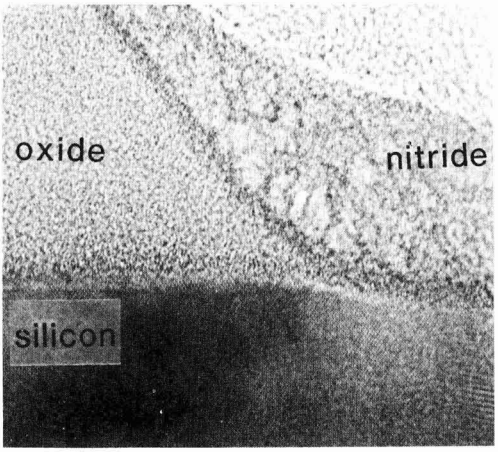

Fig. 4. TEM micrograph of the nitrided film

reaction. The most remarkable point of this TEM photograph is the difference in the interface levels between the silicon-nitrided film and the original silicon-silicon dioxide film. This phenomenon is generally observed on the thermal oxidation of silicon. With the oxidation of silicon, the interface between silicon and silicon dioxide drops down into the bulk silicon, and the thickness ratio of the upper and lower parts of the oxidized film divided by the original silicon surface is generally about half and half. Therefore, in this nitridation experiment, it is supposed that the nitridant species also diffused into silicon and that the silicon surface is actually nitrided like the oxidation of silicon surface.

Growth kinetics.—Figure 5 illustrates the variation of growth rate with the dc power applied to the wafers. The RF power and the temperature were fixed at 500W and 900°C, respectively. The enhancement of the growth rate by the externally applied voltage (V_{dc}) is shown in this figure. It is obvious that the growth rate is remarkably enhanced by the application of the dc bias. The uniformity of the films grown in this system is quite good except in the upper area. For example, with a typical film about 17 nm thick, the standard deviation of the thickness was about 0.8 nm thick within the 4 in. wafer areas.

The dependence of the film thickness on the growth temperature is plotted against the inverse of nitridation temperature in Fig. 6. These lines were obtained from the samples under nitridation conditions listed in the insert.

The nitridation temperature dependences are indicated by the two pairs of parallel curves. From the straight lines shown as solid and dotted, one can obtain apparent activation energies of 0.12 and 0.25 eV, respectively.

Activation energies of the plasma nitridation with or without the external dc voltage indicate only a very weak temperature dependence in the range of 680°-920°C. The gradient difference of the curves is considered to be caused by the application of the external dc voltage on the nitridation. However, these activation energies are somewhat smaller than those reported by Murarka *et al.* for the thermal nitridation of silicon (7).

Next, we will discuss the kinetics of the plasma anodic nitridation of silicon and propose a theory for the anodization mechanisms of silicon. For this purpose, at first, we referred to the model of thermal oxidation of silicon.

In thermal oxidation, there are three basic steps theoretically established by Deal and Grove (8). These three steps are the transportation of oxidant gases, the diffusion of oxidant species in oxide film, and the reaction with the silicon surface. The theory consists of the flux correspondence to each step at each boundary and well explains the experimental results of thermal oxidation. The same analysis based on the solution of the continuity equation has been applied to thermal nitridation (9). It was concluded that the experimental results were adequately explained by the three step model.

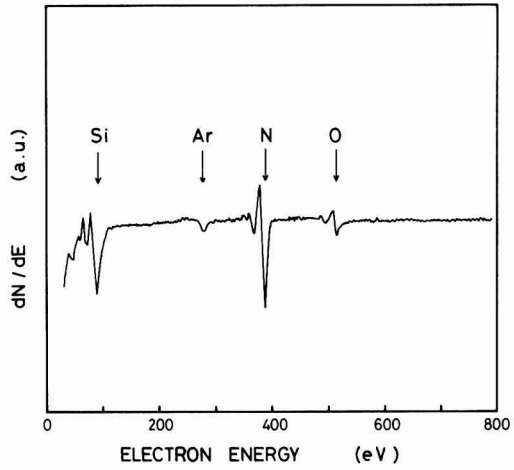

Fig. 3. Typical Auger electron spectrum of plasma anodic nitrided film.

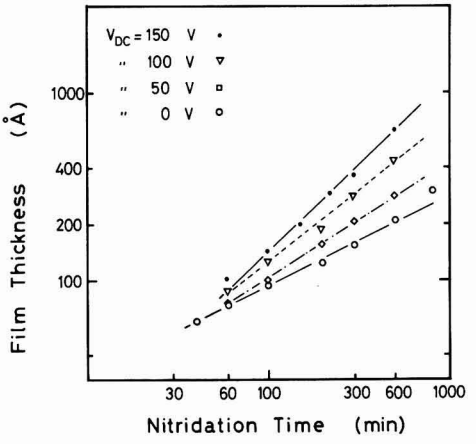

Fig. 5. Dependence of the film thickness on nitridation time

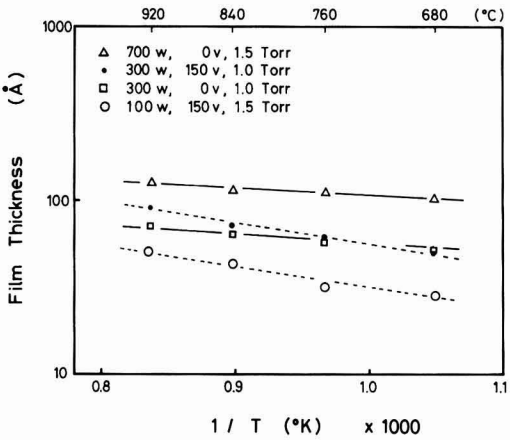

Fig. 6. Dependence of the film thickness on nitridation temperature

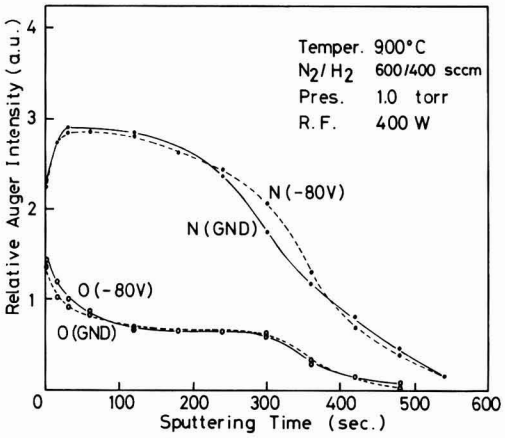

Fig. 8. In-depth Auger profile of the nitrided silicon in nitrogen-hydrogen plasma with negative external voltage.

In the plasma anodic nitridation of a silicon surface, the growth rate constants and characteristic parameters of nitridation were deduced. When the nitridation time is long, the growth rate has an exact parabolic relationship for the plasma nitridation without the external dc voltage supply. The relationship between the nitridation time and the thickness of the growth film shown with open circles in Fig. 5 can be expressed in functional form as $x_n^2 = Bt$, where x_n and t are the silicon nitride thickness and nitridation time, respectively, and B is the temperature-dependent constant. In this relationship, the constant B is calculated as 0.86×10^{-6} $\mu m^2/s$.

The significant effect of an external dc voltage on nitridation growth kinetics was suggested by the experimental data. It is clear that the gradient of these curves increases as the external dc voltage increases, as shown in Fig. 5. The growth rate of nitride film on the silicon surface was accelerated with the positive dc voltage supplied on the silicon substrate. Therefore, the relationship between the nitridation time and the nitride film thickness is empirically described as $x_n (2 - mV_{dc}) = Bt$, where the constant m was given as 0.00695 V^{-1}.

The effect of the external dc voltage was investigated from the in-depth Auger profile of the nitrided film. Figure 7 shows a typical profile of the plasma anodic nitrided film. The film was grown for 400 min in a nitrogen-hydrogen mixture at an external dc voltage of +80V. The peak-to-peak heights of the N_{KLL} and O_{KLL} lines were plotted as a function of the sputtering time. The nitrogen and oxygen profiles are described with filled and open circles, respectively, for both the samples loaded on the anode and the ground side of silicon carbide rods. The thickness of the films of the anodized sample loaded on the anode was almost twice that of the ground sample. The most interesting feature in Fig. 7 is that the tail of the nitrogen profile reaches deeply into the silicon substrate compared with that of the oxygen profile. Nitrogen apparently diffused into silicon more easily than oxygen, even though the nitridant species seems to diffuse slower through the nitride film in comparison to oxygen through the oxide. The nitrogen fraction is highest near the film surface and decreases toward the interface. It is also shown that the nitridant species has difficulty diffusing through the film and that the surface region is preferentially nitrided.

The effects of the anodization by the application of the external negative dc voltage were studied. The in-depth Auger profiles of nitrided films grown for 400 min in a nitrogen-hydrogen mixture plasma at an external dc voltage of −80V is shown in Fig. 8. Nitrogen profiles for both samples loaded on the cathode (the supplied voltage po-

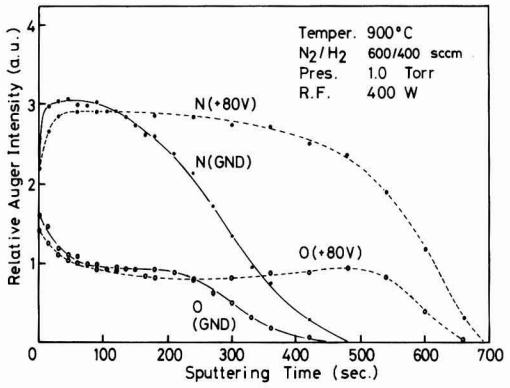

Fig. 7. In-depth Auger profile of the nitrided silicon in nitrogen-hydrogen plasma with positive external voltage.

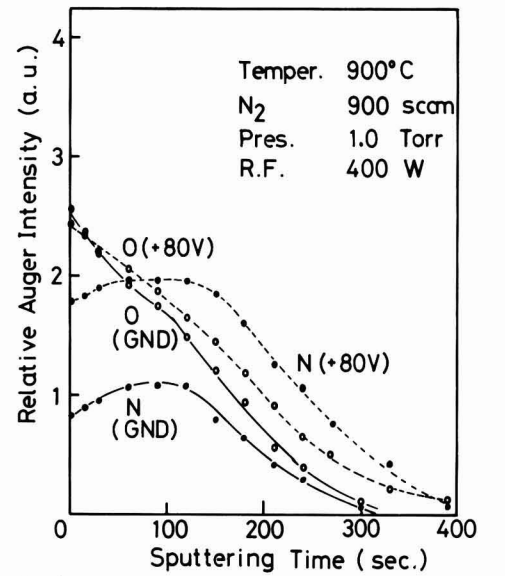

Fig. 9. In-depth Auger profile of the nitrided silicon in nitrogen plasma with positive external voltage.

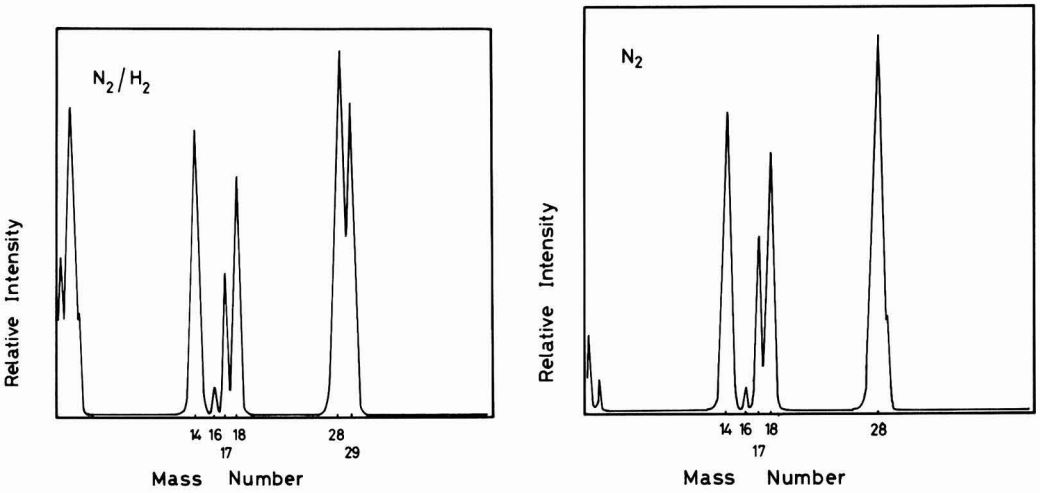

Fig. 10. Quadrupole mass spectra for nitrogen-hydrogen mixture plasma (a,left) and nitrogen plasma (b,right)

larity was changed) and the ground show almost the same curve. Beside the oxygen profiles were drawn almost the same curve one above another for the external dc positive and negative voltages. There exists no difference of film thickness between the samples loaded on the cathode and the ground level.

Role of hydrogen content.—Nitridation using plasma anodization is considerably more complex, and, at present, we can only present a tentative description of the anodization mechanism. It has been previously suggested that the nitridation of silicon is generally subject to parabolic growth behavior. Analysis of growth behavior in plasma anodization indicates that nitridation is essentially a diffusion-limited process and, presumably, the nitridant species migrate to react with silicon at the interface. Figure 9 illustrates in-depth Auger profile of the film grown for 400 min in nitrogen only. The nitrogen profiles were shrunk abruptly for both samples loaded on the anode and the ground. However, the oxygen profiles fully broadened in the direction of the depth of the films. It is quite different from the former profiles of the nitrided film obtained in the hydrogen-nitrogen mixture plasma. The tail of the nitrogen profiles disappeared before the decline and fall of the oxygen profile for both samples loaded on the anode and the ground.

To investigate the difference between the nitrogen-hydrogen mixture plasma and the nitrogen plasma, the quadrupole mass spectrometer was operated during each nitridation process. The base pressure of the spectrometer was kept at 1×10^{-6} torr, and the measurements were started after the nitridation pressure became stable. In Fig. 10a and 10b, mass spectra obtained from the nitrogen-hydrogen mixture plasma and nitrogen plasma are shown. The peaks observed in both spectra at atomic mass unit (amu) 14 and 28 were coincident with N and N_2. The intensities at amu 16, 17, and 18 were the residual oxygen and hydro-oxygen. The amu 2 and 29 peaks appear on the nitrogen-hydrogen mixture spectrum, and the amplitude of the other peak intensities has not changed between the two kinds of plasma. In the nitrogen-hydrogen plasma, $H^{\cdot}$ $H_2^{\cdot}$, nitrogen-hydrogen molecular ions of $NH^{\cdot}$, $NH_2^{\cdot}$, and $NH_3^{\cdot}$ were identified. Those ions might play the role of nitridant species. Also, it is considered that electrically neutral particles such as nitrogen and nitrogen-hydrogen radicals contribute to the nitridation reaction in plasma discharge. One possibility is that the energetic bombardment of these nitridant species in the plasma promotes the reaction of nitridation on the silicon surface to form the thick nitride film.

Conclusions

Growth kinetics of the plasma anodic nitridation of silicon were investigated using the nitrogen-hydrogen mixture plasma. Results of infrared absorption spectrum and the Auger profile indicated the formation of nitrided films on the silicon surface and the TEM micrograph actually showed the nitridation of silicon. The relationship between the nitridation time and the nitride film thickness can be expressed as $x_n (2 - mV_{dc}) = Bt$. In this equation, the temperature dependent constant B is calculated as 0.86×10^{-6} $\mu m^2/s$ and m is given as 0.00695 V^{-1}. The activation energy of anodization is about twice that of plasma nitridation. Therefore, the external dc voltage is effective in obtaining a higher growth rate of nitrided film on silicon surface. Hydrogen content also greatly contributes to the nitridation of silicon in plasma glow discharge. Some kinds of nitrogen-hydride ions in plasma work as the nitridant species to promote the reaction of nitridation.

Acknowledgments

The authors wish to acknowledge the encouragement of Dr. H. Oka and are also grateful to Professor Dr. W. G. Oldham of California University for valuable discussions.

Manuscript received March 4, 1985. This was Paper 59 presented at the Toronto, Ontario, Canada, Meeting of the Society, May 12-17, 1985.

Mitsubishi Electric Corporation assisted in meeting the publication costs of this article.

REFERENCES

1. R. Dennard, F. Gaensslen, H. Yu, V. Rideout, E. Bassous, and A. LeBlac, *IEEE J. Solid-State Circuits*, **sc-9,** 256 (1974).
2. R. G. Frieser, *This Journal*, **115,** 1092 (1968).
3. E. J. M. Kendall, *J. Phys. D, Ser. 2*, **1,** 1409 (1968).
4. T. Ito, S. Hijiya, T. Nozaki, H. Arakawa, M. Shinoda, and F. Fukukawa, *This Journal*, **125,** 448 (1978).
5. V. Q. Ho and T. Sugano, *IEEE Trans. Electron Devices*, **ed-27,** 1436 (1980).
6. M. Hirayama, T. Matsukawa, H. Arima, Y. Ohno, N. Tsubouchi, and H. Nakata, *This Journal*, **131,** 664 (1984).
7. C. P. Murarka, C. C. Chang, and A. C. Adams, *ibid.*, **126,** 994 (1979).
8. B. E. Deal and A. S. Grove, *J. Appl. Phys.*, **16,** 3770 (1965).
9. C. Y. Wu, C. W. King, M. H. Lee, and C. T. Chen, *This Journal*, **129,** 1559 (1982).

Solubilities of α-Fe_2O_3 and Fe_3O_4 in Fused Na_2SO_4 at 1200 K

Y. S. Zhang and Robert A. Rapp*

Department of Metallurgical Engineering, The Ohio State University, Columbus, Ohio 43210

ABSTRACT

The solubility of mixed α-Fe_2O_3 and Fe_3O_4 in fused Na_2SO_4 was measured at 1200 K as a function of the melt basicity at 2.14×10^{-7} atm O_2. At lower P_{O_2}, in separate ranges of basicity where either Fe_3O_4 or else FeS is the stable phase, the solubilities of these compounds in Na_2SO_4 were determined. From these solubility measurements, the activity coefficients of $NaFeO_2$, FeS, and $FeSO_4$ in fused Na_2SO_4 were calculated to be 430, 180, and 0.83, respectively. On this basis, the solubilities of the iron oxides α-Fe_2O_3 and Fe_3O_4 and the dominant acidic and basic solutes were calculated for the entire regimes of P_{O_2} and melt basicity in which these phases are stable in Na_2SO_4.

Hot corrosion occurs at high temperatures in oxidizing environments when a molten salt deposit contacts a metal surface. Hot corrosion by molten Na_2SO_4 can cause significant damage in gas turbine and other combustion-product environments. Metal oxides are often the stable phases in contact with fused Na_2SO_4. Therefore, a knowledge of the solubility behavior of metal oxides in molten Na_2SO_4 should assist in understanding hot corrosion processes, especially the initiation of hot corrosion. The solubilities of NiO (1, 2), Co_3O_4 (1, 2), Al_2O_3 (3), and Y_2O_3 (4) in Na_2SO_4 have been reported recently.

The solubility of α-Fe_2O_3 in fused Na_2SO_4 (5) has been previously measured at 1 atm O_2 and 1200 K as a function of the melt basicity, defined as log a_{Na_2O}. However, α-Fe_2O_3 is stable only at high P_{O_2} and in a certain basicity regime. As the P_{O_2} in a Na_2SO_4 melt is reduced, Fe_3O_4 becomes stable. From the thermodynamic phase stability diagram for the Na-Fe-S-O system shown as Fig. 1, the solute species and solubilities of the two iron oxides would be expected to depend upon both the melt basicity and the P_{O_2} in the melt. Obviously, solubility measurements at reduced oxygen pressures are needed to provide an overview of the dissolution behavior in the iron-oxygen-sulfur system in Na_2SO_4, and to provide insight for extension to other systems.

In the present work, the solubility of the coexisting oxides, α-Fe_2O_3 and Fe_3O_4, was measured at 1200 K and 2.14×10^{-7} atm O_2. (See Fig. 1.) This measured P_{O_2} corresponds exactly to the thermodynamic value from Ref. (6) for α-Fe_2O_3/Fe_3O_4 equilibrium at 1200 K. However, this result is inconsistent with the JANAF thermodynamic data used previously (5). Furthermore, as shown in the previous work (5) as well as in this work, a plateau in the basic solubility for α-Fe_2O_3 occurs for log $a_{Na_2O} > -8.9$, which is inconsistent with the only available data for $\Delta G^\circ_{NaFeO_2}$. Therefore, in this work, to retain an internal consistency for the calculation of solute activity coefficients and in the construction of Fig. 1, values of ΔG°_f used for compounds in the system are the same as those listed in the preceding papers (3, 5) except for the use of $\Delta G^\circ_{Fe_3O_4} = -730$ kJ/mol and $\Delta G^\circ_{NaFeO_2} = -479$ kJ/mol. These changes are not great, but are thought to represent an improvement over other reported values (7, 8). The dashed lines of Fig. 1 are calculated lines of isoactivity for the several solute species in the system. Figure 1 shows that at $P_{O_2} = 2.14 \times 10^{-7}$ atm, $NaFeO_2$ and $FeSO_4$ should be the dominant basic and acidic solutes, respectively. From the solubility measurements reported here, activity coefficients of $NaFeO_2$ and $FeSO_4$ in Na_2SO_4 are estimated later. At even lower P_{O_2}, dissolved FeS should be the predominant acidic solute of Fe_3O_4. In order to obtain the activity coefficient of FeS in fused Na_2SO_4, the solubility of FeS was also measured within the field of FeS stability. Finally, a generalized map for the solubility behavior in the Fe-O-S system has been calculated for the entire ranges of P_{O_2} and melt basicity in which α-Fe_2O_3 and Fe_3O_4 are stable in Na_2SO_4 at 1200 K. The method may serve as a model for the analysis of other metal-oxygen-sulfur systems.

* Electrochemical Society Active Member.

Experimental Apparatus and Procedure

The experimental setup is illustrated in Fig. 2. A closed-end mullite tube served as the reaction chamber which was closed by a gastight, water-cooled stainless steel flange joined by epoxy. Solid-state electrodes were inserted into the Na_2SO_4 melt through stainless steel adaptors with O-rings. Fused Na_2SO_4 and iron oxide powder were contained in an internal alumina crucible supported by an alumina tube which also sheathed a Pt-Pt/10% Rh thermocouple. The temperature was controlled at 1200 ± 3 K using an Electromax (L&N) temperature controller.

The basicity and oxygen pressure in the Na_2SO_4 melt were measured at a Pt wire working electrode by two immersed reference electrodes: a sodium sensor and an oxygen probe. The sodium sensor consisted of a silver wire contacting a Na_2SO_4-10 mole percent (m/o) Ag_2SO_4 melt contained in a closed-end mullite ($3Al_2O_3 \cdot 2SiO_2$) tube (McDanel MV30), which is a sodium ion conductor (over a grain boundary glass phase) at high temperatures. A platinum wire, spot welded to the silver wire, served as the lead wire. The mullite tube was sealed at the top with an Al_2O_3-base ceramic cement to prevent the loss of SO_3 by the thermal decomposition of the sulfate. The oxygen probe consisted of a painted porous platinum electrode connected to a Pt wire inside a partially stabilized zirconia [3.5 weight percent (w/o) CaO] tube. At 1200 K, the open-circuit voltage (1) between these two reference electrodes is given by

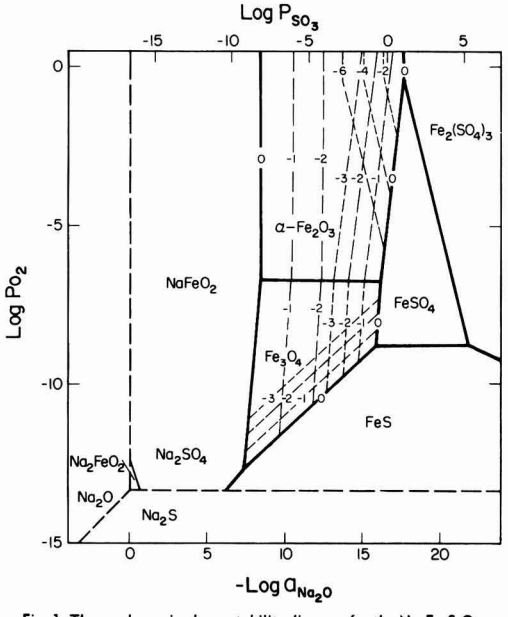

Fig. 1. Thermodynamic phase stability diagram for the Na-Fe-S-O system at 1200 K.

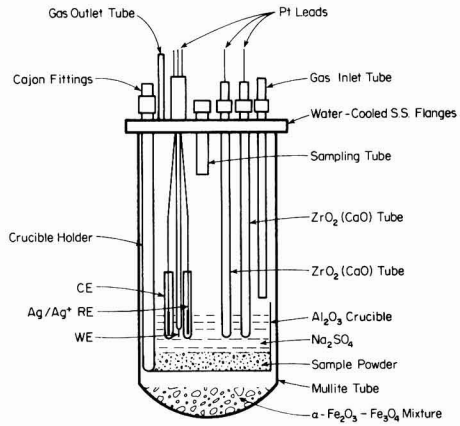

Fig. 2. Experimental setup for solubility measurements

$$E(\text{V}) = 1.4943 + 0.119 \log a_{Na_2O}\ (\text{melt}) \qquad [1]$$

The open-circuit voltage (1) between the Pt working electrode and the oxygen probe is given by

$$E(\text{V}) = 0.0403 + 0.0595 \log P_{O_2} \qquad [2]$$

The basicity of the Na_2SO_4 melt was adjusted by pumping oxide ions into or out of the melt using another partially stabilized ZrO_2 tube. A platinum wire in another mullite tube containing only Na_2SO_4 served as a counterelectrode for the titration. As shown recently (2, 9), upon applying a voltage in this circuit, the oxide ion concentration of the melt may be increased or decreased by driving the reaction

$$\frac{1}{2}\,O_2 + 2e^- \rightleftharpoons O^{2-}\ (\text{in melt}) \qquad [3]$$

to the left or the right. In this study, different values of voltage were applied to change the electrochemically measured melt basicity, $\log a_{Na_2O}$, from -7.5 to -13.6.

About 25g of reagent-grade Na_2SO_4 and 5g of mixed α-Fe_2O_3 (99.9% purity) and Fe_3O_4 (99.99% purity) powder (1:1 molar ratio) were charged into the alumina crucible, and about 150g of an equimolar α-Fe_2O_3 and Fe_3O_4 powder mixture was placed on the floor of the mullite reactor. After drying the salt and the mixed iron oxides at 150°-200°C in a slowly flowing purified argon gas for at least 24h, the system was heated to 1200 K and closed to further gas flow. A suitable voltage was applied to the ZrO_2 pumping electrode with a potentiostat (Wenking ST72). After a few hours, the P_{O_2} in the melt decreased to 2.14×10^{-7} atm, corresponding to the equilibrium oxygen pressure of α-Fe_2O_3 and Fe_3O_4 at 1200 K. Various times were required for the melt basicity to reach a desired value, and thereafter the basicity remained constant. After a day of equilibration, samples of the melt were taken by freezing a small amount of salt onto a cool alumina rod. Each salt sample, about 0.2g, was weighed to an accuracy of 0.1 mg, and dissolved into 100 or 1000 ml of 0.02*N* HCl solution, depending upon the expected iron concentration in the salt. An atomic absorption spectrophotometer (Perkin-Elmer, Series 360) with a graphite furnace was used to determine the iron content of the aqueous solutions. Only a small amount, 10 μliter, of the sample solution was added to the graphite furnace in order to avoid any uncertainty introduced by the Na_2SO_4 salt in the solution.

For determining the activity coefficient of FeS in fused Na_2SO_4, the solubility of FeS was measured in the range on Fig. 1 where FeS is the stable phase. The oxygen pressure was kept at 3.5×10^{-12} atm by placing nickel powder in the system, and the melt basicity was adjusted to -12 and -14 by titration. To substantiate the FeS activity coefficient determined in this way, the solubilities of Fe_3O_4 were measured at the same P_{O_2} and at basicities of -8.5, -9.0 and -9.5, respectively.

Results and Discussion

The measured solubility values for mixed α-Fe_2O_3 and Fe_3O_4 in fused Na_2SO_4 at 1200 K and 2.14×10^{-7} atm O_2 are shown in Fig. 3. Each data point in Fig. 3 is the average of several measurements of the concentration of soluble iron in Na_2SO_4 for each salt sample, compared with a certified standard solution for iron.

In basic dissolution, the measured dependence of the solubility on the melt basicity indicates that FeO_2^- is the solute species for the mixed iron oxides. The dependence is consistent with the following dissolution reaction

$$m\text{Fe}_2\text{O}_3 + \text{Fe}_3\text{O}_4 + \left(\frac{2m+3}{2}\right)\text{Na}_2\text{O} + \frac{1}{4}\,\text{O}_2 = (2m+3)\,\text{NaFeO}_2 \qquad [4]$$

For excess Fe_2O_3 and Fe_3O_4 at constant P_{O_2}

$$\frac{\partial(\log a_{NaFeO_2})}{\partial(-\log a_{Na_2O})} = -\frac{1}{2} \qquad [5]$$

The individual oxide Fe_2O_3 or Fe_3O_4 obeys this same dependence. Above 2.14×10^{-7} atm oxygen, oxygen is not involved in the basic dissolution of α-Fe_2O_3, so that no oxygen dependence is expected for the soluble $NaFeO_2$ concentration. At oxygen pressures below 2.14×10^{-7} atm, the basic solubility of Fe_3O_4 is dependent upon P_{O_2} according to the reaction

$$2\text{Fe}_3\text{O}_4 + 3\text{Na}_2\text{O} + \frac{1}{2}\,\text{O}_2 = 6\text{NaFeO}_2 \qquad [6]$$

For excess Fe_3O_4 at constant a_{Na_2O}

$$\frac{\partial(\log a_{NaFeO_2})}{\partial(\log P_{O_2})} = \frac{1}{12} \qquad [7]$$

The FeO_2^- concentration plateau at the left of Fig. 3 results because O^{2-} ions are not involved in the dissolution of $NaFeO_2$ to form FeO_2^- ions.

In the acidic dissolution of Fe_3O_4 + α-Fe_2O_3, the Fe^{2+} solute ion is indicated by the $\log a_{Na_2O}$ dependence of the solubility. The dependence of the soluble $FeSO_4$ concentration upon the melt basicity is consistent with the following dissolution reaction

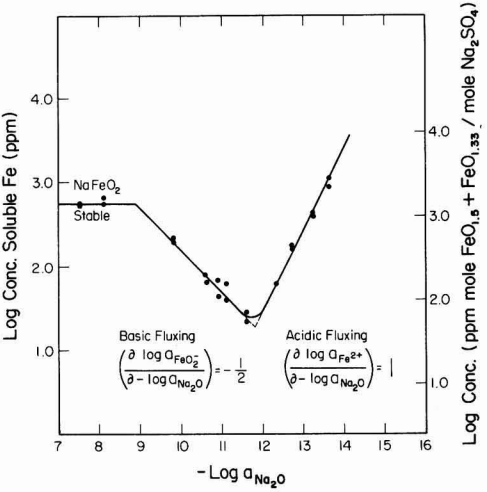

Fig. 3. Solubilities of α-Fe_2O_3 + Fe_3O_4 in fused Na_2SO_4 at 1200 K

$$m\mathrm{Fe_2O_3} + \mathrm{Fe_3O_4} + (2m+3)\mathrm{Na_2SO_4} = (2m+3)\mathrm{FeSO_4} + (2m+3)\mathrm{Na_2O} + \left(\frac{m+1}{2}\right)\mathrm{O_2} \quad [8]$$

$$\frac{\partial(\log a_{\mathrm{FeSO_4}})}{\partial(-\log a_{\mathrm{Na_2O}})} = 1 \quad [9]$$

The dependences of the acidic solubilities of α-Fe_2O_3 and Fe_3O_4 on P_{O_2} can be predicted from the reactions

$$\mathrm{Fe_2O_3} + 2\mathrm{Na_2SO_4} = 2\mathrm{FeSO_4} + 2\mathrm{Na_2O} + \frac{1}{2}\mathrm{O_2} \quad [10]$$

$$\frac{\partial(\log a_{\mathrm{FeSO_4}})}{\partial(\log P_{O_2})} = -\frac{1}{4} \quad [11]$$

and

$$\mathrm{Fe_3O_4} + 3\mathrm{Na_2SO_4} = 3\mathrm{FeSO_4} + 3\mathrm{Na_2O} + \frac{1}{2}\mathrm{O_2} \quad [12]$$

$$\frac{\partial(\log a_{\mathrm{FeSO_4}})}{\partial(\log P_{O_2})} = -\frac{1}{6} \quad [13]$$

The activity coefficient of soluble $NaFeO_2$ in fused Na_2SO_4 was calculated to be 460, which is close to the value of 400 derived from the previous work (using adjusted $\Delta G°_{\mathrm{NaFeO_2}}$) (5). The activity coefficient of the $FeSO_4$ solute in Na_2SO_4 was calculated to be 0.83. These activity coefficient values possess significant uncertainties resulting from the uncertainties in $\Delta G°_f$ for $NaFeO_2$ and $FeSO_4$. The minimum solubility for the mixed oxides, α-Fe_2O_3 and Fe_3O_4, lies at $-\log a_{\mathrm{Na_2O}} = 11.8$, which generally meets thermodynamic expectation from Fig. 1.

Four measurements of FeS solubility within the range of FeS stability gave an average concentration of 5.68×10^{-3} mole fraction FeS. From these measurements, the activity coefficient of FeS in fused Na_2SO_4 is estimated to be 180. According to Fig. 1, at very low oxygen pressures, Fe_3O_4 can experience acidic dissolution as soluble FeS. The dissolution reaction should be

$$\mathrm{Fe_3O_4} + 3\mathrm{Na_2SO_4} = 3\mathrm{FeS} + 3\mathrm{Na_2O} + \frac{13}{2}\mathrm{O_2} \quad [14]$$

From Eq. [14], the dependences of Fe_3O_4 solubility as soluble FeS upon the melt basicity and P_{O_2} can be derived as follows

$$\frac{\partial(\log a_{\mathrm{FeS}})}{\partial(-\log a_{\mathrm{Na_2O}})} = 1 \quad [15]$$

and

$$\frac{\partial(\log a_{\mathrm{FeS}})}{\partial(\log P_{O_2})} = -\frac{13}{6} \quad [16]$$

This model for Fe_3O_4 dissolution at low P_{O_2}, as well as the FeS activity coefficient, was proved by the three Fe_3O_4 solubility data points in Fig. 4, which were measured at 3.5×10^{-12} atm oxygen ($\log P_{O_2} = -11.46$) for three different basicities. As seen in Fig. 4, the two acidic solubility measurements agree exactly with those calculated using the measured activity coefficient for FeS and Eq. [15] and [16]. The other point fits the calculated line for basic solubility.

Based on an assumption of constant activity coefficients from these measurements in combination with the previous work (5), the solubilities of the iron oxides, α-Fe_2O_3 and Fe_3O_4 in fused Na_2SO_4 were calculated for wide ranges of P_{O_2} and melt basicity, as shown in Fig. 4. In the construction of Fig. 4, the activity coefficient of soluble $NaFeO_2$ was chosen to be 430, the average of the values estimated from the previous study and this work.

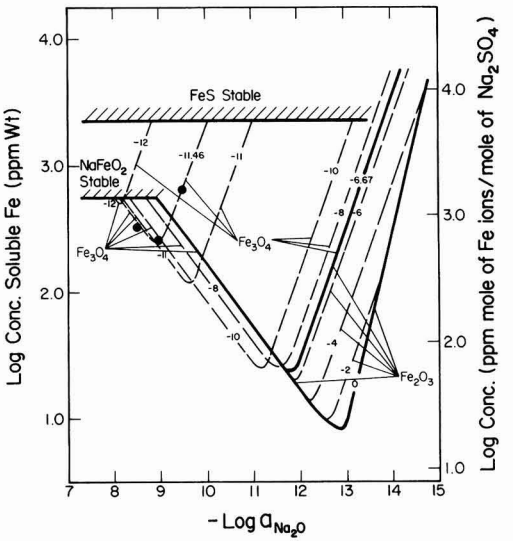

Fig. 4. Measured and calculated solubilities of α-Fe_2O_3 and Fe_3O_4 in fused Na_2SO_4 at 1200 K.

In Fig. 4, the solid lines represent the measured dependencies of solubilities upon the melt basicity at certain P_{O_2}, while the dashed lines are calculated values. For a specific log P_{O_2} value (indicated on the lines), each solubility curve is composed of two segments: the left segment for basic dissolution, and the right for acidic dissolution. In Fig. 4, the basic solubility decreases with decreasing P_{O_2}, except for P_{O_2} equal to or higher than 1.24×10^{-7} atm, whereas the acidic solubility increases with decreasing P_{O_2}. The melt basicity corresponding to the solubility minimum moves to a more basic value with a decrease in P_{O_2}. The only basic solute species of α-Fe_2O_3 and Fe_3O_4 is FeO_2^- (dissolved $NaFeO_2$), regardless of the P_{O_2}. The principal acidic solute of α-Fe_2O_3 is either Fe^{3+} [dissolved $Fe(SO_4)_{1.5}$] or Fe^{2+} (dissolved $FeSO_4$), depending upon both the P_{O_2} and melt basicity. Although the acidic solute for Fe_3O_4 is only Fe^{2+}, it can be described in terms of either dissolved $FeSO_4$ or else dissolved FeS, depending on the P_{O_2}. In Fig. 4, the acidic solubility lines for Fe_3O_4 at P_{O_2} higher than about 10^{-8} atm represent the concentrations of dissolved $FeSO_4$ in Na_2SO_4, while the solubility lines at P_{O_2} lower than about 10^{-10} atm represent the concentrations of dissolved FeS in Na_2SO_4. Between these two values for P_{O_2}, both solutes are significant.

Figure 4 should be important in understanding the iron oxide fluxing mechanism in the hot corrosion of iron. As an example, consider a piece of iron covered by molten Na_2SO_4, with a log $a_{\mathrm{Na_2O}}$ value in the acidic melt of log $a_{\mathrm{Na_2O}} = -13$, with 10^{-1} atm oxygen in the gas phase. At the oxide/melt interface, P_{O_2} should be much lower than 10^{-1} atm resulting from the SO_3- or O_2-diffusion limited oxidation of iron, say, 10^{-8} atm. The stable oxide phase at this interface is then Fe_3O_4, and the solute species is Fe^{2+}. According to Fig. 4, the solubility of Fe_3O_4 at the oxide/melt interface is much higher than that at the melt/gas interface for log $a_{\mathrm{Na_2O}} = -13$. Therefore, the migration of Fe^{2+} ions from the oxide/melt interface to the melt/gas interface results in their oxidation to form Fe_2O_3 with a lower solubility

$$2\mathrm{Fe^{2+}} + 2\,\mathrm{O^{2-}} + \frac{1}{2}\mathrm{O_2} = \mathrm{Fe_2O_3} \quad [17]$$

and the Fe_2O_3 may precipitate near the melt/gas interface as porous particles. In this case, the Rapp and Goto criterion (10)

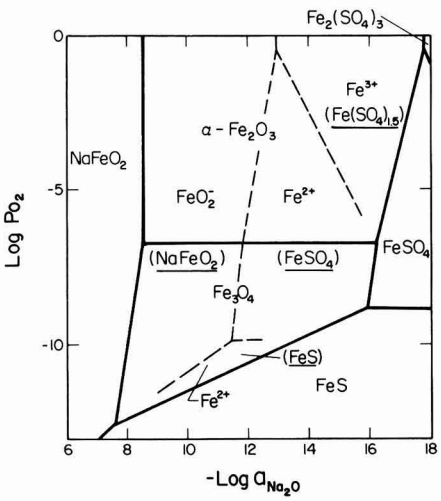

Fig. 5. Dominant solute iron species sections in Na_2SO_4-iron oxide system at 1200 K.

$$\left(\frac{d\,[\text{Solubility of oxide}]}{dx} \right)_{x=0} < 0 \qquad [18]$$

is satisfied. In such a way, hot corrosion continues as the protective Fe_3O_4 scale is dissolved. This model was used by Luthra to interpret the low temperature hot corrosion of cobalt-base alloys (11).

It is useful to identify each of the predominant solute species in the Na_2SO_4-iron oxide system, as shown in Fig. 5. The regimes in P_{O_2} and melt basicity where α-Fe_2O_3 and Fe_3O_4 are stable in Na_2SO_4 are separated by dashed lines into four sectors where different solute species are dominant. The dashed lines denote points of equal solute concentrations (not activities) and therefore possess uncertainties relating back to the solute activity coefficients. The predominance plot may be helpful in the evaluation of the electrochemical reactions in the Na_2SO_4-iron oxide system.

Conclusions

From the solubility measurements and their discussion, the following conclusions can be drawn.

1. The basic solutes of α-Fe_2O_3 and Fe_3O_4 in fused Na_2SO_4 at 1200 K are FeO_2^- ions while the acidic solutes are either Fe^{3+} or Fe^{2+}, depending upon the P_{O_2} and the melt basicity.

2. The activity coefficient for the basic solute $NaFeO_2$ in molten Na_2SO_4 at 1200 K was estimated to be 430, and those for $Fe(SO_4)_{1.5}$, FeS, and $FeSO_4$ are 3.6×10^{-3} (5), 180, and 0.83, respectively.

3. The solubility measurements and calculations may assist in understanding any fluxing mechanism for the hot corrosion of iron, and may aid in the interpretation of electrochemical studies for the Na_2SO_4-iron oxide system.

Acknowledgments

This research was sponsored by the National Science Foundation, Metallurgy Program of the Division of Material Research under Grant DMR 791190. Y. S. Zhang is supported as a Visiting Scientist from People's Republic of China.

Manuscript submitted March 25, 1985; revised manuscript received June 18, 1985.

The National Science Foundation assisted in meeting the publication costs of this article.

REFERENCES

1. D. K. Gupta and R. A. Rapp, *This Journal*, **127,** 2194, 2656 (1980).
2. M. L. Deanhardt and K. H. Stern, *ibid.*, **128,** 2577 (1981).
3. P. D. Jose, D. K. Gupta, and R. A. Rapp, *ibid.*, **132,** 735 (1985).
4. M. L. Deanhardt and K. H. Stern, *ibid.*, **129,** 2228 (1982).
5. Y. S. Zhang and R. A. Rapp, *ibid.*, **132,** 734 (1985).
6. R. A. Rapp and D. A. Shores, in "Techniques of Metals Research," Vol. IV, Part 2, R. A. Rapp, Editor, p. 159, John Wiley and Sons, New York (1970).
7. B. J. Shain, P. C. S. Wu, and P. Chiotti, *J. Nucl. Mater.*, **67,** 13 (1977).
8. JANAF Thermochemical Tables, 2nd ed., National Bureau of Standards 37, U.S. Dept. of Commerce (1971) and supplements.
9. M. L. Deanhardt and K. H. Stern, *J. Phys. Chem.*, **84,** 2831 (1980).
10. R. A. Rapp and K. S. Goto, in "Molten Salts," J. Braunstein and J. R. Selman, Editors, p. 159, The Electrochemical Society Softbound Proceedings Series, Pennington, NJ (1981).
11. K. L. Luthra, in "High Temperature Corrosion," NACE-6, R. A. Rapp, Editor, p. 507, NACE, Houston (1981).

Destabilization of Yttria-Stabilized Zirconia Induced by Molten Sodium Vanadate-Sodium Sulfate Melts

A. S. Nagelberg*

Sandia National Laboratories, Livermore, California 94550

ABSTRACT

The extent of surface destabilization of ZrO_2-8 weight percent Y_2O_3 ceramic disks was determined after exposure to molten salt mixtures of sodium sulfate containing up to 15 mole percent sodium metavanadate ($NaVO_3$) at 1173 K. The ceramic surface was observed to transform from the cubic/tetragonal to the monoclinic phase, concurrent with chemical changes in the molten salt layer in contact with the ceramic. Significant attack rates were observed in both sodium sulfate and sodium metavanadate-sulfate melts in the presence of sulfur trioxide. The rate of attack was found to be quite sensitive to the mole fraction of vanadate in the molten salt solution and the partial pressure of sulfur trioxide (1×10^{-6} to 1×10^{-3} atm) in equilibrium with the salt melt. The observed approximately parabolic rate of attack was interpreted to be caused by a reaction controlled by diffusion in the salt that penetrated into the porous layer formed by the destabilization. The parabolic rate constant in mixed sodium metavanadate-sodium sulfate melts was found to be proportional to the SO_3 partial pressure and the square of the metavanadate concentration.

Operating temperatures of today's gas turbines are limited by the high temperature mechanical properties of the nickel- and cobalt-based superalloys used for rotating components and by the high temperature corrosion of the metallic coatings on these components. The use of insulating surface layers on critical combustion turbine components is expected to allow higher gas turbine inlet temperatures, thus increasing operating efficiencies.

A thin insulating surface layer is provided by a thermal barrier coating that reduces the underlying metal surface temperature by as much as 150 K and provides a barrier to the ingress of corrosive species from the gas phase. Improved component reliability can be achieved by this reduction in operating temperature. Alternatively, increased gas turbine operating efficiencies are possible since higher inlet gas temperatures can be tolerated.

Several ceramics have been proposed for use as thermal barrier coatings, including Y_2O_3- and MgO-stabilized zirconia, MgO, and $CaSiO_3$ (1-3). Of these ceramics, zirconia-based ceramics containing 6-12 weight percent (w/o) Y_2O_3 showed superior resistance to cracking and spallation in laboratory tests (1, 3). Clean fuel burner rig tests have shown extended lifetimes. Unfortunately, burner rig tests using sodium or vanadium containing fuels show much shorter ceramic coating lifetimes. Levine (3) reported lifetimes in excess of 10,000 cycles when burning clean fuels. In contrast, when 5 ppm of sodium and 2 ppm vanadium were added to the fuel, lifetimes were less than 100 cycles. The shorter lifetimes have been attributed to chemical attack by fuel impurities and to destabilization of the zirconia-based coating and/or condensation of high thermal expansion phases in the coating pores (1, 3-6).

Zirconia ceramics are partially or totally stabilized by the addition of oxides such as MgO, CaO, and Y_2O_3. Stabilization refers to the retention of the cubic or tetragonal phases at temperatures at which the monoclinic phase would normally occur in pure ZrO_2. This stabilization is crucial to coating adherence, since the transformation from tetragonal to monoclinic structure involves a large volume change (~9%) (7). Even though the monoclinic phase is predicted to form at lower temperatures for the stabilized compositions, the slow kinetics of the transformations allow retention of the tetragonal or cubic phases at room temperature. The phase diagram (8) shows that the monoclinic structure is favored at lower temperatures and at lower concentrations of stabilizing oxide.

The zirconia-based ceramics proposed for thermal barrier coatings (6-12 w/o yttria) are found from the phase diagram to be in a two-phase region containing tetragonal and cubic phases at typical turbine operating temperatures (1073-1373 K). As long as coatings remain in either of these two structures, cracking and spallation associated with the tetragonal to monoclinic phase transition will not occur. However, if the yttria content is reduced slightly, the tetragonal to monoclinic transition will occur upon cooling.

During operation of gas turbines, impurities in the fuel and ingested air are known to lead to the formation of molten surface deposits. The presence of vanadium in the combustion exhaust gases can significantly affect the composition and temperature stability range of the liquid surface deposit. Luthra and Spacil (9) estimated that, for a fuel containing 30 ppm vanadium and 2 ppm sodium, the $NaVO_3 + V_2O_5$ content of the condensate at 1173 K would be nearly 80 mole percent (m/o). For these conditions, a liquid condensate would be stable from 879 to 1279 K. Although these impurity levels are high for presently used clean fuels, numerous gas turbine users have considered using fuels such as residual oils which contain significantly increased impurity levels. For a fuel with only 2-4 ppm vanadium, the calculated $NaVO_3 + V_2O_5$ content of the condensate is 3-15 m/o, respectively. It is thus reasonable to expect that ceramic-coated turbine components may be exposed to salt films containing high vanadium contents (10).

Sodium sulfate in the presence of a sulfur trioxide containing environment has been found to induce destabilization of yttria-stabilized zirconia ceramics (5). The destabilization was attributed to the acidic leaching of yttria from the ceramic substrate. Hamilton and Nagelberg (11, 12) have used Raman spectroscopy to study the phase transformations of stabilized zirconia induced by exposure to molten salt solutions containing sodium metavanadate. They found that the surface attack is very rapid and strongly depended on the metavanadate concentration during exposures in air at 1173 K.

In this study, we have measured the destabilization of the surface of ZrO_2-8 w/o Y_2O_3 ceramics exposed to molten sodium sulfate and sodium metavanadate-sulfate melts in oxygen-sulfur dioxide-sulfur trioxide atmospheres at 1173 K.

Experimental

High density (greater than 96% of theoretical density) ZrO_2 disks containing 8 w/o Y_2O_3 were obtained from Corning Glass Works, Zircoa Division. Sodium metavanadate ($NaVO_3$) was obtained from Cerac Pure, Incorporated, and sodium sulfate anhydrous from Baker, Incorporated.

Yttria-stabilized zirconia ceramics were exposed to molten salt mixtures containing 0.2, 2.0, 3.9, and 7.7 m/o sodium vanadate in sodium sulfate at 1173 K. Master melts were prepared by melting premixed powders at 1223 K and crushing the solidified salt melt to obtain a uniform composition. Such prepared powders were used to fill 1 ml platinum crucibles in which the 1 cm diam stabilized zirconia disks were immersed during exposure. Initial

*Electrochemical Society Active Member.

melting and ceramic introduction to the salt was done in air. In no case were the immersed ceramics at temperature for more than 5 min during this stage. For experiments using a sulfur dioxide-sulfur trioxide containing atmosphere, the platinum crucibles containing the ceramics were then suspended in a quartz reaction tube in a cold end of the tube under an argon atmosphere. Once the furnace had reached the reaction temperature, the platinum crucibles were inserted into the constant temperature zone of the furnace and the oxygen-sulfur dioxide-sulfur trioxide exposure gas composition introduced. The initial gas mixtures and final equilibrium compositions are given in Table I. The gas mixtures were obtained by mixing either SO_2 or a 1% SO_2 in O_2 mixture with O_2 before passing the gas over a bed of platinum mesh at 1173 K in a precatalyst furnace. A small piece of platinum mesh was also positioned below the salt crucibles in the reaction tube. Exposures were for times up to 500h for sodium metavanadate-sulfate melts and 1600h for pure sodium sulfate melts. For air exposures, the platinum crucibles were placed in a muffle furnace at 1173 K. After exposure, the ceramic disks were removed from the salts by immersion in distilled water. The washed ceramics were subsequently metallographically mounted and polished for examination by optical microscopy, scanning electron microscopy, and electron microprobe analysis.

The solutions containing the dissolved salts were analyzed for elements contained in the salts and original ceramics by atomic absorption and ICP techniques.

Results

Exposure of stabilized zirconia ceramics to a pure sodium sulfate melt at 1173 K in a 1% SO_2 in O_2 environment resulted in a measurable surface destabilization. After 380h, the transformed layer is approximately 40 μm thick. Longer salt exposure showed the monoclinic layer thickness was closely approximated by parabolic growth kinetics, as shown in Fig. 1.

The surface destabilization rate was observed to increase upon the introduction of sodium metavanadate to the salt melt for all the exposures examined. Except for the lowest metavanadate concentration used (0.2 m/o), the increase in the extent of destabilization was dramatic. Figure 2 shows that yttria-stabilized zirconia exposure to a molten salt solution containing 2.0 m/o sodium metavanadate in sodium sulfate at 1173 K in an initially 1.0% SO_2 in O_2 atmosphere resulted in formation of an approximately 50 μm surface layer after 24h. The surface layer formed is identified in the photomicrograph by the increased porosity in the ceramic near the surface. Not very apparent in Fig. 2 is a slight preferential attack of the ceramic along grain boundaries. On several samples examined, a slightly uneven reaction front was observed with the center of grains near the reaction front not appearing as porous as the grain periphery. A more pronounced grain boundary attack was observed by Nagelberg (12) for the molten vanadate attack of magnesia-stabilized zirconia ceramics.

Electron microprobe analysis showed the high porosity region to be depleted in yttrium compared to the bulk ceramic. The surface layer was determined to contain approximately 1 w/o yttrium throughout with no observable concentration gradient except for the center of a few grains near the reaction front. The yttrium concentration in the bulk crystal was 8 w/o, as was expected from the initial composition, and again no observable concentration

Table I. Exposure environment composition

Initial gas composition (%)		Equilibrium composition at 1173 K (%)		
O_2	SO_2	O_2	SO_2	SO_3
90	10	90	7.7	2.4
99	1	99	0.76	0.24
99.9	0.1	99.9	7.6×10^{-2}	2.5×10^{-2}
99.985	0.015	99.99	1.1×10^{-2}	3.7×10^{-3}
1	99	0.25	97	0.15

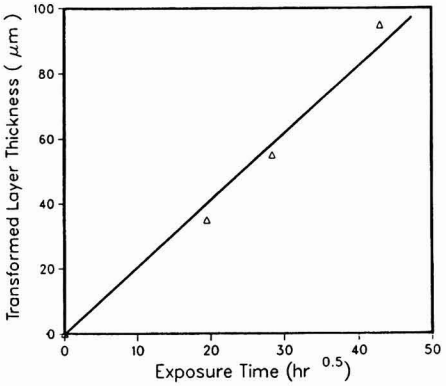

Fig. 1. Transformed layer thickness as a function of the square root of time for ZrO_2-8% Y_2O_3 exposed to Na_2SO_4 at 1173 K in a 1% SO_2 in O_2 atmosphere.

gradient was observed in the region in proximity to the surface layer.

As expected, chemical analysis of the wash solutions indicated that no zirconium was dissolved in the salt during exposure to the molten salts. The observed dissolved yttrium levels correlated well with the extent of yttrium removal from the ceramic.

The time dependence of the thickness of the yttrium-depleted surface layer for metavanadate concentrations of 0.2, 2.0, and 3.9 m/o are shown in Fig. 3 as a function of the square root of time after exposure to a 1.0% SO_2 in O_2 atmosphere at 1173 K. Similar to destabilization induced by a pure sodium sulfate salt in the presence of sulfur trioxide, an approximately parabolic time dependence appears to be approximately followed for all three vanadate concentrations in the molten salt. The measured parabolic rate constants are given in Table II. Also listed in Table II is a parabolic rate constant for a sodium metavanadate concentration of 1.0 m/o. This value was obtained by assuming parabolic kinetics and a single measured value of the monoclinic layer thickness after a 164h exposure to 1% SO_2 in O_2 atmosphere. The monoclinic layer thickness does indicate a deviation from parabolic behavior toward linear kinetics at longer times.

Variation of the sulfur dioxide (and thus sulfur trioxide) content of the atmosphere above the salt melts was found to cause significant changes in the extent of destabilization of the ceramics. For an atmosphere initially con-

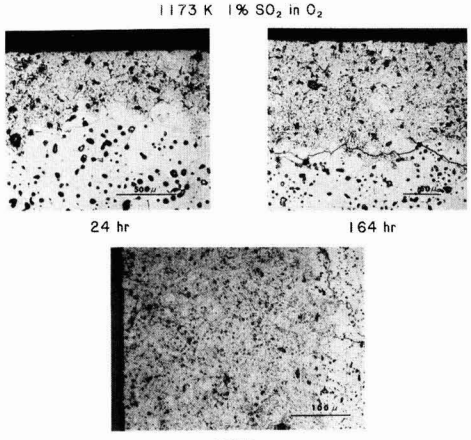

Fig. 2. Photomicrographs of ZrO_2-8 w/o Y_2O_3 exposed at 1173 K to a 1% SO_2 in O_2 atmosphere for various times.

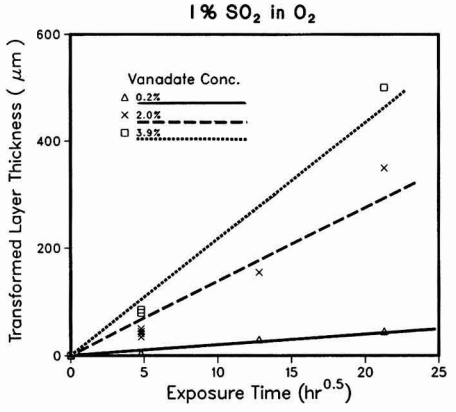

Fig. 3. Transformed layer thickness as a function of the square root of time for ZrO_2-8% Y_2O_3 exposed to $NaVO_3$-Na_2SO_4 melts at 1173 K in a 1% SO_2 in O_2 atmosphere.

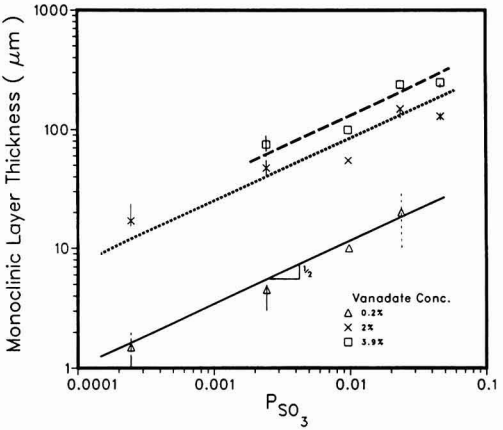

Fig. 4. Transformed layer thickness as a function of partial pressure SO_3 for ZrO_2-8% Y_2O_3 exposed to Na_2SO_4 at 1173 K.

taining 0.1% SO_2 in O_2 (P_{SO_3} = 2.5 × 10^{-4}) and 2.0% metavanadate, the transformed layer was approximately 15 μm thick after 24h. In contrast, an environment initially containing 10% SO_2 in O_2 (P_{SO_3} = 2.4 × 10^{-2}) results in a 200 μm thick layer in the same time. Results for three vanadate concentrations after a 24h exposure to various partial pressures of SO_3 at 1173 K are given in Fig. 4. The slope of all the lines drawn in Fig. 4 is 1/2.

Using the parabolic rate constants given in Table II, the metavanadate compositional dependence in the presence of an environment containing 0.0025 atm SO_3 is plotted in Fig. 5. The measured parabolic rate constant for exposures to a pure sodium sulfate melt under the same SO_3 partial pressure is also given for comparison as the filled triangle. Except for the parabolic rate constant for the lowest metavanadate concentration (0.2 m/o), the measured rate constants are fitted well by a line with a slope of 2.

Discussion

Hamilton and Nagelberg (13) have reported the rapid attack of yttria-stabilized zirconia by both pure metavanadate melts and mixed sulfate-metavanadate melts at 1173 K in air. From their salt exposures in air, it was established that the formation of a surface monoclinic layer occurred due to the acidic leaching of yttrium from the stabilized zirconia ceramic to form a Y^{+3} salt soluble species. From the phase diagram, it can be seen that the removal of yttrium results in a phase transformation to the monoclinic structure. Associated with the removal of yttrium, an increase in the pyrovanadate content of the salt was also observed. A similar reaction process is believed to be occurring in the presence of an SO_2-SO_3-O_2 atmosphere. As would be expected from their results, the monoclinic ceramic surface layers observed in this study were depleted in yttrium uniformly throughout the layer. In addition, the salt was found to contain significant quantities of dissolved yttrium but no zirconium.

The attack rates measured in SO_2-SO_3 containing atmospheres are a factor of 100-1000 faster than were reported for vanadate-sulfate melts exposed to air. Figure 6 compares the morphology of the scales formed in air with the destabilized surface layer formed in the presence of an equilibrated 99% SO_2-1% O_2 atmosphere at 1173 K. The monoclinic surface layers formed in both air and SO_2-SO_3-O_2 containing atmospheres were found to be extremely porous, as can be seen in Fig. 6. The only difference between the different salt exposures was the extent of attack.

Similar to the observations of Barkalow and Pettit (5), yttrium leaching from the ceramic was found to occur in the presence of sodium sulfate alone. The addition of sodium metavanadate was found to significantly enhance the rate of formation of a monoclinic surface layer. Since the experimental melts were buffered with respect to the sulfur trioxide partial pressure, it is assumed here that two similar yet different mechanisms are active in the mixed sulfate-vanadate melts.

In pure sodium sulfate melts, a possible dissolution mechanism for Y_2O_3 dissolved in the ZrO_2 [first proposed by Barkalow and Pettit (5)] is the acidic leaching of yttria given by

$$Y_2O_3 + 3SO_3 = 2Y^{+3} + 3SO_4^{-2} \quad [1]$$

or considering the existence of the pyrosulfate ion

$$Y_2O_3 + 3S_2O_7^{-2} = 2Y^{+3} + 6SO_4^{-2} \quad [2]$$

In either case, the reaction strongly depends on the sulfur trioxide partial pressure. Jones *et al.* (14) have determined

Table II. Parabolic rate constants (P_{SO_3} = 2.4 × 10^{-3})

$NaVO_3$ concentration (m/o)	Parabolic rate constant (cm^2/s)
0.0	1 × 10^{-11}
0.2	1 × 10^{-11}
1.0	1.7 × 10^{-10}
2.0	5.4 × 10^{-10}
3.9	1.5 × 10^{-9}

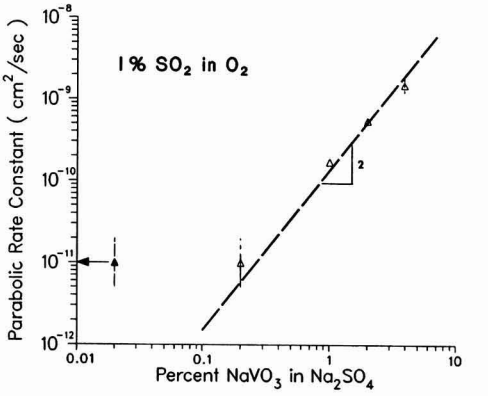

Fig. 5. Parabolic rate constant as a function of the $NaVO_3$ concentration for ZrO_2-8% Y_2O_3 exposed to Na_2SO_4 at 1173 K in a 1% SO_2 in O_2 atmosphere.

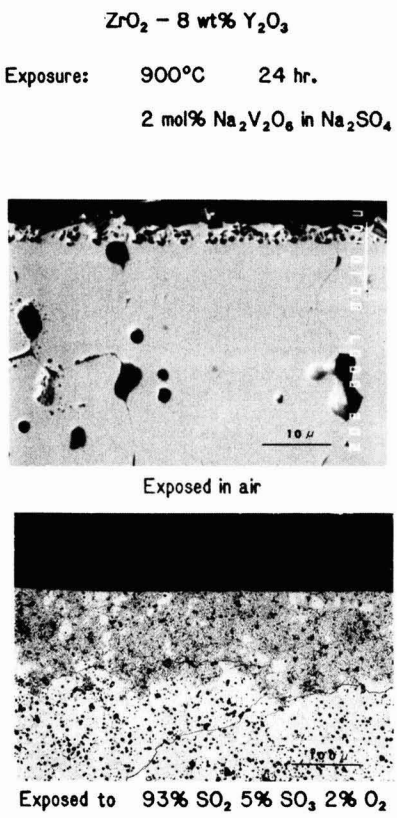

Fig. 6. Photomicrographs of ZrO_2-8 w/o Y_2O_3 exposed at 1173 K for 24h.

the minimum SO_3 partial pressure to cause sulfation of pure yttria as approximately 2.5×10^{-5} atm at 1173 K. The partial pressures utilized in this study are easily in excess of this value. These authors also noted an increased sulfation rate of the yttria in the presence of Na_2SO_4.

For salt melts containing sodium sulfate, a SO_2-SO_3-O_2 atmosphere determines the partial pressure of sulfur trioxide and thus the sodium oxide activity of the melt by Eq. [3]

$$Na_2SO_4 = Na_2O + SO_3 \quad [3]$$

$$k_1 = a_{Na_2O}P_{SO_3}/a_{Na_2SO_4} \quad [4]$$

In the absence of a sulfur dioxide-sulfur trioxide-oxygen containing cover gas the Na_2O activity of the salt melt is undefined and is not regulated. Thus, the sodium salt will decompose sufficiently to obtain local thermodynamic equilibrium, making the melt increasingly basic (high activities of Na_2O) during exposure to a flowing gas stream.

When considering mixed sodium metavanadate-sodium sulfate melts, the sodium oxide activity of the molten salt in turn affects the activity of V_2O_5 by Eq. [5]

$$Na_2O + V_2O_5 = 2NaVO_3 \quad [5]$$

$$k_3 = a_{NaVO_3}{}^2/a_{Na_2O}a_{V_2O_5} \quad [6]$$

Combining Eq. [3] and [5]

$$Na_2SO_4 + V_2O_5 = 2NaVO_3 + SO_3 \quad [7]$$

$$k_5 = a_{NaVO_3}{}^2P_{SO_3}/a_{Na_2SO_4}a_{V_2O_5} \quad [8]$$

Thus it is found that the V_2O_5 activity is proportional to the partial pressure of sulfur trioxide and the square of the sodium metavanadate concentration as $NaVO_3$, when it is assumed that the sodium sulfate activity and activity coefficient for the metavanadate are constant. The change in sodium sulfate concentration from 99.8 to 94% represents only a minor variation in comparison to the change in metavanadate concentration. Therefore, it is possible that the dissolution mechanism in metavanadate-sulfate melts is given by

$$Y_2O_3(ZrO_2) + V_2O_5(Na_2SO_4) = 2Y^{+3} + 2VO_4^{-3} \quad [9]$$

Even though Eq. [7] implies that the sodium sulfate activity and sulfur trioxide partial pressure can be influenced by the presence of metavanadate, we believe the mechanism given by Eq. [9] predominates in vanadate containing melts. Sodium sulfate is expected to behave ideally over the range of metavanadate concentrations utilized and thus varies by approximately 8%. The V_2O_5 activity of the molten salts will be modified to a very limited extent by volatilization of V_2O_5 since the vapor pressure at 1173 K is close to 10^{-8} atm. Thus the SO_3 partial pressure and the sodium metavanate concentration will have the prime influence on the V_2O_5 activity of the melt.

The parabolic rate constant for a diffusion-controlled process relates the square of the reaction layer thickness to the exposure time. In addition, for a diffusion-controlled process it is found that the parabolic rate constant is proportional to the diffusion coefficient of the rate-controlling species through an increasingly thickening reaction layer. Both Fig. 1 and 3 showed that the formation of a monoclinic surface layer can be approximately fitted to such a parabolic growth rate.

The measured parabolic rate constants given in Table II are larger than would be expected from a process controlled by cationic diffusion in the ceramic. Extrapolation of the cationic diffusion coefficients in ZrO_2 measured at higher temperatures, 1700-2100 K, give a value of D_{Zr} at 1173 K of approximately 5×10^{-20} cm^2/s or more than ten orders of magnitude smaller than the measured rate constants. In addition, the large sulfur trioxide and metavanadate concentration effects are difficult to reconcile with a cationic diffusion-controlled rate.

The monoclinic reaction layer formed is found in all cases to be very porous. For the structural conversion of the tetragonal structure to the monoclinic phase with no change in composition a net volume increase is expected (7). The observed decrease in volume of the monoclinic layer and thus the porosity can be explained by variations in the lattice parameters of the tetragonal and monoclinic phases with composition (15) and the dissolution of yttria in the molten salts. Using the lattice parameters given by Scott (15) for the tetragonal and monoclinic structures and an assumed depletion of yttria from 8 to 1 w/o, a net shrinkage of approximately 4% is expected.

Since the reaction layer forming is a porous outer monoclinic layer and no yttrium concentration gradient was observed, it would be reasonable to expect that the diffusion of $S_2O_7^{-2}$ and V_2O_5 through the porous channels of this layer was the rate-controlling species for sulfate and metavanadate-sulfate melts, respectively. Since approximately parabolic kinetics are followed, it must be assumed that the pore structure is relatively uniform throughout and thus the porous layer exhibits a nearly constant permeability.

Even though the time-dependent formation of a monoclinic reaction layer is closely fitted by a parabolic rate relationship, a small upward deviation from the square root of time dependence was observed at very long times. Haycock (16) has reported that this deviation toward a linear reaction rate can be due to the formation of a surface layer with a diffusivity increased above the rest of the reaction layer. The reaction product of the leaching reaction is soluble in the molten salts and is not expected to lead to clogging of the product layer porosity. As the transformation to the monoclinic structure progresses to completion, it is not unexpected that the size of the pores increases. No increased porosity at the outer regions is apparent in the micrographs. However, the deviation

from parabolic behavior is small and the increased porosity to induce such an effect would be difficult to observe. This deviation implies that, at exposure times significantly longer than those reported here, the rate of destabilization may be influenced by the formation of an outer porous reaction layer and make extrapolation of rates to longer times difficult.

For both sulfate and vanadate-sulfate melts, the above analysis indicates that the parabolic rate constant is strongly dependent on the SO_3 partial pressure. In the presence of sodium vanadate, Eq. [8] predicts a linear dependence of the rate of growth of the monoclinic layer with the SO_3 partial pressure. The parabolic rate constant is proportional to the scale thickness squared at any given time. Thus, the square root dependence of the monoclinic layer thickness after a fixed time exposure of 24h, shown in Fig. 4, indicates that a linear sulfur trioxide dependence of the parabolic rate constant is followed (twice the exponent of the dependence of the layer thickness on the partial pressure of SO_3).

Furthermore, for vanadate containing salts, it is expected from Eq. [7] and [9] that the parabolic rate constant is proportional to the vanadate concentration squared. Figure 5 shows that this metavanadate concentration dependence was also observed.

Comparison of the measured attack rate in a pure sodium sulfate melt and the 0.2% metavanadate melt show the two rates to be approximately identical. It thus must be assumed that the contribution of the metavanadate to the attack rate at these low concentrations is small and that the destabilization rate is essentially due to the reaction given by Eq. [1]. The dependence on metavanadate concentration squared implied by Eq. [8] would predict in association with the parabolic rate constants measured for higher metavanadate contents a parabolic rate constant for the 0.2 m/o metavanadate salt melt of approximately 5×10^{-12}, or half the experimentally measured value. This predicted value from the higher vanadate concentration measurements and the proposed compositional dependence of the vanadate-induced corrosion rate constant is larger than calculated by simply subtracting the parabolic rate constant measured in pure sulfate melt from the observed value. Nevertheless, the discrepancy is within the experimental scatter of the measurement.

The observed molten salt attack rate dependence on vanadate concentration and sulfur trioxide partial pressure strongly favors a reaction mechanism in which diffusion of V_2O_5 in the salt within the pores of the monoclinic layer is rate controlling. Associated with this mechanism would be an absence of a yttrium concentration gradient within the monoclinic product layer. Microprobe results support this conclusion, with the exception of the limited regions in which the center of the ceramic grains near the monoclinic tetragonal interface are untransformed. Even for this case there is no observed gradient in the monoclinic phase. It is felt that this is solely because of a slightly more rapid intrusion of and attack by the molten salt along the grain boundaries and pore surfaces. The observed absence of either sodium or vanadium in the internal pores of the ceramics by the electron microprobe is due to the experimental procedure of dissolving the salt in water to remove the ceramics from the salt melts.

The most extensive surface transformation found in this study or by Hamilton and Nagelberg (13) was for the exposures to the SO_2-SO_3 containing atmospheres. Comparison of monoclinic layer thickness formed in air with those formed in SO_2-SO_3 containing atmospheres show a dramatic change in the rate of leaching yttrium from the ceramics. Air exposure to a 2% $NaVO_3$ salt melt for 24h resulted in the formation of a transformed layer approximately 1.5 μm thick, while exposure to the same salt in a 1% SO_2 in O_2 atmosphere results in the formation of an ~50 μm thick monoclinic layer. If the square root dependence of layer thickness (and thus linear dependence of parabolic rate constant) on the SO_3 partial pressure holds over extended variations in partial pressure, corrosive attack in an air atmosphere over a 24h period is equivalent to exposure to an atmosphere containing a SO_3 partial pressure of approximately 2×10^{-6} atm.

The formation of a porous monoclinic reaction layer implies a process that does not simply involve the removal of yttrium from the stabilized zirconia ceramics since the density of the monoclinic product phase (5.56 g/cm^3) (7) is slightly lower than the original tetragonal phase (~5.7 g/cm^3). Even though a net expansion is expected when the density alone is considered, the significant leaching of yttrium from the ceramic (6-7 w/o) leads to a shrinkage of the ceramic within the reacted layer. Michalske (17) has observed that the transformation of tetragonal zirconia in molten silicates occurs by a dissolution-precipitation reaction. It was found that the tetragonal phase has a higher solubility in the molten salt and first dissolves before the monoclinic phase precipitates. Although no evidence for high solubilities of zirconia in the sulfates was found in this study, a similar process may be occurring in the molten sulfate-vanadate melts and represents a mechanism by which the highly porous reaction layer forms.

Conclusions

The sodium vanadate enhanced surface destabilization of yttria-stabilized zirconia occurs by a leaching of yttrium from the ceramic. Analysis of the molten salts indicated that yttrium alone was being leached from the ceramic. The removal of yttrium from the ceramic surface results in a phase transformation from the tetragonal structure to monoclinic structure. The monoclinic surface layer is observed in micrographs as a highly porous region.

The extent of transformation approximately increased with the square root of time and is believed to be controlled by a diffusion process. At long times, deviation from parabolic kinetics was observed and is believed due to the formation of an increasingly porous outer monoclinic layer. The measured parabolic rate constant was linearly dependent on the SO_3 partial pressure of the atmosphere in equilibrium with the molten salt melt. In addition, the parabolic kinetics for the growth of a monoclinic surface layer as found to be dependent on the sodium vanadate ($NaVO_3$) concentration of the salts. Since no concentration gradient was observed and a strong reaction rate dependence on the melt thermochemistry was observed, it is believed that the diffusion process controlling the observed reaction rate was diffusion of $S_2O_7^{-2}$ (in pure sulfate melts) or both $S_2O_7^{-2}$ and V_2O_5 (in mixed metavanadate-sulfate salt melts) through the salt penetrating the porous monoclinic surface layer.

Acknowledgment

This work was supported by the U.S. Department of Energy, Office of Basic Energy Sciences.

Manuscript submitted Jan. 7, 1985; revised manuscript received June 10, 1985.

Sandia National Laboratories assisted in meeting the publication costs of this article.

REFERENCES

1. R. A. Miller, "Analysis of the Response of a Thermal Barrier Coating to Sodium- and Vanadium-Doped Combustion Gases," NASA TM-79205, June 1979.
2. I. Kvernes, in "Proceedings of the Second Conference on Advanced Materials for Alternate-Fuel Capable Heat Engines," EPRI RD-2369-SR, p. 6-1, May 1982, Electric Power Research Institute, Palo Alto, CA (1982).
3. S. R. Levine, R. A. Miller, and M. A. Gedwell, in "Proceedings of the Second Conference on Advanced Materials for Alternate-Fuel Capable Heat Engines," p. 6-185, EPRI RD-2369-SR, May 1982, Electric Power Research Institute, Palo Alto, CA (1982).
4. R. J. Bratton, S. K. Lau, C. A. Andersson, and S. Y. Lee, in "Proceedings of the Second Conference on Advanced Materials for Alternate-Fuel Capable Heat Engines," p. 6-82, EPRI RD-2369-SR, May 1982, Electric Power Research Institute, Palo Alto, CA (1982).
5. R. H. Barkalow and F. S. Pettit, in "Proceedings of the First Conference on Advanced Materials for

Alternate-Fuel Capable Directly Fired Heat Engines," J. W. Fairbanks and J. Stringer, Editors, p. 704, Castine, ME, Dec. 1979.
6. P. E. Hodge, R. A. Miller, and M. A. Gedwell, "Evaluation of Hot Corrosion Behavior of Thermal Barrier Coatings," NASA TM-81520, April 1980.
7. "Engineering Property Data on Selected Ceramics: Volume III, Single Oxides," MCIC-HB-07, Vol. III, pp. 12-80, Metals and Ceramics Information Center, Columbus, OH (1981).
8. V. S. Stubican, R. C. Hink, and S. P. Ray, *J. Am. Ceram. Soc.*, **61,** 17 (1978).
9. K. L. Luthra and H. S. Spacil, *This Journal*, **129,** 649 (1982).
10. J. W. Vogan, L. L. Hsu, and A. R. Stetson, in "Proceedings of the Second Conference on Advanced Materials for Alternate-Fuel Capable Heat Engines," p. 6-54, EPRI RD-2369-SR, May 1982, Electric Power Research Institute, Palo Alto, CA (1982).
11. J. C. Hamilton and A. S. Nagelberg, in "Corrosion in Fossil Fuel Systems," I. G. Wright, Editor, pp. 435-455, The Electrochemical Society Softbound Proceedings Series, Pennington, NJ (1983).
12. A. S. Nagelberg, Unpublished research.
13. J. C. Hamilton and A. S. Nagelberg, *J. Am. Ceram. Soc.*, **67,** 686 (1984).
14. R. L. Jones, D. B. Nordman, and S. T. Gadomski, "Sulfation of Y_2O_3 and HfO_2 in Relation to MCrAlY Coatings," NRL Report 5255, Jan. 1984.
15. H. G. Scott, *J. Mater. Sci.*, **10,** 1527 (1975).
16. E. W. Haycock, *This Journal*, **106,** 771 (1959).
17. T. Michalske, Personal communication.

Cathodoluminescent Properties of Evaporated ZnS:Mn Films in the 2-6 kV Acceleration Voltage Range

D. Theis

Siemens Aktiengesellschaft, Siemens Research Laboratories, D-8000 Munich, Germany

R. Wengert

Siemens Aktiengesellschaft, Siemens Components Division, D-8000 Munich, Germany

ABSTRACT

Evaporated thin films of ZnS:Mn as used for yellow light emitting electroluminescent displays were analyzed with respect to their cathodoluminescent properties in the 2-6 kV acceleration voltage range. In these films, the light output normal to the film plane is 10-20 times lower than in yellow emitting powder phosphors. This result is explained in terms of light piping in the plane-parallel thin film structure as well as in a specific saturation process occurring at high excitation. Suitable measures to suppress the light piping could probably provide a technically useful high resolution CRT thin film faceplate.

Evaporated thin films of manganese-doped ZnS constitute the light emitting layers in ac-addressed electroluminescent displays. Scientific and industrial interest in these matrix displays is growing. [For a comprehensive review, see, e.g., Ref. (1).] Whereas highest luminance has been achieved with displays of the refresh type (2), an inherent memory and accordingly storage capability of the ZnS:Mn films fabricated under special preparational conditions have been discovered (3, 4). It was demonstrated that such panels can be addressed by electron beams and thus constitute the faceplate of a new type of storage CRT's (5, 6).

We were interested in finding out the suitability of evaporated thin ZnS:Mn films for high resolution, lower voltage CRT's without any additional storage features. Only little has been published on the cathodoluminescent properties of these films in the acceleration voltage range between 2 and 6 kV. This voltage range roughly corresponds to a complete penetration of the electrons through the films used. (Film thickness usually was less than 1 μm.) Some exploratory experiments on the cathodoluminescent properties of ZnS:Mn films evaporated on glass will be reported here.

Sample Preparation and Characterization

The samples available for the cathodoluminescent investigations were prepared by electron-beam evaporation. Mn incorporation into the ZnS film was achieved either by evaporating a Mn-doped hot-pressed ZnS pellet or by using a double-source system with separated ZnS and Mn sources. Substrate heating was performed by two 1000W quartz radiators placed in front of the samples.

Figure 1 illustrates the influence of the substrate temperature on the thickness of the film obtained at process times of equal length. One can extrapolate that in the evaporation chamber used no ZnS growth could be obtained at substrate temperatures above $\approx$ 300°C. The temperature was measured by a specially attached and gauged bimetal which could rotate together with the sample during the deposition process. It is interesting to note that the initial growth rate at a given substrate temperature is not constant. The growth rate increases with increasing film thickness and attains a (temperature-dependent) constant value only at a film thickness $t >$ 200 nm. In other words, the growth rate in the very fine grained initial layer, which we have visualized by cross-sectional TEM analysis (7), is lower than in film regions,

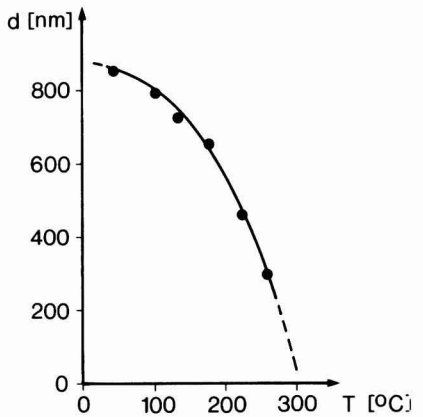

Fig. 1. Dependence of ZnS:Mn film thickness on substrate temperature *T* (at constant deposition duration, *t* = 1000s, and at constant evaporation rate).

where we observed the development of nicely shaped conical or columnar grains.

In Ref. (7), the Mn depth distribution in the bulk of our thin film samples was shown to be depending on preparational conditions. Additionally, we examined the photoluminescence intensity distribution emerging from the surface of the sample in normal direction with high spatial resolution. The luminescence observed was excited by the 488 nm line of an Ar laser and corresponds to the well-known $^4T_1$-$^6A_1$ transition between the crystal field levels of the Mn^{2+} ions, peaking at 585 nm at room temperature. The observed photoluminescence intensity normal to the surface was homogeneously distributed, indicating a correspondingly homogeneous distribution of Mn within the plane of the film. This result is important for the assessment of the cathodoluminescence intensity distribution.

Cathodoluminescence Apparatus

The specially prepared demountable cathodoluminescence (CL) apparatus is shown in Fig. 2. The rotatable sample holder carries 14 samples (25 × 25 mm²) and a current registration station which allows measurement of the incident electron-beam current with neglectable losses. The inner wall surface area of this current registration box is 460 times larger than the slit aperture area and exhibits a structure which minimizes the escape probability of backscattered electrons of the incident beam to less than 1%. This is very important in the energy range between 2 and 6 kV, where the coefficients for reflection and secondary emission of electrons are strongly dependent on material and voltage. The forward and backward CL light emission of the samples is caught by suitably arranged lightguides and registered by a calibrated photodiode.

For the measurement of fast dynamical effects we used a calibrated photomultiplier whose circuitry had response times below 50 ns. The range of electron penetration d into any material is defined by its specific properties and the kinetic energy of the electrons. An empirical formula for ZnS is given in Ref. (8)

$$d_{ZnS} = 2.83 \times 10^{-2} \times U^2 \qquad [1]$$

where d is in micrometers and U is in kilovolts. For the range of interest, this formula yields the following table for penetration depths d_{ZnS} of the electrons

U (kV)	d_{ZnS} (μm)
2	0.11
3	0.26
4	0.45
5	0.71
6	1.02

Luminance vs. Accelerating Voltage, Current Density, and Average Power

Figure 3 shows the cathodoluminescence intensity of ZnS:Mn films *vs.* the acceleration voltage of the electrons. The arrows indicate the voltage value which is sufficient for a complete penetration of the film according to the above formula (1). The cathodoluminescence intensity tends to saturate at voltages above this value. The saturation is a true bulk saturation and not due to charging effects. This is evidenced by sample 2, which has been prepared under equal conditions but additionally covered with a 30 nm Al film to ensure proper grounding of the film. The achievable saturation luminance increases with increasing substrate temperature during deposition. In Ref. (9) we have established a correlation between substrate temperature, grain size, and normalized cathodo- and photoluminescence intensities.

The current density dependence of the CL emission was measured in a pulsed mode with a 50 Hz repetition rate. We choose two different ways of excitation variation. Either the amount of charge per pulse was increased at constant pulse duration (amplitude modulation) or the pulse duration was varied, keeping $\Delta Q/\Delta t$ constant (pulse length modulation). In Fig. 4, we plot the obtained luminance values. With increasing current density the light emission tends to saturate, leading to a nonlinear dependence of light on current. This behavior has also been observed for the dissipative in-phase current flowing through the ZnS-layer during electroluminescent operation (10). There have been published a lot of speculations in the literature to explain the nature of the observed luminance saturation with increasing current [see Ref. (11) and references therein]. The most probable reason seems to be the one suggested in Ref. (11). The author proposes that saturation arises from an interaction between excited Mn^{2+} which occurs by energy transfer via unexcited Mn^{2+} and results in nonradiative decay. Furthermore, we can confirm the results of Mach and Müller (12), who find a dependence of decay time constant on the exciting beam

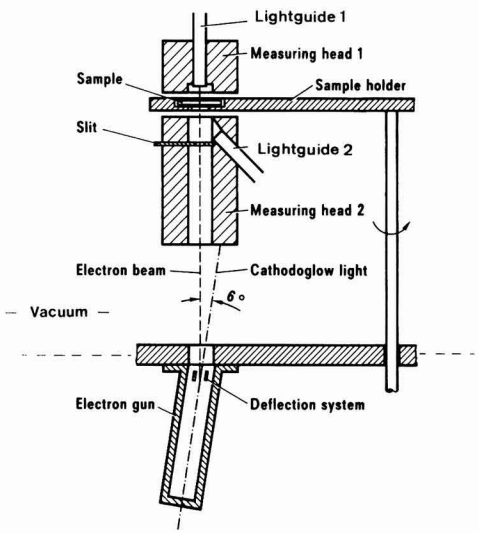

Fig. 2. Measuring system for cathodoluminescent light in forward and backward direction.

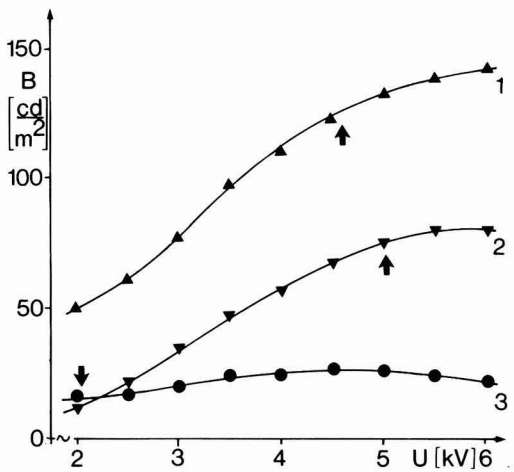

Fig. 3. Backward luminance B *vs.* accelerating voltage U for three different ZnS:Mn films. Curve 1: 630 nm, 0.4 w/o Mn, substrate temperature T_S = 180°C. Curve 2: 700 nm, 0.4 w/o Mn, T_S = 180°C (with additional 30 nm Al coverage). Curve 3: 120 nm, 0.7 w/o Mn, T_S = 180°C. The arrows indicate the voltage value where according to Eq. [1] full penetration of the bulk of the film is expected.

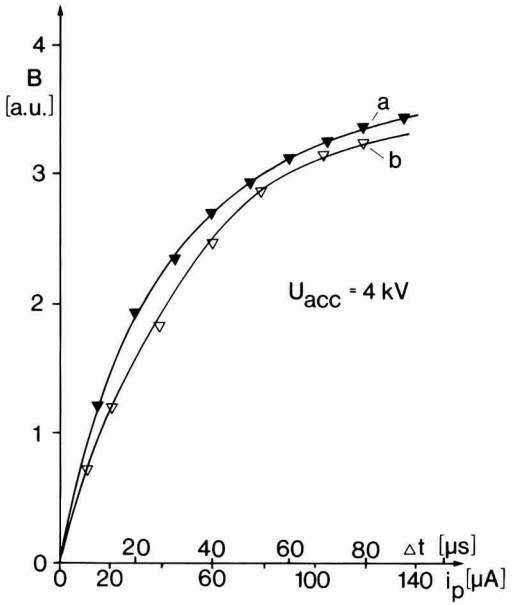

Fig. 4. Luminescence vs. exciting charge. Curve a: Keeping the current amplitude during the pulse at a constant value (100 μA) and varying the pulse duration Δt (50 Hz repetition rate). Curve b: Keeping the pulse duration constant (64 μs) and varying the current amplitude i_p during the pulse (50 Hz repetition rate). The spot diameter on the sample is 2.6 mm.

current density, *i.e.*, if we increase the charge density per pulse (60 μs, 50 Hz repetition rate) from 5 to 25 μA/mm², the decay time constant τ in samples with 0.4 weight percent Mn shrinks about 30%. This phenomenon is explained in terms of the above-mentioned nonradiative decay channel $\tau^*_{nr}([Mn^{2+}]^*)$

$$\frac{1}{\tau} = \frac{1}{\tau_r} + \frac{1}{\tau_{nr}[Mn^{2+}]} + \frac{1}{\tau^*_{nr}([Mn^{2+}]^*)} \qquad [2]$$

where τ_r is the radiative lifetime, $\tau_{nr}([Mn^{2+}])$ the concentration-dependent nonradiative lifetime, and $\tau^*_{nr}([Mn^{2+}]^*)$ the nonradiative lifetime depending on the concentration of excited centers.

In Fig. 5 (lower curve), we show how luminance saturation with current density affects the performance of an electron-beam addressed thin film faceplate when dynamical pictures should be displayed. The upper curve in Fig. 5 represents the behavior of an ordinary (Zn, Cd)S:Ag yellow emitting CRT phosphor. Although the efficiency for this phosphor also varies with excitation condition, the effect of this variation is by far not so strong as in the case of ZnS:Mn films. The thin film efficiency decreases by roughly one order of magnitude when the average power per spot (2.6 mm diam) is increased from 0.64 to 60 mW.

If we compare the light emission efficiency of the thin films under equal average power excitation, we find that higher pulse duration always yields a relative decrease in efficiency as one expects from the sublinear behavior of the pulsewidth modulation *vs.* brightness curve in Fig. 4. The obtainable efficiencies of the thin film are roughly ten times lower than the corresponding values of the phosphor at average power $P_{avg} < 3.5$ mW. This ratio increases to a factor of 20 for 3.5 mW $< P_{avg} <$ 10 mW and even to a factor of 30 for $P_{avg} > 10$ mW. For steady-state excitation with $P_{avg} = 60$ mW, the efficiency ratio between powders and thin film yields a factor of 20.

In Ref. (12), a very useful factorization of the efficiency η of thin film electroluminescent devices was suggested.

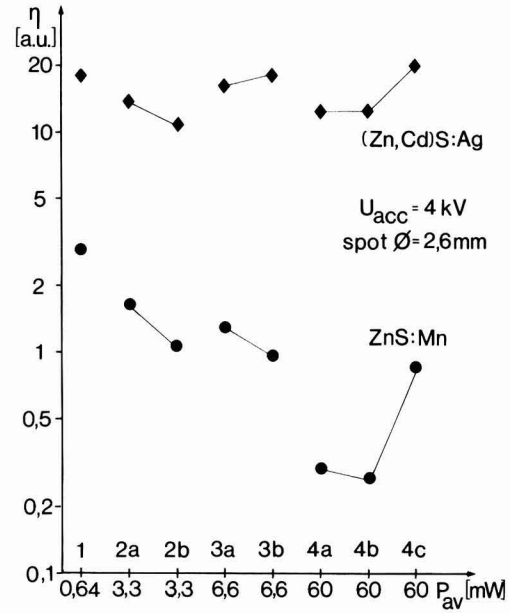

Fig. 5. Relative efficiencies of typical ZnS:Mn thin films and (Zn, Cd)S:Ag powder phosphors vs. different excitation conditions. Point 1: 50 μA; 64 μs; 50 Hz; P_{avg} = 0.64 mW. Point 2a: 130 μA; 64 μs; 100 Hz; P_{avg} = 3.328 mW. Point 2b: 130 μA; 128 μs; 50 Hz; P_{avg} = 3.328 mW. Point 3a: 130 μA; 125 μs; 100 Hz; P_{avg} = 6.656 mW. Point 3b: 130 μA; 256 μs; 50 Hz; P_{avg} = 6.656 mW. Point 4a: 120 μA; 2.5 ms; 50 Hz; P_{avg} = 60.0 mW. Point 4b: 120 μA; 5 ms; 25 Hz; P_{avg} = 60.0 mW. Point 4c: 15 μA-cw; P_{avg} = 60.0 mW. The spot diameter on the sample is 2.6 mm.

$$\eta = \eta_{exc}\eta_{lum}\eta_{opt} \qquad [3]$$

η_{exc} = centers excited (cm^{-3})/electrons transferred (cm^{-2}) [3a]

η_{lum} = centers decaying radiatively

(cm^{-3})/centers excited (cm^{-3}) [3b]

η_{opt} = photons emitted through the surface

(cm^{-2})/photons generated (cm^{-3}) [3c]

η_{opt} can be further factorized into

$$\eta_{opt} = \eta_A\eta_{Fr}\eta_{CAL} \qquad [4]$$

where η_A accounts for absorption losses (and yields the dimension distance^{-1} required from Eq. [3c], which in terms of dimensions is counterbalanced by η_{exc}, the excitation yield per unit length), η_{Fr} accounts for the Fresnel loss which occurs when light passes from a medium whose index of refraction is n_1 (ZnS) to a medium whose index of refraction is n_2 (air). The well-known formula for the reflection coefficient is

$$R = [(n_2 - n_1)/(n_2 + n_1)]^2 \qquad [5]$$

and since the transmission coefficient T is

$$T = 1 - R = 4n_2n_1/(n_2^2 + 2n_2n_1 + n_1^2) \qquad [5a]$$

The Fresnel loss efficiency factor is then defined as T/n_1n_2

$$\eta_{Fr} = 4/(2 + n_2/n_1 + n_1/n_2) \qquad [6]$$

$$\eta_{FrZnS} = 4/(2 + 1/2.4 + 2.4) = 0.83 \qquad [6a]$$

The third (and most important) efficiency loss is due to total internal reflection (Snell's law). The critical angle loss factor is determined by

$$\eta_{CAL} = (n_2/n_1)^2 \quad [7]$$

$$\eta_{CAL,ZnS} = (1/2.4)^2 = 0.17 \quad [8]$$

Hence, even if we neglect (at low excitation densities) absorption losses, the optical efficiency is

$$\eta_{opt,ZnS} = 1 \times 0.83 \times 0.17 = 0.14 \quad [9]$$

This figure accounts for a major part of the inferiority in efficiency of the thin film compared to the (Zn, Cd)S:Ag powder (which has practically no light piping losses) at least in the low excitation density region. At higher excitation densities, the above-mentioned reabsorption processes leading to nonradiative decay take place, leading to even worse optical efficiencies. In order to compare the stability of powders and thin films under heavy excitation conditions, we have measured the relative decrease of light output within a few hours. With the same amount of high average excitation energy (P = 20 mW-mm^{-2}) applied to both types of luminophors, we observed a decrease in efficiency of 60% for the powder and of only 25% for the thin film within 4h. Driven with equally high average energy, the powders degrade by nearly a factor of two faster than the thin films. Since phosphors, however, are much more efficient than the thin films, they need only a fraction of the power necessary to obtain the same level of brightness and accordingly do not degrade substantially in technical applications.

Conclusion

Mainly due to light trapping effects in the ZnS:Mn thin film layer, the cathodoluminescence efficiency of such films is lower than in a yellow light emitting (ZnCd)S:Ag powder phosphor by nearly a factor of ten at low excitation energies. At higher current densities, luminescence-current saturation effects as have been observed in electroluminescence as well further limit the cathodoluminescence efficiency of ZnS:Mn films. The main disadvantage of high light loss by waveguiding in the transparent ZnS layer can be minimized by proper surface treatment (roughening) and/or additional antireflective layers. With an estimated increase of the optical efficiency by a factor of two or three, the material seems to be quite interesting for high resolution, low degradation CL display applications.

Manuscript submitted March 21, 1985; revised manuscript received June 4, 1985.

Siemens Aktiengesellschaft assisted in meeting the publication costs of this article.

REFERENCES

1. R. Mach and G. O. Müller, *Phys. Status Solidi A*, **69,** 11 (1982).
2. M. Yoshida, Y. Kakihara, T. Yamashita, K. Taniguchi, and T. Inoguchi, *Jpn. J. Appl. Phys.*, Suppl., **17,** 127 (1978).
3. T. Inoguchi and S. Mito, "Topics in Applied Physics," p. 222, Springer, Heidelberg (1977).
4. J. M. Hurd and C. N. King, *Electron. Mater.*, **8,** 879 (1979).
5. M. E. Dunham, D. H. Smith, C. N. King, and G. S. Barta, in "Proceedings of the International Electron Devices Meeting, Washington, 1980," p. 711, New York (1980).
6. O. Sahni, P. M. Alt, D. B. Dove, W. E. Howard, and D. J. McClure, *IEEE Trans. Electron Devices*, **ed-28,** 708 (1981).
7. D. Theis, H. Oppolzer, G. Ebbinghaus, and S. Schild, *J. Cryst. Growth*, **63,** 47 (1983).
8. W. Espe, "Werkstoffkunde der Hochvakuumtechnik," Vol. III, VEB Deutscher Verlag der Wissenschaften, Berlin (1961).
9. D. Theis, *Phys. Status Solidi A*, **81,** 647 (1984).
10. H. Venghaus and D. Theis, Abstract 169, p. 420, The Electrochemical Society Extended Abstracts, Vol. 81-1, Minneapolis, MN, May 10-15, 1981.
11. R. Törnqvist, *J. Appl. Phys.*, **54,** 4110 (1983).
12. R. Mach and G. O. Müller, *Phys. Status Solidi A*, **81,** 609 (1984).

Technical Notes

A Novel Method for Growing Thin Gate Oxide

D. N. Chen[1] and Y. C. Cheng

Department of Electrical Engineering, University of Hong Kong, Hong Kong

In the present trend of miniaturization, thin oxide has become the subject of intense investigation. Recently, we proposed a novel method (1) for routinely growing thin (< 200Å) gate oxide with good stability and integrity. In this "partial-TCE" technique, a low temperature dry oxidation is followed by a high temperature dry oxidation with an appropriate amount of TCE. The former step is to provide a large portion of oxide with high dielectric strength, while the latter step gives a good Si/SiO_2 interface with a passivation ability against sodium contamination.

While it has been reported that addition of water to the oxidizing environment weakens the effect of the chlorine species (2), wet oxides have been shown (3) to possess higher dielectric strength. Taking these effects together, we are interested in examining the effectiveness of a wet partial-TCE process, aiming at obtaining thin oxides with higher dielectric strength. This paper summarizes an investigation of the properties of a wet oxygen partial TCE process consisting of two steps. The substrate is first oxidized in a wet O_2 atmosphere at a lower oxidation temperature to form an initial oxide film, and subsequently the oxidation is continued in a dry oxygen atmosphere containing TCE at a higher temperature. The overall aim is to incorporate the advantage of wet oxidation into the dry O_2 TCE technique. This oxidation process is not complicated, but the advantages of both wet O_2 and dry O_2 TCE can be fully exploited.

[1]Permanent address: South China Institute of Technology, Gaungzhou, China.

Experimental Procedure

All substrates used in the present studies are n-type silicon with a resistivity of 10 Ω-cm, and (111) orientation. These wafers were cleaned by standard cleaning procedure and were then oxidized in a resistance-heated furnace at a temperature range of 850°-1000°C for the initial oxidation period. For each oxidation temperature, wet oxidation was carried out by bubbling oxygen through water maintained at three different temperatures. Initial

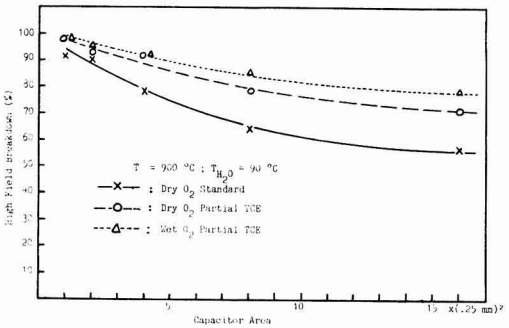

Fig. 1. Dependence of high field breakdown on capacitor area for various processes.

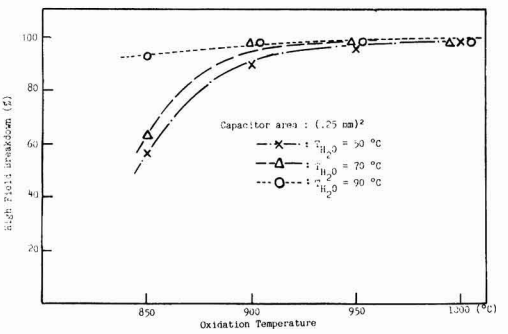

Fig. 2. Influence of water temperature on the relation of high field breakdown vs. oxidation temperature in the initial period.

oxide films were grown at 900°C in dry O_2 partial-TCE and in standard dry oxygen in order to compare with the wet O_2 partial-TCE process. Except for those oxidized with a standard dry O_2 process, all other wafers were followed by a TCE oxidation at a higher temperature. Annealing was performed in N_2 or Ar for 1h. Essential processing conditions are summarized in Table I.

Results and Discussions

Measured results on dielectric breakdown show that the distribution is generally in the high field region (*e.g.*, 8-10 MV/cm), with only a small percentage in the low field region (*e.g.*, 0.3-2 MV/cm). Figure 1 shows a plot of the percentage of high field breakdown (*i.e.*, > 5 MV/cm) as a function of capacitor areas. The results in general agree with those of a previous report (1) in that the probability of low field breakdown increases with larger capacitor area. Relatively speaking, samples fabricated by the wet O_2 partial-TCE method have the highest breakdown field compared to other processing techniques. At any oxidation temperature, the higher the water temperature, the stronger is the breakdown field, and the distinction between different water temperature diminishes as the oxidation temperature goes up. These observations confirm the notion that wet oxidation yields oxides with a greater portion of areas having higher dielectric strength, especially when the oxidation temperature is lower. These results are summarized in Fig. 2.

However, the combined influence of the oxidation temperature and water temperature is not so straightforward. At any water temperature, the general trend is that the higher the oxidation temperature, the higher the dielectric breakdown, and this is true for the water temperature

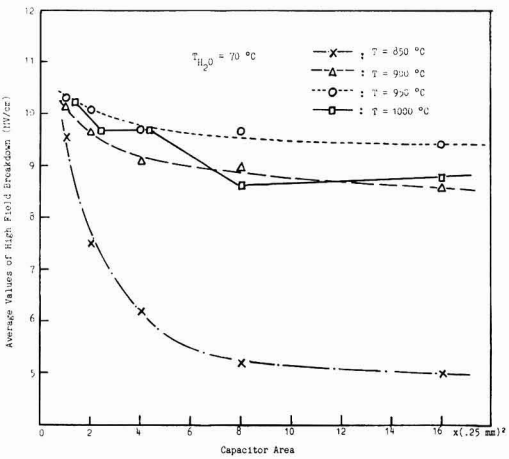

Fig. 3. Dependence of high field breakdown on capacitor area for various oxidation temperatures in the initial period.

at 50°C. Complication, however, arises when the water temperature is 70°C, and the maximum dielectric breakdown field occurs at an oxidation temperature of 950°C rather than 1000°C. These observations suggest that an optimal process condition may exist as far as dielectric breakdown field is concerned (Fig. 3). An analysis of the histograms of breakdown fields indicates that wet oxides

Table I. Processing conditions

Step	Wet TCE	Dry TCE	Standard dry O_2
1	T = 850°-1000°C T_{H_2O} (°C) = 50; 70; 90 O_2 = 500 ml/min t = 4 min	T = 900°C O_2 = 1000 ml/min t = 10 min	T = 900°C O_2 = 1500 ml/min t = 10 min
2	T = 1060°C O_2 = 500 ml/min TCE/N_2 = 80 ml/min t = 11 min	T = 1060°C O_2 = 500 ml/min TCE/N_2 = 80 ml/min t = 11 min	T = 1060°C O_2 = 1500 ml/min t = 13 min
3	Annealing in N_2 or Ar = 1500 ml/min		

Table II. High field and low field breakdown characteristics (%)

	Ref. (1) Area of capacitor = 0.204 mm²			Present work Area of capacitor = 0.25 mm²		
	Standard oxide (352Å)	Partial-TCE oxide (408Å)	Dual TCE oxide (499Å)	Standard oxide (423Å)	Partial-TCE oxide (409Å)	Wet O_2 TCE oxide (398Å)
> 8 MV-cm^{-1}	71.6	90.7	90.3	75	88	98
< 4 MV-cm^{-1}	14.7	1	0	11	3	0

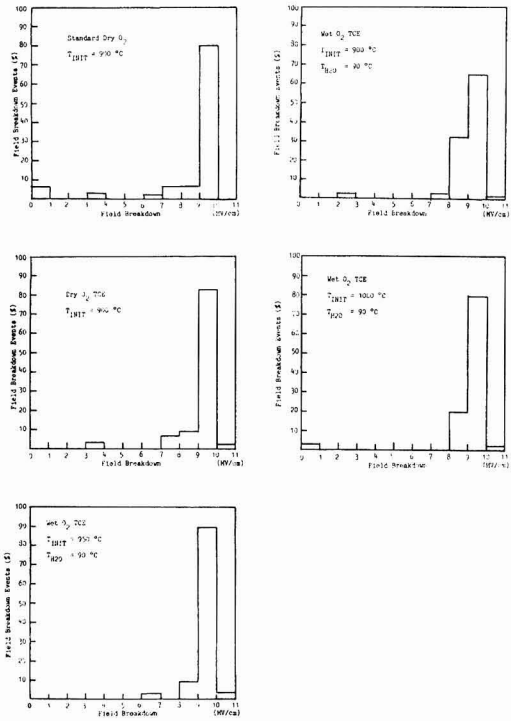

Fig. 4. Comparisons of dielectric field breakdown distribution for different oxidation processes.

grown at a furnace temperature of 950°C with a water temperature of 90°C possess the best field breakdown distribution (Fig. 4).

These results may be explained in terms of a model based on the results of Gibson and Dong (4). They found the existence of micropores in dry oxides by high resolution transmission electron microscope. The oxidant can diffuse to the interface through the micropores, with the explanation that the growth rate is linear for dry oxygen and the oxides give poor breakdown statistics. In the case of wet oxidation, it is postulated that the OH group will reduce the strain in the random network or the OH group will plug the micropores. Thus the potential fluctuation from the water-filled pores will be less than that of empty ones, resulting in a more uniform dielectric breakdown. This may probably explain the fact that there is less dependence of high field breakdown on capacitor area for wet oxides. However, some metallic ions will perhaps be attracted by the micropores, thus forming conducting channels which will cause low field breakdown. Therefore, the probability of low field breakdown will increase with the dryness of the oxidation environment.

In general, our experimental data show that raising the oxidation temperature at a fixed H_2O partial pressure will improve the relation of high field breakdown *vs.* capacitor area. This may be due to the fact that water molecules do not dissociate sufficiently at low oxidation temperatures to give enough OH radicals to plug the micropores.

In addition, we also measured the I-V characteristics of oxide films grown in wet O_2 partial TCE atmosphere with water temperature at the range of 70°-90°C. The field breakdown is nondestructive until the current is up to a few tens of microamperes, similar to that of dry O_2 partial-TCE (1). However, an abrupt transition always occurs in oxide films grown in standard dry O_2 process.

To summarize our results of investigation, we compare the high field and low field breakdown values among various oxidation techniques. Table II shows that the present technique yields the highest percentage of high field breakdown (> 8 MV-cm^{-1}) and the lowest percentage of low field breakdown (< 4 MV-cm^{-1}) when compared with other processes in the present work and with other techniques of the previous investigation. We have not examined in detail the effect of the present technique on oxide charges and defect densities. The former had been found to be comparable to that with other techniques, deducing from rough estimates of the flatband voltages. The latter quantity could possibly be lower, as suggested by the observation of a larger equilibrium current of breakdown than samples prepared by other techniques.

Conclusion

The wet O_2 partial-TCE technique has been successfully applied to grow thin oxide films with good integrity. Although the distribution of field breakdown of wet O_2 partial-TCE is very similar to that of dry O_2 partial-TCE for smaller capacitor area, the relation of field breakdown *vs.* capacitor area and the maximum breakdown current are much better in the wet case than in the dry O_2 case. The weakening effect of water vapor on TCE does not arise in the present oxidation technique, because both the wet oxidation and TCE oxidation are executed separately. Thus, the process conditions can be adjusted separately to an ideal value, if there is any, but they will not influence each other in an adverse manner. We believe that the optimum processing condition can be found if more experiments are performed. Though oxides grown by the present method appear promising, a more complete characterization is needed to perform on other oxide quality besides the dielectric breakdown in order to yield an overall picture of the quality of the thin oxides.

Acknowledgment

This work was supported in part by Industrial Development Board of Hong Kong.

Manuscript submitted Jan. 18, 1985; revised manuscript received June 14, 1985.

REFERENCES

1. Y. C. Cheng and B. Y. Liu, *This Journal*, **131,** 354 (1984); B. Y. Liu and Y. C. Cheng, *ibid.*, **131,** 683 (1984).
2. C. M. Osburn, *ibid.*, **122,** 284 (1975).
3. E. A. Irene, *ibid.*, **125,** 1708 (1978).
4. J. M. Gibson and D. W. Dong, *ibid.*, **127,** 2722 (1980).

Nickel Plating on Porous Silicon

R. Herino,[1] P. Jan, and G. Bomchil*

Centre National d'Etude des Télécommunications, 38243 Meylan Cedex, France

Porous silicon has been obtained by anodic oxidation of monocrystalline silicon in concentrated hydrofluoric acid solutions (1). Thick layers up to several microns can be obtained, with an average density ranging between 30 and 75% of that of the starting material (2), with pore radii between 20 and 100Å according to operating conditions and substrate resistivity (3). Thermal oxidation of PS can lead to thick layers of silicon dioxide, in relatively short times, because of the easy access of gaseous oxygen through the pores (4). It is why PS has been proposed to realize localized dielectric insulation and silicon-on-insulator (SOI) structures in the integrated circuit technology (5). In fact, another application of PS might be possible in the field of metallization, for contacts and interconnections. If a metal could be deposited in the porous volume, a very interesting structure would be obtained for the formation of metal silicides upon heating. Standard vacuum metallization techniques result in a quick pinching off of the pores, leading only to a thin superficial layer of metals. In this work, we report preliminary results which show that electrodeposition is an appropriate method for metallization of the porous silicon volume.

Electroplating on silicon has been studied very early in order to form electrodes. Various metals have been deposited and several solution compositions and solvents have been proposed (6). The main difficulty encountered with plating silicon is a rather poor adhesion of the deposited film when no special surface treatment (such as roughening of the surface by chemical etching) is performed before the electrolysis (7). In this preliminary work, we have been interested in the nickel deposition, which is said to present a rather good adhesion, and which is able to form silicides upon heating at relatively low temperatures. The electrolyte composition that we have used is slightly different from that described by Wurtz and Borneman (7): it was composed of 0.2*M* $NiSO_4$, $6H_2O$ and 0.1*M* tetraethylammonium perchlorate as supporting electrolyte. The solvent was a mixture of 85% ethylene glycol and 15% deionized water. Substrates were p-Si samples boron doped and (100) oriented with a 0.01 Ω-cm resistivity. The cell was a standard electrolytic cell, with a platinum counterelectrode and a Ag-AgCl reference electrode; illumination of the semiconductor surface was performed with a 100W tungsten-halogen lamp, providing intensities of the order of 10 mW/cm² at the silicon surface. Potentiostatic measurements were performed with a PAR M173 potentiostat, driven by a PAR M175 programmer. All plating experiments were conducted at room temperature. Porous samples were prepared in HF/EtOH electrolyte (25% HF and 50% EtOH), at a constant current density of 200 mA/cm², leading to a porous film of an average density of 45% of that of silicon, with pore radii of about 80Å as determined by gas adsorption experiments (3).

Nickel plating has been performed in the same experimental conditions which lead to bright and adherent films on nonporous silicon surface. Deposition occurs for potentials more negative than −0.55V *vs.* Ag/Ag^+; however, for potentials more negative than −0.90V, hydrogen bubbles form at the semiconductor surface. Plating on porous silicon was performed at constant current density, with values between 0.05 and 1 mA/cm², which corresponds to electrolysis potential greater than −0.90V. In this current density range, a faradic efficiency of 70-85% is obtained.

We have studied the Ni concentration profiles in the porous layers by x-ray microanalysis, with a LINK analyzer mounted on a JEOL electronic microscope. Primary electron energy was set to 22 keV, in order to get a good ionization of $L_{\alpha\beta}$ nickel lines. The electronic spot is fixed at a given point of the cleaved porous layer: the x-ray spectrum obtained during this analysis leads by integration (and after an initial calibration) to the atomic ratio of silicon to nickel present at the point where the spot is fixed. Concentration profiles are obtained by analyzing several points at different depths in the porous layer. Figure 1 shows the results obtained with a 10 μm thick porous layer. The cathodic current density used during metallization was 100 μA/cm², and the charges exchanged were 1.3 C/cm² for curve A and 6.7 C/cm² for curve B. It can be seen that nickel has been deposited in the whole thickness of the layers, and that the relative amount of nickel deposited decreases when depth increases. The comparison between curves A and B indicates that longer electrolysis times do not change significantly the nickel concentration at the bottom of the porous layer; on the contrary, it is observed that for longer metallization times the difference between both curves increases towards the surface, suggesting a progressive blockage of the access of nickel atoms to the pores from the bottom to the surface. Similar profiles are obtained at other plating current densities, with a slight increase in the nickel concentration gradient at the highest current density (1 mA/cm²).

When profiles obtained with rather thin porous layers (of the order of 5000Å) are investigated, x-ray microanalysis is no longer a suitable technique because of its relatively low spatial resolution. In this case, secondary ion mass spectroscopy (SIMS) can be used. However, only qualitative results will be presented, as the ratio of the intensity of the nickel signal over the intensity of the silicon signal, because the ionization rate of the element has not been determined. Profiles were not calibrated in depth, because we could not assume that the etching velocity was constant all along the thickness, so that only the depth measured with an alpha-stepper is given. A typical result is shown in Fig. 2, obtained for a 4600Å thick porous layer metallized with a plating current density of 100 μA/cm². It appears that for the small thicknesses the con-

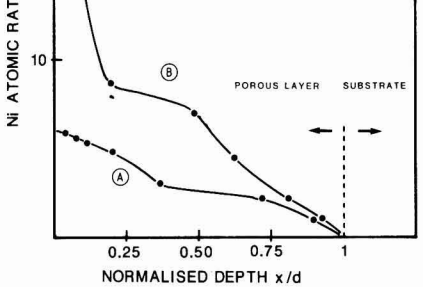

Fig. 1. Nickel concentration profile of metallized thick porous layers (10 μm) determined by x-ray microanalysis. Plating current: 100 μA/cm². Exchanged charge: 1.3 C/cm² (curve A) and 6.7 C/cm² (curve B).

*Electrochemical Society Active Member.

[1]Université Scientifique et Médicale de Grenoble, Grenoble, France.

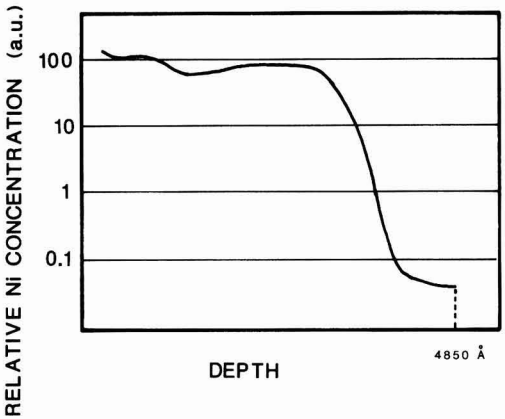

Fig. 2. Nickel concentration profile of a metallized thin porous layer (4800Å) determined by SIMS analysis.

centration profile is quite flat on mainly all the porous layer. The same result is obtained for other current densities up to 1 mA/cm^2. A rather good metallization of the porous volume is thus obtained in these conditions.

The formation of nickel silicide has been studied by annealing thin layers plated in the above conditions. X-ray diffraction of the as-plated samples (before annealing) shows the presence of a nickel layer, and from the broadening of diffraction peaks, a rather small particle size can be calculated (in the order of 50-70Å); otherwise, porous silicon presents a monocrystalline structure (8). When samples are annealed at different temperatures in the range from 400° to 800°C for 1h in dry nitrogen, nickel silicides are formed. We have observed a mixture of several silicide phases: $NiSi_2$, NiSi, and Ni_2Si_3. In addition to silicide formation, large stresses have developed, especially at the highest temperature; the diffraction pattern of monocrystalline porous silicon has disappeared, leaving place in the x-ray diagram to Bragg peaks corresponding to polycrystalline silicon.

In conclusion, this preliminary work demonstrates that metallization of the inner structure of porous silicon can be achieved by an electrochemical deposition method. The metal concentration is found uniform in depth for thin porous layers (5000Å thick), which may present a technological interest, but a large concentration gradient is obtained for thick porous layers (10 μm thick). A detailed study of the concentration profiles as a function of the cathodic current density and of the layer thickness, with porous structures presenting different pore sizes, is now necessary for getting a better understanding of the deposition mechanism in porous silicon. This would allow a comparison between the results on metal deposition on porous silicon and those obtained on microprofiles of different types, which have been studied in detail using theoretical and experimental approaches (9). Such a study, interesting from a fundamental point of view, might be of technological interest, as metallized porous layers seem to be promising structures for obtaining localized metal silicides.

Acknowledgments

The authors are very grateful to Dr. J. P. Gonchond for x-ray microanalysis and to Dr. D. Jourdain for SIMS analysis.

Manuscript submitted April 4, 1985; revised manuscript received June 26, 1985.

CNET assisted in meeting the publication costs of this article.

REFERENCES

1. D. R. Turner, in "The Electrochemistry of Semiconductors," P. J. Holmes, Editor, Chap. 4, p. 180, Academic Press, New York (1962); T. Unagami, *This Journal*, **127,** 476 (1980).
2. Y. Arita and Y. Sunohara, *ibid.*, **124,** 285 (1977).
3. G. Bomchil, R. Herino, K. Barla, and J. C. Pfister, *ibid.*, **130,** 383 (1983).
4. Y. Arita, *J. Cryst. Growth*, **45,** 383 (1978).
5. K. Imai and H. Unno, *IEEE Trans. Electron Devices*, **ed-31,** 297 (1984).
6. J. I. Pankove, in "The Electrochemistry of Semiconductors," P. J. Holmes, Editor, Chap. 7, Academic Press, New York (1962).
7. E. C. Wurtz and E. H. Borneman, *J. Appl. Phys.*, **28,** 235 (1957).
8. K. Barla, G. Bomchil, R. Herino, J. C. Pfister, and J. Baruchel, *J. Cryst. Growth*, **68,** 721 (1984).
9. O. Kardos and D. G. Foulke, in "Advances in Electrochemistry and Electrochemical Engineering," Vol. 2, C. W. Tobias, Editor, p. 145, John Wiley and Sons, New York (1962).

Interface Traps Caused by Ge Pre-Amorphization

D. S. Wen, J. Liu,** C. M. Osburn,* and J. J. Wortman***

Department of Electrical and Computer Engineering, North Carolina State University, Raleigh, North Carolina 27695 and Microelectronics Center of North Carolina, Research Triangle Park, North Carolina 27709

Modern CMOS VLSI technologies require shallow source-drain junctions for both p-channel and n-channel devices. Junction depths between 0.1 and 0.25 μm will be necessary in order to minimize both source-drain leakage currents and threshold voltage reduction due to short channel effects. This is particularly difficult for p-channel transistors because of the channeling and the high diffusivity of boron in silicon. However, these effects can be minimized by applying both preamorphization techniques and rapid thermal annealing (RTA) (1-3). More recently, silicon preamorphization using germanium implantation was shown to be a suitable choice for Si preamorphization, since it has a high solid solubility in Si and because it does not appear to alter the electrical properties of Si significantly (3). In order to be compatible with self-aligned polysilicon gate technology, the damage caused by high energy implantation must be prevented from degrading the silicon-silicon dioxide interface. MOSFET characteristics can be degraded if the damage is not removed by annealing. In our recent work, the interface traps caused by the Ge preamorphization were observed even with very low implant energy. A comparison between different isotopes of germanium showed that the effect was due to hydrogen, not germanium. The purpose of this communication is to document the effect and to alert other workers to the adverse impact of GeH implantation.

*Electrochemical Society Active Member.
**Electrochemical Society Student Member.

Experimental

Starting with <100> p-type Si wafers, a 38 nm gate oxide was thermally grown. A 0.25 μm polysilicon layer was then deposited. After $POCl_3$ doping, a 0.15 μm CVD oxide was deposited to increase the height of the gate barrier up to 0.4 μm. Then, Ge was implanted at several energies with a dose of $2E15$ cm^{-2}. Two isotopes of Ge [Ge(70) and Ge(74)] were used using GeH_4 as the source. The CVD ox-

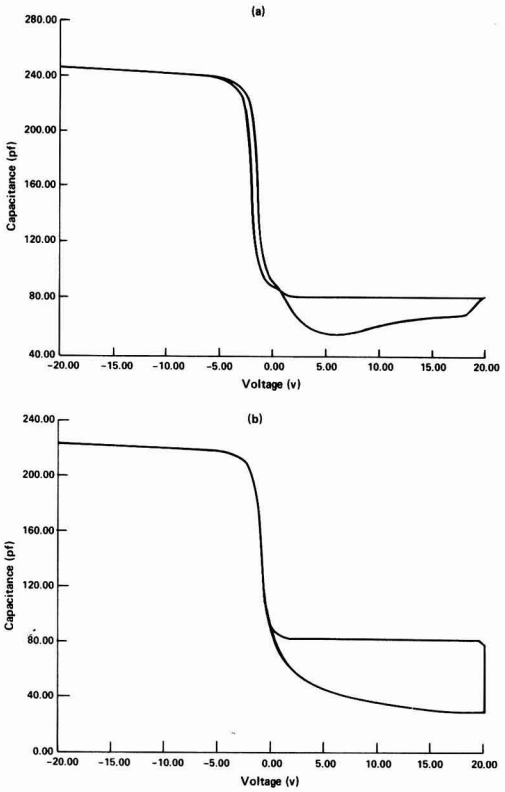

Fig. 1. The C-V characteristics of capacitor with Ge(74) implantation (energy = 75 keV, dose = 2×10^{15}). a: After RTA 1000°C, 10s. b: After RTA 1100°C, 10s.

ide layer on the top of poly was etched off and standard MOS capacitors were generated by plasma etching the polysilicon. Rapid thermal annealing was then performed at 1000° and 1100°C, respectively, for 10s. The C-V characteristics of the capacitors were obtained and the results were compared.

Results and Discussions

Figure 1a shows the C-V characteristics of the MOS capacitors with Ge(74) implantation at 75 keV, after RTA 1000°C for 10s. There is a hysteresis in the C-V characteristics between forward and retrace curves. The minority carrier lifetime of the devices is so low that the device cannot be driven into the deep depletion. Similar results had been obtained on the samples with Ge(74) implantation at the energies of 150 and 300 keV. These results indicate that the interface damage exists even with very low implant energy (75 keV). Such damage can be removed only by RTA at 1100°C for 10s (Fig. 1b) and was not observed on the control wafer without implantation. The LSS projected range and standard deviation for Ge in Si are listed in Table I. The estimated depths of amorphous layer are 0.39, 0.21, and 0.11 μm for the energies of 300, 150, and 75 keV, respectively. TEM cross-sectional analysis for Ge implantation at 300 keV showed the amorphous layer to be about 0.4 μm (3). Thus Ge penetration through the thick polygate stack (0.15 μm CVD oxide/0.25 μm

Table I. The LSS projected range of Ge in Si (4)

Energy (keV)	R_p (μm)	ΔR_p (μm)
300	0.17	0.055
150	0.087	0.030
75	0.047	0.017

Table II. The major isotopes of Ge (5)

Isotope	Percentage
Ge(70)	20.55
Ge(72)	27.37
Ge(73)	7.67
Ge(74)	36.74
Ge(76)	7.67

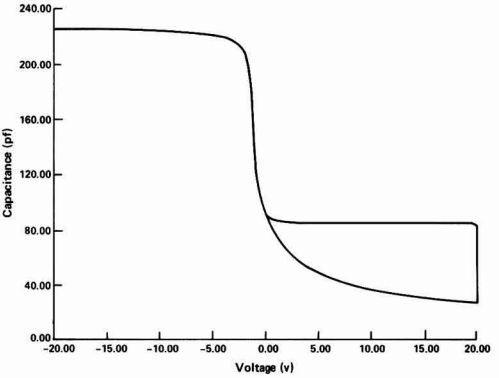

Fig. 2. The C-V characteristics of capacitor with Ge(70) implantation (energy = 150 keV, dose = 2×10^{15}), after RTA 1000°C, 10s.

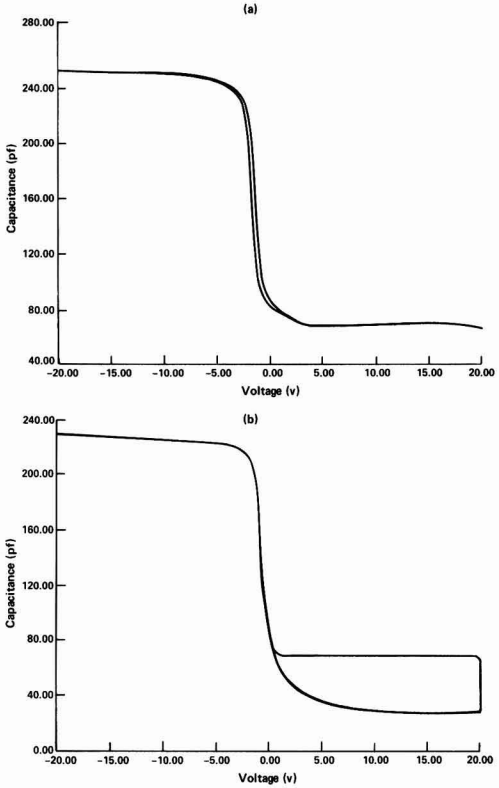

Fig. 3. The C-V characteristics of capacitor with H_2^+ implantation (energy = 100 keV, dose = 1×10^{15}). a: After RTA 1000°C, 10s. b: After RTA 1100°C, 10s.

polysilicon/oxide) was considered unlikely at 75 and 150 keV. Nevertheless, the defects were clearly caused by the implantation process.

Since Ge has several isotopes (Table II), the Ge(74) is usually selected because of the highest percentage. Unfortunately, implantation with 74 amu might include Ge(73)H and Ge(72)H_2 in addition to Ge(74). In an ion implanter with a preanalysis system, the mass analysis takes place at low extraction voltage, and the beam then passes through an acceleration stage to reach its final energy. Postanalysis dissociation of GeH(74) could occur before high energy acceleration, giving the hydrogen atoms enough energy to penetrate the polygate and gate oxide. Indeed, the hysteresis and low lifetime phenomena due to the interface defects are not seen in 150 keV Ge(70)-implanted samples after RTA at 1000°C for 10s (see Fig. 2). As a further verification that defects are due to hydrogen penetration, samples with only H_2 implantation were fabricated in the same manner. C-V hysteresis and low minority carrier lifetime were seen in the C-V curve (see Fig. 3) of 100 keV H_2-implanted wafers; furthermore, the C-V curves exhibited considerable variability from die to die. Based on these experiments, we conclude that anomalously high energy H implantation can occur during Ge(74) implantation. We are unable to determine whether this results from preacceleration dissociation, from charge exchange with residual H_2, or during dissociation of GeH at the wafer.

At 300 keV, the defects were observed in both Ge(70)- and Ge(74)-implanted wafers. It showed that the Ge penetrated the 0.4 μm gate barrier and caused damage at the oxide-silicon interface, confirming the previous work of XTEM analysis by Sadana *et al.* (3).

Acknowledgments

The authors would like to express their thanks to Dr. D. Sharma and Dr. S. Goodwin-Johansson for their helpful discussion and to Larry Simpson for help with Ge and H implantation. This work was sponsored by the Semiconductor Research Corporation and the Microelectronics Center of North Carolina.

Manuscript submitted April 22, 1985; revised manuscript received June 28, 1985.

The Microelectronics Center of North Carolina assisted in meeting the publication costs of this article.

REFERENCES

1. T. E. Seidel, *IEEE Electron Devices Lett.*, **edl-4,** 353 (1983).
2. T. E. Seidel, R. Knoell, F. A. Stevie, G. Poli, and B. Schwartz, in "VLSI Science and Technology 1984," K. Beam and G. A. Rozgonyi, Editors, p. 201, The Electrochemical Society Softbound Proceedings Series, Pennington, NJ (1984).
3. D. K. Sadana, W. Maszara, J. J. Wortman, G. A. Rozgonyi, and W. K. Chu, *This Journal,* **131,** 943 (1984).
4. J. F. Gibbons, W. S. Johnson, and S. W. Mylroie, "Projected Range Statistics, Semiconductors and Related Material," Dowden, Hutchinson & Ross, Stroudsburg, PA (1975).
5. W. H. Sullivan, "Trilinear Chart of Nuclides," Oak Ridge National Laboratory, Oak Ridge, TN (1957).

JOURNAL OF THE ELECTROCHEMICAL SOCIETY

ACCELERATED

—BRIEF COMMUNICATIONS—

OCTOBER 1985

Evidence for a Bipolar Mechanism of Passivity in Mo Bearing Stainless Steels

Y. C. Lu[1] and C. R. Clayton*

Department of Materials Science and Engineering, The State University of New York, Stony Brook, New York 11794

Variable angle XPS studies of the passive films formed on the alloys Fe-19Cr-9Ni and Fe-19Cr-9Ni-2.5Mo in deaerated 0.1M HCl is presented. Passivation in each case was carried out for 1 hour at -180mV (Vs. SCE) following cathodic removal of the air formed film by polarization at -600 mV for 15 minutes. In figure 1 we compare the Cr $2p^3/_2$ spectra for each alloy, at 20°(w.r.t. sample surface) to enhance the outer regions of the film and 50° to enhance spectra of the Cr species at the metal-film interface. The complex spectra contains two major peaks with positions corresponding to Cr_2O_3 and CrOOH or $Cr(OH)_3$*. Two minor peaks corresponding to CrO_3 and CrO_4^{2-} are also found. For each alloy the Cr_2O_3 phase appears to be situated at the metal-film interface. Independent studies to be fully presented later, indicate that CrO_3 is incorporated in Cr_2O_3 and that CrO_4^{2-} is incorporated in the $Cr(OH)_3$ or CrOOH phase. The outer layers of the anodic film in each case contain iron hydroxy-oxides. In particular we note that the Mo bearing alloy produced well defined spectra of Fe^{2+}, MoO_2 and MoO_4^{2-}. The Mo3d spectra are presented in figure 2. It is possible that $FeMoO_4$ is formed in the outer layer. The addition of Mo to the alloy also results in the development of the Cr_2O_3 phase and a marked reduction in the $Cr(OH)_3$ or CrOOH phase.

The nature of the passive film formed in 0.1M HCl appears to follow the behavior expected of a bipolar duplex membrane as described by Sakashita and Sato (1). In figure 3 is a schematic representation of the bipolar behavior of the passive films formed on stainless steel. This model proposes that CrO_4^{2-} and the more abundant MoO_4^{2-} anions may convert the otherwise anion selective hydrated oxides to cation selective phases. While deprotonation is enhanced by the field assisted egress of protons through the cation selective layer, O^{2-} anions resulting from the dissociation of OH^- groups, are able to diffuse through the anion selective phase towards the metal-film interface and to react with Cr to form Cr_2O_3. Due to the fact that Cr_2O_3 and CrO_3 have very similar standard free enthalpies it is not surprising that, as postulated by Revesz and Kruger (2) some CrO_3 is formed in the Cr_2O_3 phase. The deprotonation reaction may take the following course: $Cr(OH)_3 \rightarrow CrOOH + O^{2-} + 2H^+$, as evidenced by RHEED studies reported elsewhere (3). The resulting Cr_2O_3 layer will act as a non-selective ionic barrier for both anion and cation diffusion.

The presence of CrO_4^{2-} and MoO_4^{2-} is not expected since both ions are unstable in low pH media. However, it would appear that they are formed in the solid-state by reaction of lower valent metallic ions with lattice water trapped in the gel-like disordered state at the onset of passivity. The solid-state environment in which the lower valent cations are initially accomodated is, therefore, analogous to a neutral to high pH solution where both CrO_4^{2-} and MoO_4^{2-} are stable. We propose that there is a common link between the effect of solution born inhibitors of the type MeO_4^{n-} and MeO_4^{n-} anions incorporated in anodic films at low concentrations. It has been shown from quantum mechanical studies by Rosenfeld that anions of the form MeO_4^{n-} appear to be electron acceptors with the partial electronic charge residing on the oxygen ligands surrounding the central atom (4). Such systems would therefore provide strong negative fixed charges capable of rectifying ionic current.

A fuller discussion of the proposed mechanism of passivity of stainless steel will shortly be submitted to this journal.

ACKNOWLEDGEMENTS:

It is a pleasure to acknowledge the support of this program by the National Science Foundation under the research grant DMR8106499A01 and equipment grants DMR771831 and DMR811732

*Spectra were calibrated against the following binding energies Au 4f 83.8eV
C 1s 284.6eV

REFERENCES

1. M. Sakashita and N. Sato. Passivity of Metals, Eds., R.P. Frankenthal and J. Kruger, Electrochem. Soc., Princeton, N.J. (1978) p. 479.
2. A.G. Revesz and J. Kruger. ibid p. 479.
3. C.R. Clayton, A.R. Brooks, K. Doss and Y.C. Lu in Equilibrium Diagrams and Localized Corrosion, Eds. R.P. Frankenthal and J. Kruger, Electrochem. Soc., Princeton, N.J., (1984), p. 369.
4. I.L. Rosenfeld, Corrosion Inhibitors, McGraw-Hill Inc., New York (1981).

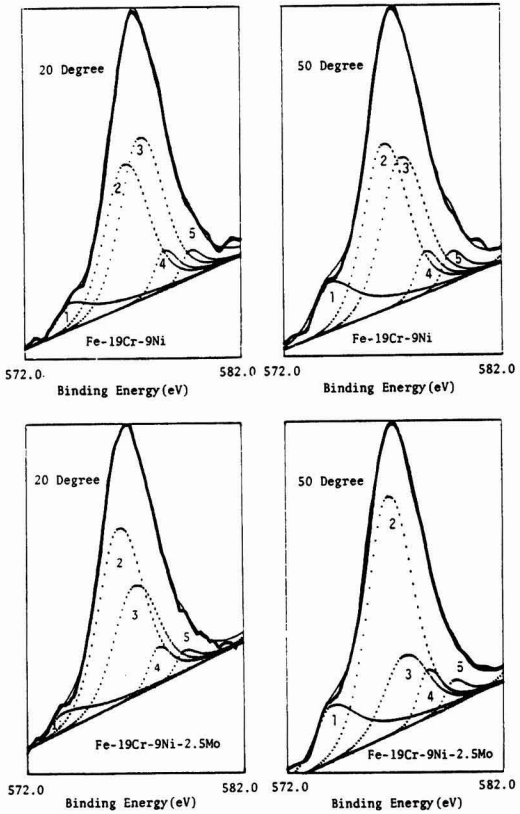

Fig. 1 Cr 2p3/2 photoelectron spectra obtained from the anodic films formed on Fe-19Cr-9Ni and Fe-19Cr-9Ni-2.5Mo alloys in 0.1M HCl at -180mV(SCE) for 1 hour.

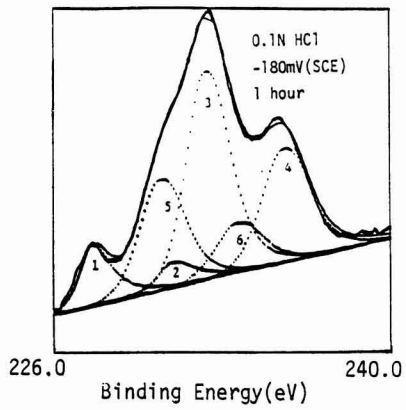

Fig. 2 Mo 3d photoelectron spectrum obtained from the anodic film formed on Fe-19Cr-9Ni-2.5Mo alloy

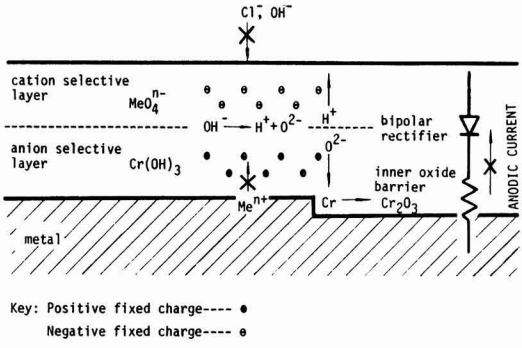

Fig. 3 Schematic representation of the bipolar behavior of the passive film formed on stainless steel

*Electrochemical Society Active Member.
[1]Permanent address: Guangzhou Research Institute of Electrical Applances, Guangzhou, China.
Manuscript received May 3, 1985.
The State University of New York assisted in meeting the publication costs of this article.

Sulfur Dioxide Gas Detection with Na_2SO_4-$Y_2(SO_4)_3$-SiO_2 Solid Electrolyte by a Solid Reference Electrode Method

N. Imanaka, Y. Yamaguchi, G. Adachi, and J. Shiokawa

Department of Applied Chemistry, Faculty of Engineering, Osaka University, Yamadaoka 2-1, Suita, Osaka 565, Japan

In recent years, sulfur dioxide exhausted into the surroundings has been seriously deteriorating the environments. The suppression of the exhausted SO_2 gas amount is an urgent necessity.

Lately, alkali-metal sulfates(1-8), have been examined to utilize as solid electrolytes for a sulfur dioxide gas detector. However, alkali-metal sulfates are not suitable materials because of the phase transformation(9-11) and their low electrical conductivities. In electromotive force(EMF) measurements, two main techniques have been investigated. One is an SO_2 gas concentration cell method(1-4,12) using an SO_2 standard gas electrode. The other is to apply the metal sulfate-metal oxide(5,6) or the silver-silver sulfate mixture(7,8) electrode as reference electrode instead of the standard reference gas. The former method is a general technique to examine whether the sample is appropriate for the solid electrolyte or not. However, the size of the SO_2 gas detector of this type becomes larger and complicated. In the case of the sulfate-oxide(5,6) electrode, it is necessary to maintain the solid electrode separated from the electrolyte completely because the electrode may react with the sulfate electrolyte to give a false EMF. The temperature in practical use should be restricted between 783 K and 833 K with a silver-silver sulfate reference electrode method(7,8).

In our previous investigation(12), rare earth sulfates(Ln=Y and Gd) and silicon dioxide have been mixed so as to enhance the electrical conductivity and to prevent the electrolyte from becoming ductile, respectively. In addition, the suppression of the phase transformation has been attempted by the mixing both $Ln_2(SO_4)_3$(Ln=Y and Gd) and SiO_2. In this study, a metal sulfate-metal oxide(M=Mg, Mn, and Ni) solid electrode has been applied as the reference electrode and directly fixed to the Na_2SO_4-$Y_2(SO_4)_3$-SiO_2 solid electrolyte.

The EMF measurement by the sulfate-oxide solid reference electrode method was conducted with the Na_2SO_4-$Y_2(SO_4)_3$-SiO_2 solid electrolyte. The apparatus is illustrated in Fig. 1. The platinum net reference electrode was tightly fixed between the electrolyte and the solid reference electrode. The sample was covered with the bonding agent(SUMICERAM from Sumitomo Chemical Industries Ltd.). A ringed glass packing was adopted so as to separate the test gas from the reference electrode compartment. The test SO_2 and air gas mixture was regulated with the Standard Gas Generator(SGGU-711SD) from Standard Technology Co.. The air gas was introduced into the reference electrode compartment in order to maintain the constant oxygen partial pressure(2.13×10^4 Pa). Platinum was sputterred on both center surfaces(5×10^{-3} m in diameter) of the electrolyte(1.3×10^{-2} m in diameter) by Shimadzu's Ion Coater IC-50. The Pt film thickness was approximately 10 nm. By this sputtering, good contact between the electrolyte and the Pt electrode was obtained. Furthermore, the formation and the decomposition of sodium sulfate might be considered to be made smoother. The preparation of the Na_2SO_4-$Y_2(SO_4)_3$-SiO_2 solid electrolyte is discussed in our previous paper(12)(The reaction between Na_2SO_4, $Y_2(SO_4)_3$, and SiO_2 has been completed by this preparation). The EMF measurements were conducted twice with each solid reference electrode and almost the same results were obtained. The EMF results with the $MgSO_4$-MgO solid reference electrode at 973 K are shown in Fig. 2. The values obtained were approximately 280 mV higher than the calculated EMF(6). The $MgSO_4$-MgO reference electrode seemed to react with the Na_2SO_4-$Y_2(SO_4)_3$-SiO_2 solid electrolyte during measurement. This chemical reaction might be considerably enhanced the EMF value. The variation of the EMF with the $MnSO_4$-Mn_2O_3 solid reference electrode at 973 K is also presented in Fig. 2. In all measurements, the measured EMF was about 80 mV larger than the calculated value. The $MnSO_4$-Mn_2O_3 electrode, however, did not react with the electrolyte. The difference between the measured and the calculated EMF can be mainly ascribed to the fact that manganese oxides of different oxidation states may have been produced. The results of the EMF measurements with the $NiSO_4$-NiO solid reference electrode at 973 K are shown in Fig. 3 together with the results of Na_2SO_4 as a comparison. The EMF characteristics for Na_2SO_4 decreased significantly in the inlet SO_2 gas concentration less than 0.1 %($\log(P_{SO_2})_{in}=-3.0$)

because of the gas permeation through cracks occurred in the electrolyte. In the case of the Na_2SO_4-$Y_2(SO_4)_3$-SiO_2 electrolyte, the measured EMF was in good accordance with the calculated EMF(6), in the inlet SO_2 gas concentration from 30 ppm($\log(P_{SO_2})_{in}$=-4.52) to 1 %($\log(P_{SO_2})_{in}$=-2.0). No chemical reaction between the electrolyte and the $NiSO_4$-NiO reference electrode was observed. The EMF characteristics for the Na_2SO_4-$Y_2(SO_4)_3$-SiO_2 were appreciably improved both the mixing of $Y_2(SO_4)_3$ and SiO_2 simultaneously into sodium sulfate and by the Pt sputtering. In addition, the Na_2SO_4-$Y_2(SO_4)_3$-SiO_2 solid electrolyte can be fixed directly to the solid reference electrode.

The $NiSO_4$-NiO solid reference electrode technique has a potential in practical utilization for a sulfur dioxide gas detector.

REFERENCES

1. K. T. Jacob and D. B. Rao, J. Electrochem. Soc., 126, 1842 (1979).
2. M. Gauthier and A. Chamberland, J. Electrochem. Soc., 124, 1579 (1977).
3. N. Imanaka, G. Adachi, and J. Shiokawa, Bull. Chem. Soc. Jpn., 57, 687 (1984).
4. N. Imanaka, G. Adachi, and J. Shiokawa, Proc. the International Meeting on Chemical Sensors, Fukuoka, 348 (1983).
5. M. Gauthier, R. Bellemare, and A. Bélanger, J. Electrochem. Soc., 128, 371 (1981).
6. M. Gauthier and C. W. Bale, Metall. Trans. B, 14B, 117 (1983).
7. W. L. Worrell, Proc. the International Meeting on Chemical Sensors, Fukuoka, 332 (1983).
8. W. L. Worrell and Q. G. Liu, J. Electroanal. Chem., 168, 355 (1984).
9. E. L. Kreidl and Ivan Simon, Nature, 181, 1529 (1958).
10. F. A. I. El-Kabbany, Phys. Stat. Sol., (a) 58, 373 (1980).
11. A. Kvist and A. Lundén, Z. Naturforschg., 20a, 235 (1965).
12. N. Imanaka, Y. Yamaguchi, G. Adachi, and J. Shiokawa, Bull. Chem. Soc. Jpn., 58, 5 (1985).

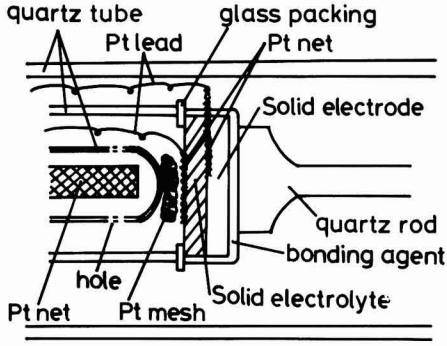

Fig. 1 The apparatus for the EMF measurements (A solid reference electrode method)

Manuscript submitted April 18, 1985; revised manuscript received Aug. 13, 1985.

Osaka University assisted in meeting the publication costs of this article.

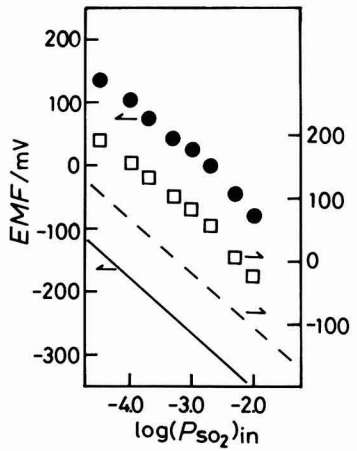

Fig. 2 The variation of the EMF for Na_2SO_4-$Y_2(SO_4)_3$-SiO_2(48.1:11.8:40.1) with $MgSO_4$-MgO(●) and $MnSO_4$-Mn_2O_3(□) solid reference electrodes at 973 K
— and – – are calculated EMF(6)

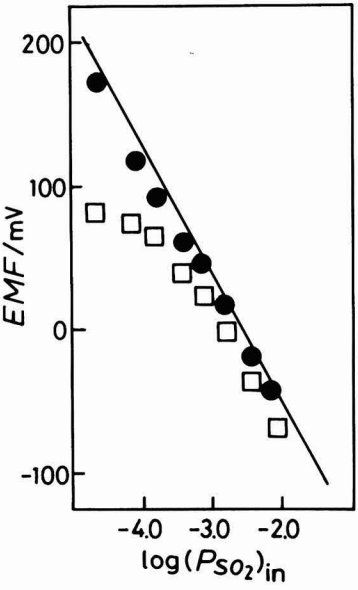

Fig. 3 The variation of the EMF for Na_2SO_4-$Y_2(SO_4)_3$-SiO_2(48.1:11.8:40.1) and Na_2SO_4 solid electrolytes with $NiSO_4$-NiO solid reference electrode at 973 K
● Na_2SO_4-$Y_2(SO_4)_3$-SiO_2
□ Na_2SO_4
— calculated EMF(6)

RN

Call for Papers
Symposium on
Silicon on Insulators
169th Meeting of The Electrochemical Society
Boston, Massachusetts
May 4-9, 1986

Focus will be placed on recent advances in the various approaches to the formation of device-quality silicon on insulating substrates.

Approaches to be discussed:
- Lateral growth from the melt and by CVD and SPE.
- Buried insulating layer formation.
- Growth on patterned relief structures.
- Heteroepitaxial growth.

Topics to be included:
- Preparative procedures.
- Properties crystalline and electronic.
- Characterization.
- Advantages and limitations.
- Applicability to device structures.

Invited Speakers

H. Baumgart, Philips Laboratories
M. Bomchil, CNET
J. B. Butcher, Middlesex Polytechnics
S. Furukawa, Tokyo Institute of Technology
P. Hemment, University of Surrey
L. Jastrzebski, RCA Laboratories
J-P. Joly, LETI
T. I. Kamins, Hewlett-Packard
H. W. Lam, Texas Instruments
S. Muramoto, NTT Atsugi Laboratory
I. Ohdomori, Waseda University
L. Pfeiffer, AT&T Bell Laboratories
N. Sasaki, Fujitsu Semiconductor Division
H. Tango, Toshiba VLSI Laboratory
L. E. Trimble and G. K. Celler, AT&T Bell Laboratories
B-Y. Tsaur, MIT Lincoln Laboratory
G. Zimmer, Fraunhofer Institute

Symposium Co-Chairmen

G. W. Cullen, RCA Laboratories, Princeton, NJ 08540; J. Butcher, Microelectronic Center, Middlesex Polytechnic, London, England N11 1NQ; G. K. Celler, AT&T Bell Laboratories, Rm. 6F-217, Murray Hill, NJ 07974; J. C. C. Fan, MIT Lincoln Laboratory, 244 Wood St., Lexington, MA 02173; S. Furukawa, Dept. of Applied Electronics, Tokyo Institute of Technology, Nagatsuta, Midori-ku, Yokohama 227, Japan; V. A. Wells, Sandia National Laboratories, Div. 2147, Albuquerque, NM 87175.

Extended and 75-word abstracts must be received by **December 1, 1985** by The Electrochemical Society, 10 South Main St., Pennington, NJ 08534-2896.

Nominations Invited for Edward Goodrich Acheson Award and Prize

The Edward Goodrich Acheson Award and Prize was established in 1928 to recognize a person who, in the judgment of the directors of the Society, has made contributions to the advancement of any of the objects, purposes, or activities of The Electrochemical Society as to merit the award. Such contributions may consist of, but shall not be limited to, (a) a discovery pertaining to electrochemistry, electrometallurgy, or electrothermics, (b) an invention of a plan, process, or device, or research evidenced by a paper embodying information useful, valuable, or significant in the theory or practice of electrochemistry, electrometallurgy, or electrothermics, and/or (c) distinguished services rendered to the Society.

The Award consists of a gold medal, a bronze replica, and two thousand dollars ($2000). The following have received the Award:

1929—Edward G. Acheson
1931—Edwin F. Northrup
1933—Colin Garfield Fink
1935—Frank J. Tone
1937—Frederick M. Becket
1939—Francis C. Frary
1942—Charles F. Burgess
1944—William Blum
1946—H. Jermain Creighton
1948—Duncan A. MacInnes
1951—George W. Vinal
1953—J. W. Marden
1954—George W. Heise
1956—Robert M. Burns
1958—William J. Kroll
1960—Henry B. Linford
1962—C. L. Faust
1964—Earl A. Gulbransen
1966—Warren C. Vosburgh
1968—Francis L. LaQue
1970—Samuel Ruben
1972—Charles W. Tobias
1974—Cecil V. King
1976—N. Bruce Hannay
1978—David A. Vermilyea
1980—Ernest B. Yeager
1982—Harry C. Gatos
1984—Norman Hackerman

Nominations for the next Award to be presented at the Fall Meeting of the Society in 1986 in San Diego, California, are invited. Nominees do not have to be members of the Society to be considered. Furthermore, there are no distinctions, restrictions, or reservations regarding age, sex, race, citizenship, or place of origin or residence.

Please send nominations before March 1, 1986 with supporting documents to Wayne L. Worrell, Dept. of Metal and Materials Science, University of Pennsylvania, 3231 Walnut St., K1, Philadelphia, PA 19104.

POSITIONS WANTED

Please address replies to the box number shown, c/o The Electrochemical Society, Inc., 10 South Main Street, Pennington, NJ 08534-2896.

Ph.D. Electrochemist—15 years experience in applied electrochemical R&D. Recent experience in corrosion measurement, electrochemical instrumentation and sensor development for high temperature aqueous environments, modeling of corrosion environment in SCC cracks, and electrochemistry of ceramics. Desires university or industrial R&D position. Reply Box C-257.

Senior Electrochemist—Ph.D. industrial/academic background. Industrial electrolytes, chlor-alkali, fused salt electrolysis, hydrometallurgy, electrodeposition, metal finishing, speciality and electronic materials, plasma chemistry. R&D as well as plant support and operation experience. Versatile, innovative, and highly self-motivated. Patents and Publications. Reply Box C-258.

MEETINGS CALENDAR

Society of Women Engineers
on
"Insuring the Future with Technology"
June 22-29, 1986
Hartford, Connecticut

For further information, contact S. W. E. 1986 Convention, P.O. Box 9242, Wethersfield, CT 06109.

U.S. Army Electronics Technology and Devices Laboratory
on
"32nd International Power Sources Symposium"
June 9-12, 1986
Cherry Hill, New Jersey

For further information, contact Carl Berger, Power Sources Div., Attn.: DELET-P, ERADCOM, Fort Monmouth, NJ 07703-5302.

NEW MEMBERS

It is a pleasure to announce the following new members of The Electrochemical Society as recommended by the Admissions Committee and approved by the Board of Directors in July 1985.

Active Members

Ambrosiano, N. A., Cincinnati, OH
Bakhshai, A., Arlington, TX
Baum, S. K., Wilmington, MA
Bertram, R., West Allis, WI
Bleiler, R. J., St. Louis, MO
Bryant, R. G., Houston, TX
Bugge, K., Stavanger, Norway
Clinton, C., Elgin, TX
Davignon, J. J., Stafford, TX
Eppley, W. J., Horsham, PA
Hansen, R. L., St. Peters, MO
Jovanckevic, V., College Station, TX
Kwiatkowski, J. H., Long Branch, NJ
Lee, H.-L., Sunnyvale, CA
McGrath, R. L., Reading, PA
Melnicki, L. S., Palo Alto, CA
O'Hara, A., Surgarland, TX
Plichon, V., Paris, France
Riggott, G., Wilmington, MA
Sarrazin, C., Paris, France
Scharifker, B. R., College Station, TX
Smith, R. A., Horsham, PA
Soubeyrand, M. J., Toledo, OH
Tam, N. K. M., Vancouver, B.C., Canada
Tsai, V. Y., San Francisco, CA
Tsang, S., Oakland, CA
Tzeng, Y., Auburn, AL
Wallace, J. L., Coatesville, PA
Wright, J. K., Houston, TX
Youngjai, K., Kanagawa, Japan

Student Members

Basu, S. N., Cambridge, MA
Boucher, C. F., Jr., Cambridge, MA
Chung, J.-H., Hoboken, NJ
Comeau, T. C., Kingston, RI
Denuzzio, J. D., Philadelphia, PA
Ila, D., Lowell, MA
Kim, S. T., Hoboken, NJ
Misra, D., Waterloo, Ont., Canada
Moslehi, M., Stanford, CA
O'Grady, D. S., Bethlehem, PA
Torosian, K., Belmont, MA
Trese, U., New York, NY
Turner, C. D., Baltimore, MD
White, J. H., Santa Barbara, CA
Wulu, H.-C., Stanford, CA
Yu, J., Los Angeles, CA

Reinstatement

Wright, R. C., Pilot Point, TX

REVIEWS & NEWS INDEX

ADVERTISERS' INDEX

Corrosion Division Award for Summer Study in Corrosion Science

The Corrosion Division of The Electrochemical Society is offering its new Award for Summer Study in Corrosion Science to a qualified graduating senior or advanced undergraduate for the summer of 1986. This award provides a minimum grant-in-aid of $1000 and travel expenses toward a summer's (at least two months) research and study in a laboratory of a recognized institute or institution of higher learning.

The objectives of this award are as follows.

1. To stimulate and encourage active and continued participation in the field of corrosion science and corrosion protection by outstanding students of science and engineering.
2. To encourage education in this field for a student likely to attend graduate school for an advanced degree.

To be eligible for the award, the entrant must qualify in at least one of two following categories. He or she must be either (1) a graduating senior of demonstrated ability, regularly enrolled in any recognized college, university, or institute of technology in the United States or Canada, who intends to seek an advanced degree, or (2) an advanced undergraduate similarly enrolled, within six months of graduation who intends to seek an advanced degree. No limitations of sex, race, nationality, or religion are to be imposed by the Award Committee in determining the recipient of the Award.

The award shall be presented on the basis of the following material.

1. A complete transcript of the student's academic record.
2. The original and two copies of a letter, over the signature of the head of the college or department in which the student is enrolled, describing briefly the student's academic work, campus activities, and abilities.
3. The original and two copies of a letter, over the student's signature, containing a brief biographical sketch, a detailed description of the nature and extent of the student's academic work, particularly as it may relate to the field of the Award, and an outline of future plans. The student shall suggest the topic and site for the intended research and his or her basis for this choice. The student's letter should also contain a statement signifying willingness to fulfill the requirements of the Award as described in the Award Rules.

Application forms are available from the Executive Secretary, V. H. Branneky, The Electrochemical Society, 10 South Main St., Pennington, NJ 08534-2896. Deadline for receipt of completed applications is December 1, 1985, and the award winner will be announced by April 1, 1986.

The Electrochemical Society, Incorporated Society Awards

The Edward Goodrich Acheson Award

Given for distinguished "contributions to the advancement of any of the objects, purposes, or activities of The Electrochemical Society."

Presented in the Fall of even-numbered years.

The Vittorio de Nora-Diamond Shamrock Award

Given for distinguished "contributions to the field of electrochemical technology."

Presented in the Spring of even-numbered years.

The Henry B. Linford Award for Distinguished Teaching

Given for "excellence in teaching in subject areas of interest to the Society."

Presented in the Spring of even-numbered years.

The Olin Palladium Award

Given for distinguished "contributions to the field of electrochemical science and corrosion."

Presented in the Fall of odd-numbered years.

The Electrochemical Society Award in Solid State Science and Technology

Given for distinguished "contributions to the field of solid state science."

Presented in the Spring of odd-numbered years.

The Electrochemical Society Carl Wagner Memorial Award

Given to "recognize mid-career achievement and excellence in research in areas of interest of the Society, and significant contributions in the teaching or guidance of students or colleagues in education, industry, or government."

Presented in the Fall of odd-numbered years.

The Electrochemical Society, Inc.
10 South Main Street, Pennington, New Jersey 08534 • Telephone: 609-737-1902

Instructions to Authors

The **JOURNAL OF THE ELECTROCHEMICAL SOCIETY** is the official monthly journal of the Society. It contains three sections: Electrochemical Science and Technology, Solid-State Science and Technology, and Reviews and News. Technical Papers, Technical Notes, and Accelerated Brief Communications are published in the first two sections and Review Papers in the third. **All manuscripts (in English) submitted are considered for publication, with the understanding that they have not been submitted, accepted for publication, or published elsewhere. Material, e.g., figures and tables, may not be reproduced from another publication unless it absolutely cannot be described in words. If this material must be used, it must be properly referenced and acknowledged, and permission to reproduce it must be obtained from the publisher.** A wide range of subject matter is acceptable. Manuscripts can be handled promptly and efficiently if these instructions are followed.

TYPES OF PAPERS

Technical Papers describe fundamental or applied studies in depth. They contain new data and/or new interpretations of existing data. Abstracts summarizing the results are required.

Technical Notes report briefly on limited research or development that is not being pursued further. No abstracts are required.

Accelerated Brief Communications present, in camera-ready format of limited length, scientific or technological information warranting rapid dissemination. No abstracts are required.

Review Papers furnish critical analyses of topical subjects. Abstracts are required.

SUBMISSION

Submit three complete, clear copies of each manuscript and the originals of all figures and illustrations to:

Editorial Office
The Electrochemical Society, Inc.
10 South Main Street
Pennington, New Jersey 08534

A letter accompanying the manuscript should give (a) the name and mailing address of the author to whom correspondence should be sent, (b) reference to any presentation of the work at a meeting of The Electrochemical Society, (c) the Division or Group of the Society or the Divisional or Group Editor (both are listed in the front of each issue of the Journal) whose interests are most closely related to the work being discussed, (d) the section of the Journal in which the work should appear, and (e) the names and addresses of people able to act as reviewers.

EDITORIAL PRACTICES

Following receipt by the Editorial Office, each manuscript is sent to a Divisional or Group Editor with knowledge of the subject matter. This editor arranges for review of the manuscript and communicates with the author(s) regarding revisions. Final acceptance or rejection of a manuscript is determined by the Editor.

Accelerated Brief Communications are handled as rapidly as possible, ordinarily with a response to the author(s) from the Divisional Editor, the Group Editor, or the Editor within three weeks of their arrival at Pennington. Response to the authors of other manuscripts usually takes place within six weeks. Following acceptance, authors are notified of the Journal issue in which publication is scheduled; about one month before publication, page proofs and an order blank for reprints are provided. Proofs must be promptly corrected and returned. Extensive alterations by the author may delay publication; their cost will be billed to the author(s).

PUBLICATION CHARGE

To help meet publication costs, a payment of $65.00 per printed page is requested for the publication of technical material. If at least one author is a Society member or an employee of a Patron or Sustaining member, a 10% reduction is allowed. Acceptance of manuscripts for publication is, however, based on merit and is in no way dependent on such payment, which may be waived in individual cases upon request.

PRESENTATION

Organization and clarity are essential elements of successful written communication. Identify the subject matter in the title, using words useful in indexing. State the purpose of the work early in the text. Avoid introductory and explanatory material that is overly familiar to those in the field. Present the work and the arguments in an order that leads naturally to clearly specified conclusions. Provide enough information for the work to be reproduced and the logic behind it to be understood. Identify and justify any assumptions that are made; avoid tacit assumptions. Omit details that are generally known or that can be covered by reference to other publications. Give the magnitude and define the significance of experimental errors. Use headings and subheadings as appropriate. Avoid proprietary and trade names, but capitalize them where their use is necessary. Define unusual technical terms and abbreviations. Where symbols are used extensively, list them with their definitions at the end of the paper. Avoid repetition in the text and duplication of material in figures and tables. Be brief but clear.

Edit and proofread the manuscript carefully; these are not the responsibilities of the editors or reviewers.

MANUSCRIPT PREPARATION

Accelerated Brief Communications must be typewritten or printed on standard forms obtained, with detailed instructions for their use, from the Pennington Editorial Office.

All other manuscripts must be typewritten or printed, double-spaced throughout, on one side only of white 21.6 x 27.0 cm paper, with 2.5-3.8 cm margins. Do not use single spacing anywhere, in title, abstract, text, references, tables, or figure captions.

For general matters of style and format, see papers in recent issues of the **Journal** and consult a style manual such as that of the American Chemical Society or that of the American Institute of Physics. These also provide lists of common abbreviations and units. The following specific items should be noted:

(a) Système Internationale (SI) units are to be used; a description may be found in NBS Special Publication 330 or ASTM Metric Practice Guide E-380-72.

(b) The signs of cell and electrode potentials are to follow the IUPAC conventions of 1953.

(c) **Mathematical equations** should be written on a single line, if possible, using parentheses, brackets, the solidus, negative exponents, etc.

(d) **References** are to be listed separately at the end of the paper in the order they are cited in the text, being sure that each listed reference is cited. Authors' initials must be given, and Chemical Abstracts abbreviations must be used. Citations of other than the generally available literature should be avoided if possible.

(e) **Tables** are to be presented on individual sheets, with both captions and body double-spaced.

(f) **Figure captions** and numbers are to be included on a separate sheet and must not appear in the body of any figure or illustration.

(g) **Drawings** and **graphs** will ordinarily be reduced to column width (8.3 cm) and after such reduction should have lettering at least 0.15 cm high. Lettering must be of letter-guide quality. Originals in India ink on tracing cloth or paper are preferred, but India ink on coordinate paper with blue ruling is acceptable. When several curves are shown, each may be lettered and identified in the caption. The Editorial Office will not make corrections or additions to figures.

(h) **Photographs** should be used sparingly. The originals supplied must be glossy prints and should be protected against bending. Micrographs must have a labeled unit length within the body of the picture; reduction for printing makes magnifications meaningless.

Revised August 1, 1984

Printed in the United States of America

APPLICATION FOR ADMISSION

TO

The Electrochemical Society, Inc.

Return completed application to:

Secretary
The Electrochemical Society, Inc.
10 South Main Street, Pennington, New Jersey 08534-2896
609-737-1902

For office use only

Date Rec'd. _____ $ _____

Notice of Ackn. _____

Checked: _____

Approved: _____

To the Board of Directors of The Electrochemical Society, Inc:

Please print complete name and address as it should appear on mailings.

Name: _____

Address: _____

_____

_____

_____

_____

Business Telephone: (include area code) _____

I hereby make application for admission to The Electrochemical Society, Inc., as an _____ member, and enclose the amount of $_____ covering the first year's dues. (Please see reverse side for proper class of membership and dues applying thereto, noting the options with regard to the date of election and active life membership and the credit available for nonmember meeting registration.)

1. Date of Birth: _____ (month) _____ (day) _____ (year)

2. Please check LOCAL SECTION with which you wish to affiliate:

—— Boston (05)	—— Detroit (25)	—— Midland (Mich.) (40)	—— Philadelphia (70)	—— So. Calif.-Nevada (90)
—— Canadian (60)	—— European (27)	—— Natl. Capital Area (45)	—— Pittsburgh (75)	—— Southern Wisconsin (92)
—— Chicago (10)	—— Indianapolis (30)	—— North Texas (55)	—— Rocky Mountain (80)	—— Twin Cities (96)
—— Cleveland (15)	—— Japan (33)	—— Oregon (62)	—— San Francisco (85)	—— None (99)
—— Columbus (20)	—— Metropolitan N.Y. (35)	—— Pacific Northwest (65)	—— South Texas (88)	

3. Please indicate your DIVISIONAL and GROUP interests, noting your primary interest(s) with the number 1 and secondary interest(s) with the number 2.

—— Battery (AO)	—— Electronics (EO)	—— Industrial Electrolytic (IO)
—— Corrosion (BO)	☐ New Electronic Technologies (E1)	—— Luminescence and Display Materials (KO)
—— Dielectrics and Insulation (CO)	☐ Semiconductors (E3)	—— Organic and Biological Electrochemistry (FO)
—— Electrodeposition (DO)	—— Energy Technology (GO)	—— Physical Electrochemistry (JO)
	—— High Temperature Materials (HO)	

4. Education:

Institution	Dates Attended	Major Subject	Degree Earned

5. Work Experience:

Name of Employer (current, followed by previous)	Dates	Position

6. The Society's Constitution provides that two Active Members of the Society (who can substantiate the above record) must recommend you for admission to membership. It will facilitate the handling of your application if you are able to have your references sign this application form; if this is not convenient, please list their names and addresses. On a student application, only a single faculty member recommendation with signature (including title and and institution) is required.

Name (please print)	Signature	Address
Name (please print)	Signature	Address

The undersigned certifies that the above statements are correct and agrees, if elected to the Society, to be governed by its Constitution and Bylaws and to promote the objects of the Society as stated in its Constitution.

Date _____ 19 __

_____
(Signature)

Rev. 7/85

EXTRACTS FROM THE CONSTITUTION AND BYLAWS

CONSTITUTION—Article II

Membership

Section 1. The individual membership shall consist of Active, Honorary and Emeritus Members. The Board of Directors may from time to time authorize other classifications of membership as defined in the Bylaws of the Society.

(Active Member—Annual Dues $50.00)

Active Member

Section 2. An Active Member shall be interested in electrochemistry or allied subjects and possess a Bachelor's degree, or its equivalent, in engineering or natural science. In lieu of a Bachelor's degree, or its equivalent, any combination of years of undergraduate study and years of relevant work experience in electrochemistry or allied subjects adding to at least seven years shall be required. Election to Active Membership shall require the recommendation of two Active Members in good standing.

BYLAWS—Article II

Non-Voting Membership
(Student Member—Annual Dues $10.00)

Student Member

Section 1. Student Member. A Student Member shall be a full-time undergraduate or graduate student registered for a degree in natural science or engineering. The applicant for Student Membership shall be recommended by a member of the faculty of the school. Upon graduation with a Bachelor's degree or equivalent in natural science or engineering, the Student Member may apply for Active Membership. The application shall be approved by two Active Members of the Society in good standing. If the Student Member enters graduate school as a full-time student, the person may choose to apply for Active Membership or remain a Student Member.

BYLAWS—Article XXI

Dues and Fees

Dues

Section 1. The annual dues for Active Members shall be fifty dollars. The annual dues for Student Members shall be ten dollars. Each member shall receive the JOURNAL OF THE ELECTROCHEMICAL SOCIETY.

Date of Election

Section 2. When individuals are elected to membership, they must elect to initiate their membership as of January 1 or July 1 of the year of election; or, if elected during the last quarter, January 1 of the year following election. In the case of a July 1 election for starting membership, dues will be prorated.

Active Life Membership

Section 3. Any Active Member who shall pay in one lump sum the amount equivalent to two-thirds of the remaining dues to age sixty-five at the time of payment, but not less than an amount of 5 years of full dues, shall be exempt from payment of any further dues and shall be considered an Active Member during the remainder of his or her life.

Nonmember Meeting Registration Credit

BOARD OF DIRECTORS ACTION OF OCTOBER 9, 1960

If application for new membership is received within four months of the payment of nonmember registration at a Society Meeting by the applicant, the difference between the nonmember and member registration fees shall be credited toward the first year's dues.

CONSTITUTION—Article III

Admission and Dismissal of Members

Section 1. Application for individual membership shall be in writing on a form adopted by the Board of Directors.

Section 2. The Admissions Committee shall be a rotating committee consisting of three members. One member shall be appointed each year by the President with the approval of the Board of Directors for a term of three years to replace the outgoing member. This Committee shall receive from the Secretary all properly executed and properly recommended applications for admission which he has received from persons desirous of becoming members of the Society. It shall be the duty of this Committee, after examining the credentials of applicants, to make appropriate recommendation to the Board as to approval or rejection of the applications. Unanimous approval of an applicant by this Committee shall be required before the candidate's name may be submitted to the Board of Directors for election. The election to membership shall be by a mail vote of the Board of Directors. The candidate shall be considered elected two weeks after the date the proposed membership list is mailed to the Board if no negative votes have been received by the Secretary. If a candidate receives one negative vote, his application shall then be considered and voted upon at the next meeting of the Board of Directors. Two negative votes cast at this meeting shall exclude a candidate. The Board of Directors may refuse to elect a candidate who, in its opinion, is not qualified for membership. The names of those elected shall be announced to the Society. Duly elected candidates shall have all the rights and privileges of membership as soon as their entrance fee, if any, and dues for the current year have been paid.

Section 3. A member desiring to resign shall send a written resignation to the Office of the Society.

Section 4. Upon the written request of ten or more Active Members that, for cause stated therein, a member be dismissed, the Board of Directors shall consider the matter and, if there appears to be sufficient reason, shall advise the accused of the charges against him. He shall then have the right to present a written defense, and to appear in person before a meeting of the Board of Directors, of which meeting he shall receive notice at least twenty days in advance. Not less than two months after such meeting the Board of Directors shall finally consider the case and, if in the opinion of the majority of the Board of Directors a satisfactory defense has not been made and the accused member has not in the meantime tendered his resignation he shall be dismissed from the Society.

Section 7. The entrance fee, if any, annual dues and any other payments to be made by the members of the Society shall be paid in accordance with regulations set forth in the Bylaws.

Section 8. Any member delinquent in dues after April 1 shall not receive the Society's publications and will not be allowed to vote in any Society election until such dues are paid. All members in arrears for one year after April 1 shall lose their membership status and can be reinstated only by action of the Board of Directors.

The NEW BENCHMARK for Electrochemical Research Instrumentation

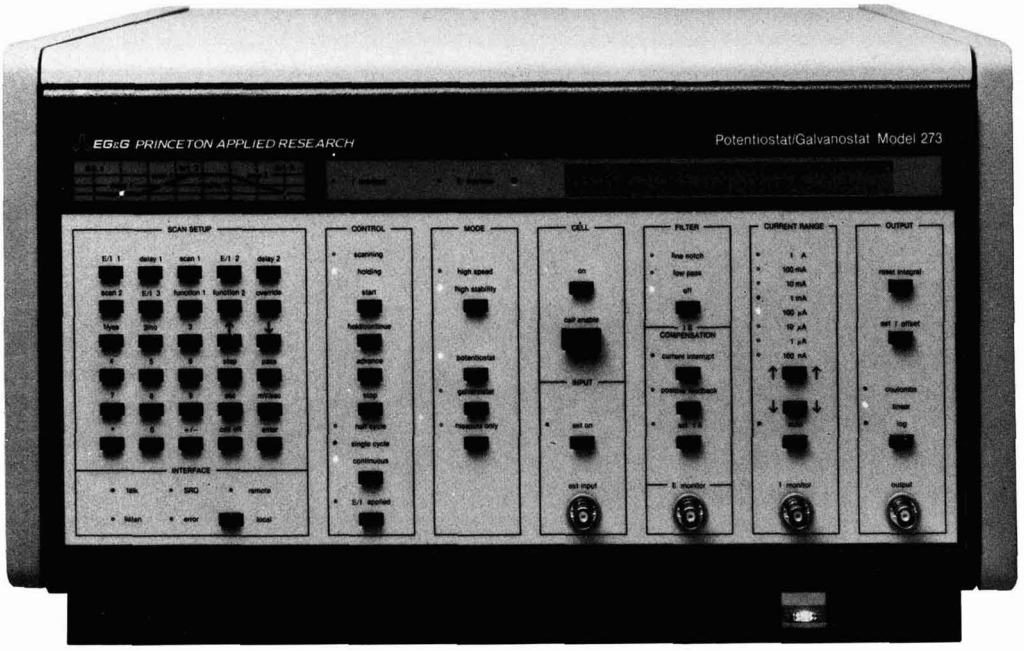

Our new MODEL 273 POTENTIOSTAT/GALVANOSTAT is the most versatile electrochemical research instrument you can buy. As a manually-controlled potentiostat, it provides features such as waveform generation and current, log current, and coulomb outputs. As a computer-controlled potentiostat, it offers both RS232 and GPIB Interfaces together with an expanded version of our easy to use Electrochemical Command Set.

The Model 273 is functionally equivalent to a rack of research instruments, yet its price is significantly lower and its performance is remarkably better. A completely new design allows both extraordinarily low noise operation and a hefty compliance of ±100 V. Current measurements can autorange over eight decades from 1 A to 100 nA full scale! A front panel control lets you optimize the Model 273 for either high-speed or high stability operation. The Model 273/97 IR compensation option uses the current-interrupt technique and includes a 5 μs A/D converter.

We even offer a less expensive version of the Model 273 without front-panel controls. It's called the Model 272. For corrosion studies, up to eight Model 272's or 273's can be used with our new Model 351 Corrosion Measurement Console.

Sound intriguing? Write or call for more details.

EG&G PRINCETON APPLIED RESEARCH

P.O. BOX 2565 • PRINCETON, NJ 08540. U.S.A. • 609/452-2111 • TELEX: 843409

660

You don't have to be made of money to afford Electrochemistry

Chemical instrumentation is expensive! Acquisition of MS, NMR, FTIR, and ESCA can involve a capital expense measured in multiples of $100,000. The information gained justifies the investment. Electrochemical techniques provide unique thermodynamic, kinetic, and mechanistic information which is simply not available from spectroscopic instrumentation. The cost-benefit analysis is in your favor if you work with transition metal complexes, biochemical redox reactions, thin-films, and chemically modified surfaces. For an order of magnitude less, you could learn more. Our BAS-100 Electrochemical Analyzer does most of the work, giving you time to think.

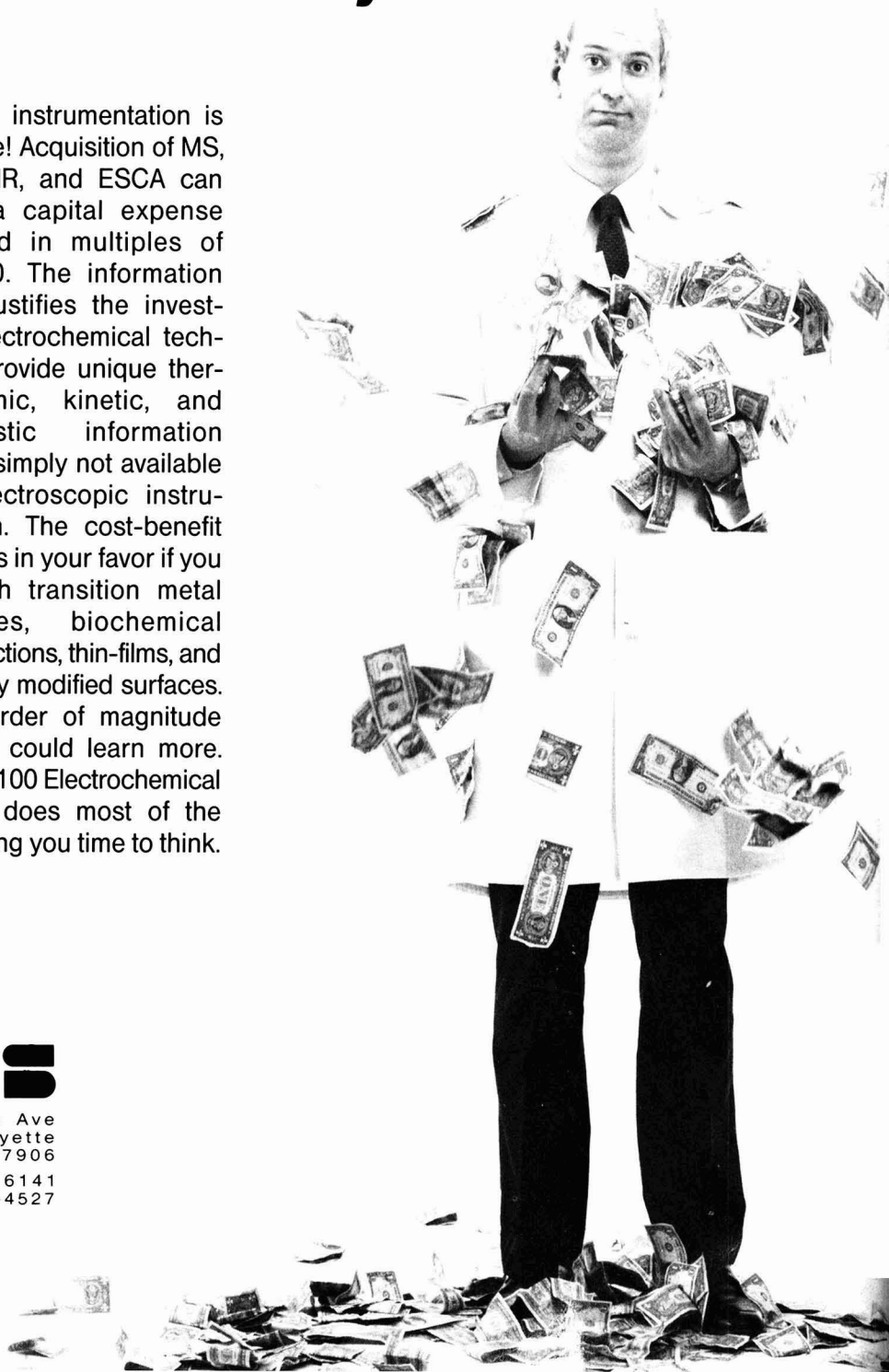

BAS

2701 Kent Ave
West Lafayette
Indiana 47906
Telex: 276141
(317) 463-4527

Off-the-shelf electrochemical cells for lab, pilot plant and production are now available for a variety of applications.

Expertly designed and engineered flow cells are available for applications including chloralkali and synthesis of a wide range of inorganic and organic chemicals. These modular membrane cells have found application world-wide! Start with a laboratory unit as small as 0.01 m^2 (Electro MP Cell) or 0.04 m^2 (ElectroSynCell) and expand to a pilot scale module, and then to production plant size by adding on modules, or installing the NEW Electro Prod Cell especially designed for production. Injection molded cell parts are available in a wide range of inert materials. Electrodes can be of DSA^R, Pt on Ti, PbO_2 on Ti, graphite and many others. Further advantages: leakproof, uniform hydrodynamics and current distribution, and narrow inter-electrode gap.

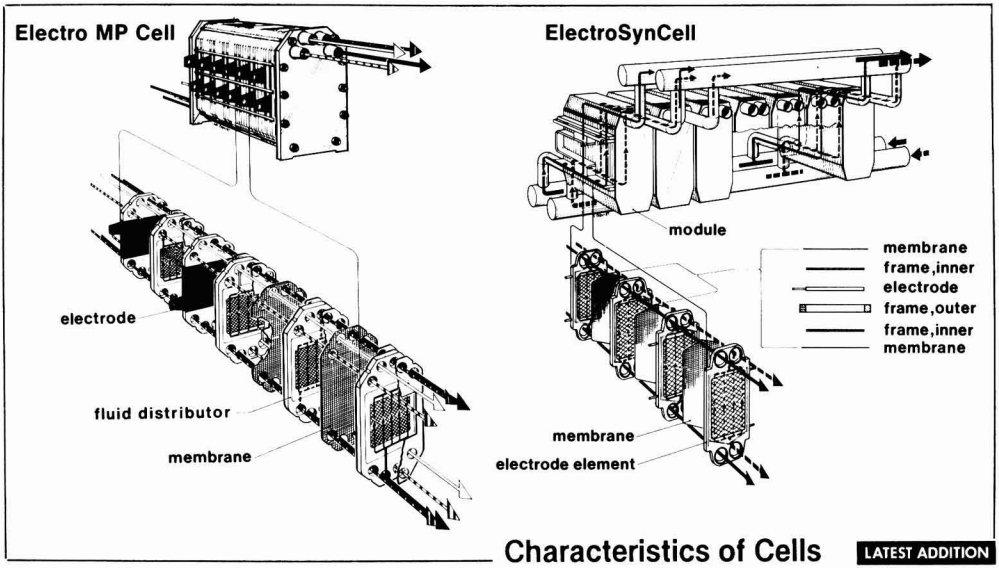

Characteristics of Cells

	Electro MP Cell	ElectroSynCell	LATEST ADDITION ElectroProdCell
Electrode area (min):	0.01 m^2	0.04 m^2	0.4 m^2
(max):	0.2 m^2/module	1.04 m^2/module	16.0 m^2/module
Current density (max):	4 kA/m^2	4kA/m^2	4 kA/m^2
Interelectrode gap:	6-12 mm	5 mm	0.5-4 mm
Electrolyte flow, per cell:	1-5 l/min	5-15 l/min	10-30 l/min
Flow Rate in each cell:	0.03-0.15 m/s	0.2-0.6 m/s	0.15-0.45 m/sek

ElectroCell AB
P.O. Box 34,
S-184 00 Akersberga,
Sweden.
Int. + 46 764-600 40
Telex 15313 ECAB S

Write or call for further technical information and a quotation.

REPRESENTATIVES:

USA, Canada:
THE ELECTRO SYNTHESIS CO., INC.
P.O. Box 16,
E. Amherst, N.Y.,
14051 U.S.A.
(716)684-0513.

France:
SORAPEC.
192 rue Carnot,
94120 Fontenay Sous-Bois,
France.
(1) 8774959

Germany:
SIGRI ELEKTROGRAPHIT GMBH
Werner-von-Siemens Strasse 18
D-8901 Meitingen
West Germany
(08 271) 83-0

Spain:
AFORA S.A.
Aribau 240
Barcelona-6
Spain
(93) 200 9911

Southeast Asia:
SHOKO CO. LTD.
8-3 Nishi Shimabashi,
3-chome, Minato-ku,
Tokyo 105,
Japan.
(03) 459-5280~6

If you're doing multi-sample corrosion research . . . the ESC 440 MULTICHANNEL POTENTIOSTAT should be in your lab . . .

Ten independent potentiostats for control of corrosion coupons during extended testing. The ESC 440 is *the* most cost effective method for individual control of multiple samples.

Interchangeable electronic modules for each channel. Separate current monitor outputs for connection to your data collection system.

Call us today for the details.

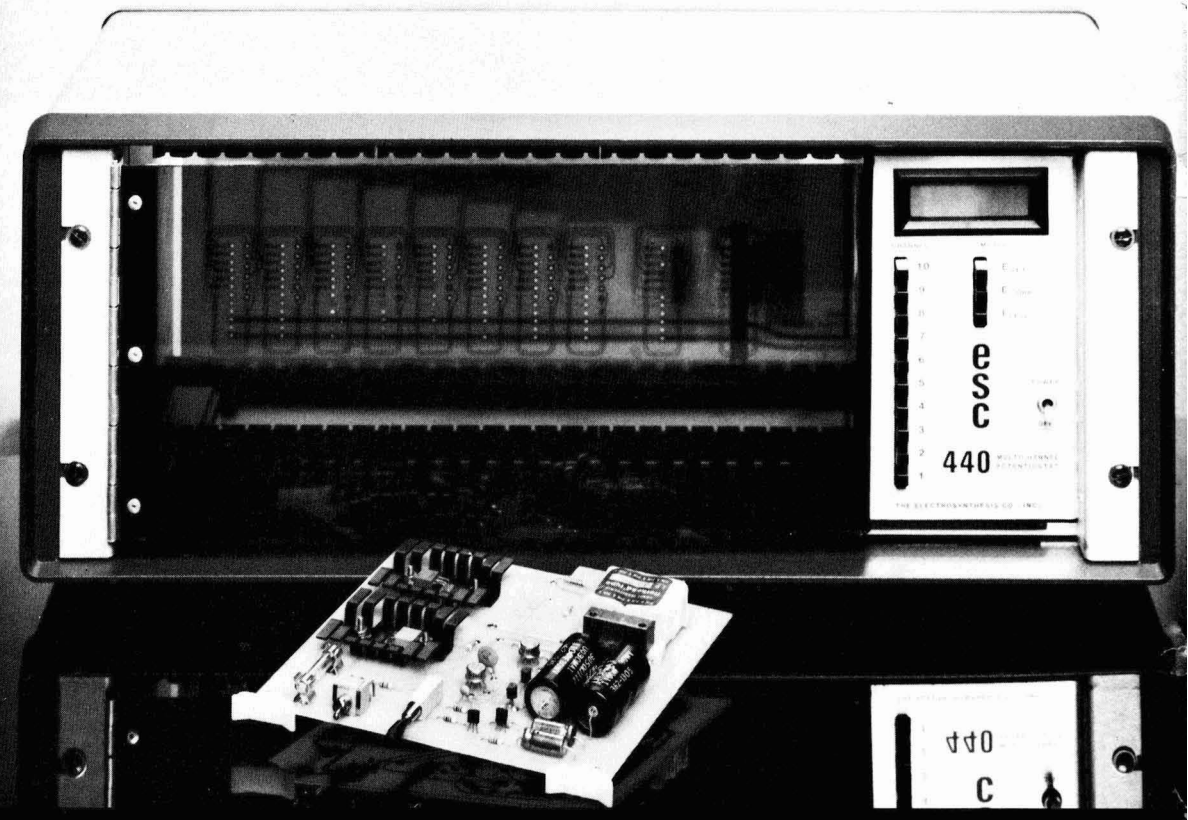

THE ELECTROSYNTHESIS CO., INC.
P.O. Box 16, E. Amherst, N.Y. 14051 • 716-684-0513

Call for Papers
169th Meeting
Boston, Massachusetts, May 4-9, 1986

Selected symposium topics and planned General Sessions are described in the following pages.

Procedure for Submitting Papers

1. Submit one original 75-Word Abstract on the attached form or a facsimile together with one original Extended Abstract to The Electrochemical Society, Inc., 10 South Main St., Pennington, NJ 08534-2896. The deadline for receipt of **both** the 75-Word and Extended Abstract at The Electrochemical Society Headquarters Office is **December 1, 1985.**

2. Send a copy of **both** the 75-Word and Extended Abstract to the appropriate organizing symposium or General Session chairman listed. **No paper will be considered unless both the 75-Word and Extended Abstract are received at Society Headquarters by December 1, 1985. Both abstracts and the oral presentation are required in English.**

Instructions for Preparation of Extended Abstract

1. New Deadline—Extended Abstract must be submitted with the 75-Word Abstract by **December 1, 1985.**

2. All scheduled papers will be published in the EXTENDED ABSTRACTS volume for this meeting. The volume is published photo-offset directly from typewritten copy submitted by the author. The volume will be 7 × 10 in.; therefore, it is essential that the typing be clear and all lettering should be the size of ordinary type or at least 1/16 in. high so that it will be legible after reduction. The EXTENDED ABSTRACTS volume is in a double-column format. Camera-ready typing mats may be obtained from The Electrochemical Society, Inc., 10 South Main St., Pennington, NJ 08534-2896, or you may use any white bond paper 11 × 17 in. The diagram below gives the dimensions of the Extended Abstract form.

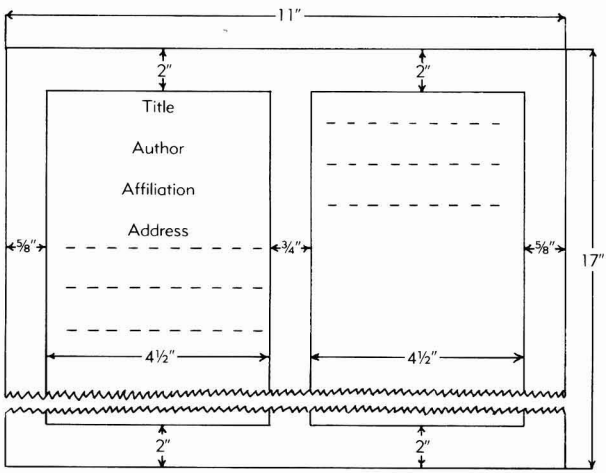

A. Use black typewriter ribbon only; type single-spaced.

B. Opaque lacquer may be used for corrections.

C. Type title, author(s), affiliation(s), and address(es) at top of first column (see diagram).

D. Tables and figures must be securely mounted within the margins with rubber cement.

E. Place references and figures after text.

3. The text of the abstract, including references, must not exceed one page (two columns) in length. An additional two columns are permitted for figures, if necessary. Papers exceeding this limit will be returned or rejected.

Mailing Instructions

Mail the original Extended Abstract together with the original 75-Word Abstract to The Electrochemical Society, Inc., 10 South Main St., Pennington, NJ 08534-2896 and a copy to the organizing chairman **for receipt before December 1, 1985.**

Notification of Paper Acceptance

Programming for this meeting will occur in early January. Organizing chairmen will notify those authors whose papers have not been accepted. In early March, a complete packet of program materials, including an Advance Program, will be sent to the presenting authors. Coauthors will receive a meeting packet without an Advance Program.

Manuscript Publication in the JOURNAL OF THE ELECTROCHEMICAL SOCIETY

Upon presentation, all meeting papers become the property of The Electrochemical Society, Inc. However, presentation incurs no obligation to publish. If publication in the JOURNAL OF THE ELECTROCHEMICAL SOCIETY is desired, papers should be submitted as promptly as possible in full manuscript form in order to be considered. "Instructions to Authors" for JOURNAL publication are available from the Society Headquarters office and are published monthly in the JOURNAL. If publication elsewhere is desired after presentation, written permission from Society Headquarters is required.

Boston, Massachusetts, Meeting Symposia Plans—Spring 1986
May 4-9, 1986

Extended Abstract must be submitted with the 75-Word Abstract by December 1, 1985.

CORROSION

General Session

Papers on all aspects of low and high temperature corrosion and associated phenomena will be considered. Experimental techniques for the study of corrosion processes and corrosion products are also of interest.

Suggestions and inquiries should be sent to the Session Chairman: E. McCafferty, Code 6314, Naval Research Laboratory, Washington, DC 20375-5000.

DIELECTRICS AND INSULATION/ELECTRONICS

Electrochemistry in Electronic Packaging

Papers on electrochemical process are solicited in areas of: 1. microwave as well as electronic packaging; 2. electroless copper catalysis and deposition on insulators; 3. metallization of silicon; 4. photoenhanced metal deposition; 5. materials and processing considerations in high density/high frequency packaging; 6. sensor (biomedical, pressure, etc.) packaging; 7. corrosion mechanisms and failure testing; 8. electromigration, with special attention to fundamentals and scientific understanding.

Suggestions and inquiries should be sent to the Symposium Chairman: E. A. Giess, IBM T. J. Watson Research Center, P.O. Box 218, Yorktown Heights, NY 10598.

DIELECTRICS AND INSULATION/ ELECTRONICS/CORROSION

Aluminum Surface Treatment Technology

This symposium is for people who are involved with the diverse products that are made from oxide-coated aluminum. It will be a forum for the exchange of ideas and information concerning the electrochemical and related chemical processing of aluminum surfaces, as well as the properties of the finished surface or device. The goal will be technology transfer between different applications through consideration of common fundamental aspects.

Presentations on recent advances, either from a scientific or an engineering viewpoint, are encouraged. Principal areas of interest are as follows. 1. Adhesive bonding of aluminum alloys. The relationship of anodic oxide film structure and composition to the integrity of the adhesive bond; aging, humidity, and other environmental effects; failure mechanism and evaluation of accelerated test methods. 2. Electrolytic capacitors, both wet and solid types. New processes and materials for ac and dc etching; improved types of oxide dielectrics; mechanisms of aluminum dissolution and oxide growth; novel capacitor materials such as Ti-Al sintered bodies and TCNQ solid electrolyte; capacitor performance related to use of advanced materials. 3. Lithographic plate. Relationship of surface roughness, texture, and anodic oxide properties to image quality and plate life; etch and anodizaton processes for high speed production lines; plate surfaces for new printing technologies. 4. Porous anodic oxide coating for architectural, corrosion protection, electrical insulation, decorative, and wear-resistant applications. Fundamental aspects of oxide growth, structure and environmental effects; improved processes, new products, shifting markets. 5. Surface treatments of new aluminum alloys and composites. 6. Emerging applications such as electrochromic and luminescent displays, memory storage disks, and solar heat collector panels.

Publication of a proceedings volume is planned. Papers published in a proceedings volume may also be submitted to the **Journal**, but must be received no later than 6 months after the date of the symposium at which the paper was presented.

Suggestions and inquiries should be sent to the Symposium Co-Chairman: R. S. Alwitt, Boundary Technologies, Inc., 3000 Dundee Rd., Suite 309, Northbrook, IL 60062; or G. E. Thompson, Corrosion and Protection Centre, University of Manchester Institute of Technology, P.O. Box 88, Manchester, England M60 1QD.

DIELECTRICS AND INSULATION/ ELECTRONICS/LUMINESCENCE AND DISPLAY MATERIALS

Patterning Science and Technology

Papers on advances in the technology of pattern transfer in the optical, E-beam, and x-ray regimes are solicited. Relevant ion beam topics will also be considered.

The emphasis will be on materials, and processes, to maximize the fidelity of the pattern-transfer step (in the radiation-sensitive layer) both by incremental improvements in current technology and by novel systems. Modeling papers to increase understanding and predict performance are also invited.

Suggestions and inquiries should be sent to the Symposium Co-Chairmen: A. W. McCullough, Shipley Co., Inc., 2300 Washington St., Newton, MA 02162; or M. J. Watts, AZ Corp., 615 Palomar Ave., Sunnyvale, CA 94086.

ELECTRONICS/DIELECTRICS AND INSULATION

Silicon on Insulators

In this symposium, focus will be placed on recent advances in the various approaches to the formation of device-quality silicon on insulating substrates. This forum should provide the opportunity to develop a perspective on the advantages and limitations of the individual approaches with respect to preparative procedures, crystalline and electronic properties, applicability to various device configurations, and economics. An important aspect of the symposium will be the crystalline and electronic characterization of SOI materials. SOI approaches to be discussed include: 1. lateral growth from the melt (seeded and unseeded); 2. lateral growth by solid phase epitaxy; 3. lateral growth by CVD; 4. the formation of an insulating layer beneath a layer of bulk silicon; 5. oriented growth induced by a patterned relief structure; and 6. the heteroepitaxial growth of silicon on single-crystal insulating substrates.

Suggestions and inquiries should be sent to the Symposium Co-Chairmen: G. W. Cullen, RCA Laboratories, Princeton, NJ 08540; J. Butcher, Microelectronic Center, Middlesex Polytechnic, London, England N11 1NQ; G. K. Celler, AT&T Bell Laboratories, Rm. 6F-217, Murray Hill, NJ 07974; J. C. C. Fan, MIT Lincoln Laboratory, 244 Wood St., Lexington, MA 02173; S. Furukawa, Dept. of Applied Electronics, Tokyo Institute of Technology, Nagatsuta, Midori-ku, Yokohama 227, Japan; or V. A. Wells, Sandia National Laboratories, Div. 2147, Albuquerque, NM 87175.

Electrochemical Sensors for Biomedical Applications

This symposium will explore a variety of novel electronic and electrochemical sensors important in biology and medicine. Presentations will address sensor fabrication, principles of operation, applications, and measurement sensitivities. The types of sensors to be discussed include, but are not limited to, 1. solid-state chemical sensors, 2. membrane electrodes, 3. potentiometric sensors of immunological reactions, 4. electronic detectors of nucleic acids, and 5. enzyme-mediated electrochemical detectors.

Publication of a proceedings volume is being considered. Papers published in a proceedings volume may also be submitted to the **Journal,** but must be received no later than 6 months after the date of the symposium at which the paper was presented.

Suggestions and inquiries should be sent to the Symposium Chairman: C. Li, Cambridge Research Laboratory, 195 Albany St., Cambridge, MA 02139.

Tutorial on Medical Electronics

This symposium will be presented for the benefit of the nonexpert. Its focus is on implanted devices. Topics to be covered include the following: 1. implantable electronics, sensors, and actuators in acute and long-term use; 2. neural prostheses; 3. electronic interface with physical prostheses; 4. the interface between electronic components and body fluids, both acute and long term; 5. electrical stimulation; 6. regulatory issues and processes; 7. safety issues; 8. body response to materials and stimulation, including biocompatibility, induced bone growth, and excapsulation; 9. materials: polymers, metals, and substrates; 10. testing and reliability; 11. percutaneous and transcutaneous signal transmission: leads, coupling methods; 12. passivation and protection of unencapsulated integrated circuits. Topics specifically excluded are imaging systems and electronics not related to implanted devices.

Some contributed papers may be included. Publication of a proceedings volume is being considered. Papers published in a proceedings volume may also be submitted to the **Journal**, but must be received no later than 6 months after the date of the symposium at which the paper was presented.

Suggestions and inquiries should be sent to one of the Symposium Co-Chairmen: P. W. Barth and L. A. Roberts, Integrated Circuits Laboratory, Stanford University, Stanford, CA 94305; or R. J. Huber, Dept. of Electrical Engineering, University of Utah, Salt Lake City, UT 84112.

Fifth International Symposium on Silicon Materials Science and Technology

The symposium will cover a wide range of topics related to silicon material phenomena accompanying the fabrication of advanced devices, integrated circuits, and, in particular, very large scale integration (VLSI). This includes the preparation, properties, and characterization of silicon crystals and thin films, as well as the chemical impurities and structural imperfections accompanying VLSI processing. Particular emphasis will be accorded the manifold interactive effects of silicon starting material properties and the multiple IC processing steps on VLSI circuit performance.

Initial plans call for a selection of papers to be comprehensive reviews of fundamental research as well as items of technological importance. The remainder of the papers will be selected from a representative sampling, but not necessarily inclusive of, contributed original research papers not previously published in the areas listed below. Authors are encouraged to recommend the appropriate session for their submitted abstracts.

The sessions will include: 1. crystal growth; 2. thin film and interfaces; 3. oxidation and nitridation; 4. diffusion and ion implantation; 5. silicon defects; 6. gettering phenomena; and 7. silicon materials/IC process failure analysis.

Suggestions and inquiries should be sent to the Symposium Co-Chairmen: H. R. Huff, Monsanto Electronic Materials Co., P.O. Box 10123, Palo Alto, CA 94303; T. Abe, SEH R&D Center, Shin-Etsu Handotai Co., Ltd., 2-13-1 Isobe, Annaka-Shi, Gunma-Ken 379-01, Japan; or B. O. Kolbesen, Siemens AG, Zentralbereich Technik, Zentrale Forschung und Entwicklung, Postfach 832729, D-8000 Muenchen 83, Germany.

Detailed instructions concerning participation in this symposium appear in the special Call for Papers in the **Journal of the Electrochemical Society,** April 1985, p. 183C.

Joint General Session

Papers are solicited on all aspects of electronic materials and processing technologies except those covered by special symposia. Topics of interest include electronic materials preparation, characterization, interactions, and device applications, basic chemistry and physics of materials processing, process and device modeling, sensor technology, and computer-aided manufacturing of electron devices. Of particular interest are new or novel materials and processes.

Suggestions and inquiries should be sent to the Session Co-Chairmen: W. M. Bullis, Siltec Silicon, 423 National Ave., Mountain View, CA 94043; H. R. Huff, Monsanto Electronic Materials Co., P.O. Box 10123, Palo Alto, CA 94303; or G. C. Schwartz, IBM Corp., Dept. 206, Bldg. 300-48A, Hopewell Junction, NY 12533.

Joint Recent News Papers Session

Recent News Papers and Extended Recent News Papers consisting of topics covered by the symposia and sessions being sponsored or cosponsored by the Electronics and Dielectrics and Insulation Divisions are invited for presentation.

A special Call for Recent News Papers will appear in the January, February, and March 1986 issues of the **Journal**.

Suggestions and inquiries should be sent to the Session Chairman: W. A. Pliskin, IBM Corp., Dept. 04A, Zip 48A, Hopewell Junction, NY 12533.

ELECTRONICS/DIELECTRICS AND INSULATION/LUMINESCENCE AND DISPLAY MATERIALS

State-of-the-Art Program on Compound Semiconductors (SOTAPOCS IV)

SOTAPOCS IV is the fourth of a new series of special symposia intended to provide a forum for discussion on the latest developments in areas involving compound semiconductors. Original papers and reviews relating to all aspects of compound semiconductor processing are solicited and welcomed. Of particular interest are papers which correlate materials properties with fabrication processes for high speed, microwave, photonic, optoelectronic and sensing devices, and integrated circuits.

The symposia are also aimed at providing a forum for synergistic interactions between those working in compound semiconductors and those involved in silicon technologies. A recent example of such synergism in materials research is the new area of silicon/compound semiconductor heteroepitaxy.

To ensure the timely nature of the SOTAPOCS IV effort, a special deadline has been set. Abstracts will be accepted until February 1, 1986. The standard 75-word Electrochemical Society abstract (refer to form in this Call for Papers) is sufficient for paper presentation at SOTAPOCS. There is no need to submit an extended abstract.

Suggestions, inquiries, and the abstracts should be sent to the Symposium Co-Chairmen: S. N. G. Chu, AT&T Bell Laboratories, Rm. 7C-226, Murray Hill, NJ 07974; R. E. Enstrom, RCA Laboratories, Princeton, NJ 08540; or V. G. Keramidas, Bell Communications Research, Rm. 7B-402, Murray Hill, NJ 07974.

ELECTRONICS/PHYSICAL ELECTROCHEMISTRY/ENERGY TECHNOLOGY/NEW TECHNOLOGY

Organic Semiconductors at the Molecular Level

This symposium will be devoted to the fundamental physical, chemical, and electrochemical properties of organic semiconductors and related electroactive organic materials. Contributions relating to the synthesis, oxidation-reduction, charge transport, charge compensation and stability properties, theory and potential use of these materials in sensors, photovoltaics, molecular electronics, and other nonbattery applications are invited. Papers on structure-property relationships, the design synthesis of large organic molecules with significantly delocalized pi networks and organic superconductors are welcome. Emphasis will be on results which provide an understanding of the fundamental principles governing the structures, properties, and behavior of the materials and mechanisms involved in their electrochemically important characteristics.

Publication of a proceedings volume is being considered. Papers published in proceedings volumes may also be submitted to the **Journal**, but must be received no later than 6 months after the date of the symposium at which the paper was presented.

Suggestions and inquiries should be sent to the Symposium Co-Chairmen: D. S. Ginley, Sandia National Laboratories, Org. 1154, Albuquerque, NM 87185; or J. J. Smith, Office of Naval Research, Chemistry Div., Arlington, VA 22217-5000.

ENERGY TECHNOLOGY

General Session

Papers are solicited in the fundamental and applied aspects of energy conversion, storage, and transmission not covered by current symposia. Of particular interest are new developments in photoelectrochemistry and novel methods for energy storage, conversion, and transmission. Papers on the application of electrochemistry for environmental cleanup are also welcome.

Suggestions and inquiries should be sent to Session Co-Chairmen: H. C. Maru, Energy Research Corp., 3 Great Pasture Rd., Danbury, CT 06810; or D. S. Ginley, Sandia National Laboratories, Div. 1154, Albuquerque, NM 87185.

ENERGY TECHNOLOGY/ DIELECTRICS AND INSULATION/ELECTRONICS

Materials and New Processing Technologies for Photovoltaics VI

This symposium will focus on the new developments in the rapidly growing field of photovoltaics with special emphasis on processing techniques that help lower the cost of manufacturing PV modules and approaches that are needed to develop high efficiency solar cells.

Papers are solicited on the following main topics: 1. thin film amorphous silicon solar cells; 2. thin film polycrystalline solar cells; 3. crystalline silicon solar cells; 4. tandem-structure solar cells; 5. new materials and advanced concepts in photovoltaics. Papers that deal with the material properties and characterization, growth mechanisms, structure of thin films, nature of interfaces, stability of photoactive materials, defects that affect the performance of solar cells, and papers on processes for uniform deposition of thin films, and monolithic integration of solar cells and silicon sheet growth are welcome.

Publication of a proceedings volume is planned. Camera-ready copies of manuscripts must be provided at the time of presentation. Papers published in a proceedings volume may also be submitted to the **Journal**, but must be received no later than 6 months after the date of the symposium at which the paper was presented.

Suggestions and inquiries should be sent to the Symposium Co-Chairmen: V. K. Kapur, International Photovoltaic Systems, 9540 Donna Ave., Northridge, CA 91324; P. Rai-Choudhary, Westinghouse Research and Development Center, 1310 Beulah Rd., Pittsburgh, PA 15235; or S. Pizzini, Dept. of Physical and Electrochemistry, University of Milan, Via Golgi-20133, Milan, Italy.

ENERGY TECHNOLOGY/ ELECTRODEPOSITION/ ELECTRONICS

Electrodeposition of Semiconductors

This symposium will focus on mechanism, applications, and end use of electrochemically deposited semiconductor thin films and on electrochemical deposition of thin films on semiconducting substrates.

Papers are solicited in the following areas: 1. mechanisms, including correlation of solid-state properties of the deposit and solution chemistry, correlation between deposition parameters and the electronic and optical properties of the film, control of stoichiometry and doping, and correlations between the mechanism of the deposition and the morphology of the film; 2. photoelectrochemical and photothermal deposition; 3. electrodeposition of organic semiconductors; 4. post-treatment including nonelectrochemical post-treatment to electrochemical deposits and electrochemical post-treatment to thin films in general; 5. adhesion; and 6. economic analysis, utilization, and comparison of electrochemical and nonelectrochemical deposition methods.

Suggestions and inquiries should be sent to the Symposium Co-Chairmen: M. Tomkiewicz, Dept. of Physics, Brooklyn College of CUNY, Brooklyn, NY 11210; R. Noufi, Solar Energy Research Institute, 1617 Cole Blvd., Golden, CO 80401; or G. Hodes, Dept. of Plastic Research, The Weizmann Institute of Science, Rehovot 76100, Israel.

ENERGY TECHNOLOGY/ PHYSICAL ELECTROCHEMISTRY

Strong Metal-Support Interaction in Electrocatalysis

There are many scattered evidences of metal-support interactions in electrocatalysis, such as enhanced activity and reduced degradation, the causes of which have been postulated to be simple physical attraction, electronic interaction, and even chemical reaction between metal and support. Even for gas phase catalysis, on which a considerable amount of research has been reported, no comprehensive understanding of metal-support interaction exists. This symposium will attempt to bring together researchers in the catalyst field, to produce a common forum for discussion, and to guide future advances in electrocatalysis.

Topics of interest include catalysis in electrochemical energy conversion, industrial electrolytics, electrometallurgy, and organic and biological electrochemistry. The proposed papers may cover all studies ranging from preliminary experiments to commercial processes and theoretical considerations.

Suggestions and inquiries should be sent to the Symposium Co-Chairmen: V. M. Jalan, Giner, Inc., 14 Spring St., Waltham, MA 02154; or J. A. Horsley, Exxon Research and Engineering Co., Corporate Research-Science Laboratories, Annandale, NJ 08801.

HIGH TEMPERATURE MATERIALS/CORROSION

Fundamental Aspects of High Temperature Corrosion II

This is the second in a series of symposia that will deal with the mechanistic aspects of high temperature corrosion. Papers are solicited in the following areas: 1. fundamental mechanisms of scale growth in single or multiple gaseous oxidants; 2. fundamental mechanisms of complex scale growth on alloys; 3. fundamental mechanisms of reaction product growth on nonmetallics, structural ceramics; 4. chemical and electrochemical mechanisms of hot corrosion; 5. studies of the relationship of alloy or scale microstructure to corrosion; 6. studies of the development of growth stresses, thermal stresses, and/or cracking of scale; and 7. theoretical considerations in high temperature corrosion.

Publication of a proceedings volume is being considered. Papers published in a proceedings volume may also be submitted to the **Journal**, but must be received no later than 6 months after the date of the symposium at which the paper was presented.

Suggestions and inquiries should be sent to the Symposium Co-Chairmen: D. A. Shores, University of Minnesota Corrosion Research Center, 221 Church St., Minneapolis, MN 55455; or G. Yurek, Massachusetts Institute of Technology, 77 Massachusetts Ave, Rm. 4-136, Cambridge, MA 02139.

HIGH TEMPERATURE MATERIALS/CORROSION/ DIELECTRICS AND INSULATION

Surface Modification of High Temperature Materials

Oxidation, corrosion, erosion, and wear of materials modified by surface treatment are to be covered. Examples of such surface treatments could include ion implantation, ion plating, ion mixing, coatings effected by sputtering, electron-beam-physical vapor deposition (EB-PVD), plasma spraying, chemical vapor deposition (CVD), and diffusion processes, as well as modifications produced by laser and electron-beam techniques.

Suggestions and inquiries should be sent to the Symposium Co-Chairmen: J. G. Smeggil, United Technologies Research Center, M/S 22, Silver Lane, East Hartford, CT 06108; or K. Grabowski, Naval Research Laboratory, Code 6671, 4555 Overlook Ave. SW, Washington, DC 20375.

HIGH TEMPERATURE MATERIALS/DIELECTRICS AND INSULATION

Contemporary Film Structures and Their Properties

This symposium will focus on recent advances in multicomponent thin film structures that owe their unique properties in part to the geometry of their individual components. Modulated thin metal film structures, as well as multilayered Langmuir-Blodgett-type films, and composite thin film structures, such as metal dispersions in dielectric thin film matrices, will be considered. Contributions are being solicited that deal with novel synthetic or characterization techniques with emphasis on microstructure/physical property correlations, both theoretical and experimental. Discussions of existing or unique potential applications are welcome.

Suggestions and inquiries should be sent to the Symposium Co-Chairmen: E. Kay, IBM Research Laboratory, Dept. K33/281, 5600 Cottle Rd., San Jose, CA 95193; or J. Susko, R. D. 1, Box 401, Owego, NY 13827.

High-Technology Silicon-Based Structural Ceramics

This symposium will focus on physical, chemical, mechanical, and tribological properties of SiC, Si_3N_4, and related compounds. Topics include powder synthesis, processing characterization,and microstructure-property relationships. There is interest in applications, manufacture, and design of ceramic components for use in high performance turbine engines, automobile engines, and cutting tools. Contributions may be state-of-the-art review articles or from research in a related field.

Suggestions and inquiries should be sent to Symposium Co-Chairmen: K. S. Mazdiyasni, AFWAL/MLLM, WPAFB, Dayton, OH 45433; or T. Johansson, KemaNord, S-840 10, Ljungaverk, Sweden.

INDUSTRIAL ELECTROLYTIC

Nonaqueous Electrolytic Processes

This symposium focuses on the industrial applications of nonaqueous systems in electrolysis and related electrochemical processes. A broad spectrum of contributions is being sought, with special emphasis on nonaqueous electrolytic areas such as molten salts, organic solvents, solid electrolytes, membranes, and room temperature ionic liquids. Metal electrowinning, electrorefining, electroplating, nonmetallic production processes, and surface treatment are particularly solicited. The chemistry, design, development, current and

potential distribution, optimization, and economic evaluation are among the various aspects of the symposium.

Publication of a proceedings volume is planned. Papers published in a proceedings volume may also be submitted to the **Journal**, but must be received no later than 6 months after the date of the symposium at which the paper was presented.

Suggestions and inquiries should be sent to the Symposium Co-Chairmen: J. Jorné, Dept. of Chemical Engineering, University of Rochester, Rochester, NY 14627; or K. Hanson, AT&T Bell Laboratories, Rm. 7D-208, Murray Hill, NJ 07974.

General Session

Papers are solicited in the areas of industrial electrochemistry or electrochemical engineering not covered by the special symposia. Of particular interest are papers concerning the application of statistics, parameter estimation, or experimental design to industrial electrochemical systems.

Suggestions and inquiries should be sent to the Session Chairman: J. Van Zee, Dept. of Chemical Engineering, University of South Carolina, Columbia, SC 29208.

INDUSTRIAL ELECTROLYTIC/BATTERY/ ENERGY TECHNOLOGY

Load Leveling and Energy Conservation in Industrial Processes

The objective of this symposium is to bring together the technical experts who are working on electrochemical energy storage and energy conservation in industrial electrochemical processes. The spectrum of the symposium covers the research and development, conceptual design, economic analysis, prototype test, and operating results of full-scale installations.

Papers are solicited on the following or related areas: 1. secondary batteries for energy storage and on-site load leveling applications; 2. fuel cells for power generation; 3. solar and photovoltaic energy conversion systems; 4. hydrogen energy storage and utilization in the process industry; 5. on-site power generation and storage using wing, geothermal, and small hydroelectric energy resources; 6. depolarized air or oxygen cathode for industrial electrolysis; 7. electrocatalysis and development of energy efficient electrodes; 8. novel cell design, cell separator and membrane for energy savings; 9. use of pulsating or alternating current in industrial electrolysis; 10. other energy conservation measures in industrial electrochemical processes including electro-organic synthesis, electroplating, electrowinning, etc.; 11. cost analysis, mass and energy balance, and optimization of electrochemical energy storage systems.

Publication of a proceedings volume is being considered. Papers published in a proceedings volume may also be submitted to the **Journal**, but must be received no later than 6 months after the date of the symposium at which the paper was presented.

Suggestions and inquiries should be sent to the Symposium Chairman: D.-T. Chin, Dept. of Chemical Engineering, Clarkson University, Potsdam, NY 13676.

INDUSTRIAL ELECTROLYTIC/BATTERY/ PHYSICAL ELECTROCHEMISTRY

Diaphragms, Separators, and Ion-Exchange Membranes

Papers are solicited for this symposium which deal with separators for batteries, fuel cells, or electrochemical cells used for the production of chemicals. Papers that deal with the preparation techniques, characterization methods, transport properties, applications, and, especially, ones that combine these aspects will be of interest. Papers should contain both theoretical and experimental work, but papers dealing with either will be considered.

Publication of a proceedings volume is being considered. Papers published in a proceedings volume may also be submitted to the **Journal**, but must be received no later than 6 months after the date of the symposium at which the paper was presented.

Suggestions and inquiries should be sent to the Symposium Co-Chairmen: R. E. White, Dept. of Chemical Engineering, Texas A&M University, College Station, TX 77843; H. S. Burney, Dow Chemical Co., B-2234, Freeport, TX 77541; or K. Kinoshita, Applied Science Div., 90-3026, Lawrence Berkeley Laboratory, Berkeley, CA 94720.

ORGANIC AND BIOLOGICAL ELECTROCHEMISTRY

Electrochemical and Ionic Mechanisms in Electromagnetic Cell Stimulation

Electromagnetic stimulation has been found useful in certain forms of therapy. There have also been reports of harmful effects in living systems due to exposure to electromagnetic radiation. Papers in this symposium should be devoted to elucidating the basic electrochemical and ionic mechanisms involved in these effects.

Suggestions and inquiries should be addressed to the Symposium Chairman: G. Rein, Dept. of Orthopedic Surgery, Mt. Sinai Medical School, New York, NY 10029.

Organic Reaction Mechanisms

Papers devoted to studies of organic reactions accompanying electron transfers using electrochemical and auxiliary techniques are solicited. Biochemically important and catalytic reactions will also be considered.

Suggestions and inquiries should be addressed to the Symposium Co-Chairmen: J. F. Russling, Dept. of Chemistry, University of Connecticut, Storrs, CT 06268; or P. Zuman, Dept. of Chemistry, Clarkson University, Potsdam, NY 13676.

PHYSICAL ELECTROCHEMISTRY

Electrode Processes IV

The symposium will consist primarily of invited papers. The focus is on aspects of structure and microscopic dynamics influencing processes at electrochemical interfaces. Subtopics that will receive emphasis include kinetics of simple systems, interfacial structure, spectroscopic probes of electrode processes, electrochemical microstructures, and organic and inorganic mechanisms. Persons interested in contributing papers to this symposium should contact one of the organizers.

Suggestions and inquiries should be sent to the Symposium Co-Chairmen: B. E. Conway, Dept. of Chemistry, University of Ottawa, Ont., Canada K1N 9B4; M. J. Weaver, Dept. of Chemistry, Purdue University, West Lafayette, IN 47907; or L. R. Faulkner, Dept. of Chemistry, University of Illinois, Urbana, IL 61801.

General Session

Papers concerning any aspect of physical electrochemistry not included in the topic areas of the symposia are welcome.

Suggestions and inquiries should be sent to the Session Chairman: B. Miller, AT&T Bell Laboratories, Rm. 1D-350, Murray Hill, NJ 07974.

PHYSICAL ELECTROCHEMISTRY/ ORGANIC AND BIOLOGICAL ELECTROCHEMISTRY

Ion Transfer at Liquid-Liquid Interfaces

This symposium will provide a forum for discussion of theoretical and applied research on ion-transport kinetics and mechanisms at immiscible electrolyte interfaces (ITIES). Among the relevant topics are: 1. single ion partition equilibrium theory; 2. double layer structures; 3. double layer potential profiles in relation to kinetics of single-ion transfers; 4. ionophore/carrier-induced ion transport; 5. ITIES in relation to ion transport through lipid bilayers; 6. metal ion/chelate interfacial transport; 7. electrolyte/ion-exchanger interfacials transport; 8. protein-modified interfacial transport; and 9. heterophase catalysis mechanisms. New points of view, new applications, new techniques and instrumentation from a variety of interdisciplinary specialists will be welcomed in this symposium.

Suggestions and inquiries should be sent to the Symposium Chairman: R. P. Buck, Dept. of Chemistry, University of North Carolina, Chapel Hill, NC 27514.

NEW TECHNOLOGY SUBCOMMITTEE

Electrochemistry and Solid-State Science Education at the Graduate and Undergraduate Level

The advancement and accomplishment of electrochemical and solid-state science and engineering are objectives of The Electrochemical Society. The goal of this symposium is to identify means of enhancing the role of education in achieving these objectives. Batteries, electronics, corrosion, dielectrics, insulation, electrodeposition, high temperature materials, energy technology, industrial electrolytic, luminescence and display materials, organic, biological, and physical electrochemistry have developed rapidly and successfully as major areas of interest of this Society. Maintaining the breadth of these multidisciplinary fields and increasing their applications are extremely important pedagogical aims of this symposium. The progress of theoretical and applied science and engineering in the coming decades will be connected with the underlying need for acquiring greater and deeper knowledge. Both theoretical and experimental topics are requested that will advance the process of educating scientists and engineers in electrochemistry and solid-state science.

Publication of a proceedings volume is being considered. Papers published in a proceedings volume may also be submitted to the **Journal**, but must be received no later than 6 months after the date of the symposium at which the paper was presented.

Suggestions and inquiries should be sent to the Symposium Co-Chairmen: W. H. Smyrl, Dept. of Chemical Engineering and Materials Science, University of Minnesota, Minneapolis, MN 55455; A. Landgrebe, Dept. of Energy, MS 5E052, Washington, DC 20585; R. C. Alkire, Dept. of Chemical Engineering, University of Illinois, Urbana; IL 61801; F. McLarnon, Applied Science Div., Lawrence Berkeley Laboratory, University of California, Berkeley, CA 94720; G. C. Farrington, Dept. of Materials Science, University of Pennsylvania, Philadelphia, PA 19104; E. H. Nicollian, Dept. of Mechanical Engineering and Engineering Science, University of North Carolina, Charlotte, NC 28223; or L. R. Faulkner, Dept. of Chemistry, University of Illinois, 1209 West California St., Urbana, IL 61801.

NEW TECHNOLOGY SUBCOMMITTEE/CORROSION/ BATTERY

Electrochemistry of Reactive Metal Electrodes in Aqueous Solution

Papers are solicited concerning the aqueous electrochemistry of reactive metal electrodes such as aluminum and alkali or alkaline earth metals. Relevant topics include ionic and electronic transport in surface films, physical and morphological properties of films, kinetics or mechanisms of competing reactions (*e.g.*, metal dissolution and water reduction) and technological applications in energy storage, corrosion protection, etc.

Suggestions and inquiries should be sent to the Symposium Co-Chairmen: J. F. Cooper, Lawrence Livermore National Laboratory, L-490, P.O. 808, Livermore, CA 94550; or S. Gross, 7201 26th NE, Seattle, WA 98115.

Extended Abstract must be submitted with the 75-Word Abstract by December 1, 1985.

75-Word Abstract Form

Extended Abstract must be submitted with the 75-Word Abstract by December 1, 1985

Boston, Massachusetts—May 4-9, 1986

Submit to: The Electrochemical Society, Inc.
10 South Main Street, Pennington, NJ 08534-2896

Abstract No. .....
(to be assigned by the Society)

Schedule for .....
(Title of Symposium)

Sponsored by .....
(Division/Group)

Title of paper .....

.....

Authors (Underline name of author presenting paper.) .....

.....

Business affiliation and address .....

.....

.....
(State or Country) (ZIP Code) (Telephone No.)

(Type abstract in this area—double-spaced.)

Do you require any audiovisual equipment?

- ☐ **35 mm (2 x 2 in.) slide projector**
- ☐ **Vu-Graph**
- ☐ **other (specify)**

Has the information in this abstract been presented verbally, submitted for publication, or published?

☐ **Yes** ☐ **No**

If the answer is yes, please provide the reference (**except in the case of invited review presentations**). _____

Is a full length paper on this work to be submitted for Society Journal publication? ☐ **Yes** ☐ **No**

Papers presented before a Society technical meeting become the property of the Society and may not be published elsewhere without written permission of the Society. Papers presented at Society technical meetings must be authored by a member or sponsored by an active member.

.....
Insert name of Society member author or sponsor

This form should accompany your Extended Abstract.

THE ELECTROCHEMICAL SOCIETY PATRON MEMBERS

AT&T Bell Laboratories
Murray Hill, NJ

Dow Chemical Co.
Inorganic Chemicals Dept.
Midland, MI

ELTECH Systems Corp.
Chardon, OH

Exxon Research and Engineering Co.
Corporate Research
Advanced Energy Systems Laboratory,
Materials and Catalysis Sciences Laboratory
Linden, NJ
Technology Department
Chemical Engineering Technology Div.
Materials Technology Div.
Florham Park, NJ

Fujitsu Limited
Tokyo, Japan

General Electric Co.
Chemical Laboratory, Knolls Atomic Power Laboratory,
Schenectady, NY
Chemical Products, Engineering
& Technical Support, Cleveland, OH
Materials & Process Laboratory, Large Steam
Turbine-Generator Dept., Schenectady, NY
Research and Development Center,
Inorganic Materials Laboratory
Schenectady, NY

General Electric Co. (continued)
Signal Processing & Communication Laboratory,
Schenectady, NY
Semiconductor Products Dept.,
Syracuse, NY

International Business Machines Corp.
New York, NY

Olin Corp.
Chemicals Div.
Charleston Technology Center
Charleston, TN

Philips Research Laboratories
Eindhoven, The Netherlands

Tadiran, Israel Electronics Industries, Ltd.
Tel Aviv, Israel

Union Carbide Corp.
Battery Products Div.
Corporate Research Dept.
Danbury, CT

Westinghouse Electric Corp.
Electronic Tube Div., Elmira, NY
Nuclear Center, Monroeville, PA
Semiconductor Div., Youngwood, PA
Research Laboratories, Pittsburgh, PA

THE ELECTROCHEMICAL SOCIETY SUSTAINING MEMBERS

The Aerospace Corp.
Los Angeles, CA

Airco Industrial Gases
Murray Hill, NJ

Allen Clark Research Centre
Plessey Research (Caswell) Ltd.
Towcester, Northants, England

Allied Corporation
C&D Power Systems
Plymouth Meeting, PA

Aluminum Co. of America
New Kensington, PA

AMAX Inc.
Greenwich, CT

AMP Inc.
Harrisburg, PA

Analog Devices, Inc.
Norwood, MA

Applied Materials, Inc.
Santa Clara, CA

ASARCO, Inc.
South Plainfield, NJ

AT&T Technologies
Princeton, NJ

AT&T Teletype Corp.
Skokie, IL

Ballard Research, Inc.
North Vancouver, B.C., Canada

Battelle Memorial Institute
Columbus, OH

Bioanalytical Systems Inc.
West Lafayette, IN

Boeing Co.
Seattle, WA

BP Research Centre
Middlesex, England

Brown, Boveri & Co., Ltd.
Research Center
Baden, Switzerland

C-I-L Inc.
Industrial Chemicals Div.
Montreal, Que., Canada

Comdial Semiconductor, Inc.
Sunnyvale, CA

Cominco Ltd.
Trail, B.C., Canada

Corning Glass Works
Corning, NY

Crawford & Russell Inc.
Stamford, CT

CSIRO Division of Mineral Chemistry
Port Melbourne, Victoria, Australia

Diamond Shamrock Chemicals Co.
Painesville, OH

Duracell Inc.
A Division of Duracell International
Tarrytown, NY (2 memberships)

Duro-Test Corp.
North Bergen, NJ

Eagle-Picher Industries, Inc.
Electronics Div.
Joplin, MO

Eastman Kodak Co.
Rochester, NY

ECO Energy Conversion
Newton, MA

EG&G Princeton Applied Research Corp.
Princeton, NJ

Elcap Electronics Ltd.
Tai Po, Hong Kong

Electric Power Research Institute
Palo Alto, CA

Electrochemical Technology Corp.
Seattle, WA

Energy Conversion Devices, Inc.
Troy, MI

Energy Development Associates
A Gulf and Western Co.
Greensboro, NC

Engelhard Corp.
Engelhard Industries Div.
Iselin, NJ

Ever Ready Co. (Holdings) Ltd.
Whetstone, London, England

Exide Corp.
Yardley, PA

Exmet Corp.
Bridgeport, CT

SUSTAINING MEMBERS (CONTINUED)

Fairchild Camera & Instrument Corp.
Research & Development Laboratory
Palo Alto, CA

Focus Semiconductor Systems, Inc.
Sunnyvale, CA

Ford Motor Co.
Dearborn, MI

The Gates Corporation
Denver, CO

General Motors Corp.
Delco-Remy Div., Anderson, IN
Research Laboratories Div.
Warren, MI

Gould Inc.
Gould Research Center
Rolling Meadows, IL

GTE Laboratories
Waltham, MA

GTE Sylvania Inc.
Chemical & Metallurgical Div.
Towanda, PA

Heliotronic GmbH
Burghausen, Germany

Hewlett Packard Co.
Loveland, CO

Hewlett Packard Laboratories
Palo Alto, CA

Hill Cross Co., Inc.
West New York, NJ

Hitachi, Ltd.
Central Research Laboratory
Tokyo, Japan

Hoechst-Uhde Corp.
Englewood Cliffs, NJ

Honeywell, Inc.
Power Sources Center
Horsham, PA

Hughes Research Laboratories
Div. of Hughes Aircraft Co.
Malibu, CA

IMI Marston Limited
Wolverhampton, England

International Lead Zinc Research Organization, Inc.
New York, NY

Johnson Controls, Inc.
Milwaukee, WI

Kaiser Aluminum & Chemical Corp.
Pleasanton, CA

KBI
a division of Cabot Corp.
Boyertown, PA

Kerr-McGee Chemical Corp.
Oklahoma City, OK

Lockheed Missiles & Space Co., Inc.
Research Laboratory
Palo Alto, CA

LSI Logic Corp.
Santa Clara, CA

Marathon Battery Co.
Waco, TX

Medtronic Energy Technology
Minneapolis, MN

Mepco/Electra, Inc.
Columbia, SC

Microwave Associates, Inc.
Burlington, MA

Molycorp, Inc.
New York, NY

Monsanto Co.
St. Louis, MO

Motorola Inc.
Phoenix, AZ

M&T Chemicals Inc.
Detroit, MI

NEC Corporation Central Research Laboratories
Kawasaki, Japan

Nippon Telegraph and Telephone Public Corporation
Tokyo, Japan

Noranda Research Centre
Pointe Claire, Que., Canada

North American Philips Lighting Corp.
Bloomfield, NJ

Northern Telecom
Ottawa, Ont., Canada

Occidental Chemical Corporation
Research & Development
(2 memberships)
Grand Island, NY

Olin Corp.
Metals Research Laboratories
New Haven, CT

OMI International Corp.
Udylite/Sel-Rex
Warren, MI

Ovonic Battery Co.
Troy, Michigan

Perkin-Elmer Corp.
Norwalk, CT

Philips Laboratories, Inc.
Briarcliff Manor, NY

Prototech Co.
Newton Highlands, MA

Public Service Electric and Gas Co.
PSE&G Research Corp.
Newark, NJ

Rayovac Corp.
Madison, WI

RCA Corp.
Color Picture Tube Div.
Lancaster, PA

Reynolds Metals Co.
Reduction Research Div.
Sheffield, AL

Rockwell International
El Segundo, CA

SAB NIFE AB
Oskarshamn, Sweden

SAFT America, Inc.
Power Sources Division,
Valdosta, GA
Advanced Battery Systems Division,
Cockeysville, MD

Sandia National Laboratories
Albuquerque, NM

Sanyo Electric Co., Ltd.
Osaka, Japan

Schlumberger-Doll Research
Ridgefield, CT

J. C. Schumacher Co.
Oceanside, CA

Shipley Company, Inc.
Newton, MA

Siemens Aktiengesellschaft
Munich, Germany

Siltec Corp.
Menlo Park, CA

Sonnenschein GmbH
Budingen, Germany

Sprague Electric Co.
North Adams, MA

Standard Telecommunication Laboratories Ltd.
Essex, England

St. Joe Minerals Corp.
Monaca, PA

Tektronix, Inc.
Beaverton, OR

Texas Instruments Inc.
Attleboro, MA
Dallas, TX

Toshiba Corp.
Toshiba Research and
Development Center
Kawasaki, Japan

Toyota Central Research and Development Labs, Inc.
Nagoya, Japan

Tracor Applied Science, Inc.
Alexandria, VA

Varian Associates
Palo Alto, CA

VARTA Batterie AG
Kelkheim, Germany

Wacker Chemitronic
Burghausen, Germany

Wilson Greatbatch Ltd.
Clarence, NY

Xerox Corp.
Webster Research Center
Rochester, NY

Yardney Corp.
Pawcatuck, CT

Yuasa Battery Co., Ltd.
Osaka, Japan